Vol. 64 ■ No. 7 ■ July 2023

JNM

The Journal of Nuclear Medicine

FEATURED ARTICLE

PSMA PET Tumor–to–Salivary Gland Ratio to Predict Response to [^{177}Lu]PSMA Radioligand Therapy: An International Multicenter Retrospective Study. Masatoshi Hotta et al. See page 1024.

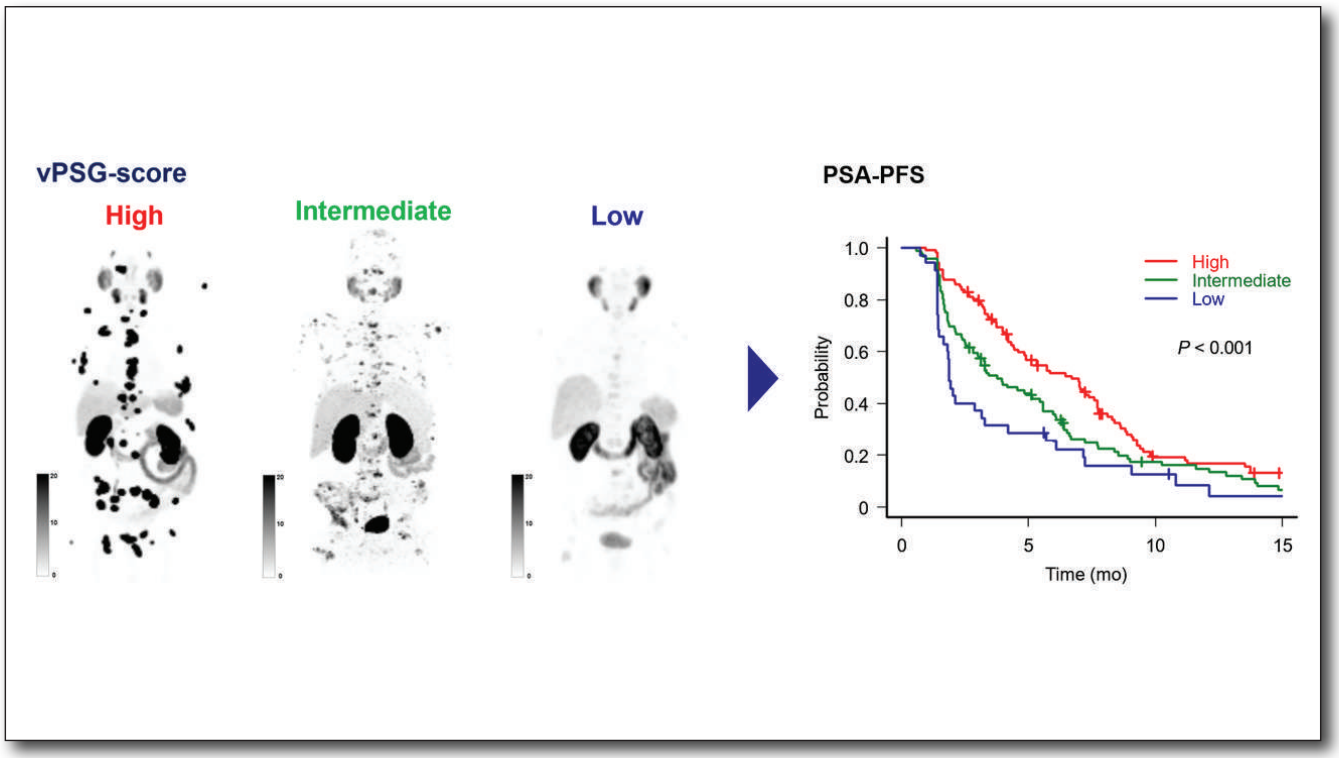

Enhancing NET treatment: Can combined PRRT and immune checkpoint inhibition improve response in neuroendocrine tumors? Shadi Esfahani et al. See page 1056.

SNMMI SOCIETY OF NUCLEAR MEDICINE & MOLECULAR IMAGING

BEDPRC23-0033 05/23

JNM

Volume 64 • Number 7 • July 2023

JNM The Journal of NUCLEAR MEDICINE

The Official Publication of **SNMMI**

MISSION STATEMENT: *The Journal of Nuclear Medicine* advances the knowledge and practice of molecular imaging and therapy and nuclear medicine to improve patient care through publication of original basic science and clinical research.

JNM (ISSN 0161-5505 [print]; ISSN 2159-662X [online]) is published monthly by SNMMI, 1850 Samuel Morse Drive, Reston, VA 20190-5316. Periodicals postage is paid at Herndon, VA, and additional mailing offices. Postmaster, send address changes to *The Journal of Nuclear Medicine,* 1850 Samuel Morse Drive, Reston, VA 20190-5316. The costs of publication of all nonsolicited articles in *JNM* were defrayed in part by the payment of page charges. Therefore, and solely to indicate this fact, these articles are hereby designated "advertisements" in accordance with 18 USC section 1734.

DISCLOSURE OF COMMERCIAL INTEREST: Johannes Czernin, MD, editor-in-chief of *The Journal of Nuclear Medicine,* has indicated that he is a founder of Sofie Biosciences and holds equity in the company and in intellectual property invented by him, patented by the University of California, and licensed to Sofie Biosciences. He is also a founder and board member of Trethera Therapeutics and holds equity in the company and in intellectual property invented by him, patented by the University of California, and licensed to Triangle. He also serves on the medical advisory board of Actinium Pharmaceuticals and on the scientific advisory boards of POINT Biopharma, RayzeBio, and Jubilant Pharma and is a consultant for Amgen. No other potential conflicts of interest were reported. Manuscripts submitted to *JNM* with potential conflicts are handled by a guest editor.

EDITORIAL COMMUNICATIONS should be sent to: Editor-in-Chief, Johannes Czernin, MD, *JNM* Office, SNMMI, 1850 Samuel Morse Drive, Reston, VA 20190-5316. Phone: (703) 326-1185; Fax: (703) 708-9018. To submit a manuscript, go to https://submit-jnm.snmjournals.org.

BUSINESS COMMUNICATIONS concerning permission requests should be sent to the publisher, SNMMI, 1850 Samuel Morse Drive, Reston, VA 20190-5316; (703) 708-9000; home page address: jnm.snmjournals.org. Subscription requests and address changes should be sent to Membership Department, SNMMI at the address above. Notify the Society of change of address and telephone number at least 30 days before date of issue by sending both the old and new addresses. Claims for copies lost in the mail are allowed within 90 days of the date of issue. Claims are not allowed for issues lost as a result of insufficient notice of change of address. For information on advertising, contact Team SNMMI (Kevin Dunn, Rich Devanna, and Charlie Meitner; (201) 767-4170; fax: (201) 767-8065; TeamSNMMI@cunnasso.com). Advertisements are subject to editorial approval and are restricted to products or services pertinent to nuclear medicine. Closing date is the first of the month preceding the date of issue.

INDIVIDUAL SUBSCRIPTION RATES for the 2023 calendar year are $633 within the United States and Canada; $680 elsewhere. Make checks payable to the SNMMI. CPC IPM Sales Agreement No. 1415158. Sales of individual back copies from 1999 through the current issue are available for $60 at http://www.snmmi.org/subscribe (subscriptions@snmmi.org; fax: (703) 667-5134). Individual articles are available for sale online at http://jnm.snmjournals.org.

Discussions with leaders: Czernin and Bengel interview Franz Weidinger, president of the European Society of Cardiology, about his career in advancing cardiac medicine initiatives. . . . . ***Page 998***

FAPI-based radionuclide therapy: Ora and colleagues summarize the current status of preclinical and clinical fibroblast activation protein inhibitor–based radionuclide therapies, as well as associated dosimetry, safety profiles, and efficacy. . . . . ***Page 1001***

Theranostics in hematooncology: Buck and colleagues provide an educational overview of radiopharmaceuticals for treatment of hematologic neoplasms, potential for targeted theranostic agents, and advantages and disadvantages of lymphoma treatment using radioimmunoconjugates. . . . . ***Page 1009***

Immuno-PET in liver cancer: Fayn and colleagues develop and evaluate glypican-3–selective single-domain antibody PET probes for imaging liver tumors, with superior in vivo target engagement and pharmacokinetic properties. . . . . ***Page 1017***

PSG score and [^{177}Lu]PSMA response: Hotta and colleagues test a quantitative and visual PSMA PET tumor-to-salivary gland ratio in prediction of outcomes after [^{177}Lu]PSMA treatment in a cohort of patients with metastatic castration-resistant prostate cancer. . . . . ***Page 1024***

Biopsy before PSMA PET: Kesler and colleagues evaluate clinical characteristics and PSMA PET-based staging of elderly prostate cancer patients without preimaging biopsy results, explore whether biopsy status affects therapeutic approach, and propose a relevant decision-making algorithm. . . . . ***Page 1030***

Late PSMA SPECT improves detection: Berliner and colleagues compare postinjection imaging timepoints in [^{99m}Tc]Tc-PSMA-I&S SPECT/CT detection of lymph node metastases in early biochemically recurrent prostate cancer. . . . . ***Page 1036***

^{68}Ga-FAPI PET interobserver agreement: Mei and colleagues prospectively assess interobserver agreement and accuracy for ^{68}Ga-fibroblast activation protein inhibitor PET/CT interpretations in different tumor entities and compare findings among readers with various levels of experience. . . . . ***Page 1043***

^{68}Ga-FAPI PET/CT in cholangiocarcinoma: Pabst and colleagues report on the accuracy of PET/CT with the novel cancer fibroblast–directed ^{68}Ga-fibroblast activation protein inhibitor-46 tracer for cholangiocarcinoma staging and management guidance.. . . . . ***Page 1049***

PRRT and ICIs in NETs: Esfahani and colleagues investigate whether combining peptide receptor radionuclide therapy using [^{177}Lu]DOTATATE and immune checkpoint inhibition therapy improves treatment response in a preclinical neuroendocrine tumor model. . . . . ***Page 1056***

Tetravalent theranostic chelators: Abou and colleagues evaluate antibody-chelator conjugates for stability using ofatumumab, a human anti-CD20 antibody, and explore tumor targeting with a ^{227}Th chelator conjugate in mice, highlighting potential for quantitative imaging and treatment. . . . . ***Page 1062***

Assessing PSMA-GCK01: Cardinale and colleagues detail development of a PSMA-targeted ^{99m}Tc/^{188}Re theranostic tandem and summarize preclinical results and initial first-in-humans applications in metastatic castration-resistant prostate cancer. . . . . ***Page 1069***

PET imaging surrogate for ^{225}Ac: Bobba and colleagues determine the potential of positron-emitting ^{134}Ce/^{134}La as a surrogate for ^{225}Ac in PET imaging, including chelation processes, imaging and distribution characteristics, and assessment of ^{134}Ce-labeled tumor-targeting agents in prostate cancer models. . . . . ***Page 1076***

Scintigraphic changes after tafamidis: Papathanasiou and colleagues perform a comprehensive analysis of visual, semiquantitative, and quantitative measures of ^{99m}Tc-DPD imaging uptake in patients with cardiac transthyretin-type amyloidosis undergoing transthyretin stabilizer therapy. . . . . ***Page 1083***

^{18}F-FET PET/MR for brain tumors: Smith and colleagues report on clinical application of hybrid ^{18}F-FET PET/MRI in patients with malignant brain tumors to differentiate disease progression from treatment-related changes, identifying complementary information from the combined modalities. . . . . ***Page 1087***

^{18}F-FET PET in recurrent brain tumors: Galldiks and Langen provide perspective on growing data supporting the use of PET with radiolabeled amino acids and advanced perfusion-weighted MRI methods and preview a related article in this issue of *JNM*. . . . . ***Page 1093***

Activity infiltration in PET: Sunderland and colleagues report on a large multicenter study of dose infiltration using PET imaging to provide dose estimates taking into account specific infiltration geometries and the impact of tissue radiosensitivity. . . . . ***Page 1095***

Voxel-based dosimetry for radioembolization: Watanabe and colleagues analyze whether voxel-based dosimetry can be more accurate in predicting hepatotoxicity in patients with hepatocellular carcinoma undergoing radioembolization with ^{90}Y glass microspheres. . . . . ***Page 1102***

Variabilities in dosimetry calculations: Brosch-Lenz and colleagues assess the source and magnitude of variability in absorbed dose estimates for organs and lesions, in response to the SNMMI ^{177}Lu Dosimetry Challenge and to inform standardization efforts. . . . . ***Page 1109***

MIRDcalc, a community dosimetry tool: Kesner and members of an SNMMI special committee on medical internal radiation dose describe a new and freely available computational tool (MIRDcalc, version 1) intended to support organ-level and sub-organ tissue dosimetry. . . . . ***Page 1117***

Dosimetry in advanced thyroid cancer: Taprogge and colleagues analyze quantitative increases in radioiodine uptake due to selumetinib, absorbed doses delivered to metastatic disease from fixed levels of administered activity, and predictive contributions from pretherapy diagnostic studies.. . . . . ***Page 1125***

Optimal SPECT of ^{224}Ra and ^{212}Pb: Mikalsen and colleagues detail studies intended to elucidate the feasibility and suitability of SPECT/CT imaging in an α-particle therapy trial using 1–7 MBq of ^{224}Ra, including development of an extensible optimizing routine. . . . . ***Page 1131***

^{161}Tb and radiolabeling for the clinic: Favaretto and colleagues characterize ^{161}Tb and outline a protocol for synthesis and quality control of ^{161}Tb-DOTATOC with a fully automated process conforming to Good Manufacturing Practice guidelines. . . . . ***Page 1138***

Whole-body PET motion correction: Shiyam Sundar and colleagues introduce the Fast Algorithms for Motion Correction software, which allows correction of both rigid and nonlinear motion artifacts in dynamic whole-body images, irrespective of PET/CT system or tracer. . . . . ***Page 1145***

Total-body PET lung kinetic modeling: Wang and colleagues investigate the need for additional corrections to the input function for kinetic modeling in high-temporal-resolution dynamic PET imaging of the lungs.. . . . . ***Page 1154***

FAPI PET in tenosynovial giant cell tumor: Sellmann and colleagues present a case study demonstrating the high sensitivity of [^{68}Ga]Ga-fibroblast activation protein inhibitor PET/CT in detecting previously unknown tumors.. . . . . ***Page 1162***

JNM Editors' Choice Awards for 2022

Johannes Czernin

David Geffen School of Medicine at UCLA, Los Angeles, California

As editor-in-chief of *The Journal of Nuclear Medicine* (*JNM*), I have the pleasure each year of working with our associate editors and editorial board to select by anonymous vote the outstanding contributions to the journal for recognition at the annual meeting of the Society of Nuclear Medicine and Molecular Imaging. The *JNM* Editors' Choice Awards for articles published in the journal in 2022 were chosen from a group of extraordinarily high-quality and innovative submissions. This year, the research and findings of the awardees represent the advances in theranostics, both clinical and preclinical, that are positioning nuclear medicine at the leading edge of cancer treatment.

Richard P. Baum

Ronnie C. Mease

In the category of Best Clinical Article, the award went to Richard P. Baum, from the Theranostics Center for Molecular Radiotherapy and Molecular Imaging, Zentralklinik Bad Berka, Germany (currently with Curanosticum Wiesbaden–Frankfurt, Center for Advanced Radiomolecular Precision Oncology, Wiesbaden, Germany), and coauthors Christiane Schuchardt, Aviral Singh, Maythinee Chantadisai, Franz C. Robiller, Jingjing Zhang, Dirk Mueller, Alexander Eismant, Frankis Almaguel, Dirk Zboralski, Frank Osterkamp, Aileen Hoehne, Ulrich Reineke, Christiane Smerling, and Harshad R. Kulkarni for "Feasibility, Biodistribution, and Preliminary Dosimetry in Peptide-Targeted Radionuclide Therapy of Diverse Adenocarcinomas Using ^{177}Lu-FAP-2286: First-in-Humans Results" (*J Nucl Med.* 2022;63:415–423). This contribution was also named the best overall article in the journal for 2022.

Ronnie C. Mease, from the Russell H. Morgan Department of Radiology and Radiological Science, Johns Hopkins University School of Medicine (Baltimore, MD), and coauthors Choong Mo Kang, Vivek Kumar, Sangeeta Ray Banerjee, Il Minn, Mary Brummet, Kathleen L. Gabrielson, Yutian Feng, Andrew Park, Ana P. Kiess, George Sgouros, Ganesan Vaidyanathan, Michael R. Zalutsky, and Martin G. Pomper were the recipients of the Best Basic Science Article award for "An Improved ^{211}At-Labeled Agent for PSMA-Targeted α-Therapy" (*J Nucl Med.* 2022;63:259–267).

These and similar efforts ensure that *JNM* remains the international journal of choice for publishing clinical, basic, and translational research in nuclear medicine, molecular imaging, radiopharmaceutical therapy, and theranostics.

Received May 11, 2023; revision accepted May 11, 2023.

DOI: 10.2967/jnumed.123.266027

Leading the European Society of Cardiology

A Conversation Between Franz Weidinger, Frank Bengel, and Johannes Czernin

Franz Weidinger[1], Frank Bengel[2], and Johannes Czernin[3]

[1]Landstrasse Clinic, Vienna, Austria; [2]Hannover Medical School, Hanover, Germany; and [3]David Geffen School of Medicine, UCLA, Los Angeles California

Frank Bengel, MD, a professor at the Hannover Medical School (Hanover, Germany), and Johannes Czernin, MD, editor-in-chief of *The Journal of Nuclear Medicine* (*JNM*) and a professor at the David Geffen School of Medicine at UCLA, talked with Franz Weidinger, MD, president of the European Society of Cardiology (ESC), about his career of leadership in cardiac medicine. The ESC represents more than 105,000 individuals in the field of cardiology from Europe, the Mediterranean Basin, and beyond and includes 28 cardiovascular subspecialty communities of clinicians and researchers.

Dr. Weidinger is head of cardiology at the Klinik Landstrasse (previously the Rudolfstiftung Hospital), a teaching hospital affiliated with Vienna Medical University in Austria. He previously served as deputy head of the Division of Cardiology at the Medical University of Innsbruck (Austria; 1997–2007). His clinical focus is on percutaneous coronary interventions (PCIs) and acute coronary syndromes, with more than 200 peer-reviewed publications. He has been active as a leader in numerous medical societies, including as president of the Austrian Society of Cardiology (2013–2015).

Dr. Czernin: *Thank you very much for taking the time to talk with us. It has been a long time since we both trained in cardiology at the University of Vienna. You have had a remarkable career culminating in your current role as president of the ESC. Let's start with the early days of your research career. You spent 2 years at Brigham and Women's Hospital (Boston, MA) working on coronary vasomotion. Why did you pick Boston?*

Dr. Weidinger: At that time, we were supposed to first train in clinical cardiology. Toward the end of our training, we were encouraged to go to the United States for a research fellowship. I read a paper in *The New England Journal of Medicine* (1986;315: 1046–1051) that described paradoxical vasoconstriction in response to acetylcholine in human coronaries, from the group led by Peter Ganz, MD, and Andrew Selwyn, MD, at Brigham and Women's. This sounded very exciting and translatable. That's why I applied.

Dr. Czernin: *Can you describe the setup of the research there? You did animal experimental work without having prior experience. How did you learn this?*

Dr. Weidinger: It was there that I discovered the beauty of science and how to do research. I spent my first 2–3 months writing the proposal for my project. This was a big project, because it dealt with endothelial dysfunction after balloon angioplasty in a rabbit iliac artery model. I had to learn how to anesthetize and operate on New Zealand White rabbits. I was trained by the fellows in the cath lab and the animal lab. I developed my own project looking at dysfunction of regenerated endothelium after balloon angioplasty, which at that time was quite interesting, because we didn't yet have stents. We could distinguish what the mechanical injury of balloon angioplasty did to the endothelium and the underlying smooth muscle cells.

Franz Weidinger, MD

Dr. Czernin: *How did the mentoring with Ganz and Selwyn work? How often did they interact with you?*

Dr. Weidinger: At that time, I would have appreciated seeing them more often. We had rounds once or twice a week with all the fellows, who discussed progress. I gradually became acquainted with a group of specialists in pathology, vascular biology, physiology, and, of course, catheter techniques. The great thing was that for every question, a relevant specialist could be found either in the same building or just across the street.

Dr. Czernin: *How did you apply your research later on in your career, and did it translate into patient care?*

Dr. Weidinger: Together with other colleagues, we started working with the same rabbit model at the University of Vienna. Later on, we were able to study endothelial dysfunction in humans noninvasively with ultrasound methods. The topic of endothelial dysfunction remained important for a long time. I don't think that endothelial function testing has been established as one of the office tests to screen for early atherosclerosis or progression of atherosclerosis, but it remained an important research tool.

Dr. Czernin: *Did it inform any risk factor modification strategies?*

Dr. Weidinger: I think so. Look at the effects of lowering cholesterol with statins or the effects of vitamin E and other antioxidants on endothelial function. It's a nice way to demonstrate that at least part of vascular dysfunction in early atherosclerosis can be reversed.

Dr. Czernin: *Before I turn the discussion over to Frank, I have a political question. You lived in the American and the European health-care systems. Are there advantages of the American over the European system or vice versa?*

Dr. Weidinger: I once had to go to an emergency department. Nothing serious, but I needed to go there and couldn't even pass the entrance without showing my credit card. "Are you insured? Are you entitled to be here?" This is unlikely to happen in our system. Most European systems are still based on socially supported health care, based on mandatory health insurance. In Austria, everyone gets good treatment and care. The hospital doors are perhaps too wide open, which drives health-care costs; nevertheless, I do prefer the Austrian and European healthcare systems.

Revised May 9, 2023; Accepted May 9, 2023.

DOI: 10.2967/jnumed.123.266017

Dr. Bengel: *I'm going to get back to your research and its clinical translation. You've been working in animal models using pharmacologic interventions. You have also reported on the effects of mechanical manipulation of arteries. This is the dichotomy of cardiovascular care, where we have catheter-based interventions on the one hand and pharmacologic and lifestyle interventions on the other. If you had to define the most important aspect of cardiovascular care today, would it be intervention or drug therapy? Or both?*

Dr. Weidinger: It's certainly both. And maybe we are at something of a turning point, because at least with chronic stable angina or chronic coronary syndrome (as we call it now), things have changed since the International Study of Comparative Health Effectiveness with Medical and Invasive Approaches (ISCHEMIA) trial and other trials have shown the limitations of too much intervention. At least in stable patients with few symptoms, we have very powerful pharmacologic approaches to improve patient outcomes. On the other hand, primary PCI in the acute setting of myocardial infarction can save lives. There is no doubt that we need rapid restoration of blood flow and stenting. More recently, we can also save lives in structural heart disease by noninvasive transcatheter aortic valve implantation for aortic stenosis. Progress and innovation come from both interventional and pharmacologic therapies.

Dr. Bengel: *How do you view the current role of functional testing for myocardial ischemia? How is that going to guide therapy?*

Dr. Weidinger: We have to deal with the discrepancies between the amount of ischemia, the impact of the invasive strategy, and the outcome. What the ISCHEMIA trial put into question is whether we can improve outcome by intervening in those patients with extensive ischemia independent of symptoms. In the many patients in whom symptoms are not so clear, perfusion imaging still has a strong role, at least in my clinical setting. It remains well established here in Austria and Europe.

Dr. Bengel: *In Germany, the numbers of nuclear perfusion imaging procedures are going up almost every year, despite the success of alternative noninvasive tests using MRI and CT. Clearly there is a role for noninvasive testing, but the question is: What kind of therapy will imaging guide in the future? Everyone is talking about precision medicine. How would you define precision cardiology?*

Dr. Weidinger: That's an interesting question, because the term comes from oncology, where targeted drug therapies are guided by biomarkers to the right patients. We like to talk about personalized medicine and precision medicine in cardiology, too. However, those are buzzwords that should be filled out with more content. It's still too early to say how precision medicine in cardiology can change clinical practice. It will involve "omics" technologies and demonstrate how these could better guide us in both preventive cardiology and in choosing the right treatment. The latest prevention guidelines of the ESC already talk about lifetime risk and better ways of assessing cardiovascular risk in individual patients.

Dr. Czernin: *Are any predictive or prognostic imaging biomarkers already on the horizon for precision cardiology?*

Dr. Bengel: *Yes, cardiac amyloidosis is a nice example in which imaging, including bone scans, is specifically used to guide application of novel and highly effective disease-modifying drugs—which are also very expensive.*

Dr. Weidinger: I agree. The search for amyloidosis has really surged in the last few years. We should be realistic and not expect that every patient in whom we have a suspicion for the presence of amyloidosis will be a good candidate for these very costly treatment strategies. However, I think it's an important new avenue for refining our search for causes of cardiomyopathies or poor ventricular function, and it serves as a role model for where novel targeted therapies can go in cardiology.

Dr. Bengel: *I have two more questions before I hand the ball back to Johannes. You talked about buzzwords; have you heard of the buzzword "theranostics"?*

Dr. Weidinger: Yes, I have, because my wife is a nuclear medicine physician. I think it's a way to visualize a target and then treat the target with a similar molecule labeled with a therapeutic isotope.

Dr. Bengel: *Indeed. I was asking this because the* JNM *associate editors have recently discussed how we as nuclear physicians would define theranostics. The terminology is a mixture of therapy and diagnostics, and it could be expanded beyond the use of a radiopharmaceutical for diagnosis and subsequent therapy toward a more general setting in which a specific, targeted therapy is informed by a diagnostic test. Perhaps cardiology is a very early example of that, because you perform coronary angiography followed immediately by coronary intervention guided by that angiography.*

Dr. Weidinger: Another example would be the vulnerable plaque that we have been following for decades, investigating whether it's possible to distinguish stable from unstable plaque and whether we can intervene more effectively, perhaps using nuclear techniques as well. I think that's fascinating.

"The best way to reach a good decision, whether in a clinical team or on the board of the ESC, is to convince with your arguments."

Dr. Bengel: *We are getting new technology, such as total-body PET imaging, that will increase sensitivity for small lesions. Thus, vulnerable plaque may be detectable in the not-so-distant future using this advanced technology.*

Theranostics is currently a driving force in nuclear medicine, leading to much greater interest in our methods from industry. Major companies, such as Novartis, are now getting involved. Industry and the scientific and clinical cardiology communities have for a long time collaborated very closely. However, certain risks are involved. Could you share with us a little bit about how you're managing this as president of the ESC while still maintaining independence in clinical and scientific decisions?

Dr. Weidinger: That's a great challenge. Large, randomized trials are increasingly expensive, and larger numbers of patients are needed to show meaningful benefits for a given therapy. Industry and medicine must collaborate to get this done. We have to be very careful to determine and establish the most independent way of guiding these interactions. We need the support of industry both in discovery of new treatments as well as to interact with the scientific and clinical communities. It's a delicate balance to preserve unbiased, independent research. We have established cardiovascular roundtables at which industry partners interact with experts in a given field of cardiovascular medicine to then publish papers on potential collaborations.

Dr. Czernin: *Another field of the future is artificial intelligence (AI). Radiologists have feared that AI could take away their jobs. How do you see the role of AI in cardiology in interpreting test results or creating algorithms?*

Dr. Weidinger: Just today I have on my desk an issue of *The New England Journal of Medicine* (2023;388:e49) with a review article on AI in medicine and what it's about. AI provides a huge opportunity in cardiology. In the ESC, we try to find the right experts who already have experience with AI in their subspecialty areas, such as imaging or arrhythmia. We have to manage big datasets, and that's where AI has a bright future. However, if you don't combine the clinician with the data scientists and the AI experts you will get more garbage than useful data. We don't know what we can expect in terms of decision support from these new technologies. Probably the best use for AI is that it should liberate us from too much bureaucratic work so that we gain time for our patients.

Dr. Czernin: *How much time do your young colleagues want to spend in research, given the quest for a life/work balance?*

Dr. Weidinger: The younger generation often sees doing research as a phase of their careers, and then they leave it. Our congresses more and more focus on educational than purely scientific content, including basic research. A recent paper in *Nature* (2023;613:138–144) showed that "disruptive" science has declined over the past decades. We have to offer ways to stimulate interest in discovery research.

Dr. Czernin: *Frank, how do you create interest in fundamental research in your department?*

Dr. Bengel: *It is mostly about reserved time for research. Young students respond well if you offer them structured programs that lead to publications and to their MD theses. Later, during clinical training, they may enroll in a clinician scientist program, which gives them 50% research time and 50% for clinical work. We still need to find better ways to integrate clinical and research training. If you want to find motivated young people, this is what you have to offer to them.*

Dr. Czernin: *Franz, when I learned that you had become president of the ESC, I wondered what motivated you.*

Dr. Weidinger: I was on the board of the ESC for about 6 years, and some colleagues tried to convince me to run for the presidency. I talked to my family, because I anticipated that this would be a lot of work—and it is! But it's still gratifying, because I interact with a very international community, learn much about different health systems, and also have the opportunity to appreciate different points of view and cultures. I can also introduce new ideas and try to influence the course of the ESC in Europe. It is a great privilege and opportunity to work with so many bright people from different countries.

Dr. Czernin: *This series is called Discussions with Leaders: What is your leadership style in your hospital and in the ESC?*

Dr. Weidinger: I prefer to listen rather than to speak too much—to integrate others' opinions rather than dictate. The best way to reach a good decision, whether in a clinical team or on the board of the ESC, is to convince with your arguments. Listening to the opinions of others and then arriving at a synthesis to provide solutions is the best way of governing and leading a society and its board. It is important to stay humble but have a clear vision communicated in the right way to stimulate interest in our common topics and concerns.

Dr. Czernin: *What is the most impactful thing you have done in your professional career?*

Dr. Weidinger: I like to think back to my years in Innsbruck. This was the time when primary PCI for acute myocardial infarction started. I was very deeply involved in the regional ST-segment elevation myocardial infarction (STEMI) network that we established there. It was gratifying to see how much we could improve outcomes of acute myocardial infarction by doing primary PCI. To be able to interact with the emergency physicians to convince them to bring in patients very quickly by helicopter, rather than doing thrombolysis in the field, was a very impactful thing.

Dr. Czernin: *My final question for you: What kind of advice do you have for the next generation, not only cardiologists, but physicians in general?*

Dr. Weidinger: We have to be mindful. We are often dealing with elderly patients, and we should spend more time explaining, in very simple terms, what we can provide and offer. We need to maintain a high interest in documenting detailed medical histories and listening carefully to the patients entrusted to us. These communication skills that we learned before smartphones should also be taught to the young. My advice would be to communicate in a very understandable, simple, and convincing way with patients after carefully listening to their stories.

Dr. Czernin: *Thank you, Franz. We are grateful to you for spending time with us and for sharing your experiences and insights with our readers.*

Fibroblast Activation Protein Inhibitor–Based Radionuclide Therapies: Current Status and Future Directions

Manish Ora*[1], Neetu Soni*[2], Aftab Hasan Nazar[1], Manish Dixit[1], Rohit Singh[3], Savita Puri[2], Michael M. Graham[4], and Sanjay Gambhir[1]

[1]*Department of Nuclear Medicine, SGPGIMS, Lucknow, India;* [2]*Department of Radiology, University of Rochester Medical Center, Rochester, New York;* [3]*Division of Hematology–Oncology, University of Vermont Medical Center, Burlington, Vermont; and* [4]*Division of Nuclear Medicine, Department of Radiology, University of Iowa Health Care, Iowa City, Iowa*

Metastatic malignancies have limited management strategies and variable treatment responses. Cancer cells develop beside and depend on the complex tumor microenvironment. Cancer-associated fibroblasts, with their complex interaction with tumor and immune cells, are involved in various steps of tumorigenesis, such as growth, invasion, metastasis, and treatment resistance. Prooncogenic cancer-associated fibroblasts emerged as attractive therapeutic targets. However, clinical trials have achieved suboptimal success. Fibroblast activation protein (FAP) inhibitor–based molecular imaging has shown encouraging results in cancer diagnosis, making them innovative targets for FAP inhibitor–based radionuclide therapies. This review summarizes the results of preclinical and clinical FAP-based radionuclide therapies. We will describe advances and FAP molecule modification in this novel therapy, as well as its dosimetry, safety profile, and efficacy. This summary may guide future research directions and optimize clinical decision-making in this emerging field.

Key Words: cancer-associated fibroblasts; fibroblast activation protein; radionuclide therapy; PET/CT; cancer management; FAPI

J Nucl Med 2023; 64:1001–1008
DOI: 10.2967/jnumed.123.265594

Cancer remains a significant cause of mortality and morbidity despite early detection and management advancements. Functional cancer imaging is crucial in staging, response evaluation, restaging, and prognostication. The commonly used molecular imaging radiopharmaceuticals target metabolism (glucose, amino acid, or lipid) and cell surface receptors (e.g., somatostatins and prostate-specific membrane antigen). However, another approach to tumor imaging and novel therapies has recently created interest—that is, targeting of the tumor stroma. As tumors grow, the tumor microenvironment (TME) stimulates the growth of adjacent nonmalignant cells, which play a complex role in tumor pathogenesis.

Cancer-associated fibroblasts (CAFs) are a critical and abundant component of TME. These are involved in tumor progression, including tumorigenesis, neoangiogenesis, metastasis, immunosuppression, and drug resistance (*1,2*). Activated CAFs have fibroblast activation protein (FAP) α receptors, which are imaged using several small FAP inhibitors (FAPIs). This approach has shown superiority to [^{18}F]-FDG in diagnosing various neoplasms (*3–5*). However, it is premature to conclude that there is an advantage over [^{18}F]-FDG regarding diagnostic ability, management changes, and cost effectiveness. [^{68}Ga]-FAPI PET/CT shows a remarkably high tumor-to-background ratio. Consequently, a new approach to noninvasive TME characterization, tumor staging, and radioligand therapy has commenced (*6*). Several preclinical and clinical studies have investigated the role of FAPI-based radionuclide therapy in various malignancies. Preliminary results have shown safety in all studies and efficacy to a variable extent (*7–28*).

This review provides nuclear medicine physicians with a concise overview of TME, CAFs, and FAPI and their role in tumorigenesis. There is heterogeneity in the origin of CAFs, their subtypes, and their functions. CAFs differ in biomarkers and FAP expression (*2,29*). These factors become pertinent in deciding the targets for imaging and therapy. The current literature on targeting of CAFs is reviewed, including preliminary results from preclinical and clinical FAPI-based radionuclide therapies. Potential future research areas include selective FAP targeting, FAPI radiopharmaceuticals, the choice of optimal radioisotopes, and follow-up strategies. The evolving role of concurrent chemotherapy and immunotherapy therapy is also covered.

NONTUMOR COMPONENT OF CANCER

TME

Malignant tissue consists of tumor cells and several noncancer components. TME includes nonmalignant components supporting continuous tumor progression and dissemination. TME comprises CAFs, myeloid-derived suppressor cells, immune cells, the extracellular matrix, endothelial cells, and pericytes (*1*). TME is active and has several tumor–stroma interactions directed by a complex system of cytokines, chemokines, inflammatory molecules, and matrix-remodeling enzymes (*30*). TME is proposed as an indispensable soil for developing malignant tumor seeds (*1*).

Origin and Role of CAFs in Tumor Pathogenesis (Fig. 1)

CAFs interact with and evolve with tumor cells. They transform into a protumor phenotype, which enables them to survive, populate, and contribute to tumor development (*31*). CAFs are derived from normal tissue fibroblasts that are activated by tumor cells. This activation involves stimuli such as oxidative stress, hypoxia, and growth factors from the tumor and immune cells. They may also be recruited from the bone marrow (*32*). Sometimes CAFs develop from a nonfibroblastic origin by epithelial-to-mesenchymal

Received Feb. 13, 2023; revision accepted Mar. 30, 2023.
For correspondence or reprints, contact Manish Ora (drmanishora@yahoo.com).
*Contributed equally to this work.
Published online Jun. 2, 2023.

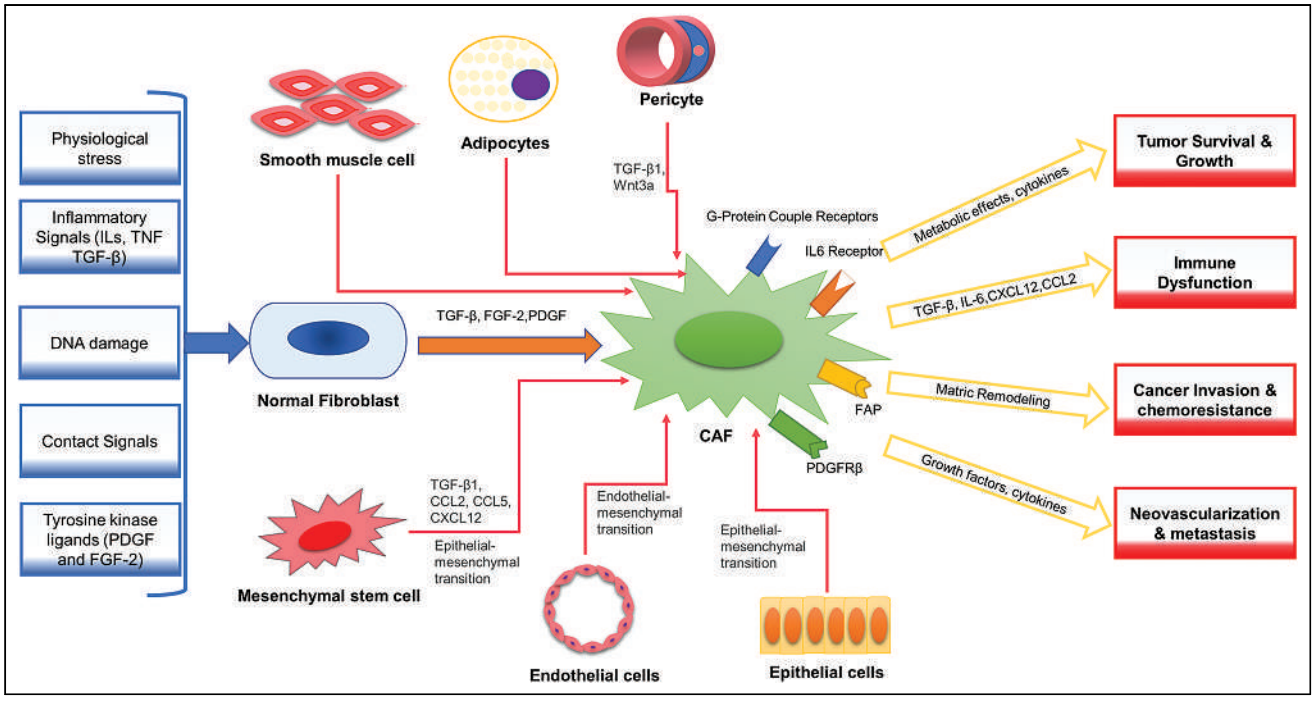

FIGURE 1. Activating pathways, sources, and important functions of CAFs in TME. CAFs may arise from quiescent fibroblasts by physiologic stresses and inflammatory signals, including TGF-β, platelet-derived growth factor, fibroblast growth factor 2, interleukins, and tumor-necrosis factor. Proinflammatory conditions (TGF-β and reactive oxygen species) cause deficiency in base excision repair. This deficiency generates unrepaired DNA strand breaks and may reprogram fibroblasts into CAFs. Other differentiation pathways involve adipocytes, pericytes, and smooth muscle cells. Mesenchymal stem cells may transform into CAFs by epithelial–mesenchymal transition. This pathway involves stimulating molecules such as TGF-β, C–C chemokine ligand 2, C–C chemokine ligand 5, and C-X-C chemokine ligand 12. Endothelial and epithelial cells may also be transformed into CAFs through endothelial-to-mesenchymal transition and epithelial-to-mesenchymal transition. These activated CAFs interact with tumor and immune cells to produce prooncogenic environment. CCL = chemokine ligand; CXCL = C-X-C chemokine ligand; FGF = fibroblast growth factor; IL = interleukin; PDGF = platelet-derived growth factor; PDGFR = platelet-derived growth factor receptor; TNF = tumor-necrosis factor.

or endothelial-to-mesenchymal transition (*33*). Transforming growth factor β (TGF-β), epidermal growth factor, platelet-derived growth factor, and fibroblast growth factor 2 are pivotal to CAF activation (*32*). Usually, fibroblasts have inhibitory effects on the in vitro proliferation and motility of tumor cells (*34*), but these modified fibroblasts stimulate tumor progression (*1*). Modified CAFs help in paracrine signaling, tumorigenesis, neoangiogenesis, metastases, and drug resistance (*1*). There is heterogeneity in the CAF population.

NOTEWORTHY

- CAFs are abundant cells in TME. There is an increased awareness of the origin, function, and role of CAFs in tumorigenesis.
- Novel radionuclides targeting FAP have shown excellent accuracy and tumor-to-background ratios in PET/CT imaging of malignancies.
- Preliminary preclinical and clinical studies have demonstrated the potential role of FAPI-based radionuclide therapy in metastasized cancers. The initial result promises safety and an antitumoral effect.
- Selective targeting of tumor-promoting CAFs, use of specific FAPI radionuclides with better pharmacokinetic and pharmacodynamic properties, and application of concurrent treatment may open an era in personalized oncology.

CD146-negative CAFs suppress estrogen receptor expression, and estrogen responsiveness of tumor cells results in tamoxifen resistance. In contrast, CD146-positive CAFs lead to estrogen-dependent proliferation and tamoxifen sensitivity (*35*). CAFs perform complex functions, and apart from the protumorigenic effect, subsets of CAFs demonstrate a substantial tumor-suppressive effect (*36*).

CAF Receptors, with Highlights on FAP

Activated CAFs have several upregulated receptors, including FAP, platelet-derived growth factor receptor ß, caveolin 1, CD10, and G-protein–coupled receptors (*1*). FAP is a type II transmembrane serine protease, and pioneer research was done by Rettig et al. (*37*). FAP has low expression in normal tissues and appears to be a redundant or nonessential protease in developmental processes. However, it upregulates during various malignant and nonmalignant pathologic processes, including healing, inflammation, and fibrosis. FAP expression has been implicated in various cancer-related signaling pathways. It contributes to tumor progression, invasion, metastasis, immunosuppression, and chemotherapy resistance (*38*).

TARGETING OF CAFS AS AN ANTITUMOR TREATMENT (FIG. 2)

Nonradionuclide Targeting Strategies

The role of CAFs in oncogenesis led to research on the development of CAF-directed therapy. Various FAP-targeting strategies have been tried, including anti-FAP monoclonal antibodies (*39–41*), blocking of FAP enzymatic activity (*42*), FAP-antigen vaccination (*43*),

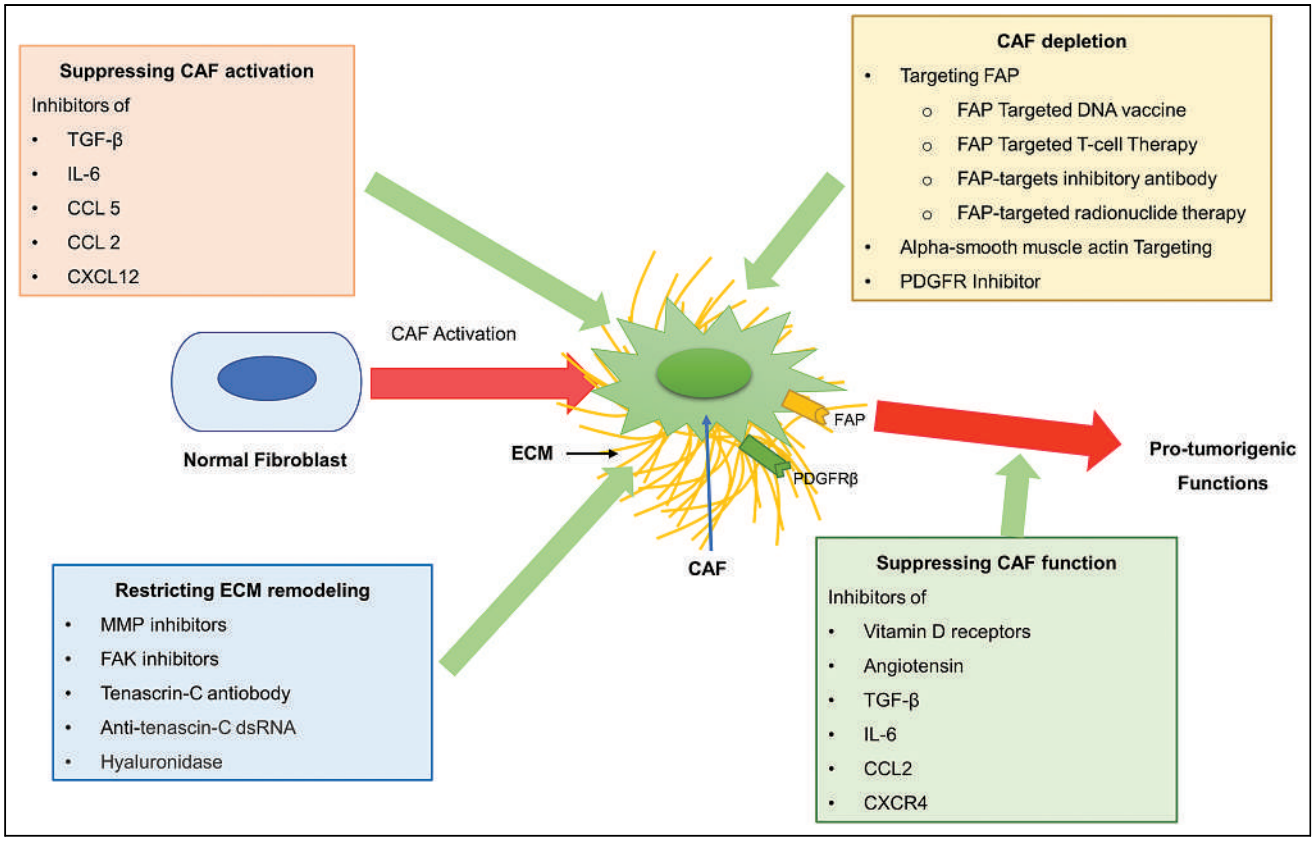

FIGURE 2. CAF-targeting strategies for anti-CAF therapies. CAF activation and function can be suppressed by inhibiting signaling pathways leading to activation. These include TGF-β, interleukin-6, C–C chemokine ligand 2, C–C chemokine ligand 5, and C-X-C chemokine ligand 12. CAF depletion may be achieved by targeting FAP, α-smooth muscle actin, and platelet-derived growth factor receptors. Another strategy is to restrict extracellular matrix remodeling by targeting matrix proteins such as matrix metalloproteinases, hyaluronan, tenascin-C, and focal adhesion kinase. CCL = chemokine ligand; CXCL = C-X-C chemokine ligand; dsRNA = double-stranded RNA; ECM = extracellular matrix; FAK = focal adhesion kinase; IL = interleukin; MMP = matrix metalloproteinase; PDGFR = platelet-derived growth factor receptor.

genetic deletion (*42*), and CAR-T cells directed against FAP (*44*). Sibrotuzumab (antibody against FAP) has been studied in colorectal and non–small cell lung carcinoma. It was well tolerated and safe (*40,41*). Another possible approach is anticytokine therapy against interleukin-6, C-X-C motif chemokine ligand 12, and TGF-β. These reduce recruitment and CAF activation, decreasing CAF-secreted cytokines and chemokines (*1,45*). The extracellular matrix is a physical barrier to tumor drug delivery. Targeting of extracellular matrix protein production or degradation of the extracellular matrix favors drug delivery and may enhance the tumoricidal effect (*46*). AVA6000 is a doxorubicin prodrug that FAP activates and is expected to have enhanced tumor killing with fewer systemic side effects (NCT04969835, Avacta Life Sciences Ltd. A Phase 1, Open Label, Dose-Escalation and Expansion Study to Evaluate the Safety, Pharmacokinetics and Initial Therapeutic Activity of AVA6000, a Novel FAP-activated Doxorubicin Prodrug Administered Intravenously in Patients With Locally Advanced or Metastatic Selected Solid Tumours [Internet]. clinicaltrials.gov; 2023 Apr [cited 2023 Apr 13]. Report No.: NCT04969835. Available from: https://clinicaltrials.gov/ct2/show/NCT04969835). Despite a trial of several drugs, an improved outcome has been shown in only a few preclinical studies. Those drugs that underwent clinical trials had limited success. FAP-targeting immunotherapy has demonstrated a nonselective recognition of FAP-reactive T cells on pluripotent bone marrow stem cells. It led to lethal bone marrow hypocellularity, necrosis, and cachexia (*47*). The current status of anti-CAF therapies is still in an early-phase clinical trial (*48*).

Principle of Targeting CAFs with FAPI-Based Radionuclide Therapy

Other CAF-directed therapy approaches are the radiolabeling of FAPI, peptides, and small-molecule radioconjugates targeting FAP (*23,49,50*). Radiopharmaceuticals are internalized by CAFs and emit α- or β-particles. α-emitters have theoretic advantages over β-particles for tumoricidal effect. α-emitters create dense ionization, leading to double-strand DNA breaks and unrepairable complex chromosomal rearrangements. This tumoricidal effect is independent of the cell cycle and oxygen level. Treatment with α-emitters may overcome resistance toward β- or γ-irradiation. Short-range α-particles have minimal effects on normal tissues (*51*). Some tumor cells also express FAP, such as pancreas (*52*), stomach (*53*), breast (*54*), and sarcoma (*55*). In these scenarios, α-therapy may have a direct tumoricidal effect. However, for other tumors, the radiopharmaceuticals are deposited in CAFs close to targeted tumor cells. Crossfire and bystander effects from long-range, β-particle–emitting radiopharmaceuticals may affect the tumor cells (*56*). The crossfire effect is particle-induced destruction of cells neighboring tracer-accumulating cells. The radiation-induced bystander effect on cells not exposed to ionizing radiation occurs through free-radical diffusion and stress signal factors from irradiated cells, leading to lethal changes (*57*).

PRELIMINARY RESULTS ON FAPI-BASED RADIONUCLIDE THERAPY

Lessons from Preclinical Studies

Preclinical in vitro and animal studies aim to accurately model a drug's desired biologic effect to predict efficacy, safety, and potential toxicities. These studies assess pharmacokinetics, pharmacodynamics, dosing, dosimetry, and side effects. Even after testing of safety in animal studies, high toxicity–related failure rates are noted in human drug trials (*58*). Tranel et al. compared absorbed dose estimates in 3-dimensional cellular models with CAFs and tumors intermingling (*55*). The efficacy of [^{225}Ac] decreases as tumor cluster size increases. In such situations, [^{177}Lu] (β-emitter with a longer range) may be more effective because of the crossfire effect. However, with larger (>600–700 μm) cluster sizes, the benefit of ^{177}Lu was also limited (*55*). The theranostic potential of radionuclide FAPI therapy has been evaluated in preclinical studies. Studies have used FAPI-based radionuclide therapy with ^{131}I (*7*), ^{177}Lu (*8,9,11*), and ^{225}Ac (*8,10*). Several FAPI agents such as FAPI-02 (*7*), FAPI-04 (*10*), FAPI-46 (*8,9*), FAP-2286 (*9*), and EB-FAPI B1-B4 (*11*) were used (Supplemental Table 1; supplemental materials are available at http://jnm.snmjournals.org). All the studies have shown variable tumor size reduction. However, tumoral uptake, clearance, and tracer retention varied with the agent and tumor type. Watabe et al. used 34 kBq of [^{225}Ac]-FAPI-04 per mouse (*10*). That corresponds to the 1.5 MBq/kg human dose, higher than the 50–200 kBq/kg dose given for other ^{225}Ac therapies. It shows rapid urinary excretion (89% at 3 h), resulting in low residual radiopharmaceutical for potential therapeutic effect (*10*). In another mouse study, [^{177}Lu]-FAPI-46 and [^{225}Ac]-FAPI-46 also showed low tumor uptake at 3 h (0.3 percentage injected dose [%ID]/g) and 24 h (0.1 %ID/g), respectively (*8*). A novel class of FAP-targeting modalities using cyclic peptides as binding motifs has been proposed. FAP-2286 is linked to DOTA and has better binding affinity, selectivity, and plasma stability. It showed a 12- and 9-fold higher time-integrated activity coefficient and tumor-absorbed dose than FAPI-46 (*9*). The Evans blue–conjugated FAPI-02–based radiotracer [^{177}Lu]-EB-FAPI-B1 has excellent FAP-targeting specificity and tumor retention. It showed remarkable tumor growth suppression in U87MG tumor–bearing mice, with negligible side effects (*11*).

Preliminary Knowledge from Clinical Studies

Current knowledge on FAPI radionuclide therapy in humans is limited to case reports, case series, and small prospective studies (Supplemental Table 2) (*12,14–24,26–28,59,60*). The studies have used the β-emitters ^{90}Y, ^{177}Lu, and ^{153}Sm. FAPI agents include FAPI-04 (*12,20*), FAPI-46 (*14,15,20–22,24,26,59*), FAP-2286 (*23,28*), 3BP-3940 (*27*), SA.FAPI, and $(SA.FAPi)_2$ (*17–19*). Recently, Baum et al. used ^{225}Ac-based radionuclide therapy in combination with ^{90}Y and ^{177}Lu (*27*). Patients with diverse malignancies were included in all studies except that of Ballal et al., which included thyroid cancer (*19*). Overall, the therapy appears safe, with few toxicities and no reportable allergic reactions. Some studies have found grade 3 and 4 hematologic and hepatobiliary toxicities (*23,24,26*). Toxicities should be interpreted cautiously, given the inclusion of heavily pretreated patients with metastases. Repeated therapy was feasible and safe. Few studies performed posttherapy scanning and dosimetry. In most studies, the dose-limiting organ was the colon or kidneys, with no safety concerns. The average radiation dose of [^{90}Y]-FAPI-46 for kidney and bone marrow was comparable to that of [^{177}Lu]-FAP-2286 and [^{177}Lu]-FAPI-46 (*16,23,26*). Tumor dosimetry (Supplemental Table 3) varied among the studies and among metastatic lesions in the same patient (*16–20,23,24,26*). Some studies found poor tumoral uptake and rapid washout (*60*). Absorbed dose and effective half-life differ among the various FAPI agents.

Early studies reported disease progression or stable disease (*15–17,21–25*). Recent studies have reported partial responses to novel therapy (*19,26,28*). Fendler et al. evaluated RECIST/PERCIST responses up to 18 mo after radionuclide therapy (*26*). Median overall survival was significantly longer for RECIST responders (P = 0.013). Higher survival was noted in those with a partial response or stable disease (14.4 mo) than in those with progressive disease (6.6 mo) after [^{90}Y]-FAPI-46 therapy. However, a partial response and stable disease were seen in sarcoma patients (*26*). The fact that sarcomas express FAP receptors on tumor cells could result in a higher tumor dose and tumoricidal effect. A complete response to FAPI therapy has not been documented. However, some published images have shown promising results (*19,28*). Some studies have reported follow-up imaging with [^{68}Ga]-FAPI PET/CT. Only Fendler et al. used [^{18}F]-FDG PET/CT in the follow-up (*26*). Tumor marker (serum thyroglobulin) correlation is available only for the study that included thyroid cancer patients (*19*).

Limitations of Existing Research and Literature

[^{68}Ga]-FAPI PET/CT has shown excellent accuracy in detecting malignant lesions. Several studies have shown advantages over [^{18}F]-FDG PET/CT (*3–6*). Most studies have not been histopathologically validated. Tumors can have variable expression of CAFs and FAP. Mona et al. studied FAP expression using immunohistochemistry on a pan-cancer human tissue microarray (*61*). FAP was expressed across several cancer types with variable intensity and frequency, ranging from 25% to 100% (mean, 76.6% ± 25.3%). Low expression of FAP in the tumor may lead to a false-negative scan. Microscopic metastases, lesions near the physiologic uptake site, and small lesion size can be causes of a false-negative scan (*61–63*). Several trials (NCT04504110, Peking Union Medical College Hospital. A Prospective Study to Evaluate 68Ga-FAPI-04 and 18F-FDG PET/CT in Patients With Epithelial Ovarian Cancer: Compared With Histological Findings [Internet]. clinicaltrials.gov; 2020 Aug [cited 2023 Apr 13]. Report No.: NCT04504110. Available from: https://clinicaltrials.gov/ct2/show/NCT04504110; NCT04459273, Jonsson Comprehensive Cancer Center. PET Biodistribution Study of 68Ga-FAPI-46 in Patients With Different Malignancies: An Exploratory Biodistribution Study With Histopathology Validation [Internet]. clinicaltrials.gov; 2023 Mar [cited 2023 Apr 13]. Report No.: NCT04459273. Available from: https://clinicaltrials.gov/ct2/show/NCT04459273; NCT04457232, Jonsson Comprehensive Cancer Center. PET Biodistribution Study of 68Ga-FAPI-46 in Patients With Prostate Cancer: A Prospective Exploratory Biodistribution Study With Histopathology Validation [Internet]. clinicaltrials.gov; 2023 Mar [cited 2023 Apr 13]. Report No.: NCT04457232. Available from: https://clinicaltrials.gov/ct2/show/NCT04457232; and NCT05209750, The Netherlands Cancer Institute. Pilot Study of FAPI PET/CT for Locoregional (re)Staging of Lymph Nodes in Colorectal Carcinoma [Internet]. clinicaltrials.gov; 2022 Aug [cited 2023 Apr 13]. Report No.: NCT05209750. Available from: https://clinicaltrials.gov/ct2/show/NCT05209750) are exploring the role of [^{68}Ga]-FAPI PET/CT along with histopathologic validation for assessing diagnostic accuracy. A multimodal imaging approach and careful interpretation of clinical and pathologic data are essential to ensure accurate cancer diagnosis and management. The current understanding of FAP radionuclide therapy is based on small studies with limited follow-up. The main goal was to evaluate safety

and perform a preliminary assessment of efficacy. It is difficult to draw meaningful conclusions because of the patient diversity, type of tumor, metastatic burden, previous therapies, FAPI ligand used, and radionuclide used. Patients have had suboptimal performance scores and poor expected survival. Long-term follow-up data are unavailable to evaluate disease progression, morbidity, and mortality.

CHALLENGES AHEAD AND POTENTIAL AREAS OF FUTURE RESEARCH

Selective Targeting of Tumor-Promoting CAFs and FAP Receptors

Most currently available anticancer agents target tumor cells, ignoring TME. Interest in TME-directed imaging and therapy research is expanding because of recognition of the importance of TME (*48*). Significant heterogeneity in origin, biomarkers, subtype, FAP expression, and CAF functions have been noted (*29*). CAF subsets are noted in triple-negative breast cancer, with various properties and levels of activation. The CAF-S1 subset is associated with an immunosuppressive microenvironment and expresses FAP. However, CAF-S2, CAF-S3, and CAF-S4 do not express FAP (*2*). Özdemir et al. observed that depleting the myofibroblast population in pancreatic ductal adenocarcinoma led to immunosuppression in animal models (*36*). It resulted in cancer progression with poor survival (*36*). This observation suggests that nonselective targeting of tumor-suppressive CAFs may be ineffective or even deleterious (*1*).

FAP expression is heterogeneous among tumors and even among different metastatic sites. Normal fibroblasts show minimal FAP expression. Uterus and breast usually show mild FAP expression but have sometimes shown intense uptake (*64*). Colon and pancreatic cancers have shown high desmoplastic reactions but moderate [^{68}Ga]-FAPI uptake (*6*). FAP expression is also associated with several benign etiologies. These include cardiovascular (myocardial infarction, atherosclerosis), musculoskeletal (degenerative disease), hepatobiliary (focal nodular hyperplasia, pancreatic lesions), and IgG4-related diseases (*65*). It is prudent for theranostics to rule out the benign and inflammatory FAP expression that may occur in healing, chronic inflammation, and physiologic uptake (*65,66*).

Changes in Structure and Properties of FAPI Radiopharmaceuticals

Diagnostic and therapeutic applications of radiopharmaceuticals need specific and rapid tracer uptake. Small-molecule FAPIs (UAMC-1110) are based on the 4-quinolinyl-glycyl-2-cyanopyrrolidine scaffold and have overcome the disadvantages of pyrrolidine-2-boronic acid derivatives of FAP antibody B12 IgG. They have nanomolar FAP affinity with high selectivity (*67*). Recent research has focused on chemical modification to achieve superior pharmacokinetics (*5*). It resulted in rapid internalization and fast circulatory clearance, with high-contrast imaging even 10 min after administration (*5*).

Pharmacokinetic prerequisites for therapeutic radiopharmaceuticals include prolonged blood circulation, serum stability, lessened nonspecific uptake, and persistent tumor retention. These characteristics result in a high effective half-life and tumor radiation dose, facilitating minimization of the radiation dose to healthy surrounding tissue and systemic toxicity and allowing higher administered doses to patients. The pharmacokinetics of FAPI-01 and FAPI-02 were reported in 2018. FAPI-02 had improved binding affinity to human FAP compared with FAPI-01 (*68*). Lindner et al. did a preclinical pharmacokinetics study on tumor-bearing animals, studying 15 synthesized FAPIs (FAPI-02 to FAPI-15) (*12*). They found FAPI-04 to be the most promising tracer for clinical application. Given the low FAPI retention time of FAPI-02 and FAPI-04, Loktev et al. further developed several other derivatives (*69*). FAPI-21, FAPI-36, FAPI-46, and FAPI-55 demonstrated higher tumor uptake than FAPI-04. Progressively increasing tumor uptake was noted in FAPI-21 from 1 to 4 h. FAPI-21 revealed the highest 24-h tumor retention (6.03 ± 0.68 %ID/g), followed by FAPI-35 and FAPI-46. Slow clearance and high retention were noted for FAPI-21 at 24 h (64% of the maximum tumor activity), followed by FAPI-35 (37%), FAPI-46, and FAPI-55 (~20% each). However, FAPI-21 had physiologic uptake in oral mucosa, thyroid, and salivary glands (*69*). FAPI-46 has better pharmacokinetics than FAPI-04. DOTA ligand is used as a chelator for FAPI-46, which makes it a suitable agent to label with ^{90}Y, ^{177}Lu, and ^{153}Sm (*13–16,21,22,24,25*).

Moon et al. reported FAPI derivatives (DOTA.SA.FAPI and DATA5m.SA.FAPI) created by replacing the heterocyclic nitrogen portion of FAPI-04 to form a squaramide unit (*70*). The Moon et al. group reported transforming FAPI into a homodimeric system (*70*). DOTA $(SA.FAPI)_2$ and DOTAGA (SA.FAPI) have 2 inhibitor groups. Compared with monomers, these have an excellent affinity to FAP, slower renal excretion, and longer blood pool retention (*70*). Ballal et al. have studied these in various cancers (*17–19*). [^{68}Ga]-FAP-2286 showed tumor uptake similar to that of [^{68}Ga]-FAPI-46. However, [^{177}Lu]-FAPI-2286 showed excellent retention at 24 and 72 h compared with [^{177}Lu]-FAPI-46 (15.8 vs. 3.8 %ID/g, respectively [$P = 0.001$], and 16.4 vs. 1.6 %ID/g, respectively [$P = 0.002$]). Significantly sustained suppressed tumor growth was seen in FAP-2286–treated animals compared with FAPI-46–treated animals (metabolic tumor volumes, 12 vs. 1,210 mm^3; $P < 0.0001$) (*71*). The tumor half-life of FAP-2286 (44 h for bone metastases) is prolonged compared with FAPI-02 and FAPI-04. Nevertheless, the effective tumor half-life is still shorter than the tumor half-life of PSMA-based radioligand therapy (*23,72*).

Albumin-binding FAPIs (TE-FAPI-01 to TE-FAPI-04) have an increased blood concentration and delayed excretion and are stable in saline and plasma. They have high FAP-binding affinity with minimum physiologic uptake. TE-FAPI-03 and TE-FAPI-04 exhibited persistent tumor accumulation 24 h after administration (2.84 ± 1.19 %ID/g and 3.86 ± 1.15 %ID/g, respectively) (*73*). Albumin binder–truncated Evans blue ([^{177}Lu]-EB-FAPI-B1) has shown excellent pharmacokinetics and tumoricidal effect (*11*). Zhao et al. have synthesized DOTA-2P$(FAPI)_2$ with 2 FAPI-46 monomers (*74*). Multimerization increased tumor uptake and retention compared with [^{68}Ga]-FAPI-46. There is a need for a pan-tumor-imaging–specific FAP radiopharmaceutical that localizes in protumor CAF subpopulations and precludes tumor-suppressive CAFs and inflammatory fibroblasts.

Choice of Radionuclide for Radionuclide Therapy

The radiation dose delivered to the target depends on type of particle, range, half-life, and energy. α-particle–based therapy might kill the CAFs but may have a minimal direct effect on tumor cells. At the same time, the inverse is true for β-particles. Another ideal characteristic is to have a radionuclide's half-life coincide with a radiopharmaceutical's retention half-life. Otherwise, the result would be a higher radiation dose and possible side effects once the radioligand is released from the target. The initial FAPI molecules had a short retention time. Thus, ^{90}Y, which has a higher energy per decay and a shorter half-life, was more suitable for labeling (*26*). With improvement in tumor retention in newer

FAPI tracers, the radionuclides with a longer half-life, such as ^{177}Lu, ^{131}I, or ^{225}Ac, will be helpful. Combined use of α- and β-emitting compounds is also proposed. This strategy involves one carrier molecule labeled with both emitters. However, superiority over the single emitter remains unexplored (*56*). Rosar et al. evaluated treatment responses of [^{225}Ac]-PSMA-617/[^{177}Lu]-PSMA-617 tandem therapy in prostate cancer patients who had progressed on [^{177}Lu]-PSMA-617 monotherapy (*75*). A partial response and stable disease were noted in 5 (29.4%) and 7 (41.2%) patients, respectively. Baum et al. reported the human results of a theranostic approach using combinations (^{177}Lu + ^{225}Ac and ^{90}Y + ^{225}Ac) with the FAP-binding peptide 3BP-3940 (*27*). The preliminary result showed safety and feasibility. However, the superiority of the α-particle–based therapy over β-emitters may not be replicated in FAPI-based therapy. Animal studies have shown marginal superiority for [^{177}Lu]-FAPI-46 compared with [^{225}Ac]-FAPI-46. A likely explanation is the inefficient energy transfer by α-emission from the stroma to the tumor (*8*).

Assessment of Response to Radionuclide Therapy, Follow-up Imaging, and Selection of Endpoint of Therapy

There are several ongoing trials for FAPI therapy (Supplemental Table 4). Most include a heterogeneous patient population with different malignancies and multiple tracers. These trials are phases I and II and evaluate feasibility and safety. However, tumor response assessment and survival analysis will be complex and challenging. Repetitive invasive biopsy for primary tumors and metastatic disease is impractical. Assessing the tumor size seems straightforward. However, RECIST for response assessment has significant pitfalls, including baseline selection of lesions and reassessment of the target, nontarget, and new lesions (*76*). After FAPI radionuclide therapy, size may decrease as CAFs form a significant part of tumor. Tumor cell number may remain unchanged. Some preclinical studies have noted an initial decrease in size followed by rapid tumor growth (*8*). Response evaluation with the FAPI-based diagnostic tracer may not reflect tumor burden if there is a transient fall in CAFs or FAP expression. Another surrogate tumor marker, such as [^{18}F]-FDG PET/CT, might give a holistic evaluation. There is a possibility of obtaining false-positive results from ongoing inflammation after radionuclide therapy.

Concurrent Treatment Options for Synergistic Effect

The role of TME in treatment resistance and disease recurrence is largely ignored in cancer management. Dense fibrosis hinders drug delivery by creating an extracellular matrix barrier, elevated interstitial pressure, and stromal cytochrome P450–mediated drug degradation. CAFs suppress immune cells. Drug resistance may be due to decreased hormonal receptors in prostate and breast cancer (*48*). Targeting CAFs by inhibiting surface markers (FAP and α-smooth muscle actin) has been tested in phase I clinical trials of colorectal and lung carcinoma. Sibrotuzumab (antibody against FAP) was safe, with limited efficacy (*40,41*). Similarly, Val-boroPro (inhibitor of FAP enzymatic activity; Talabostat, Point Therapeutics, Boston, MA) was used in phase II trials in patients with metastatic colorectal cancer, with minimal clinical activity (*77*). Several trials have combined antitumor treatment and CAF inhibitors to overcome these obstacles. Metastatic pancreatic cancer patients who are not responding to gemcitabine were given ruxolitinib (JAK1/JAK2 inhibitor) combined with capecitabine. The patients had longer overall survival with better prognoses (*78*). Depletion of FAP-positive CAFs demonstrated the enhanced antitumor effects of programmed-death ligand 1 immunotherapy. T-cell accumulation was noted in the autochthonous model of pancreatic ductal adenocarcinoma, resulting in diminished cancer cells (*79*). These findings indirectly indicated that treatment strategies targeting CAFs alone may be less effective.

Many ongoing nonradionuclide therapy trials have proposed a combination of treatment strategies. Clinical trials targeting Wnt/b-catenin signaling related to CAFs in colorectal cancer (NCT04094688, Alliance for Clinical Trials in Oncology. Randomized Double-Blind Phase III Trial of Vitamin D3 Supplementation in Patients With Previously Untreated Metastatic Colorectal Cancer (SOLARIS) [Internet]. clinicaltrials.gov; 2023 Mar [cited 2023 Apr 13]. Report No.: NCT04094688. Available from: https://clinicaltrials.gov/ct2/show/NCT04094688; high-dose vitamin D3 with FOLFOX/FOLFIRI and bevacizumab), pancreatic cancer (NCT03520790, MD KP. Vitamin D Receptor Agonist Paricalcitol Plus Gemcitabine and Nab-paclitaxel in Patients With Metastatic Pancreatic Cancer [Internet]. clinicaltrials.gov; 2023 Jan [cited 2023 Apr 13]. Report No.: NCT03520790. Available from: https://clinicaltrials.gov/ct2/show/NCT03520790; paricalcitol with gemcitabine and nab-paclitaxel), and gynecologic cancer (NCT03192059, University Hospital, Ghent. A Phase II Investigation of Pembrolizumab (Keytruda) in Combination With Radiation and an Immune Modulatory Cocktail in Patients With Cervical and Uterine Cancer (PRIMMO Trial) [Internet]. clinicaltrials.gov; 2021 Sep [cited 2023 Apr 13]. Report No.: NCT03192059. Available from: https://clinicaltrials.gov/ct2/show/NCT03192059; cyclophosphamide with lansoprazole, pembrolizumab, and radiotherapy) have incorporated various chemotherapeutic agents. Pathways involving interleukin-6 and TGF-β have been targeted by the anti–interleukin-6 antibody tocilizumab in pancreatic cancer (NCT02767557, MD IC. A Multinational, Randomized, Phase II Study of the Combination of Nab-Paclitaxel and Gemcitabine With or Without Tocilizumab, an IL-6R Inhibitor, as First-line Treatment in Patients With Locally Advanced or Metastatic Pancreatic Cancer. [Internet]. clinicaltrials.gov; 2023 Feb [cited 2023 Apr 13]. Report No.: NCT02767557. Available from: https://clinicaltrials.gov/ct2/show/NCT02767557, with nab-paclitaxel and gemcitabine), melanoma (NCT03999749, NYU Langone Health. A Phase II Study of the Interleukin-6 Receptor Inhibitor Tocilizumab in Combination With Ipilimumab and Nivolumab in Patients With Unresectable Stage III or Stage IV Melanoma [Internet]. clinicaltrials.gov; 2023 Jan [cited 2023 Apr 13]. Report No.: NCT03999749. Available from: https://clinicaltrials.gov/ct2/show/NCT03999749, with nivolumab and ipilimumab), and prostate cancer (NCT03821246, Fong L. An Open-Label Multi-Center Phase II Study of Neoadjuvant Atezolizumab-Based Combination Therapy in Men With Localized Prostate Cancer Prior to Radical Prostatectomy [Internet]. clinicaltrials.gov; 2022 Oct [cited 2023 Apr 13]. Report No.: NCT03821246. Available from: https://clinicaltrials.gov/ct2/show/NCT03821246, with atezolizumab and etrumadenant). Bintrafusp, a bifunctional antibody against TGF-β and programmed-death ligand 1, is being studied in esophageal cancer (NCT04481256, Laarhoven HWM van. TGF-β And PDL-1 Inhibition in Esophageal Squamous Cell Carcinoma Combined With Chemoradiation TheRapY [Internet]. clinicaltrials.gov; 2022 Dec [cited 2023 Apr 13]. Report No.: NCT04481256. Available from: https://clinicaltrials.gov/ct2/show/NCT04481256) along with paclitaxel, carboplatin, and radiotherapy. Simlukafusp alfa (RO6874281) immunocytokine is being tried in combination with pembrolizumab in melanoma (NCT03875079, Hoffmann-La Roche. An Open-Label, Multicenter, Phase Ib Study To Evaluate Safety And Therapeutic Activity Of

RO6874281, An Immunocytokine, Consisting Of Interleukin-2 Variant (IL-2v) Targeting Fibroblast Activation Protein-A (FAP), In Combination With Pembrolizumab (Anti-PD-1), In Participants With Advanced Or Metastatic Melanoma [Internet]. clinicaltrials.gov; 2023 Mar [cited 2023 Apr 13]. Report No.: NCT03875079. Available from: https://clinicaltrials.gov/ct2/show/NCT03875079). Results from these trials may reshape advanced tumor management. Investigating radionuclide therapy in conjunction with chemotherapy and immunotherapy will be worthwhile.

CONCLUSION

CAFs remain a dominant cell type in TME and are a worthwhile target for novel anticancer therapies. Nonradioisotopic and FAP-based radionuclide approaches against CAFs have shown variable responses in preclinical and clinical studies. FAPI-based radionuclide therapy has shown encouraging outcomes despite CAF heterogeneity, variable FAP expression, radiopharmaceutical challenges, diversity in patient selection, and advanced malignancies. We are only beginning to understand the potential of FAP-based radionuclide therapy. Extensive research on FAPI ligands is under way. Combining FAP radionuclide therapy with chemotherapy and immunotherapies remains an unexplored research area. Detailed insight into CAF biology, radiopharmacy, and dosimetry may open a new area of precise and personalized oncology.

DISCLOSURE

No potential conflict of interest relevant to this article was reported.

REFERENCES

1. Chen X, Song E. Turning foes to friends: targeting cancer-associated fibroblasts. *Nat Rev Drug Discov.* 2019;18:99–115.
2. Costa A, Kieffer Y, Scholer-Dahirel A, et al. Fibroblast heterogeneity and immunosuppressive environment in human breast cancer. *Cancer Cell.* 2018;33:463–479.e10.
3. Treglia G, Muoio B, Roustaei H, Kiamanesh Z, Aryana K, Sadeghi R. Head-to-head comparison of fibroblast activation protein inhibitors (FAPI) radiotracers versus [^{18}F]F-FDG in oncology: a systematic review. *Int J Mol Sci.* 2021;22:11192.
4. Veldhuijzen van Zanten SEM, Pieterman KJ, Wijnhoven BPL, et al. FAPI PET versus FDG PET, CT or MRI for staging pancreatic-, gastric- and cholangiocarcinoma: systematic review and head-to-head comparisons of diagnostic performances. *Diagnostics (Basel).* 2022;12:1958.
5. Sollini M, Kirienko M, Gelardi F, Fiz F, Gozzi N, Chiti A. State-of-the-art of FAPI-PET imaging: a systematic review and meta-analysis. *Eur J Nucl Med Mol Imaging.* 2021;48:4396–4414.
6. Kratochwil C, Flechsig P, Lindner T, et al. ^{68}Ga-FAPI PET/CT: tracer uptake in 28 different kinds of cancer. *J Nucl Med.* 2019;60:801–805.
7. Ma H, Li F, Shen G, et al. Synthesis and preliminary evaluation of ^{131}I-labeled FAPI tracers for cancer theranostics. *Mol Pharm.* 2021;18:4179–4187.
8. Liu Y, Watabe T, Kaneda-Nakashima K, et al. Fibroblast activation protein targeted therapy using [^{177}Lu]FAPI-46 compared with [^{225}Ac]FAPI-46 in a pancreatic cancer model. *Eur J Nucl Med Mol Imaging.* 2022;49:871–880.
9. Zboralski D, Hoehne A, Bredenbeck A, et al. Preclinical evaluation of FAP-2286 for fibroblast activation protein targeted radionuclide imaging and therapy. *Eur J Nucl Med Mol Imaging.* 2022;49:3651–3667.
10. Watabe T, Liu Y, Kaneda-Nakashima K, et al. Theranostics targeting fibroblast activation protein in the tumor stroma: ^{64}Cu- and ^{225}Ac-labeled FAPI-04 in pancreatic cancer xenograft mouse models. *J Nucl Med.* 2020;61:563–569.
11. Wen X, Xu P, Shi M, et al. Evans blue-modified radiolabeled fibroblast activation protein inhibitor as long-acting cancer therapeutics. *Theranostics.* 2022;12:422–433.
12. Lindner T, Loktev A, Altmann A, et al. Development of quinoline-based theranostic ligands for the targeting of fibroblast activation protein. *J Nucl Med.* 2018;59:1415–1422.
13. Lindner T, Altmann A, Krämer S, et al. Design and development of ^{99m}Tc-labeled FAPI tracers for SPECT imaging and ^{188}Re therapy. *J Nucl Med.* 2020;61:1507–1513.
14. Jokar N, Velikyan I, Ahmadzadehfar H, et al. Theranostic approach in breast cancer: a treasured tailor for future oncology. *Clin Nucl Med.* 2021;46:e410–e420.
15. Rathke H, Fuxius S, Giesel FL, et al. Two tumors, one target: preliminary experience with ^{90}Y-FAPI therapy in a patient with metastasized breast and colorectal cancer. *Clin Nucl Med.* 2021;46:842–844.
16. Assadi M, Rekabpour SJ, Jafari E, et al. Feasibility and therapeutic potential of ^{177}Lu-fibroblast activation protein inhibitor-46 for patients with relapsed or refractory cancers: a preliminary study. *Clin Nucl Med.* 2021;46:e523–e530.
17. Ballal S, Yadav MP, Moon ES, et al. First-in-human results on the biodistribution, pharmacokinetics, and dosimetry of [^{177}Lu]Lu-DOTA.SA.FAPi and [^{177}Lu]Lu-DOTAGA (SA.FAPi)$_2$. *Pharm Basel Switz.* 2021;14:1212.
18. Ballal S, Yadav MP, Kramer V, et al. A theranostic approach of [^{68}Ga]Ga-DOTA.SA.FAPi PET/CT-guided [^{177}Lu]Lu-DOTA.SA.FAPi radionuclide therapy in an end-stage breast cancer patient: new frontier in targeted radionuclide therapy. *Eur J Nucl Med Mol Imaging.* 2021;48:942–944.
19. Ballal S, Yadav MP, Moon ES, et al. Novel fibroblast activation protein inhibitor-based targeted theranostics for radioiodine-refractory differentiated thyroid cancer patients: a pilot study. *Thyroid.* 2022;32:65–77.
20. Kuyumcu S, Kovan B, Sanli Y, et al. Safety of fibroblast activation protein-targeted radionuclide therapy by a low-dose dosimetric approach using ^{177}Lu-FAPI04. *Clin Nucl Med.* 2021;46:641–646.
21. Kratochwil C, Giesel FL, Rathke H, et al. [^{153}Sm]samarium-labeled FAPI-46 radioligand therapy in a patient with lung metastases of a sarcoma. *Eur J Nucl Med Mol Imaging.* 2021;48:3011–3013.
22. Fu K, Pang Y, Zhao L, et al. FAP-targeted radionuclide therapy with [^{177}Lu]Lu-FAPI-46 in metastatic nasopharyngeal carcinoma. *Eur J Nucl Med Mol Imaging.* 2022;49:1767–1769.
23. Baum RP, Schuchardt C, Singh A, et al. Feasibility, biodistribution, and preliminary dosimetry in peptide-targeted radionuclide therapy of diverse adenocarcinomas using ^{177}Lu-FAP-2286: first-in-humans results. *J Nucl Med.* 2022;63:415–423.
24. Ferdinandus J, Costa PF, Kessler L, et al. Initial clinical experience with ^{90}Y-FAPI-46 radioligand therapy for advanced-stage solid tumors: a case series of 9 patients. *J Nucl Med.* 2022;63:727–734.
25. Fu H, Huang J, Sun L, Wu H, Chen H. FAP-targeted radionuclide therapy of advanced radioiodine-refractory differentiated thyroid cancer with multiple cycles of ^{177}Lu-FAPI-46. *Clin Nucl Med.* 2022;47:906–907.
26. Fendler WP, Pabst KM, Kessler L, et al. Safety and efficacy of ^{90}Y-FAPI-46 radioligand therapy in patients with advanced sarcoma and other cancer entities. *Clin Cancer Res.* 2022;28:4346–4353.
27. Baum RP, Greifenstein L, Kramer C, et al. Peptide targeted radiotherapy using cancer-associated fibroblasts as target in solid tumors: first clinical experience with the ^{177}Lu-, ^{225}Ac- and ^{90}Y-labeled peptide 3BP-3940 (single isotope and TANDEM) targeting the fibroblast activating protein [abstract]. *J Nucl Med.* 2022;63(suppl 2):2269.
28. Rao Z, Zhang Y, Liu L, Wang M, Zhang C. [^{177}Lu]Lu-FAP-2286 therapy in a case of right lung squamous cell carcinoma with systemic metastases. *Eur J Nucl Med Mol Imaging.* 2023;50:1266–1267.
29. Chen P-Y, Wei W-F, Wu H-Z, Fan L-S, Wang W. Cancer-associated fibroblast heterogeneity: a factor that cannot be ignored in immune microenvironment remodeling. *Front Immunol.* 2021;12:671595.
30. Koustoulidou S, Hoorens MWH, Dalm SU, et al. Cancer-associated fibroblasts as players in cancer development and progression and their role in targeted radionuclide imaging and therapy. *Cancers (Basel).* 2021;13:1100.
31. Öhlund D, Elyada E, Tuveson D. Fibroblast heterogeneity in the cancer wound. *J Exp Med.* 2014;211:1503–1523.
32. Bu L, Baba H, Yoshida N, et al. Biological heterogeneity and versatility of cancer-associated fibroblasts in the tumor microenvironment. *Oncogene.* 2019;38:4887–4901.
33. Zeisberg EM, Potenta S, Xie L, Zeisberg M, Kalluri R. Discovery of endothelial to mesenchymal transition as a source for carcinoma-associated fibroblasts. *Cancer Res.* 2007;67:10123–10128.
34. Alkasalias T, Flaberg E, Kashuba V, et al. Inhibition of tumor cell proliferation and motility by fibroblasts is both contact and soluble factor dependent. *Proc Natl Acad Sci USA.* 2014;111:17188–17193.
35. Brechbuhl HM, Finlay-Schultz J, Yamamoto TM, et al. Fibroblast subtypes regulate responsiveness of luminal breast cancer to estrogen. *Clin Cancer Res.* 2017;23:1710–1721.
36. Özdemir BC, Pentcheva-Hoang T, Carstens JL, et al. Depletion of carcinoma-associated fibroblasts and fibrosis induces immunosuppression and accelerates pancreas cancer with reduced survival. *Cancer Cell.* 2014;25:719–734.
37. Rettig WJ, Su SL, Fortunato SR, et al. Fibroblast activation protein: purification, epitope mapping and induction by growth factors. *Int J Cancer.* 1994;58:385–392.

38. Cheng C-S, Yang P-W, Sun Y, Song S-L, Chen Z. Fibroblast activation protein-based theranostics in pancreatic cancer. *Front Oncol.* 2022;12:969731.
39. Ostermann E, Garin-Chesa P, Heider KH, et al. Effective immunoconjugate therapy in cancer models targeting a serine protease of tumor fibroblasts. *Clin Cancer Res.* 2008;14:4584–4592.
40. Scott AM, Wiseman G, Welt S, et al. A phase I dose-escalation study of sibrotuzumab in patients with advanced or metastatic fibroblast activation protein-positive cancer. *Clin Cancer Res.* 2003;9:1639–1647.
41. Hofheinz R-D, al-Batran S-E, Hartmann F, et al. Stromal antigen targeting by a humanised monoclonal antibody: an early phase II trial of sibrotuzumab in patients with metastatic colorectal cancer. *Onkologie.* 2003;26:44–48.
42. Gunderson AJ, Yamazaki T, McCarty K, et al. Blockade of fibroblast activation protein in combination with radiation treatment in murine models of pancreatic adenocarcinoma. *PLoS One.* 2019;14:e0211117.
43. Duperret EK, Trautz A, Ammons D, et al. Alteration of the tumor stroma using a consensus DNA vaccine targeting fibroblast activation protein (FAP) synergizes with antitumor vaccine therapy in mice. *Clin Cancer Res.* 2018;24:1190–1201.
44. Wang L-CS, Lo A, Scholler J, et al. Targeting fibroblast activation protein in tumor stroma with chimeric antigen receptor T cells can inhibit tumor growth and augment host immunity without severe toxicity. *Cancer Immunol Res.* 2014;2:154–166.
45. Maia A, Wiemann S. Cancer-associated fibroblasts: implications for cancer therapy. *Cancers (Basel).* 2021;13:3526.
46. Laklai H, Miroshnikova YA, Pickup MW, et al. Genotype tunes pancreatic ductal adenocarcinoma tissue tension to induce matricellular fibrosis and tumor progression. *Nat Med.* 2016;22:497–505.
47. Tran E, Chinnasamy D, Yu Z, et al. Immune targeting of fibroblast activation protein triggers recognition of multipotent bone marrow stromal cells and cachexia. *J Exp Med.* 2013;210:1125–1135.
48. Valkenburg KC, de Groot AE, Pienta KJ. Targeting the tumour stroma to improve cancer therapy. *Nat Rev Clin Oncol.* 2018;15:366–381.
49. Fischer E, Chaitanya K, Wüest T, et al. Radioimmunotherapy of fibroblast activation protein positive tumors by rapidly internalizing antibodies. *Clin Cancer Res.* 2012;18:6208–6218.
50. Galbiati A, Zana A, Bocci M, et al. A dimeric FAP-targeting small-molecule radioconjugate with high and prolonged tumor uptake. *J Nucl Med.* 2022;63:1852–1858.
51. Kratochwil C, Giesel FL, Bruchertseifer F, et al. ^{213}Bi-DOTATOC receptor-targeted alpha-radionuclide therapy induces remission in neuroendocrine tumours refractory to beta radiation: a first-in-human experience. *Eur J Nucl Med Mol Imaging.* 2014;41:2106–2119.
52. Shi M, Yu D-H, Chen Y, et al. Expression of fibroblast activation protein in human pancreatic adenocarcinoma and its clinicopathological significance. *World J Gastroenterol.* 2012;18:840–846.
53. Mori Y, Kono K, Matsumoto Y, et al. The expression of a type II transmembrane serine protease (Seprase) in human gastric carcinoma. *Oncology.* 2004;67:411–419.
54. Kelly T, Kechelava S, Rozypal TL, West KW, Korourian S. Seprase, a membrane-bound protease, is overexpressed by invasive ductal carcinoma cells of human breast cancers. *Mod Pathol.* 1998;11:855–863.
55. Tranel J, Palm S, Graves SA, Feng FY, Hope TA. Impact of radiopharmaceutical therapy (^{177}Lu, ^{225}Ac) microdistribution in a cancer-associated fibroblasts model. *EJNMMI Phys.* 2022;9:67.
56. Haberkorn U, Giesel F, Morgenstern A, Kratochwil C. The future of radioligand therapy: α, β, or both? *J Nucl Med.* 2017;58:1017–1018.
57. Mulford DA, Scheinberg DA, Jurcic JG. The promise of targeted α-particle therapy. *J Nucl Med.* 2005;46(suppl 1):199S–204S.
58. Polson AG, Fuji RN. The successes and limitations of preclinical studies in predicting the pharmacodynamics and safety of cell-surface-targeted biological agents in patients. *Br J Pharmacol.* 2012;166:1600–1602.
59. Lindner T, Altmann A, Krämer S, et al. Design and development of ^{99m}Tc-labeled FAPI tracers for SPECT imaging and ^{188}Re therapy. *J Nucl Med.* 2020;61:1507–1513.
60. Kaghazchi F, Aghdam RA, Haghighi S, Vali R, Adinehpour Z. ^{177}Lu-FAPI therapy in a patient with end-stage metastatic pancreatic adenocarcinoma. *Clin Nucl Med.* 2022;47:e243–e245.
61. Mona CE, Benz MR, Hikmat F, et al. Correlation of ^{68}Ga-FAPi-46 PET biodistribution with FAP expression by immunohistochemistry in patients with solid cancers: interim analysis of a prospective translational exploratory study. *J Nucl Med.* 2022;63:1021–1026.
62. Wegen S, Roth KS, Weindler J, et al. First clinical experience with [^{68}Ga]Ga-FAPI-46-PET/CT versus [^{18}F]F-FDG PET/CT for nodal staging in cervical cancer. *Clin Nucl Med.* 2023;48:150–155.
63. Unterrainer LM, Lindner S, Eismann L, et al. Feasibility of [^{68}Ga]Ga-FAPI-46 PET/CT for detection of nodal and hematogenous spread in high-grade urothelial carcinoma. *Eur J Nucl Med Mol Imaging.* 2022;49:3571–3580.
64. Kessler L, Ferdinandus J, Hirmas N, et al. Pitfalls and common findings in ^{68}Ga-FAPI PET: a pictorial analysis. *J Nucl Med.* 2022;63:890–896.
65. van den Hoven AF, Keijsers RGM, Lam MGEH, et al. Current research topics in FAPI theranostics: a bibliometric analysis. *Eur J Nucl Med Mol Imaging.* 2023;50:1014–1027.
66. Egger C, Cannet C, Gérard C, et al. Effects of the fibroblast activation protein inhibitor, PT100, in a murine model of pulmonary fibrosis. *Eur J Pharmacol.* 2017;809:64–72.
67. Jansen K, Heirbaut L, Cheng JD, et al. Selective inhibitors of fibroblast activation protein (FAP) with a (4-quinolinoyl)-glycyl-2-cyanopyrrolidine scaffold. *ACS Med Chem Lett.* 2013;4:491–496.
68. Loktev A, Lindner T, Mier W, et al. A tumor-imaging method targeting cancer-associated fibroblasts. *J Nucl Med.* 2018;59:1423–1429.
69. Loktev A, Lindner T, Burger E-M, et al. Development of fibroblast activation protein–targeted radiotracers with improved tumor retention. *J Nucl Med.* 2019;60:1421–1429.
70. Moon ES, Ballal S, Yadav MP, et al. Fibroblast activation protein (FAP) targeting homodimeric FAP inhibitor radiotheranostics: a step to improve tumor uptake and retention time. *Am J Nucl Med Mol Imaging.* 2021;11:476–491.
71. Zboralski D, Hoehne A, Bredenbeck A, et al. Comparative biodistribution and radiotherapeutic efficacy of the fibroblast activation protein (FAP)-targeting agents FAP-2286 and FAPI-46 [abstract]. *Cancer Res.* 2022;82:3317.
72. Kulkarni HR, Singh A, Schuchardt C, et al. PSMA-based radioligand therapy for metastatic castration-resistant prostate cancer: the Bad Berka experience since 2013. *J Nucl Med.* 2016;57(suppl 3):97S–104S.
73. Ding J, Xu M, Chen J, et al. ^{86}Y-labeled albumin-binding fibroblast activation protein inhibitor for late-time-point cancer diagnosis. *Mol Pharm.* 2022;19:3429–3438.
74. Zhao L, Niu B, Fang J, et al. Synthesis, preclinical evaluation, and a pilot clinical PET imaging study of ^{68}Ga-labeled FAPI dimer. *J Nucl Med.* 2022;63:862–868.
75. Rosar F, Hau F, Bartholomä M, et al. Molecular imaging and biochemical response assessment after a single cycle of [^{225}Ac]Ac-PSMA-617/[^{177}Lu]Lu-PSMA-617 tandem therapy in mCRPC patients who have progressed on [^{177}Lu]Lu-PSMA-617 monotherapy. *Theranostics.* 2021;11:4050–4060.
76. Abramson RG, McGhee CR, Lakomkin N, Arteaga CL. Pitfalls in RECIST data extraction for clinical trials: beyond the basics. *Acad Radiol.* 2015;22:779–786.
77. Narra K, Mullins SR, Lee H-O, et al. Phase II trial of single agent Val-boroPro (Talabostat) inhibiting fibroblast activation protein in patients with metastatic colorectal cancer. *Cancer Biol Ther.* 2007;6:1691–1699.
78. Hurwitz HI, Uppal N, Wagner SA, et al. Randomized, double-blind, phase II study of ruxolitinib or placebo in combination with capecitabine in patients with metastatic pancreatic cancer for whom therapy with gemcitabine has failed. *J Clin Oncol.* 2015;33:4039–4047.
79. Feig C, Jones JO, Kraman M, et al. Targeting CXCL12 from FAP-expressing carcinoma-associated fibroblasts synergizes with anti-PD-L1 immunotherapy in pancreatic cancer. *Proc Natl Acad Sci USA.* 2013;110:20212–20217.

Theranostics in Hematooncology

Andreas K. Buck*[1], Sebastian E. Serfling*[1], Sabrina Kraus[2], Samuel Samnick[1], Niklas Dreher[1], Takahiro Higuchi[1], Leo Rasche[2], Hermann Einsele[2], and Rudolf A. Werner[1,3]

[1]*Department of Nuclear Medicine, University Hospital Würzburg, Würzburg, Germany;* [2]*Department of Internal Medicine II, University Hospital Würzburg, Würzburg, Germany; and* [3]*Russell H. Morgan Department of Radiology and Radiological Science, Johns Hopkins University School of Medicine, Baltimore, Maryland*

Learning Objectives: On successful completion of this activity, participants should be able to (1) describe novel and already established radiopharmaceuticals for treatment of hematologic neoplasms such as leukemia or lymphoma; (2) explain why small molecules specifically binding to C-X-C motif chemokine receptor 4 may serve as theranostic agents, particularly for hematologic applications; and (3) describe advantages and disadvantages of lymphoma treatment using radioimmunoconjugates.

Financial Disclosure: Dr. Buck has received speaker honoraria from Novartis/AAA and PentixaPharm, is a board member/officer/trustee for PentixaPharm, and is involved in [^{68}Ga]Ga-Pentixafor PET Imaging in PAN Cancer (FORPAN), sponsored and planned by PentixaPharm. Dr. Werner has received speaker honoraria from Novartis/AAA and PentixaPharm, reports advisory board work for Novartis/AAA and Bayer, has received funding from the German Research Foundation (453989101, 507803309), and is involved in [^{68}Ga]Ga-Pentixafor PET Imaging in PAN Cancer (FORPAN), sponsored and planned by PentixaPharm. Dr. Higuchi has received funding from the German Research Foundation (453989101). Dr. Rasche reports support from, is a consultant/advisor to, and is a meeting participant/lecturer for BMS, GSK, Pfizer, Janssen, and Amgen. The authors of this article have indicated no other relevant relationships that could be perceived as a real or apparent conflict of interest.

CME Credit: SNMMI is accredited by the Accreditation Council for Continuing Medical Education (ACCME) to sponsor continuing education for physicians. SNMMI designates each *JNM* continuing education article for a maximum of 2.0 AMA PRA Category 1 Credits. Physicians should claim only credit commensurate with the extent of their participation in the activity. For CE credit, SAM, and other credit types, participants can access this activity through the SNMMI website (http://www.snmmilearningcenter.org) through July 2026.

In the early 2000s, major clinical trials provided evidence of a favorable outcome from antibody-mediated radioimmunotherapy for hematologic neoplasms, which then led to Food and Drug Administration approval. For instance, the theranostic armamentarium for the referring hematooncologist now includes ^{90}Y-ibritumomab tiuxetan for refractory low-grade follicular lymphoma or transformed B-cell non-Hodgkin lymphoma, as well as ^{131}I-tositumomab for rituximab-refractory follicular lymphoma. Moreover, the first interim results of the SIERRA phase III trial reported beneficial effects from the use of ^{131}I-anti-CD45 antibodies (Iomab-B) in refractory or relapsed acute myeloid leukemia. During the last decade, the concept of theranostics in hematooncology has been further expanded by C-X-C motif chemokine receptor 4–directed molecular imaging. Beyond improved detection rates of putative sites of disease, C-X-C motif chemokine receptor 4–directed PET/CT also selects candidates for radioligand therapy using β-emitting radioisotopes targeting the identical chemokine receptor on the lymphoma cell surface. Such image-piloted therapeutic strategies provided robust antilymphoma efficacy, along with desired eradication of the bone marrow niche, such as in patients with T- or B-cell lymphoma. As an integral part of the treatment plan, such radioligand therapy–mediated myeloablation also allows one to line up patients for stem cell transplantation, which leads to successful engraftment during the further treatment course. In this continuing education article, we provide an overview of the current advent of theranostics in hematooncology and highlight emerging clinical applications.

Key Words: theranostics; C-X-C motif chemokine receptor 4; CXCR4; lymphoma; radioimmunotherapy; hematooncology

Received Mar. 14, 2023; revision accepted May 8, 2023.

For correspondence or reprints, contact Andreas K. Buck (buck_a@ukw.de).

*Contributed equally to this work.

Published online Jun. 8, 2023.

J Nucl Med 2023; 64:1009–1016
DOI: 10.2967/jnumed.122.265199

Fueled by the favorable results of prospective clinical trials, recent years have witnessed a more widespread adoption of prostate-specific membrane antigen–targeted theranostics (*1,2*) or somatostatin receptor–targeted theranostics (*3,4*). These molecular image–guided therapeutic approaches have focused on solid tumor entities, such as prostate carcinoma or neuroendocrine neoplasms (*1,4*), but there is also a growing body of evidence of favorable outcomes in hematooncology (*5–7*). For instance, with roots back to the 80s (*8*), radioimmunotherapy exploits the concept of monoclonal antibodies labeled with radioisotopes, thereby allowing for β-emission mediated by antigenic binding sites that are overexpressed on the tumor cell surface but not in unaffected tissue (*9,10*). In this regard, radiolabeled CD20 antibodies that are conjugated to ^{90}Y or ^{131}I have been extensively evaluated in clinical trials (*5,6*), leading to overall response rates of up to 80% in patients with B-cell lymphoma (*6*) and durable remissions for years (*11*). Not surprisingly, these beneficial results of radioimmunotherapy then led to the Food and Drug Administration approval of nonmyeloablative antibody-mediated hot treatments, including ^{90}Y-ibritumomab tiuxetan (Zevalin; Acrotech Biopharma) for refractory low-grade follicular lymphoma or transformed B-cell non-Hodgkin lymphoma (NHL), as well as ^{131}I-tositumomab (Bexxar; GlaxoSmithKline) for rituximab-refractory follicular lymphoma (*12,13*). In patients scheduled for radioimmunotherapy, pretherapeutic imaging has also allowed estimation of absorbed doses to tumor and normal organs, thereby rendering radioimmunotherapy a true theranostic approach (*6,14*).

In the last decade, however, novel peptide-based tracers targeting the C-X-C motif chemokine receptor 4 (CXCR4) have been applied in varying hematooncologic scenarios, including ^{68}Ga-pentixafor

for imaging and ^{177}Lu-/^{90}Y-pentixather for treatment (*7,15,16*). In a physiologic context, CXCR4 may emerge as a promising theranostic target. First, it is crucially involved in homing of stem and progenitor cells and in hematopoiesis (*17,18*). Second, in a pathophysiologic context, this G-protein–coupled receptor and its ligand stromal cell–derived factor 1 also mediate metastatic spread via various subcellular mechanisms, including paracrine stimulation of angiogenesis or migration of CXCR4-positive tumor cells to other organs with increasing stromal cell–derived factor 1 expression (*17*). As such, CXCR4-seeking radiotracers for imaging and therapy can leverage these physiologic and pathophysiologic aspects to improve diagnostic accuracy or determine the chemokine receptor extent before CXCR4-directed radioligand therapy (RLT). Systemic whole-body irradiation can then bring about antilymphoma cell kill and bone marrow (BM) eradication for hematopoietic stem cell transplantation (HSCT), in particular when combined with established radioimmunotherapeutics (NHL; Fig. 1) (*7,19*).

In the present review, we provide an overview of extensively tested radiolabeled immunotherapies and introduce the growing clinical applications of novel CXCR4-mediated theranostics in hematooncology.

RADIOIMMUNOTHERAPY

Concept and Targets

In patients with lymphoma, varying targets on disease manifestations have been exploited on a cellular level to deliver β-emitting radiation. For B-cell lymphoma, these include designated antigens, in particular CD20, CD22, and CD37 (*9*). In this article, we focus on major clinical trials that triggered Food and Drug Administration approval for selected compounds, including ^{90}Y-ibritumomab tiuxetan and ^{131}I-tositumomab. We also highlight recent favorable results for ^{131}I-anti-CD45 antibodies (^{131}I-anti-CD45-apamistamab [Iomab-B]; Actinium Pharmaceuticals), which are currently being tested in a phase III trial on acute myeloid leukemia (AML) (*20*).

NHL

DeNardo et al. were among the first to apply fractionated radioimmunotherapy to refractory NHL that had been subjected to a mean of 4 previous treatment lines. ^{131}I-labeled Lym-1, a monoclonal antibody interacting with class II histocompatibility antigens, led to a complete response (CR) in 33%, with a mean duration of 1.2 y, along with activity-dependent myeloablation (*21*). Mainly spearheaded by Witzig et al., clinical trials on rituximab-refractory NHL led to the approval of CD20-targeting ^{90}Y-ibritumomab tiuxetan. Pretreatment with rituximab ensured B-cell depletion; radioimmunotherapy followed, which led to CR in 15% and a partial response (PR) in 59% (overall response rate, 74%) (*22*). Enrolling subjects with relapsed, refractory, or transformed CD20-positive NHL, the same research group reported on a phase III trial comparing ^{90}Y-ibritumomab tiuxetan with rituximab serving as a cold reference. Objective response rates were significantly higher for radioimmunotherapy (80%) than for rituximab (56%), with CR in 30% of the patients scheduled for ^{90}Y-ibritumomab tiuxetan (vs. only 16% in the rituximab arm). The radioimmunotherapy off-target effect most often recorded was BM toxicity with reversible myelosuppression (*6*). Figure 2A shows a patient with NHL achieving PR after injection of ^{90}Y-ibritumomab tiuxetan, along with the response rates in selected clinical trials evaluating radioimmunotherapy in lymphoma patients (Fig. 2B).

Kaminski et al. were among the first to evaluate the antilymphoma efficacy of the ^{131}I-labeled murine anti-CD20 monoclonal antibody tositumomab in patients with refractory or transformed NHL. When compared with a patient's last qualifying chemotherapy, a single injection of the hot compound led to disease control (PR or CR) in 65%, whereas the last chemotherapy achieved such a favorable outcome in only 28%, indicating that a single ^{131}I-tositumomab treatment is highly effective (*23*). In subjects experiencing progressive disease under rituximab, a phase II trial then demonstrated overall and CR rates of 65% and 38%, respectively. Median progression-free survival was more than 2 y in responders to radioimmunotherapy (*24*).

Follicular Lymphoma

In a phase III trial, patients with advanced stage III or IV follicular lymphoma in the first remission were randomized into a radioimmunotherapy arm (consisting of rituximab over 7 d, followed by ^{90}Y-ibritumomab tiuxetan) or no treatment. CD20-targeted radioimmunotherapy doubled progression-free survival, with a high PR-to-CR rate, leading to a final response rate of 87%. Again, the most commonly observed side effects were hematologic, with a grade of at least 3 in 8% (*25*). In a follow-up study evaluating long-term response, the time to the next treatment was 8.1 y for patients who had received radioimmunotherapy, a time that was significantly prolonged when compared with the control arm without treatment (time to next treatment, 3 y) (*26*). In a phase III trial initiated by the Southwest Oncology Group and by Cancer and Leukemia Group B (SWOG S0016), 554 treatment-naïve subjects with advanced follicular lymphoma received cyclophosphamide, doxorubicin, vincristine, and prednisone (CHOP) along with immunotherapy using cold rituximab (CHOP-R). In the comparative arm, CHOP was combined with ^{131}I-tositumomab consolidation (CHOP-radioimmunotherapy). Over 24 mo, however, both protocols achieved comparable progression-free survival (CHOP-R, 76%, vs. CHOP-radioimmunotherapy, 80%) and overall survival rates (CHOP-R, 97%, vs. CHOP-radioimmunotherapy, 93%) (*27*).

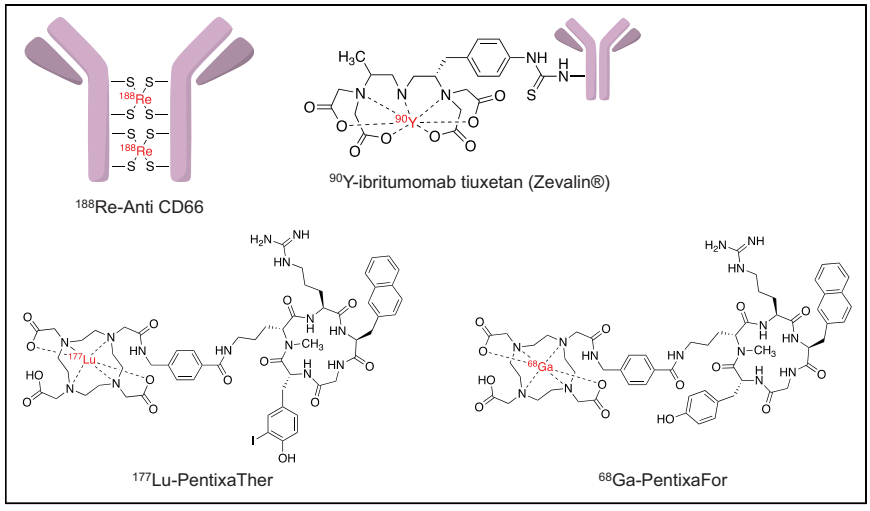

FIGURE 1. Structures of established (^{188}Re-CD66 antibodies, ^{90}Y-ibritumomab tiuxetan) and novel (^{68}Ga-pentixafor, ^{90}Y-pentixather) theranostic agents applied in hematooncology.

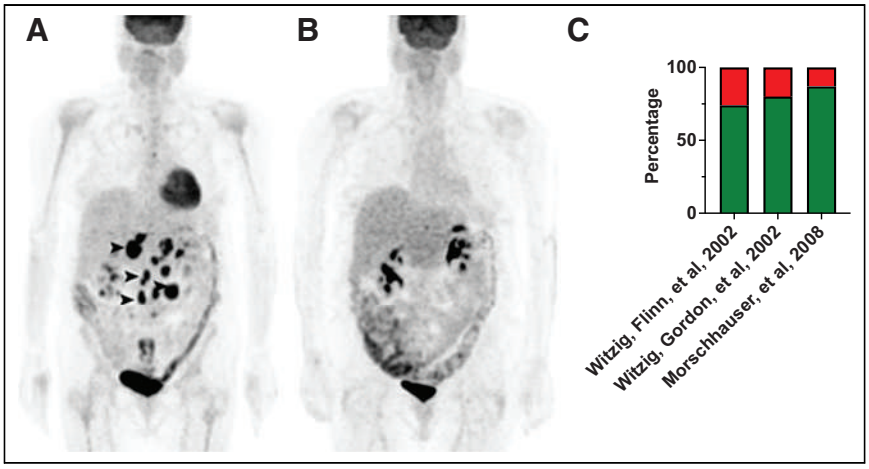

FIGURE 2. Patient with NHL treated with ^{90}Y-ibritumomab tiuxetan. (A) Pretherapeutic maximum-intensity projection derived from ^{18}F-FDG PET revealed multiple lymphoma manifestations in abdomen (arrowheads). (B) PR with inactive disease was achieved as visualized on ^{18}F-FDG PET at 3-mo follow-up. (Modified from (*67*).) (C) Response rates of major clinical trials using ^{90}Y-ibritumomab tiuxetan (*6,22,25*) (green indicates disease control depending on study's definition; red indicates uncontrolled disease).

Diffuse Large B-Cell Lymphoma

Recent efforts also turned toward the use of ^{90}Y-ibritumomab tiuxetan in diffuse large B-cell lymphoma patients for whom HSCT has failed—a clinical scenario associated with poor prognosis (*28*). As such, Lugtenburg et al. exploited synergistic effects using ^{90}Y-ibritumomab tiuxetan along with rituximab, prednisolone, etoposide, chlorambucil, and lomustine. Such combination treatments achieved 1-y survival in almost half of these difficult-to-treat patients (*28*).

Acute Myeloid Leukemia (AML)

Using a combination regimen of Iomab-B, fludarabine, and 2 Gy of total-body irradiation, Pagel et al. reported on 58 patients (with either AML or high-risk myelodysplastic syndrome) in a phase II trial demonstrating complete remission in all subjects, followed by successful HSCT (*29*). The currently recruiting phase III SIERRA trial will then shed light on the beneficial use of Iomab-B in relapsed and refractory AML by comparing this agent with conventional care. Because of an increasing rate of comorbidities, HSCT in the elderly AML patient is conducted with caution (*30*), and in the SIERRA trial, this issue will be addressed. Relapsed or refractory AML patients at least 55 y old receive either conventional care or Iomab-B, and subjects treated with conventional care can cross over to radioimmunotherapy. An interim analysis reported on 63 patients allocated to the conventional-care arm, and of those, 11 (17.4%) achieved CR and were then scheduled for HSCT. The remaining 52 subjects (83%) did not achieve a response; thus, 38 crossed over to Iomab-B. All patients with Iomab-B then received HSCT, which led to engraftment. This was independent of whether they had initially been randomized into the Iomab-B arm (60/60; 100%) or whether they crossed over (38/38; 100%). The rate of sepsis was also lower in the radioimmunotherapy group than in subjects with conventional-care–mediated HSCT. As such, this interim report indicated that Iomab-B conditioning enabled HSCT even in subjects for whom approved conventional care failed, led to successful neutrophile reconstitution, and was associated with fewer side effects than conventional-care–based transplantation (*31*).

Reasons for Declining Use of Radioimmunotherapy

Both ^{90}Y-ibritumomab tiuxetan and ^{131}I-tositumomab are associated with extensive costs—approximately $25,000 for a single injection—leading to reimbursement challenges in the United States and Europe. Despite the remarkable outcome benefits, this obstacle may partially explain the declining application of radioimmunotherapy using ^{90}Y-ibritumomab tiuxetan or ^{131}I-tositumomab in recent years (*32*). Radioimmunotherapy can also cause long-term adverse effects on BM function, including a severe decrease in platelets and leukocytes or the occurrence of myelodysplastic syndrome in selected cases (*33*). Moreover, in recent years, novel and effective therapies have also entered the clinical arena, such as CAR T-cell therapies or bispecific T-cell engagers (*34*).

PEPTIDE-MEDIATED THERANOSTICS

Concept and Targets

Mediating angiogenesis and tumor cell dissemination along with resistance to treatment, chemokine receptors have emerged as an attractive pan-hematologic cancer target (*17,35*). For instance, in marginal zone lymphoma (MZL), AML, B-cell chronic lymphocytic leukemia, or multiple myeloma (MM), CXCR4 expression may have prognostic value (*36–39*). Targeting this chemokine receptor in patients with hematologic neoplasms may offer a better rate of detection of putative sites of disease or even determine a high risk of therapeutic or chemotherapeutic resistance.

First, to evaluate the diagnostic performance, a recent study pooled retrospective data on the PET agent ^{68}Ga-pentixafor in 690 subjects scheduled for 777 scans. Among all tested tumor entities (in total, $n = 35$), hematologic malignancies revealed the highest in vivo CXCR4 expression (determined by SUV_{max}) and elevated target-to-background ratios. For solid cancers, however, only small cell lung and adrenocortical carcinomas showed an increased SUV_{max} and target-to-background ratio (Fig. 3) (*40*). As such, ^{68}Ga-pentixafor may emerge as a pan-hematologic tumor agent, in particular for MM, MZL, and leukemia.

On the basis of these favorable imaging results, patients were also scheduled for chemokine receptor–directed RLT. In this regard, administration of pentixather causes myeloablation due to CXCR4-moderated maintenance of hematopoietic stem progenitor cells in the BM (*41*). Such a pentixather-mediated myeloablation, however, can be used to prepare the patient for HSCT as an integral component of the treatment algorithm. Pretherapeutic dosimetry using ^{177}Lu-pentixather allowed for a scintigraphically visible accumulation of radiotracer in normal organs. Absorbed doses to the hepatic or splenic parenchyma were acceptable, with a range of 0.6–0.7 Gy/GBq, whereas for the kidneys, as the dose-limiting organ, the reported dose was 0.9 Gy/GBq of ^{177}Lu-pentixather, corresponding to 3.8 Gy/GBq of ^{90}Y-pentixather (*42*). The commonly applied limit of 23 Gy for renal tissue is therefore not exceeded (*43*), which would be reached after 20–30 GBq of ^{177}Lu-pentixather (5–8 GBq of ^{90}Y-pentixather) (*42*). These doses, however, could be reduced through coinfusion of nephroprotective amino acids (*44*), and chemokine receptor–directed RLT is also normally restricted to 1 cycle. On-target doses in lymphoma tissue are substantial (*42*) and, thus, may also be associated with other relevant off-target effects due to lymphoma cell kill. For instance, Maurer et al. reported side effects among a broad range of patients

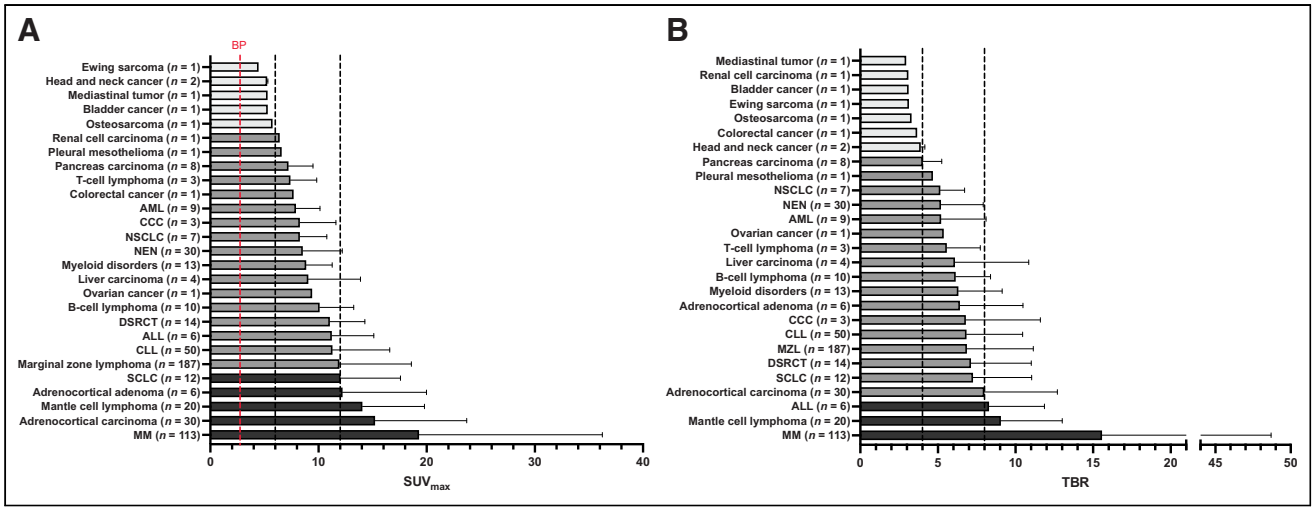

FIGURE 3. SUV_{max} (A) and target-to-background ratios (B) for 690 patients scanned with ^{68}Ga-pentixafor PET/CT for assessment of in vivo CXCR4 extent. Black dashed lines show SUV_{max} of 6 and 12 and target-to-background ratio of 4 and 8, respectively. ALL = acute lymphoblastoid leukemia; BP = blood pool; CCC = cholangiocarcinoma; CLL = chronic lymphocytic leukemia; DSRCT = desmoplastic small round cell tumor; NEN = neuroendocrine neoplasm; NSCLC = non–small cell lung carcinoma; SCLC = small cell lung carcinoma; adrenocortical adenoma = aldosterone-producing adrenocortical adenoma. (Modified from (*40*).)

with hematologic malignancies who were scheduled for last-line CXCR4-directed RLT in a salvage setting. Right after treatment, vital signs were normal, indicative of no acute toxicity. Further corroborating previous reports, however, a substantial fraction of patients died from neutropenic sepsis or progressive disease before successful engraftment after HSCT (*45*). To avoid these lethal events, countermeasures have been incorporated, including protocols to prevent tumor lysis syndrome before initiation of RLT (*19*). Another elegant approach exploits the physical properties of the used radionuclides. The short half-life of ^{90}Y (2.7 d) led to significantly reduced intervals between CXCR4 RLT and the onset of conditioning regimens, particularly when compared with the β-emitting alternative ^{177}Lu (6.7 d). The aplastic phase was thus reduced, thereby avoiding life-threatening infections (*45*).

MM

In MM, CXCR4 triggers the onset of distant manifestations, such as by osteoclastogenesis and multidrug resistance (*46*), suggesting that targeting of this receptor may provide not only an improved diagnostic read-out but also prognostic capabilities (*39*). When subjects who were scheduled for a lesion-based comparison of ^{18}F-FDG and ^{68}Ga-pentixafor were investigated, the latter agent detected more MM manifestations in 21% (the 2 agents were equal in 42%, and ^{18}F-FDG was superior in the remaining 37%). CXCR4-targeted PET positivity was also associated with survival, with negative findings on PET being linked to improved outcome. This was even more pronounced for subjects showing no extramedullary lesions on ^{68}Ga-pentixafor PET/CT. A substantially elevated SUV_{max} has been recorded, indicating that CXCR4-targeted RLT is feasible in MM (*47*). Providing further evidence of the role of ^{68}Ga-pentixafor as a noninvasive biomarker of disease activity, a recent prospective trial reported associations between uptake in disease sites with end-organ damage and the extent of β2-microglobulin, serum free light chains, and urine light chains (*48*). We also investigated the usefulness of CXCR4-directed molecular imaging in the context of pseudoprogression under CAR T-cell therapy as a strategy to disentangle immune-mediated causes for such flare-ups from true progression. Relative to ^{18}F-FDG, chemokine receptor PET was able to differentiate between an autoimmune phenomenon and a true relapse, with single-cell RNA sequencing of biopsy samples serving as a reference. First, 3 mo after CAR T-cell therapy, ^{68}Ga-pentixafor PET in the lung was negative. Respective biopsies then revealed Th17.1 T-helper cells associated with a sarcoidotic reaction, suggestive of pseudoprogression. Six months after treatment, however, ^{68}Ga-pentixafor PET was then positive in novel extramedullary lesions, which also showed high CXCR4 expression on single-cell RNA sequencing, indicative of a true relapse (Fig. 4) (*49*).

Given the intense radiotracer accumulation after administration of ^{68}Ga-pentixafor in MM, the theranostic counterpart ^{177}Lu-pentixather was first applied in 3 subjects with heavily pretreated, advanced MM with intra- and extramedullary manifestations. In 2 of these individuals, a short-term response with reduced uptake on follow-up ^{18}F-FDG PET/CT was recorded, indicative of therapeutic benefit (*50*). Another 8 MM patients were then scheduled for CXCR4-directed RLT, and myeloma doses of up to 70 Gy were reported, with CR in 1 patient and PR in 5 subjects (overall survival, 7.5 mo). Another patient, however, died of sepsis during the aplastic phase, whereas the remaining individual experienced lethal tumor lysis caused by RLT (*51*).

MZL

In a recent ex vivo analysis investigating extranodal MZL (or mucosa-associated lymphoid tissue [MALT] lymphomas), chemokine receptor expression was recorded in virtually all cases, whereas somatostatin receptors (as another theranostic target) were absent in half the samples (*52*). Duell et al. were among the first to evaluate the diagnostic benefit for imaging of MZL and investigated varying subtypes, including 22 patients with extranodal, nodal, and splenic origin. When compared with guideline-compatible routine diagnostic procedures (colonoscopy, BM biopsy, and CT as part of hybrid imaging using ^{18}F-FDG PET), ^{68}Ga-pentixafor detected all true-positive and all true-negative cases (22/22) whereas conventional staging was correct in only 17 of the investigated subjects (Fig. 5).

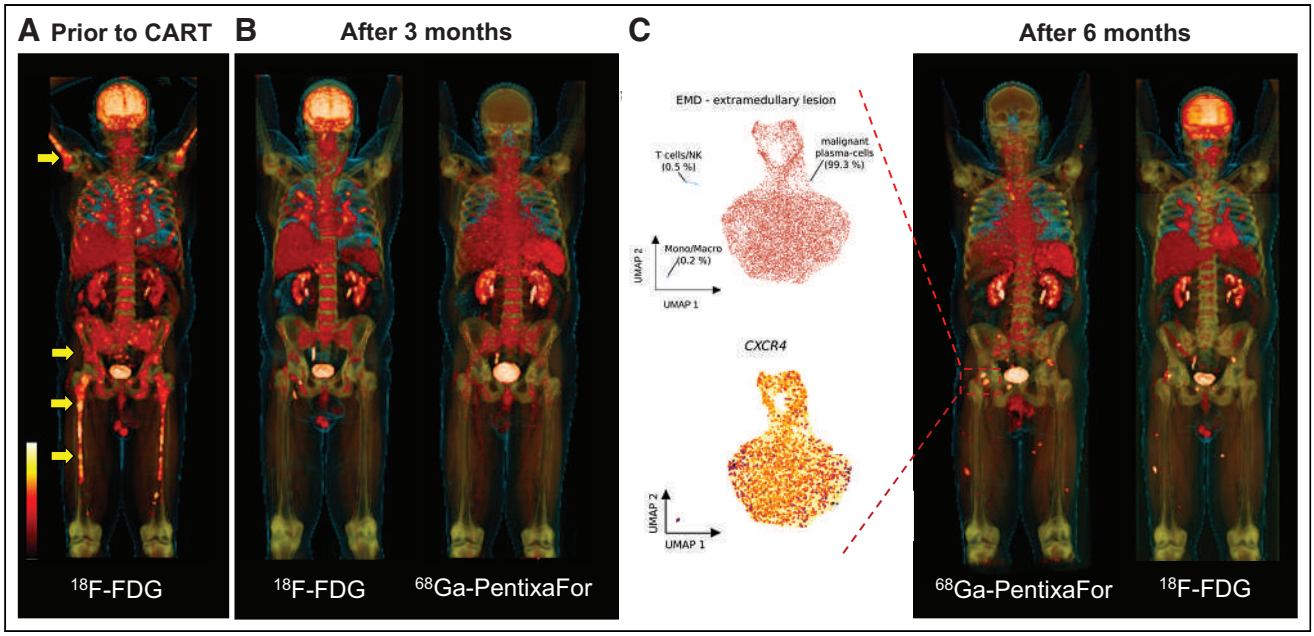

FIGURE 4. CXCR4-targeting ^{68}Ga-pentixafor PET/CT for dissecting true relapse and autoimmune-mediated side effects in MM patient scheduled for B-cell maturation antigen–targeting CAR T-cell therapy (idecabtagene vicleucel). (A) Before CAR T-cell therapy, ^{18}F-FDG showed osseous lesions (arrows). (B) On restaging 3 mo after CAR T-cell therapy, myeloma clearance in skeleton was observed on maximum-intensity projections of ^{18}F-FDG and ^{68}Ga-pentixafor PET. Only ^{18}F-FDG, however, revealed uptake in pulmonary system; no such radiotracer accumulation was observed on CXCR4-directed imaging. Single-cell RNA sequencing on lung specimen demonstrated upregulation of Th17.1-positive T cells, which are associated with autoimmune diseases such as sarcoidosis. (C) Six months after CAR T-cell therapy, both imaging modalities showed novel manifestations (red box) suggestive of relapse. ^{68}Ga-pentixafor PET–guided biopsy was conducted, and single-cell RNA sequencing then revealed malignant plasma cells along with increased CXCR4 expression (leftmost panel in C). CART = CAR T-cell therapy. (Modified from (*15*).)

The latter radiotracer identified advanced disease (Ann Arbor stage ≥ 3) in more than half the patients, which led to an upstaging in 7 of 22 (31.8%) and a change in treatment in 8 of 22 (36.4%). These modifications in oncologic management included intensified treatment in 6 of 8 (75%) (*53*). Future studies should also evaluate the role of assessing treatment response (*53*), such as under chemotherapeutic regimens (Fig. 6). These retrospective investigations triggered further prospective phase I/II trials focusing on MALT lymphomas.

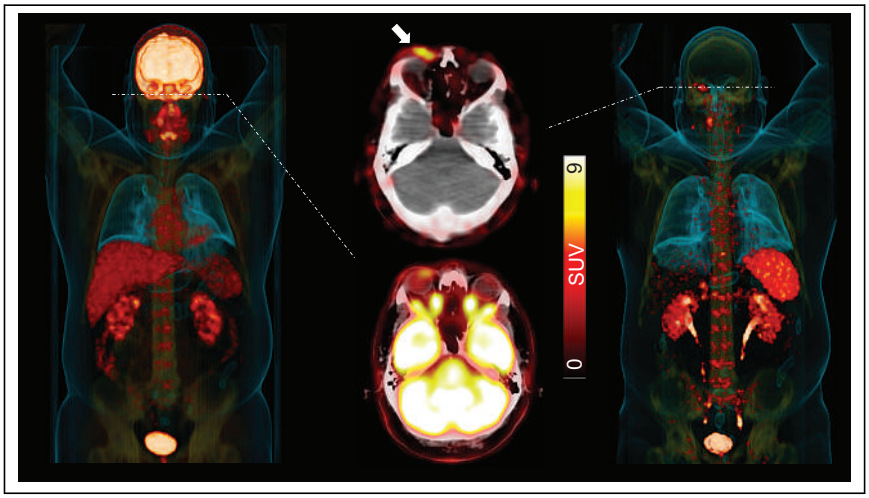

FIGURE 5. MZL patient with additional periorbital disease site (white arrow) identified on ^{68}Ga-pentixafor PET/CT. On ^{18}F-FDG maximum-intensity projection (MIP, left) and transaxial PET/CT (middle, bottom), periorbital manifestation was masked by normal biodistribution in brain. On CXCR4-targeted ^{68}Ga-pentixafor (MIP, right; transaxial PET/CT, middle top), this additional site of disease can be identified because of missing brain accumulation. (Modified from (*53*).)

Mayerhoefer et al. enrolled 26 patients with a gastric disease origin and determined the value of CXCR4 PET/CT for assessing incomplete remission on follow-up after guideline-compatible eradication of *Helicobacter pylori* (*54,55*). ^{68}Ga-pentixafor PET and MRI were conducted on all subjects, and comparison with biopsy-derived specimens revealed accuracy of 97%, specificity of 100%, and a slightly lower sensitivity of 95% (*54,55*). Thus, to identify residual disease during follow-up, ^{68}Ga-pentixafor PET may replace the currently recommended intense diagnostic work-up of invasive procedures, including endoscopy and histologic assessments twice per year (*54,55*). To date, however, CXCR4-directed RLT has not been applied to MZL.

Leukemia and Lymphoma

Patients with AML may benefit from CXCR4-directed molecular imaging because of the origin of this disease in the protective BM niche, along with the antileukemia effects of CXCR4 antagonists (*56,57*). Herhaus et al. first investigated the primary blasts of patients and reported on an association of blast counts with CXCR4 upregulation using flow cytometry. In a dedicated animal model, ^{68}Ga-pentixafor small-animal PET was positive only in CXCR-positive, not CXCR4-negative, xenografts, whereas in patients with AML, PET positivity was noted in half the subjects, which was further corroborated on MRI (*58*). PET positivity in

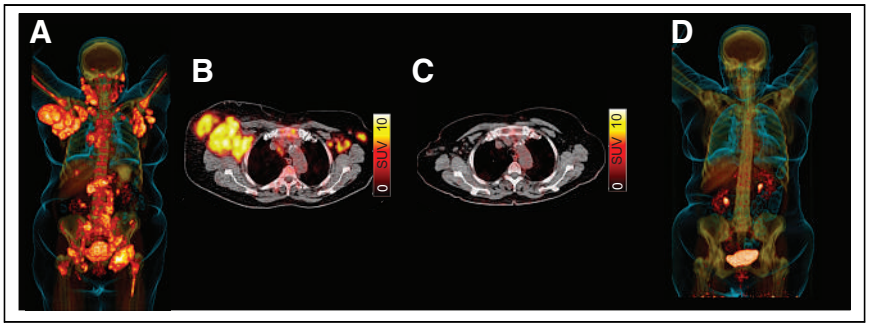

FIGURE 6. Patient with MZL and scheduled for rituximab-bendamustine. (A and B) Maximum-intensity projection (A) of ^{68}Ga-pentixafor PET revealed multiple lymphoma manifestations, in particular in axilla as seen on transaxial PET/CT (B). (C and D) After treatment, complete remission was achieved on follow-up imaging, indicating that CXCR4-targeted PET/CT may be useful to monitor treatment response. (Modified from (*53*).)

AML, however, may be exploited to identify candidates for disrupting CXCR4/CXCL12 interactions, such as plerixafor as an adjunct to chemotherapeutic regimens (*59,60*). In a prospective setup, ^{68}Ga-pentixafor PET/MRI was also used in chronic lymphocytic leukemia (*61*), as CXCR4 has been advocated to play a crucial role in BM infiltration in this leukemia subtype (*62*). When compared with solid tumors or other types of hematologic malignancies (MALT), the highest SUVs were recorded in the BM in this patient population, indicating that ^{68}Ga-pentixafor may be useful for biopsy planning (*61*).

CXCR4-directed RLT was then also applied to AML and patients with lymphoma. In patients with relapsed T-cell lymphoma, doses in extramedullary lesions ranged from 17.4 to 33.2 Gy, exerting relevant antilymphoma efficacy as revealed by longitudinal monitoring of lactate dehydrogenase. All 4 treated patients were also scheduled for chemotherapeutic conditioning or high-dose therapy. Lactate dehydrogenase had already peaked shortly after injection of ^{177}Lu-pentixather (but before the onset of additional conditioning), suggesting a direct antilymphoma effect mediated by CXCR4 RLT. One of 4 patients died of septicemia 16 d after RLT, whereas the remaining 3 achieved disease control (PR or CR) with successful leukocyte reconstitution during follow-up. Patients with a favorable outcome were also scheduled for additional radioimmunotherapy using ^{188}Re-labeled anti-CD66 (Fig. 7) (*7*). Also investigating a small case series of 6 patients with relapsed diffuse large B-cell lymphoma, Lapa et al. reported that 2 died of central nervous system aspergillosis and sepsis. In the remaining subjects, PR was again noted in those individuals who also received concomitant radioimmunotherapy. RLT-mediated eradication of the BM niche then also led to full engraftment after HSCT (*63*). The respective pretherapeutic dosimetry and baseline ^{68}Ga-pentixafor PET results for a patient with diffuse large B-cell lymphoma treated with such a tandem therapy (^{90}Y-pentixather and ^{90}Y-ibritumomab tiuxetan) is provided in Figure 8. PR was then observed 4 mo after treatment.

Last, in acute leukemia, an observational study reported on 3 subjects also treated with pentixather. Only in the patient who also received additional CD66-targeted radioimmunotherapy was long-lasting CR after RLT achieved (*64*).

Future Directions

During the annual conference of the German Society for Hematology and Oncology in 2022, an expert panel of hematooncologists and nuclear medicine physicians discussed potential clinical applications of CXCR4-targeted theranostics. There were several key findings. First, CXCR4-targeted PET/CT may have the potential to emerge as a novel diagnostic reference standard in patients with MZL, including its use for disease monitoring, such as for identifying individuals prone to transformation to large B-cell lymphoma. Second, aggressive lymphomas with involvement of

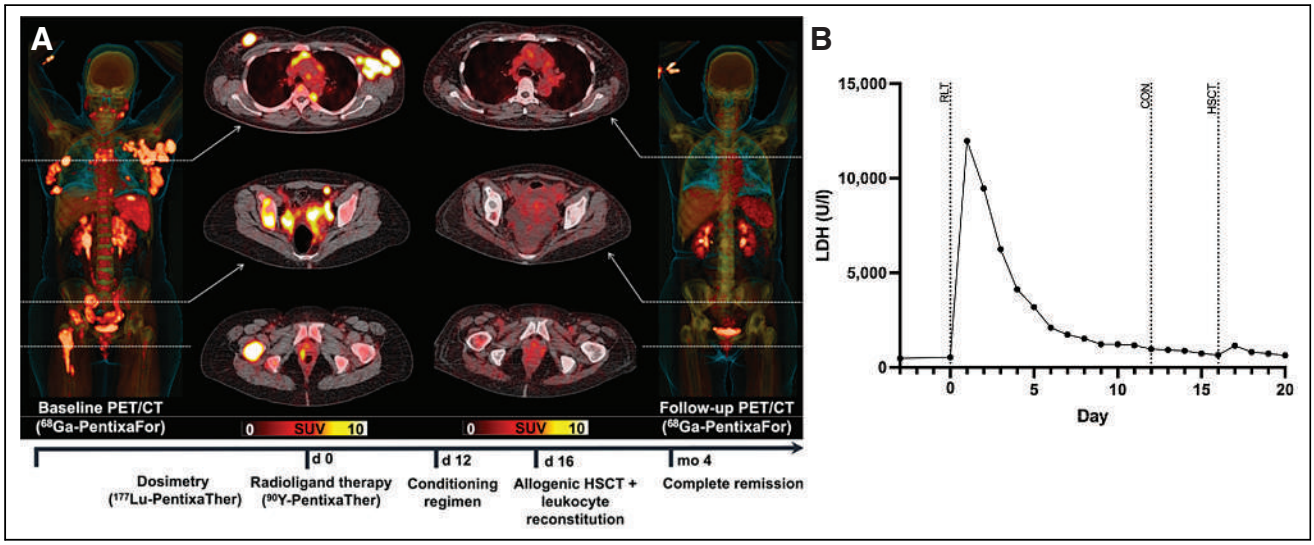

FIGURE 7. Patient with relapsed T-cell lymphoma treated with CXCR4-directed RLT and achieving complete remission. (A) Maximum-intensity projection and transaxial ^{68}Ga-pentixafor PET/CT at baseline showed extensive disease in skeleton and lymph nodes. Four months after treatment, CR was noted on follow-up ^{68}Ga-pentixafor PET/CT. (B) Lactate dehydrogenase as surrogate marker of antilymphoma efficacy peaked directly after RLT and then rapidly declined till conditioning regimen and HSCT, thereby suggesting direct antilymphoma effect caused by CXCR4 RLT. CON = conditioning regimen; LDH = lactate dehydrogenase. (Modified from (*7*).)

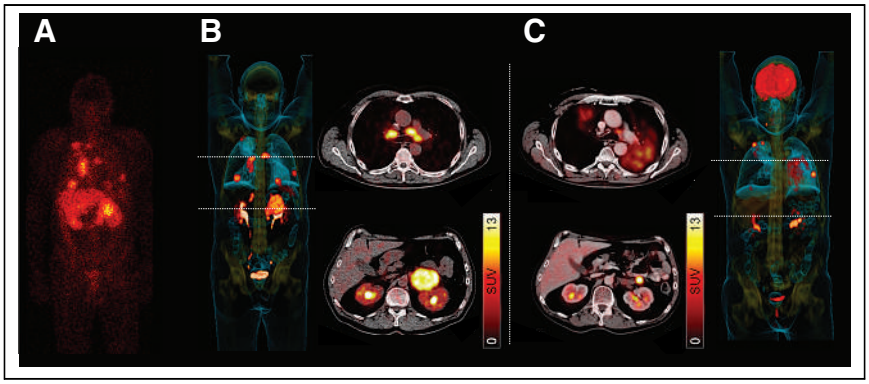

FIGURE 8. Synergistic effects of radioimmunotherapy and CXCR4-targeted RLT in patient with heavily pretreated diffuse large B-cell lymphoma. (A) Pretherapeutic scintigraphy 24 h after ^{177}Lu-pentixafor injection revealed multiple disease sites, allowing for calculations of absorbed doses. (B) Baseline maximum-intensity projection and transaxial ^{68}Ga-pentixafor PET/CT showed multiple CXCR4-expressing mediastinal and abdominal lesions. (C) ^{90}Y-ibritumomab tiuxetan combined with ^{90}Y-pentixather was initiated. On ^{18}F-FDG PET/CT 4 mo later, sites of disease were smaller, indicating PR. (Modified from (*63*).)

the central nervous system may benefit from CXCR4-directed PET/CT, as the use of ^{18}F-FDG is hampered by the physiologic biodistribution of ^{18}F-FDG in the central nervous system (*65*). Third, CXCR4-targeted RLT may be most promising in patients with T-cell lymphoma, as case series reported favorable outcomes in these otherwise difficult-to-treat patients (*7,66*). Finally, the expert panel concluded that prospective studies on imaging of MZL and treatment of T-cell lymphoma are urgently needed.

Taken together, increasing levels of evidence on chemokine receptor–targeted imaging and therapy will guide toward implementation in national and international guidelines, ultimately leading to more widespread clinical use of CXCR4-directed theranostics. Titration studies should be conducted as a first step to determine the most appropriate activity for RLT (for both antilymphoma and myeloablative effects or for lymphoma cell kill only). These should be followed by multicenter phase II trials on the safety and efficacy of CXCR4 RLT alone. Last, competitive or additive concepts should be tested, such as through sequential tandem treatment approaches using chemokine receptor RLT and CAR T-cell therapies (*15*).

CONCLUSION

Given the favorable results in major clinical trials, antibody-mediated radioimmunotherapy has been approved by the Food and Drug Administration for patients with refractory follicular lymphoma or transformed B-cell NHL. Inadequate reimbursement in Europe and the United States, however, has restricted more widespread adoption in clinical routine. The interim results of the SIERRA phase III trial, however, showed a favorable outcome from using Iomab-B in relapsed or refractory AML and may soon trigger a revival of radioimmunotherapy. CXCR4-targeted molecular imaging has been extensively evaluated across different hematologic and solid neoplasms, and the results indicate that ^{68}Ga-pentixafor may emerge as a novel pan-hematologic tumor agent. For CXCR4-targeted PET/CT, promising applications include MM and MZL, whereas refractory T-cell lymphoma may benefit from CXCR4 RLT. Patients treated with chemokine receptor–targeting radiotherapeutics also experience the desired myeloablation, which then allows scheduling for HSCT. Such an eradication of the BM niche is then an integral component of the therapeutic algorithm beyond antilymphoma effects in selected cases. Last, observational studies also hinted that synergism may be achieved when combining CD20- or CD66-directed radioimmunotherapy with CXCR4-targeted RLT in advanced disease.

REFERENCES

1. Sartor O, de Bono J, Chi KN, et al. Lutetium-177-PSMA-617 for metastatic castration-resistant prostate cancer. *N Engl J Med.* 2021;385:1091–1103.
2. Hofman MS, Emmett L, Sandhu S, et al. [^{177}Lu]Lu-PSMA-617 versus cabazitaxel in patients with metastatic castration-resistant prostate cancer (TheraP): a randomised, open-label, phase 2 trial. *Lancet.* 2021; 397:797–804.
3. Strosberg JR, Caplin ME, Kunz PL, et al. ^{177}Lu-Dotatate plus long-acting octreotide versus high-dose long-acting octreotide in patients with midgut neuroendocrine tumours (NETTER-1): final overall survival and long-term safety results from an open-label, randomised, controlled, phase 3 trial. *Lancet Oncol.* 2021;22:1752–1763.
4. Strosberg J, El-Haddad G, Wolin E, et al. Phase 3 trial of ^{177}Lu-Dotatate for midgut neuroendocrine tumors. *N Engl J Med.* 2017;376:125–135.
5. Kaminski MS, Tuck M, Estes J, et al. ^{131}I-tositumomab therapy as initial treatment for follicular lymphoma. *N Engl J Med.* 2005;352:441–449.
6. Witzig TE, Gordon LI, Cabanillas F, et al. Randomized controlled trial of yttrium-90-labeled ibritumomab tiuxetan radioimmunotherapy versus rituximab immunotherapy for patients with relapsed or refractory low-grade, follicular, or transformed B-cell non-Hodgkin's lymphoma. *J Clin Oncol.* 2002;20:2453–2463.
7. Buck AK, Grigoleit GU, Kraus S, et al. C-X-C motif chemokine receptor 4-targeted radioligand therapy in patients with advanced T-cell lymphoma. *J Nucl Med.* 2023;64:34–39.
8. DeNardo SJ, DeNardo GL, O'Grady LF, et al. Treatment of a patient with B cell lymphoma by I-131 LYM-1 monoclonal antibodies. *Int J Biol Markers.* 1987;2: 49–53.
9. Larson SM, Carrasquillo JA, Cheung NK, Press OW. Radioimmunotherapy of human tumours. *Nat Rev Cancer.* 2015;15:347–360.
10. Witzig TE. Efficacy and safety of ^{90}Y ibritumomab tiuxetan (Zevalin) radioimmunotherapy for non-Hodgkin's lymphoma. *Semin Oncol.* 2003;30:11–16.
11. Gordon LI, Witzig T, Molina A, et al. Yttrium 90-labeled ibritumomab tiuxetan radioimmunotherapy produces high response rates and durable remissions in patients with previously treated B-cell lymphoma. *Clin Lymphoma.* 2004;5:98–101.
12. Friedberg JW, Fisher RI. Iodine-131 tositumomab (Bexxar): radioimmunoconjugate therapy for indolent and transformed B-cell non-Hodgkin's lymphoma. *Expert Rev Anticancer Ther.* 2004;4:18–26.
13. Sánchez Ruiz AC, de la Cruz-Merino L, Provencio Pulla M. Role of consolidation with yttrium-90 ibritumomab tiuxetan in patients with advanced-stage follicular lymphoma. *Ther Adv Hematol.* 2014;5:78–90.
14. Larson SM, Pentlow KS, Volkow ND, et al. PET scanning of iodine-124-3F9 as an approach to tumor dosimetry during treatment planning for radioimmunotherapy in a child with neuroblastoma. *J Nucl Med.* 1992;33:2020–2023.
15. Leipold AM, Werner RA, Dull J, et al. Th17.1 cell driven sarcoidosis-like inflammation after anti-BCMA CAR T cells in multiple myeloma. *Leukemia.* 2023;37: 650–658.
16. Lewis R, Habringer S, Kircher M, et al. Investigation of spleen CXCR4 expression by [^{68}Ga]pentixafor PET in a cohort of 145 solid cancer patients. *EJNMMI Res.* 2021;11:77.
17. Chatterjee S, Behnam Azad B, Nimmagadda S. The intricate role of CXCR4 in cancer. *Adv Cancer Res.* 2014;124:31–82.
18. Karpova D, Ritchey JK, Holt MS, et al. Continuous blockade of CXCR4 results in dramatic mobilization and expansion of hematopoietic stem and progenitor cells. *Blood.* 2017;129:2939–2949.
19. Buck AK, Serfling SE, Lindner T, et al. CXCR4-targeted theranostics in oncology. *Eur J Nucl Med Mol Imaging.* 2022;49:4133–4144.
20. Gyurkocza B, Natgh R, Seropian S, et al. Clinical experience in the randomized phase 3 SIERRA trial: anti-CD45 iodine (^{131}I) apamistamab [Iomab-B] conditioning enables hematopoietic cell transplantation with successful engraftment and acceptable safety in patients with active, relapsed/refractory AML not responding to targeted therapies. *Blood.* 2021;138:1791–1793.

21. DeNardo GL, DeNardo SJ, Goldstein DS, et al. Maximum-tolerated dose, toxicity, and efficacy of ^{131}I-Lym-1 antibody for fractionated radioimmunotherapy of non-Hodgkin's lymphoma. *J Clin Oncol.* 1998;16:3246–3256.
22. Witzig TE, Flinn IW, Gordon LI, et al. Treatment with ibritumomab tiuxetan radioimmunotherapy in patients with rituximab-refractory follicular non-Hodgkin's lymphoma. *J Clin Oncol.* 2002;20:3262–3269.
23. Kaminski MS, Zelenetz AD, Press OW, et al. Pivotal study of iodine I 131 tositumomab for chemotherapy-refractory low-grade or transformed low-grade B-cell non-Hodgkin's lymphomas. *J Clin Oncol.* 2001;19:3918–3928.
24. Horning SJ, Younes A, Jain V, et al. Efficacy and safety of tositumomab and iodine-131 tositumomab (Bexxar) in B-cell lymphoma, progressive after rituximab. *J Clin Oncol.* 2005;23:712–719.
25. Morschhauser F, Radford J, Van Hoof A, et al. Phase III trial of consolidation therapy with yttrium-90-ibritumomab tiuxetan compared with no additional therapy after first remission in advanced follicular lymphoma. *J Clin Oncol.* 2008;26:5156–5164.
26. Morschhauser F, Radford J, Van Hoof A, et al. ^{90}Yttrium-ibritumomab tiuxetan consolidation of first remission in advanced-stage follicular non-Hodgkin lymphoma: updated results after a median follow-up of 7.3 years from the international, randomized, phase III first-line indolent trial. *J Clin Oncol.* 2013;31:1977–1983.
27. Press OW, Unger JM, Rimsza LM, et al. Phase III randomized intergroup trial of CHOP plus rituximab compared with CHOP chemotherapy plus ^{131}iodine-tositumomab for previously untreated follicular non-Hodgkin lymphoma: SWOG S0016. *J Clin Oncol.* 2013;31:314–320.
28. Lugtenburg PJ, Zijlstra JM, Doorduijn JK, et al. Rituximab-PECC induction followed by ^{90}Y-ibritumomab tiuxetan consolidation in relapsed or refractory DLBCL patients who are ineligible for or have failed ASCT: results from a phase II HOVON study. *Br J Haematol.* 2019;187:347–355.
29. Pagel JM, Gooley TA, Rajendran J, et al. Allogeneic hematopoietic cell transplantation after conditioning with ^{131}I-anti-CD45 antibody plus fludarabine and low-dose total body irradiation for elderly patients with advanced acute myeloid leukemia or high-risk myelodysplastic syndrome. *Blood.* 2009;114:5444–5453.
30. Deeg HJ. Not all patients with AML over 60 years of age should be offered early allogeneic stem cell transplantation. *Blood Adv.* 2022;6:1623–1627.
31. Gyurkocza B, Nath R, Seropian S, et al. High rates of transplantation in the phase III Sierra trial utilizing anti-CD45 (iodine) ^{131}I-apamistamab (Iomab-B) conditioning with successful engraftment and tolerability in relapsed refractory (R/R) acute myeloid leukemia (AML) patients after lack of response to conventional care and targeted therapies. Tandem Meetings website. https://tandem.confex.com/tandem/2022/meetingapp.cgi/Paper/19041. Published April, 23, 2022. Accessed May 18 2023.
32. Ostuni E, Taylor MRG. Commercial and business aspects of alpha radioligand therapeutics. *Front Med (Lausanne).* 2023;9:1070497.
33. Hohloch K, Delaloye AB, Windemuth-Kieselbach C, et al. Radioimmunotherapy confers long-term survival to lymphoma patients with acceptable toxicity: registry analysis by the International Radioimmunotherapy Network. *J Nucl Med.* 2011;52:1354–1360.
34. Kegyes D, Constantinescu C, Vrancken L, et al. Patient selection for CAR T or BiTE therapy in multiple myeloma: which treatment for each patient? *J Hematol Oncol.* 2022;15:78.
35. Sison EA, McIntyre E, Magoon D, Brown P. Dynamic chemotherapy-induced upregulation of CXCR4 expression: a mechanism of therapeutic resistance in pediatric AML. *Mol Cancer Res.* 2013;11:1004–1016.
36. Deutsch AJ, Steinbauer E, Hofmann NA, et al. Chemokine receptors in gastric MALT lymphoma: loss of CXCR4 and upregulation of CXCR7 is associated with progression to diffuse large B-cell lymphoma. *Mod Pathol.* 2013;26:182–194.
37. Peled A, Tavor S. Role of CXCR4 in the pathogenesis of acute myeloid leukemia. *Theranostics.* 2013;3:34–39.
38. Barretina J, Junca J, Llano A, et al. CXCR4 and SDF-1 expression in B-cell chronic lymphocytic leukemia and stage of the disease. *Ann Hematol.* 2003;82:500–505.
39. Bao L, Lai Y, Liu Y, et al. CXCR4 is a good survival prognostic indicator in multiple myeloma patients. *Leuk Res.* 2013;37:1083–1088.
40. Buck AK, Haug A, Dreher N, et al. Imaging of C-X-C motif chemokine receptor 4 expression in 690 patients with solid or hematologic neoplasms using ^{68}Ga-pentixafor PET. *J Nucl Med.* 2022;63:1687–1692.
41. Ratajczak MZ, Serwin K, Schneider G. Innate immunity derived factors as external modulators of the CXCL12-CXCR4 axis and their role in stem cell homing and mobilization. *Theranostics.* 2013;3:3–10.
42. Hänscheid H, Schirbel A, Hartrampf P, et al. Biokinetics and dosimetry of ^{177}Lu-pentixather. *J Nucl Med.* 2022;63:754–760.
43. Emami B, Lyman J, Brown A, et al. Tolerance of normal tissue to therapeutic irradiation. *Int J Radiat Oncol Biol Phys.* 1991;21:109–122.
44. Bodei L, Mueller-Brand J, Baum RP, et al. The joint IAEA, EANM, and SNMMI practical guidance on peptide receptor radionuclide therapy (PRRNT) in neuroendocrine tumours. *Eur J Nucl Med Mol Imaging.* 2013;40:800–816.
45. Maurer S, Herhaus P, Lippenmeyer R, et al. Side effects of CXC-chemokine receptor 4-directed endoradiotherapy with pentixather before hematopoietic stem cell transplantation. *J Nucl Med.* 2019;60:1399–1405.
46. Ullah TR. The role of CXCR4 in multiple myeloma: cells' journey from bone marrow to beyond. *J Bone Oncol.* 2019;17:100253.
47. Lapa C, Schreder M, Schirbel A, et al. [^{68}Ga]pentixafor-PET/CT for imaging of chemokine receptor CXCR4 expression in multiple myeloma: comparison to [^{18}F]FDG and laboratory values. *Theranostics.* 2017;7:205–212.
48. Pan Q, Cao X, Luo Y, Li J, Feng J, Li F. Chemokine receptor-4 targeted PET/CT with ^{68}Ga-pentixafor in assessment of newly diagnosed multiple myeloma: comparison to ^{18}F-FDG PET/CT. *Eur J Nucl Med Mol Imaging.* 2020;47:537–546.
49. Leipold AM, Werner RA, Dull J, et al. Th17.1 cell driven sarcoidosis-like inflammation after anti-BCMA CAR T cells in multiple myeloma. *Leukemia.* 2023;37:650–658.
50. Herrmann K, Schottelius M, Lapa C, et al. First-in-human experience of CXCR4-directed endoradiotherapy with ^{177}Lu- and ^{90}Y-labeled pentixather in advanced-stage multiple myeloma with extensive intra- and extramedullary disease. *J Nucl Med.* 2016;57:248–251.
51. Lapa C, Herrmann K, Schirbel A, et al. CXCR4-directed endoradiotherapy induces high response rates in extramedullary relapsed multiple myeloma. *Theranostics.* 2017;7:1589–1597.
52. Stollberg S, Kammerer D, Neubauer E, et al. Differential somatostatin and CXCR4 chemokine receptor expression in MALT-type lymphoma of gastric and extragastric origin. *J Cancer Res Clin Oncol.* 2016;142:2239–2247.
53. Duell J, Krummenast F, Schirbel A, et al. Improved primary staging of marginal-zone lymphoma by addition of CXCR4-directed PET/CT. *J Nucl Med.* 2021;62:1415–1421.
54. Mayerhoefer ME, Raderer M, Lamm W, et al. CXCR4 PET/MRI for follow-up of gastric mucosa-associated lymphoid tissue lymphoma after first-line *Helicobacter pylori* eradication. *Blood.* 2022;139:240–244.
55. Zucca E, Copie-Bergman C, Ricardi U, et al. Gastric marginal zone lymphoma of MALT type: ESMO clinical practice guidelines for diagnosis, treatment and follow-up. *Ann Oncol.* 2013;24(suppl 6):vi144–vi148.
56. Behrmann L, Wellbrock J, Fiedler W. Acute myeloid leukemia and the bone marrow niche: take a closer look. *Front Oncol.* 2018;8:444.
57. Nervi B, Ramirez P, Rettig MP, et al. Chemosensitization of acute myeloid leukemia (AML) following mobilization by the CXCR4 antagonist AMD3100. *Blood.* 2009;113:6206–6214.
58. Herhaus P, Habringer S, Philipp-Abbrederis K, et al. Targeted positron emission tomography imaging of CXCR4 expression in patients with acute myeloid leukemia. *Haematologica.* 2016;101:932–940.
59. Konoplev S, Rassidakis GZ, Estey E, et al. Overexpression of CXCR4 predicts adverse overall and event-free survival in patients with unmutated FLT3 acute myeloid leukemia with normal karyotype. *Cancer.* 2007;109:1152–1156.
60. Uy GL, Rettig MP, Motabi IH, et al. A phase 1/2 study of chemosensitization with the CXCR4 antagonist plerixafor in relapsed or refractory acute myeloid leukemia. *Blood.* 2012;119:3917–3924.
61. Mayerhoefer ME, Jaeger U, Staber P, et al. [^{68}Ga]Ga-pentixafor PET/MRI for CXCR4 imaging of chronic lymphocytic leukemia: preliminary results. *Invest Radiol.* 2018;53:403–408.
62. Burger JA, Burger M, Kipps TJ. Chronic lymphocytic leukemia B cells express functional CXCR4 chemokine receptors that mediate spontaneous migration beneath bone marrow stromal cells. *Blood.* 1999;94:3658–3667.
63. Lapa C, Hanscheid H, Kircher M, et al. Feasibility of CXCR4-directed radioligand therapy in advanced diffuse large B-cell lymphoma. *J Nucl Med.* 2019;60:60–64.
64. Habringer S, Lapa C, Herhaus P, et al. Dual targeting of acute leukemia and supporting niche by CXCR4-directed theranostics. *Theranostics.* 2018;8:369–383.
65. Kawai N, Miyake K, Yamamoto Y, Nishiyama Y, Tamiya T. ^{18}F-FDG PET in the diagnosis and treatment of primary central nervous system lymphoma. *BioMed Res Int.* 2013;2013:247152.
66. Nandagopal L, Mehta A. Treatment approaches of hard-to-treat non-Hodgkin lymphomas. *Expert Rev Hematol.* 2017;10:259–273.
67. Iagaru A, Gambhir SS, Goris ML. ^{90}Y-ibritumomab therapy in refractory non-Hodgkin's lymphoma: observations from ^{111}In-ibritumomab pretreatment imaging. *J Nucl Med.* 2008;49:1809–1812.

Site-Specifically Conjugated Single-Domain Antibody Successfully Identifies Glypican-3–Expressing Liver Cancer by Immuno-PET

Stanley Fayn*[1], A. Paden King*[1], Nicholas T. Gutsche[1], Zhijian Duan[2], Jesse Buffington[2], Colleen P. Olkowski[1], Ying Fu[3], Jessica Hong[3], Deepak Sail[4], Kwamena E. Baidoo[1], Rolf E. Swenson[4], Ross W. Cheloha[5], Mitchell Ho[2,3], Peter L. Choyke[1], and Freddy E. Escorcia[1,6]

[1]*Molecular Imaging Branch, Center for Cancer Research, National Cancer Institute, National Institutes of Health, Bethesda, Maryland;* [2]*Antibody Engineering Program, Center for Cancer Research, National Cancer Institute, National Institutes of Health, Bethesda, Maryland;* [3]*Laboratory of Molecular Biology, Center for Cancer Research, National Cancer Institute, National Institutes of Health, Bethesda, Maryland;* [4]*Chemistry and Synthesis Center, National Heart, Lung, and Blood Institute, National Institutes of Health, Rockville, Maryland;* [5]*Chemical Biology in Signaling Section, National Institute of Diabetes and Digestive and Kidney Diseases, National Institutes of Health, Bethesda, Maryland; and* [6]*Radiation Oncology Branch, Center for Cancer Research, National Cancer Institute, National Institutes of Health, Bethesda, Maryland*

Primary liver cancer is the third leading cause of cancer-related deaths, and its incidence and mortality are increasing worldwide. Hepatocellular carcinoma (HCC) accounts for 80% of primary liver cancer cases. Glypican-3 (GPC3) is a heparan sulfate proteoglycan that histopathologically defines HCC and represents an attractive tumor-selective marker for radiopharmaceutical imaging and therapy for this disease. Single-domain antibodies are a promising scaffold for imaging because of their favorable pharmacokinetic properties, good tumor penetration, and renal clearance. Although conventional lysine-directed bioconjugation can be used to yield conjugates for radiolabeling full-length antibodies, this stochastic approach risks negatively affecting target binding of the smaller single-domain antibodies. To address this challenge, site-specific approaches have been explored. Here, we used conventional and sortase-based site-specific conjugation methods to engineer GPC3-specific human single-domain antibody (HN3) PET probes. **Methods:** Bifunctional deferoxamine (DFO) isothiocyanate was used to synthesize native HN3 (nHN3)-DFO. Site-specifically modified HN3 (ssHN3)-DFO was engineered using sortase-mediated conjugation of triglycine-DFO chelator and HN3 containing an LPETG C-terminal tag. Both conjugates were radiolabeled with ^{89}Zr, and their binding affinity in vitro and target engagement of GPC3-positive ($GPC3^+$) tumors in vivo were determined. **Results:** Both ^{89}Zr-ssHN3 and ^{89}Zr-nHN3 displayed nanomolar affinity for GPC3 in vitro. Biodistribution and PET/CT image analysis in mice bearing isogenic A431 and A431-$GPC3^+$ xenografts, as well as in HepG2 liver cancer xenografts, showed that both conjugates specifically identify $GPC3^+$ tumors. ^{89}Zr-ssHN3 exhibited more favorable biodistribution and pharmacokinetic properties, including higher tumor uptake and lower liver accumulation. Comparative PET/CT studies on mice imaged with both ^{18}F-FDG and ^{89}Zr-ssHN3 showed more consistent tumor accumulation for the single-domain antibody conjugate, further establishing its potential for PET imaging. **Conclusion:** ^{89}Zr-ssHN3 showed clear advantages in tumor uptake and tumor-to-liver signal ratio over the conventionally modified ^{89}Zr-nHN3 in xenograft models. Our results establish the potential of HN3-based single-domain antibody probes for GPC3-directed PET imaging of liver cancers.

Key Words: glypican-3; GPC3; liver cancer; immuno-PET; molecular imaging; Nanobody

J Nucl Med 2023; 64:1017–1023
DOI: 10.2967/jnumed.122.265171

Primary liver cancer is the third most common cause of cancer death and has an 18% 5-y survival (*1*). New cases of primary liver cancer are on the rise, with the incidence projected to increase by more than 55% in the next 20 y (*2*). Hepatocellular carcinoma (HCC) accounts for around 80% of primary liver cancer cases worldwide, affecting over 600,000 individuals annually (*3*). Chronic hepatitis B virus infection is currently the main contributor to the disease. However, diabetes and obesity-related nonalcoholic fatty liver disease and nonalcoholic steatohepatitis are of growing etiologic concern (*4*).

MR- and CT-based imaging are the standard of care for diagnosing and surveilling patients with a high risk of developing HCC (*5*). Although these modalities have been critical in diagnosing HCC, distinguishing treatment effect from residual or recurrent disease remains a challenge. ^{18}F-FDG PET, used in these circumstances for other cancers, is of limited use in HCC because of the heterogeneous glucose uptake by this tumor type (*6*). As such, HCC tumor-selective or tumor microenvironment–selective imaging agents are needed to address this unmet clinical need.

Technological developments have allowed targeted radionuclide diagnostic agents, as well as β- and α-emitting radionuclide therapies, to play a role in precision oncology (*7*). Diverse biomolecules, including monoclonal antibodies, antibody fragments, small proteins, peptides, and small molecules, have been explored as tumor-targeting vectors for PET imaging and radiopharmaceutical therapy (*8,9*).

Glypican-3 (GPC3) is a glycosylphosphatidylinositol-anchored heparan sulfate proteoglycan expressed in 75%–90% of HCCs (*10*). Therefore, it is an attractive HCC-selective target that, if leveraged for molecular imaging, may help characterize postablation lesions and allow for more comprehensive screening, early diagnosis, and

Received Nov. 10, 2022; revision accepted Feb. 22, 2023.
For correspondence or reprints, contact Freddy E. Escorcia (freddy.escorcia@nih.gov).
*Contributed equally to this work.
Published online Mar. 30, 2023.

posttreatment surveillance. Full-length antibodies specific to GPC3 have been evaluated for immuno-PET imaging in preclinical (*11,12*) and clinical (*13*) studies. However, despite good imaging characteristics, the long blood half-life of full-length antibodies precludes same-day imaging, compromising existing patient workflows in the clinic. Furthermore, monoclonal antibodies typically exhibit hepatobiliary excretion, which can result in poor tumor-to-tissue ratios in patients with primary liver tumors. Although a smaller GPC3-specific $F(ab')_2$ (110 kDa) has been explored for imaging, it was not suited for same-day imaging (*14*).

Single-domain antibodies, (15 kDa), derived from camelids or sharks (*15,16*) are alternate scaffolds being explored for PET diagnostics (NCT04674722 and NCT05156515). Notably, one recent report describes the preclinical development of a GPC3-targeting single-domain antibody radiolabeled with ^{68}Ga or ^{18}F for immuno-PET, providing a proof of concept for HCC imaging with GPC3-directed single-domain antibodies (*16*). This conjugate was prepared using lysine conjugation, which is stochastic. Unlike full-size antibodies, single-domain antibodies have fewer lysine residues for conjugation. Modification of these residues by attaching prosthetic groups may worsen their binding affinity and pharmacokinetic properties. These drawbacks can be mitigated by site-specific conjugation or sequence alteration (*17–20*).

Here, we engineered the GPC3-specific single-domain antibody HN3 (*21*) to be compatible with sortase-based site-specific modification (*22*), which has previously been exploited for site-specific single-domain antibody radiolabeling (*23–25*), and labeled it with the radionuclide ^{89}Zr for use as a PET probe. The performance of this construct was compared with that of a lysine-conjugated HN3 single-domain antibody that did not require sequence engineering. We determined that both radioconjugates exhibit GPC3-specific tumor targeting in vivo, and the site-specific conjugate has superior performance to the traditional lysine-conjugated HN3 tracer and ^{18}F-FDG.

MATERIALS AND METHODS

Production of HN3 Single-Domain Antibody and Bifunctional HN3-Chelate Constructs

The HN3 human single-domain antibody, containing both -His_6 and -FLAG tags at its C terminus, was produced following a protocol previously described (*26,27*). A full description of HN3 production and plasmid maps of the transformation are provided in Supplemental Figures 1 and 2 (supplemental materials are available at http://jnm.snmjournals.org). A sortase-reactive deferoxamine (DFO) chelator (GGGK-DFO) was prepared as described in Figure 1, Supplemental Scheme 1, and Supplemental Figures 3–6. Site-specific C-terminal conjugation of GGGK-DFO to HN3-LPETG-His_6 (*28*) and stochastic lysine-directed conjugation of DFO to HN3 (*29*) were accomplished using previously reported methods detailed in the supplemental materials.

Biolayer Interferometry

The binding kinetics and equilibria for the binding of native HN3 (nHN3)-DFO and site-specifically modified HN3 (ssHN3)-DFO to recombinant GPC3 were evaluated using biolayer interferometry. Full experimental details are provided in the supplemental materials.

Radiolabeling with ^{89}Zr

Radiolabeling of DFO-conjugated single-domain antibodies was conducted using a modification of established methods (*12,29*). Gentisic acid (10 μL, 10 mg/mL) was added to a solution of $^{89}Zr(oxalate)_2$ (40 μL, 92.5 MBq, cyclotron at the National Institutes of Health Clinical Center) in oxalic acid. *N*-2-hydroxyethylpiperazine-*N*′-2-ethanesulfonic acid buffer (2 μL, 1 M) was added. A solution of 2 M Na_2CO_3 was then added until the pH reached 7. ssHN3-DFO or nHN3-DFO conjugate in 0.1 M ammonium acetate (45 μL, 1.5 mg/mL) was added to the mixture, and the reaction was heated for 1 h at 37°C. The reaction mixture was then purified using a PD-10 gel filtration column with phosphate-buffered saline containing bovine serum albumin (1 mg/mL) as the mobile phase. Radiochemical yield and purity were determined by radio–instant thin-layer chromatography with silica gel–impregnated glass microfiber paper strips (Varian) using an aqueous solution of ethylenediaminetetraacetic acid (50 mM) and NH_4OAc (100 mM, pH 5.5) as the mobile phase. An AR-2000 (Eckert-Ziegler) radio–thin-layer chromatography scanner was used to calculate the percentage total activity at the origin.

Saturation Binding Assays

To assess binding affinity, radioligand binding assays were performed as detailed in the supplemental materials by incubating varying amounts of radiolabeled single-domain antibodies with immobilized recombinant GPC3 for 2 h.

Cell Culture

The A431 human epithelioid cancer cell line and the GPC3-positive ($GPC3^+$) HepG2 human hepatoblastoma cell line were purchased from

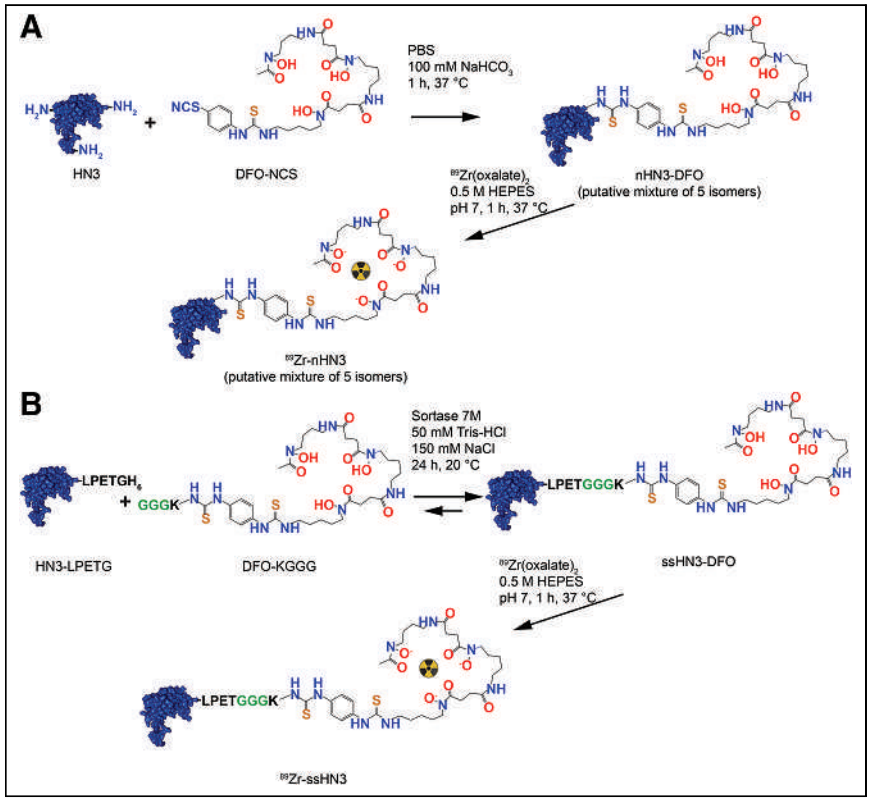

FIGURE 1. Conventional lysine conjugation vs. site-specific conjugation. Shown are synthetic schema and structures of ^{89}Zr-nHN3 (A) and ^{89}Zr-ssHN3 (B). HEPES = 4-(2-hydroxyethyl)-1-piperazineethanesulfonic acid; PBS = phosphate-buffered saline.

ATCC and cultured according to vendor instructions. A431-GPC3$^+$, a transfected A431 cell line engineered to overexpress GPC3 (*30,31*), was obtained from Dr. Mitchell Ho (National Cancer Institute). Cells were cultured in Dulbecco modified Eagle medium (Life Technologies) supplemented with 10% FetaPlex (Gemini Bio-Products). All cell lines were used within 15 passages.

Murine Subcutaneous Xenograft Models

All mouse experiments were approved by the Institutional Animal Care and Use Committee at the National Institutes of Health under protocol ROB-105. Female athymic nu/nu 8- to 10-wk-old mice (Charles River Laboratories) were implanted subcutaneously with 2.5×10^6 HepG2, A431, or A431-GPC3$^+$ cells in a 200-μL solution of phosphate-buffered saline (for A431 and A431-GPC3$^+$) or a 1:1 mixture of Matrigel (Corning) and Dulbecco modified Eagle medium (HepG2). Tumors were grown to approximately 100 mm^3 before biodistribution and imaging experiments. HepG2 and A431-GPC3$^+$ cells were chosen for their high expression of GPC3. A431 cells were used as a negative control.

PET/CT Imaging of Mice Bearing A431 or A431-GPC3$^+$ Tumors

Mice bearing A431 or A431-GPC3$^+$ xenografts ($n = 3$ per tumor type) were injected with 1,961 ± 30 kBq (2.8 μg) of ^{89}Zr-ssHN3 or 1,970 ± 40 kBq (10.9 μg) of ^{89}Zr-nHN3. At 1 and 3 h after injection, images were obtained using PET/CT (BioPET/CT; Sedecal) as follows. The mice were anesthetized using 2% isoflurane, and static PET scans were acquired over 10 min. Whole-body CT scans (8.5 min, 50 kV, 180 μA) were obtained immediately after PET images and were used to provide attenuation correction and anatomic coregistration for the PET scans. PET data were reconstructed using 3-dimensional ordered-subsets expectation maximization and were normalized, decay-corrected, and dead-time–corrected before analysis using MIM software (MIM Software Inc.). After the final imaging time point, the mice were euthanized by CO_2 asphyxiation, and 12 tissues, including tumor, were collected. All samples were weighed and counted on a γ-counter (2480 Wizard^3; Perkin Elmer Inc.). The counts were converted to percentage injected activity (%IA) using a standard solution of known activity prepared from the injection solution. %IA/g was calculated by dividing the activity in each organ by its weight.

Ex Vivo Biodistribution Study in HepG2 Tumor–Bearing Mice

Mice ($n = 4$) were injected with ^{89}Zr-labeled single-domain antibodies (370 ± 40 kBq/mouse for both the ssHN3 [0.90 μg] and the nHN3 [0.52 μg] conjugate) through a lateral tail vein. The biodistribution of ^{89}Zr-nHN3 and ^{89}Zr-ssHN3 was then evaluated at 1, 3, and 24 h after administration as described in the previous section.

PET/CT Imaging Comparison of ^{18}F-FDG and ^{89}Zr-ssHN3 in Mice Bearing HepG2 Tumors

Mice bearing HepG2 xenografts ($n = 4$) were kept fasting for 4 h before injection of approximately 4,180 ± 240 kBq of ^{18}F-FDG. After 1 h, PET/CT images were obtained and processed as described above. One day later, the same mice were injected with 3,680 ± 130 kBq (5.1 μg) of ^{89}Zr-ssHN3 and imaged 1, 3, and 24 h after injection. For comparison, another set of mice bearing HepG2 xenografts ($n = 4$) was injected with 4,110 ± 40 kBq (6.1 μg) of ^{89}Zr-nHN3 and imaged after 1, 3, and 24 h. After the 24-h image acquisition, the mice were euthanized and the ex vivo biodistribution of the ^{89}Zr conjugates was evaluated.

Statistical Analysis

Statistics were analyzed using Prism (version 9.0, GraphPad Software). Organ uptake, tumor volume, SUV, and stability were compared using the Student *t* test (unpaired, parametric, 2-tailed).

RESULTS

Synthesis of ssHN3 and nHN3 DFO Conjugates Was Successful

We successfully prepared derivatives of the GPC3-targeting single-domain antibody HN3 using previously reported methods (*28,29*). Analysis of the original single-domain antibodies and resulting DFO conjugates by size-exclusion high-performance liquid chromatography and high-resolution mass spectrometry confirmed their purity and identity (Supplemental Figs. 3–14). Synthetic schema for nHN3 and ssHN3 are presented in Figure 1. The nHN3 construct was conjugated to the commercially available bifunctional chelator DFO isothiocyanate using stochastic lysine labeling methods, yielding nHN3-DFO. Mass spectrometry analysis of this conjugate indicated a DFO:HN3 ratio of 0.2:1, consistent with minimal modification of the HN3 single-domain antibody. The ssHN3 single-domain antibody was conjugated specifically at the -LPETG sequence to GGGK-DFO, yielding ssHN3-DFO, which has a 1:1 HN3:DFO ratio. This conjugation reaction also results in cleavage of the -His_6 sequence from the C terminus of ssHN3.

Single-Domain Antibody Radioconjugates Were Synthesized with Satisfactory Radiochemical Yield and Purity

Both conjugates were successfully radiolabeled with ^{89}Zr using ^{89}Zr-oxalate, resulting in 10%–30% yield. After radiolabeling, both conjugates exhibited similar specific activities, varying on the basis of the radiolabeling efficiency (610 ± 140 kBq/μg for ssHN3 and 520 ± 240 kBq/μg for nHN3), and the radiochemical purity of both conjugates was found to be more than 99% using instant thin-layer chromatography (Supplemental Figs. 15 and 16).

Single-Domain Antibody Conjugates Exhibited Nanomolar Binding Affinities for GPC3

Biolayer interferometry assays showed that affinities (dissociation constant, or K_D) for human GPC3 were 11 ± 2 nM and 15 ± 7 nM for nHN3-DFO and ssHN3-DFO, respectively (Fig. 2). Cell-free saturation binding assays showed K_D to be 30 ± 12 and 10 ± 4 nM for ^{89}Zr-nHN3 and ^{89}Zr-ssHN3, respectively ($P = 0.14$) (Fig. 2), indicating that the 2 radioconjugates have comparable binding affinities for GPC3. The somewhat lower binding affinity determined for ^{89}Zr-nHN3 in the saturation assay versus the biolayer interferometry assay

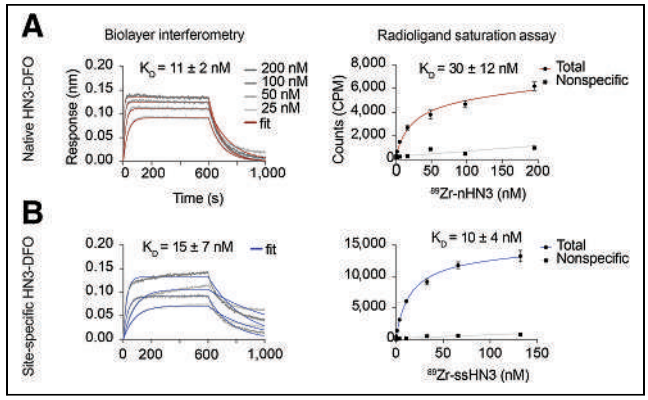

FIGURE 2. Single-domain antibody conjugates retain GPC3 affinity. Shown are biolayer interferometry (left) and radioligand saturation binding assay (right) results for stochastically modified single-domain antibody nHN3-DFO (A) and ssHN3-DFO (B), with determined K_D values. K_D values for biolayer interferometry assays are average of measurements using 4 different HN3 concentrations, whereas K_D values for saturation assays are average of 3 independent replicates.

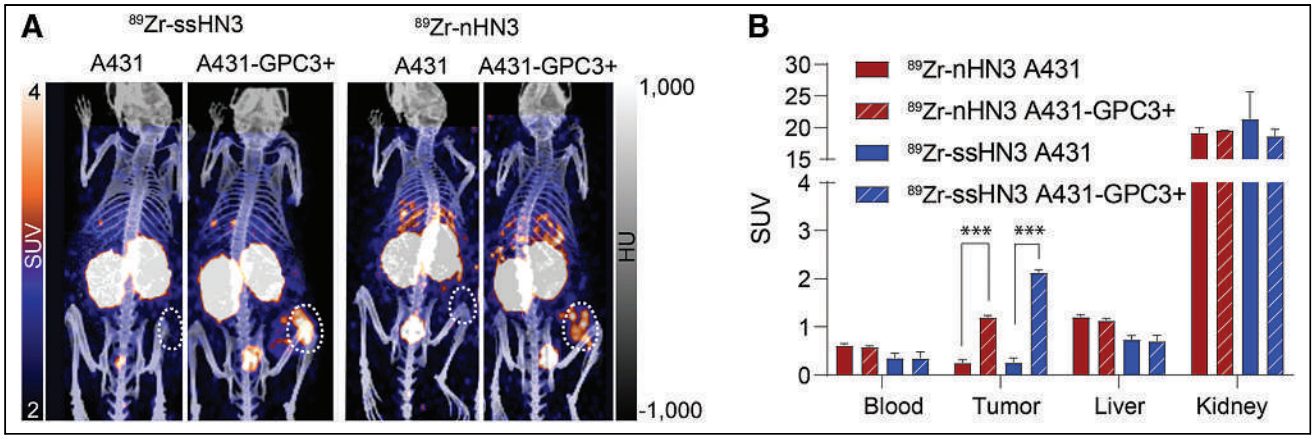

FIGURE 3. Single-domain antibody PET tracers successfully image tumors engineered to express GPC3. Shown are representative PET/CT images (A) and calculated SUVs (B) of ^{89}Zr-ssHN3 and ^{89}Zr-nHN3 in A431 and A431-GPC3$^+$ tumor–bearing mice (n = 3) 1 h after injection. Full ex vivo biodistribution data for mice bearing A431 and A431-GPC3$^+$ tumors are reported in Supplemental Figures 17 and 18. ***$P < 0.005$.

may arise from the biolayer interferometry's detecting unmodified nHN3 in addition to the nHN3-DFO present in the sample. In contrast, the saturation assay detects only nHN3-DFO that has been radiolabeled with ^{89}Zr.

In Vivo Studies Confirmed That Single-Domain Antibody Radioconjugates Specifically Bind to GPC3$^+$ Tumors

After confirming the high affinity of both radioconjugates for GPC3, we evaluated their performance in vivo. Mice bearing subcutaneous xenografts were administered the radioconjugates and underwent PET/CT imaging and ex vivo biodistribution analysis. We first compared the performance of the 2 radioconjugates in mice bearing GPC3-negative (A431) or expressing (A431-GPC3$^+$) tumors. As shown in Figure 3, both conjugates exhibited highly specific tumor accumulation at 1 h after administration, with approximately 10-fold higher tumor uptake in the A431-GPC3$^+$ model than in the otherwise isogenic A431 model. The two ^{89}Zr-single-domain antibody conjugates showed rapid blood clearance and high kidney accumulation as expected. Notably, in ex vivo biodistribution analysis of these mice, ^{89}Zr-ssHN3 exhibited both lower blood and liver accumulation and higher tumor uptake at 3 h (14.4 ± 1.8 %IA/g) than ^{89}Zr-nHN3 (7.4 ± 1.2 %IA/g) in the A431-GPC3$^+$ model (P = 0.0018) (Supplemental Figs. 17 and 18). These results likely stem from the fact that ssHN3 has a preserved GPC3-binding domain whereas the nHN3 conjugate represents a heterogeneous mixture of products, including ones with DFO modifications at lysine residues critical for binding (Fig. 1). Furthermore, the ssHN3 conjugate also lacks the polar -His$_6$ and -FLAG tags present on nHN3, potentially increasing nonspecific uptake of nHN3 (*20*).

Encouraged by the biodistribution and imaging results in the A431-GPC3$^+$ model, we next investigated the targeting ability of ^{89}Zr-nHN3 and ^{89}Zr-ssHN3 in mice bearing more clinically relevant HepG2 liver cancer xenografts (Fig. 4; Supplemental Figs. 19 and 20), which have lower GPC3 expression than the transfected A431-GPC3$^+$ cell line (*32*). Generally, biodistribution results for both radiotracers in HepG2 tumor-bearing mice were comparable to those observed in the A431-GPC3$^+$ model. ^{89}Zr-ssHN3 demonstrated numerically higher tumor uptake at 1 h (7.2 ± 1.2 %IA/g) than did ^{89}Zr-nHN3 (5.7 ± 1.8 %IA/g) (P = 0.235), as well as lower accumulation in the blood (P = 0.001), liver (P = 0.008), and spleen (P = 0.013). Kidney uptake of both tracers was quite high (~140 %IA/g at 1 h after injection). Longitudinal analysis of the

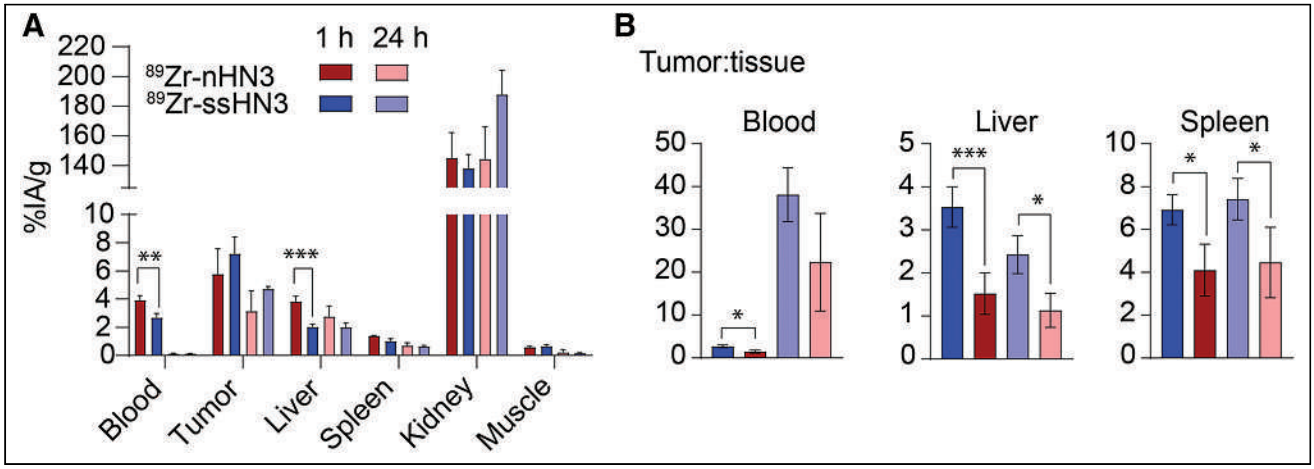

FIGURE 4. Single-domain antibody PET tracers successfully image GPC3$^+$ liver tumor xenografts. Shown are selected ex vivo biodistribution of ^{89}Zr-ssHN3 and ^{89}Zr-nHN3 (A) and tumor-to-tissue ratios of HepG2 tumor-bearing mice (n = 4) (B). Full 12-organ biodistribution results for mice bearing HepG2 tumors are reported in Supplemental Figures 19 and 20. *$P < 0.05$. **$P < 0.01$. ***$P < 0.005$.

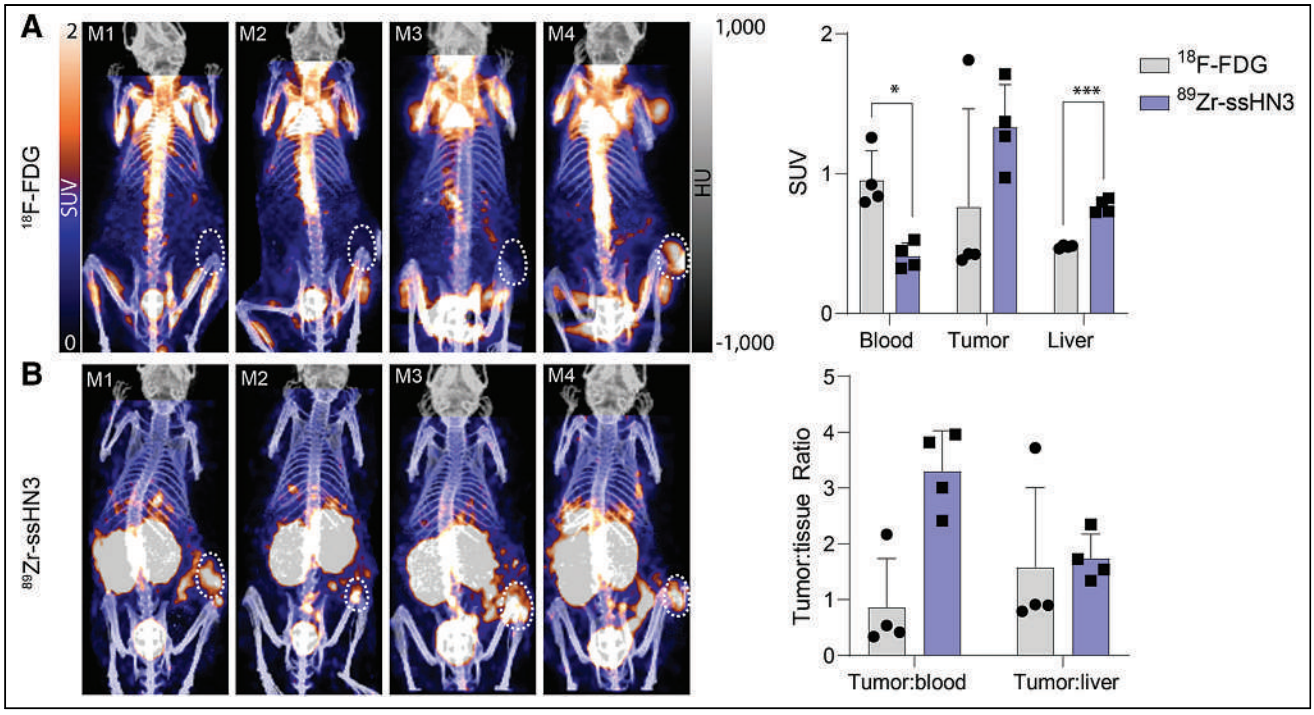

FIGURE 5. ^{89}Zr-ssHN3 PET tracer is superior to ^{18}F-FDG for imaging liver tumors. Shown are PET/CT images of mice ($n = 4$) bearing HepG2 tumors injected with ^{18}F-FDG (A) and ^{89}Zr-ssHN3 (B). At top is SUV comparison, and at bottom is tumor-to-tissue ratios for both tracers. Error bars represent SD. Full SUV analysis of ^{89}Zr-ssHN3 and ^{89}Zr-nHN3 is reported in Supplemental Figures 21–22. *$P < 0.05$. ***$P < 0.005$.

radioconjugates' biodistribution indicates some elimination from both tumor and nontarget organs at 3 and 24 h after administration, but the highest tumor-to-nontarget tissue ratios were obtained at 1 h after injection for both probes (Supplemental Table 1). The tumor-to-liver ratio at 1 h was nearly 3-fold higher for ^{89}Zr-ssHN3 (3.5 ± 0.5) than for ^{89}Zr-nHN3 (1.5 ± 0.5) ($P < 0.005$), indicating that ^{89}Zr-ssHN3 has superior performance as a liver cancer diagnostic.

Tumor Imaging with ^{89}Zr-ssHN3 Was Superior to That with ^{89}Zr-nHN3 or ^{18}F-FDG in Mice Bearing HepG2 Tumors

After evaluating the ex vivo biodistribution and PET imaging of ^{89}Zr-ssHN3 and ^{89}Zr-nHN3 in engineered models, we sought to assess their performance for imaging in HepG2 liver cancer xenografts. The ^{89}Zr-ssHN3 tracer displayed both higher tumor accumulation and lower liver uptake than ^{89}Zr-nHN3 (Supplemental Figs. 21–22). ^{89}Zr-ssHN3 also showed positive tumor accumulation (SUV > 1) in all 4 animals, whereas ^{18}F-FDG displayed an SUV of more than 1 in only 1 tumor (Fig. 5; Supplemental Fig. 21). ^{18}F-FDG also exhibited a higher blood pool signal in all animals, indicating ^{89}Zr-ssHN3's better specificity. However, ^{18}F-FDG did show a lower liver SUV and a much lower kidney signal than ^{89}Zr-ssHN3. Together, our work confirms the potential of the ^{89}Zr-ssHN3 conjugate for GPC3$^+$ tumor detection, having superior imaging performance to either the lysine conjugation-based ^{89}Zr-nHN3 or the clinically available ^{18}F-FDG in models of human liver cancer.

DISCUSSION

Here, we have shown that the GPC3-targeting single-domain antibody HN3 can be engineered as a PET agent for same-day imaging of models of liver cancer. ^{89}Zr-ssHN3 and ^{89}Zr-nHN3 demonstrate high GPC3 affinity in vitro and tumor uptake in GPC3$^+$ tumors in vivo. Notably, ^{89}Zr-ssHN3 demonstrated clear advantages, including higher tumor uptake and lower accumulation in nontarget organs, especially the liver and spleen. The significantly better tumor-to-liver ratio for ^{89}Zr-ssHN3 than for ^{89}Zr-nHN3 (3.5:1 vs. 1.5:1, respectively) would result in a much higher signal-to-noise ratio for PET and thus the ability to better differentiate between cancerous and noncancerous liver lesions. ^{89}Zr-ssHN3 also outperformed ^{18}F-FDG, demonstrating more consistent localization in HepG2 tumor xenografts.

Although its tumor-targeting ability makes ^{89}Zr-ssHN3 attractive for GPC3-directed PET, its high kidney uptake impedes single-domain antibody–based radiopharmaceutical therapy, and the long half-life of ^{89}Zr leads to an unnecessarily high deposition of radioactivity in the kidneys. Strategies to reduce kidney uptake of single-domain antibodies include coadministration of lysine or Gelofusine (B. Braun Melsungen), alteration of the single-domain antibody sequence, or addition of an albumin-binding moiety (*20,33,34*). Efforts to decrease the kidney uptake of HN3 conjugates and prepare short-lived ^{68}Ga or ^{18}F conjugable derivatives are currently under way in our lab.

The GPC3-specific imaging capabilities of ^{89}Zr-ssHN3 place it among a select few radiotracers with clinical potential for liver tumor PET imaging. Although GPC3-targeted antibody conjugates have demonstrated specific tumor accumulation, these agents suffer from slow tumor uptake kinetics and are generally unsuitable for same-day imaging (*11–13*). Single-domain antibodies represent an alternative targeting biomolecule with excellent specificity and rapid clearance. An et al. were the first to demonstrate the feasibility of using a GPC3-targeting single-domain antibody (G2) for immuno-PET (*17*). The authors reported relatively low tumor uptake (2.6 %IA/g) and tumor-to-liver ratios (1.67 ± 0.09) in animals bearing GPC3$^+$ Hep3B liver cancer xenografts, likely resulting from the use of conventional lysine-based conjugation. Our

work confirms that sortase-based site-specific modification of a GPC3-targeting single-domain antibody is superior to conventional lysine-based modification for immuno-PET of liver tumors.

The development of a tumor-specific imaging agent for HCC is critically needed to improve diagnosis, monitor treatment efficacy, and inform management. Local therapies such as stereotactic body radiation therapy, radiofrequency or microwave ablation, and transarterial embolization have proven effective against local disease (*1*). The efficacy of radiation-based treatments highlights the sensitivity of liver tumors to radiotherapy (*1,35*). Notable in leveraging this HCC radiosensitivity is ^{131}I-metuximab, a F(ab′)$_2$ specific to basigin or CD147 that is expressed on 60% of HCCs. This radioconjugate was approved as adjuvant therapy in China after demonstrating a survival benefit compared with observation after surgical resection in a randomized controlled phase 2 trial (*36*). These results are buoyed by clinical data showing noninferiority of proton stereotactic body radiation therapy compared with radiofrequency ablation in patients with small recurrent or residual HCC in a randomized phase 3 trial (*35*), survival benefit using adjuvant external-beam radiotherapy in a phase 2 trial (*37*), and promising results in the neoadjuvant setting as well (*38*). However, assessing the response of tumors to these liver-directed therapies is difficult because existing imaging modalities cannot differentiate viable from nonviable tumors. Our novel GPC3-selective immuno-PET probe might be used under these circumstances to help clinical decision making and improve patient outcomes.

In addition, tumor-selective imaging of GPC3 might serve as a noninvasive predictive biomarker to identify patients who may preferentially respond to GPC3-directed therapy, including chimeric antigen receptor T-cell strategies (NCT05003895). Tumor-selective targeting of GPC3 might also be extended toward the development of a therapeutic radiopharmaceutical. HN3-based PET agents may be particularly suitable for this application, given that therapies based on chimeric antigen receptor T cells and immunotoxins using the HN3 single-domain antibody have already shown preclinical success (*39,40*).

CONCLUSION

We successfully designed, synthesized, and characterized novel GPC3-selective single-domain antibody PET probes for imaging liver tumors, and these probes showed superiority to conventional imaging with ^{18}F-FDG. Comparative analysis of ^{89}Zr-nHN3 and ^{89}Zr-ssHN3 showed that ^{89}Zr-ssHN3 has superior in vivo target engagement and pharmacokinetic properties in GPC3$^+$ liver cancer xenograft models. We confirmed that the sortase-mediated conjugation successfully preserves the affinity of the single-domain antibody, an approach that can be extended to other radioconjugates with a lower molecular weight. Efforts are ongoing toward developing second-generation ssHN3 conjugates that have short-lived radionuclides for imaging and improved kidney uptake for therapy.

DISCLOSURE

This work was supported in part by the National Cancer Institute from Intramural Research Program funds ZIA BC 011800 and ZIA BC 010891. Dr. Mitchell Ho holds the patent (WO2012145469) assigned to the National Institutes of Health for the HN3 single-domain antibody specific for GPC3. No other potential conflict of interest relevant to this article was reported.

KEY POINTS

QUESTION: Can we engineer a GPC3-specific single-domain antibody for tumor-selective PET imaging of liver cancer?

PERTINENT FINDINGS: We used a GPC3-specific single-domain antibody to engineer ^{89}Zr-nHN3 and ^{89}Zr-ssHN3 immuno-PET probes and confirmed specific GPC3 binding in vitro and in vivo. Our ^{89}Zr-ssHN3 immuno-PET tracer outperformed a lysine-conjugated probe and ^{18}F-FDG for PET imaging of liver cancer xenografts.

IMPLICATIONS FOR PATIENT CARE: ^{89}Zr-ssHN3 represents a promising same-day immuno-PET agent for diagnosis and posttreatment surveillance of liver cancer.

REFERENCES

1. Vogel A, Meyer T, Sapisochin G, Salem R, Saborowski A. Hepatocellular carcinoma. *Lancet.* 2022;400:1345–1362.
2. Rumgay H, Arnold M, Ferlay J, et al. Global burden of primary liver cancer in 2020 and predictions to 2040. *J Hepatol.* 2022;77:1598–1606.
3. Rumgay H, Ferlay J, de Martel C, et al. Global, regional and national burden of primary liver cancer by subtype. *Eur J Cancer.* 2022;161:108–118.
4. Estes C, Razavi H, Loomba R, Younossi Z, Sanyal AJ. Modeling the epidemic of nonalcoholic fatty liver disease demonstrates an exponential increase in burden of disease. *Hepatology.* 2018;67:123–133.
5. Choi J-Y, Lee J-M, Sirlin CB. CT and MR imaging diagnosis and staging of hepatocellular carcinoma: part I. Development, growth, and spread: key pathologic and imaging aspects. *Radiology.* 2014;272:635–654.
6. Lu R-C, She B, Gao W-T, et al. Positron-emission tomography for hepatocellular carcinoma: current status and future prospects. *World J Gastroenterol.* 2019;25:4682–4695.
7. Marcu L, Bezak E, Allen BJ. Global comparison of targeted alpha vs targeted beta therapy for cancer: in vitro, in vivo and clinical trials. *Crit Rev Oncol Hematol.* 2018;123:7–20.
8. Strosberg J, El-Haddad G, Wolin E, et al. Phase 3 trial of ^{177}Lu-Dotatate for midgut neuroendocrine tumors. *N Engl J Med.* 2017;376:125–135.
9. Sartor O, de Bono J, Chi KN, et al. Lutetium-177–PSMA-617 for metastatic castration-resistant prostate cancer. *N Engl J Med.* 2021;385:1091–1103.
10. Wang HL, Anatelli F, Zhai Q, Adley B, Chuang S-T, Yang XJ. Glypican-3 as a useful diagnostic marker that distinguishes hepatocellular carcinoma from benign hepatocellular mass lesions. *Arch Pathol Lab Med.* 2008;132:1723–1728.
11. Sham JG, Kievit FM, Grierson JR, et al. Glypican-3–targeted ^{89}Zr PET imaging of hepatocellular carcinoma. *J Nucl Med.* 2014;55:799–804.
12. Kelada OJ, Gutsche NT, Bell M, et al. ImmunoPET as stoichiometric sensor for glypican-3 in models of hepatocellular carcinoma. bioRxiv website. https://www.biorxiv.org/content/10.1101/2020.01.31.926972v1.full. Published February 2, 2020. Accessed March 21, 2023.
13. Carrasquillo JA, O'Donoghue JA, Beylergil V, et al. I-124 codrituzumab imaging and biodistribution in patients with hepatocellular carcinoma. *EJNMMI Res.* 2018;8:20.
14. Sham JG, Kievit FM, Grierson JR, et al. Glypican-3–targeting F(ab′)2 for ^{89}Zr PET of hepatocellular carcinoma. *J Nucl Med.* 2014;55:2032–2037.
15. Hamers-Casterman C, Atarhouch T, Muyldermans S, et al. Naturally occurring antibodies devoid of light chains. *Nature.* 1993;363:446–448.
16. Greenberg AS, Avila D, Hughes M, Hughes A, McKinney EC, Flajnik MF. A new antigen receptor gene family that undergoes rearrangement and extensive somatic diversification in sharks. *Nature.* 1995;374:168–173.
17. An S, Zhang D, Zhang Y, et al. GPC3-targeted immunoPET imaging of hepatocellular carcinomas. *Eur J Nucl Med Mol Imaging.* 2022;49:2682–2692.
18. Massa S, Xavier C, De Vos J, et al. Site-specific labeling of cysteine-tagged camelid single-domain antibody-fragments for use in molecular imaging. *Bioconjug Chem.* 2014;25:979–988.
19. Chatalic KLS, Veldhoven-Zweistra J, Bolkestein M, et al. A novel ^{111}In-labeled anti–prostate-specific membrane antigen nanobody for targeted SPECT/CT imaging of prostate cancer. *J Nucl Med.* 2015;56:1094–1099.
20. D'Huyvetter M, Vincke C, Xavier C, et al. Targeted radionuclide therapy with a ^{177}Lu-labeled anti-HER2 nanobody. *Theranostics.* 2014;4:708–720.

21. Feng M, Gao W, Wang R, et al. Therapeutically targeting glypican-3 via a conformation-specific single-domain antibody in hepatocellular carcinoma. *Proc Natl Acad Sci USA.* 2013;110:E1083–E1091.
22. Mao H, Hart SA, Schink A, Pollok BA. Sortase-mediated protein ligation: a new method for protein engineering. *J Am Chem Soc.* 2004;126:2670–2671.
23. Massa S, Vikani N, Betti C, et al. Sortase A-mediated site-specific labeling of camelid single-domain antibody-fragments: a versatile strategy for multiple molecular imaging modalities. *Contrast Media Mol Imaging.* 2016;11:328–339.
24. Rashidian M, Keliher EJ, Bilate AM, et al. Noninvasive imaging of immune responses. *Proc Natl Acad Sci USA.* 2015;112:6146–6151.
25. Truttmann MC, Wu Q, Stiegeler S, Duarte JN, Ingram J, Ploegh HL. HypE-specific nanobodies as tools to modulate HypE-mediated target AMPylation. *J Biol Chem.* 2015;290:9087–9100.
26. Feng M, Bian H, Wu X, et al. Construction and next-generation sequencing analysis of a large phage-displayed VNAR single-domain antibody library from six naïve nurse sharks. *Antib Ther.* 2019;2:1–11.
27. Duan Z, Buffington J, Hong J, Ho M. Production and purification of shark and camel single-domain antibodies from bacterial and mammalian cell expression systems. *Curr Protoc.* 2022;2:e459.
28. Guimaraes CP, Witte MD, Theile CS, et al. Site-specific C-terminal and internal loop labeling of proteins using sortase-mediated reactions. *Nat Protoc.* 2013;8:1787–1799.
29. Vosjan MJWD, Perk LR, Visser GWM, et al. Conjugation and radiolabeling of monoclonal antibodies with zirconium-89 for PET imaging using the bifunctional chelate p-isothiocyanatobenzyl-desferrioxamine. *Nat Protoc.* 2010;5:739–743.
30. Phung Y, Gao W, Man Y-G, Nagata S, Ho M. High-affinity monoclonal antibodies to cell surface tumor antigen glypican-3 generated through a combination of peptide immunization and flow cytometry screening. *MAbs.* 2012;4:592–599.
31. Berman RM, Kelada OJ, Gutsche NT, et al. In vitro performance of published glypican 3-targeting peptides TJ12P1 and L5 indicates lack of specificity and potency. *Cancer Biother Radiopharm.* 2019;34:498–503.
32. Fu Y, Urban DJ, Nani RR, et al. Glypican-3 specific antibody drug conjugates targeting hepatocellular carcinoma (HEP-10-1020). *Hepatology.* 2019;70:563–576.
33. Tijink BM, Laeremans T, Budde M, et al. Improved tumor targeting of anti–epidermal growth factor receptor Nanobodies through albumin binding: taking advantage of modular Nanobody technology. *Mol Cancer Ther.* 2008;7:2288–2297.
34. Gainkam LO, Caveliers V, Devoogdt N, et al. Localization, mechanism and reduction of renal retention of technetium-99m labeled epidermal growth factor receptor-specific nanobody in mice. *Contrast Media Mol Imaging.* 2011;6:85–92.
35. Kim TH, Koh YH, Kim BH, et al. Proton beam radiotherapy vs. radiofrequency ablation for recurrent hepatocellular carcinoma: a randomized phase III trial. *J Hepatol.* 2021;74:603–612.
36. Li J, Xing J, Yang Y, et al. Adjuvant ^{131}I-metuximab for hepatocellular carcinoma after liver resection: a randomised, controlled, multicentre, open-label, phase 2 trial. *Lancet Gastroenterol Hepatol.* 2020;5:548–560.
37. Chen B, Wu J-X, Cheng S-H, et al. Phase 2 study of adjuvant radiotherapy following narrow-margin hepatectomy in patients with HCC. *Hepatology.* 2021;74:2595–2604.
38. Wu F, Chen B, Dong D, et al. Phase 2 evaluation of neoadjuvant intensity-modulated radiotherapy in centrally located hepatocellular carcinoma: a nonrandomized controlled trial. *JAMA Surg.* 2022;157:1089–1096.
39. Fleming BD, Urban DJ, Hall MD, et al. Engineered anti-GPC3 immunotoxin, HN3-ABD-T20, produces regression in mouse liver cancer xenografts through prolonged serum retention. *Hepatology.* 2020;71:1696–1711.
40. Kolluri A, Li D, Li N, Ho M. Engineered, fully human nanobody-based CAR T cells have enhanced antitumor activity against hepatocellular carcinoma in preclinical models [abstract]. *J Clin Oncol.* 2022;40(suppl):e14512–e14512.

PSMA PET Tumor–to–Salivary Gland Ratio to Predict Response to [^{177}Lu]PSMA Radioligand Therapy: An International Multicenter Retrospective Study

Masatoshi Hotta*[1], Andrei Gafita*[1], Vishnu Murthy[1], Matthias R. Benz[1], Ida Sonni[1], Irene A. Burger[2], Matthias Eiber[3], Louise Emmett[4], Andrea Farolfi[1,5], Wolfgang P. Fendler[6], Manuel M. Weber[6], Michael S. Hofman[7], Thomas A. Hope[8], Clemens Kratochwil[9], Johannes Czernin[1], and Jeremie Calais[1]

[1]*Ahmanson Translational Theranostics Division, UCLA, Los Angeles, California;* [2]*Department of Nuclear Medicine, University Hospital Zurich, University of Zurich, Zurich, Switzerland;* [3]*Department of Nuclear Medicine, Technical University Munich, Munich, Germany;* [4]*Department of Theranostics and Nuclear Medicine, St. Vincent's Hospital, Sydney, New South Wales, Australia;* [5]*Nuclear Medicine, IRCCS Azienda Ospedaliero–Universitaria di Bologna, Bologna, Italy;* [6]*Department of Nuclear Medicine, University of Duisburg–Essen and German Cancer Consortium–University Hospital Essen, Essen, Germany;* [7]*Prostate Cancer Theranostics and Imaging Centre of Excellence, Molecular Imaging Therapeutic Nuclear Medicine, Cancer Imaging, Peter MacCallum Cancer Centre, and Sir Peter MacCallum Department of Oncology, University of Melbourne, Melbourne, Victoria, Australia;* [8]*Department of Radiology and Biomedical Imaging, University of California, San Francisco, San Francisco, California; and* [9]*Department of Nuclear Medicine, University Hospital Heidelberg, Heidelberg, Germany*

Prostate-specific membrane antigen (PSMA)–targeted radioligand therapy can improve the outcome of patients with advanced metastatic castration-resistant prostate cancer, but patients do not respond uniformly. We hypothesized that using the salivary glands as a reference organ can enable selective patient stratification. We aimed to establish a PSMA PET tumor–to–salivary gland ratio (PSG score) to predict outcomes after [^{177}Lu]PSMA. **Methods:** In total, 237 men with metastatic castration-resistant prostate cancer treated with [^{177}Lu]PSMA were included. A quantitative PSG (qPSG) score (SUV_{mean} ratio of whole-body tumor to parotid glands) was semiautomatically calculated on baseline [^{68}Ga]PSMA-11 PET images. Patients were divided into 3 groups: high (qPSG $>$ 1.5), intermediate (qPSG = 0.5–1.5), and low (qPSG $<$ 0.5) scores. Ten readers interpreted the 3-dimensional maximum-intensity-projection baseline [^{68}Ga]PSMA-11 PET images and classified patients into 3 groups based on visual PSG (vPSG) score: high (most of the lesions showed higher uptake than the parotid glands) intermediate (neither low nor high), and low (most of the lesions showed lower uptake than the parotid glands). Outcome data included a more than 50% prostate-specific antigen decline, prostate-specific antigen (PSA) progression-free survival, and overall survival (OS). **Results:** Of the 237 patients, the numbers in the high, intermediate, and low groups were 56 (23.6%), 163 (68.8%), and 18 (7.6%), respectively, for qPSG score and 106 (44.7%), 96 (40.5%), and 35 (14.8%), respectively, for vPSG score. The interreader reproducibility of the vPSG score was substantial (Fleiss weighted κ, 0.68). The more than 50% prostate-specific antigen decline was better in patients with a higher PSG score (high vs. intermediate vs. low, 69.6% vs. 38.7% vs. 16.7%, respectively, for qPSG [$P < 0.001$] and 63.2% vs 33.3% vs 16.1%, respectively, for vPSG [$P < 0.001$]). The median PSA progression-free survival of the high, intermediate, and low groups by qPSG score was 7.2, 4.0, and 1.9 mo ($P < 0.001$), respectively, by qPSG score and 6.7, 3.8, and 1.9 mo ($P < 0.001$), respectively, by vPSG score. The median OS of the high, intermediate, and low groups was 15.0, 11.2, and 13.9 mo ($P = 0.017$), respectively, by qPSG score and 14.3, 9.6, and 12.9 mo ($P = 0.018$), respectively, by vPSG score. **Conclusion:** The PSG score was prognostic for PSA response and OS after [^{177}Lu]PSMA. The visual PSG score assessed on 3-dimensional maximum-intensity-projection PET images yielded substantial reproducibility and comparable prognostic value to the quantitative score.

Key Words: PSMA PET; [^{177}Lu]PSMA; radioligand therapy; visual criteria; parotid glands

J Nucl Med 2023; 64:1024–1029
DOI: 10.2967/jnumed.122.265242

Patients with advanced metastatic castration-resistant prostate cancer (mCRPC) do not respond uniformly to [^{177}Lu]prostate-specific membrane antigen (PSMA) (*1,2*). Thus, identification of patients who will likely benefit from PSMA-targeted radioligand therapy remains an unmet clinical need.

High PSMA expression as assessed by PET and whole-body (WB) tumor SUV_{mean} is associated with better outcomes (*3–7*). PSMA PET should be used to select patients on the basis of tumor PSMA expression (*8*). However, the inclusion criteria based on baseline PSMA PET vary among major clinical trials and therapy centers across the world (Supplemental Table 1; supplemental materials are available at http://jnm.snmjournals.org) (*1,2,6,9–17*). The VISION trial applied qualitative (i.e., tumor uptake $>$ liver uptake, assessed visually) thresholds (*18*). These criteria are relevant in identifying patients with absence of or low [^{68}Ga]PSMA-11 expression, and 13% (126/1003) of patients were screening failures (*1*). Men with screening failure according to the VISION PET criteria had worse short-term outcomes than those who were eligible (*19*). However, even after selection of patients by VISION PET criteria, many patients do not respond favorably to [^{177}Lu]PSMA, suggesting the need for further refinements of PSMA PET and other screening parameters.

Received Nov. 22, 2022; revision accepted Feb. 10, 2023.
For correspondence or reprints, contact Masatoshi Hotta (mhotta.11.11@gmail.com).
*Contributed equally to this work.
Guest Editor: Todd Peterson, Vanderbilt University.
Published online Mar. 30, 2023.

TABLE 1
Visual PSMA PET vPSG Score

PSMA expression	Finding of MIP image
High	Most of lesions show higher uptake than parotid glands
Intermediate	Neither low nor high
Low	Most of lesions show lower uptake than parotid glands

When assessing PSMA expression, 3 anteroposterior MIP images adjusted to 0–10, 0–20, and 0–30 SUV window range should be used. "Most of lesions" refers to 80% of extent (total area) of lesion (not number). If parotid glands show heterogeneous uptake, area showing lower uptake should be used as reference. When more than half of parotid glands are out of scan range, patient should not be evaluated with these criteria.

When measured quantitatively, [^{68}Ga]PSMA-11 uptake in the parotid glands exceeds liver uptake 2- to 3-fold (median SUV_{max} for liver vs. parotids, 9.7 vs. 21.3 (*20*)), which is close to the criteria used in the TheraP trial (lesion SUV_{max}, 20) (*2*). We hypothesized that use of the parotid glands rather than the liver as a reference organ would improve patient stratification for [^{177}Lu]PSMA. The aim of this study was to test a quantitative and visual PSMA PET tumor–to–salivary gland ratio (PSG score) to predict outcomes after [^{177}Lu]PSMA in a cohort of patients with mCRPC established retrospectively from multiple institutions.

MATERIALS AND METHODS

Study Design

This was a retrospective multicenter study using a published dataset (n = 270) (*4,19*). Images were visually analyzed by 10 masked central, independent readers. The informed consent requirement was waived by the UCLA institutional review board (waiver 19-000896).

Patients

Patients received [^{177}Lu]PSMA-617 or [^{177}Lu]PSMA-I&T between December 10, 2014, and July 19, 2019, in phase 2 clinical trials (NCT03042312 and ACTRN12615000912583) or via compassionate-use access programs (Supplemental Table 2). The [^{68}Ga]PSMA-11 PET/CT protocol is provided in the supplemental Materials and Methods (*20*) and in Supplemental Table 3. Treatment details are provided in the supplemental Materials and Methods (*21–23*). Patients were excluded from the current analysis if more than 50% of the parotid glands was outside the PET field of view (as described in the eligibility criteria in Supplemental Table 4).

Image Analysis

Quantitative PSG (qPSG) Score. We first assessed the WB tumor burden quantitatively using the [^{68}Ga]PSMA-11 PET qPSG score. Parotid glands and WB tumors were segmented semiautomatically on baseline [^{68}Ga]PSMA-11 PET images using qPSMA software (*24*). Output parameters included WB SUV_{mean}, the SUV_{max} of the lesion with the highest uptake (H-lesion), WB PSMA tumor volume, and bilateral parotid gland SUV_{mean}. The ratio of WB tumor to parotid gland SUV_{mean} (qPSG = mean tumor WB SUV/mean parotid gland SUV_{mean}) was calculated. Patients were divided into 3 groups according to qPSG score: high (>1.5), intermediate (0.5–1.5), and low (<0.5). In addition, patients were grouped as high SUV versus low SUV to compare SUV-based criteria (*2,6*) with PSG scores (supplemental Materials and Methods).

Visual PSG (vPSG) Score. In a second step, we assessed the reproducibility and prognostic value of visual criteria using the parotid glands as an organ of reference (vPSG score). All readers were board-certified nuclear medicine physicians with more than 2 y of experience in PSMA PET interpretation. To assess whether the reader experience in treating patients with [^{177}Lu]PSMA therapy influences image scoring, both readers with extensive experience (>50 treatments; 5 readers) and readers with limited experience (≤50 treatments; 5 readers) were selected (Supplemental Table 5).

Three-dimensional maximum-intensity-projection (MIP) baseline [^{68}Ga]PSMA-11 PET images adjusted to 3 different SUV window ranges (0–10, 0–20, and 0–30) were generated by a single lead investigator not involved in image analysis. Each reader was provided with the images (portable document format). Readers were asked to classify the patients into 3 groups (i.e., high, intermediate, and low) according to the vPSG score as described in Table 1. Representative images of each group are shown in Figure 1.

At more than 2 wk after the first reads, 50 cases were randomly selected for rereading to determine intrareader agreement. One lead investigator conducted the final analysis. A central majority rule (6 vs. 4) was applied in cases of disagreement to obtain the final reads. If disagreement persisted on intermediate versus high or on low versus intermediate (e.g., 5 vs. 5), the cases were classified as high or low, respectively, avoiding the intermediate category.

Clinical Outcomes

The clinical outcomes included a more than 50% prostate-specific antigen (PSA) decline (PSA50), PSA progression-free survival (PFS), and overall survival (OS). PSA50 was defined by a PSA decline of more than 50% compared with baseline at any time during the treatment (best response). PSA PFS was defined as the time from treatment initiation to PSA progression or death from any cause, as per the criteria of Prostate Cancer Clinical Trials Working Group 3 (*25*). OS was defined as time from treatment initiation to death of any cause.

Statistical Analysis

The R software package was used for statistical analysis. Two-tailed P values of less than 0.05 were considered significant. Clinical characteristics were compared among PSMA expression groups using the Mann–Whitney U and Fisher exact tests for continuous and

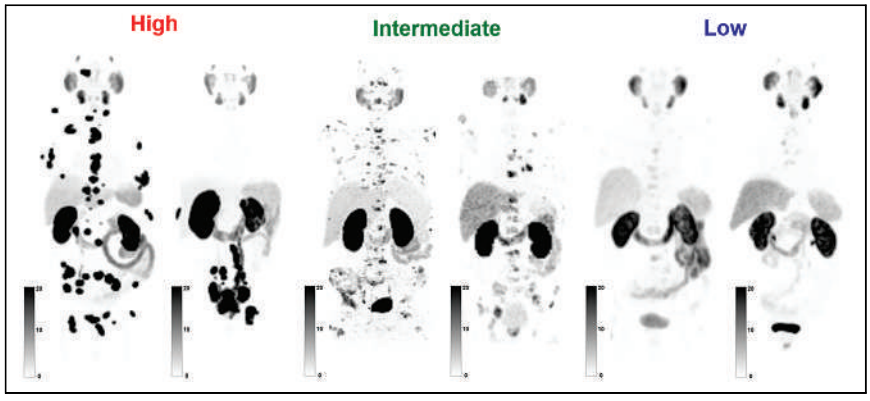

FIGURE 1. Representative MIP images of 6 patients classified as having high, intermediate, and low vPSG scores (MIP SUV range, 0–20).

categoric variables. The proportion of patients who had a PSA50 was assessed by the Fisher exact test, and the odds ratio from logistic regression was calculated. Kaplan–Meier analysis with the log-rank test and Cox hazard ratio regression was performed to evaluate survival outcomes. Multivariate Cox and logistic regression analyses were performed to test the PSG scores and previously reported prognostic factors for [^{177}Lu]PSMA (*4*). Intra- and interreader agreement was evaluated by weighted Fleiss κ-coefficients. Agreement between vPSG score (majority rule) and qPSG score was assessed by weighted Cohen κ-coefficients.

RESULTS

Patients

Between April 23, 2019, and January 13, 2020, 414 patients were retrospectively screened, and 177 men were excluded as specified in Supplemental Figure 1. Thus, 237 men were included in the final analysis. Seventy-five and 162 men were treated with [^{177}Lu]PSMA-617 and [^{177}Lu]PSMA-I&T, respectively. Table 2 depicts the clinical characteristics of the cohort. The median follow-up time was 21.2 mo (interquartile range, 14.1–30.6 mo).

PSG Score

Of the 237 patients, the numbers in the high-, intermediate-, and low-PSG groups were 56 (23.6%), 163 (68.8%), and 18 (7.6%), respectively, by qPSG score and 106 (44.7%), 96 (40.5%), and 35 (14.8%), respectively, by vPSG score (majority rule) (Supplemental Tables 6 and 7 show the clinical and PSMA PET characteristics of each qPSG and vPSG score group). There was no difference between the baseline clinical characteristics of any groups, except for the lower proportion of patients with prior docetaxel treatment in the low-qPSG group. The number of patients with PSMA PET nodal metastasis (N1) was lowest in the low groups both by qPSG score (33.3%) and by vPSG score (20.0%) ($P < 0.001$). The number of distant metastases (≥20) was lower in the low group (45.7%) than the intermediate (75.0%) and high (76.4%) groups by vPSG score ($P = 0.001$). WB tumor SUV_{mean} and PSMA tumor volume were highest in the high group, followed by the intermediate and low group, both by qPSG score and by vPSG score.

PSG Score and Clinical Outcome

Clinical outcomes for each of the 3 groups by vPSG and qPSG scores are summarized in Table 3. Comparisons between PSA PFS and OS in patients with a nonhigh PSG score (intermediate + low) versus a high PSG score (2 groups) are provided in Supplemental Figures 2 and 3, respectively. The PSA50, PSA PFS, and OS obtained by PSG scores and SUV-based criteria (high SUV vs. low SUV) are compared in the supplemental Materials and Methods.

PSA Response. A higher PSA50 was observed in the groups with a high PSG score than in those with an intermediate or low PSG score ($P < 0.001$) (PSA50 odds ratios for qPSG and vPSG scores are shown in Supplemental Tables 8 and 9). Both qPSG score and vPSG score were independent predictors of PSA50. Moreover, PSA50 in patients with a high PSG score was significantly better than in those with an H-lesion SUV_{max} of at least 20 (supplemental Materials and Methods).

PSA PFS. PSA PFS was longest in the groups with a high qPSG or vPSG score (Fig. 2). The corresponding hazard ratios are shown in Supplemental Tables 10 and 11, respectively.

OS. The longest OS was in the groups with a high qPSG or vPSG score (Fig. 3). The hazard ratios of the high groups were lower than those of the intermediate groups but were not significantly different from the low groups in univariate and multivariate analyses (Supplemental Tables 12 and 13). There was no difference in OS between patients with an H-lesion SUV_{max} of at least 20 and those with an H-lesion SUV_{max} of less than 20. In contrast, OS was longer in patients with a WB SUV_{mean} of at least 10 than in those with a WB SUV_{mean} of less than 10. OS did not significantly differ between patients with a high PSG score and patients with a WB SUV_{mean} of at least 10 (Supplemental Fig. 3).

TABLE 2
Patient Characteristics and Clinical Outcome

Characteristic	Data
Total patients	237
Age (y)	72 (IQR, 66, 76)
PSA (ng/mL)	116.3 (IQR, 34.2, 388.1)
Initial NCCN risk group	
Low risk	9 (3.8%)
Intermediate risk	42 (17.7%)
High risk	92 (38.8%)
Metastatic	94 (39.7%)
Treatment history	
Previous docetaxel	190 (80.2%)
Second-line chemotherapy	86 (36.3%)
Androgen receptor signaling inhibitor	225 (94.9%)
Extent of disease on PSMA PET/CT	
Number of metastases ≥ 20	169 (71.3%)
Number of metastases < 20	68 (28.7%)
Sites of disease on PSMA PET/CT	
Pelvic nodal metastasis (N1)	113 (47.7%)
Distant nodal metastasis (M1a)	156 (65.8%)
Bone metastasis (M1b)	218 (92.0%)
Other organ metastasis (M1c)	72 (30.4%)
Cycles of [^{177}Lu]PSMA received	
1	37 (15.6%)
2	64 (27.0%)
3	34 (14.3%)
4	78 (32.9%)
>4	24 (10.1%)
Injected activity per cycle (GBq)	7.4 (IQR, 7.4, 7.4)
OS (mo)	12.6 (95% CI, 11.0–14.2)
OS events	195 (82.3%)
PSA progression-free survival (mo)	4.6 (95% CI, 3.7–5.6)
PSA progression-free survival events	210 (88.6%)
PSA decline ≥ 50%	105 (44.3%)

IQR = interquartile range; NCCN = National Comprehensive Cancer Network.
Qualitative data are number; continuous data are median.

TABLE 3
Outcomes of qPSG Score and vPSG Score for High, Intermediate, and Low Patients

Outcome	High	Intermediate	Low	*P*
qPSG score				
PSA decline ≥ 50% (*n*)	39/56 (69.6%)	63/163 (38.7%)	3/18 (16.7%)	<0.001
PSA PFS	7.2 (4.9–8.3)	4.0 (3.3–5.4)	1.9 (1.4–4.2)	<0.001
OS	15.0 (12.0–19.0)	11.2 (9.1–13.1)	13.9 (8.0–30.6)	0.017
vPSG score				
PSA decline ≥ 50% (*n*)	67/106 (63.2%)	32/96 (33.3%)	6/35 (17.1%)	<0.001
PSA PFS	6.7 (4.6–7.7)	3.8 (2.8–5.6)	1.9 (1.5–3.1)	<0.001
OS	14.3 (12.0–17.8)	9.6 (8.0–12.9)	12.9 (9.0–18.8)	0.018

Survival data are median, in months, followed by 95% CI in parentheses.

Agreement

Agreement between qPSG and vPSG scores was moderate (weighted Cohen κ, 0.60; 95% CI, 0.52–0.68). Complete agreement between qPSG and vPSG scores was seen in 160 (67.5%) of the 237 patients.

The inter- and intrareader reproducibility of the vPSG score for all readers ($n = 10$) showed substantial agreement (Fleiss weighted κ, 0.68; 95% CI, 0.63–0.73) or almost perfect agreement (Cohen weighted κ [mean], 0.83 ± 0.06), respectively (supplemental Materials and Methods). Agreement among readers with and without prior ^{177}Lu-PSMA experience is shown in Supplemental Table 14 and Supplemental Figure 4.

DISCUSSION

Quantitative (qPSG) and visual (vPSG) PET-derived scores for tumor [^{68}Ga]PSMA-11 expression relative to parotid gland uptake predicted the PSA response and PSA PFS to [^{177}Lu]PSMA of patients with mCRPC. The 3-dimensional MIP image–based vPSG score was substantially reproducible and did not require extensive experience with [^{177}Lu]PSMA.

In the VISION study, the liver was used as the reference organ, and 87.4% of patients were eligible after [^{68}Ga]PSMA-11 PET screening (*1*). PSMA tumor uptake equal to or greater than liver uptake appears to be the minimum target expression requirement for response to [^{177}Lu]PSMA. The [^{68}Ga]PSMA-11 uptake of the parotid gland is 2–3 times higher than that of the liver (*20*). Therefore, use of the parotid gland as a reference organ would make the criteria more stringent and specific.

Only MIP images were used for visual analysis. MIP images display WB tumor PSMA expression and disease extent in a single image. However, vPSG score should be used in combination with cross-sectional image analysis to determine the presence of PSMA-negative lesions (*1,18,19*). The greatest value of the PSG score may be in its use to exclude patients less likely to benefit from [^{177}Lu]PSMA—those with a low PSG score. Also, when available, [^{18}F]FDG PET/CT may complement the PSG score and potentially improve prognostication. The presence of [^{18}F]FDG-positive/PSMA-negative lesions was associated with poor response to [^{177}Lu]PSMA (*9,26–28*). We propose that patients with a low PSG score be deprioritized from [^{177}Lu]PSMA. PSMA PET–based exclusion criteria for [^{177}Lu]PSMA may encompass patients with PSMA-negative lesions by CT or by FDG, patients with lesion uptake below liver uptake, and patients with a low vPSG score.

Three different SUV-scale windows were used for interpreting MIP images. A MIP image with a narrow window (SUV, 0–10) is useful to observe the distribution of lesions with low PSMA expression, and MIP images with a wider window (SUVs, 0–20 and 0–30) are helpful to compare lesion uptake with parotid gland uptake. Using MIP images enables rapid and reproducible evaluations, which can facilitate clinical implementation.

Agreement between qPSG score and vPSG score (majority rule) was moderate, because vPSG score is based on the extent (>80%) of lesions with uptake greater than that of the parotid gland, whereas qPSG score is independent of disease extent (based on SUV ratio only). Despite the methodologic difference, the outcomes of each group by qPSG and vPSG score were similar, suggesting that both criteria are valuable. qPSG score enables higher reproducibility as it is obtained semiautomatically; however, segmentation software is necessary.

Recently developed nomograms to predict outcome after [^{177}Lu]PSMA require WB SUV_{mean} as a parameter (*4*). A classification using a WB SUV_{mean} of at least

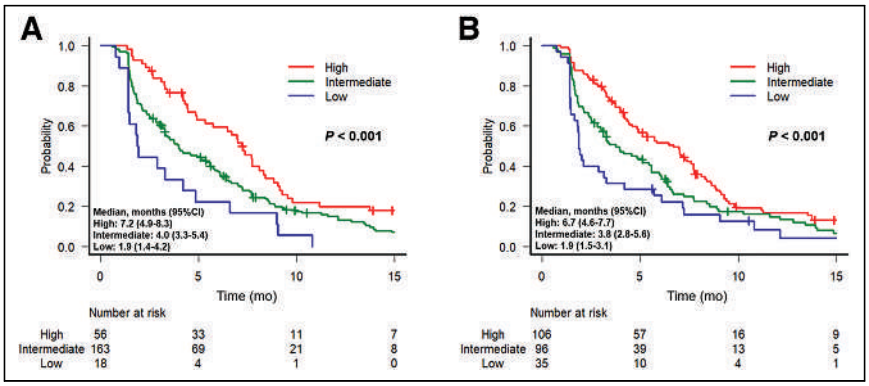

FIGURE 2. Kaplan–Meier curves for PSA PFS comparing groups with high, intermediate, and low PSMA expression classified by qPSG score (A) and vPSG score (B).

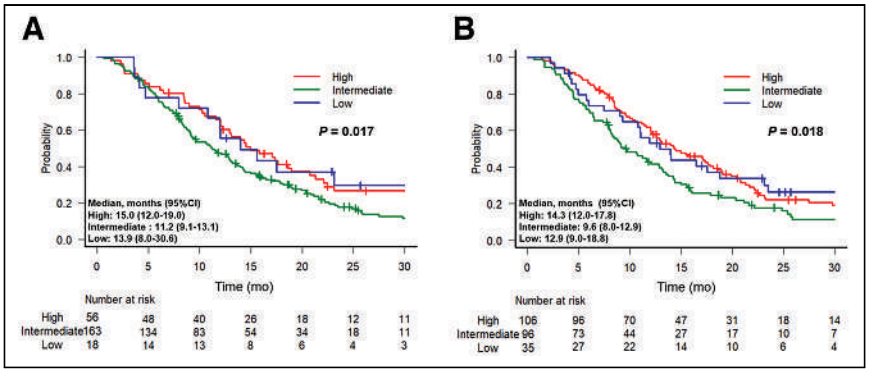

FIGURE 3. Kaplan–Meier curves for OS comparing groups with high, intermediate, and low PSMA expression classified by qPSG score (A) and vPSG score (B).

10 identified treatment responders in the VISION and TheraP cohorts (*6*). In our cohort, both qPSG score and vPSG score had similar prognostic value to a WB SUV_{mean} of at least 10. The qPSG score is based on an SUV ratio (WB tumor to parotid glands) rather than a fixed SUV threshold to reduce some inherent variability in SUV measurements across patients, scanners, and reconstruction algorithms (*29*). The need for tumor segmentation software precludes current clinical use of quantitative parameters such as WB tumor volume/SUV_{mean}. There are multiple WB segmentation tools under clinical development (*24,30–33*), but none are yet validated and widely available.

We propose a simple visual score to derive prognostic information from the screening 3-dimensional MIP [^{68}Ga]PSMA-11 PET images. In contrast, a binary SUV_{max} classification (H-lesion $SUV_{max} \geq 20$ vs. < 20) was not prognostic of patient OS, because H-lesion SUV_{max} does not account for disease heterogeneity, a key determinant of treatment response to [^{177}Lu]PSMA (*3,12*). The 3-dimensional MIP-based vPSG score can be implemented quickly and at no cost in the clinic after further validation. Integration of the vPSG score in the [^{177}Lu]PSMA nomogram approach (*4*) may improve its accuracy and further support clinical adoption.

We divided patients into 3 rather than 2 groups. The rationale was to capture, in the intermediate group, patients with heterogeneous PSMA expression. This grouping predicted PSA responses well. However, the group with an intermediate PSG score tended to show worse OS than the group with a low PSG score. Possible explanations include the small population, partial-volume effects, less advanced disease stage, and lower tumor burden in the low group. As such, the 3-group PSG score is more suitable as a biomarker for PSA response than for OS.

Limitations of this study include the lack of independent PSG score validation and the retrospective design. Moreover, the cohort did not include patients who were excluded from [^{177}Lu]PSMA by the local treating sites. Thus, patients with low PSMA expression may be underrepresented. Also, the PSG score was tested only with [^{68}Ga]PSMA-11 PET, and its efficacy with other PSMA-targeted PET tracers (e.g., [^{18}F]DCFPyL) is unknown. Considering similar normal-organ and tumor biodistribution patterns between [^{68}Ga]PSMA-11 and [^{18}F]DCFPyL (*34*), we anticipate that the PSG score may be applicable to [^{18}F]DCFPyL PET as well. Nevertheless, confirmatory studies have yet to be conducted. Finally, our criteria focus on only PSMA expression. Although high PSMA expression increases the likelihood of sufficient delivery of radiopharmaceutical to tumor, various factors (e.g., administered and absorbed dose, genomic DNA repair mechanism, radiosensitivity, and other biologic tumor characteristics) are associated with radioresistance (*35*). More comprehensive inclusion criteria may be necessary to refine patient selection.

CONCLUSION

This study proposes a PSG score derived from pretherapeutic [^{68}Ga]PSMA-11 PET as a novel predictive and prognostic biomarker for response to [^{177}Lu]PSMA. After further clinical validation, this score, together with other cross-sectional or metabolic imaging, may improve patient selection.

DISCLOSURE

Andrei Gafita is supported by the Prostate Cancer Foundation (21YOUN18), a UCLA Jonsson Comprehensive Cancer Center fellowship award, and a Dr. Christiaan Schiepers postdoctoral fellowship award. Jeremie Calais is supported by the Prostate Cancer Foundation (20YOUN05) and reports previous consulting activities for Astellas, Blue Earth Diagnostics, Curium Pharma, DS Pharma, GE Healthcare, IBA Cyclopharma, Isoray, Janssen Pharmaceuticals, Lantheus, Lightpoint Medical, Novartis, Point Biopharma, and Telix outside the submitted work. Michael Hofman is supported by a PCF Special Challenge Award through the Prostate Cancer Foundation with funding from CANICA, Oslo, Norway, and a Prostate Cancer Research Alliance Grant funded by Movember and the Australian Government Medical Research Future Fund; receives personal fees from Janssen (lecture honorarium), Mundipharma (lecture honorarium), Astellas (lecture honorarium), AstraZeneca (lecture honorarium), and MSD (advisory forum); receives research support from Endocyte, AAA, and Novartis, outside the submitted work; receives grant support from AAA/Novartis; and receives consulting fees for lectures or advisory boards from Astellas, AstraZeneca, Janssen, Merck/MSD, Mundipharma, and Point Biopharma. Wolfgang Fendler is supported by the German Research Foundation (FE1573/3-1/659216) and receives fees from SOFIE Bioscience (research funding), Janssen (consultant, speakers bureau), Calyx (consultant), Bayer (consultant, speakers bureau, research funding), and Parexel (image review) outside the submitted work. Johannes Czernin is a founder, board member, and holds equity in Sofie Biosciences and Trethera Therapeutics (intellectual property is patented by the University of California and licensed to Sofie Biosciences and Trethera Therapeutics) and was a consultant for Endocyte (VISION trial steering committee), Actinium Pharmaceuticals, and Point Biopharma, outside the submitted work. Thomas Hope reports consulting activities with Curium, RayzeBio, and ITM; receives research support from Clovis Oncology and Philips; and is supported by the NCI (R01CA212148 and R01CA235741) and the Prostate Cancer Foundation. Matthias Eiber reports previous consulting activities for BED, Novartis, Telix, Progenics, Bayer, PointBiopharma and Janssen and has submitted a patent application for rhPSMA, outside the submitted work.

No other potential conflict of interest relevant to this article was reported.

KEY POINTS

QUESTION: Can the PSMA PET criteria using salivary glands as a reference organ (i.e., PSG score) optimize stratification of patients with mCRPC based on the response to [^{177}Lu]PSMA?

PERTINENT FINDINGS: WB tumor uptake was compared with salivary gland uptake visually and quantitatively on baseline [^{68}Ga]PSMA-11 PET images, and patients were classified into groups with high, intermediate, and low PSMA expression. Patients with high expression classified visually and by qPSG score showed a significantly better PSA response and OS after [^{177}Lu]PSMA.

IMPLICATIONS FOR PATIENT CARE: The PSG score can be a valuable biomarker for response to [^{177}Lu]PSMA and may assist in individual clinical decision making and future clinical trial design.

REFERENCES

1. Sartor O, de Bono J, Chi KN, et al. Lutetium-177-PSMA-617 for metastatic castration-resistant prostate cancer. *N Engl J Med.* 2021;385:1091–1103.
2. Hofman MS, Emmett L, Sandhu S, et al. [^{177}Lu]Lu-PSMA-617 versus cabazitaxel in patients with metastatic castration-resistant prostate cancer (TheraP): a randomised, open-label, phase 2 trial. *Lancet.* 2021;397:797–804.
3. Seifert R, Seitzer K, Herrmann K, et al. Analysis of PSMA expression and outcome in patients with advanced prostate cancer receiving ^{177}Lu-PSMA-617 radioligand therapy. *Theranostics.* 2020;10:7812–7820.
4. Gafita A, Calais J, Grogan TR, et al. Nomograms to predict outcomes after ^{177}Lu-PSMA therapy in men with metastatic castration-resistant prostate cancer: an international, multicentre, retrospective study. *Lancet Oncol.* 2021;22:1115–1125.
5. Ferdinandus J, Violet J, Sandhu S, et al. Prognostic biomarkers in men with metastatic castration-resistant prostate cancer receiving [^{177}Lu]-PSMA-617. *Eur J Nucl Med Mol Imaging.* 2020;47:2322–2327.
6. Buteau JP, Martin AJ, Emmett L, et al. PSMA and FDG-PET as predictive and prognostic biomarkers in patients given [^{177}Lu]Lu-PSMA-617 versus cabazitaxel for metastatic castration-resistant prostate cancer (TheraP): a biomarker analysis from a randomised, open-label, phase 2 trial. *Lancet Oncol.* 2022;23:1389–1397.
7. Kuo P, Hesterman J, Rahbar K, et al. [^{68}Ga]Ga-PSMA-11 PET baseline imaging as a prognostic tool for clinical outcomes to [^{177}Lu]Lu-PSMA-617 in patients with mCRPC: a VISION substudy [abstract]. *J Clin Oncol.* 2022;40(suppl):5002.
8. Highlights of prescribing information. Pluvicto® (lutetium Lu 177 vipivotide tetraxetan) injection, for intravenous use. Food and Drug Administration website. https://www.accessdata.fda.gov/drugsatfda_docs/label/2022/215833s000lbl.pdf. Revised March 2022. Accessed March 15, 2023.
9. Hofman MS, Violet J, Hicks RJ, et al. [^{177}Lu]-PSMA-617 radionuclide treatment in patients with metastatic castration-resistant prostate cancer (LuPSMA trial): a single-centre, single-arm, phase 2 study. *Lancet Oncol.* 2018;19:825–833.
10. Calais J, Gafita A, Eiber M, et al. Prospective phase 2 trial of PSMA-targeted molecular RadiothErapy with ^{177}Lu-PSMA-617 for metastatic castration-reSISTant Prostate Cancer (RESIST-PC): efficacy results of the UCLA cohort. *J Nucl Med.* 2021;62:1440–1446.
11. Calais J, Czernin J, Thin P, et al. Safety of PSMA-targeted molecular radioligand therapy with ^{177}Lu-PSMA-617: results from the prospective multicenter phase 2 trial RESIST-PC (NCT03042312). *J Nucl Med.* 2021;62:1447–1456.
12. Vlachostergios PJ, Niaz MJ, Skafida M, et al. Imaging expression of prostate-specific membrane antigen and response to PSMA-targeted β-emitting radionuclide therapies in metastatic castration-resistant prostate cancer. *Prostate.* 2021;81:279–285.
13. Rathke H, Holland-Letz T, Mier W, et al. Response prediction of ^{177}Lu-PSMA-617 radioligand therapy using prostate-specific antigen, chromogranin A, and lactate dehydrogenase. *J Nucl Med.* 2020;61:689–695.
14. Derlin T, Werner RA, Lafos M, et al. Neuroendocrine differentiation and response to PSMA-targeted radioligand therapy in advanced metastatic castration-resistant prostate cancer: a single-center retrospective study. *J Nucl Med.* 2020;61:1602–1606.
15. Sartor O, Morris MJ, Chi KN, et al. PSMAfore: a phase 3 study to compare ^{177}Lu-PSMA-617 treatment with a change in androgen receptor pathway inhibitor in taxane-naïve patients with metastatic castration-resistant prostate cancer [abstract]. *J Clin Oncol.* 2022;40(suppl):211.
16. Chi KN, Metser U, Czernin J, et al. Study evaluating metastatic castrate resistant prostate cancer (mCRPC) treatment using ^{177}Lu-PNT2002 PSMA therapy after second-line hormonal treatment (SPLASH) [abstract]. *J Clin Oncol.* 2021;39(suppl):5087.
17. Yu EY, Laidley D, Pouliot F, et al. A multicenter, randomized, controlled phase II study: efficacy and safety of PSMA-targeted radioligand therapy I-131-1095 (1095) plus enzalutamide (enza) in ^{18}F-DCFPyL PSMA scan avid, metastatic castration-resistant prostate cancer (mCRPC) patients post-abiraterone (abi) progression (ARROW) [abstract]. *J Clin Oncol.* 2020;38(suppl):5596.
18. Kuo PH, Benson T, Messmann R, Groaning M. Why we did what we did: PSMA-PET/CT selection criteria for the VISION trial. *J Nucl Med.* 2022;63:816–818.
19. Hotta M, Gafita A, Czernin J, Calais J. Outcome of patients with PSMA-PET/CT screen failure by VISION criteria and treated with ^{177}Lu-PSMA therapy. *J Nucl Med.* 2022;63:1484–1488.
20. Gafita A, Wang H, Robertson A, et al. Tumor sink effect in ^{68}Ga-PSMA-11 PET: myth or reality? *J Nucl Med.* 2022;63:226–232.
21. Weineisen M, Simecek J, Schottelius M, Schwaiger M, Wester HJ. Synthesis and preclinical evaluation of DOTAGA-conjugated PSMA ligands for functional imaging and endoradiotherapy of prostate cancer. *EJNMMI Res.* 2014;4:63.
22. Calais J, Fendler WP, Eiber M, et al. RESIST-PC phase 2 trial: ^{177}Lu-PSMA-617 radionuclide therapy for metastatic castrate-resistant prostate cancer [abstract]. *J Clin Oncol.* 2019;37(suppl):5028.
23. Kratochwil C, Giesel FL, Stefanova M, et al. PSMA-targeted radionuclide therapy of metastatic castration-resistant prostate cancer with ^{177}Lu-labeled PSMA-617. *J Nucl Med.* 2016;57:1170–1176.
24. Gafita A, Bieth M, Krönke M, et al. qPSMA: semiautomatic software for whole-body tumor burden assessment in prostate cancer using ^{68}Ga-PSMA11 PET/CT. *J Nucl Med.* 2019;60:1277–1283.
25. Scher HI, Morris MJ, Stadler WM, et al. Trial design and objectives for castration-resistant prostate cancer: updated recommendations from the Prostate Cancer Clinical Trials Working Group 3. *J Clin Oncol.* 2016;34:1402–1418.
26. Wang B, Liu C, Wei Y, et al. A prospective trial of ^{68}Ga-PSMA and ^{18}F-FDG PET/CT in nonmetastatic prostate cancer patients with an early PSA progression during castration. *Clin Cancer Res.* 2020;26:4551–4558.
27. Michalski K, Ruf J, Goetz C, et al. Prognostic implications of dual tracer PET/CT: PSMA ligand and [^{18}F]FDG PET/CT in patients undergoing [^{177}Lu]PSMA radioligand therapy. *Eur J Nucl Med Mol Imaging.* 2021;48:2024–2030.
28. Khreish F, Ribbat K, Bartholomä M, et al. Value of combined PET imaging with [^{18}F]FDG and [^{68}Ga]Ga-PSMA-11 in mCRPC patients with worsening disease during [^{177}Lu]Lu-PSMA-617 RLT. *Cancers (Basel).* 2021;13:4134.
29. Boellaard R. Standards for PET image acquisition and quantitative data analysis. *J Nucl Med.* 2009;50(suppl 1):11S–20S.
30. Klyuzhin IS, Chaussé G, Bloise I, Ferres JL, Uribe C, Rahmim A. PSMA-Hornet: fully-automated, multi-target segmentation of healthy organs in PSMA PET/CT images. medRxiv website. https://www.medrxiv.org/content/10.1101/2022.02.02.22270344v1. Published February 5, 2022. Accessed March 15, 2023.
31. Seifert R, Herrmann K, Kleesiek J, et al. Semiautomatically quantified tumor volume using ^{68}Ga-PSMA-11 PET as a biomarker for survival in patients with advanced prostate cancer. *J Nucl Med.* 2020;61:1786–1792.
32. Nickols N, Anand A, Johnsson K, et al. aPROMISE: a novel automated PROMISE platform to standardize evaluation of tumor burden in ^{18}F-DCFPyL images of veterans with prostate cancer. *J Nucl Med.* 2022;63:233–239.
33. Johnsson K, Brynolfsson J, Sahlstedt H, et al. Analytical performance of aPROMISE: automated anatomic contextualization, detection, and quantification of [^{18}F]DCFPyL (PSMA) imaging for standardized reporting. *Eur J Nucl Med Mol Imaging.* 2022;49:1041–1051.
34. Ferreira G, Iravani A, Hofman MS, et al. Intra-individual comparison of ^{68}Ga-PSMA-11 and ^{18}F-DCFPyL normal-organ biodistribution. *Cancer Imaging.* 2019;19:23.
35. Sandhu S, Guo C, Hofman MS. Radionuclide therapy in prostate cancer: from standalone to combination PSMA theranostics. *J Nucl Med.* 2021;62:1660–1668.

Staging Prostate Cancer with ^{68}Ga-PSMA-11 PET/CT in the Elderly: Is Preimaging Biopsy Imperative?

Mikhail Kesler*[1], Dan Cohen*[1], Charles Levine[1,2], David Sarid[2,3], Daniel Keizman[2,3], Ofer Yossepowitch[2,4], and Einat Even-Sapir[1,2]

[1]*Department of Nuclear Medicine, Tel Aviv Sourasky Medical Center, Tel Aviv, Israel;* [2]*Sackler Faculty of Medicine, Tel Aviv University, Tel Aviv, Israel;* [3]*Department of Oncology, Tel-Aviv Sourasky Medical Center, Tel Aviv, Israel; and* [4]*Department of Urology, Tel Aviv Sourasky Medical Center, Tel Aviv, Israel*

Although prostate-specific membrane antigen (PSMA) PET/CT has been shown valuable for staging biopsy-proven [B(+)] high-risk prostate cancer, elderly patients are occasionally referred for PSMA PET/CT without a preimaging confirming biopsy [B(−)]. The current study evaluated the rate, clinical characteristics, and PET-based stage of elderly B(−) patients and explored whether biopsy status affects therapeutic approach. **Methods:** One hundred consecutive patients at least 80 y old who underwent staging ^{68}Ga-PSMA-11 PET/CT were included. For each patient, we documented whether preimaging biopsy was performed, the clinical parameters, the PET-based staging parameters, and the primary therapy received. **Results:** Thirty-four (34%) of the elderly patients included in the study had no preimaging biopsy. Compared with B(+) patients, B(−) patients were older (median age, 87 vs. 82 y; $P < 0.01$), with worse performance status ($P < 0.01$) and higher prostate-specific antigen (PSA) levels (median, 57 vs. 15.4 ng/mL; $P < 0.01$). On ^{68}Ga-PSMA-11 PET/CT, all B(−) patients had avid disease, with trends toward higher rates of bone metastases (47.1% vs. 28.8%) and overall advanced disease (50% vs. 33.3%) than in B(+) patients. Among patients with localized ($n = 36$) or locally advanced ($n = 25$) disease, B(−) patients were less commonly referred than B(+) patients for definitive therapies ($P < 0.01$). However, higher age, Eastern Cooperative Oncology Group performance status, and PSA were other probable factors determining their therapeutic approach. Among 39 patients with advanced disease, 38 received hormonal therapy irrespective of their biopsy status. Among B(−) patients with advanced disease who were referred for hormonal therapy, 12 of 13 with follow-up data showed a biochemical or imaging-based response. **Conclusion:** Real-life experience with ^{68}Ga-PSMA-11 PET/CT indicates that around one third of elderly patients are referred for imaging without a preimaging confirming biopsy. These patients are likely to be older, with a worse clinical status and higher PSA levels. Advanced disease might be more likely to be identified on their ^{68}Ga-PSMA-11 PET/CT images, and if it is, their biopsy status does not preclude them from receiving hormonal therapy.

Key Words: prostate cancer; staging; PSMA PET/CT; elderly patients; biopsy

J Nucl Med 2023; 64:1030–1035
DOI: 10.2967/jnumed.122.265371

The prostate cancer (PCa) staging algorithm is continually undergoing adjustments. Prostate-specific membrane antigen (PSMA)–based PET imaging is gaining popularity and posing an alternative to traditional imaging modalities (*1–3*). Although first granted a limited approval in the United States in late 2020 (*4*), PSMA PET/CT was included in the Israeli medical services basket in early 2016 for initial staging of high-risk PCa (*5*), replacing the traditional use of CT and bone scanning in this group of patients.

On staging, several therapeutic approaches exist for patients with high-risk PCa. Although dictated by guidelines (*6–8*), treatment is generally patient-tailored on the basis of both disease-related and patient-related factors. Patients presenting with high-risk localized cancer are usually considered for definitive therapy by radical prostatectomy or radiotherapy with or without hormonal therapy. Therapy of patients with locally advanced disease usually includes pelvic radiotherapy. Patients with advanced disease are usually offered hormonal therapy aiming to achieve androgen deprivation and delay disease progression. Accurate staging is therefore crucial for optimal treatment planning.

The definition of high-risk PCa is based on clinical T stage (cT3–4), blood prostate-specific antigen (PSA) level (>20 ng/mL), or Gleason score (≥7) (*9*), and these are the criteria that usually guide clinicians on whether to refer patients for PSMA PET/CT once PCa is histopathologically confirmed. Focusing on elderly patients, however, our impression was that at least some patients are referred for PSMA PET/CT on the basis of high clinical suspicion but without biopsy-proven PCa, probably because of the known inconvenience and potential complications of prostate biopsies (*10,11*).

In the current study, we focused on patients at least 80 y old who were referred for PSMA PET/CT with or without a preimaging biopsy confirming the existence of PCa. The aims of the study were to assess the proportion of patients undergoing PSMA PET/CT based on clinical suspicion but without biopsy-proven PCa, identify the characteristics of patients referred on the basis of high clinical suspicion only, calculate the PSMA PET positivity rate in such cases, and explore whether lack of pathologic proof impacted the therapeutic approach selected for these patients.

MATERIALS AND METHODS

Patient Population

We retrospectively included all patients who met the following criteria: had an age of at least 80 y, underwent whole-body ^{68}Ga-PSMA-11 PET/CT in the department of nuclear medicine at Tel-Aviv Sourasky Medical Center for primary staging between January 2016 and

Received Dec. 25, 2022; revision accepted Feb. 16, 2023.
For correspondence or reprints, contact Einat Even-Sapir (evensap@tlvmc.gov.il).
*Contributed equally to this work.
Published online Apr. 28, 2023.

September 2021, and were clinically evaluated and treated at Tel-Aviv Sourasky Medical Center. A total of 100 patients fulfilled the study's inclusion criteria. The study protocol was approved by the local institutional ethics committee, which waived the requirement for written informed consent (approval TLV-0327-20).

Preimaging Clinical Data. For all included patients, we documented the following clinical parameters: age, PSA level, Eastern Cooperative Oncology Group performance status, and whether a preimaging biopsy was performed, B(+), or not performed, B(−). If the patient underwent a biopsy, we documented the highest International Society of Urological Pathology group grade reported on histopathologic assessment.

PET/CT-Based Staging Data. For all included studies, we documented the disease extent identified on PSMA PET/CT imaging using the European Association of Nuclear Medicine standardized reporting guidelines for PSMA PET (*12*): miT stage, that is, evidence of a local avid tumor (organ-confined, suspected extracapsular extension, seminal vesicle invasion, invasion to other adjacent structures); miN stage, that is, evidence of regional avid nodal disease (pelvic nodes); and miM stage, that is, evidence of avid distant metastases (extrapelvic nodes, bone or visceral metastases). Accordingly, patients' malignancies were categorized into 3 groups: localized disease (malignancy that involves the prostate only), locally advanced disease (extraprostatic extension or regional nodal disease, without distant metastases), and advanced disease (evident distant metastases) (*13–15*). For each case, the PET/CT-based staging parameters were recorded in the dataset on the basis of the data interpretation and categorization that appeared in the final PET/CT report. Beyond the PET/CT imaging data, all available data regarding the patient's previous clinical history and course of the disease, and all available data from previous laboratory, pathologic, and imaging studies, were used to assist in imaging interpretation and categorization.

Therapy Data. For each included patient, we documented which of the following therapies were used after staging PET/CT: radical prostatectomy, pelvic radiotherapy, hormonal therapy (androgen deprivation therapy or other hormonal therapies), or other systemic therapies. If none of these were given, the patient was considered to have been put under surveillance (a watch-and-wait strategy).

PET/CT Imaging

PET/CT studies were performed from the tip of the skull to mid thigh using Discovery 690 or Discovery MI PET/CT systems (GE Healthcare). An activity of 148–166 MBq of ^{68}Ga-PSMA-11 was intravenously injected 60 min before acquisition. The patients were instructed to void their bladder immediately before the acquisition. Contrast material was administered orally and intravenously, unless contraindicated. CT was performed using automatic mA-modulation and 120 kV. CT scans were reconstructed to a slice thickness of 2.5 mm. PET was performed with an acquisition time of 2.5–3 min per bed position in 3-dimensional mode. PET images were reconstructed in a matrix size of 128 × 128, pixel size of 5.5 mm, and slice thickness of 3.3 mm for the Discovery 690 system and a matrix size of 256 × 256, pixel size of 2.7 mm, and slice thickness of 2.8 mm for the Discovery MI system. The reconstruction method was VUE Point FX (GE Healthcare), which uses time-of-flight information and includes a fully 3-dimensional ordered-subsets expectation maximization algorithm with 3 iterations. Reconstruction used 24 subsets and a filter cutoff of 8 mm for the Discovery 690 system and 8 subsets and a filter cutoff of 6 mm for the Discovery MI system. The VUE Point FX algorithm also includes normalization and image corrections for attenuation, scatter, randoms, and dead time. A heavy Z-filter was applied to smooth between transaxial slices.

Statistical Analysis

Categoric data were described with contingency tables that included frequency and percentage. Continuous variables were evaluated for normal distribution and reported as median and interquartile range. The Pearson χ^2 test and Fisher exact test were used to compare rates of categoric variables. The Mann–Whitney *U* test was used to compare medians of continuous variables between 2 unpaired groups. A 2-sided *P* value of less than 0.05 was considered statistically significant. SPSS software (IBM SPSS Statistics, version 27; IBM Corp.) for Microsoft Windows was used for statistical analysis.

RESULTS

Patient Characteristics

The median patient age was 82 y (interquartile range, 80–86.8 y; range, 80–94 y). At the time of imaging, 33% and 11% of patients were at least 85 y old and at least 90 y old, respectively. The median blood PSA level was 22.6 ng/mL, with 53% and 13% of patients having a PSA level above 20 and 100 ng/mL, respectively.

From their ^{68}Ga-PSMA-11 PET/CT studies, 36 and 25 patients were categorized as having localized and locally advanced disease, respectively. The other 39 patients had advanced disease: 35 had bone metastases, 10 had distal nodal disease, 3 had liver metastases, 2 had lung metastases, and 1 had peritoneal involvement. Table 1 summarizes the clinical, staging, and therapy data of the total study patients.

Characteristics of Patients Undergoing PSMA PET/CT Without Preimaging Biopsy

Of the 100 patients, 34 (34%) were referred for ^{68}Ga-PSMA-11 PET/CT on the basis of high clinical suspicion only, without

TABLE 1
Patient Characteristics (n = 100)

Variable	Value
Preimaging clinical data	
Age (y)	82 (80–86.8)
ECOG PS = 0	52 (52%)
ECOG PS = 1	39 (39%)
ECOG PS ≥ 2	9 (9%)
PSA (ng/mL)	22.6 (9.4–59.0)
PSA < 5	6 (6%)
5 ≤ PSA < 10	22 (22%)
10 ≤ PSA < 20	19 (19%)
PSA > 20	53 (53%)
PSMA PET–based staging data	
Avid disease	100 (100%)
Localized disease	36 (36%)
Locally advanced disease	25 (25%)
Advanced disease	39 (39%)
Therapy data	
Radical prostatectomy	2 (2%)
Radiotherapy	36 (36%)
Hormonal therapy	79 (77%)
Surveillance	14 (14%)

ECOG PS = Eastern Cooperative Oncology Group performance status.

Categoric variables are reported as frequency and percentage. Continuous variables are reported as median and interquartile range.

preimaging histopathologic confirmation of PCa (Table 2. Eighteen (53%) of these 34 were referred after documentation of significantly elevated PSA levels (>50 ng/mL), 15 (44.1%) were referred because of prominent clinical symptoms (11 had urinary symptoms, 4 had bone pain), and 1 (2.8%) was referred because of focal prostatic ^{18}F-FDG uptake observed on ^{18}F-FDG PET/CT performed for colon cancer follow-up. Among these 34 B(−) patients, 10 (29.4%) underwent prostate MRI before referral for PSMA PET/CT, with the highest reported Prostate Imaging–Reporting and Data System score (4 or 5) documented in 9 of them.

Compared with B(+) patients (Table 2), B(−) patients were older (median age, 87 vs. 82 y; $P < 0.01$) and had worse performance status scores (Eastern Cooperative Oncology Group performance status ≥ 2 in 23.5% vs. 1.5%, $P < 0.01$). The PSA level of these patients was significantly higher (median, 57 vs. 15.4 ng/mL; $P < 0.01$), with 79.4% and 17.7% of them having PSA levels higher than 20 and 100 ng/mL, respectively.

TABLE 2
Comparison Between B(+) and B(−) Patients

Variable	B(+) (n = 66)	B(−) (n = 34)	P
Preimaging clinical data			
Age (y)	82 (80–83)	87 (83–90)	<0.01*
ECOG PS = 0	43 (65.2%)	9 (26.5%)	<0.01*
ECOG PS = 1	22 (33.3%)	17 (50%)	0.10
ECOG PS ≥ 2	1 (1.5%)	8 (23.5%)	<0.01*
PSA (ng/mL)	15.4 (8.3–43.2)	57 (22.4–82.5)	<0.01*
PSA < 5	6 (9.1%)	0 (0%)	0.09
5 ≤ PSA < 10	19 (28.8%)	3 (8.8%)	0.02*
10 ≤ PSA < 20	15 (22.7%)	4 (11.8%)	0.19
PSA > 20	26 (39.4%)	27 (79.4%)	<0.01*
ISUP GG 1	4 (6.1%)	—	—
ISUP GG 2	16 (24.2%)	—	—
ISUP GG 3	14 (21.2%)	—	—
ISUP GG 4	10 (15.2%)	—	—
ISUP GG 5	22 (33.3%)	—	—
PSMA PET-based staging data			
Avid disease	66 (100%)	34 (100%)	—
Localized disease	27 (40.9%)	9 (26.5%)	0.15
Locally advanced disease	17 (25.8%)	8 (23.5%)	0.81
Advanced disease	22 (33.3%)	17 (50%)	0.11
Therapy data			
Radical prostatectomy	2 (3%)	0 (0%)	0.55
Pelvic radiotherapy	35 (53%)	1 (2.9%)	<0.01*
Hormonal therapy	54 (81.8%)	25 (73.5%)	0.34
Surveillance	5 (7.6%)	9 (26.5%)	0.02*

*Statistically significant.
ECOG PS = Eastern Cooperative Oncology Group performance status; ISUP GG = International Society of Urological Pathology grade group.
Categoric variables are reported as frequency and percentage. Continuous variables are reported as median and interquartile range.

In B(−) patients and B(+) patients, 100% of them (34/34 and 66/66, respectively) had at least 1 avid lesion that was considered to represent PCa on their ^{68}Ga-PSMA-11 PET/CT scan. Examples of a B(−) patient with localized disease and a B(−) patient with findings that required special clinical attention are presented in Figures 1 and 2, respectively. In terms of staging parameters, the B(−) patients had no staging parameters significantly different from the B(+) patients, although trends toward higher rates of bone metastasis (47.1% vs. 28.8%) and overall advanced disease (50% vs. 33.3%) were noted in these patients.

Is Preimaging Biopsy a Factor in Choosing Therapeutic Approach?

Comparing therapy approaches among the total study cohort (Table 2), similar proportions of B(+) and B(−) elderly patients were referred for hormonal therapy (81.8% and 73.5%, respectively, $P = 0.34$). In contrast, whereas 63% of B(+) patients were referred for radiotherapy after imaging, only 8.8% of B(−) were referred for radiotherapy ($P < 0.01$, Table 2). To better assess the differences in therapeutic approach selected for B(−) versus B(+) patients, therapies given to patients in 3 different stage groups were analyzed: localized disease, locally advanced disease, and advanced disease (Table 3).

Localized Disease. Among the 36 patients with localized disease, 22 were referred for definitive therapy (20 patients underwent pelvic radiotherapy and 2 patients underwent radical prostatectomy), and 14 patients were given nondefinitive therapy (4 received hormonal therapy, and 10 were put under surveillance). B(−) patients were less commonly referred for definitive therapies than B(+) patients (0/9 vs. 22/27, 0% vs. 81.5%, $P < 0.01$). Still, beyond biopsy status, those referred for definitive therapy also had a statistically significant better performance status ($P = 0.01$) and a trend toward a younger median age ($P = 0.10$).

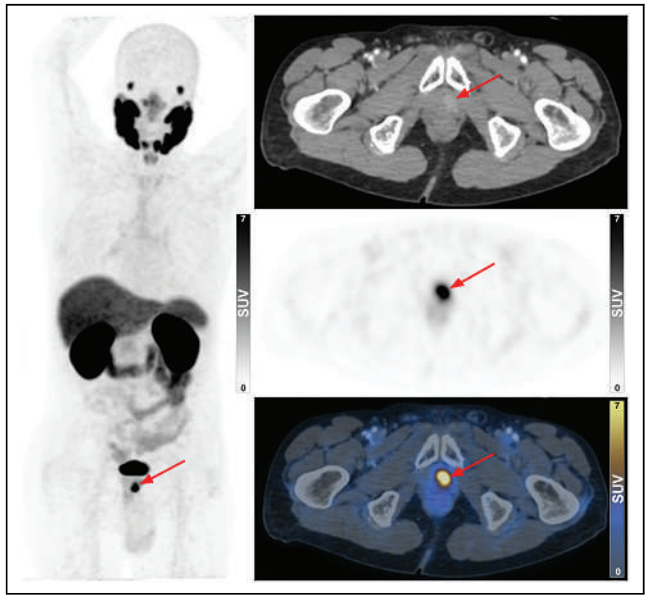

FIGURE 1. ^{68}Ga-PSMA-11 PET/CT of 84-y-old B(−) man with rising PSA levels. Focus of increased uptake was identified at left apex of prostate (arrow), indicating localized disease.

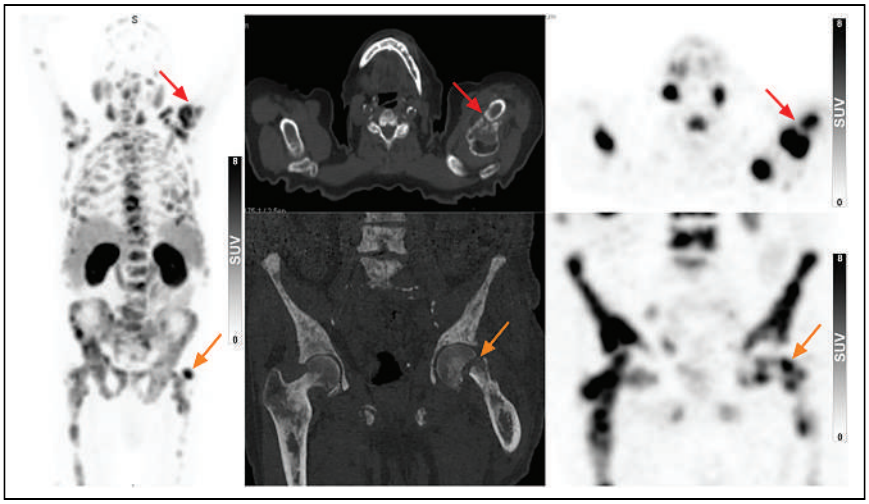

FIGURE 2. ^{68}Ga-PSMA-11 PET/CT of 82-y-old B(−) man with bone pain and PSA levels of 960 ng/mL. Not only effective in identifying disease extent, study also detected pathologic fractures of left humerus and left femur (arrows). Patient was immediately referred for radiotherapy for humeral lesion and surgery for femoral lesion.

Locally Advanced Disease. Among the 25 patients with locally advanced disease, 16 were referred for pelvic radiotherapy (14 received hormonal therapy as well). The other 9 received hormonal therapy only ($n = 6$) or were put under surveillance only ($n = 3$). Similarly to patients with localized disease, among patients with locally advanced disease, B(−) patients received pelvic radiotherapy at significantly lower rates than B(+) patients (1/8 vs. 15/17, 12.5% vs. 88.2%, $P < 0.01$). However, age and PSA level were significantly lower in those receiving radiotherapy ($P < 0.01$ for both variables).

Advanced Disease. Among the 39 patients with advanced disease, 38 received hormonal therapy (9 were referred for radiotherapy as well) and 1 was put under surveillance. In contrast to patients with localized or locally advanced disease, B(−) and B(+) patients with advanced disease received hormonal therapy at similar rates (16/17 and 22/22, 94.1% and 100%, $P = 0.44$), indicating that biopsy was not a factor determining the therapy approach in these patients.

Focusing on the 16 B(−) patients whose PSMA PET/CT revealed advanced disease and were then put on hormonal therapy (with no preimaging or pretherapy confirming biopsy), follow-up data on their next PSA level and next PSMA PET/CT were available for 13 and 9 patients, respectively. In 12 (92.3%) of the 13 patients with documented PSA

TABLE 3
Factors Affecting Therapeutic Approach, Stratified by Disease Extent

Parameter	Therapeutic approach 1	Therapeutic approach 2	*P*
Localized disease ($n = 36$)			
Therapy type	Definitive therapy* ($n = 22$)	Other therapy ($n = 14$)	
B(+) patients ($n = 27$)	22	5	<0.01†
B(−) patients ($n = 9$)	0	9	<0.01†
Age (y)	82 (80–83)	82.5 (81.8–86.5)	0.10
ECOG PS ≥ 1	5/22 (22.7%)	9/14 (64.3%)	0.01†
PSA (ng/mL)	10.4 (7.2–18.2)	14.8 (8.4–22.3)	0.31
Locally advanced disease ($n = 25$)			
Therapy type	Pelvic radiotherapy ($n = 16$)	Other therapy ($n = 9$)	
B(+) patients ($n = 17$)	15	2	<0.01†
B(−) patients ($n = 8$)	1	7	<0.01†
Age (y)	80 (80–81.8)	87 (85.5–92)	<0.01†
ECOG PS ≥ 1	6/16 (37.5%)	6/9 (66.7%)	0.23
PSA (ng/mL)	13.5 (6.7–29.5)	56 (28.4–74)	<0.01†
Extraprostatic extension	8/16 (50%)	6/9 (66.6%)	0.68
Regional nodal disease	11/16 (68.8%)	8/9 (88.9%)	0.36
Advanced disease ($n = 39$)			
Therapy type	Hormonal therapy ($n = 38$)	Other therapy ($n = 1$)	
B(+) patients ($n = 22$)	22	0	0.44
B(−) patients ($n = 17$)	16	1	0.44

*Radical prostatectomy or pelvic radiotherapy.
†Statistically significant.
ECOG PS = Eastern Cooperative Oncology Group performance status.
Categoric variables are reported as frequency and percentage. Continuous variables are reported as median and interquartile range.

levels, a dramatic decrease in PSA levels was found (mean change, 95.6%; interquartile range, 95.0%–98.2%). In 8 (88.9%) of the 9 patients with repeated PSMA PET/CT, either a significant decrease in PSMA-avid disease extent ($n = 5$, Fig. 3) or stable disease ($n = 3$) was documented. Only 1 patient was found to have increasing PSA levels and progressive disease on imaging after hormonal therapy initiation.

DISCUSSION

Although ^{68}Ga-PSMA-11 PET/CT is indicated primarily for staging of patients with biopsy-proven high-risk PCa, real-life experience indicates that elderly patients are occasionally referred for imaging on the basis of high clinical suspicion alone without prior histopathologic confirmation of PCa. This single-center retrospective study explored this practice among elderly patients and found it to occur in around one third of patients at least 80 y old.

Previous literature indicates that in elderly patients, prostate biopsies are associated with longer hospital stays (*10*), and postbiopsy complications such as infection, bleeding, or urinary retention might occur in of up to 17% of cases (*11*). Moreover, elderly patients are prone to delayed clinical management and reduced compliance with invasive procedures (*16*). Therefore, reduction of unnecessary biopsies and effective diagnosis of clinically significant PCa in elderly patients should be a medical priority. Previous studies that contain data on the application of PSMA PET/CT before biopsy were not directed to the population of elderly patients and did not focus on the potential of imaging to eliminate the need for biopsy in the elderly (or in other predefined populations). Instead, these studies evaluated mainly the diagnostic performance and the prognostic information provided by PSMA PET/CT, using postimaging histopathologic data as a reference (*17,18*). The results of the current study indicate that 100% of the elderly patients who were referred for PSMA PET/CT on the basis of clinical suspicion only (mainly a rising PSA level or prominent urinary or musculoskeletal symptoms) were found to have avid disease on PSMA PET/CT. Given that positive PSMA PET/CT results usually indicate clinically significant rather than clinically insignificant PCa (*19*), and together with insignificant negative biologic effect of radiation exposure in elderly patients (*20*), this practice of waiving the need for preimaging biopsy when the clinical suspicion is high proves to be effective and to have no apparent negative cost. This practice is not common in the field of PET/CT but has been shown cost-effective and adopted in the assessment algorithm of solitary pulmonary nodules (*21*).

By characterizing the patients undergoing PSMA PET/CT without preimaging biopsy, whose PET-positivity rate was 100%, the current study provides practical tools for clinicians. It seems that PSMA PET/CT is highly likely to identify and stage PCa in patients at least 80 y old with a PSA level of at least 20 ng/mL, even without histopathologic confirmation.

As for postimaging therapy, our results indicate that preimaging biopsy may play a role in selecting the therapeutic approach toward localized or locally advanced PCa cases. Those patients in our cohort who did not undergo preimaging biopsy were less likely to get definitive therapies if having localized or locally advanced disease. However, it seems that those not referred for definitive therapies were usually older, with worse performance status or higher PSA levels. These data support the probability that biopsy status was not the

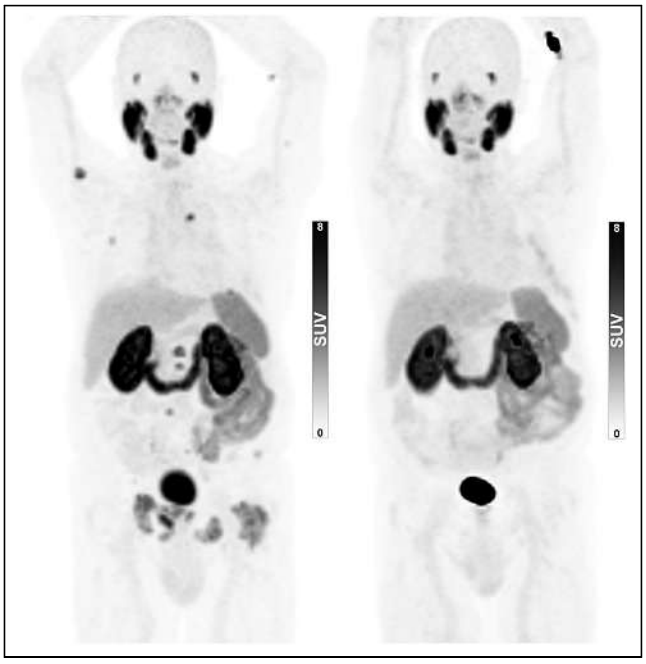

FIGURE 3. ^{68}Ga-PSMA-11 PET/CT scans of 83-y-old B(−) man before (left) and after (right) initiation of hormonal therapy. Staging scan (left) was performed without preimaging biopsy, revealing advanced disease. On imaging performed 10 mo later (right), all previous PSMA-positive lesions demonstrated no uptake of ^{68}Ga-PSMA-11. PSA level of this patient decreased dramatically on therapy initiation as well (from 67 to 3.1 ng/mL).

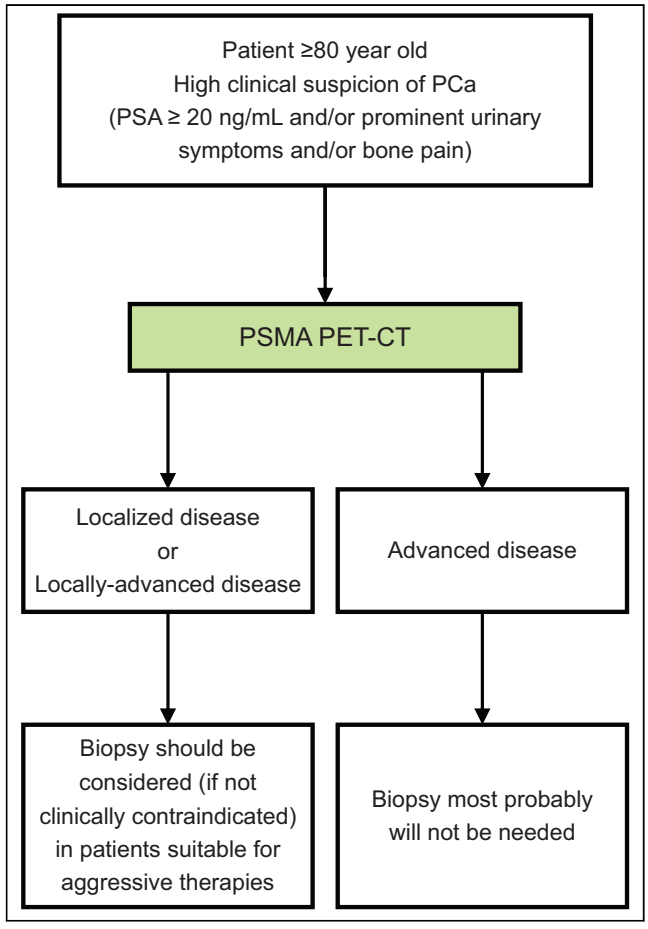

FIGURE 4. Adjusted staging algorithm for elderly patients for whom there is high clinical suspicion of PCa.

sole factor on which the therapy approach was based and that other patient-related factors probably affected therapy selection as well. These observations suggest that a selected group of patients with localized or locally advanced PCa, who are candidates for more aggressive therapies after PSMA PET/CT, should be considered for a complete postimaging histopathologic assessment.

When PSMA PET/CT identified advanced disease in patients who had no preimaging biopsy, as happened in half of such patients in the current study, our results indicate that the lack of tissue diagnosis did not preclude them from receiving hormonal therapy, which biochemical and imaging follow-up data indicated had been beneficial.

On the basis of our results, we outlined in Figure 4 an adjusted PCa staging algorithm for elderly patients. Adoption of this suggested algorithm can potentially reduce the numbers of prostate biopsies and associated complications in the elderly while providing accurate staging data. If patients are selected correctly for imaging, the risk of performing unnecessary PSMA PET/CT seems negligible. Still, larger studies are required to validate our results. If confirmed in additional series, our proposed algorithm could be implemented in the PCa staging algorithm for elderly patients.

DISCLOSURE

No potential conflict of interest relevant to this article was reported.

KEY POINTS

QUESTION: How commonly are elderly patients referred for staging PSMA PET/CT without preimaging biopsy, what is the PET-positivity rate in such patients, are their clinical and PET-based staging parameters different from those of patients referred with biopsy, and does biopsy status affect the selected therapeutic approach?

PERTINENT FINDINGS: In real life, around one third of elderly patients are referred for PSMA PET/CT without a preimaging confirming biopsy. These patients are likely to be older, with worse clinical status and a higher PSA level, and avid disease is expected to be identified on their PSMA PET/CT images. Identification of advanced disease may be more likely in these patients, and if it is, their biopsy status does not preclude them from receiving hormonal therapy, which results in a biochemical and imaging-based response.

IMPLICATIONS FOR PATIENT CARE: In elderly patients with a high clinical suspicion of PCa, an excellent PET-positivity rate is provided by PSMA PET/CT, even without preimaging biopsy. Advanced disease identified on PSMA PET/CT can be considered confirmatory of PCa and serve as a criterion to initiate hormonal therapy, potentially waiving the need for preimaging biopsy in frail patients.

REFERENCES

1. Cytawa W, Seitz AK, Kircher S, et al. ^{68}Ga-PSMA I&T PET/CT for primary staging of prostate cancer. *Eur J Nucl Med Mol Imaging.* 2020;47:168–177.
2. Sonni I, Eiber M, Fendler WP, et al. Impact of ^{68}Ga-PSMA-11 PET/CT on staging and management of prostate cancer patients in various clinical settings: a prospective single-center study. *J Nucl Med.* 2020;61:1153–1160.
3. Satapathy S, Singh H, Kumar R, Mittal BR. Diagnostic accuracy of ^{68}Ga-PSMA PET/CT for initial detection in patients with suspected prostate cancer: a systematic review and meta-analysis. *AJR.* 2021;216:599–607.
4. FDA approves first PSMA-targeted PET imaging drug for men with prostate cancer. U.S. Food and Drug Administration website. https://www.fda.gov/news-events/press-announcements/fda-approves-first-psma-targeted-pet-imaging-drug-men-prostate-cancer. Published December 1, 2020. Accessed March 30, 2023.
5. Israel Ministry of Health – updates in the Israeli medical services basket [in Hebrew]. Israel Ministry of Health website. https://www.health.gov.il/hozer/mr02_2016.pdf. Published February 2016. Accessed March 30, 2023.
6. Mottet N, van den Bergh RC, Briers E, et al. EAU-EANM-ESTRO-ESUR-SIOG guidelines on prostate cancer—2020 update. Part 1: screening, diagnosis, and local treatment with curative intent. *Eur Urol.* 2021;79:243–262.
7. Cornford P, van den Bergh RC, Briers E, et al. EAU-EANM-ESTRO-ESUR-SIOG guidelines on prostate cancer. Part II—2020 update: treatment of relapsing and metastatic prostate cancer. *Eur Urol.* 2021;79:263–282.
8. Mohler JL, Antonarakis ES. NCCN guidelines updates: management of prostate cancer. *J Natl Compr Canc Netw.* 2019;17:583–586.
9. Carroll PR, Parsons JK, Andriole G, et al. NCCN guidelines insights: prostate cancer early detection, version 2.2016. *J Natl Compr Canc Netw.* 2016;14:509–519.
10. Iwamoto H, Izumi K, Kadomoto S, et al. A novel screening strategy for clinically significant prostate cancer in elderly men over 75 years of age. *Asian J Androl.* 2021;23:36–40.
11. Gershman B, Van Houten HK, Herrin J, et al. Impact of prostate-specific antigen (PSA) screening trials and revised PSA screening guidelines on rates of prostate biopsy and postbiopsy complications. *Eur Urol.* 2017;71:55–65.
12. Ceci F, Oprea-Lager DE, Emmett L, et al. E-PSMA: the EANM standardized reporting guidelines v1.0 for PSMA-PET. *Eur J Nucl Med Mol Imaging.* 2021;48:1626–1638.
13. American Joint Committee on Cancer. Prostate. In: *AJCC Cancer Staging Manual.* 8th ed. Springer; 2017:715–725.
14. Ruhl JL, Callaghan C, Schussler N, eds. *Summary Stage 2018: Codes and Coding Instructions.* National Cancer Institute; 2021.
15. Barbosa FG, Queiroz MA, Nunes RF, et al. Revisiting prostate cancer recurrence with PSMA PET: atlas of typical and atypical patterns of spread. *Radiographics.* 2019;39:186–212.
16. De Geest S, von Renteln-Kruse W, Steeman E, Degraeve S, Abraham IL. Compliance issues with the geriatric population: complexity with aging. *Nurs Clin North Am.* 1998;33:467–480.
17. Albisinni S, Sarkis J, Diamand R, De Nunzio C. Prebiopsy ^{68}Ga-PSMA PET imaging: can we improve the current diagnostic pathway for prostate cancer? *Prostate Cancer Prostatic Dis.* 2023;26:47–49.
18. Caracciolo M, Castello A, Urso L, et al. The role of [^{68}Ga] PSMA PET/CT for clinical suspicion of prostate cancer in patients with or without previous negative biopsy: a systematic review. *Cancers (Basel).* 2022;14:5036.
19. Demirci E, Kabasakal L, Şahin OE, et al. Can SUVmax values of Ga-68-PSMA PET/CT scan predict the clinically significant prostate cancer? *Nucl Med Commun.* 2019;40:86–91.
20. Sandgren K, Johansson L, Axelsson J, et al. Radiation dosimetry of [^{68}Ga] PSMA-11 in low-risk prostate cancer patients. *EJNMMI Phys.* 2019;6:2.
21. Tang K, Wang L, Lin J, Zheng X, Wu Y. The value of ^{18}F-FDG PET/CT in the diagnosis of different size of solitary pulmonary nodules. *Medicine (Baltimore).* 2019;98:e14813.

Delayed Imaging Improves Lesion Detectability in [^{99m}Tc]Tc-PSMA-I&S SPECT/CT in Recurrent Prostate Cancer

Christoph Berliner*[1,2], Lisa Steinhelfer*[3], Maythinee Chantadisai[3], Markus Kroenke[3], Daniel Koehler[1], Randi Pose[4], Peter Bannas[1], Sophie Knipper[4], Matthias Eiber†[4], and Tobias Maurer†[4,5]

[1]*Department of Diagnostic and Interventional Radiology and Nuclear Medicine, Universitätsklinikum Hamburg–Eppendorf, Hamburg, Germany;* [2]*Department of Nuclear Medicine, Universitätsklinikum Essen, Essen, Germany;* [3]*Department of Nuclear Medicine, Klinikum Rechts der Isar, Technische Universität München, München, Germany;* [4]*Martini-Klinik Prostate Cancer Center, University Hospital Hamburg–Eppendorf, Hamburg, Germany; and* [5]*Department of Urology, University Hospital Hamburg–Eppendorf, Hamburg, Germany*

Our objective was to compare the ability to detect histopathologically confirmed lymph node metastases by early and delayed [^{99m}Tc]Tc-PSMA-I&S SPECT/CT in early biochemically recurrent prostate cancer. **Methods:** We retrospectively analyzed 222 patients selected for radioguided surgery using [^{99m}Tc]Tc-PSMA-I&S SPECT/CT at different time points after injection (≤4 h and >15 h). In total, 386 prostate-specific membrane antigen (PSMA) PET predetermined lesions were analyzed on SPECT/CT using a 4-point scale, and the results were compared between early and late imaging groups, with uni- and multivariate analyses performed including prostate-specific antigen, injected [^{99m}Tc]Tc-PSMA-I&S activity, Gleason grade group, initial TNM stage, and, stratified by size, PSMA PET/CT–positive lymph nodes. PSMA PET/CT findings served as the standard of reference. **Results:** [^{99m}Tc]Tc-PSMA-I&S SPECT/CT had a significantly higher positivity rate for detecting lesions in the late than the early imaging group (79%, $n = 140/178$, vs. 27%, $n = 12/44$ [$P < 0.05$] on a patient basis; 60%, $n = 195/324$, vs. 21%, $n = 13/62$ [$P < 0.05$] on a lesion basis). Similar positivity rates were found when lesions were stratified by size. Multivariate analysis found that SUV_{max} on PSMA PET/CT and the uptake time of [^{99m}Tc]Tc-PSMA-I&S were independent predictors for lesion detectability on SPECT/CT. **Conclusion:** Late imaging (>15 h after injection) should be preferred when [^{99m}Tc]Tc-PSMA-I&S SPECT/CT is used for lesion detection in early biochemical recurrence of prostate cancer. However, the performance of PSMA SPECT/CT is clearly inferior to that of PSMA PET/CT.

Key Words: prostate carcinoma; scintigraphy; radioguided; salvage surgery; biochemical recurrence; PET

J Nucl Med 2023; 64:1036–1042
DOI: 10.2967/jnumed.122.265252

Prostate cancer is one of the most diagnosed cancers and the fourth leading cause of cancer-related death in men worldwide (*1*). Definitive surgery or radiotherapy is currently the curative therapy of choice (*2*). Success rates are measured in biochemical recurrence (BCR)–free survival. However, a portion of patients experiences recurrence after initial surgical treatment (*3–6*) as determined by a rising blood level of prostate-specific antigen (PSA). A confirmed increase in PSA greater than 0.2 ng/mL during follow-up after radical prostatectomy (RP) defines BCR (*2*). For further therapy and management, it is crucial to recognize and differentiate between local, regional, and systemic prostate recurrence (*7,8*).

In the last decade, hybrid imaging with prostate-specific membrane antigen (PSMA) ligands has emerged as the most accurate imaging modality to detect lesions in early BCR (*9–12*). Several radiopharmaceuticals targeting PSMA are available and in clinical use (*13–15*). PSMA ligands labeled with γ-emitters allow new therapeutic options in BCR, such as PSMA radioguided surgery (RGS) (*16,17*). Their signal can also be used for SPECT imaging (*18*). Compared with PET/CT scanners, SPECT/CT scanners are less costly and more accessible in most parts of the world. Therefore, the diagnostic performance of ^{99m}Tc-labeled PSMA ligands for SPECT imaging and its comparison to PET imaging is of the utmost interest, but so far, data are sparse, especially in early BCR (*19*).

PSMA-targeting radiopharmaceuticals are internalized, and lesion-to-background contrast improves over time (*20*). These dynamics may be especially relevant for PSMA ligands labeled by nuclides with longer half-lives. Despite established use in RGS, the optimal time interval for [^{99m}Tc]Tc-PSMA-I&S injection and SPECT imaging is not known to date.

The aim of this retrospective analysis was to compare early (≤4 h after injection) and late (≥15 h after injection) [^{99m}Tc]Tc-PSMA-I&S SPECT/CT imaging for the identification of pelvic lymph node metastases in early BCR.

MATERIALS AND METHODS

Study Population

We retrospectively reviewed the databases at 2 centers for all patients who underwent RGS using [^{99m}Tc]Tc-PSMA-I&S between September 2015 and April 2020.

Patients were included if they had BCR after RP and PSMA PET/CT–positive pelvic or retroperitoneal soft-tissue metastases, had undergone [^{99m}Tc]Tc-PSMA-I&S SPECT/CT before RGS, and had all imaging data available in a digital format. The obtained PSMA PET/CT scan served as the diagnostic gold standard, and only PET-positive

Received Dec. 6, 2022; revision accepted Mar. 7, 2023.
For correspondence or reprints, contact Christoph Berliner (christoph.berliner@uk-essen.de).
*Contributed equally to this work.
†Contributed equally to this work.
Published online May 25, 2023.

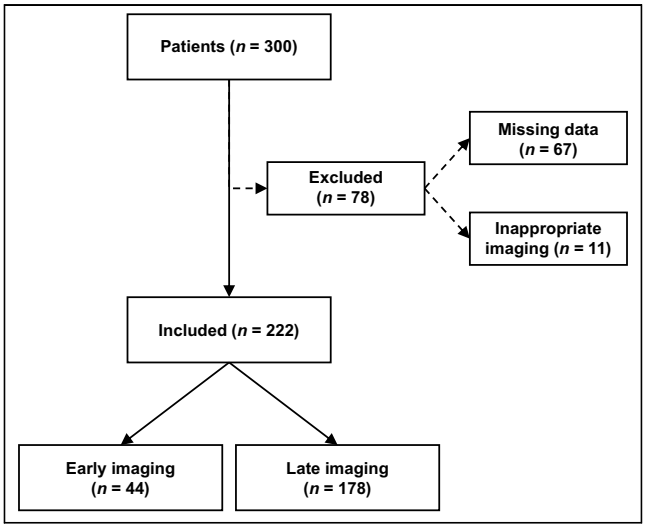

FIGURE 1. Flowchart of included patients. Total of 222 of 300 patients in our institutional databases met inclusion criteria for analysis. We excluded 78 patients (incomplete availability of imaging data [$n = 67$], staging images provided as PSMA PET/MRI [$n = 10$], or staging images provided as choline PET/CT [$n = 1$]).

patients were included in the analysis. All lesions were histopathologically confirmed after salvage surgery.

Patients were excluded from analysis if data were missing (unavailable image data) or if inappropriate imaging had been performed (an imaging modality other than PSMA PET/CT or a tracer for SPECT/CT and PSMA RGS other than [^{99m}Tc]Tc-PSMA-I&S).

Finally, 222 patients could be included in the retrospective analysis (Fig. 1). The initial patient characteristics and findings before RGS are shown in Table 1 and Supplemental Table 1 (supplemental materials are available at http://jnm.snmjournals.org). The local ethics committees (PV7316 and 226/18S) approved this retrospective study, and the requirement to obtain informed consent was waived.

[^{99m}Tc]Tc-PSMA-I&S SPECT/CT Imaging and Interpretation

The application of [^{99m}Tc]Tc-PSMA-I&S was part of the RGS (*21*). [^{99m}Tc]Tc-PSMA-I&S was prepared as described previously (*17*). The administration of [^{99m}Tc]Tc-PSMA-I&S complied with the German Medicinal Products Act, Arzneimittelgesetz §13 2b, and the responsible regulatory bodies. All patients underwent whole-body planar imaging and pelvic [^{99m}Tc]Tc-PSMA-I&S-SPECT/CT no more than 4 h after injection or at least 15 h after injection (Supplemental Table 2).

PSMA PET/CT and [^{99m}Tc]Tc-PSMA-I&S SPECT/CT images were reanalyzed independently by 2 physicians experienced in nuclear medicine and radiology. Axial, sagittal, and coronal SPECT, PET, and

TABLE 1
Characteristics of 222 Patients Treated with RGS Between 2014 and 2020 at 2 Centers*

Parameter	Early SPECT (≤4 h after injection; $n = 44$)	Late SPECT (≥15 h after injection; $n = 178$)	*P*
Year of initial RP	2010 (2005–2013)	2014 (2010–2016)	<0.001
PSA at RP (ng/mL)	10 (6–16)	9 (6–15)	0.8
Lymph node yield at RP	13 (8–20)	13 (8–20)	0.6
Positive lymph nodes at RP			0.6
0	32 (73)	115 (65)	
1	3 (6.8)	19 (11)	
2	3 (6.8)	9 (5.1)	
≥3	2 (4.5)	5 (2.8)	
Unknown	4 (9.1)	30 (17)	
Surgical margin status			0.05
R0	29 (66)	130 (73)	
R1	9 (20)	41 (23)	
RX/NA	6 (14)	7 (3.9)	
RT after RP			0.1
No RT	15 (34)	59 (33)	
RT after RP	28 (64)	119 (67)	
NA	1 (2.3)	0 (0)	
Time from RP to SPECT (mo)	70 (22–128)	46 (22–88)	0.2
Age at PSMA RGS (y)	72 (65–75)	66 (61–70)	<0.001
PSA before SPECT (ng/mL)	1.4 (0.7–3.0)	1.0 (0.5–2.0)	0.09

*Patients received [^{99m}Tc]Tc-PSMA-I&S SPECT/CT before surgery and presented with BCR after RP with histopathology-confirmed positive lesions at PSMA PET/CT.

NA = not assigned; RT = radiotherapy.

Qualitative data are number and percentage; continuous data are median and IQR.

TABLE 2
PSMA PET/CT and SPECT/CT Imaging Characteristics of 222 Patients with BCR After RP Treated with RGS Between 2014 and 2020 at 2 Centers Within Early and Late [^{99m}Tc]Tc-PSMA-I&S SPECT/CT Groups

Parameter	Early SPECT (≤4 h after injection; n = 44)	Late SPECT (≥15 h after injection; n = 178)	P
Lesions on PSMA PET			0.7
1	30 (68%)	94 (53%)	
2	11 (25%)	53 (30%)	
3	2 (4.5%)	16 (9.0%)	
4	1 (2.3%)	7 (3.9%)	
≥5	0 (0%)	8 (4.5%)	
Maximum lesion size on PET/CT (mm)	8 (7–12)	9 (6–12)	0.7
Maximum lesion SUV on PET	9 (6–17)	8 (5–16)	0.1
Ratio of maximum lesion SUV to background on PET	12 (7–22)	8 (5–16)	0.02
miTNM-Tr	0 (0%)	28 (16%)	0.01
miTNM-N1	34 (77%)	112 (63%)	0.1
miTNM-N2	10 (23%)	53 (30%)	0.5
miTNM-M1a	0 (0%)	15 (8.4%)	0.1
[^{99m}Tc]Tc-PSMA-I&S activity (MBq)	550 (416–702)	752 (695–786)	<0.001
Corrected [^{99m}Tc]Tc-PSMA-I&S activity at time of SPECT (MBq)	488 (370–632)	99 (91–108)	<0.001
Interval between [^{99m}Tc]-Tc-PSMA-I&S tracer injection and SPECT imaging (h)	1.0 (1.0–2.0)	18.0 (17.0–18.0)	<0.001
Lesions on SPECT			<0.001
0	33 (75%)	45 (25%)	
1	9 (20%)	90 (51%)	
2	1 (2%)	27 (15%)	
3	1 (2%)	13 (7%)	
4	0 (0%)	2 (1%)	
≥5	0 (0%)	1 (1%)	
Maximum lesion size on SPECT/CT (mm)	11.5 (7.8–17.1)	9.0 (7.0–13.0)	0.07

Qualitative data are number and percentage; continuous data are median and IQR.

CT images as well as fused images were analyzed using OsiriX MD (Pixmeo) (*22*).

For PET data analysis, a 40% isocontour volume of interest was drawn around suggestive areas, with added volumes of interest in the background (blood pool, gluteal muscle). SUV_{max} and SUV_{mean} were recorded. SPECT lesion detectability was assessed qualitatively using a 4-point scale (Supplemental Table 3).

To assess potential differences between early (≤4 h after injection) and late (≥15 h after injection) [^{99m}Tc]Tc-PSMA-I&S SPECT/CT imaging, the patient cohort was divided into 2 groups. Patients in the early imaging group underwent [^{99m}Tc]Tc-PSMA-I&S-I&S 1–4 h after injection (median, 1 h; interquartile range [IQR], 1–2 h), and patients in the late imaging group underwent imaging at 15–20 h after injection (median, 18 h; IQR, 17–18 h). The mean injected activities were 560 ± 201 MBq (IQR, 417–702 MBq) and 733 ± 90 MBq (IQR, 695–786 MBq) in the early and late imaging groups, respectively (Table 2).

Statistical Analysis

Descriptive statistics included frequencies and proportions for categoric variables and means, medians, and IQR for continuous variables. Test power was calculated using a t-statistical power calculator with a medium effect size of 0.5 and a significance level of 0.05. Differences in medians and proportions between early and late imaging were evaluated using Kruskal–Wallis, Mann–Whitney U, Fisher exact, and χ^2 tests (*23,24*).

Univariable and multivariable logistic regression models tested the relationship between visibility of lesions on SPECT before PSMA RGS and the following clinical variables: Gleason grade group at RP (I-II vs. III-V), pT stage at RP (pT2 vs. pT3a/b), pN stage at RP (pN0/NX vs. pN1), margin status at RP (R0 vs. R1), radiation therapy after RP before PSMA RGS (yes vs. no), time between initial RP and SPECT, age at SPECT, number of PSMA PET–positive lesions, maximal size of PSMA PET–positive lesions on PET/CT, SUV_{max} of PSMA PET–positive lesions, [^{99m}Tc]Tc-PSMA-I&S activity, and time interval between [^{99m}Tc]Tc-PSMA-I&S tracer injection and SPECT imaging. Predictors were included in the multivariable models if significantly associated with the outcome in the univariable analysis.

For all statistical analyses, the R software environment for statistical computing and graphics (version 3.4.3) was used. All tests were 2-sided, with the level of significance set at a P value of less than 0.05.

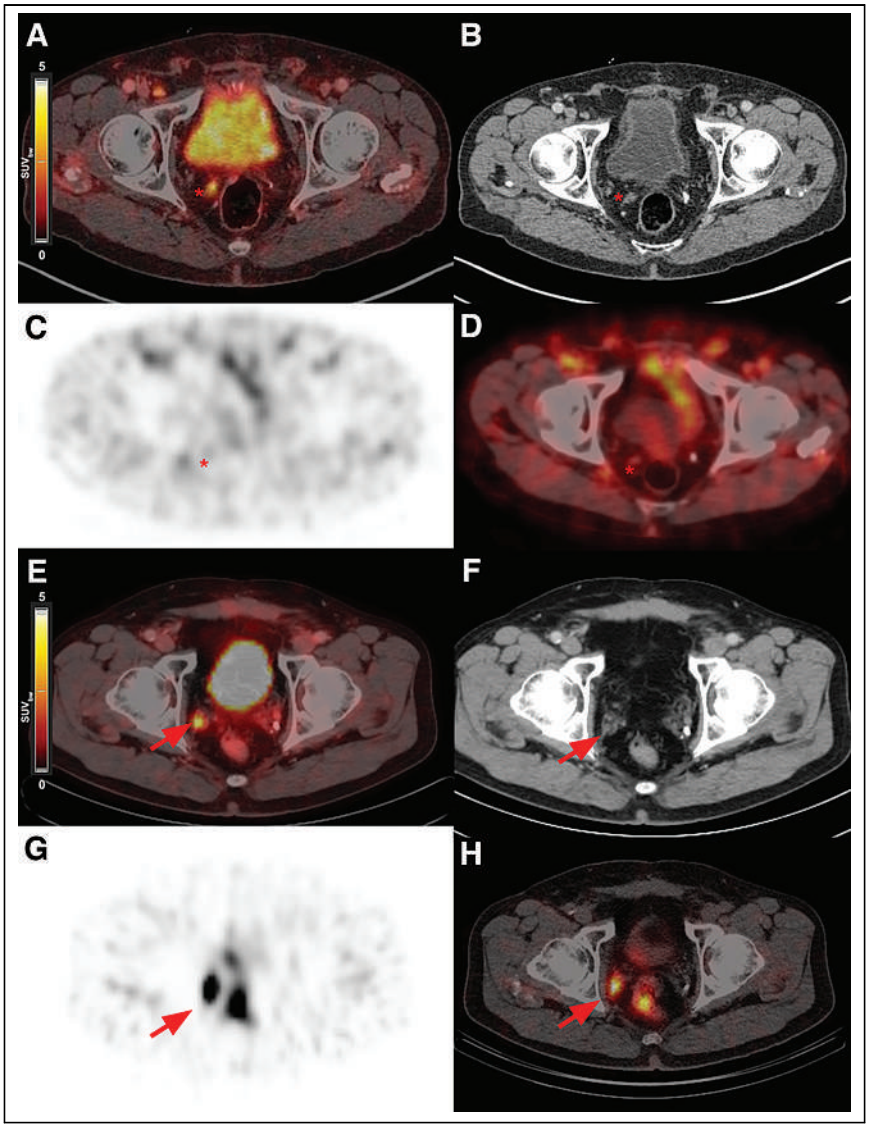

FIGURE 2. Examples of early (A–D) and late (E–H) [^{99m}Tc]Tc-PSMA-I&S SPECT/CT imaging. (A–D) In 74-y-old patient who had RP in 2004 and BCR in 2016 (PSA, 0.66 ng/mL), PSMA PET (A and B) shows local recurrence in right prostate fossa with intense PSMA expression (SUV_{max}, 12.7 [asterisk]); 4 h after [^{99m}Tc]Tc-PSMA I&S injection, SPECT/CT (C and D) morphologically identifies known local recurrent cancer (asterisk) but uptake is not above background, with overall score of 2. (E–H) In 66-y-old patient who had RP in 2012 and BCR in 2018 (PSA, 0.59 ng/mL), PSMA PET (E and F) shows right internal iliac lymph node metastasis with intense PSMA expression (SUV_{max}, 5.0 [arrow]); 18 h after [^{99m}Tc]Tc-PSMA-I&S injection, SPECT/CT (G and H) confirms metastasis with significant uptake above background (score 4, arrow).

RESULTS

Patient-Based Analysis

Overall, 65% (144/222) of all patients had at least 1 lesion scored as visible on SPECT (Table 2). On a patient basis, at least 1 lesion was present in 25% (11/44) and 75% (133/178) of patients in the early versus late imaging groups. Representative patient examples are shown in Figure 2. There was a strong power (0.84) in the t-statistical test. No difference between groups was found in number of lesions, SUV_{max} of the hottest lesion, or lesion size. However, the early imaging group had a higher lesion-to-background SUV_{max} ratio on PET (Table 2).

Lesion-Based Analysis

In total, 386 lesions could be identified in 222 patients on PET/CT imaging. Of these, 208 (54%) were scored as detectable on SPECT/CT. Late SPECT/CT imaging revealed a significantly higher percentage of lesions than was seen on early SPECT/CT (60%, $n = 195/324$, vs. 21%, $n = 13/62$ [$P < 0.05$]). Similar results were present when lesions were stratified by size, at 0%, 10%, 11%, and 62% vs. 52%, 50%, 66%, and 78% for lesions sized 1–3, 4–7, 8–10, and greater than 10 mm on early versus late imaging, respectively (Fig. 3).

The results were stratified into different PSA subgroups. Only in patients with a PSA of less than 0.2 ng/mL was no significant difference in lesion detectability seen on late versus early SPECT/CT imaging (56%, 9/16, vs. 100%, 2/2 [$P = 0.49$]). Lesion detectability was higher on late than early imaging in patients with a PSA of 0.2 to less than 0.5 ng/mL (41%, 25/61, vs. 0%, 0/0 [$P < 0.001$]), a PSA of 0.5 to less than 1 ng/mL (57%, 38/67, vs. 0%, 0/9 [$P < 0.002$]), a PSA of 1 to less than 2 ng/mL (60%, 52/86, vs. 0%, 0/11 [$P < 0.001$]), and PSA of more than 2 ng/mL (76%, 71/94, vs. 34%, 11/32 [$P < 0.001$]).

PET SUV_{max} and Interval Between Tracer Injection and SPECT Imaging as Independent Factors Predicting SPECT Detectability

Univariate regression found PSA, number of lesions on prior PSMA PET, maximum lesion size on PSMA PET/CT, SUV_{max} of lesions on prior PSMA PET, injected tracer activity ([^{99m}Tc]Tc-PSMA-I&S), and interval between tracer injection and SPECT imaging significant for lesion detectability (all $P < 0.05$, Table 3).

Multivariate regression showed only SUV_{max} of prior PET/CT lesions and time interval between tracer injection and SPECT as independent SPECT detectability factors ($P < 0.05$, respectively). PSA at SPECT imaging ($P = 0.09$), number of PET/CT-detected lesions ($P = 0.07$), maximum size of lesions ($P = 0.2$), and activity of injected [^{99m}Tc]Tc-PSMA-I&S ($P = 0.6$) failed to show a significant correlation in our patient cohort.

DISCUSSION

Our study compared early (1–4 h) versus late (15–20 h) [^{99m}Tc]Tc-PSMA-I&S SPECT/CT imaging for detecting tumors in prostate cancer patients. Late imaging was found to be more advantageous, especially for tumors smaller than 10 mm, and was an independent predictor for detecting lesions. Lesion SUV_{max} on PSMA PET and detectability on late SPECT/CT were the main factors for depicting PSMA PET–avid lesions, with PSA, number of

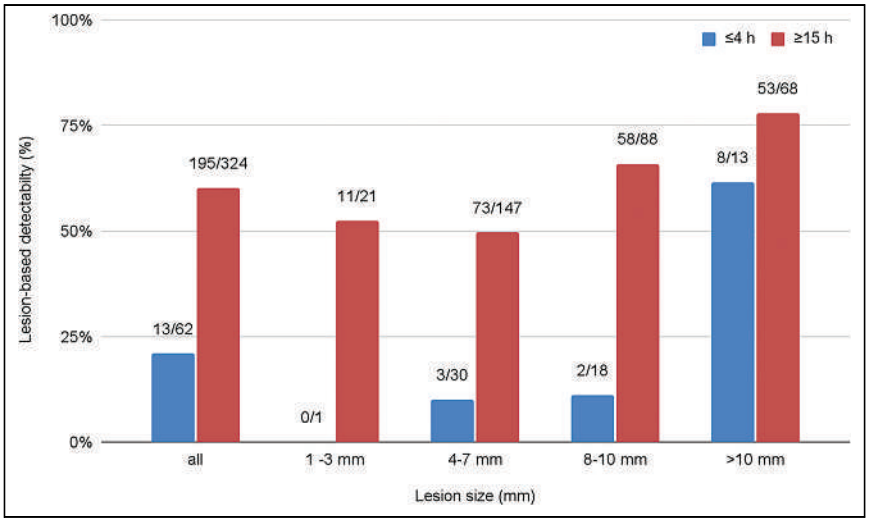

FIGURE 3. Overall and size-dependent lesion-based detectability by early (≤4 h) vs. late (≥15 h) [^{99m}Tc]Tc-PSMA-I&S SPECT/CT imaging.

lesions, and size not having a significant impact. Overall, the results indicate a preference for late-time-point imaging.

PSMA ligands attached to the binding sites of PSMA are usually internalized into the cell and degraded (*25*), entrapping the PSMA ligand. This active internalization process provides an advantage for small diagnostic molecules, as they are pooled over time in cells with high PSMA expression, such as most prostate cancer cells. On the other hand, the physical decay of radioisotopes lowers the absolute measurable activity within PSMA-positive cells over time. For ^{68}Ga-based PSMA PET tracers, reports indicate that a late time point at 3 h shows slight advantages for lesion detection (*26*), although for practical reasons the clinically recommended time window is 1 h after injection (*27*). For most ^{18}F-based PSMA

TABLE 3
Uni- and Multivariable Logistic Regression Models Regarding Visibility of Lesions in [^{99m}Tc]Tc-PSMA-I&S SPECT/CT Imaging

	Univariable				Multivariable			
Variable	OR	CI, 2.5%	CI, 97.5%	*P*	OR	CI, 2.5%	CI, 97.5%	*P*
Gleason grade group at RP								
I–II	Ref.							
III–V	0.34	0.74	2.42	0.3				
pT stage at RP								
pT2	Ref.							
pT3a/b	0.65	0.34	1.21	0.2				
pN stage at RP								
pN0/X	Ref.							
pN1	0.53	0.27	1.05	0.07				
Margin status at RP								
R0	Ref.							
R1	1.0	0.51	2.06	0.9				
RT after RP								
No	Ref.							
Yes	0.82	0.43	1.49	0.5				
Time from RP to SPECT (continuous)	0.99	0.99	1.0	0.8				
Age at SPECT (continuous)	0.99	0.95	1.03	0.6				
PSA at SPECT (continuous)	1.21	1.03	1.47	0.03	1.25	0.99	1.66	0.09
Lesions on PET (continuous)	2.03	1.38	3.21	0.001	1.57	1.02	2.67	0.07
Maximum lesion size on PET (continuous)	1.13	1.05	1.22	0.002	1.06	0.97	1.17	0.2
Maximum lesion SUV on PET (continuous)	1.10	1.05	1.16	<0.001	1.15	1.07	1.27	<0.001
Activity of injected [^{99m}Tc]Tc-PSMA-I&S (continuous)	1.00	1.00	1.00	<0.001	0.99	0.99	1.0	0.6
Interval between injection and SPECT (continuous)	1.16	1.11	1.22	<0.001	1.27	1.17	1.40	<0.001

OR = odds ratio; RT = radiotherapy.

tracers, an uptake time of between 90 and 120 min is typically recommended (*28*). For ^{99m}Tc-based PSMA tracers, data in the literature are sparse and only a few publications indicate an average time range of 3–5 h (*19,29,30*). However, initial studies with PSMA RGS have shown an advantage of imaging after 18–24 h after injection (*17,31*).

In our retrospective analysis, significantly more pelvic lymph node metastases were detected on late than early SPECT/CT imaging, both on a patient basis and on a lesion basis. In comparison, Werner et al. showed in 2 cases that uptake remained high in lymph node metastases on planar scintigraphy at 20 h after injection (*19*). Of note, even on late SPECT/CT imaging, the total number of lesions was substantially less than on the PSMA PET/CT serving as the standard of reference. This finding is congruent with a report by Albalooshi et al. of a high and comparable sensitivity in bone metastasis with a PSA cutoff of more than 2.1 ng/mL but an inferior sensitivity with lower PSA levels (*29*). [^{99m}Tc]Tc-PSMA-I&S is currently only seldom used for staging purposes. Our study sheds new light on potential application scenarios for imaging with [^{99m}Tc]Tc-PSMA-I&S. We can envision that the use of late imaging [^{99m}Tc]Tc-PSMA-I&S SPECT/CT is adequate when the focus is more on the extent of disease before or during systemic treatment than on depiction of all lesions for potential metastasis-directed treatments. Here, patients with advanced disease could represent a cohort suitable for [^{99m}Tc]Tc-PSMA-I&S SPECT, for example, in therapy monitoring of metastatic castration-sensitive as well as castration-resistant patients after chemotherapy or [^{177}Lu]-Lu-PSMA radioligand therapy. Werner et al. have already delivered their first experiences (*19*). The advantage of SPECT/CT imaging lies in its lower costs and broader availability.

The advantages of late imaging were most apparent in small lesions and low PSA levels. The advantages are related to a significantly higher tumor-to-background ratio at late imaging, as a lower count rate in lesions is overcompensated by a diminishing activity in background tissue at the time of imaging. The overall decay of background activity was shown nicely by Urbán et al. in their dosimetry study (*32*). Nevertheless, the tumor-to-background ratio is still clearly inferior to that of PET imaging. These results are not unexpected given the physiologic characteristics of PSMA and the technical and physical limitations of SPECT compared with PET. To exclude test influences due to group invariance, we proved that there was no significant difference between patient characteristics, lesion size, and SUV_{max} of lesions on PET.

Our analysis had several limitations. First, the focus was on a specific cohort of patients with biochemically recurrent prostate cancer and PSMA PET–positive, histologically proven lymph node metastases within the pelvic region. This is a narrow patient population, and our results therefore might not be transferable to other patient populations without further investigation. Second, the size of the early and late imaging groups substantially differed, with 44 patients in the early group and 178 patients in the late group. Although we performed a t-statistical power analysis and Kruskal–Wallis tests, the results of these tests do not cover all eventualities and a possible bias remains. Third, the activity levels injected into the patients in both groups differed significantly, with a lower remaining physical activity in the late imaging group. Nevertheless, lesion detectability was still superior in this group, making the observation even more robust. Fourth, the exact kinetics of [^{99m}Tc]Tc-PSMA-I&S over time are still not known, and we had to use an approximation based on physical decay, which neglects potential trapping or detrapping of the agent over time. Finally, the retrospective nature of this study cannot exclude other influencing factors and invariances besides the tested factors.

CONCLUSION

For lesion detection in early BCR of prostate cancer, late imaging (≥15 h after injection) is preferred using [^{99m}Tc]Tc-PSMA-I&S SPECT/CT. It requires a 2-d protocol and is still clearly inferior to PET/CT imaging for primary staging, but it significantly improves image quality and the detectability of pelvic lesions.

DISCLOSURE

Christoph Berliner reports fees from ABX (consultant) and Janssen (speakers' bureau). Tobias Maurer reports fees from ABX, Advanced Accelerator Applications, Novartis, Telix, ROTOP Pharma, GEMoAb, Astellas, and Blue Earth Diagnostics (consultant) and from Bayer, Sanofi-Aventis, Astellas, and Phillips (speakers' bureau). Matthias Eiber holds parts of the patent for rhPSMA and received payments from third party funding from Blue Earth Diagnostics as well as consulting fees from Blue Earth Diagnostics, Novartis, Telix, Bayer, Point Biopharma, and Janssen. No other potential conflict of interest relevant to this article was reported.

KEY POINTS

QUESTION: Does delayed imaging improve the detectability of soft-tissue lesions on [^{99m}Tc]Tc-PSMA-I&S SPECT/CT?

PERTINENT FINDINGS: Late [^{99m}Tc]Tc-PSMA-I&S SPECT/CT imaging requires a 2-d protocol but significantly improves image quality and the detectability of soft-tissue lesions.

IMPLICATIONS FOR PATIENT CARE: [^{99m}Tc]Tc-PSMA-I&S SPECT/CT is still clearly inferior to PET/CT imaging for primary staging but could play a role in certain clinical scenarios focusing more on determining the extent of disease (e.g., for monitoring of systemic treatment) than on visualizing every lesion before metastasis-directed therapy.

REFERENCES

1. Sung H, Ferlay J, Siegel RL, et al. Global cancer statistics 2020: GLOBOCAN estimates of incidence and mortality worldwide for 36 cancers in 185 countries. *CA Cancer J Clin.* 2021;71:209–249.
2. Prostate cancer. European Association of Urology website. https://uroweb.org/guideline/prostate-cancer/. Accessed May 2, 2023.
3. Boehm K, Schiffmann J, Tian Z, et al. Five-year biochemical recurrence-free and overall survival following high-dose-rate brachytherapy with additional external beam or radical prostatectomy in patients with clinically localized prostate cancer. *Urol Oncol.* 2016;34:119.e11–119.e18.
4. Brockman JA, Alanee S, Vickers AJ, et al. Nomogram predicting prostate cancer-specific mortality for men with biochemical recurrence after radical prostatectomy. *Eur Urol.* 2015;67:1160–1167.
5. Lee BH, Kibel AS, Ciezki JP, et al. Are biochemical recurrence outcomes similar after radical prostatectomy and radiation therapy? Analysis of prostate cancer-specific mortality by nomogram-predicted risks of biochemical recurrence. *Eur Urol.* 2015;67:204–209.
6. Tyson MD, Penson DF, Resnick MJ. The comparative oncologic effectiveness of available management strategies for clinically localized prostate cancer. *Urol Oncol.* 2017;35:51–58.
7. Bott SRJ. Management of recurrent disease after radical prostatectomy. *Prostate Cancer Prostatic Dis.* 2004;7:211–216.
8. Valle LF, Lehrer EJ, Markovic D, et al. A systematic review and meta-analysis of local salvage therapies after radiotherapy for prostate cancer (MASTER). *Eur Urol.* 2021;80:280–292.
9. Anttinen M, Ettala O, Malaspina S, et al. A prospective comparison of ^{18}F-prostate-specific membrane antigen-1007 positron emission tomography computed

tomography, whole-body 1.5 T magnetic resonance imaging with diffusion-weighted imaging, and single-photon emission computed tomography/computed tomography with traditional imaging in primary distant metastasis staging of prostate cancer (PROSTAGE). *Eur Urol Oncol.* 2021;4:635–644.
10. Hofman MS, Lawrentschuk N, Francis RJ, et al. Prostate-specific membrane antigen PET-CT in patients with high-risk prostate cancer before curative-intent surgery or radiotherapy (proPSMA): a prospective, randomised, multicentre study. *Lancet.* 2020;395:1208–1216.
11. Sonni I, Eiber M, Fendler WP, et al. Impact of ^{68}Ga-PSMA-11 PET/CT on staging and management of prostate cancer patients in various clinical settings: a prospective single-center study. *J Nucl Med.* 2020;61:1153–1160.
12. Fendler WP, Calais J, Eiber M, et al. Assessment of ^{68}Ga-PSMA-11 PET accuracy in localizing recurrent prostate cancer: a prospective single-arm clinical trial. *JAMA Oncol.* 2019;5:856–863.
13. Afshar-Oromieh A, Malcher A, Eder M, et al. PET imaging with a [^{68}Ga]gallium-labelled PSMA ligand for the diagnosis of prostate cancer: biodistribution in humans and first evaluation of tumour lesions. *Eur J Nucl Med Mol Imaging.* 2013; 40:486–495.
14. Robu S, Schmidt A, Eiber M, et al. Synthesis and preclinical evaluation of novel ^{18}F-labeled Glu-urea-Glu-based PSMA inhibitors for prostate cancer imaging: a comparison with ^{18}F-DCFPyl and ^{18}F-PSMA-1007. *EJNMMI Res.* 2018;8:30.
15. Herrmann K, Bluemel C, Weineisen M, et al. Biodistribution and radiation dosimetry for a probe targeting prostate-specific membrane antigen for imaging and therapy. *J Nucl Med.* 2015;56:855–861.
16. Maurer T, Gschwend JE, Eiber M. Prostate-specific membrane antigen-guided salvage lymph node dissection in recurrent prostate cancer. *Curr Opin Urol.* 2018;28:191–196.
17. Robu S, Schottelius M, Eiber M, et al. Preclinical evaluation and first patient application of ^{99m}Tc-PSMA-I&S for SPECT imaging and radioguided surgery in prostate cancer. *J Nucl Med.* 2017;58:235–242.
18. Brunello S, Salvarese N, Carpanese D, Gobbi C, Melendez-Alafort L, Bolzati C. A review on the current state and future perspectives of [^{99m}Tc]Tc-housed PSMA-i in prostate cancer. *Molecules.* 2022;27:2617.
19. Werner P, Neumann C, Eiber M, Wester HJ, Schottelius M. [^{99cm}Tc]Tc-PSMA-I&S-SPECT/CT: experience in prostate cancer imaging in an outpatient center. *EJNMMI Res.* 2020;10:45.
20. Rajasekaran SA, Anilkumar G, Oshima E, et al. A novel cytoplasmic tail MXXXL motif mediates the internalization of prostate-specific membrane antigen. *Mol Biol Cell.* 2003;14:4835–4845.
21. Maurer T, Robu S, Schottelius M, et al. ^{99m}Technetium-based prostate-specific membrane antigen-radioguided surgery in recurrent prostate cancer. *Eur Urol.* 2019;75:659–666.
22. Rosset A, Spadola L, Ratib O. OsiriX: an open-source software for navigating in multidimensional DICOM images. *J Digit Imaging.* 2004;17:205–216.
23. Rasch D, Kubinger KD, Moder K. The two-sample t test: pre-testing its assumptions does not pay off. *Stat Pap (Berl).* 2011;52:219–231.
24. Ruxton GD. The unequal variance t-test is an underused alternative to Student's t-test and the Mann-Whitney U test. *Behav Ecol.* 2006;17:688–690.
25. Q04609 FOLH1_HUMAN. UniProt website. https://www.uniprot.org/uniprot/Q04609. Accessed May 2, 2023.
26. Afshar-Oromieh A, Hetzheim H, Kübler W, et al. Radiation dosimetry of ^{68}Ga-PSMA-11 (HBED-CC) and preliminary evaluation of optimal imaging timing. *Eur J Nucl Med Mol Imaging.* 2016;43:1611–1620.
27. Fendler WP, Eiber M, Beheshti M, et al. ^{68}Ga-PSMA PET/CT: joint EANM and SNMMI procedure guideline for prostate cancer imaging—version 1.0. *Eur J Nucl Med Mol Imaging.* 2017;44:1014–1024.
28. Rahbar K, Afshar-Oromieh A, Bögemann M, et al. ^{18}F-PSMA-1007 PET/CT at 60 and 120 minutes in patients with prostate cancer: biodistribution, tumour detection and activity kinetics. *Eur J Nucl Med Mol Imaging.* 2018;45:1329–1334.
29. Albalooshi B, Al Sharhan M, Bagheri F, et al. Direct comparison of ^{99m}Tc-PSMA SPECT/CT and ^{68}Ga-PSMA PET/CT in patients with prostate cancer. *Asia Ocean J Nucl Med Biol.* 2020;8:1–7.
30. Fallahi B, Khademi N, Karamzade-Ziarati N, et al. ^{99m}Tc-PSMA SPECT/CT versus ^{68}Ga-PSMA PET/CT in the evaluation of metastatic prostate cancer. *Clin Nucl Med.* 2021;46:e68–e74.
31. Rauscher I, Düwel C, Wirtz M, et al. Value of ^{111}In-prostate-specific membrane antigen (PSMA)-radioguided surgery for salvage lymphadenectomy in recurrent prostate cancer: correlation with histopathology and clinical follow-up. *BJU Int.* 2017;120:40–47.
32. Urbán S, Meyer C, Dahlbom M, et al. Radiation dosimetry of ^{99m}Tc-PSMA I&S: a single-center prospective study. *J Nucl Med.* 2021;62:1075–1081.

^{68}Ga-FAPI PET/CT Interobserver Agreement on Tumor Assessment: An International Multicenter Prospective Study

Riccardo Mei*[1,2], Lukas Kessler*[1,3], Kim M. Pabst[1,3], Manuel Weber[1,3], Christian Schmidkonz[4], Christoph Rischpler[1,3], Helle Damgaard Zacho[5], Thomas Hope[6], Sarah M. Schwarzenböck[7], Martin Allen-Auerbach[8,9], Louise Emmett[10], Justin Ferdinandus[11], Marcus Unterrainer[12], Benedikt M. Schaarschmidt[13], Lale Umutlu[13], Andrea Farolfi[2], Paolo Castellucci[2], Cristina Nanni[2], Silvi Telo[2], Stefano Fanti[2], Ken Herrmann[1,3], and Wolfgang P. Fendler[1,3]

[1]Department of Nuclear Medicine, University Hospital Essen, University of Duisburg–Essen, Essen, Germany; [2]Nuclear Medicine Department, IRCCS Azienda Ospedaliero–Universitaria di Bologna, Bologna, Italy; [3]German Cancer Consortium, Partner Site University Hospital Essen, and German Cancer Research Center, Essen, Germany; [4]Department of Nuclear Medicine, University Hospital Erlangen, Erlangen, Germany; [5]Department of Clinical Medicine, Aalborg University Hospital, Aalborg, Denmark; [6]Department of Radiology and Biomedical Imaging, University of California, San Francisco, California; [7]Department of Nuclear Medicine, Rostock University Medical Centre, Rostock, Germany; [8]Ahmanson Translational Theranostics Division, Department of Molecular and Medical Pharmacology, David Geffen School of Medicine, UCLA, Los Angeles, California; [9]Institute of Urologic Oncology, David Geffen School of Medicine, UCLA, Los Angeles, California; [10]Department of Theranostics and Nuclear Medicine, St. Vincent's Hospital, and Faculty of Medicine, UNSW Sydney, Sydney, New South Wales, Australia; [11]Department of Internal Medicine I, University of Cologne, Cologne, Germany; [12]Department of Radiology, University Hospital LMU Munich, Munich, Germany; and [13]Department of Diagnostic and Interventional Radiology and Neuroradiology, University Hospital Essen, University of Duisburg–Essen, Essen, Germany

^{68}Ga-fibroblast activation protein inhibitors (FAPIs) are promising radiotracers for cancer imaging, with emerging data in the recent years. Nonetheless, the interobserver agreement on ^{68}Ga-FAPI PET/CT study interpretations in cancer patients remains poorly understood. **Methods:** ^{68}Ga-FAPI PET/CT was performed on 50 patients with various tumor entities (sarcoma [n = 10], colorectal cancer [n = 10], pancreatic adenocarcinoma [n = 10], genitourinary cancer [n = 10], and other types of cancer [n = 10]). Fifteen masked observers reviewed and interpreted the images using a standardized approach for local, local nodal, and metastatic involvement. Observers were grouped by experience as having a low (<30 prior ^{68}Ga-FAPI PET/CT studies; n = 5), intermediate (30–300 studies; n = 5), or high level of experience (>300 studies; n = 5). Two independent readers with a high level of experience and unmasked to clinical information, histopathology, tumor markers, and follow-up imaging (CT/MRI or PET/CT) served as the standard of reference (SOR). Observer groups were compared by overall agreement (percentage of patients matching SOR) and Fleiss κ with mean and corresponding 95% CI. We defined acceptable agreement as a κ value of at least 0.6 (substantial or higher) and acceptable accuracy as at least 80%. **Results:** Highly experienced observers agreed substantially on all categories (primary tumor: κ = 0.71; 95% CI, 0.71–0.71; local nodal involvement: κ = 0.62; 95% CI, 0.61–0.62; distant metastasis: κ = 0.75; 95% CI, 0.75–0.75), whereas observers with intermediate experience showed substantial agreement on primary tumor (κ = 0.73; 95% CI, 0.73–0.73) and distant metastasis (κ = 0.65; 95% CI, 0.65–0.65) but moderate agreement on local nodal stages (κ = 0.55; 95% CI, 0.55–0.55). Observers with low experience had moderate agreement on all categories (primary tumor: κ = 0.57; 95% CI, 0.57–0.58; local nodal involvement: κ = 0.51; 95% CI, 0.51–0.52; distant metastasis: κ = 0.54; 95% CI, 0.53–0.54). Compared with SOR, the accuracy for readers with high, intermediate, and low experience was 85%, 83%, and 78%, respectively. In summary, only highly experienced readers showed substantial agreement and a diagnostic accuracy of at least 80% in all categories. **Conclusion:** The interpretation of ^{68}Ga-FAPI PET/CT for cancer imaging had substantial reproducibility and accuracy among highly experienced observers only, especially for local nodal and metastatic assessments. Therefore, for accurate interpretation of different tumor entities and pitfalls, we recommend training or experience with at least 300 representative scans for future clinical readers.

Key Words: cancer imaging; FAPI; fibroblast activation protein; PET; interobserver agreement

J Nucl Med 2023; 64:1043–1048
DOI: 10.2967/jnumed.122.265245

Fibroblast activation protein is expressed by carcinoma-associated fibroblasts and cells of certain solid tumors (*1*). Radiolabeled fibroblast activation protein inhibitors (FAPIs) such as ^{68}Ga-FAPI-46 have been developed as novel theranostic tools for cancer (*2–5*). Increasing data suggest a high sensitivity for tumor detection and less background uptake than with ^{18}F-FDG (*6–8*). Mainly retrospective trials have demonstrated superior detection rates and higher accuracy for the localization for various tumor entities, but larger cohorts and prospective data are lacking. Nonetheless, multiple prospective trials to evaluate the accuracy and management impact of ^{68}Ga-FAPI PET/CT are currently under way at our site and worldwide (NCT05160051, NCT04023240, NCT05262855) (*7,9,10*).

To serve as a reliable clinical and research tool in the future, findings from ^{68}Ga-FAPI PET/CT must be accurate and reproducible. However, interobserver agreement on ^{68}Ga-FAPI PET/CT interpretations remains poorly understood, and consistent interpretation might be challenging given the heterogeneity of tumor diseases and limited

Received Nov. 23, 2022; revision accepted Feb. 21, 2023.
For correspondence or reprints, contact Riccardo Mei (riccardo.mei@studio.unibo.it).
*Contributed equally to this work.
Published online May 25, 2023.

availability of these novel radiotracers. Regardless of the diagnostic value of an imaging method, the overall performance is closely linked to interobserver agreement and variability, which need to be established before implementation into clinical routine (*11,12*). To address this need, we prospectively evaluated interobserver agreement and accuracy for ^{68}Ga-FAPI PET/CT interpretations in different tumor entities and compared findings among readers with various levels of experience.

MATERIALS AND METHODS

Study Design and Patients

Fifty patients who underwent ^{68}Ga-FAPI-46 PET/CT for imaging of the following tumor types were retrospectively selected from 2 institutional databases (University Hospital Essen and University Hospital Bologna): sarcoma (n = 10), pancreatic adenocarcinoma (n = 10), colorectal cancer (n = 10), genitourinary cancer (n = 10) and miscellaneous cases (n = 10) consisting of various other cancer entities (breast cancer [n = 1]; lung cancer [n = 2]; pleural mesothelioma [n = 2]; cholangiocarcinoma [n = 2]; hepatocellular carcinoma [n = 1]; head and neck cancer [n = 1]; and lymphoma [n = 1]).

PET/CT-positive lesions were defined by consensus during a joint reading session by 2 expert readers, each with more than 500 prior clinical or research ^{68}Ga-FAPI-46 PET/CT readings. Expert readers had access to all clinical data. Clinical information, histopathology, tumor markers, and follow-up imaging (CT/MRI or PET/CT) were used as the standard of reference (SOR) for lesion validation. Cases were selected to represent clinical routine, ranging from negative cases (n = 8, 16%) to extensive disease (n = 28, 56%), with typical pitfalls. Data were analyzed as part of the prospective interobserver study (NCT04990882) and approved by the local Ethics Committee (permits 19-8991-BO and 20-9485-BO). Patients gave written informed consent to undergo clinical ^{68}Ga-FAPI-46 PET/CT, and the respective institutional review boards waived individual patient consent for anonymized assessment of their datasets as part of the interobserver study.

Image Acquisition and Reconstruction

Patient preparation and image acquisition were performed as previously described (*13*).

In brief, PET was performed on a PET/CT system (Biograph mCT or Vision; Siemens). Scanning was performed at a mean (±SD) of 14 ± 9 min after injection (minimum, 10 min; maximum, 48 min). The injected activity of ^{68}Ga-FAPI was 150 ± 38 MBq. All PET images were iteratively reconstructed (Vision: 4 iterations, 5 subsets, 220 × 220 matrix, 5-mm Gauss filtering; mCT: 3 iterations, 21 subsets; 200 × 200 matrix, 4-mm Gauss filtering) with time-of-flight information, using the manufacturer's dedicated software (syngo.via for MI; Siemens Healthineers). In all patients, a low-dose CT scan was acquired for attenuation correction (30 mAs, 120 keV, 512 × 512 matrix, 3-mm slice thickness). If available, diagnostic CT scans (with or without contrast enhancement, within 2 wk of ^{68}Ga-FAPI PET/CT) were provided for the respective case.

Observers

Fifteen nuclear medicine physicians (5 with additional radiology training) who had at least 1 y of experience with other tracers (^{18}F-FDG, ^{18}F/^{68}Ga-PSMA, ^{68}Ga-DOTA-peptides) were prospectively recruited as observers. They were from 10 centers in Europe (n = 12), North America (n = 2), and Australia (n = 1). On the basis of the previously reported number of ^{68}Ga-FAPI PET/CT interpretations, observers were classified as having a low (<30 prior ^{68}Ga-FAPI PET/CT studies; n = 5), intermediate (30–300 studies; n = 5, 4 of whom also had radiology education), or high level of experience (>300 studies; n = 5, 1 of whom also had radiology education). The observers reviewed all provided ^{68}Ga-FAPI PET/CT datasets (n = 50). Each dataset included low-dose CT and attenuation-corrected PET images and, if available, diagnostic CT images.

Guidelines for Visual Interpretation

For standardized visual interpretation of datasets, the observers were provided a written guide (Supplemental Data File 1; supplemental materials are available at http://jnm.snmjournals.org), 4 teaching cases (Supplemental Data File 2), an electronic case report form, and 1 test patient dataset with disclosed data entries. Furthermore, the observers were asked to learn about ^{68}Ga-FAPI-46 PET/CT pitfalls (*13*).

Only necessary patient information was disclosed to the observers before image interpretation: indication for ^{68}Ga-FAPI PET/CT (primary diagnosis, prior surgery/therapy, staging or restaging of metastatic disease), age (y), weight (kg), injected dose (MBq), and uptake time (min). The observers were masked to all other clinical data. Visual image interpretation for the presence or absence of malignant disease was reported for predefined organ and region categories.

Statistical Analyses and Reference Standard

Agreement among observer groups was evaluated using the Fleiss κ (*14*).

Ninety-five percent CIs are reported for κ. The interpretation of κ was based on a classification provided by Landis and Koch (*15*): 0.0, poor; 0.0–0.20, slight; 0.21–0.40, fair; 0.41–0.60, moderate; 0.61–0.80, substantial; and 0.81–1.00, almost-perfect reproducibility. SOR was defined as the decision of the experienced expert readers, unmasked to all clinical information (e.g., histopathology, follow-up imaging, and tumor markers).

Overall agreement, defined as the total agreement of an observer on all categories (primary tumor, local nodal involvement, distant metastasis), and sensitivity, specificity, and positive and negative predictive value compared with SOR were calculated. The difference between 2 groups was assessed by the Student t test at a significance level of P less than 0.05. Statistical analyses were performed using SSPS software (version 26.0, SPSS Inc.) for all other statistical analyses, and graphs were generated using GraphPad Prism (version 9.1.0; GraphPad Software). At least substantial agreement ($\kappa \geq 0.6$) on visual interpretation of all scans for the 3 major staging categories (primary tumor, local nodal involvement, distant metastasis) and diagnostic accuracy of at least 80% were defined as acceptable performance.

RESULTS

Patient Characteristics

Table 1 summarizes the patient characteristics. Twenty-seven male (54.0%) and 23 female (46.0%) patients were included in this study, with a mean age of 58 ± 18 y (range, 19–83 y). Twenty-one patients were imaged at initial diagnosis (42.0%), and 29 patients (58.0%) underwent ^{68}Ga-FAPI PET/CT for disease restaging. Diagnostic CT was available for 68% of the patients (34 patients: 9 with sarcoma, 9 with pancreatic adenocarcinoma, 5 with colorectal cancer, 4 with genitourinary cancer, and 7 with miscellaneous cancers), and low-dose CT was performed on 16 (32%) patients. ^{68}Ga-FAPI PET/CT studies were interpreted as positive for local or metastatic cancer lesions in 42 of 50 (84.0%) patients by the reference readers: primary tumor was present in 10 patients (20.0%); 4 patients (8.0%) had lymph node–positive disease, whereas 28 (56.0%) were staged as bone-positive or organ-positive (distant metastasis), respectively.

Image Interpretation: Interobserver Agreement

The interobserver agreement on visual image interpretation is summarized in Figure 1 and Table 2. Highly experienced observers agreed substantially on all categories (primary tumor, κ = 0.71;

TABLE 1
Patient Characteristics (n = 50)

Characteristic	Data
Age (y)	
Mean	58 (SD, 16)
Median	61 (range, 19, 83)
Sex	
Female	23 (46.0%)
Male	27 (54.0%)
Indication	
Initial staging	21 (42.0%)
Restaging	29 (58.0%)
Tumor stage	
No tumor	8 (16.0%)
Local	10 (20.0%)
Local nodal metastatic	4 (8.0%)
Metastatic (organ and bone)	28 (56.0%)

Data are number followed by percentage in parentheses, except for age.

local nodal involvement, κ = 0.62; distant metastasis, κ = 0.75), whereas observers with intermediate experience showed substantial agreement on primary tumor (κ = 0.73) and distant metastasis (κ = 0.65) and moderate agreement on nodal involvement (κ = 0.55). Observers with low experience had moderate agreement on all categories (primary tumor, κ = 0.57; local nodal involvement, κ = 0.51; distant metastasis, κ = 0.54). Regardless of the experience level, the overall interobserver agreement was moderate for primary tumor (κ = 0.56) and local nodal involvement (κ = 0.55) but substantial for other metastatic lesions (κ = 0.69).

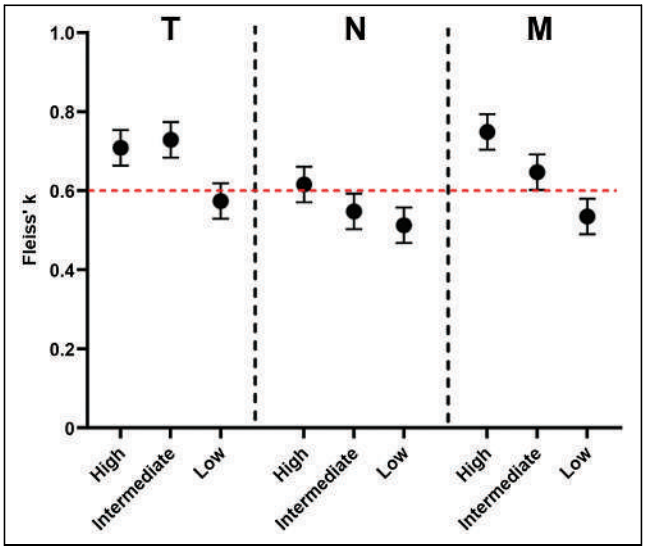

FIGURE 1. Interobserver agreement by primary tumor (T), local nodal involvement (N), distant metastasis (M), and experience level (high, intermediate, and low).

TABLE 2
Interobserver Agreement on Visual Image Interpretation

Category	Agreement level	Mean κ	Inferior 95% CI	Superior 95% CI
T	High	0.709	0.705	0.710
	Intermediate	0.729	0.727	0.732
	Low	0.574	0.572	0.577
	Any	0.563	0.490	0.633
N	High	0.616	0.613	0.619
	Intermediate	0.548	0.546	0.551
	Low	0.513	0.510	0.516
	Any	0.547	0.472	0.616
M	High	0.749	0.746	0.752
	Intermediate	0.647	0.645	0.650
	Low	0.535	0.532	0.538
	Any	0.686	0.614	0.757

Image Interpretation: Comparison to SOR

Table 3 summarizes—by category—sensitivity, specificity, positive and negative predictive value, and accuracy for the entire group and separately for observers with a low, intermediate, or high level of experience. Independent of the experience level, all observers reported primary tumor and distant metastasis stages with high sensitivity (89.0% and 91%). Sensitivity was lower for local nodal involvement stages (79.0%). Because of higher rates of false-positive lesions, specificity was lower for primary tumor stages than for local nodal involvement and distant metastasis stages (65% vs. 81% vs. 77%). Five representative patient examples of disagreement among observers are given in Figure 2.

Mean overall agreement with SOR for primary tumor, local nodal involvement, and distant metastasis staging had a κ value

TABLE 3
Sensitivity and Specificity for Observer with High, Intermediate, and Low Experience and for All Observers

Category	Agreement level	SE	SP	PPV	NPV	ACC
T	High	0.91	0.63	0.81	0.79	0.81
	Intermediate	0.89	0.73	0.86	0.80	0.84
	Low	0.88	0.59	0.79	0.73	0.77
	All combined	0.89	0.65	0.82	0.77	0.81
N	High	0.77	0.89	0.73	0.91	0.86
	Intermediate	0.83	0.77	0.59	0.92	0.79
	Low	0.88	0.59	0.79	0.73	0.77
	All combined	0.79	0.81	0.61	0.91	0.80
M	High	0.87	0.88	0.91	0.83	0.87
	Intermediate	0.96	0.73	0.83	0.93	0.86
	Low	0.90	0.70	0.80	0.83	0.81
	All combined	0.91	0.77	0.84	0.86	0.85

SE = sensitivity; SP = specificity; PPV = positive predictive value; NPV = negative predictive value; ACC = accuracy.

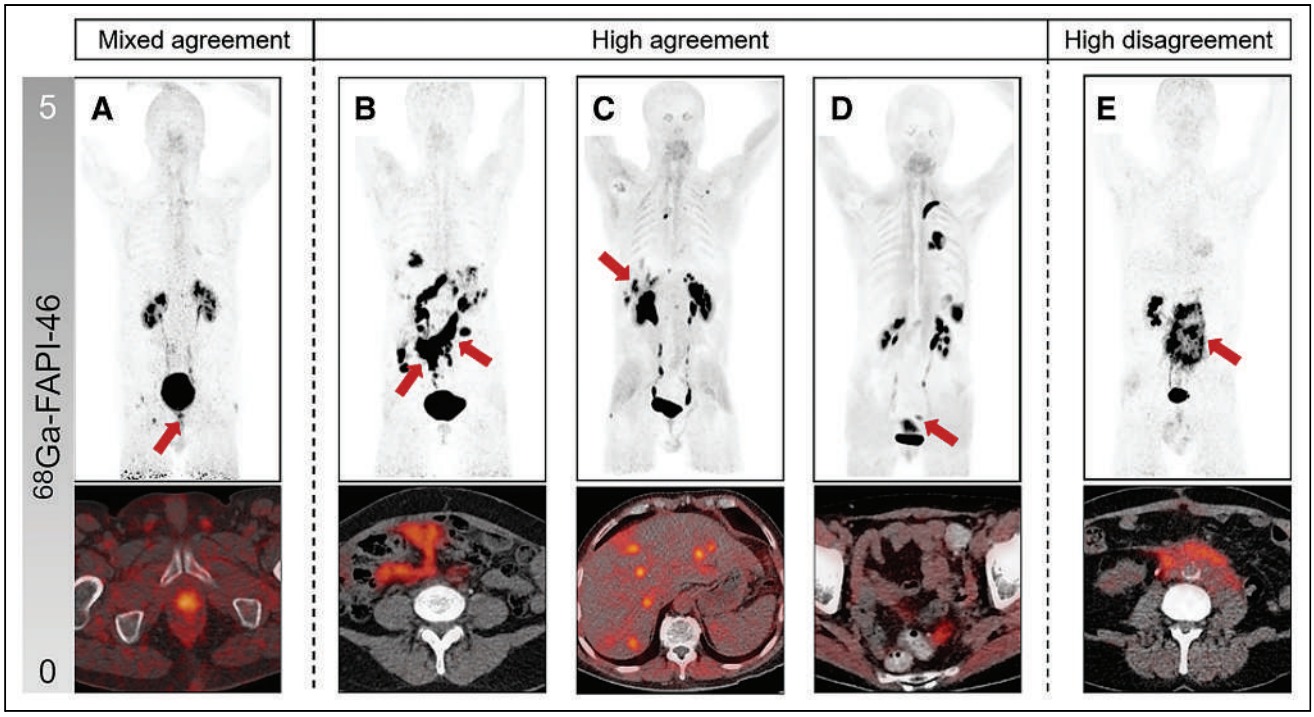

FIGURE 2. Example cases and lesions (arrows) with high agreement, high disagreement, and mixed agreement with SOR. Maximum intensity projections (MIPs) are represented above, and fused transaxial PET/CT images are represented below. (A) Patient with local relapse of urothelial cancer confirmed by histopathology; 7 readers rated positive (2 high, 3 intermediate, 2 low experience), and 8 readers rated lesion negative (3 high, 2 intermediate, 3 low experience). (B) Patient with ovarian cancer; all readers agreed with expert on peritoneal involvement. (C) All readers agreed with expert on liver metastasis in patient with colorectal carcinoma. (D) All readers correctly identified diverticulosis in sarcoma patient. (E) Patient with urothelial cancer and retroperitoneal fibrosis; all readers falsely rated retroperitoneal lesions as malignant and disagreed with expert panel and histopathology.

of 0.64 for the entire group of observers. Observers with high and intermediate experience showed substantial agreement with SOR (high, $\kappa = 0.69$; intermediate, $\kappa = 0.66$), whereas readers with low experience had moderate agreement with SOR ($\kappa = 0.56$) (Table 4). Observers with low and intermediate experience had significantly lower agreement than did highly experienced observers ($\kappa = 0.56$ and 0.66 vs. 0.69, $P < 0.001$). Irrespective of the stage categories, observers with high and intermediate experience had higher sensitivity, specificity, positive and negative predictive values, and accuracy than did observers with low experience (sensitivity, 87% vs. 91% vs. 74%; specificity, 82% vs. 75% vs. 70%; accuracy, 85% vs. 83% vs. 78%) (Table 4).

The interobserver agreement and accuracy of observers were analyzed separately for the different tumor entities (Table 5). Substantial overall agreement was observed for the miscellaneous ($\kappa = 0.75$), sarcoma ($\kappa = 0.74$), colorectal ($\kappa = 0.70$), and genitourinary cases ($\kappa = 0.63$). Only interpretation of pancreatic cancer cases revealed slight overall agreement ($\kappa = 0.33$). Readers were most sensitive for sarcoma and miscellaneous cases (96% and 97%) and had high accuracy (87% and 89%). Pancreatic cases had the lowest diagnostic performance (sensitivity, 73%; specificity, 61%; accuracy, 66%) (Table 5).

TABLE 4
Overall Sensitivity and Specificity for Observer with High, Intermediate, or Low Experience

Experience level	κ	SE	SP	PPV	NPV	ACC
High	0.69	0.87	0.82	0.83	0.86	0.85
Intermediate	0.66	0.91	0.75	0.79	0.89	0.83
Low	0.56	0.74	0.70	0.74	0.84	0.78

SE = sensitivity; SP = specificity; PPV = positive predictive value; NPV = negative predictive value; ACC = accuracy.

DISCUSSION

This prospective study involving 50 ^{68}Ga-FAPI46 PET/CT patients with various tumor entities demonstrated substantial reproducibility for highly experienced observers, as well as—with limitations—for observers with intermediate experience.

TABLE 5
Agreement and Accuracy per Tumor Entity Irrespective of Reader Experience

Tumor entity	κ	SE	SP	PPV	NPV	ACC
Colorectal	0.68	0.84	0.85	0.83	0.86	0.85
Genitourinary	0.63	0.63	0.82	0.75	0.87	0.82
Miscellaneous	0.75	0.97	0.73	0.88	0.93	0.89
Pancreas	0.33	0.73	0.61	0.59	0.75	0.66
Sarcoma	0.74	0.96	0.77	0.83	0.95	0.87

SE = sensitivity; SP = specificity; PPV = positive predictive value; NPV = negative predictive value; ACC = accuracy.

On the basis of our predefined criteria, we recommend initial training with at least 300 representative patient cases (high experience) to reach an acceptable diagnostic performance for clinical and research interpretations of ^{68}Ga-FAPI PET/CT scans. This is comparable to other recent radiotracer training recommendations (*16*). Training cases should include not just tumor findings (low and extensive tumor burden) but also common pitfalls, such as inflammatory changes or degenerative or posttraumatic bone lesions (*13*).

In recent years, ^{68}Ga-FAPI PET/CT has been promoted as a novel highly tumor-specific imaging modality with beneficial radiotracer kinetics and low background uptake (*17*). Nonetheless, because of the heterogeneity of tumor diseases, variance in fibroblast activation protein expression of tumor and stromal cells, and potential pitfalls, the interpretation of ^{68}Ga-FAPI PET/CT scans might prove more challenging than expected (*8,9,13,18–22*). Sources of misinterpretations and false-positive ratings of lesions include a variety of pitfalls similar to those for ^{18}F-FDG but differing from those for other recent targeted radioligands such as ^{68}Ga-PSMA (*23,24*). Examples of these pitfalls include inflammatory uptake (e.g., pancreatitis and myocarditis), degenerative bone lesions, and benign tumors (*8,13,25*). Because ^{68}Ga-FAPI is relatively new, the list of pitfalls and benign findings is still evolving and therefore must be constantly updated. Radiotracers such as ^{68}Ga-PSMA for prostate cancer or ^{68}Ga-DOTATATE/DOTATOC for neuroendocrine tumors are entity-specific. On the other hand, ^{68}Ga-FAPI is not specific for any malignancy and can be used for a variety of cancers. This might explain why physicians need to be trained on a high number of cases (300) for ^{68}Ga-FAPI PET to achieve substantial reproducibility, compared with less than 50 patient cases for ^{68}Ga-PSMA and ^{68}Ga-DOTATATE/DOTATOC PET (*16,26*). Our data underline the necessity of high reader experience for best ^{68}Ga-FAPI PET agreement and diagnostic performance, although intermediate-level readers do show appropriate results as well. As compared with our study on the ^{68}Ga-FAPI tracer, other interobserver agreement studies on ^{68}Ga-PSMA and ^{68}Ga-DOTATATE PET/CT reported higher reproducibility with lower numbers of recommended initial training cases. This difference is partly due to higher specificity and tumor signal given by receptor radiotracers.

Our cohort consisted of a high proportion of patients with metastatic disease, which reflects the likely clinical-use scenario for ^{68}Ga-FAPI PET/CT as a whole-body staging tool. We observed that despite high sensitivity for local staging, specificity was only 63% even for highly experienced readers. This is likely due to high nonmalignant tracer uptake after surgery or tracer uptake due to inflammatory changes, both frequently noted in pancreatic cancer patients in our cohort and likely reflecting chronic pancreatitis or scarred tissue after pancreatectomy (*8,27*). A careful review of the patient's history before image interpretation, and sufficient experience, will therefore be required to avoid a negative impact on clinical management.

This study comes with limitations. Because ^{68}Ga-FAPI PET/CT is applied for different indications, we decided on a balanced oncologic patient cohort from 2 centers. Only a small proportion of tumor entities was reflected by the patient cohort, and a larger number of patients would be necessary to draw conclusions on agreement and diagnostic performance for distinct tumor entities or imaging of benign disease. Although previous interobserver studies were focused on a single tumor entity (i.e., neuroendocrine tumors for ^{68}Ga-DOTATATE and prostate cancer for ^{68}Ga-PSMA) (*16,26*), ^{68}Ga-FAPI could be used for a variety of malignancies. For this purpose, we aimed to include representative patients with different tumor entities. We acknowledge that only one fifth of the cases presented with primary tumor and that PET/CT was performed after the primary treatment in almost 60% of the patients. However, we consider restaging of disease to be a representative scenario to test the reproducibility of ^{68}Ga-FAPI PET interpretation among readers with various levels of experience. The skill of a reader is determined by multiple factors, including clinical knowledge and general experience in imaging and may vary with the oncologic focus of the reader or center (e.g., lung cancer vs. breast cancer vs. sarcoma). We tried to address this limitation by recruitment of readers worldwide and by inclusion of different tumor entities.

CONCLUSION

Before clinical implementation of ^{68}Ga-FAPI PET/CT, we recommend a high experience level based on at least 300 training cases for substantial agreement and diagnostic performance in all categories (primary tumor, local nodal involvement, and distant metastasis). On the basis of the different clinical scenarios and pitfalls, more extensive training is required for ^{68}Ga-FAPI PET/CT than for other radiotracers.

DISCLOSURE

Lukas Kessler is a consultant for BTG and AAA and received fess from Sanofi outside the submitted work. Manuel Weber reports personal fees from Boston Scientific, Terumo, Advanced Accelerator Applications, and Eli Lilly. Wolfgang Fendler reports fees from SOFIE Biosciences (research funding), Janssen (consultant, speakers' bureau), Calyx (consultant), Bayer (consultant, speakers' bureau, research funding), Parexel (image review), and AAA (speakers' bureau) outside the submitted work. Benedikt Schaarschmidt received a research grant from PharmaCept for an undergoing investigator-initiated study not related to this paper. No other potential conflict of interest relevant to this article was reported.

KEY POINTS

QUESTION: To what extent do ^{68}Ga-FAPI PET/CT interpretations agree on various tumor entities for observers with different levels of experience?

PERTINENT FINDINGS: We observed substantial overall agreement and high accuracy for observers with a high experience level and also, partially, for intermediate-level observers.

IMPLICATIONS FOR PATIENT CARE: Before clinical implementation of ^{68}Ga-FAPI PET/CT, we recommend a high level of reader experience based on at least 300 training cases.

REFERENCES

1. Puré E, Blomberg R. Pro-tumorigenic roles of fibroblast activation protein in cancer: back to the basics. *Oncogene.* 2018;37:4343–4357.
2. Loktev A, Lindner T, Burger EM, et al. Development of fibroblast activation protein-targeted radiotracers with improved tumor retention. *J Nucl Med.* 2019;60:1421–1429.
3. Lindner T, Loktev A, Altmann A, et al. Development of quinoline-based theranostic ligands for the targeting of fibroblast activation protein. *J Nucl Med.* 2018;59:1415–1422.
4. Ferdinandus J, Fragoso Costa P, Kessler L, et al. Initial clinical experience with ^{90}Y-FAPI-46 radioligand therapy for advanced stage solid tumors: a case series of nine patients. *J Nucl Med.* 2022;63:727–734.
5. Fendler WP, Pabst KM, Kessler L, et al. Safety and efficacy of ^{90}Y-FAPI-46 radioligand therapy in patients with advanced sarcoma and other cancer entities. *Clin Cancer Res.* 2022;28:4346–4353.

6. Giesel FL, Kratochwil C, Schlittenhardt J, et al. Head-to-head intra-individual comparison of biodistribution and tumor uptake of ^{68}Ga-FAPI and ^{18}F-FDG PET/CT in cancer patients. *Eur J Nucl Med Mol Imaging.* 2021;48:4377–4385.
7. Kessler L, Ferdinandus J, Hirmas N, et al. ^{68}Ga-FAPI as a diagnostic tool in sarcoma: data from the ^{68}Ga-FAPI PET prospective observational trial. *J Nucl Med.* 2022;63:89–95.
8. Röhrich M, Naumann P, Giesel FL, et al. Impact of ^{68}Ga-FAPI PET/CT imaging on the therapeutic management of primary and recurrent pancreatic ductal adenocarcinomas. *J Nucl Med.* 2021;62:779–786.
9. Dendl K, Koerber SA, Finck R, et al. ^{68}Ga-FAPI-PET/CT in patients with various gynecological malignancies. *Eur J Nucl Med Mol Imaging.* 2021;48:4089–4100.
10. Syed M, Flechsig P, Liermann J, et al. Fibroblast activation protein inhibitor (FAPI) PET for diagnostics and advanced targeted radiotherapy in head and neck cancers. *Eur J Nucl Med Mol Imaging.* 2020;47:2836–2845.
11. Bankier AA, Levine D, Halpern EF, Kressel HY. Consensus interpretation in imaging research: is there a better way? *Radiology.* 2010;257:14–17.
12. Reid MC, Lachs MS, Feinstein AR. Use of methodological standards in diagnostic test research: getting better but still not good. *JAMA.* 1995;274:645–651.
13. Kessler L, Ferdinandus J, Hirmas N, et al. Pitfalls and common findings in ^{68}Ga-FAPI-PET: a pictorial analysis. *J Nucl Med.* 2022;63:890–896.
14. Hale CA, Fleiss JL. Interval estimation under two study designs for kappa with binary classifications. *Biometrics.* 1993;49:523–534.
15. Landis JR, Koch GG. The measurement of observer agreement for categorical data. *Biometrics.* 1977;33:159–174.
16. Fendler WP, Calais J, Allen-Auerbach M, et al. ^{68}Ga-PSMA-11 PET/CT interobserver agreement for prostate cancer assessments: an international multicenter prospective study. *J Nucl Med.* 2017;58:1617–1623.
17. Giesel FL, Kratochwil C, Lindner T, et al. ^{68}Ga-FAPI PET/CT: biodistribution and preliminary dosimetry estimate of 2 DOTA-containing FAP-targeting agents in patients with various cancers. *J Nucl Med.* 2019;60:386–392.
18. Dendl K, Koerber SA, Adeberg S, et al. Physiological FAP-activation in a postpartum woman observed in oncological FAPI-PET/CT. *Eur J Nucl Med Mol Imaging.* 2021;48:2059–2061.
19. Gündoğan C, Güzel Y, Can C, Alabalik U, Kömek H. False-positive ^{68}Ga-fibroblast activation protein-specific inhibitor uptake of benign lymphoid tissue in a patient with breast cancer. *Clin Nucl Med.* 2021;46:e433–e435.
20. Liu H, Wang Y, Zhang W, Cai L, Chen Y. Elevated ^{68}Ga-FAPI activity in splenic hemangioma and pneumonia. *Clin Nucl Med.* 2021;46:694–696.
21. Lin R, Lin Z, Zhang J, Yao S, Miao W. Increased ^{68}Ga-FAPI-04 uptake in Schmorl node in a patient with gastric cancer. *Clin Nucl Med.* 2021;46:700–702.
22. Kratochwil C, Flechsig P, Lindner T, et al. ^{68}Ga-FAPI PET/CT: tracer uptake in 28 different kinds of cancer. *J Nucl Med.* 2019;60:801–805.
23. Rischpler C, Beck TI, Okamoto S, et al. ^{68}Ga-PSMA-HBED-CC uptake in cervical, celiac, and sacral ganglia as an important pitfall in prostate cancer PET imaging. *J Nucl Med.* 2018;59:1406–1411.
24. Ibrahim N, Cho S, Hall L, Perlman S. Is it cancer? Potential pitfalls of FDG PET/CT imaging [abstract]. *J Nucl Med.* 2016;57(suppl 2):1315.
25. Zhang X, Song W, Qin C, Liu F, Lan X. Non-malignant findings of focal ^{68}Ga-FAPI-04 uptake in pancreas. *Eur J Nucl Med Mol Imaging.* 2021;48:2635–2641.
26. Fendler WP, Barrio M, Spick C, et al. ^{68}Ga-DOTATATE PET/CT interobserver agreement for neuroendocrine tumor assessment: results of a prospective study on 50 patients. *J Nucl Med.* 2017;58:307–311.
27. Ferdinandus J, Kessler L, Hirmas N, et al. Equivalent tumor detection for early and late FAPI-46 PET acquisition. *Eur J Nucl Med Mol Imaging.* 2021;48:3221–3227.

Superior Tumor Detection for ^{68}Ga-FAPI-46 Versus ^{18}F-FDG PET/CT and Conventional CT in Patients with Cholangiocarcinoma

Kim M. Pabst[1,2], Marija Trajkovic-Arsic[2,3], Phyllis F.Y. Cheung[2,3], Simone Ballke[4], Katja Steiger[4], Timo Bartel[1,2], Benedikt M. Schaarschmidt[5], Aleksandar Milosevic[5], Robert Seifert[1,2,6], Michael Nader[1,2], Lukas Kessler[1,2], Jens T. Siveke[2,3,7,8], Katharina Lueckerath[1,2], Stefan Kasper[2,7], Ken Herrmann[1,2], Nader Hirmas[1,2], Hartmut H. Schmidt[9,10], Rainer Hamacher[2,7], and Wolfgang P. Fendler[1,2]

[1]Department of Nuclear Medicine, West German Cancer Center, University Hospital Essen, Essen, Germany; [2]German Cancer Consortium, partner site University Hospital Essen, Essen, Germany; [3]Division of Solid Tumor Translational Oncology, German Cancer Research Center, Heidelberg, Germany; [4]Institute of Pathology, School of Medicine, Technical University of Munich, Munich, Germany; [5]Department of Diagnostic and Interventional Radiology, University Hospital Essen, University of Duisburg–Essen, Essen Germany; [6]Department of Nuclear Medicine, University Hospital Münster, Münster, Germany; [7]Department of Medical Oncology, West German Cancer Center, University Hospital Essen, Essen, Germany; [8]Bridge Institute of Experimental Tumor Therapy, West German Cancer Center, University Hospital Essen, Essen, Germany; [9]Medical Clinic B, Department of Gastroenterology, Hepatology, Endocrinology, and Infectiology, University Hospital Münster, Münster, Germany; and [10]Department of Gastroenterology and Hepatology, University Hospital Duisburg–Essen, Essen, Germany

Management of cholangiocarcinoma is among other factors critically determined by accurate staging. Here, we aimed to assess the accuracy of PET/CT with the novel cancer fibroblast–directed ^{68}Ga-fibroblast activation protein (FAP) inhibitor (FAPI)-46 tracer for cholangiocarcinoma staging and management guidance. **Methods:** Patients with cholangiocarcinoma from a prospective observational trial were analyzed. ^{68}Ga-FAPI-46 PET/CT detection efficacy was compared with ^{18}F-FDG PET/CT and conventional CT. SUV_{max}/tumor-to-background ratio (Wilcoxon test) and separately uptake for tumor grade and location (Mann–Whitney *U* test) were compared. Immunohistochemical FAP and glucose transporter 1 (GLUT1) expression of stromal and cancer cells was analyzed. The impact on therapy management was investigated by pre- and post-PET/CT questionnaires sent to the treating physicians. **Results:** In total, 10 patients (6 with intrahepatic cholangiocarcinoma and 4 with extrahepatic cholangiocarcinoma; 6 with grade 2 tumor and 4 with grade 3 tumor) underwent ^{68}Ga-FAPI-46 PET/CT and conventional CT; 9 patients underwent additional ^{18}F-FDG PET/CT. Immunohistochemical analysis was performed on the entire central tumor plain in 6 patients. Completed questionnaires were returned in 8 cases. Detection rates for ^{68}Ga-FAPI-46 PET/CT, ^{18}F-FDG PET/CT, and CT were 5, 5, and 5, respectively, for primary tumor; 11, 10, and 3, respectively, for lymph nodes; and 6, 4, and 2, respectively, for distant metastases. ^{68}Ga-FAPI-46 versus ^{18}F-FDG PET/CT SUV_{max} for primary tumor, lymph nodes, and distant metastases was 14.5 versus 5.2 ($P = 0.043$), 4.7 versus 6.7 ($P = 0.05$), and 9.5 versus 5.3 ($P = 0.046$), respectively, and tumor-to-background ratio (liver) was 12.1 versus 1.9 ($P = 0.043$) for primary tumor. Grade 3 tumors demonstrated a significantly higher ^{68}Ga-FAPI-46 uptake than grade 2 tumors (SUV_{max}, 12.6 vs. 6.4; $P = 0.009$). Immunohistochemical FAP expression was high on tumor stroma (~90% of cells positive), whereas GLUT1 expression was high on tumor cells (~80% of cells positive). Overall, average expression intensity was estimated as grade 3 for FAP and grade 2 for GLUT1. Positive ^{68}Ga-FAPI-46 PET findings led to a consequent biopsy workup and diagnosis of cholangiocarcinoma in 1 patient. However, patient treatment was not adjusted on the basis of ^{68}Ga-FAPI-46 PET. **Conclusion:** ^{68}Ga-FAPI-46 demonstrated superior radiotracer uptake, especially in grade 3 tumors, and lesion detection in patients with cholangiocarcinoma. In line with this result, immunohistochemistry demonstrated high FAP expression on tumor stroma. Accuracy is under investigation in an ongoing investigator-initiated trial.

Key Words: ^{68}Ga-FAPI-46 PET/CT; ^{18}F-FDG PET/CT; conventional CT; cholangiocarcinoma; immunohistochemistry

J Nucl Med 2023; 64:1049–1055
DOI: 10.2967/jnumed.122.265215

Cholangiocarcinomas originate from intra- and extrahepatic locations of the biliary tract (*1*). They are the second most common liver malignancy (*2*), are rising in incidence (*3*) and are often diagnosed late, frequently leading to a fatal outcome (*4*). Primary tumors are typically diagnosed by contrast-enhanced and diffusion-weighted MRI with MR cholangiopancreatography (*5*). Additional imaging by whole-body CT is offered for the detection of distant metastases and vascular involvement (*6*).

Current guidelines do not routinely recommend PET/CT for the diagnosis and staging of biliary tract malignancies. These recommendations refer to imaging using the radioactive tracer ^{18}F-FDG (*6*). The accuracy of ^{18}F-FDG is limited by intertumoral heterogeneous uptake, that is, a high glycolytic rate for high-grade cholangiocarcinoma and a low glycolytic rate for low-grade cholangiocarcinoma (*7,8*).

In recent years, quinoline-based fibroblast activation protein (FAP)–specific inhibitors (*9*) coupled to ^{68}Ga have been developed for

Received Nov. 18, 2022; revision accepted Feb. 2, 2023.
For correspondence or reprints, contact Kim M. Pabst (kim.pabst@uk-essen.de).
Published online Apr. 6, 2023.

PET imaging. FAP is expressed by predominantly cancer-associated fibroblasts in the stroma of various tumor entities, leading to highly tumor-specific expression (*10*).

Because of an abundant tumor stroma whose main cellular components are cancer-associated fibroblasts, cholangiocarcinoma is a promising tumor entity for ^{68}Ga-FAP inhibitor (FAPI)-46 PET imaging (*11*).

Previous publications without a systematic histopathologic workup indicated FAP-directed PET to be highly accurate for the imaging of cholangiocarcinoma (*12,13*). Here, we performed a head-to-head comparison of ^{68}Ga-FAPI-46 PET, ^{18}F-FDG PET, and contrast-enhanced CT and compared the efficacy of these 3 modalities for cholangiocarcinoma detection. Furthermore, we investigated immunohistochemical FAP and glucose transporter 1 (GLUT1) expression from tumor samples of our patient cohort and assessed the impact of ^{68}Ga-FAPI-46 PET/CT on cholangiocarcinoma management.

MATERIALS AND METHODS

Patient Population

The patient flowchart is shown in Figure 1. This is a subgroup analysis of the ongoing observational trial (NCT04571086) at the University Hospital Essen. Until August 2021, 10 patients with cholangiocarcinoma were included (1.8% of the entire trial). Before enrollment, patients gave written informed consent to undergo ^{68}Ga-FAPI-46 PET for a clinical indication. Inclusion criteria were scheduling a ^{68}Ga-FAPI PET examination for staging or restaging of cholangiocarcinoma in routine clinical practice and being at least 18 y old. Pregnant, lactating, or breastfeeding women, as well as patients unable to tolerate PET scanning, were excluded. This study was approved by the local Ethics Committee (permits 19-8991-BO and 20-9485-BO).

Image Acquisition

^{68}Ga-FAPI-46 Synthesis and Administration. Radiosynthesis of ^{68}Ga-FAPI-46 was described previously (*14*). Briefly, a pharmaceutical-grade ^{68}Ge/^{68}Ga generator was applied for the labeling of FAPI-46 using the cassette-based synthesis module Trasis EasyOne.

Patients were not required to be fasting at the time of application and did not require specific preparation. The median intravenously administered activity was 89 MBq (interquartile range [IQR], 79–128 MBq). The median uptake time was 15 min after injection (IQR, 10–38 min). Low-dose CT was performed without application of intravenous contrast medium. Clinical PET/CT scans were obtained in the craniocaudal direction on a Biograph mCT Vision scanner (Siemens Healthineers) (*15*).

^{18}F-FDG PET/CT. ^{18}F-FDG PET/CT was performed in 8 of 10 (80%) patients and ^{18}F-FDG PET/MRI in 1 of 10 (10%). One patient did not undergo additional ^{18}F-FDG PET/CT. The median injected activity was 317 MBq (IQR, 266–344 MBq). The median uptake time was 63 min after injection (IQR, 54–80 min after injection). Diagnostic CT was performed, and intravenous contrast medium was given to 6 of 9 (66.7%) patients. The PET protocol was in accordance with the European Association of Nuclear Medicine procedure guidelines for tumor imaging, version 2.0 (*16*).

Conventional CT. Conventional CT was performed on all patients either as part of ^{18}F-FDG PET/CT ($n = 5$) or as a stand-alone examination before PET/CT ($n = 5$); the median interval between ^{68}Ga-FAPI-46 PET/CT and CT was 17 d (range, 0–36 d). In all patients, diagnostic CT was acquired after application of intravenous contrast medium in the arterial and portal venous phases.

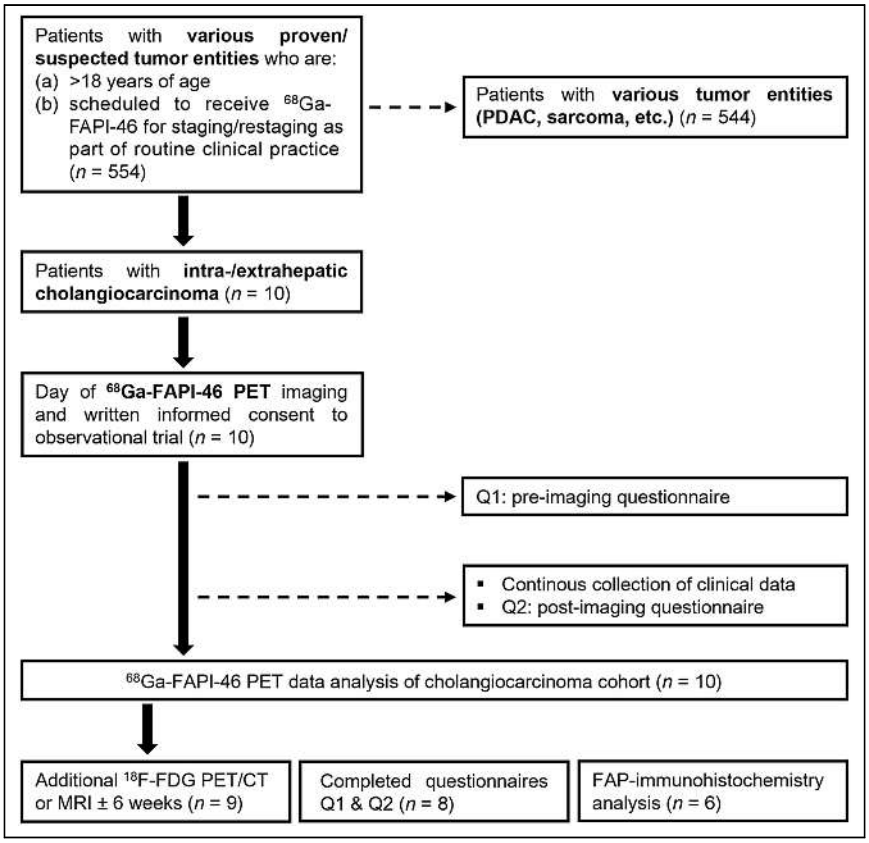

FIGURE 1. Enrollment flowchart. PDAC = pancreatic ductal adenocarcinoma; Q = questionnaire.

Image Evaluation

For comparison of ^{68}Ga-FAPI-46 and ^{18}F-FDG PET/CT, a lesion-based analysis of SUV_{max}, SUV_{mean}, SUV_{peak}, and metabolic tumor volume was performed in consensus by 2 independent, masked readers. For calculation of SUV_{mean} and metabolic tumor volume, volumes of interest were determined by an isocontour threshold of 41% of SUV_{max}. Syngo.via software (Siemens Healthineers) was used for measurements of SUV and metabolic tumor volume (*16*). Lesions visible on only one PET modality were compared with the background of the other PET modality in the same region for statistical reasons. Three regions were selected for evaluation of tumor-to-background ratios (TBRs) using a spheric region of interest: mediastinal blood pool (center of the aortic arch), liver (noninvolved area of the right lobe), and left gluteal muscle (center of the left gluteus). Diagnostic CT was analyzed in consensus by 2 independent, masked radiologists.

Detection Efficacy

Detection efficacy was assessed through lesion-based evaluation of ^{68}Ga-FAPI-46 PET/CT, ^{18}F-FDG PET/CT, and conventional CT in 9 of 10 patients. Each detected lesion was considered positive, regardless of the imaging modality. On PET, areas with focal uptake above the background level, not attributable to physiologic findings, were rated positive. On CT, lymph nodes

TABLE 1
Visual FAP/GLUT1 Grading

Grade	Definition
0	Absence of FAP/GLUT1 positivity
1	Slight FAP/GLUT1 positivity
2	Moderate FAP/GLUT1 positivity
3	Strong FAP/GLUT1 positivity

larger than 1 cm in short diameter with suggestive features (contrast enhancement and a round shape, among others) were considered positive. Furthermore, on CT, morphologically delineated or hyperarterialized organ lesions were considered suggestive of malignancy. Follow-up imaging (CT or PET/CT), clinical data, or histologic confirmation were used as the standard of truth.

Management Questionnaires

To assess changes in intended management after ^{68}Ga-FAPI-46 PET/CT, referring physicians completed one questionnaire (questionnaire 1, Supplemental Fig. 1; supplemental materials are available at http://jnm.snmjournals.org) before PET and another questionnaire (questionnaire 2, Supplemental Fig. 2) after reviewing the written ^{68}Ga-FAPI-46 PET/CT report.

Immunohistochemical Analysis of FAP and GLUT1 Expression

Immunohistochemistry was performed on formalin-fixed paraffin-embedded human tissue samples according to the standard laboratory procedures (*17*). The following antibodies were used: anti-GLUT1 Abcam ab652 (RRID:AB 305540), diluted 1:5,000; anti-FAP α-antibody (SP325); and Abcam ab227703, diluted 1:100. Immunohistochemical expression was evaluated on tumor cells and tumor stroma, and the percentage of intratumoral necrosis related to the tumor areas was also assessed. A simplified visual FAP/GLUT1 grading was applied for stromal and tumor cells, as well as for necrosis. A FAP/GLUT1 grading legend is shown in Table 1. For larger neoplasms, a central slice of the tumor was stained completely. Immunohistochemical analyses were performed on a resection of bioptic samples of the primary or local-recurrence tumors before ^{68}Ga-FAPI-46 or ^{18}F-FDG PET/CT and consequently do not correspond to visible PET lesions. Two pathologists and 2 biologists performed masked immunohistochemical analysis in consensus.

Statistical Analysis

Descriptive statistics and individual patient data are reported. For continuous data, the median, IQR, and range were used. SUV_{max}, SUV_{mean}, and TBR were compared using the Wilcoxon test. The Mann–Whitney *U* test was performed to compare subgroups for tumor grade and location. To demonstrate the results, visualization with scatterplots was used, with a *P* value of less than 0.05 being considered statistically significant. All analyses were performed using SPSS Statistics (version 27.0; IBM).

RESULTS

Patient Characteristics

Overall, 10 patients (6 men and 4 women) were reviewed. The median age was 55.5 y (range, 40–79 y). Included were 6 patients with intrahepatic cholangiocarcinoma and 4 patients with extrahepatic cholangiocarcinoma.

We performed initial staging in 2 patients and restaging in 8. The median interval between diagnosis and initial staging or restaging was 1 mo or 22 mo (range, 5–56 mo), respectively, whereas the median interval was 17 d (range, 0–36 d) between ^{68}Ga-FAPI-46 PET/CT and conventional CT and 0 d (range, 0–35 d) between ^{68}Ga-FAPI-46 PET/CT and ^{18}F-FDG PET/CT. Further clinical information can be found in Table 2.

Detection Efficacy

Detection efficacy is summarized in Table 3. Figure 2 shows maximum-intensity projections of all 10 patients. Overall, 22 lesions were detected across all modalities, including primary tumors (n = 5), lymph node metastases (n = 11), and distant metastases (n = 6). All primary tumors were detected by all 3 imaging modalities.

TABLE 2
Patient Characteristics

Patient no.	Age (y)	Sex	Histology	Grade	UICC (initial)	Date of initial diagnosis	Tumor sites on imaging (primary and metastatic)	SUV_{max}	
								^{68}Ga-FAPI-46	^{18}F-FDG
1	58	M	iCC	3	II	01/2020	Bone, lymph node	14.3	6.3
2	79	F	iCC	3	IIIA	01/2021	Liver	17.5	5.1
3	45	M	pCC	2	IIIC	08/2020	Liver	14.5	8.0
4	44	M	iCC	3	II	07/2016	Liver	28.6	5.2
5	57	F	dCC	3	IIIB	03/2018	Ductus hepaticus communis, peritoneal	11.4	11.6
6	70	M	pCC	2	II	12/2019	Liver, lymph node	9.3	4.0
7	40	F	iCC	2	IV	04/2021	Liver, peritoneal, lymph node	25.4	NA
8	79	F	dCC	2	IIB	03/2019	None	NA	NA
9	54	F	iCC	2	IIIA	03/2021	Lymph node	9.8	12.6
10	65	F	iCC	2	IIIB	08/2020	Lymph node	7.7	9.2

UICC = Union for International Cancer Control; iCC = intrahepatic cholangiocarcinoma; pCC = perihilar cholangiocarcinoma; dCC = distal cholangiocarcinoma; NA = not available.

SUV_{max} was determined in hottest lesion for each tracer.

TABLE 3
Lesion-Based Detection Efficacy

Location	Overall	Conventional CT	^{18}F-FDG PET/CT	^{68}Ga-FAPI-46 PET/CT
Primary tumor	5 (100)	5 (100)	5 (100)	5 (100)
Lymph nodes	11 (100)	3 (27.3)	10 (90.9)	11 (100)
Distant metastases	6 (100)	2 (33.3)	4 (66.7)	6 (100)

Data are *n* followed by percentage in parentheses.

^{68}Ga-FAPI-46 PET/CT demonstrated the highest detection efficacy for lymph nodes and distant metastases when compared with ^{18}F-FDG PET/CT and conventional CT (lymph node metastases: 11 on ^{68}Ga-FAPI-46 PET/CT, 10 on ^{18}F-FDG PET/CT, and 3 on CT; distant metastases: 6 on ^{68}Ga-FAPI-46 PET/CT, 4 on ^{18}F-FDG PET/CT, and 2 on CT).

Tumor Uptake

Figure 3 summarizes tumor SUV_{max} for ^{68}Ga-FAPI-46 versus ^{18}F-FDG PET/CT. In total, 22 lesions (6 primary tumors, 11 lymph node metastases, and 6 distant metastases) were assessed. SUV_{max} was significantly higher for ^{68}Ga-FAPI-46 PET/CT than for ^{18}F-FDG PET/CT for primary lesions (median, 14.5 [IQR, 6.1] vs. 5.2 [IQR, 2.9]; $P = 0.043$) and distant metastases (median, 9.5 [IQR, 2.4] vs. 5.3 [IQR, 2.7]; $P = 0.046$). No significant difference was noted for lymph node metastases (median, 4.7 [IQR, 2.8] vs. 6.7 [IQR, 5.0]; $P = 0.05$). Details are shown in Figure 3A.

Furthermore, tumor uptake for both tracers was investigated with respect to tumor grade (grade 2, $n = 4$; grade 3, $n = 4$) and tumor location (intrahepatic, $n = 5$; extrahepatic, $n = 3$) (Fig. 3B). Two patients were excluded from evaluation because of a missing ^{18}F-FDG PET/CT scan or the absence of tumor lesions. ^{68}Ga-FAPI-46 SUV_{max} (median, 10.9 [IQR, 5.2] vs. 5.2 [IQR, 4.5]) was significantly higher in patients with grade 3 than grade 2 tumors (Mann–Whitney *U* test, $P = 0.009$). For ^{18}F-FDG PET, no significant difference was observed (median, 5.2 [IQR, 3.3] vs. 6.7 [IQR, 4.6]; $P = 0.33$).

SUV_{max} was not significantly different between intra- and extrahepatic cholangiocarcinoma for either ^{68}Ga-FAPI-46 (median, 6.1 [IQR, 6.2] vs. 9.2 [IQR, 2.7]; $P = 0.23$) or ^{18}F-FDG (median, 5.3 [IQR, 3.6] vs. 6.6 [IQR, 4.8]; $P = 0.64$) (Fig. 3C).

Figure 4 demonstrates a patient example of primary tumor uptake for ^{68}Ga-FAPI-46 versus ^{18}F-FDG PET/CT, and Supplemental Table 1 shows patient-based, detailed tumor uptake data.

TBR

TBR for mediastinal blood pool, liver, and left gluteal muscle was assessed for both tracers (Fig. 5). For primary tumor, TBR_{blood} (median, 9.7 [IQR, 1.8] for ^{68}Ga-FAPI-46 vs. 2.4 [IQR, 2.4] for ^{18}F-FDG; $P = 0.043$) and TBR_{liver} (median, 12.1 [IQR, 18.8] vs. 1.9 [IQR, 1.1]; $P = 0.043$) were significantly higher for ^{68}Ga-FAPI-46 than for ^{18}F-FDG PET, whereas TBR_{muscle} was not significantly different (median, 8.8 [IQR, 2.1] vs. 7.4 [IQR, 4.3]; $P = 0.69$).

Lymph node metastases showed a significantly higher TBR_{liver} (median, 13.7 [IQR, 5.8] vs. 2.3 [IQR, 1.5]; $P = 0.003$) and TBR_{blood} (median, 5.9 [IQR, 2.8] vs. 2.7 [IQR, 1.7]; $P = 0.004$) for ^{68}Ga-FAPI-46 PET. In contrast, TBR_{muscle} was significantly higher for ^{18}F-FDG PET/CT (median, 5.9 [IQR, 4.0] vs. 9.6 [IQR, 7.1]; $P = 0.01$).

TBR_{blood} (median, 8.2 [IQR, 2.4] vs. 3.7 [IQR, 3.0]; $P = 0.028$) and TBR_{liver} (median, 12.3 [IQR, 10.7] vs. 2.4 [IQR, 2.0]; $P = 0.028$) were significantly higher in ^{68}Ga-FAPI-46 PET than ^{18}F-FDG PET for distant metastases but not for TBR_{muscle} (median, 6.8 [IQR, 1.3] vs. 7.9 [IQR, 3.5]; $P = 0.25$).

Change in Management

Eight of 10 questionnaire pairs were completed by the referring physicians. According to the survey, diagnostic tests were not avoided or triggered, and intended therapy did not change in any patient. In 1 patient with an unknown primary, ^{68}Ga-FAPI-46 PET/CT localized the tumor. Subsequent biopsy with immunohistochemical analysis led to a cholangiocarcinoma diagnosis.

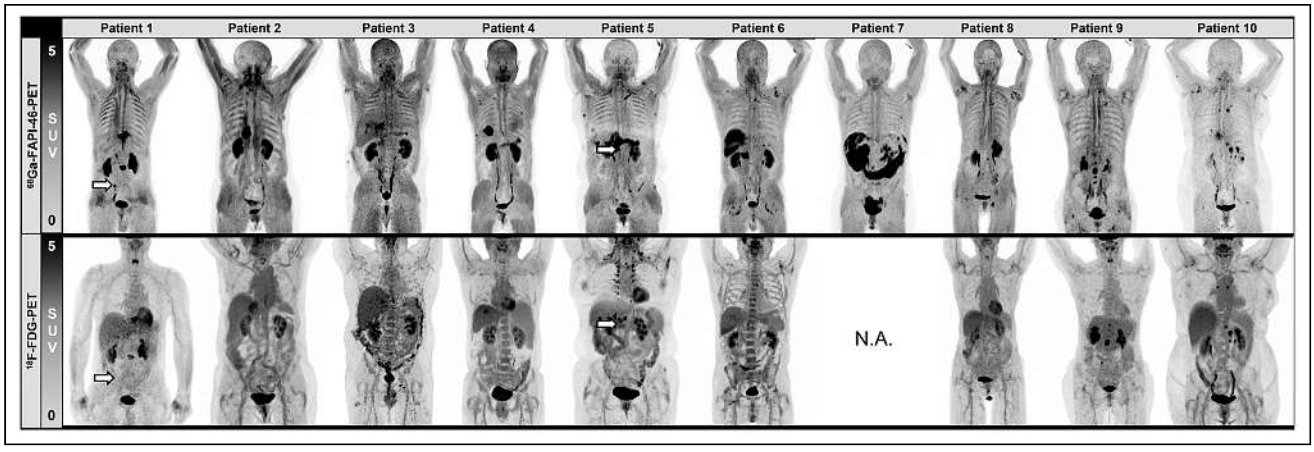

FIGURE 2. Maximum-intensity projections of ^{68}Ga-FAPI-46 and ^{18}F-FDG PET for all patients. Tumor lesions that could not be detected by ^{18}F-FDG PET are marked with arrows. Tumor sites are listed in Table 2. N.A. = not applicable.

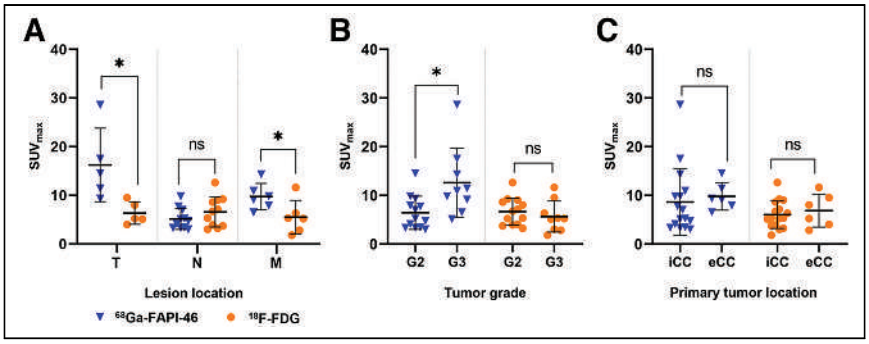

FIGURE 3. Lesion-based comparison of SUV_{max} between ^{68}Ga-FAPI-46 and ^{18}F-FDG PET/CT for lesion location (primary tumor, lymph node, distant metastases) (A), tumor grade (B), and location of primary tumor (C). *Statistically significant ($P < 0.05$). eCC = extrahepatic cholangiocarcinoma; G2 = grade 2; G3 = grade 3; iCC = intrahepatic cholangiocarcinoma; M = distant metastases; N = lymph nodes; ns = not statistically significant; T = primary tumor.

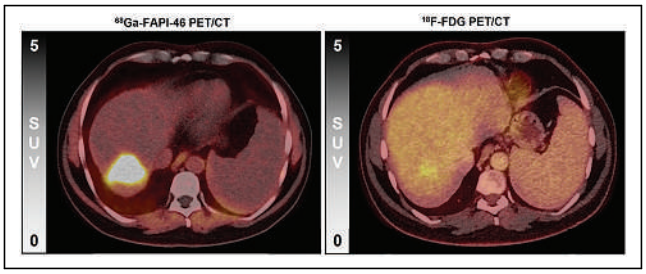

FIGURE 4. Intrahepatic primary tumor of patient 4, demonstrating 18.7-fold higher tumor-to-background uptake ratio in ^{68}Ga-FAPI-46 PET (31.8) than in ^{18}F-FDG PET (1.7).

FAP and GLUT1 Immunohistochemistry

FAP and GLUT1 immunohistochemistry findings are shown in Figures 6A–6C. Surgical samples of primary tumors ($n = 5$) or local recurrences ($n = 1$) from 6 of 10 patients were examined. Figure 6D demonstrates FAP and GLUT1 expression within a tumor sample. According to visual assessment (Table 1), there was a pronounced FAP expression intensity in the tumor stroma (median intensity grade, 3 [range, 2–3]; mean expression of stromal cells, 90% [range, 50%–95%]), whereas there was largely no FAP expression on the tumor cells themselves (median intensity grade, 0 [range, 0–1]; mean tumoral expression, <1% [range, <1%–5%]).

GLUT1 expression was seen predominantly on tumor cells (median intensity grade, 2 [range, 1–3]; mean tumoral expression, 80% [range, 70%–100%]) and only slightly in the tumor stroma (median intensity grade, 0 [range, 0–2]; mean expression of stromal cells, <1% [range, <1%–10%]). Immunohistochemical staining of central tumor slices is shown in Supplemental Figure 3.

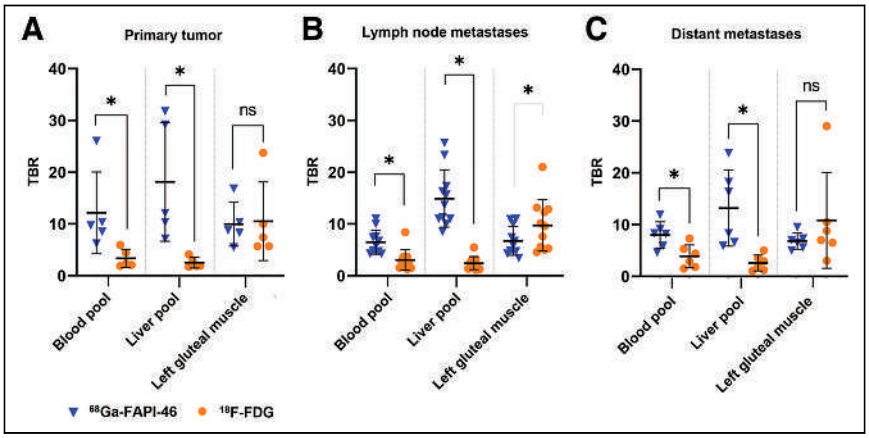

FIGURE 5. Lesion-based comparison of TBR (blood pool, liver pool, left gluteal muscle; mean ± SD) between ^{68}Ga-FAPI-46 and ^{18}F-FDG PET for primary tumor (A), lymph node metastases (B), and distant metastases (C). Statistical significance is marked in black for ^{68}Ga-FAPI-46 and in gray for ^{18}F-FDG. *Statistically significant ($P < 0.05$). ns = not statistically significant.

DISCUSSION

Here, we report superior detection efficacy and tumor-to-background uptake for ^{68}Ga-FAPI-46 PET/CT versus ^{18}F-FDG PET/CT or conventional CT in patients with cholangiocarcinoma. We further demonstrate the impact of ^{68}Ga-FAPI-46 PET/CT on diagnostic workup of cholangiocarcinoma in 1 patient.

Currently, the only curative treatment for cholangiocarcinoma is radical surgery of the primary tumor, including lymphadenectomy (*6*). Patients with unresectable intrahepatic cholangiocarcinoma may benefit from local ablative interventions, such as radioembolization with ^{90}Y-microspheres or transarterial chemoembolization (*18*). In the presence of distant metastases, systemic chemotherapy is the therapy of choice (*6*). Accurate staging is therefore crucial for management of cholangiocarcinoma.

MRI in combination with MR cholangiopancreatography is the clinical standard for local detection of cholangiocarcinoma (*6*). According to the guidelines of the European Society for Medical Oncology, additional contrast-enhanced CT determines the relationship between tumor and vasculature (*6*). Contrast-enhanced CT is currently the imaging modality of choice for staging lymph nodes and distant metastases, although sensitivity and specificity vary significantly across studies (lymph node metastases: sensitivity, 67% [95% CI, 28%–86%]; specificity, 88% [95% CI, 74%–95%]) (*19*). ^{18}F-FDG PET/CT shows advantages in detecting small cholangiocarcinomas as well as lymph node and distant metastases (*20–22*). However, extrahepatic cholangiocarcinomas and low-grade tumors are difficult to detect because of reduced ^{18}F-FDG or a high background signal (*8*). Here, we show the lowest detection rates for contrast-enhanced CT: we attribute this in particular to the size, exemplified by lymph node metastases, which partly presented at 10 mm or smaller in the investigated cohort.

^{68}Ga-FAPI-46 is a novel radioligand that binds to FAP in the tumor stroma and has shown high detection rates for stroma-rich tumors (*23*). FAP is selectively expressed at high levels by cancer-associated fibroblasts (*24,25*) in more than 90% of human epithelial cancers (*26*).

Recently, Kratochwil et al. reported a high ^{68}Ga-FAPI PET SUV_{max} for cholangiocarcinoma (*12*). In addition, Lan et al. compared detection efficacy for biliary tract

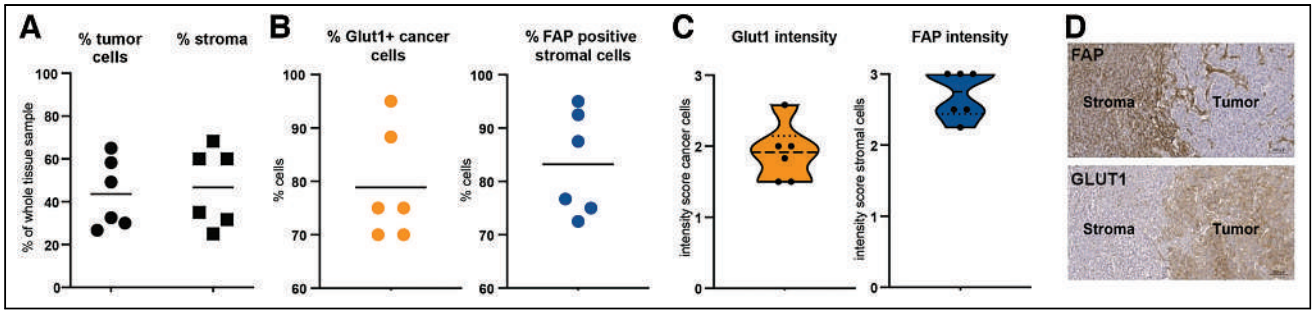

FIGURE 6. Immunohistochemical FAP/GLUT1 expression graded in accordance with Table 1. (A). Histologic evaluation of tumor cell and stromal content in analyzed samples (2–5 samples per patient, 1 dot presents 1 patient, line presents mean value); tumor cell and stromal content were mostly comparable (~50%). (B) On average, 90% of stromal cells are positive for FAP whereas 80% of cancer cells are positive for GLUT1. Line presents mean value. (C) Violin plots showing median intensity of 3 for FAP staining on stromal cells but 2 for GLUT1 staining on cancer cells. Line presents mean value. (D) Representative images of immunohistochemistry for FAP and GLUT1 on consecutive sections of 1 patient sample. FAP was strongly expressed in stroma, whereas GLUT1 was detected on tumor cells.

cancer of primary tumors, lymph nodes, and distant metastases between ^{68}Ga-FAPI and ^{18}F-FDG PET/CT and showed ^{68}Ga-FAPI to be superior in all 3 subgroups (*13*). Here, we confirm that ^{68}Ga-FAPI-46 PET/CT is superior to ^{18}F-FDG PET/CT, and also to conventional CT, for detection of primary tumor but especially for detection efficacy for lymph node and distant metastases.

In addition, ^{68}Ga-FAPI-46 PET/CT demonstrates a higher TBR than does ^{18}F-FDG PET/CT, which leads to improved delineation, especially of intrahepatic lesions. Notably, ^{68}Ga-FAPI-46 PET uptake was highest in grade 3 cholangiocarcinomas, similar to previous findings for ^{18}F-FDG PET/CT (*8*).

Here we, for the first time to our knowledge, present a systematic immunohistochemistry assessment of the imaging cohort. Immunohistochemistry showed high and very specific FAP expression in tumor stroma whereas GLUT1 was expressed mainly on cholangiocarcinoma tumor cells. A high expression level of FAP in tumor stroma was reported previously (*23,27*). Cholangiocarcinoma typically presents with a pronounced stromal compartment, which consists mainly of cancer-associated fibroblasts (*28,29*). The tumor-specific FAP expression, high stromal content in cholangiocarcinoma and good specificity and retention properties of ^{68}Ga-FAPI-46 radioligand probably led to the observed superior TBR and detection rate. In contrast, GLUT1 is a universal glucose transporter that is expressed in many healthy cells in the body, contributing to a higher background level in liver and blood pool that leads to lower TBR ratios and a lower detection specificity for ^{18}F-FDG PET.

We could not detect major changes in tumor treatment, mainly because most patients presented for restaging and metastatic stage was already known. With limited therapeutic options for cholangiocarcinoma, the treatment of choice was mostly already performed or planned.

Efficacious treatment options for cholangiocarcinoma are limited (*6*). In the past decade, target-directed radioligand therapy (RLT) combined with PET, so-called radiotheranostics, has seen unprecedented expansion (*30*). Theranostic ligands are carrier-bound small molecules that provide diagnostic imaging or therapy depending on the type of radiolabel. Novel RLT has led to prolonged survival in patients with metastatic neuroendocrine tumors (^{177}Lu-DOTATOC) (*31*) and prostate cancer (^{177}Lu-PSMA) (*32*). RLT is characterized by favorable safety and improvement of health-related quality of life (*33*).

FAP-directed ^{90}Y-FAPI and ^{177}Lu-FAPI RLT has been reported previously in several tumor entities (e.g., sarcoma, pancreatic adenocarcinoma, and breast cancer) (*34–37*). ^{90}Y-FAPI-46 RLT led to tumor control and was tolerated well in patients with sarcoma or other tumor entities (*34,35*). High ^{68}Ga-FAPI-46 uptake and strong immunohistochemical FAP expression support the future evaluation of FAP RLT in patients with advanced cholangiocarcinoma.

Our study comes with limitations. ^{18}F-FDG PET was mostly combined with contrast-enhanced CT, whereas ^{68}Ga-FAPI-46 PET/CT was performed as low-dose CT without a contrast agent. This may affect attenuation correction and SUV quantification. However, Schoen et al. (*38*) did not find a significant difference with respect to the SUV_{max} of the liver or muscle, for PET/CT with or without contrast enhancement. Other limitations are a small number of patients and the retrospective design. An ongoing prospective interventional investigator-initiated trial (NCT 05160051) aims to assess diagnostic accuracy and target expression in a larger cohort of patients.

CONCLUSION

In patients with cholangiocarcinoma, ^{68}Ga-FAPI-46 demonstrates superior radiotracer uptake, especially in grade 3 tumors, and improved lesion detection when compared with ^{18}F-FDG PET/CT. In line with this finding, immunohistochemistry demonstrates high FAP expression in the stroma of cholangiocarcinoma. Superior tumor detection by ^{68}Ga-FAPI-46 PET led to tumor diagnosis in 1 patient. FAP targeting may become a valuable option for imaging and potentially RLT of cholangiocarcinoma.

DISCLOSURE

Kim Pabst has received a Junior Clinician Scientist Stipend from the University Medicine Essen Clinician Scientist Academy (UMEA) sponsored by the faculty of medicine and Deutsche Forschungsgemeinschaft (DFG), travel fees from IPSEN, and research funding from Bayer. Robert Seifert receives research funding from Boehringer Ingelheim Funds and the Else Kröner-Fresenius Stiftung. Timo Bartel receives travel fees from PARI GmbH. Lukas Kessler is a consultant for AAA and BTG and receives fees from Sanofi. Work in the lab of Jens Siveke is supported by the German Cancer Consortium (DKTK). Jens Siveke receives honoraria as a consultant or for continuing medical education presentations from AstraZeneca, Bayer, Immunocore, Novartis, Roche/Genentech, and Servier. His institution receives research funding from Bristol-Myers Squibb, Celgene, Eisbach, Bio, and Roche/Genentech. He holds ownership in and serves on the Board of Directors of

Pharma15. Katharina Lueckerath is a consultant for SOFIE Bioscience. Stefan Kasper receives honoraria from Merck Serono, MSD, Novartis, BMS, Amgen, Roche, Sanofi-Aventis, Servier, Incyte, and Lilly and research funding from Merck Serono, Lilly, BMS, and Roche. Ken Herrmann receives personal fees from Bayer, Sofie Biosciences, SIRTEX, Adacap, Curium, Endocyte, IPSEN, Siemens Healthineers, GE Healthcare, Amgen, Novartis, ymabs, Aktis Oncology, and Pharma15; nonfinancial support from ABX; and grants or personal fees from BTG. Rainer Hamacher is supported by the Clinician Scientist Program of the University Medicine Essen Clinician Scientist Academy (UMEA) sponsored by the faculty of medicine and Deutsche Forschungsgemeinschaft (DFG); has received travel grants from Lilly, Novartis, and PharmaMar; and has received fees from Lilly and PharmaMar. Wolfgang Fendler receives research funding from SOFIE Bioscience and Bayer; is a consultant to Janssen, Calyx, and Bayer; is on the speakers bureau for Janssen, Bayer, Novartis, and Telix; and does image review for Parexel. No other potential conflict of interest relevant to this article was reported.

KEY POINTS

QUESTION: Is ^{68}Ga-FAPI-46 PET/CT superior to ^{18}F-FDG PET/CT and conventional CT in a head-to-head comparison for staging cholangiocarcinoma?

PERTINENT FINDINGS: ^{68}Ga-FAPI-46 PET/CT is superior to both other imaging modalities for detection efficacy, uptake intensity, and TBR. In line with these findings, immunohistochemistry demonstrates high FAP expression of the tumor samples.

IMPLICATIONS FOR PATIENTS CARE: ^{68}Ga-FAPI-46 is a promising novel diagnostic test for staging cholangiocarcinoma. In the future, FAP-directed RLT may represent a new treatment option.

REFERENCES

1. Nakeeb A, Pitt HA, Sohn TA, et al. Cholangiocarcinoma: a spectrum of intrahepatic, perihilar and distal tumors. *Ann Surg.* 1996;224:463–473.
2. Bergquist A, von Seth E. Epidemiology of cholangiocarcinoma. *Baillieres Best Pract Res Clin Gastroenterol.* 2015;29:221–232.
3. Shaib Y, El-Serag HB. The epidemiology of cholangiocarcinoma. *Semin Liver Dis.* 2004;24:115–125.
4. Razumilava N, Gores GJ. Cholangiocarcinoma. *Lancet.* 2014;383:2168–2179.
5. Park MJ, Kim YK, Lim S, Rhim H, Lee WJ. Hilar cholangiocarcinoma: value of adding DW imaging to gadoxetic acid-enhanced MR imaging with MR cholangiopancreatography for preoperative evaluation. *Radiology.* 2014;270:768–776.
6. Valle JW, Borbath I, Khan SA, et al. Biliary cancer: ESMO clinical practice guidelines for diagnosis, treatment and follow-up. *Ann Oncol.* 2016;27(suppl 5):v28–v37.
7. Suzuki H, Komuta M, Bolog A, et al. Relationship between ^{18}F-fluoro-deoxy-D-glucose uptake and expression of glucose transporter 1 and pyruvate kinase M2 in intrahepatic cholangiocarcinoma. *Dig Liver Dis.* 2015;47:590–596.
8. Cho KM, Oh DY, Kim TY, et al. Metabolic characteristics of advanced biliary tract cancer using F-18-fluorodeoxyglucose positron emission tomography and their clinical implications. *Oncologist.* 2015;20:926–933.
9. Jansen K, Heirbaut L, Cheng JD, et al. Selective inhibitors of fibroblast activation protein (FAP) with a (4-quinolinoyl)-glycyl-2-cyanopyrrolidine scaffold. *ACS Med Chem Lett.* 2013;4:491–496.
10. Giesel FL, Kratochwil C, Lindner T, et al. ^{68}Ga-FAPI PET/CT: biodistribution and preliminary dosimetry estimate of 2 DOTA-containing FAP-targeting agents in patients with various cancers. *J Nucl Med.* 2019;60:386–392.
11. Montori M, Scorzoni C, Argenziano ME, et al. Cancer-associated fibroblasts in cholangiocarcinoma: current knowledge and possible implications for therapy. *J Clin Med.* 2022;11:6498.
12. Kratochwil C, Flechsig P, Lindner T, et al. ^{68}Ga-FAPI PET/CT: tracer uptake in 28 different kinds of cancer. *J Nucl Med.* 2019;60:801–805.
13. Lan L, Zhang S, Xu T, et al. Prospective comparison of ^{68}Ga-FAPI versus ^{18}F-FDG PET/CT for tumor staging in biliary tract cancers. *Radiology.* 2022;304:648–657.
14. Nader M, Valla DF, Vriamont C, et al. [^{68}Ga]/[^{90}Y]FAPI-46: automated production and analytical validation of a theranostic pair. *Nucl Med Biol.* 2022;110-111:37–44.
15. Kessler L, Ferdinandus J, Hirmas N, et al. ^{68}Ga-FAPI as a diagnostic tool in sarcoma: data from the ^{68}Ga-FAPI PET prospective observational trial. *J Nucl Med.* 2022;63:89–95.
16. Boellaard R, Delgado-Bolton R, Oyen WJ, et al. FDG-PET/CT: EANM procedure guidelines for tumour imaging: version 2.0. *Eur J Nucl Med Mol Imaging.* 2015; 42:328–354.
17. Cheung JYPF, Krengel K, Althoff K, et al. Progranulin promotes immune evasion of pancreatic ductal adenocarcinoma through regulation of MHCI expression. *Nat Commun.* 2022;13:156.
18. Al-Adra DP, Gill RS, Axford SJ, Shi X, Kneteman N, Liau SS. Treatment of unresectable intrahepatic cholangiocarcinoma with yttrium-90 radioembolization: a systematic review and pooled analysis. *Eur J Surg Oncol.* 2015;41:120–127.
19. Ruys AT, van Beem BE, Engelbrecht MR, Bipat S, Stoker J, Van Gulik TM. Radiological staging in patients with hilar cholangiocarcinoma: a systematic review and meta-analysis. *Br J Radiol.* 2012;85:1255–1262.
20. Anderson CD, Rice MH, Pinson CW, Chapman WC, Chari RS, Delbeke D. Fluorodeoxyglucose PET imaging in the evaluation of gallbladder carcinoma and cholangiocarcinoma. *J Gastrointest Surg.* 2004;8:90–97.
21. Kim YJ, Yun M, Lee WJ, Kim KS, Lee JD. Usefulness of ^{18}F-FDG PET in intrahepatic cholangiocarcinoma. *Eur J Nucl Med Mol Imaging.* 2003;30:1467–1472.
22. Lee Y, Yoo IR, Boo SH, Kim H, Park HL, Hyun OJ. The role of F-18 FDG PET/CT in intrahepatic cholangiocarcinoma. *Nucl Med Mol Imaging.* 2017;51:69–78.
23. Mona CE, Benz MR, Hikmat F, et al. Correlation of ^{68}Ga-FAPi-46 PET biodistribution with FAP expression by immunohistochemistry in patients with solid cancers: a prospective translational exploratory study. *J Nucl Med.* 2022;63:1021–1026.
24. Loktev A, Lindner T, Mier W, et al. A tumor-imaging method targeting cancer-associated fibroblasts. *J Nucl Med.* 2018;59:1423–1429.
25. Park JE, Lenter MC, Zimmermann RN, Garin-Chesa P, Old LJ, Rettig WJ. Fibroblast activation protein, a dual specificity serine protease expressed in reactive human tumor stromal fibroblasts. *J Biol Chem.* 1999;274:36505–36512.
26. Lindner T, Loktev A, Altmann A, et al. Development of quinoline-based theranostic ligands for the targeting of fibroblast activation protein. *J Nucl Med.* 2018;59:1415–1422.
27. Byrling J, Sasor A, Nilsson J, Said Hilmersson K, Andersson R, Andersson B. Expression of fibroblast activation protein and the clinicopathological relevance in distal cholangiocarcinoma. *Scand J Gastroenterol.* 2020;55:82–89.
28. Gentilini A, Pastore M, Marra F, Raggi C. The role of stroma in cholangiocarcinoma: the intriguing interplay between fibroblastic component, immune cell subsets and tumor epithelium. *Int J Mol Sci.* 2018;19:2885.
29. Guedj N, Blaise L, Cauchy F, Albuquerque M, Soubrane O, Paradis V. Prognostic value of desmoplastic stroma in intrahepatic cholangiocarcinoma. *Mod Pathol.* 2021;34:408–416.
30. Herrmann K, Schwaiger M, Lewis JS, et al. Radiotheranostics: a roadmap to future development. *Lancet Oncol.* 2020;21:e146–e156.
31. Strosberg J, El-Haddad G, Wolin E, et al. Phase 3 Trial of ^{177}Lu-Dotatate for midgut neuroendocrine tumors. *N Engl J Med.* 2017;376:125–135.
32. Sartor O, de Bono J, Chi KN, et al. Lutetium-177-PSMA-617 for metastatic castration-resistant prostate cancer. *N Engl J Med.* 2021;385:1091–1103.
33. Strosberg J, Wolin E, Chasen B, et al. Health-related quality of life in patients with progressive midgut neuroendocrine tumors treated with ^{177}Lu-Dotatate in the phase III NETTER-1 trial. *J Clin Oncol.* 2018;36:2578–2584.
34. Ferdinandus J, Fragoso Costa P, Kessler L, et al. Initial clinical experience with ^{90}Y-FAPI-46 radioligand therapy for advanced stage solid tumors: a case series of nine patients. *J Nucl Med.* 2022;63:727–734.
35. Fendler WP, Pabst KM, Kessler L, et al. Safety and efficacy of ^{90}Y-FAPI-46 radioligand therapy in patients with advanced sarcoma and other cancer entities. *Clin Cancer Res.* 2022;28:4346–4353.
36. Ballal S, Yadav MP, Kramer V, et al. A theranostic approach of [^{68}Ga]Ga-DOTA.SA.FAPi PET/CT guided [^{177}Lu]Lu-DOTA.SA.FAPi radionuclide therapy in an end-stage breast cancer patient: new frontier in targeted radionuclide therapy. *Eur J Nucl Med Mol Imaging.* 2021;48:942–944.
37. Kaghazchi F, Aghdam RA, Haghighi S, Vali R, Adinehpour Z. ^{177}Lu-FAPI therapy in a patient with end-stage metastatic pancreatic adenocarcinoma. *Clin Nucl Med.* 2022;47:e243–e245.
38. Schoen M, Braun T, Manava P, Ludwigs S, Lell M. Influence of scan time point and volume of intravenous contrast administration on blood-pool and liver SUVmax and SUVmean in [^{18}F] FDG PET/CT. *Nucl Med (Stuttg).* 2018;57:50–55.

Addition of Peptide Receptor Radiotherapy to Immune Checkpoint Inhibition Therapy Improves Outcomes in Neuroendocrine Tumors

Shadi A. Esfahani[1–3], Carolina De Aguiar Ferreira[1], Priska Summer[1], Umar Mahmood[1,3], and Pedram Heidari[1,3]

[1]*Athinoula A. Martinos Center for Biomedical Imaging, Department of Radiology, Massachusetts General Hospital, Charlestown, Massachusetts;* [2]*Institute for Innovation in Imaging, Massachusetts General Hospital, Boston, Massachusetts; and* [3]*Division of Nuclear Medicine and Molecular Imaging, Department of Radiology, Massachusetts General Hospital, Boston, Massachusetts*

Neuroendocrine tumors (NETs) are often diagnosed in advanced stages. Despite the advances in treatment approaches, including somatostatin analogs and peptide receptor radionuclide therapy (PRRT), these patients have no curative treatment option. Moreover, immunotherapy often yields modest results in NETs. We investigated whether combining PRRT using [^{177}Lu]DOTATATE and immune checkpoint inhibition therapy improves treatment response in NETs. **Methods:** A gastroenteropancreatic NET model was generated by subcutaneous implantation of human QGP-1 cells in immune-reconstituted NOD.Cg-*Prkdc*^{scid} *Il2rg*^{tm1Wjl}/SzJ mice engrafted with human peripheral blood mononuclear cells (n = 96). Mice were randomly assigned to receive pembrolizumab (anti-PD1), [^{177}Lu]DOTATATE (PRRT), simultaneous anti-PD1 and PRRT (S-PRRT), anti-PD1 on day 0 followed by PRRT on day 3 (delayed PRRT [D-PRRT]), PRRT on day 0 followed by anti-PD1 (early PRRT [E-PRRT]), or vehicle as control (n = 12/group). Human granzyme-B–specific [^{68}Ga]NOTA-hGZP PET/MRI was performed before and 6 d after treatment initiation, as an indicator of T-cell activation. Response to treatment was based on tumor growth over 21 d and on histologic analyses of extracted tissues on flow cytometry for T cells, hematoxylin and eosin staining, and immunohistochemical staining. **Results:** [^{68}Ga]NOTA-hGZP PET/MRI showed significantly increased uptake in tumors treated with E-PRRT, S-PRRT, and anti-PD1 on day 6 compared with baseline (SUV_{max}: 3.36 ± 0.42 vs. 0.73 ± 0.23; 2.36 ± 0.45 vs. 0.76 ± 0.30; 2.20 ± 0.20 vs. 0.72 ± 0.28, respectively; $P < 0.001$), whereas no significant change was seen in PET parameters in the D-PRRT, PRRT, or vehicle groups ($P > 0.05$). Ex vivo analyses confirmed the PET results showing the highest granzyme-B levels and T cells (specifically CD8-positive effector T cells) in the E-PRRT group, followed by the S-PRRT and anti-PD1 groups. Tumor growth follow-up showed the most significant tumor size reduction in the E-PRRT group (baseline to day 21, 205.00 ± 30.70 mm^3 vs. 78.00 ± 11.75 mm^3; P = 0.0074). Tumors showed less growth reduction in the PRRT, D-PRRT, and S-PRRT groups than in the E-PRRT group ($P <$ 0.0001). The vehicle- and anti-PD-1–treated tumors showed continued growth. **Conclusion:** Combination of PRRT and anti-PD1 shows the most robust inflammatory response to NETs and a better overall outcome than immune checkpoint inhibition or PRRT alone. The most effective regimen is PRRT preceding anti-PD1 administration by several days.

Key Words: granzyme B; PET; neuroendocrine tumor; peptide receptor radiotherapy; immunotherapy

Received Jan. 2, 2023; revision accepted Mar. 1, 2023.

For correspondence or reprints, contact Pedram Heidari (heidari.pedram@mgh.harvard.edu).

Published online Apr. 6, 2023.

J Nucl Med 2023; 64:1056–1061
DOI: 10.2967/jnumed.123.265391

Neuroendocrine tumors (NETs) are heterogeneous neoplasms characterized by markers of neuroendocrine differentiation (*1,2*). Mostly located in the gastrointestinal tract and lungs, they are divided mainly into gastroenteropancreatic (66%) and bronchopulmonary (25%) NETs (GEP-NETs) (*1*). The GEP-NETs often present at a late stage and are associated with high morbidity due to excess hormonal secretion of biologically active amines and peptides released by metastatic lesions (*3,4*). Although there is a low annual incidence for NETs (<1% of all cancers in the United States), their indolent course results in a high prevalence, with GEP-NETs being the second most common gastrointestinal cancer after colon cancer (*1*).

Current treatment approaches for metastatic GEP-NETs include mainly the use of somatostatin receptor agonists and peptide receptor radionuclide therapy (PRRT) with somatostatin analogs (*2,4–6*). Although the main focus is to stabilize the disease and manage symptoms (*4*), this focus also improves the median overall survival from approximately 2 to 8 y after initial diagnosis (*7*). However, long-term follow-up results have shown that somatostatin analog–based therapy eventually becomes ineffective, and the disease progresses in most patients (*6,8*). Rationally, combining somatostatin analog–based treatment with other classes of therapies might improve patient outcomes.

Immune checkpoint inhibitors (ICIs) have markedly improved survival in many cancers (*9–12*). On the basis of multiple clinical trials on patients with GEP-NETs, responders to ICIs have more durable progression-free survival than patients treated with standard chemotherapy (*13*). However, the overall response rate of GEP-NETs to ICIs remains poor (*14,15*), possibly because of a low tumor mutational burden, a small number of tumor-infiltrating lymphocytes, or low expression of immune checkpoints such as PD-L1 in these tumors (*14,15*). We hypothesize that PRRT stimulates the immune system through additional exposure to antigens as a result of radiation-induced tumor cell death. Improving the response rate of GEP-NETs to ICIs might potentially lead to a curative treatment strategy or greatly expand treatment options. In this study, we evaluated whether the combination of [^{177}Lu]DOTATATE (PRRT) and the ICI pembrolizumab (anti-PD1) improves the treatment outcome in a humanized immune-reconstituted mouse

model of GEP-NET. First, we determined an optimal dose of PRRT to gauge the maximal intratumoral immune response. Then, we compared the effect of PRRT and anti-PD1 combination on treatment response to PRRT or anti-PD1 therapy alone. Last, we optimized the relative temporal administration of PRRT and anti-PD1 to improve treatment outcomes.

MATERIALS AND METHODS

Cell Culture and Development of GEP-NET Mouse Model

The experiments were approved and conducted per the Institutional Animal Care and Use Committee guidelines. The human pancreatic NET cell line QGP-1 was obtained from the Japanese Collection of Research Bioresources Cell Bank. Cells were cultured in RPMI medium (ATCC) supplemented with 10% fetal bovine serum (ThermoFisher) and 1% penicillin–streptomycin (ThermoFisher) at 37°C and 5% CO_2. *Mycoplasma* polymerase chain reaction testing was performed monthly. In total, 96 male NOD.Cg-*Prkdc*^{scid} *Il2rg*^{tm1Wjl}/SzJ mice were engrafted with human peripheral blood mononuclear cells and kept for 10 d to allow for immune reconstitution before tumor engraftment. In total, 1×10^6 QGP-1 cells were mixed with Matrigel (BD Biosciences) in a volume of 100 μL 1:1 (v/v) and injected into the subcutaneous space of the mice over the right shoulder.

[^{177}Lu]DOTATATE and [^{68}Ga]NOTA-hGZP Synthesis

^{68}Ga was eluted from a ^{68}Ge/^{68}Ga generator (Eckert and Ziegler) with 0.1 M HCl. NOTA-hGZP was radiolabeled as previously described (*16*). Briefly, 50 μg of NOTA-hGZP (1 mg/mL in metal-free water) (OmniTrace Ultra; Millipore) were mixed with 2 M *N*-2-hydroxyethylpiperazine-*N*′-2-ethanesulfonic acid buffer and pH-adjusted to 3.5–4.0. Eluted ^{68}Ga (555 ± 55 MBq) was added to the mixture, and the reaction proceeded for 10 min at room temperature. The reaction product was purified using a reverse-phase C18 Sep-Pak (Waters Corp.) mini cartridge, eluted with 200 μL of 200-proof ethanol. Ethanol was evaporated under a vacuum for 5 min, and the final product was diluted with 0.9% saline to reach a 10% ethanol concentration. Radiochemical purity was calculated through instant thin-layer chromatography (*16*). The mean yield was 72% ± 5%, and radiochemical purity was 95% ± 2%.

For [^{177}Lu]DOTATATE, the reaction cocktail comprised 4.5 μg of DOTATATE peptide (Anespec) and 370 MBq of $^{177}LuCl_3$ (Eckert and Zeigler) in 1 mL of 0.15 M sodium ascorbate (Sigma-Aldrich) with a pH ranging from 4.5 to 4.9. The reaction vial was heated for 30 min at 90°C. After cooling, [^{177}Lu]DOTATATE was purified using a C18 Sep-Pak. The final product was reconstituted in a solution containing 3.5 mM ascorbic acid, 3.5 mM gentisic acid, and 10 mM methionine (Sigma-Aldrich) to prevent radiolysis. Instant thin-layer chromatography was used to determine the radiochemical purity. The reaction yield was 87% ± 4%, and radiochemical purity was 96% ± 2%.

Experimental Design

To assess the efficacy of different doses of PRRT on intratumoral T-cell infiltration and activation, a subset of tumor-bearing mice was randomly assigned to 3 groups (n = 8/group) to receive [^{177}Lu]DOTATATE by a single tail-vein injection of either a low dose (0.03 MBq/g), a medium dose (0.15 MBq/g, equivalent to the currently approved clinical dose) (*4*), or a high dose (0.74 MBq/g). Three days after PRRT, all mice received intraperitoneal injection of pembrolizumab (anti-PD1, 2 mg/kg). To assess in vivo granzyme-B (GZB) expression as a noninvasive measure of T-cell activity within the tumors (*17,18*), we performed [^{68}Ga]NOTA-hGZP PET/MRI before and 6 d after treatment onset (at ~1 half-life interval of ^{177}Lu). Medium-dose PRRT was selected for the subsequent combination-therapy experiments.

The remaining tumor-bearing mice were randomly assigned to multiple groups (n = 12/group) to receive saline (as vehicle control); anti-PD1, pembrolizumab (2 mg/kg loading dose, followed by 1 mg/kg every 3 d, intraperitoneally); PRRT only (a single intravenous injection of a medium dose [^{177}Lu]DOTATATE); or a combination of intraperitoneal pembrolizumab and a single intravenous medium dose of PRRT, including simultaneous PRRT (S-PRRT; i.e., PRRT given simultaneously with the initial dose of pembrolizumab), delayed PRRT (D-PRRT; i.e., PRRT given 3 d after the initial dose of pembrolizumab), or early PRRT (E-PRRT; i.e., PRRT given 3 d before the initial dose of pembrolizumab). The mice underwent [^{68}Ga]NOTA-hGZP PET/MRI at baseline and 6 d after treatment initiation to assess early intratumoral T-cell response. After PET, tumors from 4 mice in each group were extracted for histologic analyses. For the remaining 8 mice in each group, tumor volume was measured every 3 d by calipers for up to 21 d after treatment initiation (40 d after tumor implantation).

In Vivo [^{68}Ga]NOTA-hGZP PET Imaging of NET Models

Approximately 7.4–8 MBq of [^{68}Ga]NOTA-hGZP were injected into the lateral tail vein of the mice 60 ± 5 min before imaging. PET/MR images were acquired on a Bruker simultaneous Si198 PET insert in a Bruker 4.7-T MRI subsystem. PET acquisition was performed in static mode for 15 min at a single bed position, and the data were reconstructed as previously described (*19*). Simultaneous fat-saturated T1- and T2-weighted MRI sequences were acquired for localization purposes. Images were analyzed using VivoQuant software, version 4 (In-Vicro). Three-dimensional regions of interest were manually drawn over the tumors guided by MR images. Standard tumor PET uptake values (SUV_{max}) were measured and compared between the baseline and 6-d-posttreatment scans for each group.

Histopathologic Analyses

The frozen tumor tissues (4/group) were evaluated by hematoxylin and eosin and immunohistochemical staining for GZB and CD3 using previously described methods (*18*). Briefly, GZB staining was performed using rabbit antihuman GZB primary antibody (ab255598; Abcam) and Alexa Fluor 647 conjugated preadsorbed goat antirabbit IgG secondary antibody (A32733; ThermoFisher), CD3 staining was performed using mouse antihuman CD3 primary antibody (ab17143; Abcam) and Alexa Fluor 448 conjugated preadsorbed donkey antimouse IgG secondary antibody (ab150109, Abcam), and nuclear staining was performed using 4′,6-diamidino-2-phenylindole (ab8961; Abcam). GZB staining was quantified and reported as the percentage of total fluorescence signal in the red channel relative to the total fluorescence signal in the blue channel (4′,6-diamidino-2-phenylindole) as a representative marker of cell density (*19*). Microscopic images were acquired using a BioTek Cytation-5 cell imaging multimode reader and analyzed by BioTek Gen-5 software.

For flow cytometry, the freshly excised tumors (4/group) were minced and strained through a 70-mm nylon mesh and incubated with phenol red-free RPMI (ATCC) with a 1 mg/mL solution of collagenase type IV (ThermoFisher) for 35 min at 37°C to generate a single-cell suspension. Zombie Aqua (Biolegend) staining was performed to distinguish between viable and nonviable cells, followed by staining against human CD3 (clone SK7; BD Biosciences), CD4 (clone OK-4; Biolegend), CD8 (clone RPA-T8; Biolegend), CD45RA (clone HI100; DB Biosciences), and CCR7 (clone G0437H; Biolegend) according to the manufacturers' protocols. Flow cytometry was performed on a BD-LSR-II cytometry cell analyzer (BD Biosciences), and gating was established using FlowJo software (version 9.1, FlowJo LLC), as previously described (*17*).

Statistical Analysis

Quantitative data analyses were performed using Prism (version 9; GraphPad). Data are presented as mean ± SD. Paired and unpaired Student t tests were used to compare the means of 2 groups when appropriate.

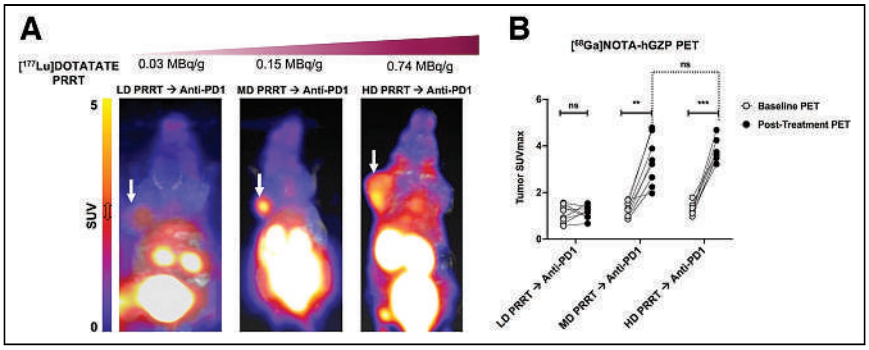

FIGURE 1. GZB expression measured on [^{68}Ga]NOTA-hGZP PET/MRI depends on dose of [^{177}Lu]DOTATATE PRRT (n = 8/group). (A) Representative [^{68}Ga]NOTA-hGZP PET/MRI maximum-intensity projections of QGP-1 tumor–bearing mice 6 d after initiation of low-, medium-, and high-dose [^{177}Lu]DOTATATE PRRT followed by pembrolizumab show higher tumor uptake (arrow) in medium- and high-dose groups than in low-dose group. (B) Both medium- and high-dose groups show significantly higher SUV_{max} on day 6 than at baseline, whereas this change is not significant in low-dose group. SUV_{max} on day 6 significantly differs between medium- and high-dose groups. HD = high-dose; LD = low-dose; MD = medium-dose; ns = not significant. $^{**}P < 0.001$, paired Student t test. $^{***}P < 0.0001$, paired Student t test.

Repeated-measure 2-way ANOVA with the Tukey test was used to compare tumor growth differences among multiple experimental groups. P values of less than 0.05 were considered statistically significant.

RESULTS

PRRT Dose Affects Intratumoral T-Cell Activity

[^{68}Ga]NOTA-hGZP PET demonstrated that the PRRT dose significantly affects the level of intratumoral T-cell activation. PET on day 6 after treatment demonstrated a significant increase in GZB probe uptake in tumors in the medium- and high-dose PRRT groups compared with baseline (SUV_{max}, 3.35 ± 1.05 vs. 1.27 ± 0.33 [P = 0.0005] and 3.77 ± 0.46 vs. 1.26 ± 0.25 [$P < 0.0001$], respectively), but this change was not significant in the low-dose group (SUV_{max}, 1.15 ± 0.27 vs. 1.09 ± 0.38 [P = 0.7013], respectively). The tumor SUV_{max} on day 6 after treatment did not significantly differ between the medium- and high-dose groups (P = 0.3164) (Fig. 1; Supplemental Fig. 1; supplemental materials are available at http://jnm.snmjournals.org). Building on these findings, we used the medium dose of [^{177}Lu]DOTATATE for the subsequent combination-therapy experiments to induce a high level of tumoral inflammation while minimizing the toxicity and direct effect of PRRT in decreasing the tumor size.

Timing of PRRT Administration Affects Intratumoral T-Cell Activity

[^{68}Ga]NOTA-hGZP PET at baseline demonstrated no significant difference in tumor SUV_{max} among the experimental groups ($P > 0.05$). Tumor SUV_{max} was significantly higher on day 6 after treatment than at baseline in the E-PRRT group (3.36 ± 0.42 vs. 0.73 ± 0.23, $P < 0.0001$), the S-PRRT group (2.36 ± 0.45 vs. 0.76 ± 0.3, $P < 0.0001$), and the anti-PD1 group (2.2 ± 0.2 vs. 0.72 ± 0.28, $P < 0.0001$). There were significant differences in SUV_{max} depending on the treatment regimen and timing of PRRT administration relative to anti-PD1 ($P < 0.0001$). The E-PRRT group had a significantly higher posttreatment SUV_{max} (3.36 ± 0.42) than the S-PRRT group (2.36 ± 0.45, P = 0.0005) or the anti-PD1–only group (2.2 ± 0.2, P = 0.0001). For the vehicle, PRRT, and D-PRRT groups, there was no significant increase in tumor SUV_{max} on posttreatment PET compared with baseline (0.74 ± 0.35 vs. 0.70 ± 0.2 [P = 0.99], 0.8 ± 0.55 vs. 0.75 ± 25 [P = 0.99], and 0.95 ± 0.55 vs. 0.68 ± 0.18 [P = 0.57], respectively) (Fig. 2; Supplemental Fig. 2).

Ex Vivo Findings Correlate with [^{68}Ga]NOTA-hGZP PET Uptake In Vivo

Immunohistochemical staining for GZB in the extracted tumor tissues showed the greatest values in the E-PRRT group, followed by the S-PRRT and anti-PD1 groups (33.00% ± 11.00%, 14.00% ± 1.50%, and 7.00% ± 3.00%, respectively). The GZB level did not significantly differ between the PRRT group and the vehicle group (P = 0.62) (Fig. 3).

Immunohistochemical staining for CD3 and flow cytometry of tumor specimens for T-cell populations agreed with the results of

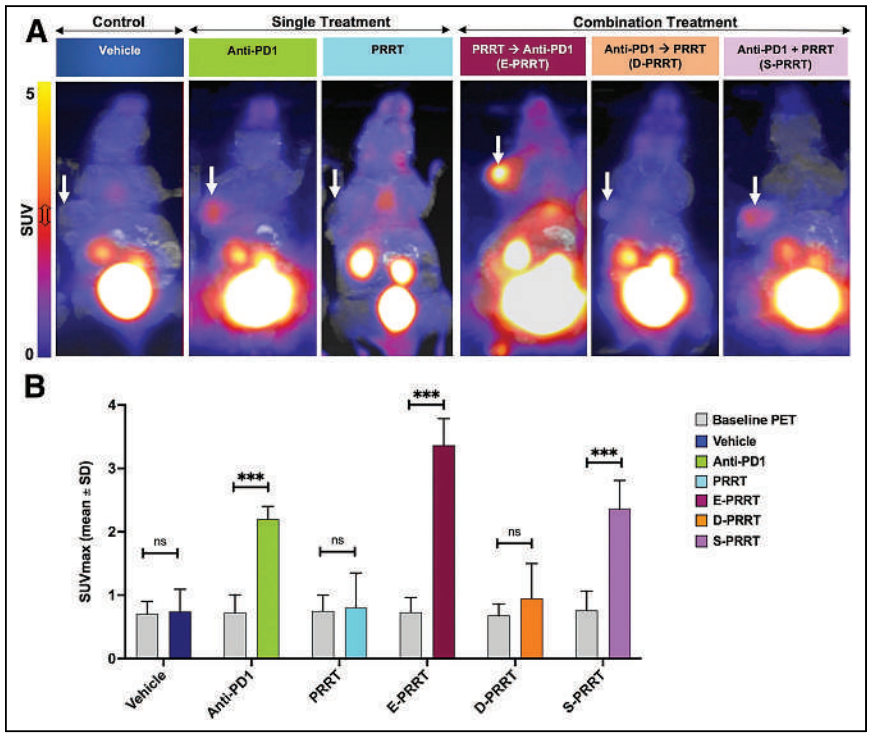

FIGURE 2. Timing of PRRT administration affects intratumoral T-cell activity measured on GZB PET (n = 12/group). (A) Coronal [^{68}Ga]NOTA-hGZP PET/MRI maximum-intensity projection of QGP-1 tumor–bearing mice on day 6 after treatment initiation (arrows point out tumor). (B) Significant increase in tumor SUV_{max} in E-PRRT, followed by S-PRRT and anti-PD1, on day 6 after treatment compared with baseline. PET measures did not significantly differ between 2 time points in remaining treatment groups. ns = not significant. $^{***}P < 0.0001$, paired Student t test.

GZB PET and immunohistochemistry. Flow cytometry demonstrated the highest percentage of CD3-positive T cells in the E-PRRT group (86.70% ± 4.50%), followed by the anti-PD1 group (11.30% ± 0.80%) and the S-PRRT group (10.50% ± 2.20%), compared with vehicle-treated tumors (1.50% ± 0.09%) ($P < 0.0001$). There was no difference in number of CD3-positive cells between the PRRT (0.80% ± 0.50%) and D-PRRT (2.60% ± 1.80%) groups and the vehicle group ($P = 0.98$). In the E-PRRT group, the percentage of CD4-positive (22.7% ± 4.0%), CD8-positive (53.3% ± 2.5%), effector CD8-positive (27.6% ± 1.37%), and naïve CD8-positive (3.5% ± 1.6%) T cells was significantly higher than in any other group ($P < 0.0001$). The percentages of these cell populations were much lower in the anti-PD1 and S-PRRT groups. Among the groups that received combination therapy, the D-PRRT group showed the lowest percentage of most tumor-infiltrating lymphocyte populations (Fig. 4).

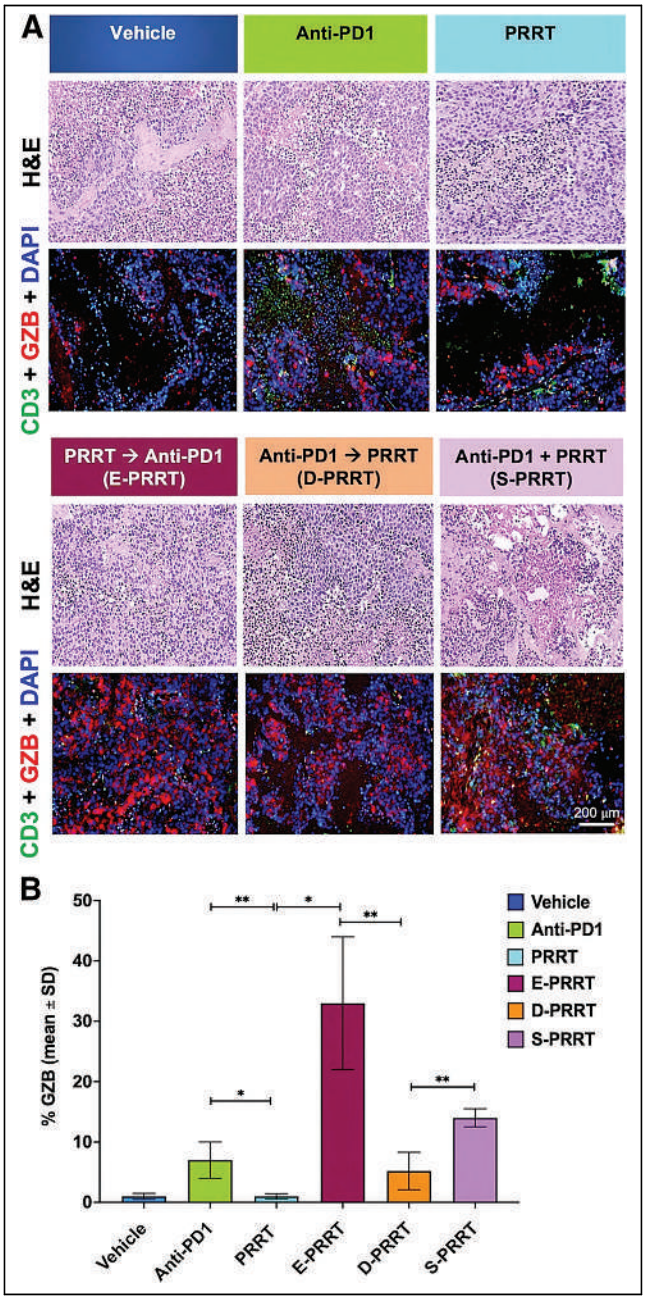

FIGURE 3. PRRT preceding anti-PD1 results in markedly increased GZB levels in NETs ($n = 4$/group). (A) Representative hematoxylin and eosin and immunohistochemical staining of extracted QGP-1 tumor tissues. (B) GZB excretion is significantly higher in tumors treated with anti-PD1 and combination of anti-PD1 and PRRT than with PRRT only or vehicle. E-PRRT–treated tumor tissues show highest GZB signal. DAPI = 4′,6-diamidino-2-phenylindole; H&E = hematoxylin and eosin. *$P < 0.01$, paired Student t test. **$P < 0.001$, paired Student t test.

E-PRRT Administration Significantly Decreases Tumor Volume

Evaluation of tumor growth over 21 d after treatment onset showed that the tumors assigned to E-PRRT were the only ones with a decreased volume at the study endpoint compared with the pretreatment day (volume, 78 ± 11.7 mm^3 vs. 205 ± 30.7 mm^3; $P = 0.0074$). The tumors that received PRRT, S-PRRT, or D-PRRT showed a modest reduction in growth; however, tumor volume at the study endpoint was overall higher than on the pretreatment day (570 ± 85.5 mm^3 vs. 209.8 ± 30.7 mm^3 [$P = 0.0076$], 538 ± 80.7 mm^3 vs. 245.2 ± 36.7 mm^3 [$P = 0.0076$], and 536.0 ± 79.6 mm^3 vs. 250 ± 37.5 mm^3 [$P = 0.0071$], respectively); the endpoint tumor volume did not significantly differ among these 3 groups ($P = 0.1155$). Tumors treated with vehicle and anti-PD1 continuously grew over time (Fig. 5).

DISCUSSION

In this study, we demonstrated the synergistic effect of PRRT and ICIs in a preclinical NET model and highlighted the effect of PRRT dose and relative timing of PRRT and ICI administration. Immunotherapy has changed the landscape of tumor treatment for multiple cancer types (*9–12*). However, to date, immunotherapy has not had a significant role in treating NETs, as evidenced by disappointing results in clinical trials (*14,15,20*). Similarly, when we administered pembrolizumab alone, we observed a weak intratumoral inflammatory response and no definite reduction in tumor growth. Factors that may contribute to the poor outcomes include the low mutational burden of NETs and the paucity of tumor-infiltrating lymphocytes in the tumor matrix (*14,15*). Therefore, combination-therapy approaches that can enhance the efficacy of ICIs by changing the tumor immune microenvironment deserve attention and warrant further exploration. One such approach is combining radiation and ICI therapy. Combination of beam radiation with ICIs in clinical trials has shown promising results, such as in melanoma, cervical NETs, pancreatic adenocarcinoma, and colon cancer (*21–23*). This systemic immune-mediated response is

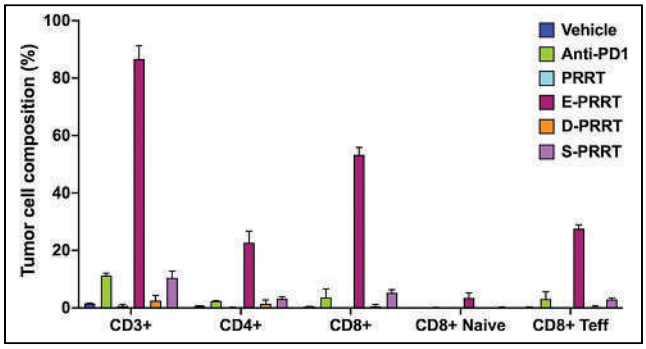

FIGURE 4. Flow cytometry of extracted QGP-1 tumor tissues 6 d after treatment initiation. Highest percentage of CD3+ tumor-infiltrating T cells, most importantly CD8-positive effector cells, is seen in E-PRRT group.

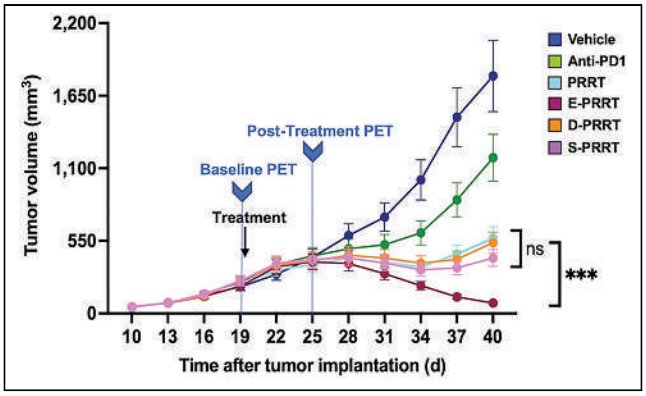

FIGURE 5. Evaluation of tumor growth over 21 d of treatment (n = 8/group). Tumors in E-PRRT group were the only ones that decreased in size by study endpoint (day 40) compared with treatment start day (day 19). Tumor growth was reduced with D-PRRT, S-PRRT, and PRRT, but tumor volume at endpoint was overall higher than on treatment start day. Vehicle- and anti-PD-1–treated tumors grew continuously. ns = not significant. ***$P < 0.0001$, ANOVA with Tukey.

due to altered expression of cell-surface antigens, enhanced cross-presentation of tumor antigens, costimulatory molecule expression, and a proinflammatory signal release caused typically by irradiating a single tumor site (*23*). We hypothesized that a similar strategy using PRRT to deliver systemic tumor radiation might change the NET microenvironment in all metastatic sites and enhance the efficacy of immune modulators. The Food and Drug Administration approval of [^{177}Lu]DOTATATE for use in GEP-NETs and multiple ICIs makes this therapy combination highly appealing to explore in large-scale clinical trials. There are 2 potentially important differences between beam radiotherapy and PRRT: most importantly, external-beam radiation targets only a single or a few tumor sites, whereas PRRT delivers radiation to each tumor focus, changing the equation of immune stimulation systematically; in addition, radiation delivery is temporally distinct, with external radiotherapy acutely applied over multiple fractions whereas PRRT is applied continuously over multiple days or weeks.

We showed that the combination of [^{177}Lu]DOTATATE and pembrolizumab resulted in a significantly lower tumor volume at the study endpoint than either of these therapies alone. This enhanced efficacy was related to increased CD3-positive cells, particularly effector CD8-positive lymphocytes, and increased GZB, a marker of active cytotoxic T-lymphocyte tumor killing. There are scarce literature data regarding the PRRT and ICI combination in NETs. Most recently, Ferdinandus et al. reported promising results for ICI and PRRT combination as a second-line treatment in a patient with Merkel cell carcinoma, a tumor of neuroendocrine origin, after initial failure of ICI treatment alone (*24*); the findings of that study were concordant with ours and anecdotally highlight the possibility of this approach. When we administered PRRT alone, there was a modest tumor growth reduction over time; this is expected as PRRT at the currently approved clinical dose rarely reduces tumor size in patients (*4*). These findings indicate that PRRT alone is noncurative but exerts a crucial effect in stabilizing disease, consistent with the findings of the NETTER-1 trial (*6*).

We demonstrated that the timing of PRRT administration relative to ICI is critical in eliciting a robust antitumor immune response and treatment efficacy. The synergistic effect of PRRT and ICI occurred only in the E-PRRT group. On the basis of data from external-beam radiotherapy, this finding was likely caused by a release of tumor antigens, altering chemokine expression and development of a proinflammatory tumor microenvironment caused by PRRT (*23,25,26*). The addition of ICI after PRRT elicits the maximal cytotoxic T-lymphocyte response. On the other hand, when ICI precedes PRRT or is given in isolation, it does not cause a robust inflammatory response, probably because of the paucity of tumor-infiltrating lymphocytes and the immunosuppressive environment of NETs. Nonetheless, these results must be interpreted with caution, as a more thorough investigation of the tumor immune microenvironment will be needed to validate them.

We used the medium dose of [^{177}Lu]DOTATATE for testing the dual PRRT and ICI experiments. We found that medium-dose PRRT induced a robust T-cell response that was not statistically different from the high-dose PRRT. The medium dose is equivalent to the clinically used dose per body weight and is often lower than what is used in most animal studies testing the efficacy of PRRT (*4*). This lower dose might decrease the risk of potential toxicities, making it more favorable for studying the synergistic effects of PRRT and ICIs.

As previously shown, GZB PET imaging can be used as a reliable biomarker for T-cell activity (*17,18*). We performed [^{68}Ga]NOTA-hGZP PET as a noninvasive method to quantify cytotoxic T-lymphocyte activation. The PET results were verified on GZB immunohistochemical and flow cytometry studies of cytotoxic T-lymphocyte populations. Given the availability of PRRT and ICIs in routine clinical practice, a similar image-guided treatment paradigm might be used to assess the efficacy of immunomodulatory treatment approaches in clinical trials for patients with NETs.

There is an overall lack of reliable preclinical models for human NETs, particularly for well-differentiated tumors, thus significantly limiting investigations of NET biology. We used QGP-1 cells, which highly express somatostatin receptor 2 (*27*). Comparison of different tumor models with variable expression levels of somatostatin receptors and sensitivity to PRRT and ICI is necessary to further investigate and compare the immune response to combination-treatment paradigms. Failure of tumor engraftment for other NET cell lines did not allow us to make such comparisons. Furthermore, we tested the combinational approaches by applying a single PRRT administration. The number and temporal administration of PRRT and ICIs require further investigation in the preclinical setting and near-term clinical trials.

CONCLUSION

Our study demonstrated that combination of ICIs and PRRT can significantly improve outcomes for GEP-NETs, while emphasizing the importance of temporal administration of these 2 treatments in enhancing treatment response. Our findings lead us to conclude that adding PRRT to ICIs is a promising paradigm for advanced, metastatic NETs. Because PRRT and ICIs are clinically available, this approach is readily translatable into the clinic.

DISCLOSURE

Umar Mahmood is a cofounder of and consultant to CytoSite Biopharma, a company focused on the development of PET probes for immunooncology, and is supported by R01DK123143 and R01CA214744. Pedram Heidari received an ASCO Young Investigator Grant for this project and is supported by NCI K08CA249047. Shadi Esfahani is supported by NCI K08CA259626. No other potential conflict of interest relevant to this article was reported.

KEY POINTS

QUESTION: Is the combination of somatostatin-targeting PRRT and ICIs synergistic in treating GEP-NETs?

PERTINENT FINDINGS: In a humanized immune-reconstituted mouse model of GEP-NETs, we showed that PRRT and ICI act synergistically. The most robust effect was seen when the PRRT administration preceded the ICI.

IMPLICATIONS FOR PATIENT CARE: The synergistic effect of ICIs and PRRT shown in this study provides a new strategy for treating GEP-NETs with curative intent; this approach can readily be tested in clinical trials.

REFERENCES

1. Taal BG, Visser O. Epidemiology of neuroendocrine tumours. *Neuroendocrinology.* 2004;80(suppl 1):3–7.
2. Uri I, Grozinsky-Glasberg S. Current treatment strategies for patients with advanced gastroenteropancreatic neuroendocrine tumors (GEP-NETs). *Clin Diabetes Endocrinol.* 2018;4:16.
3. Strosberg JR, Caplin ME, Kunz PL, et al. ^{177}Lu-Dotatate plus long-acting octreotide versus high-dose long-acting octreotide in patients with midgut neuroendocrine tumours (NETTER-1): final overall survival and long-term safety results from an open-label, randomised, controlled, phase 3 trial. *Lancet Oncol.* 2021;22:1752–1763.
4. Strosberg JR, Halfdanarson TR, Bellizzi AM, et al. The North American Neuroendocrine Tumor Society consensus guidelines for surveillance and medical management of midgut neuroendocrine tumors. *Pancreas.* 2017;46:707–714.
5. Caplin ME, Pavel M, Cwikla JB, et al. Lanreotide in metastatic enteropancreatic neuroendocrine tumors. *N Engl J Med.* 2014;371:224–233.
6. Strosberg J, El-Haddad G, Wolin E, et al. Phase 3 trial of ^{177}Lu-dotatate for midgut neuroendocrine tumors. *N Engl J Med.* 2017;376:125–135.
7. Kaltsas GA, Besser GM, Grossman AB. The diagnosis and medical management of advanced neuroendocrine tumors. *Endocr Rev.* 2004;25:458–511.
8. Kwekkeboom DJ, Kam BL, van Essen M, et al. Somatostatin-receptor-based imaging and therapy of gastroenteropancreatic neuroendocrine tumors. *Endocr Relat Cancer.* 2010;17:R53–R73.
9. Pagès F, Galon J, Dieu-Nosjean MC, Tartour E, Sautes-Fridman C, Fridman WH. Immune infiltration in human tumors: a prognostic factor that should not be ignored. *Oncogene.* 2010;29:1093–1102.
10. Ascierto PA, Kalos M, Schaer DA, Callahan MK, Wolchok JD. Biomarkers for immunostimulatory monoclonal antibodies in combination strategies for melanoma and other tumor types. *Clin Cancer Res.* 2013;19:1009–1020.
11. Borghaei H, Paz-Ares L, Horn L, et al. Nivolumab versus docetaxel in advanced nonsquamous non-small-cell lung cancer. *N Engl J Med.* 2015;373:1627–1639.
12. Motzer RJ, Escudier B, McDermott DF, et al. Nivolumab versus everolimus in advanced renal-cell carcinoma. *N Engl J Med.* 2015;373:1803–1813.
13. Gile JJ, Liu AJ, McGarrah PW, et al. Efficacy of checkpoint inhibitors in neuroendocrine neoplasms: Mayo Clinic experience. *Pancreas.* 2021;50:500–505.
14. Vijayvergia N, Dasari A, Deng M, et al. Pembrolizumab monotherapy in patients with previously treated metastatic high-grade neuroendocrine neoplasms: joint analysis of two prospective, non-randomised trials. *Br J Cancer.* 2020;122:1309–1314.
15. Strosberg J, Mizuno N, Doi T, et al. Efficacy and safety of pembrolizumab in previously treated advanced neuroendocrine tumors: results from the phase II KEYNOTE-158 study. *Clin Cancer Res.* 2020;26:2124–2130.
16. Heidari P, Wehrenberg-Klee E, Habibollahi P, Yokell D, Kulke M, Mahmood U. Free somatostatin receptor fraction predicts the antiproliferative effect of octreotide in a neuroendocrine tumor model: implications for dose optimization. *Cancer Res.* 2013;73:6865–6873.
17. Larimer BM, Bloch E, Nesti S, et al. The effectiveness of checkpoint inhibitor combinations and administration timing can be measured by granzyme B PET imaging. *Clin Cancer Res.* 2019;25:1196–1205.
18. Larimer BM, Wehrenberg-Klee E, Dubois F, et al. Granzyme b PET imaging as a predictive biomarker of immunotherapy response. *Cancer Res.* 2017;77:2318–2327.
19. Esfahani SA, de Aguiar Ferreira C, Rotile NJ, et al. HER3 PET imaging predicts response to pan receptor tyrosine kinase inhibition therapy in gastric cancer. *Mol Imaging Biol.* 2023;25:353–362.
20. Albertelli M, Dotto A, Nista F, et al. Present and future of immunotherapy in neuroendocrine tumors. *Rev Endocr Metab Disord.* 2021;22:615–636.
21. Aboudaram A, Modesto A, Chaltiel L, et al. Concurrent radiotherapy for patients with metastatic melanoma and receiving anti-programmed-death 1 therapy: a safe and effective combination. *Melanoma Res.* 2017;27:485–491.
22. Sharabi A, Kim SS, Kato S, et al. Exceptional response to nivolumab and stereotactic body radiation therapy (SBRT) in neuroendocrine cervical carcinoma with high tumor mutational burden: management considerations from the Center for Personalized Cancer Therapy at UC San Diego Moores Cancer Center. *Oncologist.* 2017;22:631–637.
23. Parikh AR, Szabolcs A, Allen JN, et al. Radiation therapy enhances immunotherapy response in microsatellite stable colorectal and pancreatic adenocarcinoma in a phase II trial. *Nat Cancer.* 2021;2:1124–1135.
24. Ferdinandus J, Fendler WP, Lueckerath K, et al. Response to combined peptide receptor radionuclide therapy and checkpoint immunotherapy with ipilimumab plus nivolumab in metastatic Merkel cell carcinoma. *J Nucl Med.* 2022;63:396–398.
25. Deng L, Liang H, Burnette B, et al. Irradiation and anti-PD-L1 treatment synergistically promote antitumor immunity in mice. *J Clin Invest.* 2014;124:687–695.
26. Weichselbaum RR, Liang H, Deng L, Fu YX. Radiotherapy and immunotherapy: a beneficial liaison? *Nat Rev Clin Oncol.* 2017;14:365–379.
27. Guenter R, Aweda T, Carmona Matos DM, et al. Overexpression of somatostatin receptor type 2 in neuroendocrine tumors for improved Ga68-DOTATATE imaging and treatment. *Surgery.* 2020;167:189–196.

Evaluation of Candidate Theranostics for ^{227}Th/^{89}Zr Paired Radioimmunotherapy of Lymphoma

Diane S. Abou[1], Mark Longtine[1], Amanda Fears[1], Nadia Benabdallah[1], Ryan Unnerstall[1], Hannah Johnston[1], Kyuhwan Shim[1], Abbie Hasson[1], Hanwen Zhang[1], David Ulmert[2], Floriane Mangin[3], Serife Ozen[4], Laurent Raibaut[4], Stéphane Brandès[3], Michel Meyer[3], Jean-Claude Chambron[4], David S. Tatum[5], Darren Magda[5], Richard L. Wahl[1], and Daniel L.J. Thorek[1,6,7]

[1]*Mallinckrodt Institute of Radiology, Washington University School of Medicine, St. Louis, Missouri;* [2]*Department of Molecular and Medical Pharmacology, UCLA, Los Angeles, California;* [3]*Institut de Chimie Moléculaire de l'Université de Bourgogne, UMR 6302, CNRS, Université de Bourgogne, Dijon, France;* [4]*Institut de Chimie de Strasbourg, UMR 7177, CNRS, Université de Strasbourg, Strasbourg, France;* [5]*Lumiphore, Inc., Berkeley, California;* [6]*Department of Biomedical Engineering, Washington University in St. Louis, St. Louis, Missouri; and* [7]*Siteman Cancer Center, Oncologic Imaging Program, Alvin J. Siteman Cancer Center, Washington University School of Medicine, St. Louis, Missouri*

^{227}Th is a promising radioisotope for targeted α-particle therapy. It produces 5 α-particles through its decay, with the clinically approved ^{223}Ra as its first daughter. There is an ample supply of ^{227}Th, allowing for clinical use; however, the chemical challenges of chelating this large tetravalent *f*-block cation are considerable. Using the CD20-targeting antibody ofatumumab, we evaluated chelation of $^{227}Th^{4+}$ for α-particle–emitting and radiotheranostic applications. **Methods:** We compared 4 bifunctional chelators for thorium radiopharmaceutical preparation: S-2-(4-Isothiocyanatobenzyl)-1,4,7,10-tetraazacyclododecane tetraacetic acid (*p*-SCN-Bn-DOTA), 2-(4-isothicyanatobenzyl)-1,2,7,10,13-hexaazacyclooctadecane-1,4,7,10,13,16-hexaacetic acid (*p*-SCN-Bn-HEHA), *p*-isothiacyanatophenyl-1-hydroxy-2-oxopiperidine-desferrioxamine (DFOcyclo*-*p*-Phe-NCS), and macrocyclic 1,2-HOPO *N*-hydroxysuccinimide (L804-NHS). Immunoconstructs were evaluated for yield, purity, and stability in vitro and in vivo. Tumor targeting of the lead ^{227}Th-labeled compound in vivo was performed in CD20-expressing models and compared with a companion ^{89}Zr-labeled PET agent. **Results:** ^{227}Th-labeled ofatumumab-chelator constructs were synthesized to a radiochemical purity of more than 95%, excepting HEHA. ^{227}Th-HEHA-ofatumumab showed moderate in vitro stability. ^{227}Th-DFOcyclo*-ofatumumab presented excellent ^{227}Th labeling efficiency; however, high liver and spleen uptake was revealed in vivo, indicative of aggregation. ^{227}Th-DOTA-ofatumumab labeled poorly, yielding no more than 5%, with low specific activity (0.08 GBq/g) and modest long-term in vitro stability (<80%). ^{227}Th-L804-ofatumumab coordinated ^{227}Th rapidly and efficiently at high yields, purity, and specific activity (8 GBq/g) and demonstrated extended stability. In vivo tumor targeting confirmed the utility of this chelator, and the diagnostic analog, ^{89}Zr-L804-ofatumumab, showed organ distribution matching that of ^{227}Th to delineate SU-DHL-6 tumors. **Conclusion:** Commercially available and novel chelators for ^{227}Th showed a range of performances. The L804 chelator can be used with potent radiotheranostic capabilities for ^{89}Zr/^{227}Th quantitative imaging and α-particle therapy.

Key Words: radioimmunotherapy; ^{227}Th; chelator; ^{89}Zr

Received Oct. 3, 2022; revision accepted Mar. 7, 2023.
For correspondence or reprints, contact Daniel Thorek (thorek.lab@wustl.edu).
Guest Editor: Jason Lewis, Memorial Sloan-Kettering Cancer Center
Published online May 4, 2023.

J Nucl Med 2023; 64:1062–1068
DOI: 10.2967/jnumed.122.264979

Radiotheranostic agents provide a unique ability to detect, characterize, treat, and monitor sites of disease with exceptional specificity. A persistent challenge for clinical theranostics is the development of suitably matched therapeutic and diagnostic agents that provide correlating pharmacokinetic data to guide therapeutic application. Ideally, this goal is realized in the form of a targeted agent that can be labeled with radionuclides for either imaging or therapy without other chemical changes. Radiometals must be stably bound to a molecularly specific vector (a small molecule, peptide, or antibody) to achieve localized uptake. The extended biologic residency time and longer radiologic half-life ($t^1/_2$) of isotopes used for antibody-based agents add a requirement for greater stability. To date, a limited number of chelates have been clinically applied, notably from the DOTA and diethylenetriaminepentaacetic acid classes (*1*). Advancements in radioisotopes available for theranostic applications necessitate radiologic and chemical efforts to achieve stable, safe, and effective radiopharmaceutical preparation.

Interest in treatments using α-particle–emitting isotopes with high linear-energy transfer continues to grow. A promising isotope that has been widely used to date is ^{225}Ac, yet the supply of isotopically pure ^{225}Ac is limited (*2*). Theranostic pairs for ^{225}Ac radioimmunotherapy typically use ^{111}In (*3,4*). Although these isotopes have reasonably close half-lives (2.8 and 9.8 d $t^1/_2$ for ^{111}In and ^{225}Ac, respectively), SPECT imaging presents challenges in image quantification for pharmacokinetics and dosimetry (*5*). Alternatively, the radiotheranostics of ^{225}Ac using ^{89}Zr ($t^1/_2$, 3.3 d) for PET have highly similar pharmacokinetics; however, different chelators are required for coordination of each isotope (*6,7*).

^{227}Th ($t^1/_2$, 18.7 d) is produced from ^{227}Ac ($t^1/_2$, 21.7 y) with a branching ratio of 98.6% and produces 5 α-particles, including from its first daughter, ^{223}Ra ($t^1/_2$, 11.4 d) (Supplemental Fig. 1; supplemental materials are available at http://jnm.snmjournals.org). Tetravalent thorium bears a $5f^0$ electronic configuration and is typically 8-, 10-, or even 12-fold coordinated. Chelation with ^{227}Th has been limited to a few bifunctional ligands, such as macrocyclic DOTA (displaying inefficient labeling yields), and newer hydroxypyridinone

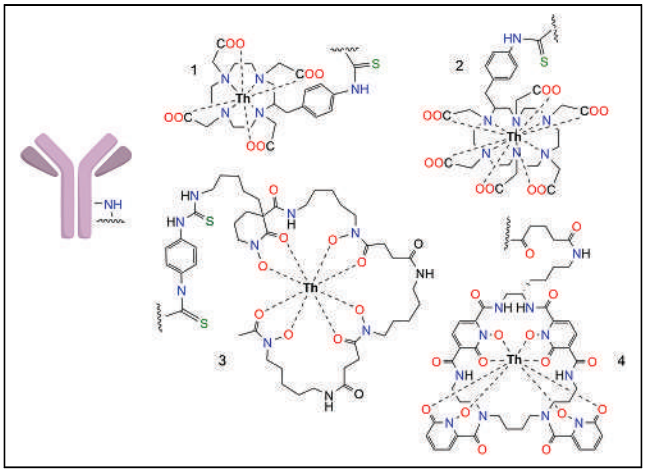

FIGURE 1. Bifunctional chelators for ^{227}Th radiolabeling: ^{227}Th-DOTA- (*1*), ^{227}Th-HEHA- (*2*), ^{227}Th-DFOcyclo*- (*3*), and ^{227}Th-L804-ofatumumab (*4*). *p*-SCN-Bn-DOTA was radiolabeled using a 2-step procedure; all others were directly labeled once conjugated to antibody.

or picolinic acid constructs. It can be challenging for such ligands to also stably complex PET isotopes (*8–11*), as chelation chemistries are often class-specific (transition metals, lanthanides, actinides, or other heavy metals). Cross-class metal radiolabeling involves different chemistries and mechanisms (*12,13*), and evaluation of single-agent theranostic precursors is ongoing (*9*).

In this work, we evaluated 4 antibody-chelator conjugates for in vitro and in vivo stability using ofatumumab, a human anti-CD20 antibody (*14,15*). The most stable ^{227}Th chelator conjugate, L804, was evaluated in vivo for tumor-targeting capability in Raji tumor–bearing mice. An ^{89}Zr-L804- theranostic analog was compared, as well as conventional ^{89}Zr-chelating DFO. Data demonstrate long-term stability and a pharmacokinetic match between ^{89}Zr tracer and ^{227}Th radiotherapy, with translational potential for quantitative imaging and treatment.

MATERIALS AND METHODS

Chemicals were from Sigma-Aldrich unless otherwise noted. Ofatumumab (Novartis) was obtained from the Washington University in St. Louis clinical pharmacy. The bifunctional chelators S-2-(4-Isothiocyanatobenzyl)-1,4,7,10-tetraazacyclododecane tetraacetic acid (*p*-SCN-Bn-DOTA) and 2-(4-isothicyanatobenzyl)-1,2,7,10,13-hexaazacyclooctadecane-1,4,7,10,13,16-hexaacetic acid (*p*-SCN-Bn-HEHA) were purchased from Macrocyclics. The desferrioxamine derivative *p*-isothiacyanatophenyl-1-hydroxy-2-oxopiperidine-desferrioxamine (DFOcyclo*-*p*-Phe-NCS) was synthesized as outlined in the supplemental materials, and macrocyclic 1,2-HOPO *N*-hydroxysuccinimide (L804-NHS) was provided by Lumiphore, Inc. Solutions were prepared with Chelex (Bio-Rad)-treated ultrapure water. ^{227}Th was supplied as dried nitrates by the U.S. Department of Energy.

Chelators and Conjugations

DFOcyclo*-*p*-Phe-NCS was prepared in 5 steps from known precursors. The synthesis and characterization are reported in Supplemental Figures 2–5 (*16–20*). Chelator-to-antibody ratios of 8:1 (*p*-Bn-SCN-HEHA), 5:1 (DFOcyclo*-*p*-Phe-NCS), and 4.2:1 (L804-NHS) were reacted in 0.1 M Na_2CO_3 (pH 9, 37°C for 1 h). L804-ofatumumab was prepared in 0.5 M NH_4OAc, pH 5.5, with 1 mM $CaCl_2$. Before ^{227}Th radiolabeling, buffer was exchanged by spin desalting columns (Zeba, 40K, 0.5 mL; Thermo Scientific) to 4-(2-hydroxyethyl)-1-piperazineethanesulfonic acid (HEPES) (1 M, pH 7). Conjugate ratios were measured by capillary mass spectrometry with an Exactive Plus (Thermo Fisher). Samples were run at a resolving power of 8,750 or 17,500 at 300 m/k and analyzed by Protein Metric Intact.

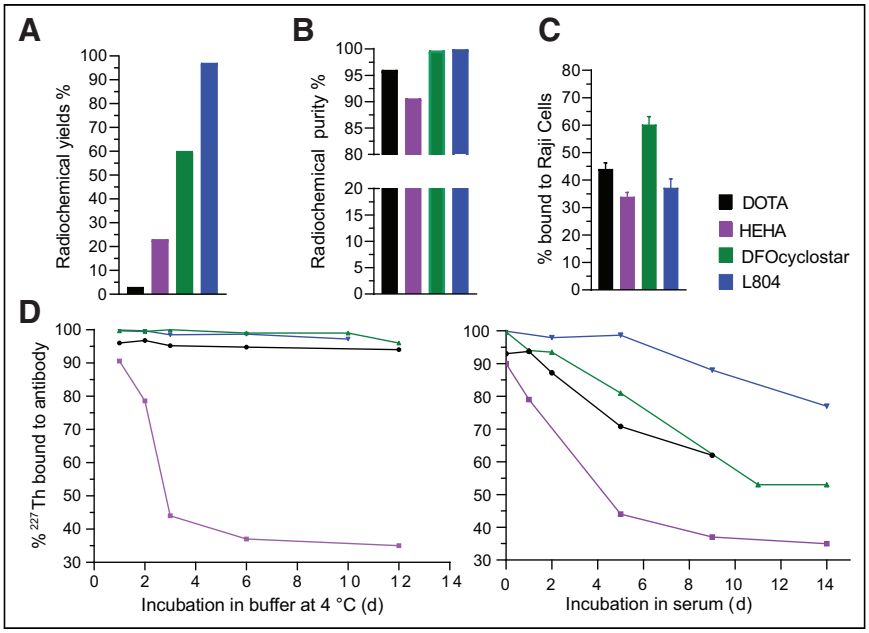

FIGURE 2. Radiopharmaceutical quality control for ^{227}Th-labeled ofatumumab. All calculations were based on ^{227}Th only. (A) Radiochemical yields of DOTA, HEHA, DFOcyclo*, and L804 conjugated to ofatumumab; highest yield (>95%) was obtained for L804 after purification. (B) Achieved RCPs of >95% for all except HEHA. (C) Raji cell binding showing that all ^{227}Th-labeled constructs preserved moderate affinities. (D) In vitro stability of ^{227}Th counts associated with antibody at 4°C in buffer (left) or human serum protein challenge at 37°C (right), over 14 d.

^{227}Th and ^{89}Zr Radiolabeling and Purification

DOTA-ofatumumab was radiolabeled following a 2-step procedure (*21,22*) in which 0.925–1.85 MBq of ^{227}Th(IV) nitrate dissolved in 0.2 M HCl was added to *p*-Bn-SCN-DOTA (10 mg/mL; 20 μL in 0.1 M NH_4OAc at pH 6). We verified a pH of 6 and incubated (65°C, 1 h) under gentle shaking. After radiocomplexation, the material was conjugated to the antibody (1 mg) at pH 9 in 0.1 M Na_2CO_3 (37°C for 2 h); 10 μL of diethylenetriaminepentaacetic acid (50 mM) was added, then the mixture was purified twice in saline using a preconditioned spin desalting column (7 kDa).

Single-step labeling (5–7 mg/mL; 1 mg) using ^{227}Th at 0.925–1.85 MBq in 0.1 M NH_4OAc at pH 6 (HEHA) or 1 M HEPES at pH 7 (DFOcyclo* and L804) occurred under gentle shaking (37°C, 2 h) and was quenched with 10 μL of diethylenetriaminepentaacetic acid (50 mM) before purification, as above. Free ^{223}Ra was adsorbed on the column resin, providing high ^{227}Th isotopic purity. Radical scavengers were either ascorbic acid (10 μL, 150 mg/mL, for DOTA) or gentisic acid (0.1 M, 20 μL, for others). ^{89}Zr radiolabeling of DFO-ofatumumab was conducted as previously described (*15*). ^{89}Zr radiolabeling of L804-ofatumumab (7 mg/mL)

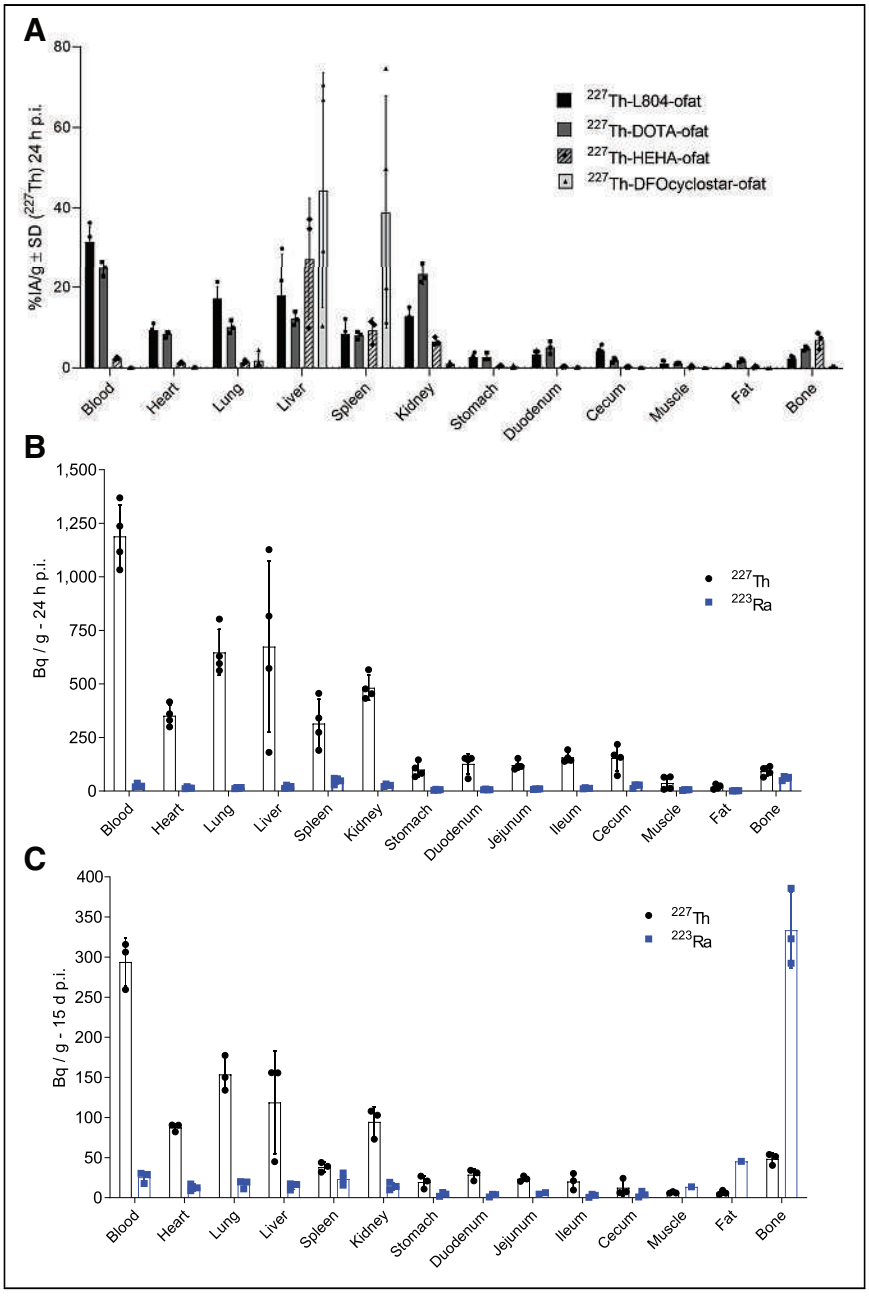

FIGURE 3. Comparative ^{227}Th organ uptake in naïve mice. (A) Organ distribution of ^{227}Th-DOTA-, HEHA-, DFOcyclo*-, and L804-ofatumumab 24 h after injection. Extended blood circulation was seen for DOTA and L804, compared with elevated liver and spleen uptake observed for DFOcyclo* and high liver uptake for HEHA constructs. (B and C) ^{227}Th-L804-ofatumumab distribution at 24 h (B) and 15 d (C) after injection for ^{227}Th and ^{223}Ra. ofat = ofatumumab; p.i. = postinjection.

was performed in 0.5 M NH_4OAc with 1 mM $CaCl_2$ at pH 5.5 and 37°C for 2 h, with purification as above.

Radiopharmaceutical Quality Control

Protein concentration was determined by bicinchoninic acid assay, with more than 90% recoveries. Radiochemical yields were calculated as the ratio of initial activity to measured activity obtained after purification, using γ-counting and calibrated high-purity germanium (GEM-50195-S; Ametek) detection (for ^{227}Th).

Radiochemical purity (RCP) evaluation used thin-layer chromatography (AR-2000; Bioscan) and fast protein liquid chromatography (AKTA; GE Healthcare) for both ^{227}Th and ^{89}Zr (Supplemental Figs. 6 and 7). Labeled antibodies were migrated on silica-coated paper with an aqueous solution of diethylenetriaminepentaacetic acid (10 mM, pH 5). A control strip of unchelated ^{227}Th dissolved in NH_4OAc displayed complete migration to the front of the strip. After thin-layer chromatography reading, samples were bisected for quantitative radioisotopic determination by high-purity germanium. Radioisotopic purity was verified after purification (Supplemental Fig. 8). Stability and purity were determined using fast protein liquid chromatography with ultraviolet light (280 nm) coupled with in-line radiodetection (Lablogic) for ^{89}Zr, with 1-mL fraction collection for ^{227}Th/^{223}Ra γ-counting.

In Vitro Stability Assay

^{227}Th-ofatumumab constructs (100 μg/0.74–0.925 MBq) were incubated in human plasma diluted 1:10 at 37°C, under gentle shaking over 1 half-life of ^{227}Th. To monitor ^{227}Th dissociation from antibody, samples were surveyed by thin-layer chromatography and size-exclusion chromatography fast protein liquid chromatography every other day. Thin-layer chromatography sections and fast protein liquid chromatography fractions were γ-counted (protocol below). ^{227}Th activities integrated at the antibody retention time (12–14 min) over the sum of eluted activity defines the RCP percentage of ^{277}Th-ofatumumab.

Immunoreactivity was evaluated by the assay of Lindmo et al. (*23*). Cells were incubated with the labeled samples (~5 ng of ^{227}Th conjugate, 16.7 ± 1.33 kBq) and blocked with unlabeled ofatumumab. Raji cells (12×10^6) were incubated for 1 h in phosphate-buffered saline and 1% bovine serum albumin and washed, in triplicate.

Administration and In Vivo Distribution

The studies were approved by the Institutional Animal Care and Use Committee. For organ distribution, female 6- to 8-wk-old Swiss Webster mice (Charles River) were intravenously administered constructs through the retroorbital sinus. The animals received 5.55–9.25 kBq of ^{227}Th-labeled antibody or 740 kBq of ^{89}Zr analogs. Injections were adjusted with unlabeled precursor to 20 μg of antibody per injection (supplemental materials).

At the times indicated, mice were killed by CO_2 asphyxiation and organs were γ-counted (Wizard^2; Perkin Elmer). ^{227}Th and ^{223}Ra (at equilibrium) activities were determined by decomposing the γ-spectra, and percentage injected activity (%IA) per gram of tissue for ^{227}Th was computed. Absolute activity per organ (Bq/g) was defined using a γ-counting methodology, applying serial dilutions of a calibrated ^{223}Ra source and Bateman equation–corrected ^{227}Th decay spectra (*24*).

PET and PET/CT

PET imaging of SU-DHL-6–bearing mice was performed using ^{89}Zr-labeled L804-ofatumumab (6.66 MBq) at 1, 2, 3, and 7 d after

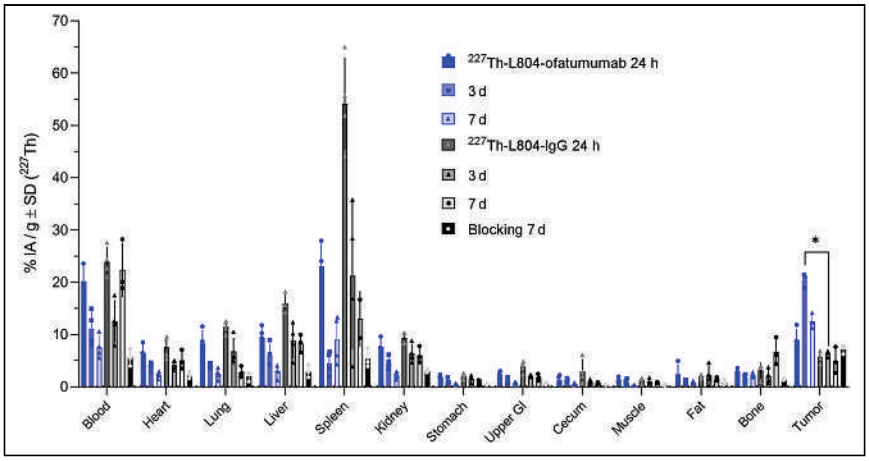

FIGURE 4. Organ distribution of ^{227}Th-L804-ofatumamab and ^{227}Th-L804-IgG and blocking with ofatumumab using Raji tumor–bearing mice (R2G2, female), reporting ^{227}Th only (%IA/g) at 24 h, 3 d, and 7 d after injection. GI = gastrointestinal tract.

injection (R4 microPET; Siemens). A blocking cohort with 200 μg of unlabeled ofatumumab (2 h before tracer) was included. The scanner was calibrated with a mouse-sized cylinder phantom of aqueous ^{18}F with a known activity concentration (*25*), energy windows of 350–650 keV, and coincidence timing of 6 ns. Corrected scanner data were reconstructed by an iterative 3-dimensional maximum a priori algorithm. Volumes of interest were defined, and %IA/mL was computed (ASIPro; Siemens).

PET/CT of the SU-DHL-6 tumor–bearing animals was performed on the Nanoscan (Mediso) on day 7. A CT acquisition of 720°, 70 kV/980 μA of 90 ms, and 4× binning was reconstructed by filtered backprojection to produce isotropic 124-μm voxels (122 × 122 × 97 mm). PET data (400–600 keV, 5-ns timing) were reconstructed using the iterative, 3-dimensional TeraTomo algorithm (4 iterations and 6 subsets; Mediso Medical Imaging Systems). Decay, attenuation, and scatter corrections were applied to quantify injected activity.

RESULTS

Ofatumumab, a second-generation humanized anti-CD20 antibody targeting non-Hodgkin lymphoma, was modified with 1 of 4 chelators, radiolabeled with ^{227}Th, and tested for yield, purity, and stability. The bifunctional chelators considered for this study were 4-arm DOTA, HEHA, DFOcyclo*, and the L804 (Fig. 1).

Radiochemical Yields, Purity, and Specific Activity

^{227}Th labeling of DOTA-ofatumumab required a 2-step procedure first chelating ^{227}Th to *p*-SCN-Bn-DOTA and then following with antibody conjugation. The final radiochemical yield reached no more than 3% because of poor conjugation efficiency. Other conjugates underwent a 1-step radiolabeling procedure resulting in radiochemical yields of 23%, 60%, and 97%, for HEHA, DFOcyclo*, and L804, respectively (Fig. 2A). The RCP of the final products was lowest for HEHA-ofatumumab (<90%), whereas the DOTA, DFOcyclo*, and L804 constructs all achieved an RCP of more than 99% (Fig. 2B; Supplemental Figs. 6 and 7). Radioisotopic purity was more than 99% for all radiopharmaceuticals, demonstrating high selectivity for ^{227}Th over ^{223}Ra and other daughters (Supplemental Fig. 8). The specific activities of ^{227}Th-ofatumumab varied widely: 0.08 GBq/g for DOTA, 1.5–3 GBq/g for DFOcyclo*, and 8 GBq/g for L804 with 3.2 chelators per antibody (Supplemental Fig. 9). L804-ofatumumab was successfully labeled with ^{89}Zr, with RCP of more than 99% (Supplemental Fig. 7), using a specific activity ranging from 330–370 GBq/g for the PET imaging study to 70–75 GBq/g for the organ distribution.

In Vitro Stability and Immunoreactivity

Radioconjugate stability varied when challenged with human serum. HEHA demonstrated the lowest coordination capability with ^{227}Th, whereas DOTA, DFOcyclo*, and L804 demonstrated stable chelation over 2 wk in buffer or plasma. DOTA and DFOcyclo* maintained adequate binding of ^{227}Th ranging between 50% and 70% over 10 d of challenge (Fig. 2D; Supplemental Fig. 6). L804 presented the highest stability, with more than 80% of ^{227}Th bound to the antibody after 2 wk (Supplemental Fig. 7). Binding to CD20-expressing cells indicated similar immunoreactivity for all 4 conjugates: DOTA construct binding at 44% ± 2.3% (similar to what was previously reported with rituximab (*26*)), HEHA at 34% ± 1.6%, DFOcyclo* at 60.2% ± 2.9%, and L804 at 32% ± 3% (Fig. 2C).

In Vivo Distribution

Acute ^{227}Th stability was assessed in vivo with naïve mice at 24 h after injection (Fig. 3). ^{227}Th-labeled HEHA and DFOcyclo* constructs were insufficiently stable, with elevated liver uptake (both) and spleen uptake (DFOcyclo*) (>20 %IA/g). In contrast, ^{227}Th-DOTA- and ^{227}Th-L804-ofatumumab presented nearly identical distributions and no significant differences in organ uptake.

The concatenated decay of ^{227}Th (Supplemental Fig. 1) presents opportunities and challenges for drug development. We decomposed ^{227}Th activities from daughter ^{223}Ra (at equilibrium) and analyzed ^{227}Th-L804-ofatumumab distribution. ^{223}Ra does not decay in place, where ^{227}Th accumulates, but rather recirculates and is sequestered in the skeleton (Figs. 3B and 3C) in agreement with

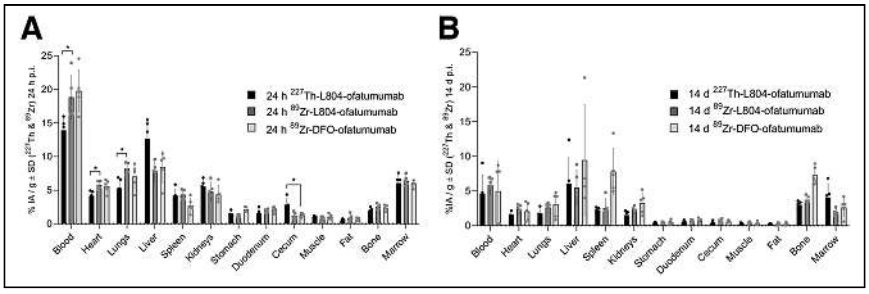

FIGURE 5. Pharmacokinetic comparison of ^{227}Th-L804-, ^{89}Zr-L804-, and ^{89}Zr-DFO-ofatumumab in naïve female mice at 1 d (A) and 14 d (B) after injection. Significant differences were observed for blood, heart, and lung accumulation of ^{227}Th-L804- vs. ^{89}Zr-L804-ofatumumab at 1 d ($P < 0.05$). At 14 d, no differences were seen between ^{227}Th-L804- and ^{89}Zr-L804-ofatumumab. ^{89}Zr bone uptake was greater for DFO (7.3 ± 1.1 %IA/g) than for L804 (^{89}Zr, 3.7 ± 0.5 %IA/g; ^{227}Th, 3.0 ± 0.4 %IA/g [$P < 0.001$]). p.i. = postinjection.

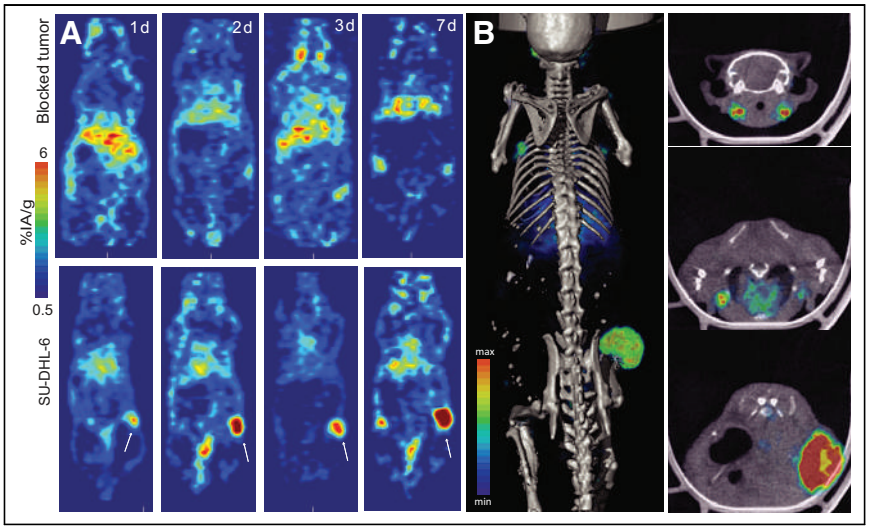

FIGURE 6. (A) Representative PET images of SU-DHL-6 tumor–bearing animal with ^{89}Zr-L804-ofatumumab, with or without blocking. (B) PET/CT at 7 d, without blocking. On right are cross-sectional images of cervical lymph nodes, brachial lymph nodes, and tumor, from top to bottom.

previous reports (*22,27*). Initial ^{227}Th uptake in lungs, liver, and kidney (>10 %IA/g) decreased over 2 wk to no more than 5%IA/g, suggesting clearance and elimination of antibody (Supplemental Fig. 10). Dosimetric evaluation of a 150 kBq/kg treatment was computed to predict human organ-absorbed doses using IDAC-Dose, version 2.1 (Supplemental Table 1) (*28–30*). The highest values for bone, kidney, liver, and spleen ranged from 71 to 65 mGy/MBq; heart wall and bone marrow were both 50 mGy/MBq.

Tumor-Targeting Evaluation

The ^{227}Th-L804 conjugate was selected as the lead agent for further evaluation. We first investigated the tumor-targeting ability of ^{227}Th-L804-ofatumumab in CD20–positive Raji tumors. Mice were randomized to receive ^{227}Th-L804-ofatumumab, control ^{227}Th-L804-IgG, or ^{227}Th-L804-ofatumumab preceded by unmodified ofatumumab. The early blood signal for the unblocked group (21.6 ± 1.9 %IA/g) decreased with time to 7.5 ± 1.8 %IA/g at 7 d (Fig. 4). Control IgG uptake was significantly greater in the spleen over the course of the experiment, whereas ^{227}Th tumor uptake was significantly higher for the targeted construct at all time points (to control IgG, $P <$ 0.01) and to blocked group at 7 d ($P < 0.05$). Peak tumor uptake at day 3 for ^{227}Th-L804-ofatumumab achieved 20 ± 1 %IA/g (Fig. 4).

^{227}Th and ^{89}Zr Theranostics

Having validated the stability and biologic activity of ^{227}Th-L804-ofatumumab, we next tested the analogous ^{89}Zr PET agent. We compared the pharmacokinetics of ^{227}Th- and ^{89}Zr-L804-ofatumumab and conventional ^{89}Zr-DFO-ofatumumab (Fig. 5). Small but statistically significant differences were observed between ^{227}Th- and ^{89}Zr-L804-ofatumumab for blood, heart, lung, and cecal tissues at 1 d (Fig. 5A). At 14 d, no differences were detected (Fig. 5B). ^{89}Zr-L804- and ^{89}Zr-DFO-ofatumumab have highly similar distributions except for longer-term skeletal uptake; bone signal was significantly higher for ^{89}Zr-DFO-ofatumumab (7.3 ± 1.3 %IA/g) than for ^{89}Zr-L804-ofatumumab (3.7 ± 0.5 %IA/g). ^{227}Th-L804 bone uptake was correspondingly low (3.0 ± 0.4 %IA/g). Free radiometal may also explain the increased liver and spleen values for ^{89}Zr-DFO- over ^{227}Th/^{89}Zr-L804-ofatumumab (*31*). Together, these data demonstrate that use of different chelators (DFO and L804) alters radiopharmaceutical distribution to a greater degree than does exchange of radiometals.

The theranostic capability of L804-ofatumumab for ^{89}Zr PET was tested in CD20–positive SU-DHL-6 xenografts (Fig. 6). Recapitulating Raji accumulation of ^{227}Th-L804-ofatumumab, we observed high-contrast delineation with ^{89}Zr-L804-ofatumumab and a low skeletal signal. To confirm specificity, blocking antibody was administered to a representative animal; the result was decreased tumor uptake (Supplemental Fig. 11). Metastatic invasion of lymph nodes was also visualized, along with primary tumor, and was confirmed by histologic analysis (Supplemental Fig. 12) (*32*).

DISCUSSION

Radiopharmaceutical therapy is an emerging cancer treatment class. Tempering enthusiasm are concerns of off-target tissue effects and the limited availability of several radionuclides. α-particle–emitting therapy confronts both concerns because demand for a key radionuclide, ^{225}Ac, greatly exceeds supply (*33*). Alternatives include ^{223}Ra (however, receptor-specific targeting is challenging) (*34*) and ^{227}Th (for which there is an ample stock for early-phase trials) (*35,36*). Labeling with ^{227}Th has been achieved in the past using DOTA, octapa, and octadentate 3,2-hydroxypyridinonate structures (*37*), with the last of these used in clinical trials (NCT03507452 and NCT02581878). However, ^{227}Th lacks suitable in vivo stability with ^{89}Zr compatible chelators, potentially precluding theranostic use (*22,36*). Here, we chose 4 chelators from different classes to test ^{227}Th coordination efficiency, stability, purity, and cancer cell receptor targeting, and we evaluated the lead conjugate as a companion ^{89}Zr diagnostic.

Chelator selection was based on chemical attributes and prior experience. DOTA is a versatile chelator and has previously been used for ^{227}Th coordination (*22,38*), which requires a 2-step procedure (*26,39*). The result was poor radiolabeling yields (<5%) and low specific activity (0.8 GBq/g). Previously reported ^{227}Th-DOTA-antibody specific activities exceed the results of this work for ^{227}Th-DOTA-ofatumumab, suggesting that antibody labeling can be further optimized (*39*). HEHA is a large cyclic chelator with 12 donor atoms, potentially amenable to Th^{4+} coordination (*40*). HEHA is an efficient in vitro chelator for $^{225}Ac^{3+}$ (*41*) but has limited in vivo applicability (*42*). Conjugated to ofatumumab, HEHA complexed ^{227}Th with limited efficiency and RCP, and data indicate that ^{227}Th-HEHA-ofatumumab lacks in vivo stability.

DFOcyclo*- and L804-ofatumumab presented the most interesting radiolabeling efficiencies, purities, and specific activities with ^{227}Th, in line with recent reports (*43*). DFOcyclo* is a linear chelator of 4 hydroxamate donors providing octadentate coordination. It presents features similar to those of DFO, with the addition of a fourth cyclic hydroxamic acid motif for additional stability to complexes embedding an 8-coordinated metal (*44*). We also investigated a macrocyclic approach using L804 articulated with four 1-hydroxypyridin-2-one chelators. Previously, L804 immune constructs have shown high affinity for ^{177}Lu and ^{89}Zr (*45*) and potential for actinides (*46*).

Both DFOcyclo* and L804 presented attractive in vitro stability, suggesting strong coordinating features for ^{227}Th formulations. Surprisingly, despite excellent DFOcyclo* in vitro results, the elevated liver and spleen accumulations suggest instability of the conjugate or metal decomplexation. ^{227}Th-L804-ofatumumab remained intact in vivo, as CD20-expressing tumor recognition was achieved for 2 tumor mouse models of lymphoma. ^{227}Th-L804-ofatumumab organ distributions were similar to the DOTA conjugate in naïve mice, with extended blood content and low bone uptake. In vitro performance and in vivo utility indicate that L804 is an effective chelator of ^{227}Th for radiopharmaceutical applications.

γ-spectroscopic analysis of the radiolabeled material showed selective ^{227}Th labeling with insignificant ^{223}Ra. However, concatenated decay leads to production of daughters over time, complicating quality control and in vivo evaluation (*47*). ^{227}Th-L804-ofatumumab was administered with high radionuclidic purity, and in vivo ingrowth of ^{223}Ra was notable for its skeletal redistribution anticipated from $^{223}RaCl_2$ distribution in mice (*27,48*) and other ^{227}Th conjugates (*49*). ^{227}Th-L804-ofatumumab organ distribution over 2 wk indicates clearance from off-target organs including lungs, liver, spleen, and kidneys. Predicted human dosimetry showed that bone, kidney, and spleen may receive the highest absorbed doses for activity administrations of 150 kBq/kg. We computed low bone marrow dose estimates (<2 Gy). Considering stable ^{227}Th coordination, the magnitude of tumor activity–delivery, and dosimetry, ^{227}Th-L804 may drive further interest in radioimmunotherapy.

Finally, we addressed the theranostic potential for quantitative imaging using ^{89}Zr-L804-ofatumumab. Subtle but significant differences were measured in blood (early time points) versus ^{227}Th, and these differences resolved at 2 wk; otherwise, a nearly identical distribution was observed. In contrast, the increasing bone uptake with DFO conjugate indicated inadequate long-term stability. PET imaging of ^{89}Zr-L804-ofatumumab further confirmed effective chelation of ^{89}Zr by L804, displaying—with clear contrast—primary tumor SU-DHL-6 and diseased lymph nodes and showing low skeletal uptake.

CONCLUSION

L804 is the most stable and versatile chelator of those tested, providing facile coordination of ^{227}Th and ^{89}Zr. Stable chelation of ^{227}Th was demonstrated and applied for tumor-targeted delivery across 2 lymphoma models. These data support the further development of ^{227}Th/^{89}Zr antibody theranostics using this chemically identical precursor.

DISCLOSURE

Financial support was received from NIH NCI (R01CA229893, R01CA240711, and R01EB02925901 to Daniel Thorek), P30 CA091842, the Children's Discovery Institute of Washington University in St. Louis and St. Louis Children's Hospital (to Diane Abou), the Centre National de la Recherche Scientifique (CNRS), the Conseil Régional de Bourgogne through the Plan d'Action Regional pour l'Innovation (program PARI II "Pharmaco-imagerie et agents théragnostiques"), the European Regional Development Fund (FEDER), and the University of Strasbourg. Floriane Mangin acknowledges the Université de Bourgogne for a postdoctoral fellowship. Darren Magda and David Tatum own intellectual property relating to L804 and are employees of Lumiphore, Inc. (Berkeley, CA). No other potential conflict of interest relevant to this article was reported.

ACKNOWLEDGMENTS

We thank Dr. Jacqueline Payton at Washington University in St. Louis for supplying SU-DHL-6 cells. Isotope was supplied in part by the U.S. Department of Energy Office of Science (Isotope Program, Office of Nuclear Physics). We thank the Cyclotron Facility for ^{89}Zr, and we thank the Small Animal Cancer Imaging Core for imaging assistance, both of Washington University in St. Louis.

KEY POINTS

QUESTION: Can we stably achieve antibody radiolabeling using an identical precursor for both ^{89}Zr imaging and ^{227}Th therapy?

PERTINENT FINDINGS: L804 is the most stable and versatile chelator of 4 tested for coordination of ^{227}Th and ^{89}Zr as a theranostic pair.

IMPLICATIONS FOR PATIENT CARE: These data support the development of suitably matched therapeutic and diagnostic agents that provide correlating pharmacokinetic and pharmacodynamic data to guide therapeutic application.

REFERENCES

1. Baidoo KE, Yong K, Brechbiel MW. Molecular pathways: targeted α-particle radiation therapy. *Clin Cancer Res.* 2013;19:530–537.
2. Morgenstern A, Apostolidis C, Bruchertseifer F. Supply and clinical application of actinium-225 and bismuth-213. *Semin Nucl Med.* 2020;50:119–123.
3. Kelly VJ, Wu S-T, Gottumukkala V, et al. Preclinical evaluation of an ^{111}In/^{225}Ac theranostic targeting transformed MUC1 for triple negative breast cancer. *Theranostics.* 2020;10:6946–6958.
4. Solomon VR, Alizadeh E, Bernhard W, et al. ^{111}In- and ^{225}Ac-labeled cixutumumab for imaging and α-particle radiotherapy of IGF-1R positive triple-negative breast cancer. *Mol Pharm.* 2019;16:4807–4816.
5. Pereira JM, Stabin MG, Lima FRA, Guimarães MICC, Forrester JW. Image quantification for radiation dose calculations: limitations and uncertainties. *Health Phys.* 2010;99:688–701.
6. Thorek DLJ, Ku AT, Mitsiades N, et al. Harnessing androgen receptor pathway activation for targeted alpha particle radioimmunotherapy of breast cancer. *Clin Cancer Res.* 2019;25:881–891.
7. Veach DR, Storey CM, Lückerath K, et al. PSA-targeted alpha-, beta-, and positron-emitting immunotheranostics in murine prostate cancer models and nonhuman primates. *Clin Cancer Res.* 2021;27:2050–2060.
8. Broer LN, Knapen DG, Suurs FV, et al. ^{89}Zr-3,2-HOPO-mesothelin antibody PET imaging reflects tumor uptake of mesothelin-targeted ^{227}Th-conjugate therapy in mice. *J Nucl Med.* 2022;63:1715–1721.
9. Roy J, Jagoda EM, Basuli F, et al. In vitro and in vivo comparison of 3,2-HOPO versus deferoxamine-based chelation of zirconium-89 to the antimesothelin antibody anetumab. *Cancer Biother Radiopharm.* 2021;36:316–325.
10. Labadie KP, Hamlin DK, Kenoyer A, et al. Glypican-3-targeted ^{227}Th α-therapy reduces tumor burden in an orthotopic xenograft murine model of hepatocellular carcinoma. *J Nucl Med.* 2022;63:1033–1038.
11. Shannon RD. Revised effective ionic radii and systematic studies of interatomic distances in halides and chalcogenides. *Acta Crystallogr A.* 1976;32:751–767.
12. Fani M, Maecke HR. Radiopharmaceutical development of radiolabelled peptides. *Eur J Nucl Med Mol Imaging.* 2012;39(suppl 1):S11–S30.
13. Bhatt NB, Pandya DN, Wadas TJ. Recent advances in zirconium-89 chelator development. *Molecules.* 2018;23:638.
14. Klein C, Lammens A, Schäfer W, et al. Epitope interactions of monoclonal antibodies targeting CD20 and their relationship to functional properties. *MAbs.* 2013;5:22–33.
15. Yoon JT, Longtine MS, Marquez-Nostra BV, Wahl RL. Evaluation of next-generation anti-CD20 antibodies labeled with ^{89}Zr in human lymphoma xenografts. *J Nucl Med.* 2018;59:1219–1224.
16. Liu Y, Jacobs HK, Gopalan AS. A new approach to cyclic hydroxamic acids: intramolecular cyclization of N-benzyloxy carbamates with carbon nucleophiles. *Tetrahedron.* 2011;67:2206–2214.
17. Feiner IVJ, Brandt M, Cowell J, et al. The race for hydroxamate-based zirconium-89 chelators. *Cancers (Basel).* 2021;13:4466.

18. Zhao Y, Chen G. Palladium-catalyzed alkylation of ortho-C(sp2)-H bonds of benzylamide substrates with alkyl halides. *Org Lett.* 2011;13:4850–4853.
19. Vugts DJ, Klaver C, Sewing C, et al. Comparison of the octadentate bifunctional chelator DFO*-pPhe-NCS and the clinically used hexadentate bifunctional chelator DFO-pPhe-NCS for ^{89}Zr-immuno-PET. *Eur J Nucl Med Mol Imaging.* 2017;44:286–295.
20. Liu J, Obando D, Schipanski LG, et al. Conjugates of desferrioxamine B (DFOB) with derivatives of adamantane or with orally available chelators as potential agents for treating iron overload. *J Med Chem.* 2010;53:1370–1382.
21. McDevitt MR, Ma D, Simon J, Frank RK, Scheinberg DA. Design and synthesis of ^{225}Ac radioimmunopharmaceuticals. *Appl Radiat Isot.* 2002;57:841–847.
22. Dahle J, Borrebaek J, Melhus KB, et al. Initial evaluation of ^{117}Th-p-benzyl-DOTA-rituximab for low-dose rate alpha-particle radioimmunotherapy. *Nucl Med Biol.* 2006;33:271–279.
23. Lindmo T, Boven E, Cuttitta F, Fedorko J, Bunn PA Jr. Determination of the immunoreactive fraction of radiolabeled monoclonal antibodies by linear extrapolation to binding at infinite antigen excess. *J Immunol Methods.* 1984;72:77–89.
24. Bateman H. The solution of a system of differential equations occurring in the theory of radioactive transformations. *Proc Camb Philos Soc.* 1910;15:423–427.
25. Tai Y-C, Ruangma A, Rowland D, et al. Performance evaluation of the microPET focus: a third-generation microPET scanner dedicated to animal imaging. *J Nucl Med.* 2005;46:455–463.
26. Dahle J, Borrebaek J, Jonasdottir TJ, et al. Targeted cancer therapy with a novel low-dose rate alpha-emitting radioimmunoconjugate. *Blood.* 2007;110:2049–2056.
27. Jiang W, Ulmert D, Simons BW, Abou DS, Thorek DLJ. The impact of age on radium-223 distribution and an evaluation of molecular imaging surrogates. *Nucl Med Biol.* 2018;62-63:1–8.
28. Andersson M, Johansson L, Eckerman K, Mattsson S. IDAC-Dose 2.1, an internal dosimetry program for diagnostic nuclear medicine based on the ICRP adult reference voxel phantoms. *EJNMMI Res.* 2017;7:88.
29. Stabin MG. Developments in the internal dosimetry of radiopharmaceuticals. *Radiat Prot Dosimetry.* 2003;105:575–580.
30. Sgouros G, Roeske JC, McDevitt MR, et al. MIRD pamphlet no. 22 (abridged): radiobiology and dosimetry of α-particle emitters for targeted radionuclide therapy. *J Nucl Med.* 2010;51:311–328.
31. Abou DS, Ku T, Smith-Jones PM. In vivo biodistribution and accumulation of ^{89}Zr in mice. *Nucl Med Biol.* 2011;38:675–681.
32. Economopoulos V, Noad JC, Krishnamoorthy S, Rutt BK, Foster PJ. Comparing the MRI appearance of the lymph nodes and spleen in wild-type and immunodeficient mouse strains. *PLoS One.* 2011;6:e27508.
33. Radchenko V, Morgenstern A, Jalilian AR, et al. Production and supply of α-particle-emitting radionuclides for targeted α-therapy. *J Nucl Med.* 2021;62:1495–1503.
34. Abou DS, Thiele NA, Gutsche NT, et al. Towards the stable chelation of radium for biomedical applications with an 18-membered macrocyclic ligand. *Chem Sci.* 2021;12:3733–3742.
35. Hagemann UB, Wickstroem K, Hammer S, et al. Advances in precision oncology: targeted thorium-227 conjugates as a new modality in targeted alpha therapy. *Cancer Biother Radiopharm.* 2020;35:497–510.
36. Lindén O, Bates AT, Cunningham D, et al. ^{227}Th-labeled anti-CD22 antibody (BAY 1862864) in relapsed/refractory CD22-positive non-Hodgkin lymphoma: a first-in-human, phase I study. *Cancer Biother Radiopharm.* 2021;36:672–681.
37. Ferrier MG, Li Y, Chyan M-K, et al. Thorium chelators for targeted alpha therapy: rapid chelation of thorium-226. *J Labelled Comp Radiopharm.* 2020;63:502–516.
38. Kent GT, Wu G, Hayton TW. Synthesis and crystallographic characterization of the tetravalent actinide-DOTA complexes [AnIV(κ8-DOTA)(DMSO)] (an = Th, U). *Inorg Chem.* 2019;58:8253–8256.
39. Larsen RH, Borrebaek J, Dahle J, et al. Preparation of TH227-labeled radioimmunoconjugates, assessment of serum stability and antigen binding ability. *Cancer Biother Radiopharm.* 2007;22:431–437.
40. Jacques V, Desreux JF. Complexation of thorium(IV) and uranium(IV) by a hexaacetic hexaaza macrocycle: kinetic and thermodynamic topomers of actinide chelates with a large cavity ligand. *Inorg Chem.* 1996;35:7205–7210.
41. Deal KA, Davis IA, Mirzadeh S, Kennel SJ, Brechbiel MW. Improved in vivo stability of actinium-225 macrocyclic complexes. *J Med Chem.* 1999;42:2988–2992.
42. Kennel SJ, Chappell LL, Dadachova K, et al. Evaluation of ^{225}Ac for vascular targeted radioimmunotherapy of lung tumors. *Cancer Biother Radiopharm.* 2000;15:235–244.
43. Heyerdahl H, Abbas N, Brevik EM, Mollatt C, Dahle J. Fractionated therapy of HER2-expressing breast and ovarian cancer xenografts in mice with targeted alpha emitting ^{227}Th-DOTA-p-benzyl-trastuzumab. *PLoS One.* 2012;7:e42345.
44. Raavé R, Sandker G, Adumeau P, et al. Direct comparison of the in vitro and in vivo stability of DFO, DFO* and DFOcyclo* for ^{89}Zr-immunoPET. *Eur J Nucl Med Mol Imaging.* 2019;46:1966–1977.
45. Foster A, Nigam S, Tatum DS, et al. Novel theranostic agent for PET imaging and targeted radiopharmaceutical therapy of tumour-infiltrating immune cells in glioma. *EBioMedicine.* 2021;71:103571.
46. Tatum D, Xu J, Magda D, Butlin N, inventors; Lumiphore Inc., assignee. Macrocyclic ligands with pendant chelating moieties and complexes thereof. U.S. patent 10239878B2. March 26, 2019.
47. Hasson A, Jiang W, Benabdallah N, et al. Radiochemical quality control methods for radium-223 and thorium-227 radiotherapies. *Cancer Biother Radiopharm.* 2023;38:15–25.
48. Abou DS, Rittenbach A, Tomlinson RE, et al. First whole-body three-dimensional tomographic imaging of alpha particle emitting radium-223. bioRxiv website. https://www.biorxiv.org/content/10.1101/414649v1.full. Published September 26, 2018. Accessed March 23, 2023.
49. Hagemann UB, Wickstroem K, Wang E, et al. In vitro and in vivo efficacy of a novel CD33-targeted thorium-227 conjugate for the treatment of acute myeloid leukemia. *Mol Cancer Ther.* 2016;15:2422–2431.

PSMA-GCK01: A Generator-Based ^{99m}Tc/^{188}Re Theranostic Ligand for the Prostate-Specific Membrane Antigen

Jens Cardinale*[1,2], Frederik L. Giesel*[1,2], Christina Wensky[1,3], Hendrik G. Rathke[1], Uwe Haberkorn[1,3], and Clemens Kratochwil[1]

[1]*Department of Nuclear Medicine, University Hospital Heidelberg, Heidelberg, Germany;* [2]*Department of Nuclear Medicine, Medical Faculty and University Hospital Duesseldorf, Heinrich Heine University Duesseldorf, Duesseldorf, Germany; and* [3]*Clinical Cooperation Unit Nuclear Medicine, German Cancer Research Center, Heidelberg, Germany*

Prostate-specific membrane antigen (PSMA) theranostics have been introduced with ^{68}Ga and ^{177}Lu, the most used radionuclides. However, ^{188}Re is a well-known generator-based therapeutic nuclide that completes a theranostic tandem with ^{99m}Tc and may offer an interesting alternative to the currently used radionuclides. In the present work, we aimed at the development of a PSMA-targeted ^{99m}Tc/^{188}Re theranostic tandem. **Methods:** The ligand HYNIC-iPSMA was chosen as the lead structure. Its HYNIC chelator has limitations for ^{188}Re labeling and was replaced by mercaptoacetyltriserine to obtain PSMA-GCK01, a precursor for stable ^{99m}Tc and ^{188}Re labeling. ^{99m}Tc-PSMA-GCK01 was used for in vitro evaluation of the ligand and comparison with ^{99m}Tc-EDDA/HYNIC-iPSMA. Planar imaging using ^{99m}Tc-PSMA-GCK01 and organ biodistribution with ^{188}Re-PSMA-GCK01 were performed using LNCaP tumor–bearing mice. Finally, the theranostic tandem was applied for imaging and therapy in 3 prostate cancer patients in compassionate care. **Results:** Efficient radiolabeling of PSMA-GCK01 with both radionuclides was demonstrated. Cell-based assays with ^{99m}Tc-PSMA-GCK01 versus ^{99m}Tc-EDDA/HYNIC-iPSMA revealed comparable uptake characteristics. Planar imaging and organ distribution revealed good tumor uptake of both ^{99m}Tc-PSMA-GCK01 and ^{188}Re-PSMA-GCK01 at 1 and 3 h after injection, with low uptake in nontarget organs. In patients, similar distribution patterns were observed for ^{99m}Tc-PSMA-GCK01 and ^{188}Re-PSMA-GCK01 and in comparison with ^{177}Lu-PSMA-617. **Conclusion:** The ligand PSMA-GCK01 labels stably with ^{99m}Tc and ^{188}Re, both generator-based radionuclides, and thus provides access to on-demand labeling at reasonable costs. Preclinical evaluation of the compounds revealed favorable characteristics of the PSMA-targeted theranostic tandem. This result was confirmed by successful translation into first-in-humans application.

Key Words: PSMA; ^{188}Re; ^{99m}Tc; theranostic; SPECT

J Nucl Med 2023; 64:1069–1075
DOI: 10.2967/jnumed.122.264944

The development of theranostics has dominated recent activities in the field of oncologic nuclear medicine. The most common theranostics are based on so-called matched pairs, in which the diagnostic and therapeutic radiopharmaceuticals are labeled with radionuclides from different elements. Sometimes, even different molecules are used. The only precondition is that both radiopharmaceuticals within the matched pair show a similar biodistribution (*1–3*).

A combination of nuclides using the same precursor that fulfills this demand is ^{99m}Tc with ^{188}Re (and ^{186}Re) (*4*). ^{99m}Tc is still one of the most widely used radionuclides worldwide, and rhenium (with its isotopes ^{186}Re and ^{188}Re) is the only element resembling its in vivo chemistry nearly perfectly. Moreover, both ^{99m}Tc and ^{188}Re are available from radionuclide generators, disclosing potential application in areas without strong nuclear infrastructure. Finally, ^{188}Re might help to surpass potential shortages in the supply of ^{177}Lu, which may arise from lack of high-flux neutron facilities (*5*). This renders ^{99m}Tc/^{188}Re-based theranostic radiopharmaceuticals an attractive combination, in particular for smaller hospitals using only SPECT in their nuclear medicine departments, as well as for application in developing countries (*6*). Another more current aspect underscores the need for SPECT-based prostate-specific membrane antigen (PSMA) imaging and therefore ^{99m}Tc-ligands: the patient selection for recently approved ^{177}Lu-PSMA-617 (Pluvicto; Advanced Accelerator Applications) affords confirmation of sufficient PSMA uptake in a preliminary diagnostic scan. For these mandatory diagnostic scans, current PET infrastructure may prove to be the bottleneck—a challenge that might be met by suitable SPECT ligands, including ligands developed primarily for diagnostic purposes, such as ^{99m}Tc-MIP-1404 (*7*) and ^{99m}Tc-EDDA/HYNIC-iPSMA (*8*).

The aim of this work was to develop a ^{99m}Tc/^{188}Re theranostic tandem targeting PSMA. The ligand HYNIC-iPSMA, which is already in an advanced clinical stage in its technetium-labeled form ^{99m}Tc-EDDA/HYNIC-iPSMA, was chosen as the lead structure (*8–10*). ^{99m}Tc is coordinated via the HYNIC chelator in ^{99m}Tc-EDDA/HYNIC-iPSMA. However, it is rather unlikely that HYNIC is a suitable chelator for ^{188}Re (*6*). Thus, we replaced the chelator in HYNIC-iPSMA with the more suitable mercaptoacetyltriserine, a classical N_3S chelator suitable for ^{188}Re coordination (Fig. 1) (*11,12*). In the following, we provide a summary of our research results thus far, including first-in-humans application under compassionate use.

MATERIALS AND METHODS

General

Precursor was synthesized using well-known standard methods as described in the supplemental materials (supplemental materials are

Received Sep. 19, 2022; revision accepted Feb. 2, 2023.
For correspondence or reprints, contact Jens Cardinale (jens.cardinale@med.uni-duesseldorf.de).
*Contributed equally to this work.
Published online Feb. 9, 2023.

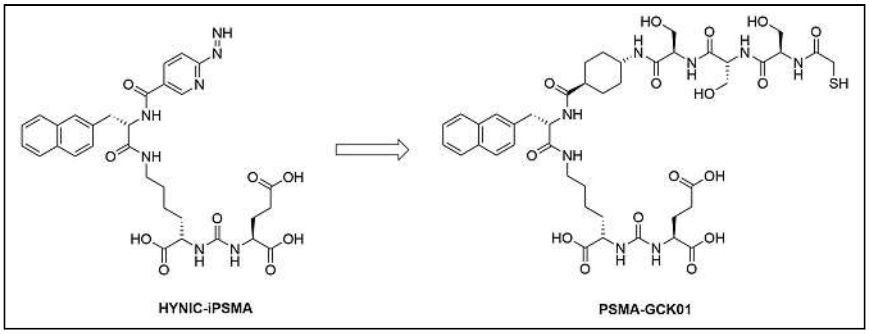

FIGURE 1. Structures of HYNIC-iPSMA and PSMA-GCK01.

available at http://jnm.snmjournals.org) (*13,14*). The $SnCl_2$ for rhenium reduction was trace metal–based and acquired from Merck. The remaining chemicals for tracer synthesis were all of European Pharmacopoeia or *ad injectabilia* grade and acquired from Merck or B. Braun. Waters Sep-Pak Alumina N Light cartridges, Sep-Pak Accell Plus QMA Plus Light cartridges, and Sep-Pak tC18 Plus Light cartridges were purchased from Macherey and Nagel. Dionex OnGuard II Ag cartridges were purchased from Thermo Fischer.

^{99m}Tc was obtained from a TekCis generator (Curium) in the form of ^{99m}Tc-$NaTcO_4$ in 0.9% saline, according to the manufacturer instructions. ^{188}Re was obtained in the form of ^{188}Re-$NaReO_4$ from a ^{188}W/^{188}Re tandem generator (OnkoBeta) by elution with 10 mL of 0.9% saline (B. Braun). ^{99m}Tc-EDDA/HYNIC-iPSMA was produced from commercial kits according to the instructions. The reagent kits were acquired from Telix Pharmaceuticals.

Chemistry and Radiochemistry

^{99m}Tc Labeling of PSMA-GCK01. Phosphate buffer for labeling was prepared from 890 mg of $Na_2PO_4{\cdot}2H_2O$ in 9.5 mL of water for injection and 0.5 mL of 2 M NaOH (pH 11.5–12.0). For ^{99m}Tc labeling, 500–800 μL of pertechnetate solution (1.5–2.5 GBq/mL in 0.9% saline) were mixed with 200 μL of phosphate buffer, 100 μL of tris(2-carboxyethyl)phosphine (28.9 mg/mL in phosphate buffer), and a 20-μL precursor solution (1 mg/mL). The resulting mixture (pH 8.0–8.5) was heated at 98°C for 10 min. The mixture was diluted with approximately 1 mL of 0.9% saline and passed through a C18 cartridge (a Sep-Pak tC18 Plus Light cartridge preconditioned with 5 mL of ethanol, followed by 10 mL of water). The product was eluted with 1 mL of 70% ethanol and diluted with 9 mL of phosphate-buffered saline (PBS), prepared from 9 mL of 0.9% saline and 1 mL of phosphate buffer concentrate, both *ad injectabilia* (B. Braun). Finally, the product was passed through a 0.22-μm sterile filter. Samples of the reaction mixture—withdrawn directly after the reaction, after cartridge separation (but before dilution with PBS)—and of the final product formulation were analyzed by reverse-phase high-performance liquid chromatography (HPLC).

^{188}Re Labeling of PSMA-GCK01. ^{188}Re was eluted from the ^{188}W/^{188}Re tandem generator using 10 mL of 0.9% NaCl. The eluate was postprocessed according to Guhlke et al. (*15*). Potential tungsten breakthrough was retained on a Sep-Pak Alumina N cartridge. The eluate was dechlorinated using a Dionex OnGuard II Ag cartridge, and the perrhenate was concentrated using a Sep-Pak QMA cartridge, preconditioned with 5 mL of 1 M K_2CO_3, followed by 10 mL of deionized water. The perrhenate was eluted from the QMA cartridge using 1 mL of 0.9% NaCl (B. Braun).

A typical ^{188}Re-labeling mixture consisted of 120 μL of citrate solution (100 mg/mL), 80 μL of GCK01 precursor solution (1 mg/mL in MeCN/H_2O 50:50 v/v), 40 μL of 30% ascorbic acid solution (in water), 800 μL of perrhenate in 0.9% NaCl (postprocessed as described earlier at 6–12 GBq), and 48 μL of $SnCl_2$ (50 mg/mL in 1 M HCl). The mixture was usually pH 2.0–3.5. The mixture was heated at 96°C for 60 min. After being cooled to ambient temperature, the mixture was neutralized to pH 7.5 using 0.5 M sodium phosphate, heated for an additional 5 min at 96°C, diluted with 1 mL of 0.9% NaCl, and passed through a Sep-Pak tC18 Plus Light cartridge (preconditioned with 5 mL of ethanol and 10 mL of water). The cartridge was washed with 2–3 mL of 0.9% NaCl, and the product was eluted with 1 mL of 70% ethanol. The solution containing the product was diluted 1:9 into PBS, prepared from 9 mL of 0.9% NaCl and 1 mL of sodium phosphate concentrate, both *ad injectabilia* (B. Braun), containing 2% sodium ascorbate solution. The radiochemical yield was determined by division of the isolated product activity by the starting activity. The radiochemical purity was determined by radio-HPLC for the isolated product (after cartridge separation and formulation).

Preclinical Evaluation

In Vitro and Toxicologic Evaluation of the ^{99m}Tc-/^{188}Re-PSMA-GCK01 Tandem. The evaluation was conducted using well-known standard methods (*16,17*). Detailed information is provided in the supplemental materials.

Cellular uptake experiments were conducted in analogy to a previously described procedure (*16*). A detailed description is provided in the supplemental materials.

In Vivo and Organ Distribution Experiments. All animal experiments were conducted in compliance with the current laws of the Federal Republic of Germany (animal license 35-9185.81/G-127/(18)). For in vivo planar imaging and organ distribution experiments, 8-wk-old BALB/c *nu/nu* mice (male) were subcutaneously inoculated in the left shoulder with 6 million LNCaP cells in 50% Matrigel (Corning) in Opti-MEM I medium. The studies were performed when the tumor size reached approximately 1 cm^3 (8–12 wk after inoculation). Mean body weight was 23 ± 2 g on the day of investigation.

In Vivo Planar Imaging. For the in vivo planar imaging, 100 μL of a formulation containing 5–10 MBq of ^{99m}Tc-labeled compound in PBS containing ~0.1 μg precursor (1 nM, 5–10 MBq/nmol) was injected into the tail vein of a LNCaP tumor–bearing mouse (n = 1). The animal was anesthetized with isoflurane (AbbVie Deutschland GmbH) and placed prone on a γ-imager (S/C) for planar imaging (using γ-acquisition and GammaVision+ (Biospace Mesures) software). The scan was started directly after administration of the activity, and the mouse was scanned for 10 min. The scan was repeated after 30, 90, and 180 min and 24 h. An activity standard (~1 MBq of the respective tracer) was prepared in a closed HPLC sample flask and placed next to the animal during all time points of the measurement.

Ex Vivo Organ Distribution with ^{188}Re-PSMA-GCK01. For ex vivo biodistribution, LNCaP tumor–bearing mice were injected with 100 μL of a PBS formulation containing approximately 1 MBq of ^{188}Re-PSMA-GCK01 (~0.1 μg of precursor or 1 μg of precursor per milliliter). The animals were killed by CO_2 asphyxiation 1 and 3 h after injection, respectively. Organs of interest were dissected, blotted dry, and weighed, and the radioactivity was determined on a γ-counter (Packard Cobra II; GMI) and calculated as percentage injected dose (%ID) per gram.

Clinical Imaging and Therapy

After giving written informed consent, 3 patients with metastatic castration-resistant prostate cancer received PSMA-radioligand therapy (RLT) and the related companion diagnostic under compassionate-care regulations. Prospective clinical trial registration is not required for compassionate care that is performed under an individual medical indication.

The ethical committee of the University Hospital Heidelberg approved the retrospective evaluation (permission S-732/18). The patients were Gleason score 9 (n = 2) or 10 (n = 1), and all cases were metastatic to lymph nodes and bone but without visceral lesions All patients had previously received standard androgen-deprivation therapy, abiraterone, prednisolone, docetaxel; 2 patients had additionally received enzalutamide, 1 patient had also received apalutamide, and 2 patients had additionally received cabazitaxel. All cases were BRCA1/2 wild-type and naïve to poly(adenosine diphosphate ribose) polymerase inhibitors, and none of the patients was a promising candidate for $^{223}RaCl_2$ (low uptake in bone scan or bulky lymph nodes). One patient had previously received ipilimumab with nivolumab and 2 cycles of ^{177}Lu-PSMA-617; the other 2 patients were ^{177}Lu-PSMA–naïve.

To demonstrate target-positive disease, a diagnostic scan was performed about 1 wk in advance of therapy using 600 MBq of ^{99m}Tc-PSMA-GCK01 (molar activity, 75–125 MBq/nmol), and images were acquired 2–4 h after injection with an low-energy, high-resolution collimator at a 140-keV (±10%) photopeak (18 cm/min; E.Cam [Siemens]). At day 1 of therapy, 3.7 GBq of ^{188}Re-PSMA-GCK01 (molar activity, 56–112 MBq/nmol) were administered, followed by serial planar scans (20 min to 48 h as clinically available) centered at the 155-keV (±10%) photopeak but with a high-energy collimator because of downscatter of up to 2.12-MeV bremsstrahlung (E.Cam [Siemens], 18 cm/min). After 1–2 d (~2–3 physical half-lives of ^{188}Re), when septum penetration of bremsstrahlung became negligible, 3.7 GBq of ^{177}Lu-PSMA-617 were injected and serial images were acquired with a medium-energy collimator; to avoid cross-talk with the primary 155-keV photons of ^{188}Re, only the upper photopeak of ^{177}Lu at 210 keV (±10%) was used. Dual-photopeak imaging within such a short time enables intraindividual comparison of 2 therapeutic ligands, even though relevant treatment-related effects have yet to be considered. The timeline of imaging time points is illustrated in Figure 2. However, under these circumstances, no scatter-subtraction techniques could be applied to obtain sufficient quantitative data.

RESULTS

Chemistry and Radiochemistry

Precursor. The identity of the precursor was confirmed by HPLC–mass spectrometry: m/z = 977.386 (calculated m/z ($[M+H^+]^+$) = 977.392) and m/z = 999.367 (calculated m/z ($[M+Na^+]^+$) = 999.374). The purity was analyzed by HPLC and was more than 95%. The only detectable impurity was the oxidized disulfide. Details are provided in Supplemental Figures 1–3.

^{99m}Tc-PSMA-GCK01. The radiosynthesis of ^{99m}Tc-PSMA-GCK01 reliably delivered the product in radiochemical yields of 81% ± 3% and purities above 97.8% ± 0.7% after cartridge separation (n = 8). Molar activity was in the range of 75–125 MBq/nmol. Residual tris(2-carboxyethyl)phosphine was removed quantitatively by cartridge separation. No signs of degradation were observed over a period of 7 h. Details are provided in Supplemental Figures 4 and 5.

^{188}Re-PSMA-GCK01. After ^{188}Re postprocessing, approximately 79% ± 6% of the total activity was retrieved in 1 mL of saline without detectable ^{188}W breakthrough (n = 9). Subsequent labeling yielded ^{188}Re-PSMA-GCK01 in radiochemical yields of 78% ± 3% and with a radiochemical purity of more than 96% ± 3% (n = 6). Molar activity was in the range of 56–112 MBq/nmol. Only minor signs of degradation were observed after 3 h (~3% degradation of radiochemical purity). Details are provided in Supplemental Figure 6.

Preclinical Evaluation

In Vitro Evaluation. The binding characteristics of PSMA-GCK01 and HYNIC-iPSMA were evaluated with the respective ^{99m}Tc-labeled tracers; the results are summarized in Table 1. ^{99m}Tc-PSMA-GCK01 showed plasma protein binding of 98%. The radiochemical purity of the free fraction showed no signs of degradation over 4 h (by repetitive HPLC measurements; Supplemental Fig. 7).

In Vivo and Organ Distribution Experiments. The images acquired by in vivo planar imaging are shown in Figure 3. Region-of-interest analysis and standardization on the internal standard provided a rough estimation of the observed uptake values of ^{99m}Tc-PSMA-GCK01.

The results of the organ distribution of ^{188}Re-PSMA-GCK01 are depicted in Figure 4. The tumor uptake of the ligand is approximately 5 %ID/g at 1 h after injection, rising to approximately 11 %ID/g at 3 h after injection. In addition, the ligand showed an uptake of 70 %ID/g (1 h after injection) and 91 %ID/g (3 h after injection) in kidneys and 11 %ID/g (1 h after injection) and approximately 4 %ID/g (3 h after injection) in the spleen. Moreover, renal excretion is reflected by urine uptake of 36 %ID/g (1 h after injection) and 71 %ID/g (3 h after injection). All further organs showed only minor tracer uptake. Detailed results are provided in the supplemental materials.

Toxicologic Investigation. No test article–related mortality was observed. No differences in organ weights or macroscopic observations were seen at terminal or recovery euthanasia.

Clinical Imaging and Therapy

In the 3 compassionate-care patients, no acute adverse events were observed after injection of ^{99m}Tc-PSMA-GCK01 or ^{188}Re-PSMA-GCK01. Visually, the gross biodistribution of diagnostic ^{99m}Tc-PSMA-GCK01 was similar to that of all other low-molecular-weight scintigraphic PSMA ligands that had been developed previously (Fig. 5A), with combined renal and hepatointestinal clearance, nontarget accumulation in salivary glands, and a low perfusion-dependent background in the remaining organs (*8,9,18,19*). Monoenergetic, 140-keV, pure γ-emitting ^{99m}Tc-PSMA-GCK01 was imaged with a low-energy, high-resolution collimator, but ^{188}Re-PSMA-GCK01 had to be measured with a high-energy collimator to cope with the high level of scatter and bremsstrahlung (up to 2.12 MeV) in relation to the only 15% coemission probability of 155-keV photons. Considering these limitations, the tagged radionuclide had no obvious influence on

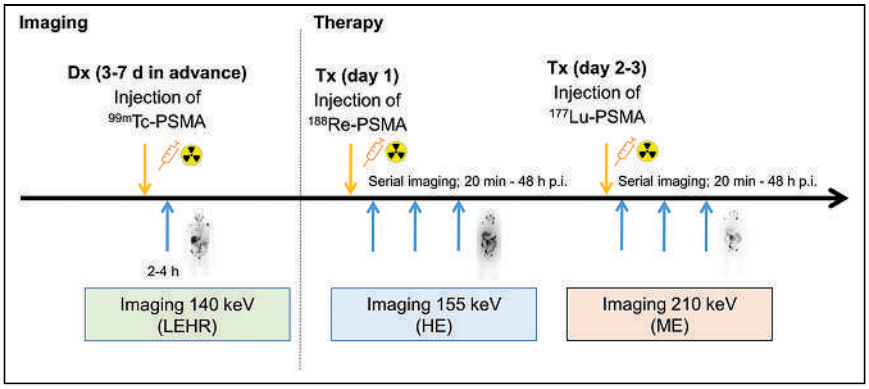

FIGURE 2. Dual-photopeak imaging for intraindividual comparison of Re-PSMA-GCK01 vs. Lu-PSMA-617 pharmacokinetics. Dx = diagnosis; HE = high-energy; LEHR = low-energy high-resolution; ME = medium-energy; p.i. = after injection; Tx = treatment;

TABLE 1
Binding Characteristics of ^{99m}Tc-EDDA/HYNIC-iPSMA and ^{99m}Tc-PSMA-GCK01

Substance	Uptake (%AD/10^6 cells)	Unspecific uptake (%AD/10^6 cells)	Specific uptake (%AD/10^6 cells)	K_i (nm)
^{99m}Tc-EDDA/HYNIC-iPSMA (reference compound)	20.3 ± 0.3	1.64 ± 0.07	18.7 ± 0.3	38
^{99m}Tc-PSMA-GCK01	19.6 ± 4.8	1.2 ± 0.6	18.4 ± 4.2	26

%AD = Applied dose; K_i = inhibition constant.

biodistribution 2–4 h after injection (Fig. 5). Already 20 min after injection, the intensity of tumor targeting exceeded the intravascular blood pool and delineation of the bladder demonstrated moderate clearance kinetics. Late images beyond 20 h after injection demonstrated prolonged trapping in tumor lesions, additional hepatobiliary clearance into the intestine, and low residual uptake in other organs (Fig. 5B); thus, to some degree, PSMA-GCK01 has tumor accumulation and excretion kinetics similar to those of other Glu-urea–based PSMA ligands, such as MIP-1095, PSMA-617, or PSMA-I&T (*20–22*).

Using the distinct photopeaks of ^{188}Re at 155 keV, followed 48 h later by ^{177}Lu imaged at 210 keV, an intraindividual comparison between ^{188}Re-PSMA-GCK01 and ^{177}Lu-PSMA-617 within a 2-d interval is demonstrated in Figure 6. Although tumor targeting is almost equal at 20–24 and 44–48 h after injection, PSMA-GCK01 initially demonstrates a higher liver-to-kidney uptake ratio, which translates into better delineation of the intestine 48 h after injection, possibly implying a slight shift from renal to hepatointestinal clearance for PSMA-GCK01 compared with PSMA-617.

DISCUSSION

The focus of our investigation was the development of a PSMA ligand suitable for ^{99m}Tc and ^{188}Re labeling based on the HYNIC-iPSMA lead structure. Because the suitability of HYNIC for ^{188}Re labeling has been controversial (*6*), we replaced the HYNIC unit with a similar-in-size spacer, linked to the mercaptoacetyltriserine sequence as a favorable chelator for radiolabeling with both ^{99m}Tc and ^{188}Re (Fig. 1). The precursor synthesis was obtained in high purity of more than 95%. The only detectable impurity was the oxidized disulfide derivate (Supplemental Figs. 2 and 3), which is reduced to the desired precursor under the reductive labeling conditions.

Technetium labeling using tris(2-carboxyethyl)phosphine as the reducing agent delivered the product ^{99m}Tc-PSMA-GCK01 in high and reproducible yields and purities. In general, the radiochemical purity would allow direct application of the product mixture containing the tracer. However, for clinical formulation, we applied cartridge separation of the tracer to remove residual tris(2-carboxyethyl)phosphine, which was confirmed by HPLC analysis (Supplemental Fig. 5). The reducing agent may impose a potential limitation. For broader application, a kit should be developed using the more commonly applied $SnCl_2$ as the reducing agent.

In the case of ^{188}Re labeling, the desired ^{188}Re-PSMA-GCK01 was produced in yields of approximately 75% (isolated after synthesis and purification) using relatively harsh conditions (low pH). The results agree well with previous reports on such reactions (*23*). However, under these conditions, the product is formed in 2 stereoisomers (Supplemental Fig. 6). We eventually converted the undesired isomer by terminal pH elevation to pH 7.0–7.5 and a short additional heating period. In the case of ^{99m}Tc labeling, the pH was sufficiently high to suppress formation of the isomer. Thus, because no isomer formation was observed in the stable plasma of ^{99m}Tc-PSMA-GCK01, we do not consider the potential isomer formation to be a drawback.

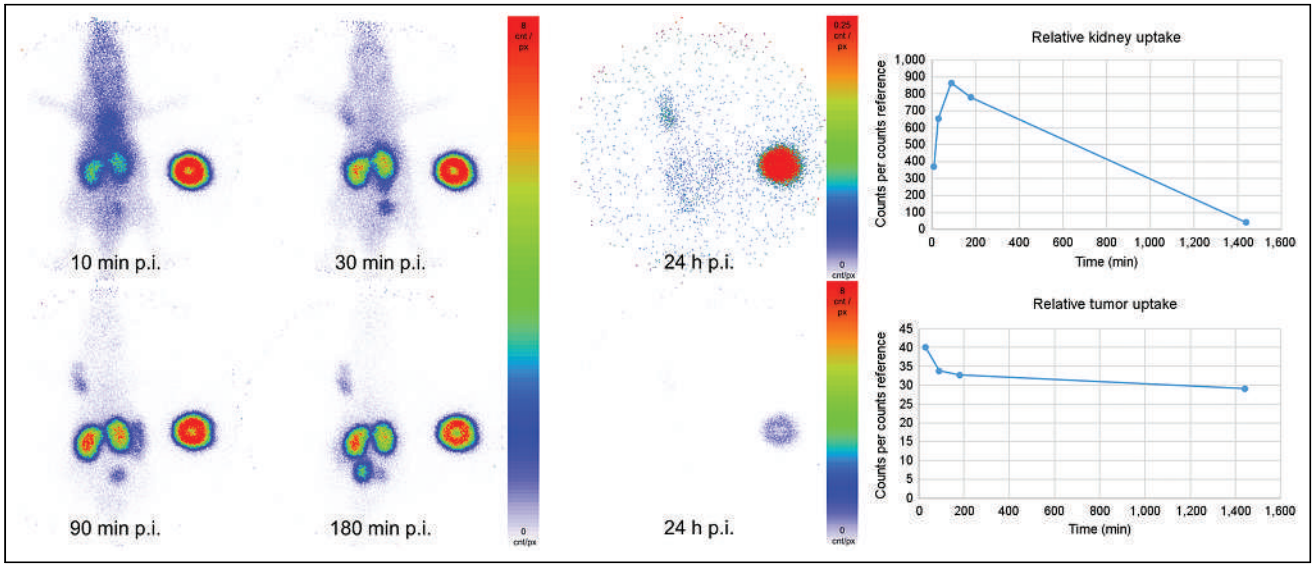

FIGURE 3. Planar imaging of ^{99m}Tc-PSMA-GCK01 in LNCaP tumor–bearing mouse. Red spot at right side is internal standard. p.i. = after injection.

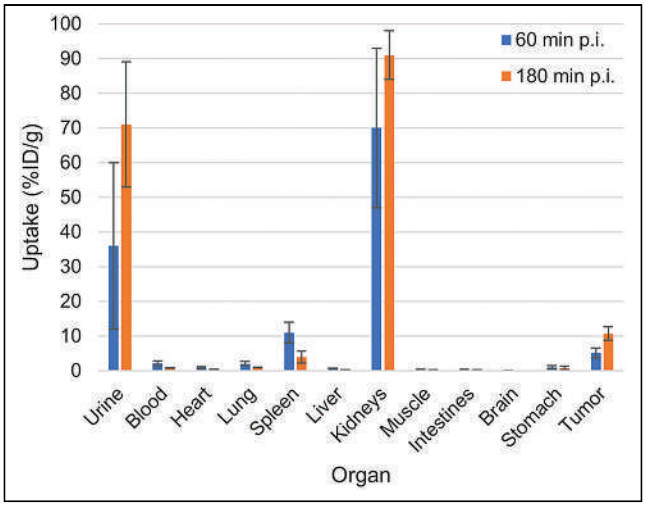

FIGURE 4. Organ distribution of approximately 1 MBq of ^{188}Re-PSMA-GCK01 in LNCaP tumor–bearing mice (3 per time point). Exact values are provided in Supplemental Table 1. p.i. = after injection.

For the preclinical evaluation, we first compared our ligand ^{99m}Tc-PSMA-GCK01 with ^{99m}Tc-EDDA/HYNIC-iPSMA in a cell-based assay. Both compounds showed a comparable and specific uptake in LNCaP cells. A further displacement experiment with ^{99m}Tc-PSMA-GCK01 also revealed a comparable inhibition constant of 26 nM (vs. 38 nM for ^{99m}Tc-EDDA/HYNIC-iPSMA). The ligand showed relatively high plasma protein binding of 98%. However, for other PSMA ligands, it is known that high plasma protein binding does not necessarily impose a problem for clinical application. Recently, even dedicated albumin-binding motifs have been suggested as an improvement when PSMA ligands should be labeled with long physical half-life nuclides (*24,25*). More importantly, the free fraction in plasma did not show signs of decomposition over a period of 4 h. Unfortunately, we were not able to confirm this for the rhenium theranostic tandem ^{188}Re-PSMA-GCK01 because of an insufficient count rate (only 15.5% probability of 155-keV emissions) in the respective HPLC samples. Hence, we decided to evaluate our ligands in a suitable animal model. In planar imaging with ^{99m}Tc-PSMA-GCK01, the ligand presents promising tumor uptake and retention in the LNCaP xenotransplant and moderate renal clearance, according to semiquantitative region-of-interest analysis. Quantitative data were obtained by further organ distribution experiments with the rhenium analog ^{188}Re-PSMA-GCK01. As expected, the results reflected the planar imaging quite well. Already at 1 h after injection, we observed intense tumor uptake, reaching approximately 11 %ID/g at 3 h after injection. In mouse-only renal clearance, minimal uptake in the liver was observed. However, it was already reported for PSMA-617 that renal versus hepatointestinal clearance is not comparable between animal studies and human application (*14,26*).

Preclinically, we achieved our goal to develop a promising PSMA ligand for labeling with both ^{99m}Tc and ^{188}Re for theranostic application. Potential limitations of the current preclinical study are the lack of a late time point (e.g., 24 or 48 h) in organ distribution and the lack of a histopathologic evaluation of eventual radiation-induced kidney toxicity from ^{188}Re-PSMA-GCK01 in mice. However, a dedicated clinical dosimetry study is already in preparation (including initial extrapolation from ^{99m}Tc-PSMA-GCK01 to ^{188}Re-PSMA-GCK01) and will probably be more predictive than the mouse-to-human extrapolation that is otherwise needed for nonradioactive therapies. Another potential limitation is the lack of ^{99m}Tc-PSMA-GCK01 organ distribution data. We considered these data to be facultative because the analogy of ^{99m}Tc/^{188}Re tandem radiopharmaceuticals is widely accepted (*4*). Consequently, we preferred to reduce our demand for laboratory animals.

Toxicologic investigation of PSMA-GCK01 according to the current Organisation for Economic Co-operation and Development guideline was ordered by a third-party preclinical research organization and revealed no toxicologic effect up to 2 mg/kg in mice. On the basis of these data, we conclude that PSMA-GCK01 has a good safety profile and that application of up to a 2 μg/kg dose of PSMA-GCK01 in humans will likely be well tolerated.

During compassionate use, the promising tumor targeting and acceptable fast clearance kinetics were confirmed in humans. Dual-photopeak imaging enabled intraindividual comparison with the current standard-of-reference compound ^{177}Lu-PSMA-617. Our preliminary investigation suggests that ^{188}Re-PSMA-GCK01 and ^{177}Lu-PSMA-617 share the combined renal and hepatointestinal clearance route and a relatively similar biodistribution between 2 and 20 h after injection. However, using a double-isotope imaging protocol, we could not yet approximate a quantitatively reliable treatment dosimetry. Nevertheless, the ligands offer some promising benefits.

One of these benefits is that the availability of a completely generator-based theranostic tandem to available ligands will help facilitate PSMA-RLT, particularly in countries or regions with a less developed nuclear medicine infrastructure, and may help reduce the cost of PSMA-RLT. Another benefit is that $^{188(/186)}$Re-PSMA-RLT might amend ^{177}Lu-PSMA-RLT in a mixed nuclide therapy, with the potential of offering an additional mean β-emission energy

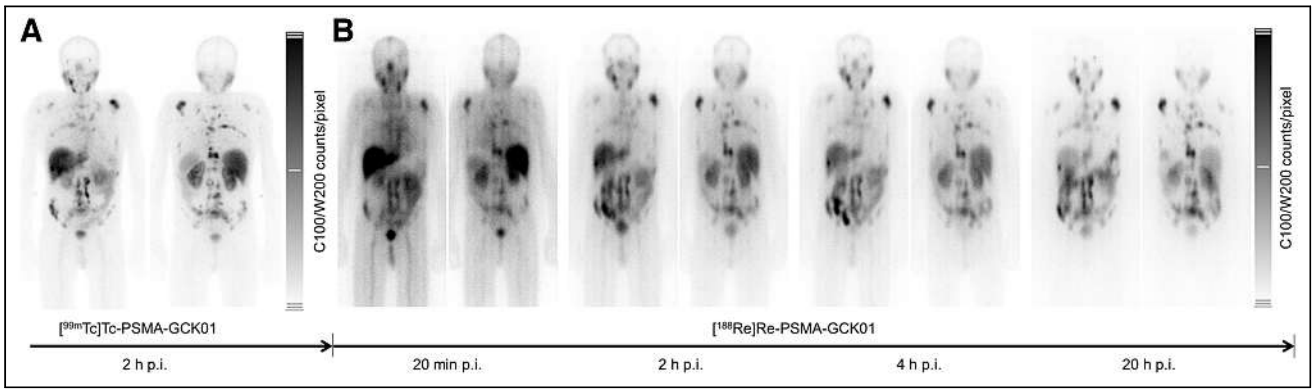

FIGURE 5. ^{188}Re-GCK01 photopeak (sequential imaging). p.i. = after injection.

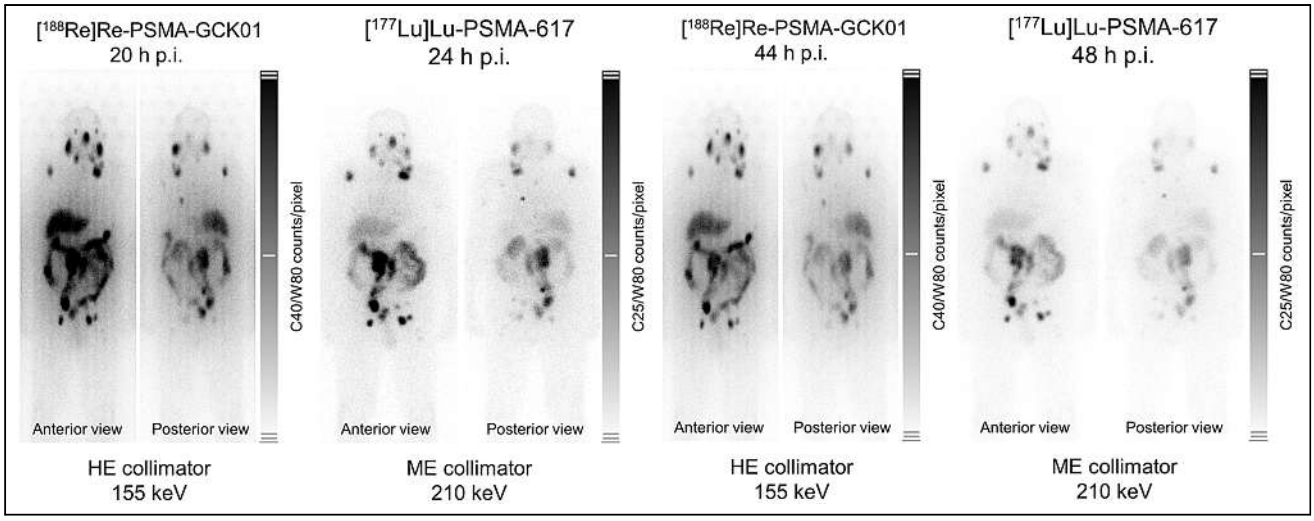

FIGURE 6. Intraindividual comparison of 3.7 GBq of Lu-PSMA-617 and 3.7 GBq of Re-PSMA-GCK01 at 20–24 and 44–48 h after injection, respectively. HE = high-energy; ME = medium-energy; p.i. = after injection.

profile (^{188}Re, 765 keV; ^{186}Re, 347 keV; ^{177}Lu, 133 keV) and improving therapy of bulk lesions (*27,28*). A third benefit is that shorter-half-life and lower-energy γ-emissions (^{188}Re, 16.9 h and 155 keV [15%]; ^{186}Re, 3.7 d and 137 keV [9%]; and ^{177}Lu, 6.7 d and 113 keV [6%] and 208 keV [10%], respectively) may enable therapy in an outpatient setting, eventually helping to circumvent the expected bottleneck in bed capacity of existing nuclear medicine departments after ^{177}Lu-PSMA-617 (half-life, 6.7 d) approval (*29*).

In summary, we consider the tandem PSMA ligands ^{99m}Tc-/^{188}Re-PSMA-GCK01 to form a versatile and promising supplement in the available PSMA ligand landscape. In particular, the broad availability of different therapeutic nuclides may lead to interesting synergetic effects that cannot yet be predicted. A phase 1 and 2 clinical trial with the ligands, including a dosimetry study, is in preparation. The additional potential that may arise from the ligand ^{186}Re-GCK01 is still to be disclosed.

CONCLUSION

PSMA-GCK01 is characterized by robust labeling with both radionuclides of the ^{99m}Tc-/^{188}Re-PSMA-GCK01 theranostic tandem; hence, they can be produced in high radiochemical yields using standard methodologies. Preliminary experiences in patients with metastatic castration-resistant prostate cancer were promising. Thus, further investigation of the ^{99m}Tc-/^{188}Re-PSMA-GCK01 tandem in a prospective phase 1 trial has already been initiated.

DISCLOSURE

This project was supported by a research grant from Telix Pharmaceuticals. The toxicologic study at Agilex Biolabs was sponsored by Telix Pharmaceuticals. Frederik Giesel is an advisor at ABX Radiopharmaceuticals, SOFIE Biosciences, Telix Pharmaceuticals, and α-Fusion. Frederik Giesel, Clemens Kratochwil, Uwe Haberkorn, and Jens Cardinale hold a patent application on PSMA-GCK01. No other potential conflict of interest relevant to this article was reported.

ACKNOWLEDGMENTS

We thank the working group Haberkorn at Otto-Meyerhof-Zentrum Heidelberg—in particular, Annette Altmann, Marlene Tesch, and Vanessa Kohl—for conducting the preclinical investigations. We thank Drs. Alesia Ivashkevich and Michael Wheatcroft for their support and assistance with the toxicologic study.

KEY POINTS

QUESTION: Can we prepare a PSMA ligand suitable for ^{99m}Tc and ^{188}Re labeling with HYNIC-iPSMA as the lead structure?

PERTINENT FINDINGS: An exchange of the chelator moiety to mercaptoacetyltriserine yielded PSMA-GCK01, a ligand suitable for ^{99m}Tc and ^{188}Re labeling that maintains the good binding characteristics of HYNIC-iPSMA.

IMPLICATIONS FOR PATIENT CARE: PSMA-GCK01 offers a suitable platform for the decentralized production of the theranostic tandem for prostate cancer patients. In particular, it provides the basis for diagnosis of prostate cancer in smaller nuclear medical centers limited to SPECT, and it may help to circumvent potential bottlenecks in the ^{177}Lu supply chain.

REFERENCES

1. Herrmann K, Schwaiger M, Lewis JS, et al. Radiotheranostics: a roadmap for future development. *Lancet Oncol.* 2020;21:e146–e156.
2. Barca C, Griessinger CM, Faust A, et al. Expanding theranostic radiopharmaceuticals for tumor diagnosis and therapy. *Pharmaceuticals (Basel).* 2021;15:13.
3. Solnes LB, Werner RA, Jones KM, et al. Theranostics: leveraging molecular imaging and therapy to impact patient management and secure the future of nuclear medicine. *J Nucl Med.* 2020;61:311–318.
4. Lepareur N, Lacoeuille F, Bouvry C, et al. Rhenium-188 labeled radiopharmaceuticals: current applications in oncology and promising perspectives. *Front Med (Lausanne).* 2019;6:132.
5. Vogel WV, van der Marck SC, Versleijen MWJ. Challenges and future options for the production of lutetium-177. *Eur J Nucl Med Mol Imaging.* 2021;48:2329–2335.
6. Blower PJ. Rhenium-188 radiochemistry: challenges and prospects. *Int J Nucl Med Res.* 2017:39–53.
7. Hillier SM, Maresca KP, Lu G, et al. ^{99m}Tc-labeled small-molecule inhibitors of prostate-specific membrane antigen for molecular imaging of prostate cancer. *J Nucl Med.* 2013;54:1369–1376.
8. García-Pérez FO, Davanzo J, López-Buenrostro S, et al. Head to head comparison performance of ^{99m}Tc-EDDA/HYNIC-iPSMA SPECT/CT and ^{68}Ga-PSMA-11

PET/CT a prospective study in biochemical recurrence prostate cancer patients. *Am J Nucl Med Mol Imaging.* 2018;8:332–340.
9. Ferro-Flores G, Luna-Gutiérrez M, Ocampo-García B, et al. Clinical translation of a PSMA inhibitor for ^{99m}Tc-based SPECT. *Nucl Med Biol.* 2017;48:36–44.
10. Santos-Cuevas C, Davanzo J, Ferro-Flores G, et al. ^{99m}Tc-labeled PSMA inhibitor and radiation dosimetry in healthy subjects and imaging of prostate cancer tumors in patients. *Nucl Med Biol.* 2017;52:1–6.
11. Chang F, Ruschkowski M, Qu T, Hnatowich DJ. Early results of the irrational design of new bifunctional chelators. *Cancer.* 1997;80(suppl 12):2347–2353.
12. Chang F, Qu T, Ruschkowski M, Hnatowich DJ. NHS-MAS_3: a bifunctional chelator alternative to NHS-MAG_3. *Appl Radiat Isot.* 1999;50:723–732.
13. Eder M, Schäfer M, Bauder-Wüst U, et al. ^{68}Ga-complex lipophilicity and the targeting property of the urea-based PSMA inhibitor for PET imaging. *Bioconjug Chem.* 2012;23:688–697.
14. Benešová M, Schäfer M, Bauder-Wüst U, et al. Preclinical evaluation of a tailor made DOTA-conjugated PSMA inhibitor with optimized linker moiety for imaging and endoradiotherapy of prostate cancer. *J Nucl Med.* 2015;56:914–920.
15. Guhlke S, Beets AL, Oetjen K, Mirzadeh S, Biersack H-J, Knapp FF. Simple new method for effective concentration of ^{188}Re solutions from alumina-based ^{188}W-^{188}Re generator. *J Nucl Med.* 2000;41:1271–1278.
16. Lindner T, Loktev A, Altmann A, et al. Development of quinoline-based theranostic ligands for the targeting of fibroblast activation protein. *J Nucl Med.* 2018;59:1415–1422.
17. Test no. 407: repeated dose 28-day oral toxicity study in rodents. Organisation for Economic Co-operation and Development iLibrary website. https://doi.org/10.1787/9789264070684-en. Accessed March 28, 2023.
18. Vallabhajosula S, Nikolopoulou A, Babich JW, et al. ^{99m}Tc-labeled small-molecule inhibitors of prostate-specific membrane antigen: pharmacokinetics and biodistribution studies in healthy subjects and patients with metastatic prostate cancer. *J Nucl Med.* 2014;55:1791–1798.
19. Urbán S, Meyer C, Dahlbom M, et al. Radiation dosimetry of ^{99m}Tc-PSMA-I&S: a single-center study. *J Nucl Med.* 2021;62:1075–1081.
20. Zechmann CM, Afshar-Oromieh A, Amor T, et al. Radiation dosimetry and first therapy results with a ^{124}I/^{131}I-labeled small molecule (MIP-1095) targeting PSMA for prostate cancer therapy. *Eur J Nucl Med Mol Imaging.* 2014;41:1280–1292.
21. Kratochwil C, Giesel FL, Stefanova M, et al. PSMA-targeted radionuclide therapy of metastatic castration-resistant prostate cancer with ^{177}Lu-labeled PSMA-617. *J Nucl Med.* 2016;57:1170–1176.
22. Weineisen M, Schottelius M, Simecek J, et al. ^{68}Ga- and ^{177}Lu-labeled PSMA I&T: optimization of a PSMA-targeted theranostic concept and first proof-of-concept human studies. *J Nucl Med.* 2015;56:1169–1176.
23. Guhlke S, Schaffland A, Zamora PO, et al. ^{188}Re- and ^{99m}Tc-MAG_3 as prosthetic groups for labeling amines and peptides: approaches with pre- and postconjugate labeling. *Nucl Med Biol.* 1998;25:621–631.
24. Benešová M, Umbricht CA, Schibli R, Müller C. Albumin-binding PSMA ligands: optimization of the tissue distribution profile. *Mol Pharm.* 2018;15:934–946.
25. Kelly JM, Amor-Coarasa A, Ponalla S, et al. Albumin-binding PSMA ligands: implications for expanding the therapeutic window. *J Nucl Med.* 2019;60:656–663.
26. Kabasakal L, AbuQbeitah M, Aygün A, et al. Pre-therapeutic dosimetry of normal organs and tissues of ^{177}Lu-PSMA-617 prostate-specific membrane antigen (PSMA) inhibitor in patients with castration-resistant prostate cancer. *Eur J Nucl Med Mol Imaging.* 2015;42:1976–1983.
27. O'Donoghue JA, Bardiès M, Wheldon TE. Relationships between tumor size and curability for uniformly targeted therapy with beta-emitting radionuclides. *J Nucl Med.* 1995;36:1902–1909.
28. Strosberg J, Kunz PL, Hendifar A, et al. Impact of liver tumour burden, alkaline phosphatase elevation, and target lesion size on treatment outcomes with ^{177}Lu-Dotatate: an analysis of the NETTER-1 study. *Eur J Nucl Med Mol Imaging.* 2020;47:2372–2382.
29. Zippel C, Giesel FL, Kratochwil C, et al. PSMA radioligand therapy could pose infrastructural challenges for nuclear medicine: results of a basic calculation for the capacity planning of nuclear medicine beds in the German hospital sector [in German]. *Nucl Med (Stuttg).* 2021;60:216–223.

Evaluation of ^{134}Ce/^{134}La as a PET Imaging Theranostic Pair for ^{225}Ac α-Radiotherapeutics

Kondapa Naidu Bobba[1], Anil P. Bidkar[1], Niranjan Meher[1], Cyril Fong[1], Anju Wadhwa[1], Suchi Dhrona[1], Alex Sorlin[1], Scott Bidlingmaier[2], Becka Shuere[1], Jiang He[3], David M. Wilson[1], Bin Liu[2,4], Youngho Seo[1], Henry F. VanBrocklin[1,4], and Robert R. Flavell[1,4,5]

[1]Department of Radiology and Biomedical Imaging, University of California, San Francisco, San Francisco, California; [2]Department of Anesthesia, University of California, San Francisco, San Francisco, California; [3]Department of Radiology and Medical Imaging, University of Virginia, Charlottesville, Virginia; [4]UCSF Helen Diller Family Comprehensive Cancer Center, San Francisco, California; and [5]Department of Pharmaceutical Chemistry, University of California, San Francisco, San Francisco, California

^{225}Ac-targeted α-radiotherapy is a promising approach to treating malignancies, including prostate cancer. However, α-emitting isotopes are difficult to image because of low administered activities and a low fraction of suitable γ-emissions. The in vivo generator ^{134}Ce/^{134}La has been proposed as a potential PET imaging surrogate for the therapeutic nuclides ^{225}Ac and ^{227}Th. In this report, we detail efficient radiolabeling methods using the ^{225}Ac-chelators DOTA and MACROPA. These methods were applied to radiolabeling of prostate cancer imaging agents, including PSMA-617 and MACROPA-PEG$_4$-YS5, for evaluation of their in vivo pharmacokinetic characteristics and comparison to the corresponding ^{225}Ac analogs. **Methods:** Radiolabeling was performed by mixing DOTA/MACROPA chelates with ^{134}Ce/^{134}La in NH_4OAc, pH 8.0, at room temperature, and radiochemical yields were monitored by radio–thin-layer chromatography. In vivo biodistributions of ^{134}Ce-DOTA/MACROPA.NH_2 complexes were assayed through dynamic small-animal PET/CT imaging and ex vivo biodistribution studies over 1 h in healthy C57BL/6 mice, compared with free $^{134}CeCl_3$. In vivo, preclinical imaging of ^{134}Ce-PSMA-617 and ^{134}Ce-MACROPA-PEG$_4$-YS5 was performed on 22Rv1 tumor–bearing male nu/nu-mice. Ex vivo biodistribution was performed for ^{134}Ce/^{225}Ac-MACROPA-PEG$_4$-YS5 conjugates. **Results:** ^{134}Ce-MACROPA.NH_2 demonstrated near-quantitative labeling with 1:1 ligand-to-metal ratios at room temperature, whereas a 10:1 ligand-to-metal ratio and elevated temperatures were required for DOTA. Rapid urinary excretion and low liver and bone uptake were seen for ^{134}Ce/^{225}Ac-DOTA/MACROPA. NH_2 conjugates in comparison to free $^{134}CeCl_3$ confirmed high in vivo stability. An interesting observation during the radiolabeling of tumor-targeting vectors PSMA-617 and MACROPA-PEG$_4$-YS5—that the daughter ^{134}La was expelled from the chelate after the decay of parent ^{134}Ce—was confirmed through radio–thin-layer chromatography and reverse-phase high-performance liquid chromatography. Both conjugates, ^{134}Ce-PSMA-617 and ^{134}Ce-MACROPA-PEG$_4$-YS5, displayed tumor uptake in 22Rv1 tumor–bearing mice. The ex vivo biodistribution of ^{134}Ce-MACROPA.NH_2, ^{134}Ce-DOTA and ^{134}Ce-MACROPA-PEG$_4$-YS5 corroborated well with the respective ^{225}Ac-conjugates. **Conclusion:** These results demonstrate the PET imaging potential for ^{134}Ce/^{134}La-labeled small-molecule and antibody agents. The similar ^{225}Ac and ^{134}Ce/^{134}La-chemical and pharmacokinetic characteristics suggest that the ^{134}Ce/^{134}La pair may act as a PET imaging surrogate for ^{225}Ac-based radioligand therapies.

Key Words: ^{134}Ce; ^{225}Ac; targeted α-radiotherapy; PET imaging; PSMA-617; YS5 antibody

J Nucl Med 2023; 64:1076–1082
DOI: 10.2967/jnumed.122.265355

Advances in targeted molecular imaging and radionuclide therapy have given rise to the field of targeted theranostics (*1*). In this paradigm, a molecular agent with a PET or SPECT imaging isotope (e.g., ^{64}Cu, ^{89}Zr, or ^{123}I) is paired with a cognate radionuclide therapy agent (e.g., ^{177}Lu, ^{225}Ac, or ^{131}I) (*2*). α-emitting radiotherapies with isotopes, including ^{227}Th, ^{225}Ac, ^{213}Bi, ^{212}Pb/^{212}Bi, ^{211}At, and ^{149}Tb, have demonstrated promise in human trials (*3,4*). α-particles have a shorter range in tissue (40–100 μm) and higher linear energy transfer than β-particles (*5*).

To date, ^{225}Ac is one of the most promising radionuclides for targeted α-therapy (*6*). However, an imaging isotope to match with ^{225}Ac to measure pharmacokinetics and dosimetry has been elusive (*7*). Actinium has 2 short-lived daughter isotopes, ^{221}Fr and ^{213}Bi, that emit low-energy γ-rays, which are challenging to image with SPECT (*8*). Thus, ^{225}Ac therapy is commonly paired with ^{68}Ga, ^{89}Zr, or ^{111}In for imaging-based pharmacokinetic or dosimetry information. However, because of substantial differences in half-life ($t_{1/2}$) (^{68}Ga) or chelation chemistry (^{89}Zr), these are imperfect PET imaging surrogates for ^{225}Ac. To overcome these limitations, lanthanum-based PET imaging agents such as ^{132}La ($t_{1/2}$ = 4.8 h, 42% β^+) and ^{133}La ($t_{1/2}$ = 3.9 h, 7% β^+) have emerged as potential imaging surrogates for ^{225}Ac (*9,10*). Unfortunately, the $t_{1/2}$ values of these isotopes are considerably shorter than for ^{225}Ac, restricting their translation to longer-$t_{1/2}$ macromolecule-based PET imaging.

In this context, the Department of Energy isotope program (*11*) has recently initiated the production of ^{134}Ce, an isotope with a 3.2-d $t_{1/2}$ that decays by electron capture to ^{134}La with the emission of low-energy Auger electrons. The ^{134}La is a positron emitter (63% β^+; endpoint energy, 2.69 MeV) with a $t_{1/2}$ of 6.45 min. The unique relationship between the $t_{1/2}$ values of ^{134}Ce and ^{134}La establishes a secular equilibrium (*12*). In pioneering work, ^{134}Ce cation in the +3 oxidation state has been shown to complex with diethylenetriamine pentaacetate (DTPA) (*11*) and DOTA (*13*) and

Received Dec. 21, 2022; revision accepted Mar. 7, 2023.
For correspondence or reprints, contact Robert R. Flavell (robert.flavell@ucsf.edu) or Henry F. VanBrocklin (henry.vanbrocklin@ucsf.edu).
Published online May 18, 2023.

to be used for in vivo PET imaging of the chelate as well as the antibody trastuzumab. It was suggested that the similar chemical characteristics between $^{225}Ac^{3+}$ and $^{134}Ce^{3+}$ and the longer ^{134}Ce $t_{1/2}$ (3.2-d) might be advantageous for tracking in vivo pharmacokinetics, especially at later time points. However, DOTA and DTPA require higher molar ratios and elevated temperatures for isotope complexation. Alternatively, MACROPA has demonstrated superior chelate properties for ^{225}Ac and a high stability (K_{LnL} = 15.1) for nonradioactive cerium (*14*), suggesting that it may function well for $^{134}Ce/^{225}Ac$ theranostic development (*15*).

^{225}Ac-based radiopharmaceutical therapy has recently attracted great interest in prostate cancer, particularly ^{225}Ac-PSMA-617 in small trials, demonstrating great efficacy, especially in the context of resistance to ^{177}Lu-PSMA-617 (*16,17*). Our own laboratories have identified the antibody YS5, which targets a tumor-selective epitope, CD46, that is highly expressed in prostate cancer (*18*). An immuno-PET agent, ^{89}Zr-DFO-YS5, has successfully imaged both PSMA-positive and PSMA-negative tumor xenografts and patient-derived PDX models (*19*). Development of cognate ^{225}Ac-YS5 radiopharmaceuticals for therapy is currently under way (*20–22*). These therapeutic approaches would significantly benefit from a companion imaging agent.

Here, we aim to evaluate the potential of positron-emitting $^{134}Ce/^{134}La$ as a PET imaging surrogate for ^{225}Ac. We describe methods for efficient chelation of ^{134}Ce using the MACROPA and DOTA chelators and demonstrate the stability of the conjugates. The imaging and distribution characteristics of the ^{134}Ce-labeled tumor-targeting agents PSMA-617 and MACROPA-PEG_4-YS5 are evaluated in prostate cancer models. These studies demonstrate the feasibility and applicability of ^{134}Ce-based radiopharmaceuticals for cancer imaging.

MATERIALS AND METHODS

Radiolabeling of DOTA, MACROPA.NH_2, and PSMA-617 with $^{134}CeCl_3$

$^{134}Ce(NO_3)_3$ in 0.1 M HCl was produced at the Isotope Production Facility of Los Alamos National Laboratory as previously described (*11*). Test batches were supplied by the Department of Energy isotope program for our studies. Radiolabeling reactions of DOTA, MACROPA.NH_2, and PSMA-617 at various ligand-to-metal molar ratios were performed using 2 M NH_4OAc buffer, pH 8.0, except when the product was used for animal injections (0.1 M NH_4OAc, pH 8.0). For radiolabeling, aliquots of $^{134}CeCl_3$ in 0.1 M HCl (5.17 μL) were mixed with MACROPA.NH_2 (23 μL, 630 μg/mL in 2 M NH_4OAc buffer) or DOTA (20 μL, 375 μg/mL in 2 M NH_4OAc buffer) in 2 M NH_4OAc buffer, pH 8.0 (100 μL) at 25°C for 30 min and PSMA-617 (1.5 μL, 0.8 μg, 500 μg/mL) at 60°C for 1 h. The reaction solution was analyzed by radio–thin-layer chromatography (TLC) using C_{18} TLC plates (Supelco; Sigma) eluted with 10% NH_4Cl:MeOH (1:1).

Radiolabeling of MACROPA-PEG_4-YS5 with $^{134}CeCl_3$

MACROPA-PEG_4-YS5 (221.4 μg; 1:1 total metal-to-YS5 molar ratio) was incubated with an aliquot of $^{134}CeCl_3$ (105 μL, 48.1 MBq) in 2 M NH_4OAc (pH 8.0) at 25°C for 1 h. The radiolabeling progress was monitored by instant thin-layer chromatography (iTLC) on Varian iTLC silica gel strips using 50 mM ethylenediaminetetraacetic acid, pH 5.5, as an eluent. The reaction mixture was purified over PD10 column gel filtration eluting with 0.9% saline solution.

Small-Animal PET Imaging

^{134}Ce-MACROPA.NH_2 and ^{134}Ce-DOTA reactions in 0.1 M NH_4OAc buffer were diluted in saline (1:1 ratio), and 4.81–5.92 MBq in 100 μL were administered via the tail vein to 5- to 6-wk-old wild-type C57BL/6 male mice under isoflurane anesthesia. The specific and molar activities were 19.24 GBq/mg and 20.4 GBq/μmol, respectively, for ^{134}Ce-MACROPA.NH_2 and 3.7 GBq/mg and 1.9 GBq/μmol, respectively, for ^{134}Ce-DOTA. Dynamic small-animal PET/CT (Inveon; Siemens Medical Solutions) was performed for 1 h simultaneously on 3 mice for both ^{134}Ce-MACROPA.NH_2 and ^{134}Ce-DOTA. Free $^{134}CeCl_3$ (~4.81–5.92 MBq) in saline (100 μL) was injected similarly to the method described above, to a group of 2 mice for dynamic small-animal PET/CT and a group of 3 mice for static small-animal PET/CT (20-min PET acquisition) at 2 h and 24 h.

For tumor imaging studies, ^{134}Ce-PSMA-617 (~4.3 MBq) in saline (100 μL) was injected via the tail vein into 22Rv1 tumor–bearing mice, and the mice were imaged at 1 h after injection using small-animal PET/CT. For ^{134}Ce-MACROPA-PEG_4-YS5 (~4.44 MBq), the conjugate was injected intravenously into mice implanted with 22Rv1 xenografts and imaged at 4 h and then at 1, 2, 4, and 7 d after injection. Small-animal PET/CT was performed with 20 min of PET at earlier time points (4 h, 1d, and 2 d) and with 60 min of PET at later time points (4 and 7 d). The specific and molar activities were 2.58 GBq/mg and 2.67 GBq/μmol, respectively, for ^{134}Ce-PSMA-617 and 0.18 GBq/mg and 26.94 GBq/μmol, respectively, for ^{134}Ce-MACROPA-PEG_4-YS5.

RESULTS

Radiolabeling of Bifunctional Chelators DOTA and MACROPA.NH_2

We assessed the radiolabeling efficiencies of MACROPA.NH_2 and compared with DOTA at varying ligand-to-metal (L/M) ratios (Fig. 1 left). The L/M ratios were calculated using the stable cerium plus lanthanum present in the $^{134}CeCl_3$ solution as per the certificate of analysis (Supplemental Fig. 1; supplemental materials are available at http://jnm.snmjournals.org). As posited, MACROPA.NH_2 complexed all the ^{134}Ce in greater than 95% yield from 0.5:1 to 10:1 L/M ratios. In contrast, DOTA complexed 94.2% ± 1.8% of the ^{134}Ce only at the 10:1 L/M ratio (Fig. 1; Supplemental Fig. 2). A slight increase in radiolabeling complexation was observed for DOTA using L/M ratios of 2:1 (32.6% vs. 23.3%) and 5:1 (88.2% vs. 72.53%) at an elevated temperature of 60°C (Supplemental Fig. 3). These studies demonstrate that MACROPA.NH_2 exhibited a radiolabeling yield superior to that of DOTA, notably allowing rapid, near-quantitative radiolabeling at a 1:1 L/M

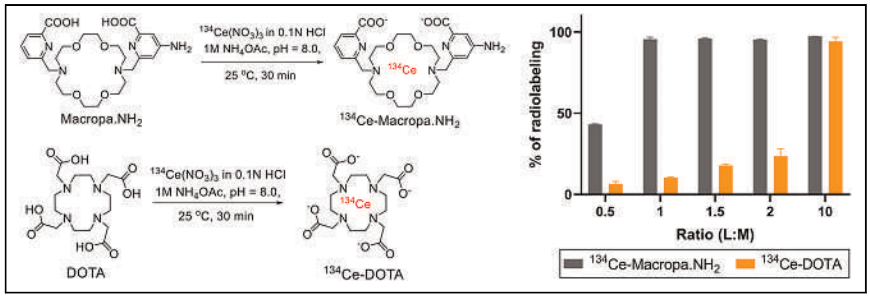

FIGURE 1. (Left) Radiolabeling of MACROPA.NH_2 and DOTA with $^{134}CeCl_3$. (Right) Percentage radiolabeling at increasing L/M ratios for MACROPA.NH_2 and DOTA (n = 2) at 25°C, as assayed by radio-TLC.

ratio at room temperature. The ^{134}Ce-MACROPA.NH$_2$ (1:1 ratio) radiocomplex was analyzed by reverse-phase radio–high-performance liquid chromatography, and the retention time was compared with the ^{Nat}Ce-MACROPA.NH$_2$ complex (Supplemental Figs. 4–8; Supplemental Scheme 1). However, the radio–high-performance liquid chromatogram showed a tailing behavior, likely due to the ejection of ^{134}La from the chelate after the decay by its parent, ^{134}Ce. The stability of the ^{134}Ce-MACROPA.NH$_2$ complex was evaluated in physiologic buffers and in human and rat serum. Over 7 d, more than 95% of the complex was intact in all buffers and serum (Supplemental Fig. 9).

In Vivo Stability of ^{134}Ce-MACROPA.NH$_2$ and DOTA Demonstrated by PET Imaging and Biodistribution Studies

After successful ^{134}Ce radiolabeling of MACROPA.NH$_2$ and DOTA, complex pharmacokinetics and stability were studied in healthy wild-type C57BL/6 mice via PET imaging and biodistribution compared with free ^{134}CeCl$_3$. ^{134}CeCl$_3$ showed a gradual increase in liver uptake, as well as in bladder and kidney uptake (Fig. 2A; Supplemental Fig. 10). In contrast, PET imaging of the ^{134}Ce-MACROPA.NH$_2$ and ^{134}Ce-DOTA complexes demonstrated clearance from most organs, with accumulation in the kidneys and bladder at over 1 h after injection, consistent with renal excretion (Fig. 2A; Supplemental Figs. 11–13). The time–activity curves in Supplemental Figure 14 show the slow blood clearance of ^{134}CeCl$_3$ in comparison with ^{134}Ce-MACROPA.NH$_2$ and ^{134}Ce-DOTA. The 1-h ex vivo biodistribution of ^{134}CeCl$_3$, ^{134}Ce-MACROPA.NH$_2$, and ^{134}Ce-DOTA are shown in Figures 2B–2D and Supplemental Table 1. High liver (71.5 ± 4.3 percentage injected dose [%ID]/g) and bone (15.54 ± 2.69 %ID/g) uptake was observed for free ^{134}CeCl$_3$, with similar results found at 2.5 and 24 h after injection (Supplemental Fig. 15). In contrast, ^{134}Ce-MACROPA.NH$_2$ (4.36 ± 2.54 %ID/g) and ^{134}Ce-DOTA (5.17 ± 2.33 %ID/g) were equally taken up in the kidney, with low accumulation in the liver and other organs, indicating low nonspecific accumulation and renal clearance. Overall, the PET imaging and biodistribution studies of ^{134}Ce-MACROPA.NH$_2$ and ^{134}Ce-DOTA versus free ^{134}Ce demonstrated high complex in vivo stability.

The ex vivo biodistribution of ^{225}AcCl$_3$, ^{225}Ac-MACROPA.NH$_2$, and ^{225}Ac-DOTA (Supplemental Fig. 16; Supplemental Table 2) was assessed and compared with the respective ^{134}Ce complexes. Free ^{225}Ac accumulates primarily in the liver (38.33 ± 6.75 %ID/g) and bone (29.56 ± 2.40 %ID/g), similarly to ^{134}Ce (Fig. 2B). ^{225}Ac-MACROPA.NH$_2$ (3.54% ± 1.07%) and DOTA (3.07 ± 0.99 %ID/g) complexes displayed a higher uptake in the kidney, with minimal uptake in the liver (0.74 ± 0.19 and 0.28 ± 0.008 %ID/g), similarly to ^{134}Ce-MACROPA.NH$_2$ and ^{134}Ce-DOTA (Figs. 2C and 2D). Notable differences were observed in bone uptake for ^{225}Ac-DOTA (2.26 ± 0.56 %ID/g) versus ^{134}Ce-DOTA (0.45 ± 0.24 %ID/g) and in blood uptake for ^{134}Ce-MACROPA.NH$_2$ (0.86 ± 0.19 %ID/g) and ^{134}Ce-DOTA (1.07 ± 0.80 %ID/g) versus ^{225}Ac-MACROPA.NH$_2$ (0.32 ± 0.08 %ID/g) and ^{225}Ac-DOTA (0.23 ± 0.02 %ID/g). Taken together, the data indicate that the biodistributions of the ^{134}Ce- and ^{225}Ac-chelated complexes are largely similar.

Radiolabeling of Prostate Cancer–Targeting Agents PSMA-617 and MACROPA-PEG$_4$-YS5

Given the encouraging in vivo results in normal mice, we investigated the ^{134}Ce radiochemistry of cancer-targeting radiopharmaceuticals, including the small-molecule prostate-specific membrane antigen (PSMA)–targeting agent PSMA-617 (*23*) and the CD46-targeting antibody derivative MACROPA-PEG$_4$-YS5. For PSMA-617, higher L/M ratios were required for quantitative ^{134}Ce-labeling, as 24.3%, 81.0%, and 100% radiolabeling yields were noted by radio-TLC for 2:1, 5:1, and 10:1 L/M ratios, respectively (Fig. 3A; Supplemental Fig. 17). The radiolabeling yields were comparable to the similar ratios (10:1) of ^{225}Ac-PSMA-617 based on the prior literature (*24*). After 1 h of incubation of ^{134}Ce with PSMA-617 (Fig. 3), iTLC showed 94.1% radiolabeling yield. Surprisingly, the radiolabeling yields were apparently reduced to about 53.2% when the reaction was diluted in saline. However, when the same TLC plate was allowed to decay and rescanned, quantitative labeling was again observed. Similarly, when the apparently 94.1% pure ^{134}Ce-PSMA-617 was analyzed on reverse-phase radio–high-performance liquid chromatography (Supplemental Fig. 18), a significant tailing behavior was observed between 4 and 9 min. These data are consistent with the release of ^{134}La due to the dechelation or recoil effect after the decay of the parent, ^{134}Ce.

On the basis of the favorable model labeling studies, we hypothesized that MACROPA would be a superior chelator to enable ^{134}Ce immuno-PET imaging. To facilitate the bioconjugation of MACROPA to the YS5 antibody, we prepared a bifunctional chelator containing MACROPA with a short PEG$_4$ linker with an activated TFP ester. MACROPA-PEG$_4$-TFP (**7 g**) was synthesized over 7 steps in 56.3% overall yield (Supplemental Figs. 19–37; Supplemental Scheme 2) (*25*). MACROPA-PEG$_4$-TFP

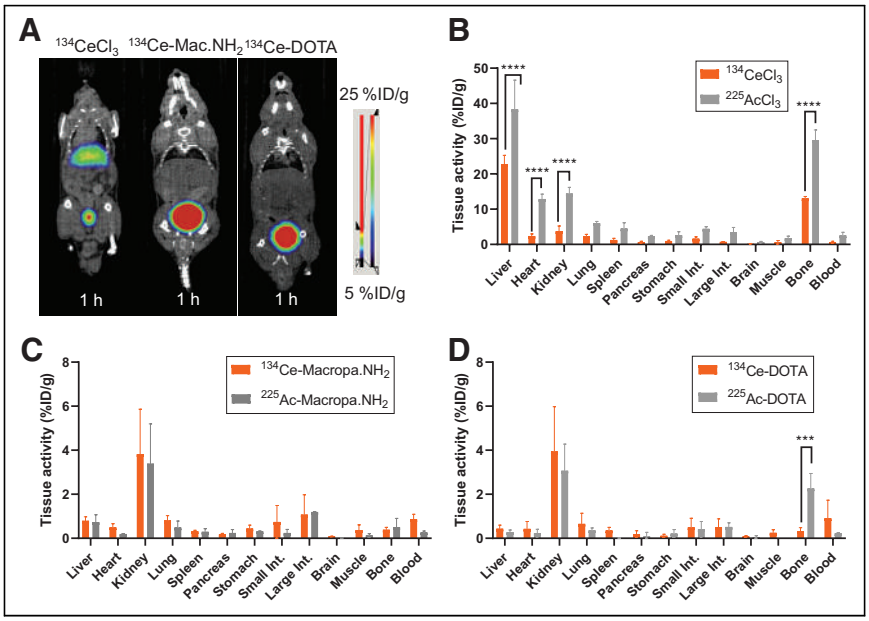

FIGURE 2. Evaluation of PET imaging of ^{134}Ce and chelated complexes in wild-type mouse studies. (A) Coronal small-animal PET/CT images of free ^{134}CeCl$_3$, ^{134}Ce-MACROPA.NH$_2$, and ^{134}Ce-DOTA in wild-type mice. (B–D) Ex vivo biodistribution of ^{134}CeCl$_3$ (n = 2) and ^{225}AcCl$_3$ (n = 3) (B), ^{134}Ce/^{225}Ac-MACROPA.NH$_2$ (n = 3) (C), and ^{134}Ce/^{225}Ac-DOTA (n = 3) (D). Error bars represent SD. ***P < 0.0008. ****P < 0.0001.

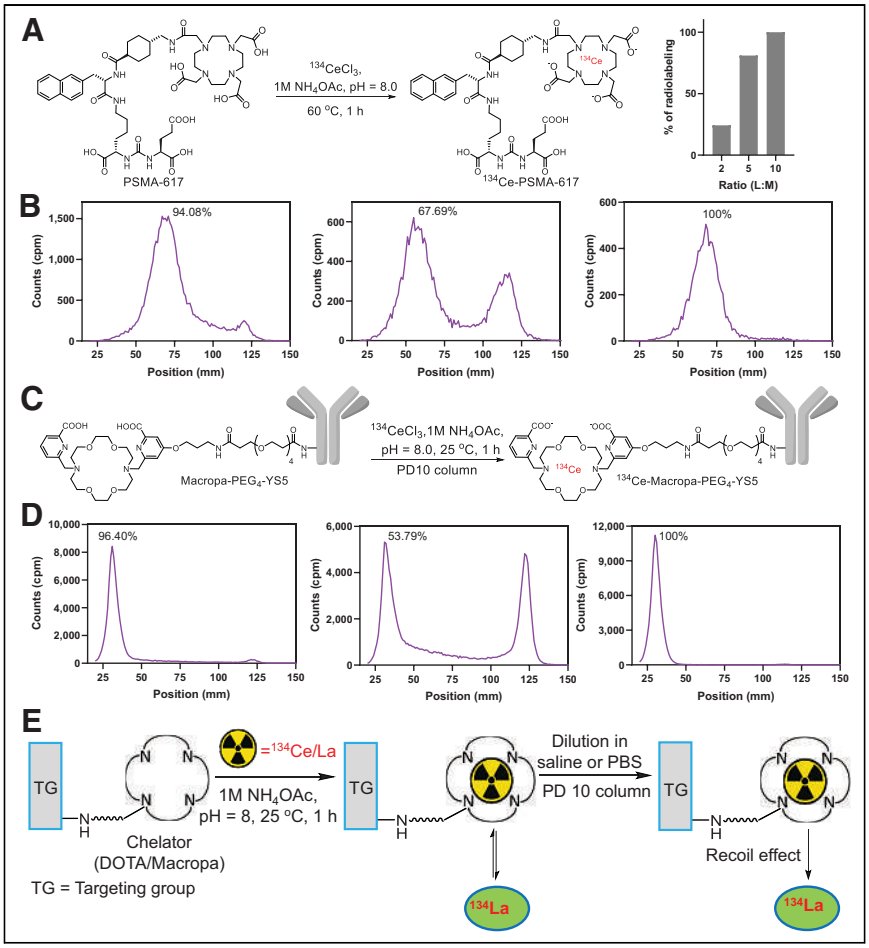

FIGURE 3. Radiolabeling of prostate cancer–targeting agents PSMA-617 and MACROPA-PEG$_4$-YS5. (A) Radiolabeling of PSMA-617 (left) and radiolabeling yields at increasing molar ratios of PSMA-617 (right). (B) Radio-iTLC of ^{134}Ce-PSMA-617 (left), same reaction mixture diluted in saline scanned without waiting for 1-h decay (middle), and same radio-iTLC scanned after 1-h decay showing quantitative radiochemical yield (right). (C) Radiolabeling of MACROPA-PEG$_4$-YS5. (D) Radio-iTLC of ^{134}Ce-MACROPA-PEG$_4$-YS5 (left), same reaction mixture after PD10 column purification immediately scanned without waiting for 1-h decay (middle), and same radio-iTLC after 1-h decay (right). (E) ^{134}La dechelation due to recoil effect. PBS = phosphate-buffered saline.

ester (**7 g**) was conjugated to lysine residues on YS5 (Supplemental Scheme 3), with an average of about 2.6 chelators per antibody as determined by MALDI-TOF MS (Supplemental Fig. 38). Optimized conditions for MACROPA ^{134}Ce-labeling were applied, and the radiochemical yield was 96.4% as confirmed by radio-iTLC, with 69.3% isolated yield after purification and a specific activity of 0.18 GBq/mg (Figs. 3C and 3D). In contrast, DOTA-YS5 was unable to complex ^{134}Ce even at higher molar ratios (L/M ratio, 2 or 4) and 40°C (Supplemental Fig. 39). Calculation of the ligand-to-metal ratios was based on the number of chelators per antibody YS5. Unexpectedly, the purified eluted fraction of ^{134}Ce-MACROPA-PEG$_4$-YS5 showed an apparent decrease in radiochemical purity to about 53.8% (Fig. 3D). As seen in the case of labeled PSMA-617, when the same TLC plate was scanned after decaying for 1 h, 100% radiochemical yield was observed (Fig. 3D). Size-exclusion chromatography demonstrated no evidence of aggregation, whereas an elevated baseline was noticed between the product peak at 9.65 to 25 min, indicating the possible dechelation of daughter isotope ^{134}La (Supplemental Fig. 40). The release of daughter ^{134}La was also evident when these reaction mixtures were diluted in saline either for purification or for mouse injections, irrespective of MACROPA or DOTA ligands (Fig. 3E).

In Vitro Analysis and In Vivo Distribution of Prostate-Targeting Agent PSMA-617

The cell-binding assay of ^{134}Ce-PSMA-617 was performed with different concentrations using the 22Rv1 cell line. The percentage of cell-bound activity was significantly higher for all the concentrations than for blocking controls. A decrease in cell-bound activity percentage for a higher concentration (0.8 nM) was observed because of the cold mass effect (Supplemental Fig. 41) (*26*). Small-animal PET/CT was performed on a 22Rv1 tumor–bearing mouse at 1 h after injection. As shown in Figure 4, most of the activity was in the bladder and kidney at 1 h after injection, with low uptake in the tumor, whereas almost all the activity was eliminated from the other organs. This pattern of tumor uptake is similar to that found using other PSMA-targeting agents in 22Rv1 tumors, which express moderate levels of PSMA (*27,28*).

In Vitro and In Vivo Analysis of ^{134}Ce-MACROPA-PEG$_4$-YS5

The properties of ^{134}Ce-MACROPA-PEG$_4$-YS5 for immuno-PET imaging of prostate cancer were evaluated. A magnetic bead–based radioligand-binding assay revealed a 80.5% ± 4.6% target binding fraction for ^{134}Ce-MACROPA-PEG$_4$-YS5 (Fig. 5A), whereas approximately 16.25% ± 4.4% for blocking and approximately 6.7% ± 2.6% for no CD46 were observed (n = 3). In a saturation binding assay, the dissociation constant of MACROPA-PEG$_4$-YS5 was 3.7 nM, similar to that previously reported for ^{89}Zr-DFO-YS5 (6.7 nM) (Fig. 5B) (*19*). These data demonstrate that ^{134}Ce-MACROPA-PEG$_4$-YS5 could be synthesized effectively with 1:1 ligand-to-metal ratios, with little or no loss of CD46 binding affinity.

Encouraged by the promising radiolabeling studies, we evaluated the PET imaging properties of ^{134}Ce-MACROPA-PEG$_4$-YS5 in prostate cancer xenografts. Figure 5C and Supplemental Figure 42 show representative small-animal PET/CT images after intravenous administration of ^{134}Ce-MACROPA-PEG$_4$-YS5 in athymic nude mice bearing 22Rv1 tumors over 7 d. The ex vivo biodistribution confirmed the elevated uptake in the tumor (37.16 ± 8.17 %ID/g) and liver (21.60 ± 1.70 %ID/g). Persistent high tumor uptake (33.11 ± 9.27 %ID/g) was seen 14 d after administration (Fig. 6; Supplemental Table 3).

^{225}Ac-MACROPA-PEG$_4$-YS5 was radiolabeled, and in vivo biodistribution studies were conducted to compare with the ^{134}Ce-labeled YS5 (Supplemental Fig. 43). The imaging and ex vivo biodistribution results for ^{134}Ce-MACROPA-PEG$_4$-YS5 were similar to those for ^{225}Ac-MACROPA-PEG$_4$-YS5 for tumor and most tissues (Fig. 6; Supplemental Table 3). High ^{225}Ac-MACROPA-PEG$_4$-YS5

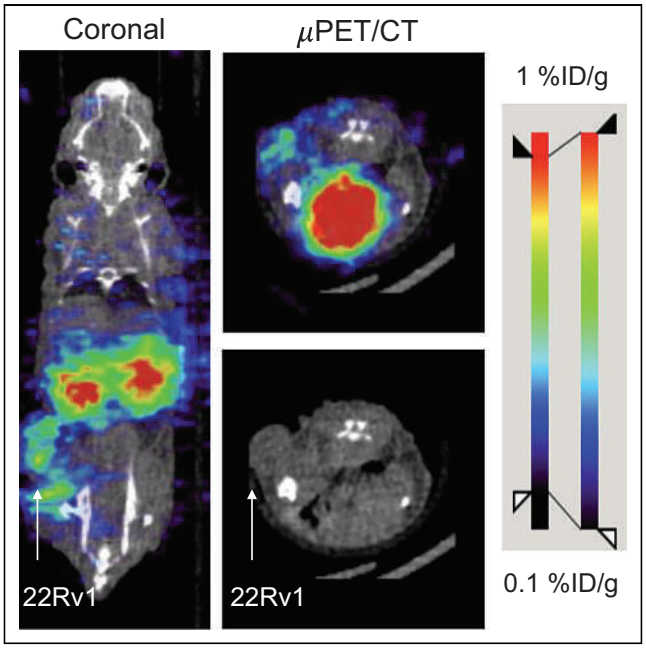

FIGURE 4. Small-animal PET imaging of ^{134}Ce-PSMA-617 in 22Rv1 xenograft at 1 h after injection.

uptake in the tumor (34.75 ± 9.07 %ID/g) was observed on day 7 after injection, similar to the ^{134}Ce-MACROPA-PEG$_4$-YS5 uptake (37.16 ± 8.17 %ID/g). However, significant differences in liver ($P < 0.0001$) and spleen ($P = 0.0109$) uptake were observed.

DISCUSSION

In the design of theranostic agents, it is essential to match the structure and biodistribution of the imaging molecule to that of the radiotherapeutic. Recently, lanthanides have been proposed as nonradioactive surrogates for actinium because of similar chemical properties. ^{132}La ($t_{1/2} = 4.8$ h) and ^{133}La ($t_{1/2} = 3.9$ h) have been studied as complementary PET imaging isotopes for targeted α-therapy with ^{225}Ac ($t_{1/2} = 9.9$ d) (*9,10*). Aluicio-Sarduy et al. reported cyclotron-produced ^{132}La-labeled alkyl phosphocholine (NM600) in a 4T1 tumor and showed in vivo uptake characteristics similar to those of ^{225}Ac (*9*). Similarly, Nelson et al. described a high-yield cyclotron method to produce ^{133}La using natural barium and isotopically enriched ^{135}BaCO$_3$ targets (*10*). Potential limitations of ^{132}La and ^{133}La include shorter $t_{1/2}$ values than for ^{225}Ac ($t_{1/2} = 9.92$ d) and elevated temperatures (80°C–90°C) required for higher radiochemical conversions (>95%). Although these may be more suitable for fast-clearing small molecules, antibody fragments, or small peptides, their $t_{1/2}$ values limit the ability to monitor the pharmacokinetics of macromolecules such as antibodies.

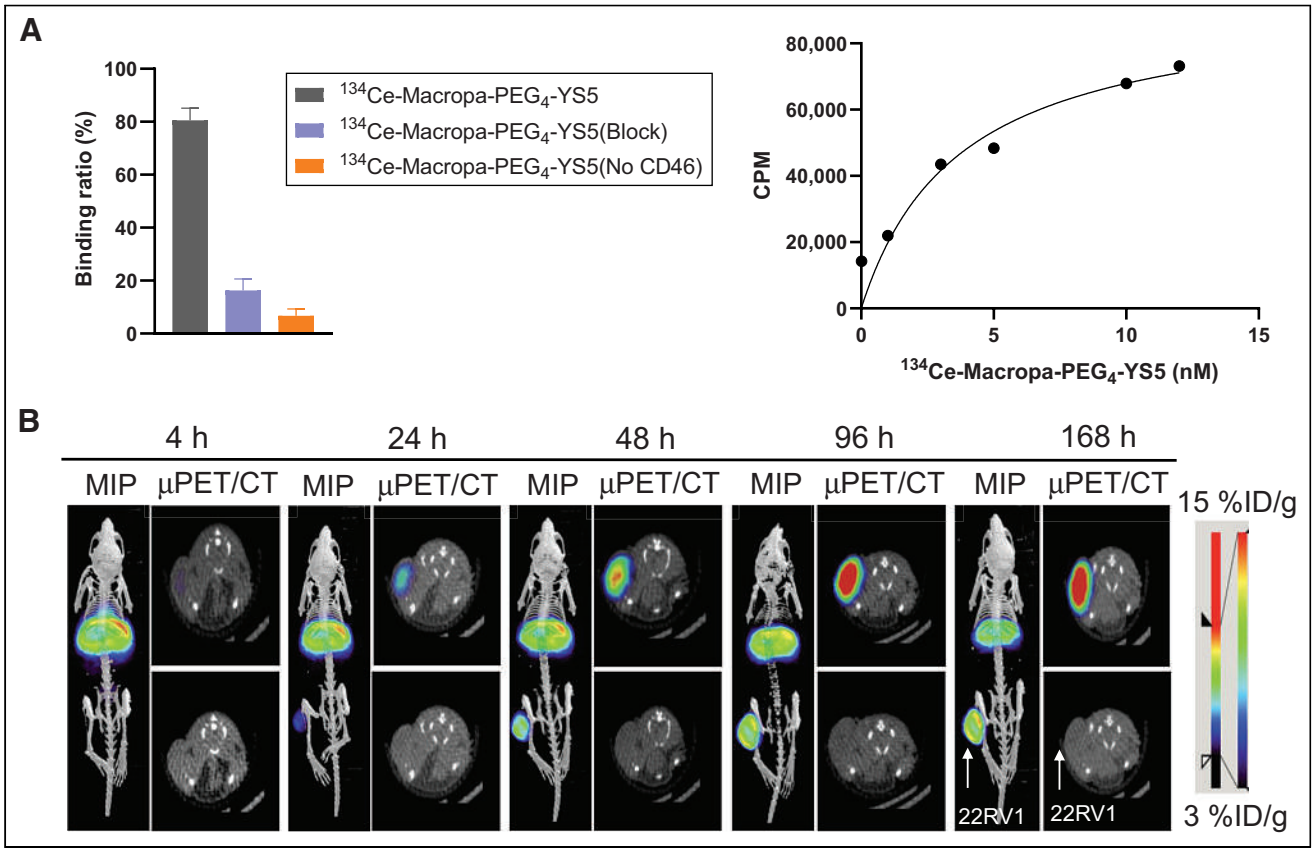

FIGURE 5. In vitro and in vivo analysis of radioimmunoconjugate ^{134}Ce-MACROPA-PEG$_4$-YS5. (A) Left: Magnetic bead–based radioligand assay for ^{134}Ce-MACROPA-PEG$_4$-YS5 ($n = 3$). Right: Saturation binding assay of ^{134}Ce-MACROPA-PEG$_4$-YS5 on 22Rv1 cells (dissociation constant, 3.7 nM) ($n = 3$). (B) Maximum-intensity-projection PET/CT and transverse small-animal PET/CT images obtained up to 7 d after ^{134}Ce-MACROPA-PEG$_4$-YS5 injection in mouse bearing 22Rv1 xenografts, demonstrating gradual increase in tumor uptake over time ($n = 4$). MIP = maximum-intensity projection.

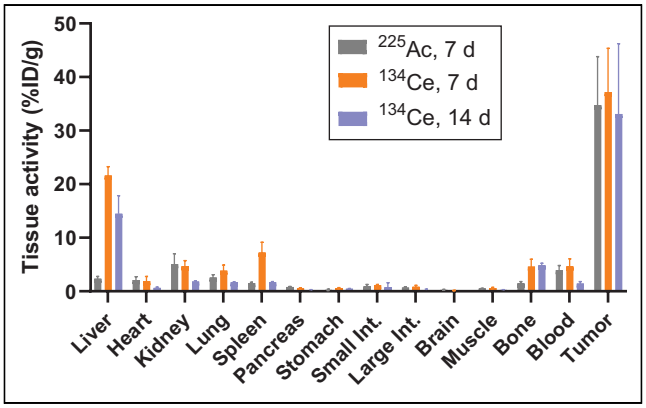

FIGURE 6. Ex vivo biodistribution analysis of ^{134}Ce/^{225}Ac-MACROPA-PEG$_4$-YS5 in mouse bearing 22Rv1 xenografts at 7 d after injection. Higher tumor and liver uptake was obtained. Error bars represent SD (n = 5 at 7 d and 2 at 14 d for ^{134}Ce; n = 4 for ^{225}Ac at 7 d).

^{134}Ce has emerged as an isotope that may be complexed by the same chelates as actinium and thorium. Its decay to ^{134}La provides an in situ generator of a positron-emitting isotope with the apparent $t_{1/2}$ of its parent. The pioneering study by Bailey et al. highlighted the cyclotron production of ^{134}Ce/^{134}La from a natural lanthanum target and established the radiochemistry with ligands DTPA (as a potential surrogate for ^{225}Ac) and hydroxypyridinone (as a potential surrogate for ^{227}Th) (*11*). Later, the same group demonstrated the in vivo distribution of ^{134}Ce-DOTA-trastuzumab, an internalizing antibody (*13*). In the present study, imaging and biodistribution of a small-molecule conjugate, PSMA-617, and the antibody YS5 conjugated with MACROPA (MACROPA-PEG$_4$-YS5) were conducted on prostate cancer xenografts. Similar tumor uptake was observed between the ^{134}Ce- and ^{225}Ac-labeled MACROPA-PEG$_4$-YS5. The ^{134}Ce/^{134}La pair allows lengthy in vivo monitoring of molecules because of its extended $t_{1/2}$ of 3.2 d, which is not possible with $^{132/133}$La radioisotopes.

Broadly speaking, the radiolabeling findings and stability using MACROPA and DOTA chelators with ^{134}Ce recapitulate the prior reports using the same chelators with ^{225}Ac (*15*). Radiolabeling efficiency of greater than 95% was achieved with 1:1 ligand-to-metal ratios for MACROPA.NH$_2$ and 10:1 for DOTA at room temperature. Dynamic PET imaging and ex vivo biodistribution studies of both ^{134}Ce-MACROPA.NH$_2$ and ^{134}Ce-DOTA confirm in vivo stability and a biodistribution similar to that of ^{225}Ac-MACROPA.NH$_2$ and DOTA complexes. Overall, the radiolabeling methodologies show that MACROPA.NH$_2$ was more efficient than DOTA and that both complexes showed excellent overall stability.

After radiolabeling and purification into saline of the tumor-targeting agents PSMA-617 and MACROPA-PEG$_4$-YS5 for mouse administration, we chromatographically observed the release of the daughter radionuclide ^{134}La from the chelate. In the reaction mixture, before dilution or purification, the ^{134}La may be rechelated after recoil effect if excess ligand is present (Fig. 3E). However, the rechelation may not occur in vivo even if the excess ligand is present, leading to possible ^{134}La redistribution. Though the stability constants were high for ^{Nat}La-MACROPA (14.91) and ^{Nat}Ce-MACROPA (15.11) (*14*), the ^{134}Ce bond dissociation occurs because of the nuclear recoil effect through electron capture decay and subsequent Auger electron emission (*29*). A similar phenomenon was seen by Severin et al. for another in vivo PET generator, ^{140}Nd ($t_{1/2}$ = 3.4 d, Electron capture (EC)/^{140}Pr ($t_{1/2}$ = 3.4 m, β^+), with DOTA-LM3 (small peptide) and DTPA-ATN 291 (antibody). In their work, small differences in tissue distribution were noted via pre- and postmortem imaging—differences that were attributed to redistribution of the daughter. The differences were greater for noninternalizing agents (*30,31*). Our imaging findings are also consistent with these prior reports.

The imaging properties of ^{134}Ce/^{134}La have been evaluated in prostate cancer models using PSMA-617 and MACROPA-PEG$_4$-YS5. Low to moderate tumor uptake of ^{134}Ce-PSMA-617 was observed at 1 h after administration. High kidney uptake of PSMA-based targeting vectors is known, as they tend to excrete through renal elimination and the mouse kidneys express PSMA (*27,28*). In contrast, ^{134}Ce-MACROPA-PEG$_4$-YS5 showed elevated tumor uptake. Our findings are consistent with our prior report demonstrating elevated uptake of ^{89}Zr-DFO-YS5, compared against ^{68}Ga-PSMA-11 in the 22Rv1 xenograft model (*19*).

Remarkably, biodistribution studies of ^{134}Ce-MACROPA-PEG$_4$-YS5 showed tissue distribution almost identical to that of ^{225}Ac-MACROPA-PEG$_4$-YS5 except for the liver and spleen. The high liver uptake observed in early images at 24 h (Fig. 5B) may be due to redistribution of daughter ^{134}La after ejection from the chelate. This possibility will be further investigated in future studies by conducting pre- and postmortem imaging and comparing it with ^{225}Ac more systematically.

One notable advantage to using ^{134}Ce is that it allows facile imaging of conjugates bearing the MACROPA chelate, which was previously limited to therapeutic radionuclides. The similar chemical properties of these radionuclides (^{134}Ce/^{225}Ac) may allow a single molecular platform by complexing with the ligands DOTA or MACROPA. This complexation could facilitate predicting the tumor distribution of ^{225}Ac-labeled targeting vectors (^{225}Ac-PSMA-617 or MACROPA-PEG$_4$-YS5) based on the (^{134}Ce-PSMA-617 or MACROPA-PEG$_4$-YS5) PET imaging results. Hence, this methodology addresses an important challenge in radiopharmaceutical sciences, namely the study of the biodistribution of ^{225}Ac radiopharmaceuticals. Overall, these studies support our premise that ^{134}Ce/^{134}La may serve as an imaging radionuclide to pair with ^{225}Ac.

CONCLUSION

MACROPA.NH$_2$ showed exceptional radiolabeling efficiency with ^{134}Ce at room temperature. PET imaging of ^{134}Ce-MACROPA.NH$_2$ and ^{134}Ce-DOTA revealed that both tracers are highly stable in vivo. The ex vivo biodistributions of both ^{134}Ce-DOTA and MACROPA.NH$_2$ were almost identical to the respective ^{225}Ac complexes. ^{134}Ce-PSMA-617 shows high binding affinity and uptake in prostate cancer 22Rv1 xenografts. A bifunctional analog for MACROPA was synthesized, conjugated with antibody YS5, and radiolabeled with ^{134}Ce and ^{225}Ac. Both the PET imaging and the biodistribution of ^{134}Ce-MACROPA-PEG$_4$-YS5 demonstrate elevated tumor retention in 22Rv1 prostate cancer xenografts. The ex vivo biodistribution is consistent with the ^{225}Ac-MACROPA-PEG$_4$-YS5 distribution in most tissues, including the tumor. These studies support the future development of ^{134}Ce-radiopharmaceuticals for cancer imaging as a companion to paired α-particle radiotherapeutics.

DISCLOSURE

Kondapa Naidu Bobba and Robert Flavell have filed a patent application, "Radioimmunoconjugates and Therapeutic Uses Thereof"

provisional patent application number 63/344537. This study was supported by U.S. Department of Energy, Office of Science, Office of Isotope R&D and Production, DOE Isotope program under Award Number DE-SC-0023467 and Department of Defense grant W81XWH2110792. No other potential conflict of interest relevant to this article was reported.

ACKNOWLEDGMENTS

We gratefully acknowledge Prof. R. Abergel for helpful discussions. The ^{134}Ce used in this research was supplied by the U.S. Department of Energy Isotope Program, managed by the Office of Isotope R&D and Production.

KEY POINTS

QUESTION: Are the radiochemistry and in vitro/in vivo characteristics of ^{134}Ce/^{134}La chelates similar to those of ^{225}Ac?

PERTINENT FINDINGS: ^{134}Ce/^{134}La efficiently forms stable complexes with ^{225}Ac-chelates, DOTA, and MACROPA. These may allow a single molecular platform for imaging and radiotherapy. The ex vivo tissue biodistribution was largely similar between ^{225}Ac- and ^{134}Ce-labeled antibody YS5, with the exception of liver and spleen.

IMPLICATIONS FOR PATIENT CARE: Identification of an imaging surrogate for ^{225}Ac may aid in the development of targeted α-radiotherapeutics and enable visualization of their distribution. Imaging with ^{134}Ce-labeled radiopharmaceuticals may guide therapeutic dosing of the concomitant ^{225}Ac-labeled molecule.

REFERENCES

1. Bodei L, Herrmann K, Schöder H, Scott AM, Lewis JS. Radiotheranostics in oncology: current challenges and emerging opportunities. *Nat Rev Clin Oncol.* 2022;19:534–550.
2. Herrero Álvarez N, Bauer D, Hernández-Gil J, Lewis JS. Recent advances in radiometals for combined imaging and therapy in cancer. *ChemMedChem.* 2021;16:2909–2941.
3. Parker C, Lewington V, Shore N, et al. Targeted alpha therapy, an emerging class of cancer agents: a review. *JAMA Oncol.* 2018;4:1765–1772.
4. Juzeniene A, Stenberg VY, Bruland ØS, Larsen RH. Preclinical and clinical status of PSMA-targeted alpha therapy for metastatic castration-resistant prostate cancer. *Cancers (Basel).* 2021;13:779.
5. Graf F, Fahrer J, Maus S, et al. DNA double strand breaks as predictor of efficacy of the alpha-particle emitter Ac-225 and the electron emitter Lu-177 for somatostatin receptor targeted radiotherapy. *PLoS One.* 2014;9:e88239.
6. Morgenstern A, Apostolidis C, Kratochwil C, Sathekge M, Krolicki L, Bruchertseifer F. An overview of targeted alpha therapy with ^{225}actinium and ^{213}bismuth. *Curr Radiopharm.* 2018;11:200–208.
7. Kratochwil C, Bruchertseifer F, Giesel FL, et al. ^{225}Ac-PSMA-617 for PSMA-targeted α-radiation therapy of metastatic castration-resistant prostate cancer. *J Nucl Med.* 2016;57:1941–1944.
8. de Kruijff RM, Raavé R, Kip A, et al. The in vivo fate of ^{225}Ac daughter nuclides using polymersomes as a model carrier. *Sci Rep.* 2019;9:11671.
9. Aluicio-Sarduy E, Barnhart TE, Weichert J, Hernandez R, Engle JW. Cyclotron-produced ^{132}La as a PET imaging surrogate for therapeutic ^{225}Ac. *J Nucl Med.* 2021;62:1012–1015.
10. Nelson BJB, Ferguson S, Wuest M, et al. First in vivo and phantom imaging of cyclotron-produced ^{133}La as a theranostic radionuclide for ^{225}Ac and ^{135}La. *J Nucl Med.* 2022;63:584–590.
11. Bailey TA, Mocko V, Shield KM, et al. Developing the ^{134}Ce and ^{134}La pair as companion positron emission tomography diagnostic isotopes for ^{225}Ac and ^{227}Th radiotherapeutics. *Nat Chem.* 2021;13:284–289.
12. Lubberink M, Lundqvist H, Tolmachev V. Production, PET performance and dosimetric considerations of ^{134}Ce/^{134}La, an Auger electron and positron-emitting generator for radionuclide therapy. *Phys Med Biol.* 2002;47:615–629.
13. Bailey TA, Wacker JN, An DD, et al. Evaluation of ^{134}Ce as a PET imaging surrogate for antibody drug conjugates incorporating ^{225}Ac. *Nucl Med Biol.* 2022;110-111:28–36.
14. Hu A, Aluicio-Sarduy E, Brown V, et al. Py-macrodipa: a Janus chelator capable of binding medicinally relevant rare-earth radiometals of disparate sizes. *J Am Chem Soc.* 2021;143:10429–10440.
15. Thiele NA, Brown V, Kelly JM, et al. An eighteen-membered macrocyclic ligand for actinium-225 targeted alpha therapy. *Angew Chem Int Ed Engl.* 2017;56:14712–14717.
16. Satapathy S, Sood A, Das CK, Mittal BR. Evolving role of ^{225}Ac-PSMA radioligand therapy in metastatic castration-resistant prostate cancer: a systematic review and meta-analysis. *Prostate Cancer Prostatic Dis.* 2021;24:880–890.
17. Sathekge M, Bruchertseifer F, Knoesen O, et al. ^{225}Ac-PSMA-617 in chemotherapy-naive patients with advanced prostate cancer: a pilot study. *Eur J Nucl Med Mol Imaging.* 2019;46:129–138.
18. Su Y, Liu Y, Behrens CR, et al. Targeting CD46 for both adenocarcinoma and neuroendocrine prostate cancer. *JCI Insight.* 2018;3:e121497.
19. Wang S, Li J, Hua J, et al. Molecular imaging of prostate cancer targeting CD46 using immunoPET. *Clin Cancer Res.* 2021;27:1305–1315.
20. Bidkar AP, Wang S, Bobba KN, et al. Treatment of prostate cancer with CD46 targeted ^{225}Ac alpha particle radioimmunotherapy. *Clin Cancer Res.* March 14, 2023 [Epub ahead of print].
21. Bobba K, Bidkar A, Wang S, et al. Influence of short PEG linkers on biodistribution of ^{225}Ac-macropa-YS5, an immunoconjugate for treating CD46 expressing cancer [abstract]. *Nucl Med Biol.* 2022;108–109(suppl):S53.
22. Li J, Huang T, Hua J, et al. CD46 targeted ^{212}Pb alpha particle radioimmunotherapy for prostate cancer treatment. bioRxiv website. https://www.biorxiv.org/content/10.1101/2022.10.14.512321v1. Published October 18, 2022. Accessed April 13, 2023.
23. Afshar-Oromieh A, Hetzheim H, Kratochwil C, et al. The theranostic PSMA ligand PSMA-617 in the diagnosis of prostate cancer by PET/CT: biodistribution in humans, radiation dosimetry, and first evaluation of tumor lesions. *J Nucl Med.* 2015;56:1697–1705.
24. Thakral P, Simecek J, Marx S, Kumari J, Pant V, Sen IB. In-house preparation and quality control of Ac-225 prostate-specific membrane antigen-617 for the targeted alpha therapy of castration-resistant prostate carcinoma. *Indian J Nucl Med.* 2021;36:114–119.
25. Chauvin A, Tripier R, Bünzli J. A new versatile methodology for the synthesis of 4-halogenated-6-diethylcarbamoylpyridine-2-carboxylic acids. *Tetrahedron Lett.* 2001;42:3089–3091.
26. Dewulf J, Hrynchak I, Geudens S, et al. Improved characteristics of RANKL immuno-PET imaging using radiolabeled antibody Fab fragments. *Pharmaceutics.* 2022;14:939.
27. Current K, Meyer C, Magyar CE, et al. Investigating PSMA-targeted radioligand therapy efficacy as a function of cellular PSMA levels and intratumoral PSMA heterogeneity. *Clin Cancer Res.* 2020;26:2946–2955.
28. Nedrow JR, Latoche JD, Day KE, et al. Targeting PSMA with a Cu-64 labeled phosphoramidate inhibitor for PET/CT imaging of variant PSMA-expressing xenografts in mouse models of prostate cancer. *Mol Imaging Biol.* 2016;18:402–410.
29. Edem PE, Fonslet J, Kjær A, Herth M, Severin G. In vivo radionuclide generators for diagnostics and therapy. *Bioinorg Chem Appl.* 2016;2016:6148357.
30. Severin GW, Kristensen LK, Nielsen CH, et al. Neodymium-140 DOTA-LM3: evaluation of an in vivo generator for PET with a non-internalizing vector. *Front Med (Lausanne).* 2017;4:98.
31. Severin GW, Fonslet J, Kristensen LK, et al. PET in vivo generators ^{134}Ce and ^{140}Nd on an internalizing monoclonal antibody probe. *Sci Rep.* 2022;12:3863.

Regression of Myocardial ^{99m}Tc-DPD Uptake After Tafamidis Treatment of Cardiac Transthyretin Amyloidosis

Maria Papathanasiou*[1], Lukas Kessler*[2], Frank M. Bengel[3], Aiste-Monika Jakstaite[1], David Kersting[2], Zohreh Varasteh[2], Peter Luedike[1], Alexander Carpinteiro[4], Ken Herrmann[2], Tienush Rassaf[1], and Christoph Rischpler[2,5]

[1]*Department of Cardiology and Vascular Medicine, West German Heart and Vascular Center, University Hospital Essen, Essen, Germany;* [2]*Department of Nuclear Medicine, University Hospital Essen, Essen, Germany;* [3]*Department of Nuclear Medicine, Hannover Medical School, Hannover, Germany;* [4]*Department of Hematology and Stem Cell Transplantation, University Hospital Essen, Essen, Germany; and* [5]*Department of Nuclear Medicine, Klinikum Stuttgart, Stuttgart, Germany*

Cardiac transthyretin amyloidosis is an infiltrative cardiomyopathy with high mortality. To date, there are no specific biomarkers to directly assess disease activity and response to specific treatments. Our aim was to evaluate scintigraphic changes after treatment with the transthyretin stabilizer tafamidis. **Methods:** We included patients who had undergone ^{99m}Tc-3,3-diphosphono-1,2-propanodicarboxylic acid (^{99m}Tc-DPD) scintigraphy before tafamidis initiation and after at least 9 mo. Tracer activity was assessed visually and quantitatively as SUV_{max}. **Results:** The study included 14 patients who were on tafamidis for 44 ± 14 mo. We observed regression of Perugini grade in 5 patients, unchanged grade in 9 patients, and regression of mean heart–to–contralateral-lung ratio ($P = 0.015$) and SUV_{max} ($P = 0.005$). There were no changes in N-terminal pro-B-type natriuretic peptide or echocardiographic measures. **Conclusion:** Treatment with tafamidis results in regression of myocardial ^{99m}Tc-DPD uptake. ^{99m}Tc-DPD scintigraphy may provide useful imaging biomarkers to assess response to treatment.

Key Words: transthyretin; tafamidis; amyloidosis; cardiomyopathy; bone tracers

J Nucl Med 2023; 64:1083–1086
DOI: 10.2967/jnumed.122.265352

Tafamidis is a first-in-class transthyretin stabilizer and currently the only approved treatment for cardiac transthyretin-type amyloidosis (ATTR). Implementation of disease-modifying therapies to stabilize or decelerate this inherently progressive disease has unveiled the need to identify reliable markers of disease activity. This is particularly challenging since it is largely unknown whether amyloid infiltration and the resulting myocardial damage are reversible and at which time point relevant changes can be expected. Current recommendations suggest the evaluation of standard clinical parameters of heart failure severity such as New York Heart Association (NYHA) class, serum biomarkers, and echocardiographic parameters (*1*). In addition to these traditional but nonspecific markers, further assays may be needed for a comprehensive assessment of response to antiamyloid treatments.

Received Dec. 21, 2022; revision accepted Apr. 14, 2023.
For correspondence or reprints, contact Christoph Rischpler (c.rischpler@klinikum-stuttgart.de).
*Contributed equally to this work.
Published online Jun. 8, 2023.

Serial imaging has the potential to identify novel markers of disease activity and disentangle the complex pathophysiology of amyloidosis. MRI with extracellular volume estimation provides a surrogate of myocardial amyloid burden. A previous study demonstrated extracellular volume regression or stabilization in 13 of 16 patients with hereditary cardiac ATTR who received patisiran (*2*). In the same study, visually assessed tracer uptake declined in 15 of 16 patients with serial ^{99m}Tc-labeled 3,3-diphosphono-1,2-propanodicarboxylic acid (^{99m}Tc-DPD) scintigraphy. Recently, Rettl et al. showed that treatment with tafamidis delayed the extracellular volume expansion compared with untreated historical controls in serial MRI scans (*3*). The current study aimed to perform a comprehensive analysis of visual, semiquantitative, and quantitative measures of ^{99m}Tc-DPD uptake in patients with cardiac ATTR under long-term tafamidis therapy.

MATERIALS AND METHODS

This analysis retrospectively included patients with cardiac ATTR under tafamidis who had undergone ^{99m}Tc-DPD scans, with SPECT/low-dose CT of the chest for diagnostic purposes before treatment initiation and after at least 9 mo of treatment. All patients received echocardiography and laboratory testing as part of a standardized follow-up. Our analysis included SPECT/CT-based quantitation of tracer uptake, which is inherently more accurate than visual or semiquantitative grading methods (*4,5*). The detailed scintigraphic protocol and quantitative method were previously published (*5*). Briefly, SPECT/CT systems (Symbia T2 and Intevo; Siemens Healthineers) were calibrated by phantom measurements. We used a whole-heart segmentation method to overcome the limitations of anatomic segmentation in noncontrast low-dose CT. The calculated voxel-based activity concentration was decay-corrected and converted to SUVs normalized to body weight. For comparative analysis, all studies were conducted with identical radiotracer, camera, and acquisition conditions. Two masked nuclear medicine physicians analyzed the images. The following quantitative measures were estimated: heart–to–contralateral-lung (H/CL) ratio, SUV_{max}, and quantitative ratios of uptake in the myocardium to the blood pool and in the myocardium to the vertebral bone. The institutional review board approved this retrospective study, and the requirement to obtain informed consent was waived (20-9278-BO).

Descriptive statistics are reported as means and SDs for continuous variables and counts and percentages for categoric variables unless indicated otherwise. Variables at baseline and follow-up imaging were compared with the paired *t* test for interval scaled variables and with the Wilcoxon matched-pairs signed rank test for ordinal scaled variables. All statistical tests and CIs were 2-sided, and *P* values of less

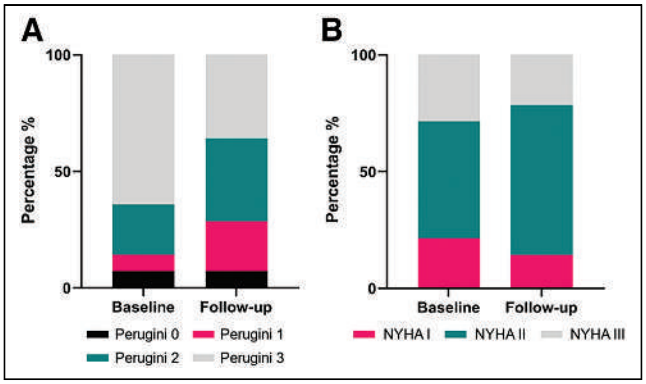

FIGURE 1. Changes in visual Perugini grade (A) and NYHA functional class (B) under treatment with tafamidis.

than 0.05 were considered statistically significant. All analyses were performed with GraphPad Prism (version 9.1.1; GraphPad Software).

RESULTS

The study included 14 patients, 11 with wild-type and 3 with hereditary cardiac ATTR. The mean age was 76 y, and 79% were male. At baseline, NYHA I class symptoms were reported in 3 patients, NYHA II in 7, and NYHA III in 4. Perugini grades of 0, 1, 2, and 3 were found in 1, 1, 3, and 9 patients, respectively. After uninterrupted tafamidis therapy with 61 mg once daily for 44 ± 14 mo, we reported a stable or improving NYHA class in all but 3 patients (Fig. 1). Scintigraphic images were acquired 197 ± 31 min after injection with a mean injected activity of 547 ± 60 MBq of ^{99m}Tc-DPD. In 1 patient, only planar scintigraphy was performed at follow-up. Our analysis showed regression of Perugini grade in 5 patients and an unchanged grade in 9 patients but no increases. One patient improved from Perugini 3 to 1, and the other 4 patients had improvement by 1 grade (Table 1). Quantitative analysis revealed regression of H/CL ratio (2.2 vs. 1.8, $P = 0.015$), SUV_{max} (11.9 vs. 7.5, $P = 0.005$), myocardium–to–blood-pool SUV_{max} ratio (8.5 vs. 5.2, $P = 0.029$), and myocardium–to–vertebral bone SUV_{max} ratio (1.9 vs. 1.1, $P = 0.038$), as depicted in Figure 2. A representative case of a 73-y-old woman after 57 mo of tafamidis treatment with regression of Perugini grade from 3 to 1 alongside decreasing H/CL ratio (from 2.1 to 1.4) and SUV_{max} (from 10.7 to 3.4) is shown in Figure 3. Scintigraphic findings of the study population are provided in Figure 4. There were no significant changes in N-terminal pro-B-type natriuretic peptide (4,872 vs. 3,919 pg/mL, $P = 0.24$) or in several echocardiographic measures of systolic and diastolic function, including left ventricular wall thickness, muscle mass index, global longitudinal strain (mean change: +1%, −11.9 vs. −10.9%, $P = 0.29$), and ejection fraction (mean change: −2.8%, 53.0 vs. 50.2%, $P = 0.08$). We found no correlation between absolute changes in laboratory and echocardiographic parameters and H/CL ratio or SUV_{max}.

DISCUSSION

The central finding of this study is that most patients exhibit regression of ^{99m}Tc-DPD uptake in response to tafamidis, as assessed by quantitative techniques. Even though the mechanism of bone tracer affinity in ATTR is not yet elucidated, the observed changes generate a new hypothesis regarding the long-term effects of tafamidis beyond the targeted stabilization of transthyretin in its tetrameric form. A possible explanation for the regression of tracer uptake is that the inhibition of de novo amyloidogenesis may enable removal or degradation of the deposited amyloid fibrils and a true reduction in the myocardial amyloid burden. A previous

TABLE 1
Study Results

Patient no.	Sex	Age (y)	Tafamidis (d)	Gillmore stage at diagnosis	ATTR type	*TTR* variant	% SUV_{max} change	% H/CL ratio change	Perugini, baseline	Perugini, follow up
1	M	82	714	3	WT	—	−56.21	−31.0	3	2
2	M	85	717	1	WT	—	22.64	11.1	0	0
3	M	84	744	2	WT	—	−39.03	−11.6	3	2
4	F	47	488	1	Variant	c.128G > A (p.Ser43Asn)	−55.72	−22.3	3	3
5	M	46	488	1	Variant	c.128G > A (p.Ser43Asn)	−32.59	−4.2	3	3
6	M	79	368	2	WT	No	−69.71	−20.4	2	1
7	M	83	292	2	WT	No	11.81	7.7	3	3
8	F	73	681	3	Variant	c.262A > T (p.Ile88Leu)	−67.88	−32.0	3	1
9	M	85	361	3	WT	—	−39.38	−19.9	3	3
10	M	83	358	1	WT	—	−27.96	−18.8	2	2
11	M	84	392	1	WT	—	NA	−18.2	3	3
12	M	82	367	2	WT	—	−34.48	−11.6	3	2
13	F	82	680	1	WT	—	26.19	−29.2	2	2
14	M	75	669	3	WT	—	−43.74	−4.3	1	1

TTR = transthyretin; WT = wild-type; NA = not applicable.

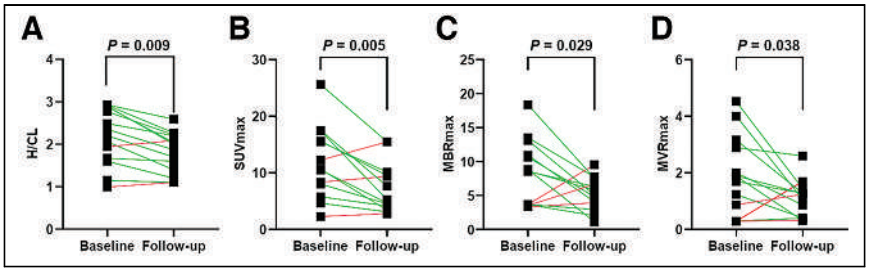

FIGURE 2. Changes in quantitative measures of ^{99m}Tc-DPD uptake at baseline (before tafamidis initiation) and follow-up: H/CL ratio (A), SUV_{max} (B), MBR_{max} (myocardium–to–blood-pool SUV_{max} ratio) (C), and MVR_{max} (myocardium–to–vertebral bone SUV_{max} ratio) (D).

report on 20 untreated cardiac ATTR patients who underwent serial scintigraphic assessment demonstrated no relevant changes in H/CL ratios after a median of 1.5 y (*6*), supporting the hypothesis that regression of tracer accumulation may reflect subsidence of the disease and a possible treatment effect.

Recently, preliminary data were reported from 2 ongoing randomized controlled trials using the small interfering RNAs vutrisiran and patisiran in patients with ATTR. The HELIOS A trial included patients with hereditary ATTR with polyneuropathy and compared vutrisiran with historic cohorts of patisiran- and placebo-treated patients from the APOLLO trial. In a subgroup of patients with cardiac involvement who were treated with vutrisiran, bone scintigraphy was repeated at 18 mo. Perugini grade was unchanged in 68% (39/57) and was decreased in 28% (16/57) of patients receiving serial scintigraphy, and only 3.5% (2/57) exhibited higher Perugini scores at follow up. H/CL ratio decreased in 65% (31/48) of patients treated with vutrisiran (*7*). In the APOLLO-B trial, which investigates patisiran versus placebo in patients with cardiac ATTR, scintigraphic changes at 12 mo were one of the selected exploratory endpoints. In 100% of evaluable patients in the patisiran arm ($n = 37$), Perugini grade decreased or demonstrated no change from baseline at 12 mo, and 38% of patients demonstrated a decrease in Perugini grade. No patients in the placebo arm ($n = 28$) demonstrated a decrease in Perugini grade at follow-up (*8*).

However, there is still a lack of robust data to provide evidence of amyloid removal, and these exploratory findings await confirmation by prospective studies with serial multiparametric assessment of myocardial function. Another hypothesis for the regression of uptake could be that antiamyloid treatments offer the myocardium

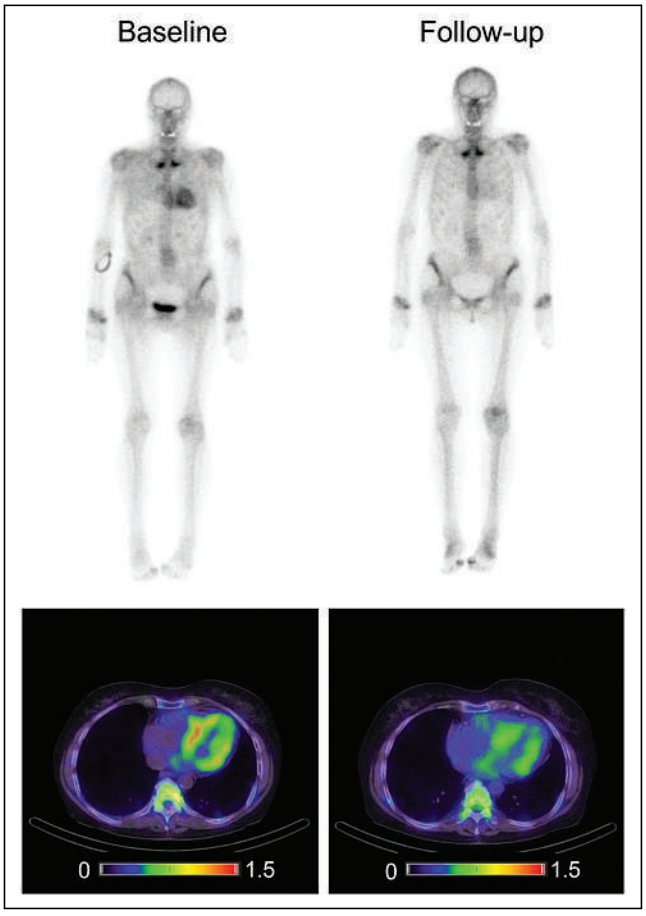

FIGURE 3. Whole-body planar ^{99m}Tc-DPD scintigraphy and corresponding SPECT/CT demonstrating regression of myocardial tracer accumulation after tafamidis treatment in 73-y-old woman with hereditary cardiac ATTR. Scintigraphic and SPECT/CT parameters from baseline to follow-up changed accordingly: visual Perugini, 3 vs. 1; SUV_{max}, 10,7 vs. 3.4; myocardium–to–blood-pool SUV_{max} ratio, 8.9 vs. 1.3; myocardium–to–vertebral bone SUV_{max} ratio, 1.9 vs. 0.3. Color scale is in kilocounts.

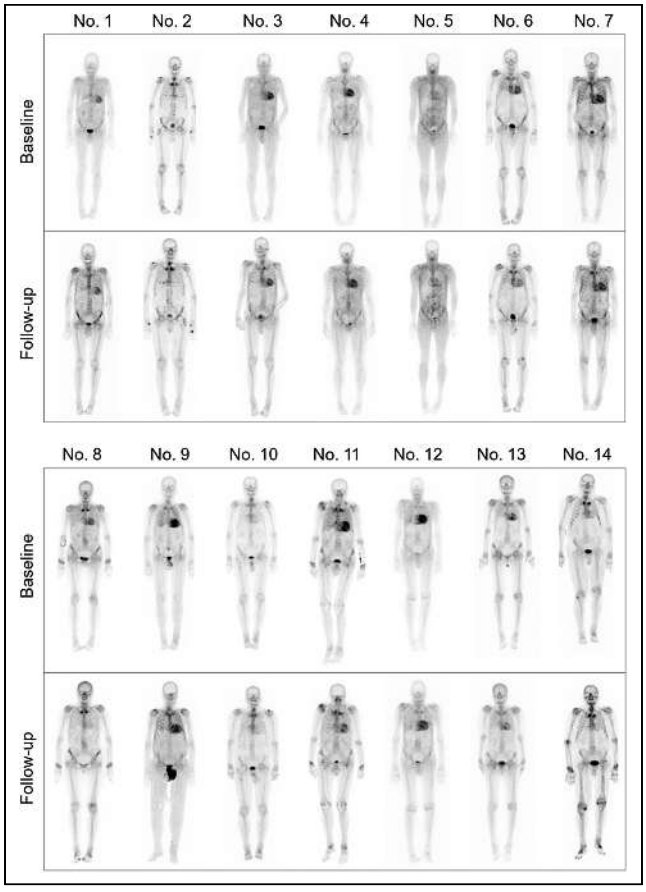

FIGURE 4. Planar scintigraphy findings at diagnosis and after treatment with tafamidis.

time to start a healing process and, thus, indirectly induce changes in the molecular properties of the deposited amyloid fibrils or the amyloid microenvironment so that the tracer affinity for amyloid is reduced. It is also possible that regression of ^{99m}Tc-DPD uptake is a perfusion-dependent phenomenon due to tracer redistribution in other compartments, such as muscles, soft tissues, and bone, despite stability or even progression of myocardial amyloid infiltration.

The strength of the current study lies in the quantitative image analysis and the multiparametric assessment over a long follow-up period. The study carries the inherent limitations of retrospective data analysis. There were no untreated patients with longitudinal ^{99m}Tc-DPD scintigraphy who could serve as a control group. The small study sample precludes a safe conclusion regarding the correlation of imaging findings with echocardiographic and biochemical indices of cardiac function or clinical outcomes.

CONCLUSION

In this report, we demonstrate the effect of tafamidis on scintigraphic and SPECT-derived biomarkers and its potential to reflect disease activity. It is of great interest to validate these results in larger cohorts and correlate the observed changes with multiple other disease markers to establish reliable biomarkers for guidance and monitoring of cardiac amyloid burden in response to disease-modifying therapy.

DISCLOSURE

This work was supported by the Universitaetsmedizin Essen Clinician Scientist Academy (UMEA) and the German Research Foundation (DFG, Deutsche Forschungs-Gemeinschaft; research grant FU356/12-1 to Maria Papathanasiou). No other potential conflict of interest relevant to this article was reported.

KEY POINTS

QUESTION: Are there any changes in myocardial bone tracer uptake after treatment with tafamidis for cardiac ATTR?

PERTINENT FINDINGS: In this study involving 14 patients with cardiac ATTR, treatment with the transthyretin stabilizer tafamidis resulted in regression of myocardial tracer uptake at a median of 44 mo after treatment initiation.

IMPLICATIONS FOR PATIENT CARE: Changes in quantitative measures of bone tracer uptake by the myocardium may reflect disease activity and facilitate assessment of response to disease-modifying therapies.

REFERENCES

1. Garcia-Pavia P, Bengel F, Brito D, et al. Expert consensus on the monitoring of transthyretin amyloid cardiomyopathy. *Eur J Heart Fail.* 2021;23:895–905.
2. Fontana M, Martinez-Naharro A, Chacko L, et al. Reduction in CMR derived extracellular volume with patisiran indicates cardiac amyloid regression. *JACC Cardiovasc Imaging.* 2021;14:189–199.
3. Rettl R, Mann C, Duca F, et al. Tafamidis treatment delays structural and functional changes of the left ventricle in patients with transthyretin amyloid cardiomyopathy. *Eur Heart J Cardiovasc Imaging.* 2022;23:767–780.
4. Scully PR, Morris E, Patel KP, et al. DPD quantification in cardiac amyloidosis: a novel imaging biomarker. *JACC Cardiovasc Imaging.* 2020;13:1353–1363.
5. Kessler L, Fragoso Costa P, Kersting D, et al. Quantitative ^{99m}Tc-DPD-SPECT/CT assessment of cardiac amyloidosis. *J Nucl Cardiol.* 2023;30:101–111.
6. Castaño A, DeLuca A, Weinberg R, et al. Serial scanning with technetium pyrophosphate (^{99m}Tc-PYP) in advanced ATTR cardiac amyloidosis. *J Nucl Cardiol.* 2016;23:1355–1363.
7. Mussinelli R, Garcia-Pavia P, Gillmore JD, et al. HELIOS-A: 18-month exploratory cardiac results from the phase 3 study of vutrisiran in patients with hereditary transthyretin-mediated amyloidosis. *Eur Heart J Suppl.* 2022;24(suppl K):suac121.654.
8. Kale P, Maurer MS, Fontana M, et al. Exploratory analyses from the APOLLO-B, a phase 3 study of patisiran in patients with ATTR amyloidosis with cardiomyopathy. Poster presented at: Heart Failure Society of America (HFSA) Annual Scientific Meeting; September 30–October 3, 2022; Washington, DC.

Hybrid ^{18}F-Fluoroethyltyrosine PET and MRI with Perfusion to Distinguish Disease Progression from Treatment-Related Change in Malignant Brain Tumors: The Quest to Beat the Toughest Cases

Nathaniel J. Smith[1,2], Tristan K. Deaton[3], Wendy Territo[1], Brian Graner[1], Andrew Gauger[1], Scott E. Snyder[1], Michael L. Schulte[1], Mark A. Green[1], Gary D. Hutchins[1], and Michael C. Veronesi[1]

[1]*School of Medicine, Indiana University, Indianapolis, Indiana;* [2]*Weldon School of Biomedical Engineering, Purdue University, West Lafayette, Indiana; and* [3]*Indiana University–Purdue University, Indianapolis, Indiana*

Conventional MRI has important limitations when assessing for progression of disease (POD) versus treatment-related changes (TRC) in patients with malignant brain tumors. We describe the observed impact and pitfalls of implementing ^{18}F-fluoroethyltyrosine (^{18}F-FET) perfusion PET/MRI into routine clinical practice. **Methods:** Through expanded-access investigational new drug use of ^{18}F-FET, hybrid ^{18}F-FET perfusion PET/MRI was performed during clinical management of 80 patients with World Health Organization central nervous system grade 3 or 4 gliomas or brain metastases of 6 tissue origins for which the prior brain MRI results were ambiguous. The diagnostic performance with ^{18}F-FET PET/MRI was dually evaluated within routine clinical service and for retrospective parametric evaluation. Various ^{18}F-FET perfusion PET/MRI parameters were assessed, and patients were monitored for at least 6 mo to confirm the diagnosis using pathology, imaging, and clinical progress. **Results:** Hybrid ^{18}F-FET perfusion PET/MRI had high overall accuracy (86%), sensitivity (86%), and specificity (87%) for difficult diagnostic cases for which conventional MRI accuracy was poor (66%). ^{18}F-FET tumor-to-brain ratio static metrics were highly reliable for distinguishing POD from TRC (area under the curve, 0.90). Dynamic tumor-to-brain intercept was more accurate (85%) than SUV slope (73%) or time to peak (73%). Concordant PET/MRI findings were 89% accurate. When PET and MRI conflicted, ^{18}F-FET PET was correct in 12 of 15 cases (80%), whereas MRI was correct in 3 of 15 cases (20%). Clinical management changed after 88% (36/41) of POD diagnoses, whereas management was maintained after 87% (34/39) of TRC diagnoses. **Conclusion:** Hybrid ^{18}F-FET PET/MRI positively impacted the routine clinical care of challenging malignant brain tumor cases at a U.S. institution. The results add to a growing body of literature that ^{18}F-FET PET complements MRI, even rescuing MRI when it fails.

Key Words: malignant brain tumors; WHO CNS grade 3 or 4 glioma; glioblastoma; brain metastasis; amino acid PET; ^{18}F-fluoroethyltyrosine (FET) PET

J Nucl Med 2023; 64:1087–1092
DOI: 10.2967/jnumed.122.265149

Malignant gliomas of World Health Organization central nervous system grade 3 or 4 (adult-type diffuse glioma, ATDG) and brain metastases (BM) cause significant morbidity and mortality annually (*1*). Although management has improved, these malignancies remain difficult to treat. Even with specialized care, patients with glioblastoma have a mean survival of 15–20 mo with standard-of-care therapy, and only about 5% survive past 5 y (*2*). BMs are 10 times more common than primary malignant brain tumors, portend a poor prognosis, and continue rising in incidence (*3,4*).

Conventional MRI is the standard clinical imaging modality for managing brain tumors; however, it remains suboptimal for response assessment and treatment monitoring when distinguishing the progression of disease (POD) from treatment-related changes (TRCs) (*5*). MRI signal abnormalities lack biologic specificity, as T2-derived abnormalities reflect tissue water content, and contrast enhancement identifies regions of high blood–brain barrier permeability.

In MRI, perfusion-weighted imaging (PWI) indirectly measures malignancy by detecting neovascularity. Dynamic susceptibility contrast PWI captures signal loss within susceptibility-weighted sequences as paramagnetic gadolinium moves through tumor tissue (*6*). Dynamic contrast-enhanced PWI evaluates T1 relaxivity as gadolinium contrast medium passes through tissue (*7*). Although PWI techniques partially overcome conventional MRI limitations, reported clinical thresholds vary widely because of differences in acquisition protocols, scanner hardware, and overlapping tumor and normal-tissue parametric distributions (*8–11*).

To help overcome MRI's limitations, international working groups recommend amino acid PET imaging for complementary assessment of malignant brain tumors given superior tumor-to-background contrast (*12–14*). ^{18}F-fluoroethyltyrosine (^{18}F-FET) is the most commonly used amino acid radiotracer, providing a high diagnostic value for differentiating POD from TRC (*15–18*). PWI combined with ^{18}F-FET PET demonstrates increased sensitivity and specificity for delineating POD from TRC in malignant brain tumors, with hybrid ^{18}F-FET PET/MRI further increasing the accuracy (*5,19,20*).

We report the clinical application of hybrid ^{18}F-FET PET/MRI to patients with malignant brain tumors at a U.S. institution to

Received Nov. 16, 2022; revision accepted Feb. 16, 2023.
For correspondence or reprints, contact Michael Veronesi (michael.veronesi@gmail.com).
Published online Apr. 28, 2023.

discern POD from TRC. This report provides additional evidence supporting the complementary nature of ^{18}F-FET PET and MRI, reinforcing the European Association of Neurooncology/Response Assessment in Neurooncology (EANO/RANO) working group recommendations.

MATERIALS AND METHODS

^{18}F-FET PET/MRI (3T Biograph mMR; Siemens) was performed for 80 adult patients with known ATDG (n = 42) or BM (n = 38). Advanced imaging discerned whether abnormalities in standard-of-care imaging corresponded to POD or TRC, with a 6-mo clinical follow-up (33 BM and 36 ATDG) or pathologic reference (5 BM and 6 ATDG) diagnosis. The institutional review board approved this study, and all subjects provided written informed consent for imaging with ^{18}F-FET, which was prepared and clinically administered under expanded-access investigational-new-drug application 150883. Patients underwent standard cranial MRI, including 3-dimensional T1-weighted sequences before and after contrast medium, T2-weighted sequences, 3-dimensional fluid-attenuated inversion recovery sequences, diffusion-weighted imaging, apparent diffusion coefficient imaging, and susceptibility-weighted imaging. Patients received a half-and-half gadobutrol (Gadavist [Bayer]; 0.1 mL/kg of body weight) injection before dynamic susceptibility contrast MRI (repetition time, 1,600 ms; echo time, 30.0 ms; 90° flip angle; 1.7 × 1.7 × 4.0 mm voxel size; 2,020-ms temporal resolution) and dynamic contrast-enhanced TWIST (time-resolved angiography with interleaved stochastic trajectories; Siemens) MRI (repetition time, 3.91 ms; echo time, 1.54 ms; dynamic temporal resolution, 2.70 s; 10° flip angle; 1.1 × 1.1 × 5.0 mm voxel size). ^{18}F-FET PET data were acquired in list mode from 0 to 40 min, concurrent with MRI acquisitions, allowing reconstruction as both single-frame late static images and a dynamic sequence for assessing regional radiopharmaceutical kinetics. ^{18}F-FET (503–810 MBq) was administered as a bolus followed by a saline flush. Relatively high ^{18}F-FET doses were used to enhance small-lesion (<10 mm) detection, with estimated critical organ doses remaining commensurate with standard clinical nuclear medicine procedures. Image analysis and interpretation followed the Society of Nuclear Medicine and European Association of Nuclear Medicine procedural recommendations for ^{18}F-FET PET/MRI of brain tumors (*14*). ^{18}F-FET analysis parameters included static (mean, maximum) and dynamic (slope, intercept, time-to-peak [TTP]) assessment for SUV and tumor-to-brain ratio (TBR) metrics (Fig. 1). PWI parameters included relative cerebral blood volume (rCBV), capillary permeability volume transfer constant (K_{trans}), and extravascular extracellular volume fraction. The Supplemental Methods contain more complete image acquisition, processing, and analysis details (supplemental materials are available at http://jnm.snmjournals.org) (*7,14,21–32*).

RESULTS

Patients

Eighty patients (47 men, 33 women) aged 17–77 y underwent ^{18}F-FET PET/MRI. Most patients were at least 50 y old (75%) and were Caucasian (91%) (Table 1). Standard-of-care treatments included MRI-localized gross (36/80) and subtotal (16/80) resection; stereotactic radiosurgery (56/80); γ-knife (13/80) and whole-brain radiation (9/80); and temozolomide (32/80), bevacizumab (10/80), monoclonal antibody (28/80), DNA alkylation (15/80), and small-molecule kinase inhibitor (5/80) chemotherapies. Equivocal MRI examinations occurred a median of 188 d (range, 52–1,252 d) after the initiation of radiotherapy, and patients received a median 4 adjuvant doses (range, 0–12) of temozolomide. ^{18}F-FET PET/MRI was performed a median of 10 mo (range, 2–95 mo) after radiation treatment, 9 mo (range, 1–76 mo) after surgery, and 38 d (range, 10–394 d) after the latest MRI exam. The supplemental materials contains additional patient information.

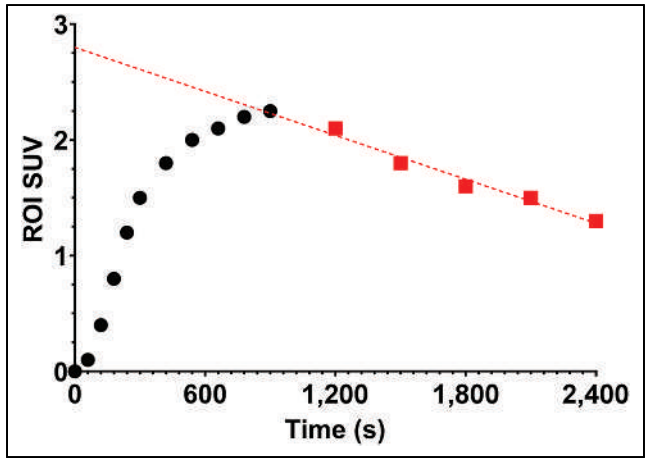

FIGURE 1. Dynamic slope and intercept estimation method. Regions of interest (ROIs) were located by neuroradiologist, and SUV_{mean} was extracted for every frame in dynamic sequence. Linear regression to scan's final 20–40 min determined slope and intercept terms. Slope is reported in units of SUV/h. For TBR analysis, ROIs were normalized by contralateral reference tissue ROI for every frame in dynamic sequence with same linear regression procedure. TTP was estimated from SUV dynamic sequence global maximum.

Forty-two ATDG patients (30 glioblastoma, 2 grade 4 diffuse astrocytoma, and 10 grade 3 diffuse astrocytoma) underwent ^{18}F-FET PET/MRI a median of 47 d after brain MRI with equivocal findings. Isocitrate dehydrogenase was wild type in 79% (33/42) patients, mutated in 19% (8/42) patients, and unknown in 1 patient. (6)-methylguanine-DNA methyltransferase was unmethylated in 43% (18/42) of patients, low-level methylated in 5% (2/42) of patients, methylated in 24% (10/42) of patients, hypermethylated in 14% (6/42) of patients, and unknown in 6 patients. Thirty-eight patients underwent ^{18}F-FET PET/MRI to assess BM treatment response. Disease origins included lung in 47% (18/38), colon or rectum in

TABLE 1
Demographics for the 80 Study Patients

Demographic	*n*
Sex	
Male	47 (59%)
Female	33 (41%)
Age (y)	
<40	6 (7.5%)
40–49	14 (18%)
50–59	29 (36%)
60–69	25 (31%)
≥70	6 (7.5%)
White/Caucasian*	73 (91%)
Black/African American	3 (4%)
Hispanic/Latinx	2 (3%)
Asian	2 (3%)

*Denotes overrepresentation relative to overall US incidence.

TABLE 2
Institutional Performance with Hybrid ^{18}F-FET PET/MRI

Index	Overall	High-grade glioma	BM
Total patients	80	42	38
True-positive (true POD)*	36	28	8
True-negative (true TRC)*	33	8	25
False-positive*	5	2	3
False-negative*	6	4	2
Accuracy	86%	86%	87%
Sensitivity	86%	88%	80%
Specificity	87%	83%	88%
Positive predictive value	88%	93%	73%
Negative predictive value	85%	67%	93%
Positive likelihood ratio	6.5	4.4	7.5
Negative likelihood ratio	0.16	0.16	0.22
False-positive rate	13%	20%	11%
False-negative rate	14%	13%	20%

*Confirmed by 6 mo of follow-up.

Performance shown demonstrates overall clinical performance with integrating ^{18}F-FET PET/MRI into care, using literature-based and institutional thresholds (rCBV > 3:1, K_{trans} > 0.26, TBR_{max} > 2.5) to assist in image-derived diagnosis.

5% (2/38), kidney in 13% (5/38), melanoma in 11% (4/38), breast in 18% (7/38), and thyroid in 3% (1/38) and were unspecified in 3% (1/38).

Observed Performance of ^{18}F-FET PET/MRI

Table 2 summarizes the institutional diagnostic performance of ^{18}F-FET PET/MRI. The accuracy, sensitivity, and specificity were similar across all disease origins (~85%). Figure 2 demonstrates an example case with hybrid ^{18}F-FET PET/PWI assisting to provide a diagnosis, and Supplemental Figures 1–4 provide examples of true-positive, true-negative, false-positive, and false-negative institutional diagnoses. Only 11 cases (14%) were misidentified in this study, 5 as false-positives and 6 as false-negatives. False-negative diagnoses occurred nearly twice as frequently in ATDG patients (4/42, 9.5%) as in BM patients (2/38, 5.3%). Of the 11 misdiagnosed patients, 7 had a tumor volumes of less than 10 cm^3. Most mischaracterized lesions had increased in size from the previous MRI exam (7/11); 3 were stable, and 1 decreased in size.

Figure 3 and Supplemental Table 1 display the combined pathology receiver-operating-characteristic (ROC) performance for all perfusion MRI, TBR normalized ^{18}F-FET PET/MRI uptake, and standardized ^{18}F-FET PET/MRI uptake parameters. The supplemental materials contain replicate ROC analyses stratified by disease origin (BM or ATDG), optimized cutoff thresholds, performance characteristics, and statistical justification. Increasing tumor volume on conventional MRI was only 60% (33/55) predictive of POD, whereas stagnant or receding MRI tumor volume was 64% (16/25) predictive of TRC. Overall, ^{18}F-FET PET/MRI metrics met or exceeded the diagnostic performance of perfusion MRI metrics. For combined ATDG and BM patients, maximum, mean, and intercept TBR metrics (TBR_{max}, TBR_{mean}, and $TBR_{intercept}$, respectively) generated area-under-the-ROC-curve (AUC) performance at or above 0.90 (Table 3). Institutional accuracy values mirrored the performance of these 3 metrics within 2% across all disease origins (BM or ATDG). In contrast, no perfusion-weighted MRI metric demonstrated an accuracy above 76%.

When directly compared, TBR_{max}, TBR_{mean}, and $TBR_{intercept}$ performed significantly better than K_{trans} and rCBV (Fig. 4; Table 4). The optimal perfusion-weighted MRI POD threshold (rCBV > 3.85) would have led to 10 false-positive and 9 false-negative mischaracterizations for this cohort without ^{18}F-FET PET. In these instances, 7 false-positives and 5 false-negatives would have been corrected by combination with the TBR_{max} threshold of more than 2.69 or the TBR_{mean} threshold of more than 2.16. Alternatively, if a TBR_{max} of more than 2.69 was the sole diagnostic metric, 7 false-negative and 3 false-positive cases would have occurred, and only 3 of the false-negative diagnoses would have been corrected by the rCBV threshold of more than 3.85.

When stratified by disease origin, select dynamic ^{18}F-FET PET/MRI metrics generated strong retrospective performance. Slope TBR metrics (TBR_{slope}) were 95% (36/38) accurate with an AUC of 0.97 for BM patients (Supplemental Fig. 5; Supplemental Table 2), and intercept SUV metrics ($SUV_{intercept}$) were 95% (40/42) accurate with an AUC of 0.96 for ATDG patients (Supplemental Fig. 6; Supplemental Table 3). Of the 5 BM patients who were incorrectly diagnosed, 4 had TBR_{slope} values that were consistent with their correct diagnosis. Perfusion-weighted MRI parameters yielded up to 90% (38/42) accuracy for ATDG patients, and 5 of 6 of the misdiagnosed ATDG patients had K_{trans} values and extravascular extracellular volume fractions consistent with their correct diagnosis. Further details on all patient disease characteristics, treatments, and imaging parameters can be found in Supplemental Tables 4–11. Supplemental Table 12 includes a small subset analysis of interrater reliability for PWI parameters, indicating strong correspondence between readers for K_{trans} and rCBV.

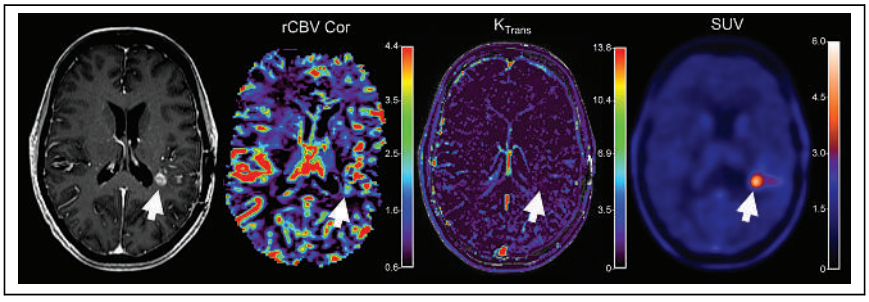

FIGURE 2. Patient with suspected recurrence of left parietal glioma (arrows) of World Health Organization central nervous system grade 4. Patient was initially evaluated with ^{18}F-FET PET/MRI for increasing contrast-enhanced T1-weighted MRI findings posterior to left resection cavity. Dynamic contrast-enhanced K_{trans} parameter met threshold for progression (0.38), but maximum rCBV value remained borderline (3.0). ^{18}F-FET PET TBR_{max} and TBR_{mean} exceeded threshold at 2.75 and 2.3, respectively, supporting diagnosis of disease progression. Bevacizumab treatment was initiated, and enhancement and perfusion pattern improved on follow-up MRI, remaining stable for 2.5 y. Serial ^{18}F-FET PET/MRI 2 y later remained stable.

DISCUSSION

This study demonstrated the utility of hybrid ^{18}F-FET PET/MRI with PWI in

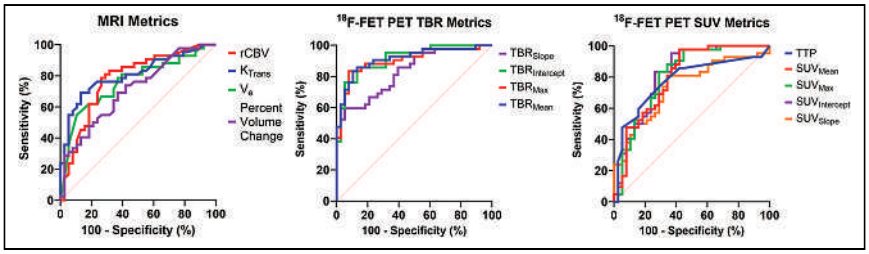

FIGURE 3. ROC curve analysis of perfusion-weighted MRI and ^{18}F-FET PET/MRI. Sensitivity was calculated as ratio of detected cases to all POD cases, and specificity was calculated as ratio of detected cases to all TRC cases. MRI metrics include rCBV, K_{trans}, and extravascular extracellular volume fraction (V_e). PET metrics included TBR, SUV, and TTP concentration. Dashed red line represents nondiagnostic test performance. Associated ROC quantitative analyses are in Table 3.

routine clinical medicine, applied across various primary and secondary disease origins, treatment regimens, and diagnostic timelines. Despite the patient heterogeneity, reported PWI and ^{18}F-FET PET performance were consistent with the literature. For ATDG patients, our rCBV (DSC MRI) sensitivity of 84%, specificity of 80%, and AUC of 0.88 were within the confidence bounds of a recent metaanalysis released by Fu et al. (*33*). Additionally, the K_{trans} (dynamic contrast-enhanced MRI) specificity of 80% and AUC of 0.88 for ATDG patients were within the confidence bounds of a metaanalysis released by Taylor et al., whereas our reported sensitivity was slightly higher, at 94% (*34*). Evidence for PWI is limited in BM patients, but Cicone et al. reported an rCBV accuracy of 76% and AUC within 0.65–0.96, which complement our 76% accuracy and AUC of 0.74 (*35*).

The complementary nature of perfusion-weighted MRI and amino acid PET uptake imaging improved clinician confidence compared with MRI alone. Importantly, when dynamic susceptibility contrast or dynamic contrast-enhanced MRI is suboptimal or nondiagnostic, ^{18}F-FET PET still supports high clinician diagnostic confidence because it resists PWI failure (*36*). Because interreader qualitative assessment varies with PWI alone (*37*), complementary imaging enables a more robust diagnostic outcome. Previous studies have advocated for sequential PWI and ^{18}F-FET PET in glioma evaluation due to a 100% reported positive predictive value for rCBV, but our reported 93% positive predictive value for rCBV did not exceed that of TBR_{mean} or TBR_{max} (96% and 97%, respectively) (*38*). ^{18}F-FET PET parameters also provided higher accuracy (TBR_{mean}, 86%; TBR_{max}, 88%) than rCBV (83%), supporting the use of simultaneous hybrid imaging, when available.

In this study, diagnostic accuracy was 89% (58/65) when PWI and ^{18}F-FET PET findings were concordant. When discordant, ^{18}F-FET PET indicated the correct diagnosis in 80% (12/15) of patients. However, 45% (5/11) of the false diagnoses occurred when hybrid imaging was discordant. In the 20% (3/15) of discordant imaging findings for which PWI indicated the correct diagnosis, ^{18}F-FET PET failed to detect POD. Overall, the institutional diagnostic accuracy mirrors that of ^{18}F-FET PET alone. Hybrid imaging exceeded the performance of perfusion MRI alone, but the impact of other useful MRI techniques, such as diffusion-weighted imaging, MR spectroscopy, and kurtosis imaging, was not evaluated in this study (*19,39–41*).

Our institution's ^{18}F-FET PET criteria included a TBR_{max} of more than 2.5 and a TBR_{mean} of more than 2.0, guided by publications cited in the EANO/RANO update (*14*). Calculated glioma

TABLE 3
Retrospective ROC-Optimized Thresholds and Analysis Results in All Patients (38 TRC, 42 POD) (for Fig. 3)

Modality	Parameter	Cutoff (%)	SN (%)	SP (%)	ACC (%)	PPV (%)	NPV (%)	AUC	95% CI	Adjusted *P*
MRI	Volume change	>13.5	69	63	66	67	65	0.71	0.60–0.82	<0.01
Perfusion MRI	rCBV	>3.85	79	74	76	77	76	0.78	0.67–0.88	<0.0001
	K_{trans}	>0.58	76	76	76	78	74	0.81	0.71–0.90	<0.0001
	V_e	>0.98	62	82	71	79	66	0.76	0.65–0.87	<0.0001
^{18}F-FET PET (TBR)	TBR_{slope}	<−0.69	67	79	73	78	68	0.83	0.74–0.92	<0.0001
	$TBR_{intercept}$	>2.39	83	87	85	88	83	0.91	0.85–0.98	<0.0001
	TBR_{max}	>2.69	83	92	88	92	83	0.90	0.84–0.97	<0.0001
	TBR_{mean}	>2.16	86	87	86	88	85	0.91	0.85–0.98	<0.0001
^{18}F-FET PET (SUV)	SUV_{slope}	<0.24	81	66	73	71	75	0.74	0.63–0.85	<0.001
	$SUV_{intercept}$	>2.07	83	74	79	78	80	0.82	0.72–0.91	<0.0001
	SUV_{max}	>2.42	83	71	76	76	77	0.81	0.71–0.91	<0.0001
	SUV_{mean}	>2.01	81	66	74	72	76	0.80	0.70–0.90	<0.0001
	TTP	<1,800	74	71	73	74	71	0.78	0.67–0.88	<0.0001

SN = sensitivity; SP = specificity; ACC = accuracy; PPV = positive predictive value; NPV = negative predictive value; V_e = extravascular extracellular volume fraction.

Significance is adjusted for multiple comparisons using Benjamini–Hochberg method and tests for AUC > 0.5. All metrics tested as significant. Cutoffs were calculated by optimizing geometric mean of sensitivity and specificity for ROC curve.

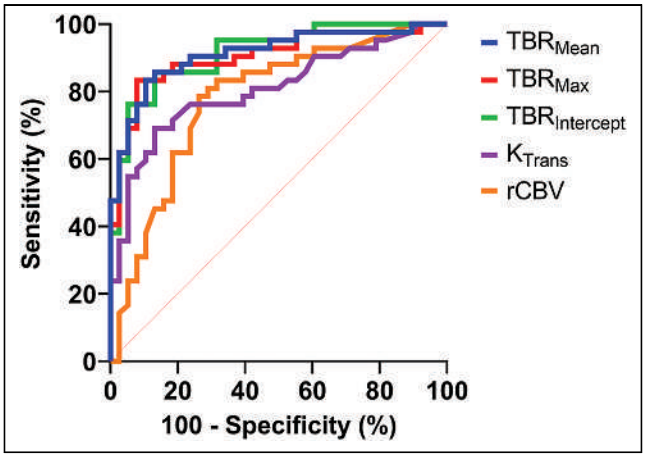

FIGURE 4. ROC curve performance comparison for select perfusion-weighted MRI and ^{18}F-FET PET parameters. Sensitivity was calculated as ratio of detected cases to all POD cases, and specificity was calculated as ratio of detected cases to all TRC cases. MRI metrics include rCBV and K_{trans}. PET metrics included $TBR_{intercept}$, TBR_{max}, and TBR_{mean}. Dashed red line represents nondiagnostic test performance. Associated comparative tests are in Table 4.

thresholds included a TBR_{max} of more than 2.42 and a TBR_{mean} of more than 2.16, in support of the criteria. Individually, these static ^{18}F-FET PET TBR parameters achieved 86%–88% diagnostic accuracy, 84%–88% sensitivity, and 90% specificity, consistent with other reports (*17,39*). For BM, our diagnostic accuracy with TBR_{max} approximates literature values, but with an elevated threshold of 2.79 relative to the 2.55 literature threshold (*15,16*). POD prevalence was only 26% (10/38) in our BM patients, which could generate a biased threshold estimate. Combined, our data support a TBR_{max} threshold of 2.69 (88% accuracy, 83% sensitivity, 92% specificity) across all disease origins. Our threshold exceeds the suggested EANO/RANO criteria of 2.5 (84% accuracy, 86% sensitivity, 82% specificity), reflecting a blend of the BM and ATDG stratified criteria. Compared with international recommendations, our threshold improves the overall accuracy for our patients, but at the cost of slightly reduced sensitivity and an increased false-negative rate.

TABLE 4
ROC Comparison of Select Perfusion-Weighted MRI and ^{18}F-FET PET/MRI Metrics (for Fig. 4)

Metrics compared	Metric 1 AUC	Metric 2 AUC	Adjusted *P*
$TBR_{intercept}$ vs. rCBV	0.9148	0.7785	0.024*
TBR_{mean} vs. rCBV	0.9123	0.7785	0.015*
TBR_{max} vs. rCBV	0.9041	0.7785	0.013*
$TBR_{intercept}$ vs. K_{trans}	0.9148	0.8058	0.025*
TBR_{mean} vs. K_{trans}	0.9123	0.8058	0.026*
TBR_{max} vs. K_{trans}	0.9041	0.8058	0.028*
K_{trans} vs. rCBV	0.8058	0.7785	0.310 (NS)

*$P < 0.05$.
NS = not significant.
P values are calculated using Hanley ROC comparison method and adjusted for multiple comparisons using Benjamini–Hochberg method. Significance tests are for overperformance of metric 1 relative to metric 2. Evaluated over entire 80-patient sample, listed TBR metrics demonstrate superior performance in AUC compared with K_{trans} and rCBV. No significant difference in performance exists between rCBV (dynamic susceptibility contrast MRI) and K_{trans} (dynamic contrast-enhanced MRI).

Guidelines for ATDG and BM evaluation recommend the use of static and dynamic ^{18}F-FET PET analysis (*13,14*), promoting slope SUV metrics (SUV_{slope}) and TTP as the most accurate dynamic metrics. Although SUV_{slope} and TTP demonstrated strong performance for BM and ATDG, with our results matching literature accuracy (*39*), our data suggest the need for an origin-specific diagnostic approach. For ATDG, $SUV_{intercept}$ enabled a 95% diagnostic accuracy, with an AUC greater than the TTP and SUV_{slope} (Supplemental Table 3). Because the $SUV_{intercept}$ varies with the TTP, SUV_{slope}, and the absolute SUV scaling of the time–activity curve, we hypothesize that performance characteristics can be attributed to this multifactorial diagnostic combination. For BM, TBR_{slope} enabled a 95% diagnostic accuracy (Supplemental Table 2), outperforming SUV_{slope}. Because TBR metrics normalize the SUV signal to a contralateral reference region, we posit that TBR_{slope} achieves high accuracy by reducing the impact of regional uptake differences and patient weight variability.

^{18}F-FET prompted false-negative conclusions more frequently when the lesion was less than 10 cm^3 in volume (Supplemental Fig. 4), consistent with other reports indicating the importance of suprathreshold tumor volumes (*42*). Partial-volume artifacts can dilute the ^{18}F-FET signal from small lesions, obscuring them with adjacent brain signals. To address this, serial ^{18}F-FET PET/MRI may enhance subclinical lesion interpretation when compared with single-session ^{18}F-FET PET/MRI and periodic follow-up PWI.

This study demonstrates the value of clinical ^{18}F-FET PET/MRI; however, there are still limitations to its clinical use. Clinical scans are inconsistent in their posttreatment timing and are subject to treatment heterogeneity. This study is also susceptible to referral bias, omitting cases in which a prior MRI exam sufficiently established a definitive diagnosis, as evidenced by the low diagnostic performance of contrast-enhanced MRI lesion volume change relative to other investigated parameters (Table 3). However, this implicit focus on challenging case referrals is consistent with other reports in the literature and with the common clinical indications for ^{18}F-FET PET (*43*). Additionally, this study was limited in sample size for stratification by disease type. When assessing ATDG alone, there was an asymmetrically higher number of cases of POD (76%, 32/42) than of METs (24%, 10/42). Conversely, there were fewer METs with POD (26%, 10/38) than with TRC (74%, 28/38). Although most analyses were considered in aggregate, the supplemental materials stratified by disease type did not have balanced outcomes and should be interpreted cautiously.

CONCLUSION

This study demonstrates the overall benefit of implementing hybrid ^{18}F-FET PET/MRI for patients with malignant brain tumors when conventional MRI and PWI were equivocal for discerning disease progression from nonmalignant treatment changes. Sample size limitations and the subjective nature of regional analysis may limit the generalizability of the study findings; however, this study provides a benchmark for prospective analyses and establishes a framework through which ^{18}F-FET PET/MRI may be clinically introduced.

DISCLOSURE

No potential conflict of interest relevant to this article was reported.

ACKNOWLEDGMENT

We thank Sharon Sidenbender for administrative support.

KEY POINTS

QUESTION: What is the clinical impact of perfusion ^{18}F-FET PET/MRI on assessing posttreatment brain malignancies?

PERTINENT FINDINGS: TBR metrics can distinguish posttreatment disease progression from treatment-related change with high accuracy.

IMPLICATIONS FOR PATIENT CARE: ^{18}F-FET PET/MRI improves clinician diagnostic confidence and informs timely, appropriate treatment modifications.

REFERENCES

1. Miller KD, Ostrom QT, Kruchko C, et al. Brain and other central nervous system tumor statistics, 2021. *CA Cancer J Clin.* 2021;71:381–406.
2. Stupp R, Taillibert S, Kanner AA, et al. Maintenance therapy with tumor-treating fields plus temozolomide vs temozolomide alone for glioblastoma: a randomized clinical trial. *JAMA.* 2015;314:2535–2543.
3. Nieblas-Bedolla E, Zuccato J, Kluger H, Zadeh G, Brastianos PK. Central nervous system metastases. *Hematol Oncol Clin North Am.* 2022;36:161–188.
4. Ostrom QT, Wright CH, Barnholtz-Sloan JS. Chapter 2: brain metastases—epidemiology. In: Schiff D, van den Bent MJ, eds. *Handbook of Clinical Neurology.* Vol 149. Elsevier; 2018:27–42.
5. Stopa BM, Juhász C, Mittal S. Comparison of amino acid PET to advanced and emerging MRI techniques for neurooncology imaging: a systematic review of the recent studies. *Mol Imaging.* 2021;2021:8874078.
6. Lev MH, Ozsunar Y, Henson JW, et al. Glial tumor grading and outcome prediction using dynamic spin-echo MR susceptibility mapping compared with conventional contrast-enhanced MR: confounding effect of elevated rCBV of oligodendroglimoas. *Am J Neuroradiol.* 2004;25:214–221.
7. Tofts PS, Brix G, Buckley DL, et al. Estimating kinetic parameters from dynamic contrast-enhanced t_1-weighted MRI of a diffusable tracer: standardized quantities and symbols. *J Magn Reson Imaging.* 1999;10:223–232.
8. Shukla-Dave A, Obuchowski NA, Chenevert TL, et al. Quantitative imaging biomarkers alliance (QIBA) recommendations for improved precision of DWI and DCE-MRI derived biomarkers in multicenter oncology trials. *J Magn Reson Imaging.* 2019;49:e101–e121.
9. Bell LC, Semmineh N, An H, et al. Evaluating the use of rCBV as a tumor grade and treatment response classifier across NCI quantitative imaging network sites: part II of the DSC-MRI digital reference object (DRO) challenge. *Tomography.* 2020;6:203–208.
10. Wang L, Wei L, Wang J, et al. Evaluation of perfusion MRI value for tumor progression assessment after glioma radiotherapy. *Medicine (Baltimore).* 2020;99:e23766.
11. Patel P, Baradaran H, Delgado D, et al. MR perfusion-weighted imaging in the evaluation of high-grade gliomas after treatment: a systematic review and meta-analysis. *Neuro Oncol.* 2017;19:118–127.
12. Albert NL, Weller M, Suchorska B, et al. Response assessment in neuro-oncology working group and European Association for neuro-oncology recommendations for the clinical use of PET imaging in gliomas. *Neuro Oncol.* 2016;18:1199–1208.
13. Galldiks N, Langen K-J, Albert NL, et al. PET imaging in patients with brain metastasis: report of the RANO/PET group. *Neuro Oncol.* 2019;21:585–595.
14. Law I, Albert NL, Arbizu J, et al. Joint EANM/EANO/RANO practice guidelines/SNMMI procedure standards for imaging of gliomas using PET with radiolabelled amino acids and [^{18}F]FDG: version 1.0. *Eur J Nucl Med Mol Imaging.* 2019;46:540–557.
15. Galldiks N, Stoffels G, Filss CP, et al. Role of *O*-(2-^{18}F-fluoroethyl)-L-tyrosine PET for differentiation of local recurrent brain metastasis from radiation necrosis. *J Nucl Med.* 2012;53:1367–1374.
16. Ceccon G, Lohmann P, Stoffels G, et al. Dynamic O-(2-^{18}F-fluoroethyl)-L-tyrosine positron emission tomography differentiates brain metastasis recurrence from radiation injury after radiotherapy. *Neuro Oncol.* 2017;19:281–288.
17. de Zwart PL, van Dijken BRJ, Holtman GA, et al. Diagnostic accuracy of PET tracers for the differentiation of tumor progression from treatment-related changes in high-grade glioma: a systematic review and metaanalysis. *J Nucl Med.* 2020;61:498–504.
18. Henriksen OM, Hansen AE, Muhic A, et al. Diagnostic yield of simultaneous dynamic contrast-enhanced magnetic resonance perfusion measurements and [^{18}F]FET PET in patients with suspected recurrent anaplastic astrocytoma and glioblastoma. *Eur J Nucl Med Mol Imaging.* 2022;49:4677–4691.
19. Sogani SK, Jena A, Taneja S, et al. Potential for differentiation of glioma recurrence from radionecrosis using integrated ^{18}F-fluoroethyl-L-tyrosine (FET) positron emission tomography/magnetic resonance imaging: a prospective evaluation. *Neurol India.* 2017;65:293–301.
20. Pyka T, Hiob D, Preibisch C, et al. Diagnosis of glioma recurrence using multiparametric dynamic ^{18}F-fluoroethyl-tyrosine PET-MRI. *Eur J Radiol.* 2018;103:32–37.
21. Rosen BR, Belliveau JW, Vevea JM, Brady TJ. Perfusion imaging with NMR contrast agents. *Magn Reson Med.* 1990;14:249–265.
22. Pöpperl G, Götz C, Rachinger W, Gildehaus F-J, Tonn J-C, Tatsch K. Value of O-(2-[^{18}F]fluoroethyl)-L-tyrosine PET for the diagnosis of recurrent glioma. *Eur J Nucl Med Mol Imaging.* 2004;31:1464–1470.
23. Louis DN, Perry A, Reifenberger G, et al. The 2016 World Health Organization classification of tumors of the central nervous system: a summary. *Acta Neuropathol (Berl).* 2016;131:803–820.
24. Louis DN, Perry A, Wesseling P, et al. The 2021 WHO classification of tumors of the central nervous system: a summary. *Neuro Oncol.* 2021;23:1231–1251.
25. McHugh ML. Interrater reliability: the kappa statistic. *Biochem Med (Zagreb).* 2012;22:276–282.
26. Shrout PE, Fleiss JL. Intraclass correlations: uses in assessing rater reliability. *Psychol Bull.* 1979;86:420–428.
27. Youden WJ. Index for rating diagnostic tests. *Cancer.* 1950;3:32–35.
28. Clopper CJ, Pearson ES. The use of confidence or fiducial limits illustrated in the case of the binomial. *Biometrika.* 1934;26:404–413.
29. Hanley JA, McNeil BJ. The meaning and use of the area under a receiver operating characteristic (ROC) curve. *Radiology.* 1982;143:29–36.
30. Hanley JA, McNeil BJ. A method of comparing the areas under receiver operating characteristic curves derived from the same cases. *Radiology.* 1983;148:839–843.
31. Benjamini Y, Hochberg Y. Controlling the false discovery rate: a practical and powerful approach to multiple testing. *J R Stat Soc B.* 1995;57:289–300.
32. Benjamini Y, Heller R, Yekutieli D. Selective inference in complex research. *Philos Trans A Math Phys Eng Sci.* 2009;367:4255–4271.
33. Fu R, Szidonya L, Barajas RF Jr, Ambady P, Varallyay C, Neuwelt EA. Diagnostic performance of DSC perfusion MRI to distinguish tumor progression and treatment-related changes: a systematic review and meta-analysis. *Neurooncol Adv.* 2022;4:vdac027.
34. Taylor C, Ekert JO, Sefcikova V, Fersht N, Samandouras G. Discriminators of pseudoprogression and true progression in high-grade gliomas: a systematic review and meta-analysis. *Sci Rep.* 2022;12:13258.
35. Cicone F, Minniti G, Romano A, et al. Accuracy of F-DOPA PET and perfusion-MRI for differentiating radionecrotic from progressive brain metastases after radiosurgery. *Eur J Nucl Med Mol Imaging.* 2015;42:103–111.
36. Overcast WB, Davis KM, Ho CY, et al. Advanced imaging techniques for neuro-oncologic tumor diagnosis, with an emphasis on PET-MRI imaging of malignant brain tumors. *Curr Oncol Rep.* 2021;23:34.
37. Zakhari N, Taccone M, Torres C, et al. Qualitative assessment of advanced MRI in post-treatment high grade gliomas follow up: do we agree? *Can Assoc Radiol J.* 2022;73:187–193.
38. Steidl E, Langen K-J, Hmeidan SA, et al. Sequential implementation of DSC-MR perfusion and dynamic [^{18}F]FET PET allows efficient differentiation of glioma progression from treatment-related changes. *Eur J Nucl Med Mol Imaging.* 2021;48:1956–1965.
39. Brendle C, Maier C, Bender B, et al. Impact of ^{18}F-FET PET/MR on clinical management of brain tumor patients. *J Nucl Med.* 2022;63:522–527.
40. Dang H, Zhang J, Wang R, et al. Glioblastoma recurrence versus radiotherapy injury: combined model of diffusion kurtosis imaging and ^{11}C-MET using PET/MRI may increase accuracy of differentiation. *Clin Nucl Med.* 2022;47:e428–e436.
41. D'Amore F, Grinberg F, Mauler J, et al. Combined ^{18}F-FET PET and diffusion kurtosis MRI in posttreatment glioblastoma: differentiation of true progression from treatment-related changes. *Neurooncol Adv.* 2021;3:vdab044.
42. Paprottka KJ, Kleiner S, Preibisch C, et al. Fully automated analysis combining [^{18}F]-FET-PET and multiparametric MRI including DSC perfusion and APTw imaging: a promising tool for objective evaluation of glioma progression. *Eur J Nucl Med Mol Imaging.* 2021;48:4445–4455.
43. Heinzel A, Dedic D, Galldiks N, et al. Two decades of brain tumour imaging with O-(2-[^{18}F]fluoroethyl)-L-tyrosine PET: the Forschungszentrum Jülich experience. *Cancers (Basel).* 2022;14:3336.

Hybrid ^{18}F-FET PET and Perfusion MRI to Differentiate Disease Progression from Treatment-Related Changes in Malignant Brain Tumors

Norbert Galldiks[1–3] and Karl-Josef Langen[2–4]

[1]*Department of Neurology, Faculty of Medicine and University Hospital Cologne, University of Cologne, Cologne, Germany;* [2]*Institute of Neuroscience and Medicine, Research Center Juelich, Juelich, Germany;* [3]*Center for Integrated Oncology, Universities of Aachen, Bonn, Cologne, and Duesseldorf, Germany; and* [4]*Department of Nuclear Medicine, RWTH University Hospital Aachen, Aachen, Germany*

Differentiation between progression of disease (POD) and treatment-related changes (TRCs) in brain tumors remains challenging. Both POD and TRCs can lead to mass effects, perilesional edema, and contrast enhancement in conventional MRI, which presents a major problem in clinical decision-making (*1*). PET using radiolabeled amino acids and advanced MRI methods such as perfusion-weighted imaging can provide substantial additional information in this crucial situation (*2*).

PET using radiolabeled amino acids is increasingly being applied in neurooncology, and its benefits have been documented in previous recommendations and guidelines of the PET task force of the Response Assessment in Neuro-Oncology Working Group (*3–7*). The longest-established amino acid tracer for PET is [^{11}C-methyl]-L-methionine, which requires an onsite cyclotron because of the short half-life of ^{11}C (20 min). Amino acids labeled with ^{18}F (half-life of 109.8 min) such as *O*-(2-^{18}F-fluoroethyl)-L-tyrosine (^{18}F-FET), 3,4-dihydroxy-6-^{18}F-fluoro-L-phenylalanine (^{18}F-FDOPA), or anti-1-amino-3-^{18}F-fluorocyclobutane-1-carboxylic acid (^{18}F-fluciclovine) offer considerable logistic advantages in clinical practice (*2*). ^{18}F-FDOPA was initially developed to evaluate dopamine synthesis in the basal ganglia, but the tracer can also be used for brain tumor imaging (*7*). In the United States and Europe, ^{18}F-FDOPA is approved for characterization of presynaptic dopaminergic activity in patients with parkinsonian syndromes. Notably, the physiologic uptake of ^{18}F-FDOPA in the striatum may hamper its use for the evaluation of brain tumor infiltration in this region (*7*). The synthetic amino acid analog anti-1-amino-3-^{18}F-fluorocyclobutane-1-carboxylic acid has gained clinical interest, particularly for the diagnosis of recurrent prostate cancer, but is now also considered for brain tumor imaging (*8*). ^{18}F-fluciclovine has been approved in the United States and Europe for evaluation of recurrent prostate cancer (*9*) and has orphan drug status for glioma imaging in the United States.

It is assumed that uptake of the mentioned amino acid tracers occurs mainly by facilitated transport via large neutral amino acid transporters of the L-type in gliomas and brain metastases (i.e., subtypes 1 and 2), which are regularly overexpressed in both brain tumor types (*7*). The tumor-to-brain contrast observed with ^{18}F-fluciclovine is higher than that of [^{11}C-methyl]-L-methionine, ^{18}F-FET, and ^{18}F-FDOPA (*10*), presumably because of the lower transport of ^{18}F-fluciclovine through the intact blood–brain barrier. Whether this feature is advantageous in brain tumor diagnosis needs to be clarified.

In Europe, ^{18}F-FET is the most frequently used amino acid tracer for brain tumor imaging, and especially in Germany, some centers have collectively performed more than 20,000 examinations because of the high clinical interest in this method (*11,12*). Furthermore, the increasing number of publications coming from Australia, China, India, and South Korea indicate a wide acceptance of this method (*13–17*). For ^{18}F-FET, approval exists in Switzerland (*18*) and in France (IASOglio; IASON). Clinical use of ^{18}F-FET and reimbursement is possible in several European countries depending on the local legislation or exemption for specialized centers.

A particular property of ^{18}F-FET is the additional information derived from time–activity curve analysis, which is useful for differential diagnosis of brain lesions (*11*). Several studies reported that high-grade gliomas characterized by older World Health Organization classifications typically show a short time to peak followed by a decreasing time–activity curve, whereas low-grade gliomas or nonneoplastic lesions usually exhibit delayed and steadily increasing tracer uptake (*19–22*). Such prominent differences in time–activity curve patterns are not provided by [^{11}C-methyl]-L-methionine or ^{18}F-FDOPA (*23,24*).

The hybrid PET/MRI study by Smith et al. including 80 patients with gliomas (n = 42) or brain metastases (n = 38) published in the current issue of *The Journal of Nuclear Medicine* represents the first study using ^{18}F-FET PET in the United States (*25*). The study provides a wide scope of data, and the results concerning the value of ^{18}F-FET PET for discerning POD from TRCs on MRI are in line with international studies as documented in a recent meta-analysis (*26*).

Smith et al. report the overall diagnostic performance of hybrid ^{18}F-FET PET/perfusion-weighted imaging (sensitivity, 86%; specificity, 87%) to differentiate POD from TRCs across all tumor types based on visual reading and analysis of tumor-to-brain ratios. The authors emphasize that ^{18}F-FET PET outperformed perfusion MRI metrics and positively impacted the routine clinical care of

Received Apr. 3, 2023; revision accepted Apr. 20, 2023.
For correspondence or reprints, contact Norbert Galldiks (norbert.galldiks@uk-koeln.de).
Published online May 18, 2023.

DOI: 10.2967/jnumed.123.265647

challenging malignant brain tumor cases. The authors could not replicate an improvement in overall performance when ^{18}F-FET PET was combined with perfusion-weighted imaging. The use of hybrid PET/MRI offers logistic advantages but seems not essential in this setting. Accordingly, a recent study demonstrated no differences between hybrid and sequential ^{18}F-FET PET MRI in the differentiation of recurrent gliomas (*27*). On the other hand, hybrid ^{18}F-FET PET/MRI offers essential advantages in pediatric patients by avoiding radiation exposure from the PET/CT scanner and repeated general anesthesia (*28*).

Special attention should be paid to the analysis of dynamic ^{18}F-FET PET data in the present study. Time to peak and the slope of the late phase of the time–activity curve (SUV_{slope}) yielded results consistent with previous literature. Of note, the authors identified the $SUV_{intercept}$ of the slope extrapolation as a novel parameter. Time to peak and SUV_{slope} influence $SUV_{intercept}$ in the same direction, and the parameter yielded higher accuracies to differentiate POD from TRCs than time to peak and SUV_{slope}. This presents an innovation that could further improve the use of dynamic ^{18}F-FET PET.

In conclusion, the study by Smith et al. suggests that the time has come to make ^{18}F-FET PET more widely available to U.S. patients. The necessary PET infrastructure is widely available, and the production of this tracer is well established, with costs comparable to those of other tracers routinely used in clinical practice. In addition, the cost-effectiveness of ^{18}F-FET PET has been demonstrated in several studies (*29–33*). A more reliable diagnostic assessment of recurrent brain tumors is desirable, as the costs of brain tumor therapy options are usually high and an efficient use of these therapies is of the utmost importance for both the patient and the treating physician. It is hoped that the study by Smith et al. represents a milestone in this process.

DISCLOSURE

Norbert Galldiks received honoraria for lectures from Blue Earth Diagnostics and honoraria for advisory board participation from Telix Pharmaceuticals. No other potential conflict of interest relevant to this article was reported.

REFERENCES

1. Galldiks N, Kocher M, Langen KJ. Pseudoprogression after glioma therapy: an update. *Expert Rev Neurother.* 2017;17:1109–1115.
2. Langen KJ, Galldiks N, Hattingen E, Shah NJ. Advances in neuro-oncology imaging. *Nat Rev Neurol.* 2017;13:279–289.
3. Law I, Albert NL, Arbizu J, et al. Joint EANM/EANO/RANO practice guidelines/SNMMI procedure standards for imaging of gliomas using PET with radiolabelled amino acids and [^{18}F]FDG: version 1.0. *Eur J Nucl Med Mol Imaging.* 2019;46:540–557.
4. Albert NL, Weller M, Suchorska B, et al. Response Assessment in Neuro-Oncology working group and European Association for Neuro-Oncology recommendations for the clinical use of PET imaging in gliomas. *Neuro Oncol.* 2016;18:1199–1208.
5. Galldiks N, Langen KJ, Albert NL, et al. PET imaging in patients with brain metastasis: report of the RANO/PET group. *Neuro Oncol.* 2019;21:585–595.
6. Galldiks N, Niyazi M, Grosu AL, et al. Contribution of PET imaging to radiotherapy planning and monitoring in glioma patients: a report of the PET/RANO group. *Neuro Oncol.* 2021;23:881–893.
7. Galldiks N, Langen KJ, Albert NL, et al. Investigational PET tracers in neuro-oncology: what's on the horizon? A report of the PET/RANO group. *Neuro Oncol.* 2022;24:1815–1826.
8. Laudicella R, Albano D, Alongi P, et al. ^{18}F-Facbc in prostate cancer: a systematic review and meta-analysis. *Cancers (Basel).* 2019;11:1348.
9. Bogsrud TV, Londalen A, Brandal P, et al. ^{18}F-fluciclovine PET/CT in suspected residual or recurrent high-grade glioma. *Clin Nucl Med.* 2019;44:605–611.
10. Albano D, Tomasini D, Bonu M, Giubbini R, Bertagna F. ^{18}F-fluciclovine (^{18}F-FACBC) PET/CT or PET/MRI in gliomas/glioblastomas. *Ann Nucl Med.* 2020;34:81–86.
11. Langen KJ, Stoffels G, Filss C, et al. Imaging of amino acid transport in brain tumours: positron emission tomography with O-(2-[^{18}F]fluoroethyl)-L-tyrosine (FET). *Methods.* 2017;130:124–134.
12. Heinzel A, Dedic D, Galldiks N, et al. Two decades of brain tumour imaging with O-(2-[^{18}F]fluoroethyl)-L-tyrosine PET: the Forschungszentrum Julich experience. *Cancers (Basel).* 2022;14:3336.
13. Puranik AD, Rangarajan V, Dev ID, et al. Brain FET PET tumor-to-white mater ratio to differentiate recurrence from post-treatment changes in high-grade gliomas. *J Neuroimaging.* 2021;31:1211–1218.
14. Chan DL, Hsiao E, Schembri G, et al. FET PET in the evaluation of indeterminate brain lesions on MRI: differentiating glioma from other non-neoplastic causes—a pilot study. *J Clin Neurosci.* 2018;58:130–135.
15. Cheng Y, Song S, Wei Y, et al. Glioma imaging by O-(2-^{18}F-fluoroethyl)-L-tyrosine PET and diffusion-weighted MRI and correlation with molecular phenotypes, validated by PET/MR-guided biopsies. *Front Oncol.* 2021;11:743655.
16. Song S, Cheng Y, Ma J, et al. Simultaneous FET-PET and contrast-enhanced MRI based on hybrid PET/MR improves delineation of tumor spatial biodistribution in gliomas: a biopsy validation study. *Eur J Nucl Med Mol Imaging.* 2020;47:1458–1467.
17. Kang SY, Moon BS, Yoo MY, Yoon HJ, Kim BS. Clinical usefulness of ^{18}F-FET PET in a pediatric patient with suspected demyelinating disease. *Clin Nucl Med.* 2022;47:e562–e564.
18. Swissmedic. Swiss Agency for Therapeutic Products. *Swissmedic J.* 2020;19:485.
19. Weckesser M, Langen KJ, Rickert CH, et al. O-(2-[^{18}F]fluorethyl)-L-tyrosine PET in the clinical evaluation of primary brain tumours. *Eur J Nucl Med Mol Imaging.* 2005;32:422–429.
20. Calcagni ML, Galli G, Giordano A, et al. Dynamic O-(2-[^{18}F]fluoroethyl)-L-tyrosine (F-18 FET) PET for glioma grading: assessment of individual probability of malignancy. *Clin Nucl Med.* 2011;36:841–847.
21. Pöpperl G, Kreth FW, Mehrkens JH, et al. FET PET for the evaluation of untreated gliomas: correlation of FET uptake and uptake kinetics with tumour grading. *Eur J Nucl Med Mol Imaging.* 2007;34:1933–1942.
22. Galldiks N, Stoffels G, Filss C, et al. The use of dynamic O-(2-^{18}F-fluoroethyl)-l-tyrosine PET in the diagnosis of patients with progressive and recurrent glioma. *Neuro Oncol.* 2015;17:1293–1300.
23. Kratochwil C, Combs SE, Leotta K, et al. Intra-individual comparison of ^{18}F-FET and ^{18}F-DOPA in PET imaging of recurrent brain tumors. *Neuro Oncol.* 2014;16:434–440.
24. Moulin-Romsée G, D'Hondt E, de Groot T, et al. Non-invasive grading of brain tumours using dynamic amino acid PET imaging: does it work for ^{11}C-methionine? *Eur J Nucl Med Mol Imaging.* 2007;34:2082–2087.
25. Smith NJ, Deaton TK, Territo W, et al. Hybrid ^{18}F-fluoroethyltyrosine PET and MRI with perfusion to distinguish disease progression from treatment-related change in malignant brain tumors: the quest to beat the toughest cases. *J Nucl Med.* 2023;64:1087–1092.
26. de Zwart PL, van Dijken BRJ, Holtman GA, et al. Diagnostic accuracy of PET tracers for the differentiation of tumor progression from treatment-related changes in high-grade glioma: a systematic review and metaanalysis. *J Nucl Med.* 2020;61:498–504.
27. Ziegenfeuter J, Delbridge C, Bernhardt D, et al. Sequential and hybrid PET/MRI acquisition in follow-up examination of glioblastoma show similar diagnostic performance. *Cancers (Basel).* 2022;15:83.
28. Marner L, Henriksen OM, Lundemann M, Larsen VA, Law I. Clinical PET/MRI in neurooncology: opportunities and challenges from a single-institution perspective. *Clin Transl Imaging.* 2017;5:135–149.
29. Heinzel A, Müller D, Langen KJ, et al. The use of O-(2-^{18}F-fluoroethyl)-L-tyrosine PET for treatment management of bevacizumab and irinotecan in patients with recurrent high-grade glioma: a cost-effectiveness analysis. *J Nucl Med.* 2013;54:1217–1222.
30. Heinzel A, Müller D, Yekta-Michael SS, et al. O-(2-^{18}F-fluoroethyl)-L-tyrosine PET for evaluation of brain metastasis recurrence after radiotherapy: an effectiveness and cost-effectiveness analysis. *Neuro Oncol.* 2017;19:1271–1278.
31. Heinzel A, Stock S, Langen KJ, Müller D. Cost-effectiveness analysis of amino acid PET-guided surgery for supratentorial high-grade gliomas. *J Nucl Med.* 2012;53:552–558.
32. Heinzel A, Stock S, Langen KJ, Müller D. Cost-effectiveness analysis of FET PET-guided target selection for the diagnosis of gliomas. *Eur J Nucl Med Mol Imaging.* 2012;39:1089–1096.
33. Rosen J, Ceccon G, Bauer EK, et al. Cost effectiveness of ^{18}F-FET PET for early treatment response assessment in glioma patients after adjuvant temozolomide chemotherapy. *J Nucl Med.* 2022;63:1677–1682.

Multicenter Evaluation of Frequency and Impact of Activity Infiltration in PET Imaging, Including Microscale Modeling of Skin-Absorbed Dose

John J. Sunderland[1], Stephen A. Graves[1], Dusty M. York[2], Christine A. Mundt[1], and Twyla B. Bartel[3]

[1]*Department of Radiology, University of Iowa, Iowa City, Iowa;* [2]*Chattanooga State Community College, Chattanooga, Tennessee; and* [3]*Global Advanced Imaging, Little Rock, Arkansas*

There has been significant recent interest in understanding both the frequency of nuclear medicine injection infiltration and the potential for negative impact, including skin injury. However, no large-scale study has yet correlated visualized injection site activity with actual activity measurement of an infiltrate. Additionally, current skin dosimetry approaches lack sufficient detail to account for critical factors that impact the dose to the radiosensitive epidermis. **Methods:** From 10 imaging sites, 1,000 PET/CT patient studies were retrospectively collected. At each site, consecutive patients with the injection site in the field of view were used. The radiopharmaceutical, injected activity, time of injection and imaging, injection site, and injection method were recorded. Net injection site activity was calculated from volumes of interest. Monte Carlo image–based absorbed dose calculations were performed using the actual geometry from a patient with a minor infiltration. The simulation model used an activity distribution in the skin microanatomy based on known properties of subcutaneous fat, dermis, and epidermis. Simulations using several subcutaneous fat-to-dermis concentration ratios were performed. Absorbed dose to the epidermis, dermis, and fat were calculated along with relative γ- and β-contributions, and these findings were extrapolated to a hypothetical worst-case (470 MBq) full-injection infiltration. **Results:** Only 6 of 1,000 patients had activity at the injection site in excess of 370 kBq (10 μCi), with no activities greater than 1.7 MBq (45 μCi). In 460 of 1,000 patients, activity at the injection site was clearly visualized. However, quantitative assessment of activities averaged only 34 kBq (0.9 μCi), representing 0.008% of the injected activity. Calculations for the extrapolated 470-MBq infiltration resulted in a hypothetical absorbed dose to the epidermis of below 1 Gy, a factor of 2 lower than what is required for deterministic skin reactions. Analysis of the dose distribution demonstrates that the dermis acts as a β-shield for the radiation-sensitive epidermis. Dermal shielding is highly effective for low-energy ^{18}F positrons but less so with the higher-energy positrons of ^{68}Ga. **Conclusion:** When quantitative activity measurement criteria are used rather than visual, the frequency of PET infiltration appears substantially below frequencies previously published. Shallow doses to the epidermis from infiltration events are also likely substantially lower than previously reported because of absorption of β-particles in the dermis.

Key Words: infiltration; extravasation; dosimetry; Monte Carlo

Received Apr. 18, 2023; revision accepted Apr. 26, 2023.

For correspondence or reprints, contact John J. Sunderland (john-sunderland@uiowa.edu).

Published online May 25, 2023.

J Nucl Med 2023; 64:1095–1101
DOI: 10.2967/jnumed.123.265891

There has been recent focus within the nuclear medicine community on the frequency and clinical consequences associated with injected activity infiltration in both diagnostic imaging and therapeutic applications. The situation is complicated by the variety of radionuclides in clinical use, the range of injected activities, their different half-lives, and their different radiation emissions, all of which affect the potential adverse impact of infiltration. The dearth of reported acute adverse events associated with activity infiltration over the last 50 y, spanning tens of millions of nuclear medicine injections, makes it difficult to draw systematic conclusions on cause and frequency. This is further complicated by an incomplete understanding of tissue-specific radiation dose effects, a lack of consistent definition of what is considered a consequential infiltration event, and the unclear impact of consequential infiltration on clinical care.

Relatively recently, several investigations into the frequency and severity of infiltration events in the nuclear medicine space have been published, including a relatively complete systematic review covering both diagnostic and therapeutic events (*1*). Several articles have been published on infiltrations in ^{18}F-FDG PET imaging (*2,3*). There are additional publications that report the dosimetric implications of infiltrated activity (*4,5*).

Infiltration can adversely impact a patient in 3 ways. The first is the safety issue associated with potential tissue damage due to local absorbed radiation dose. The second is the possibility that a suboptimal injection may negatively impact the quality of the scan, making it less diagnostic. The third is that a suboptimal injection resulting in infiltration will impact image quantitation and result in the potential for misinterpretation, particularly in the case of response to therapy. In all cases, understanding the frequency and severity of infiltration events will help inform recommended protocols.

In this work, we performed a controlled, retrospective, quantitative multicenter study of dose infiltration involving 10 imaging sites and 1,000 patients using PET imaging. The choice of PET was primarily due to its absolute quantitative nature and its superior sensitivity and resolution, providing the ability to quantitate the radioactivity at the injection site and estimate the infiltrate tissue mass at the imaging time point. Further, to better understand the potential for biologic impact on the patient, a patient-specific case of suboptimal injections was analyzed using imaging data and patient-specific Monte Carlo dose calculations accounting for

microscale anatomy of the skin to understand the respective dosimetric implications on the epidermis, dermis, and subcutaneous soft tissue. To our knowledge, dose estimates taking into account specific infiltration geometries and the impact of tissue radiosensitivity have not previously been reported. The dosimetric approach presented here can be generalized and may provide a valuable contextual approach to dose estimation in other nuclear medicine applications.

Critical to the dosimetric context of radiopharmaceutical infiltration is an understanding of the macroanatomy and microanatomy of the skin, as well as their respective thicknesses and associated fluid dynamics. The highly proliferative and radiation-sensitive epidermis, with a thickness of 50–70 μm, is the dose-critical structure (*6*). Beneath the epidermis are the largely acellular papillary dermis (~15 μm) and reticular dermis (~1,000 μm) (*7*). The papillary dermis and reticular dermis consist primarily of dense, fibrous connective tissue with little volumetric expansion capability. Beneath the dermis lies the subcutaneous fat layer, with a small proportion of structural connective tissue. Subcutaneous tissue is lightly cellular and highly deformable. Its thickness increases with patient fat content, varying between 1 and 10 mm or more. Veins with diameters large enough for cannulization lie at the base of the subcutaneous tissue and are just superior to muscle fascia. The skin anatomy and dimensions used are illustrated in Figure 1. Monte Carlo simulations performed in this work, accounting for the anatomic distribution of infiltrating activity on absorbed dose to different skin components, should provide a deeper understanding of the potential for deterministic radiation effects after radiopharmaceutical infiltration.

We hypothesize that the quantitative analysis of this large and diverse PET imaging patient cohort will better define the frequency and clinical impact of infiltrations, specifically as relates to the 3 adverse event categories (tissue damage, diminished diagnostic image quality, and quantitative accuracy). We further hypothesize that Monte Carlo–based absorbed dose calculations using patient-specific infiltration activities and geometry will better inform potential tissue damage models both in PET and, by inference, in other nuclear medicine applications.

MATERIALS AND METHODS

Patient Population

In total, 1,000 PET/CT oncology patient studies were collected from 10 different imaging institutions. To avoid bias associated with a single imaging model, a variety of institutions was chosen, including 1 academic medical center, 2 private radiology groups, 2 private oncology groups, 1 community hospital, 2 multispecialty groups, and 1 research facility. Approximately 50 patients from smaller clinics were combined into a tenth "institution." This diverse group of institutions should represent the variety of injection skills and injection techniques typically used in the clinical PET environment. At each of the institutions, consecutive patients who had the injection site in the field of view were analyzed. To avoid overrepresentation from a single site, no site contributed more than 230 patients (minimum, 37; maximum, 230; median, 74). Several radiopharmaceuticals were represented in the patient cohort, including ^{18}F-FDG, ^{18}F-fluciclovine, ^{18}F-DCFPyL, ^{68}Ga-DOTATOC, and ^{68}Ga-DOTATATE. All injection methods were allowed, including intravenous cannulation, butterfly injection, direct stick, port access, and peripheral insertion of a central catheter line. The informed consent requirement for this retrospective analysis was waived by the institutional review boards or equivalent authorities.

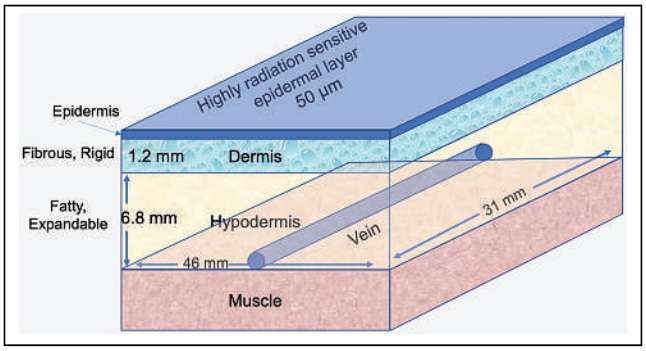

FIGURE 1. Schematic of skin anatomy with primary dimensions used in Monte Carlo absorbed dose calculations.

Imaging Data

For each patient, the following data were collected to quantitatively analyze any infiltration: radiopharmaceutical, net injected activity (Bq), time of injection, time of imaging, injection site (right or left antecubital, forearm, wrist, or hand), and injection type (e.g., intravenous catheter, port, or peripherally inserted central catheter). PET/CT images were analyzed by 1 of 2 investigators. Volumes of interest were drawn around the injection site to include all potential activity associated with the injection. A similar volume of interest of nearly equivalent volume was drawn on the contralateral side.

Injection Site Analysis

Each reader subjectively assessed whether the injection site was clearly visualized, barely visible, or not visible. Mean and maximum radioactivity concentration (Bq/cm^3) and volume of interest (cm^3) were measured at the injection site. Net activity at the injection site was calculated as the difference between activity at the injection site ([mean radioactivity concentration] × [volume of interest]) and activity on the contralateral side. The net percentage injected activity at the injection site was calculated.

A measured activity of more than 370 kBq (10 μCi) at the injection site, decay-corrected back to time of injection, was used as the threshold for further analysis of the clinical impact of infiltration. On average, this threshold represented approximately 0.1% of the average injected dose of 407 MBq (11 mCi).

Patient-Specific Dosimetry

Presented in this work is a single-sample, patient-specific skin dose calculation performed using the image-based geometry of a minor infiltration event (as no major events were found). Monte Carlo simulation was performed using MCNP, version 6.2. For each radioactive emission mode (β-particles, discrete electrons, and photons), 1×10^7 emission events were simulated, thereby providing less than 1% estimated statistical uncertainty in absorbed dose results in each skin layer for each emission type (excluding uncertainty from discrete electrons beyond their practical range). Static geometry was assumed. A subcutaneous tissue thickness of 6.8 mm (patient-specific based on CT images) and a dermal thickness of 1.2 mm were simulated. An effective clearance half-life of 30 min was modeled for the infiltrated activity based on the literature (*4*). For ^{68}Ga simulations, 25 min was used. The Monte Carlo infiltration dimensions were taken from the patient's CT scan and were 3.6 × 2.1 cm in *x* and *y*, with *z* being 1.2 mm in the dermis and 6.8 mm in the subcutaneous tissues. Because the exact equilibrium distribution of the infiltrated activity into the expandable subcutaneous tissue and the fibrous dermal tissue is unknown, multiple simulations were performed. The actual equilibrium distribution is currently under study, and preliminary experiments suggest an approximately 10:1 hypodermal-to-dermal concentration ratio. However, to be conservative, 10:1, 5:1, and 2:1 ratios were simulated. Dose contributions from

β-particles, photons, and electrons were separately estimated from the MCNP model.

RESULTS

Frequency and Severity of Infiltrations

Injected activities averaged 405 ± 78 MBq from all sites, with 952 of the injections being ^{18}F-FDG and the others distributed among other approved radiopharmaceuticals. The distribution of injection sites was approximately two-thirds (645 patients) antecubital injections, with 135 hand injections, 111 forearm injections, and 34 wrist injections. All venous access, when not performed through a peripherally inserted central catheter line (3 patients) or port access (66 patients), was performed using venous cannulation, with no reported direct sticks or butterfly access.

The distribution of net activity measured at the injection site is shown in Figure 2A. In 985 of the 1,000 patients, there was less than 74 kBq (2 μCi) at the injection site. Of the 15 patients with higher activities, none exceeded 1.65 MBq (44 μCi), with no injection site receiving more than 1% of the net injected activity. Details on the 6 patients who had more than 370 kBq (10 μCi) at the injection site are shown in Figure 2B. Interestingly, of the 6 patients with more than 370 kBq at the injection site, only 3 were infiltrations whereas the others were either external contamination or activity trapped in external tubing or fittings.

Probability of Infiltration

If we assume that data from the 10 sites were a representative sample of PET injection techniques and we use an overly conservative definition that activity of less than 1% of the injected dose at the injection site is not a clinically meaningful infiltration event (no clinically negative impact), then we will have observed 0 infiltration events in our 1,000 patient sample. This information allows us to calculate a statistical 95% CI for the probability of an infiltration of more than 1%. When a simple binomial distribution calculation with a sample size of 1,000 is used, the 95% CI for an infiltration of more than 1% is 0–0.0037. Simply stated, with 95% confidence we can say that the rate for PET infiltrations of more than 1% of injected activity is between 0.00% and 0.37%.

Dosimetry Results

Monte Carlo–generated absorbed radiation doses for the measured 0.41 MBq of ^{18}F-FDG infiltrated for patient E (left *y*-axis) and for an extrapolated full-injection infiltration of 470 MBq (right *y*-axis) are shown in Figure 3. For the actual infiltration, absorbed

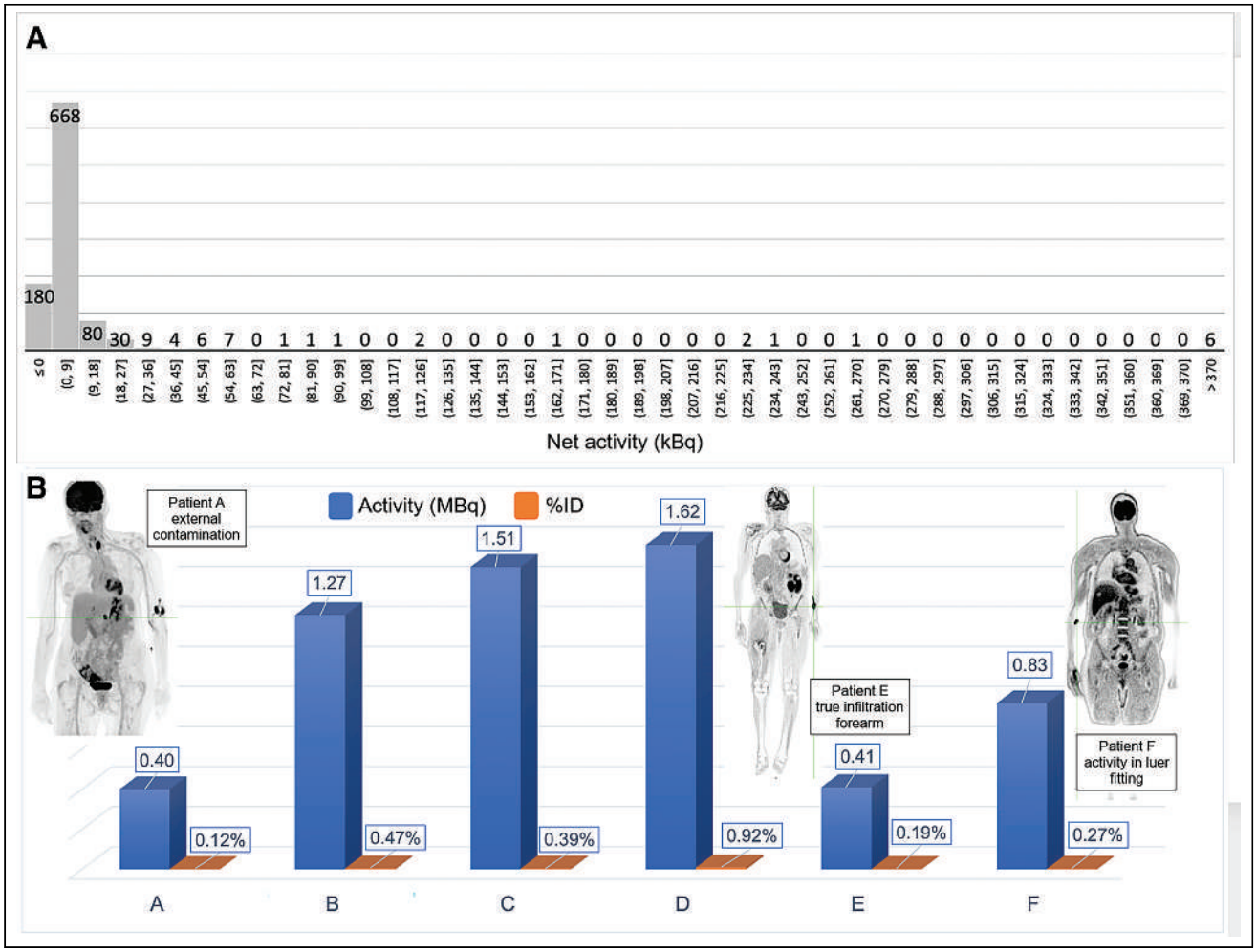

FIGURE 2. (A) Histogram distribution of net activity (MBq) at injection site. (B) Detail of 6 infiltrations above 0.4 MBq (10 μCi) with percentage injected activity. Patient E's injection geometry was used in Monte Carlo simulation.

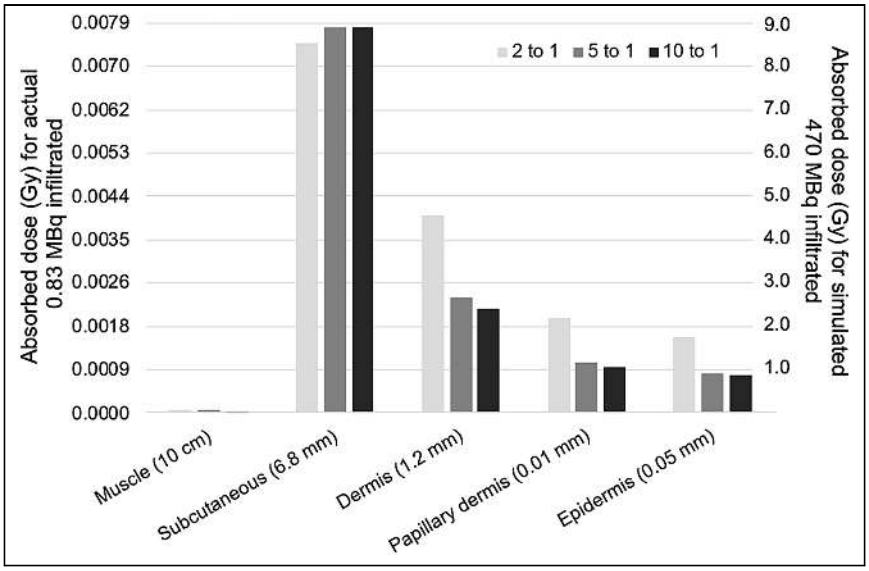

FIGURE 3. Absorbed dose for actual 0.41 MBq infiltrated (left *y*-axis scale) and for hypothetical full injection infiltration of 470 MBq (right *y*-axis scale) with 1.2-mm dermis.

doses were predictably highest in the expandable hypodermis, where most of the activity pools and delivers most of the positron energy deposition. Regardless of assumed equilibrium concentration ratios between subcutaneous and dermal tissue, absorbed doses narrowly ranged from 7 to 8 mGy. Absorbed dose in the dermis, at roughly 2 to 4 mGy, was generally more than 2 times lower than that in the subcutaneous tissue; however, at lower subcutaneous-to-dermal equilibrium concentration ratios, the dermal dose was substantially higher because of the larger proportion of the infiltrate resident in dermal tissue. The radiation-sensitive epidermal layer was estimated to receive between 1.5 and 4.2 mGy, depending on equilibrium concentration ratios. These absorbed radiation doses to the epidermis are roughly 1,000 times below the lowest absorbed doses at which even the most minor deterministic tissue injuries are reported (*8,9*). Given the small infiltrated activity, these results are not unexpected.

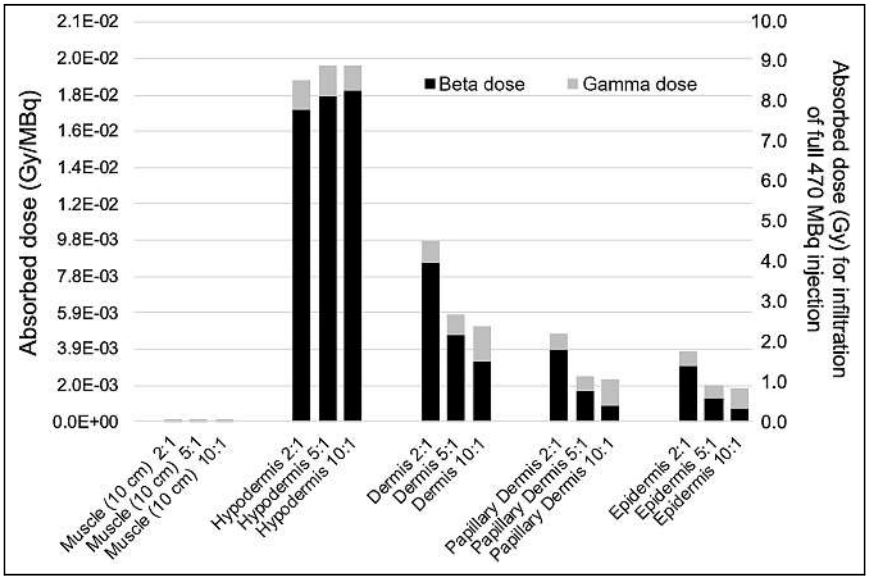

FIGURE 4. Absorbed dose per megabecquerel infiltrated for γ- and β-components for ^{18}F in 5 tissue compartments (left *y*-axis) and assuming full 470-MBq activity infiltration (right *y*-axis).

Extrapolating to a hypothetical 470-MBq infiltration, absorbed radiation doses to the radiation-resistant subcutaneous tissue range between 8 and 9 Gy, whereas the dose to the epidermis generally remains below 2 Gy, the lowest absorbed doses at which minor erythema has been seen in the most sensitive patients (reported from external-beam radiation therapy and fluoroscopy dose estimates (*8,9*)).

β- and γ-Dose Distribution

The relative absorbed dose contributions of positron, γ-particle, and electron emissions were separately tabulated during the Monte Carlo simulation. Figure 4 breaks down the absorbed radiation dose per infiltrated activity (Gy/MBq) into its respective β- and γ-components for each of the 5 skin tissues simulated using the 1.2-mm dermal thickness and also presents estimated doses for the extrapolated 470-MBq infiltration case (right *y*-axis). It is important to note that the mean range of ^{18}F positrons is approximately 0.6 mm, with only a very small fraction traveling greater than 1.2 mm, the thickness of the dermis. Also of note is the fraction of absorbed dose in the epidermal layer attributable to β-particles (positrons) relative to γ-particles for the different equilibrium concentration ratios. When the concentration in the dermal layer is low, the dermis only minimally contributes β-dose to the epidermis because of significant self-absorption, while simultaneously acting as an effective β-shield for positrons sourced in the subcutaneous tissue. Doses to other less radiosensitive tissue remain below 10 Gy for all circumstances simulated. This is likely about 5 times below the threshold for tissue damage within these largely acellular skin subanatomies.

Impact of β-Endpoint Energy

Most infiltrated activity resides within the fractures between fat cells in subcutaneous tissue. β-penetration from the subcutaneous tissue through the dermis has the potential to generate a β-particle absorbed dose into the epidermal tissue only when the endpoint β-range of the infiltrate's β-emissions is substantially longer than the dermal thickness, which is not the case with ^{18}F. However, because ^{68}Ga has a mean positron range of more than 3 mm, we simulated radiation doses to skin anatomies using patient A (Fig. 2) geometries with ^{68}Ga as a source radionuclide to determine the potential impact of β-energy on skin injury.

Results comparing the absorbed dose of ^{18}F with that of ^{68}Ga on a per-decay basis are shown in Figure 5A. ^{68}Ga predictably manifested an increase in absorbed dose per decay in all tissues, including, most significantly, the epidermis. Absorbed doses associated with a worst-case scenario of a 470-MBq ^{18}F-FDG infiltration versus a 148-MBq infiltration of ^{68}Ga (a complete activity infiltration) are shown in Figure 5B. There are substantial increases in both

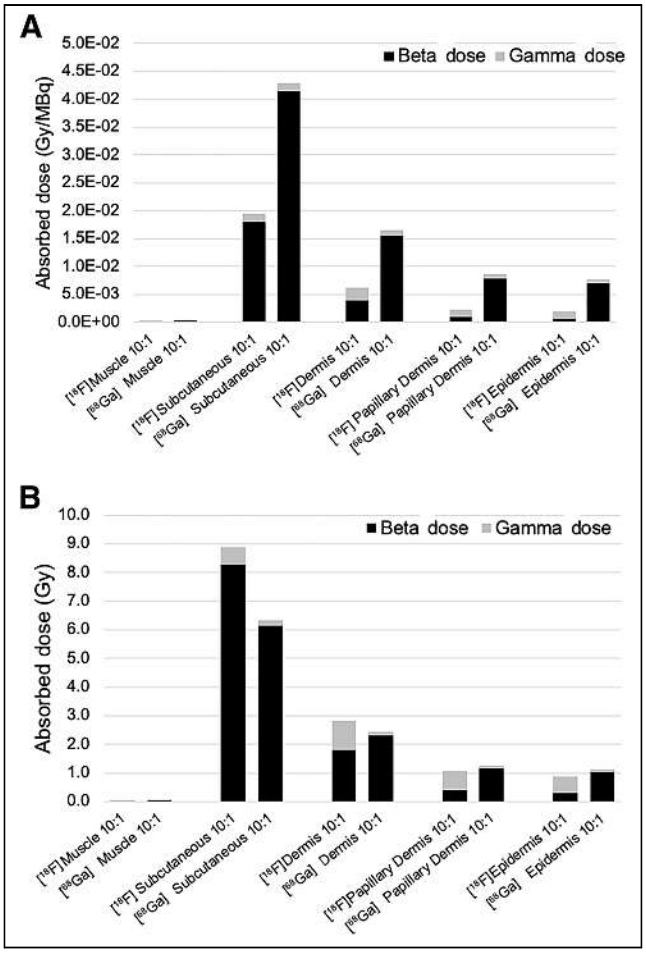

FIGURE 5. (A) γ- and β-contributions to absorbed dose for each subanatomy per megabecquerel infiltrated for ^{18}F and ^{68}Ga. (B) Relative γ- and β-contributions to absorbed dose for full infiltration of ^{18}F and ^{68}Ga.

proportional and absolute β-dose to tissues, up to and including the epidermis, when the dermis is no longer an effective β-shield. Even at an injected activity of less than a third of its ^{18}F counterpart, the total absorbed dose in the epidermis from a 148-MBq ^{68}Ga infiltration is higher than for the 470-MBq infiltrated ^{18}F activity.

DISCUSSION

To date, studies investigating the frequency of nuclear medicine activity infiltration have not reported the quantitative activities of the infiltrations (*3,10*), which would seem to be a crucial variable. Additionally, those studies investigating the risks associated with nuclear medicine infiltrations have been based on simplified models that account for neither a realistic injectate distribution within the anatomic structures of the skin nor the relative radiation sensitivity of the different layers of the skin. This work is the first attempt, to our knowledge, to address these issues systematically.

Frequency of Infiltration

With regard to the frequency and severity of infiltration, there are widely varying estimates reported in the literature. Osman et al. reported a relatively frequent 10% incidence of infiltrations in PET studies. These data, published in 2011, used exclusively 23- to 25-gauge butterfly needles for injection (*3*) rather than the currently recommended standard cannulation procedure for PET studies. In that study, an administration was considered extravasated if any remaining activity was visible at the injection site. In a smaller study in 2017, similar infiltration rates were identified with similar visually based criteria (*11*). Neither of these reports provided quantitative measurements of activity infiltrated despite the availability of these data through PET images. In our study, activity at the injection site was measured in 1,000 consecutive cases. It quickly became clear that simple visualization of activity was not evidence of meaningful infiltration, nor was it indicative of a poor, ineffective, or potentially dangerous injection. In fact, clearly visualized activity at the injection site was present in 460 of the 1,000 subjects but contained an average of only 34 kBq (0.9 μCi), which represents 0.008% of the net injected activity. We would argue that this is not representative of an actual infiltration event, which strongly suggests that visualization alone is not a meaningful criterion for infiltration and that the remarkably high sensitivity of PET imaging coupled with low background in peripheral tissues can lead to visually deceiving conclusions. Another important observation was that the activity near the injection site seen on PET was not necessarily anatomically within the patient. It is important to localize the activity on the CT portion of PET because several times the activity was actually external to the patient.

It is also important to note that venous cannulation was uniformly implemented at all 10 sites in this study and that with this practice, there was not a single clinically meaningful infiltration event observed in the 1,000 cases reviewed and analyzed.

Skin Anatomy and Fluid Dynamics

The previous literature investigating radiation dose to the skin from infiltration events has largely ignored skin anatomy and the implications of fluid behavior in these tissues. In this work we consider both, as they would seem to have potentially significant implications in any dosimetric model.

Skin is a large and complex organ, but for our purposes it is critical to at least appreciate the structure, function, and dimensions of the major layers. The behavior of fluids when purposely or accidentally injected into the subcutaneous space has been abundantly reported in the literature (*12–14*), as tumescent fluid injections into the subcutaneous tissue for purposes of local anesthesia are common for several dermatologic procedures, including liposuction, cutaneous surgery, and drug administration. On injection, the fluid, under pressure, is trapped within the intracellular matrix of the subcutaneous tissue, as the fatty tissue expands severalfold. The fluid seeks and opens channels between adipose cells, as the fluid finds paths of least resistance (Fig. 6) (*15*). The initial local distribution occurs over the first few minutes, whereas subsequent absorption and dispersion via the circulation and lymphatic system occur over several hours, as has been observed and documented in nuclear infiltration studies by Osborne et al. (*4*). Insight from the literature informed our modeling assumptions regarding the distribution of concentrations between the subcutaneous tissue and the dermis. Figure 6A (*12*) demonstrates how 10 mL of stained saline injected tumescently into the subcutaneous tissue distributes but only minimally invades the dermis, if at all. A similar tumescent injection experiment was repeated by the authors using ^{18}F-FDG in euthanized piglets (Fig. 6B), and concentration ratios of hypodermis to the dermis were measured to be 10:1 or greater. A similar pattern is shown in Figure 6C (*14*), where an injection drug was also dyed red and showed the telltale fracturing between fat cells to accommodate and drain excess fluid.

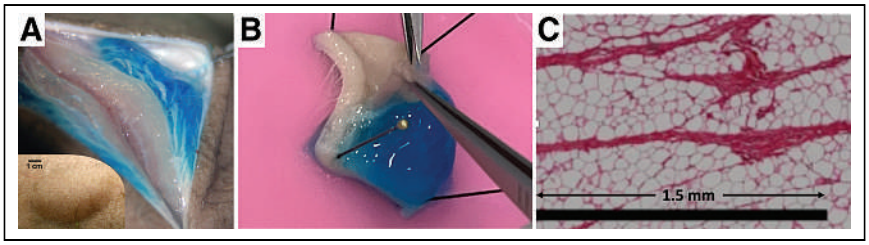

FIGURE 6. (A) Tumescent injection of 10 mL of saline (dyed blue) into porcine subcutaneous fat. Slicing into it reveals that liquid is held in subcutaneous tissue, forced to expand to accommodate in 5-cm diameter bleb (lower left insert). Lack of migration into dermis is seen. (Reprinted with permission of (*12*).) (B) ^{18}F-FDG with blue dye subcutaneously injected into euthanized pig, excised 15 min after injection. ^{18}F-FDG remains virtually exclusively in fat and does not appear to diffuse into dermis. (C) Histologic image of porcine adipose tissue. Septa are seen as magenta stripes. Scale bar is 1.5 mm. (Reprinted with permission of (*14*).)

Uncertainty of Equilibrium Concentration Between Subcutaneous Tissue and Dermis

The visual evidence in Figure 6 suggesting that the major portion of the infiltrated radiopharmaceutical remains in the subcutaneous tissue, with limited intrusion into the dermis, was independently confirmed with preliminary ^{18}F-FDG experiments in euthanized piglets. The dermis is a largely dense connective tissue, consisting primarily of collagen and elastin surrounded by glycosaminoglycans (highly polar water-binding molecules) that enable collagen fibers to retain water; this water is not freely exchangeable. For purposes of our dose calculations, hypodermis-to-dermis radioactivity concentration ratios of 10:1, 5:1, and 2:1 were simulated, but the results from the 10:1 simulations are likely closest to reality.

Prior Infiltration Dosimetry Estimates

Several methods for dose estimation of the skin from infiltration events have been reported in the literature. VARSKIN 6.1 (*16*), a Nuclear Regulatory Commission–sourced Monte Carlo computer code for calculation of superficial skin dose in the case of external skin contamination, has been used in several recent publications. However, unmodified, this model is not appropriate for shallow-dose exposure from activity in underlying tissues. Other published approaches use MIRD methods, or simplified Monte Carlo geometries assuming skin to be a uniform homogeneous tissue, which are inappropriate for a risk assessment in which different skin anatomies have different radiation sensitivities. Osborne et al. (*4*) present the most complete data on measured clearance rates from infiltration and calculate shallow-dose estimates based on the assumption of uniform distribution of activity into both the dermis and the subcutaneous tissue (equal concentrations), intimate with the sensitive epidermis. This treatment, however, does not account for the β-shielding of the dermis presented in this work, which significantly reduces the shallow dose to the epidermis from β-emissions.

Radiosensitivity of Skin Subanatomies

Formulated in 1906, the law of Bergonie and Tribondeau states that the radiosensitivity of a biologic tissue is directly proportional to the mitotic activity and inversely proportional to the degree of differentiation of its cells (*17*). This early concept is foundational to the prevailing understanding of effects from ionizing radiation, and as such, it can be applied to the relevant skin subanatomies in the context of radiopharmaceutical infiltration.

The most proliferative layer of skin is the epidermis, which has a reported mitotic index (fraction of cells undergoing mitosis at a given time) of 0.12–0.14 (*18*), with complete cell lineage turnover approximately every 40–56 d (*19*). As a result of the high mitotic rate of the epidermis, deterministic radiation effects can be observed at relatively low doses. Minor and temporary radiation effects (erythema and temporary epilation) can occur at doses of as low as 2 Gy, increasing in severity up to about 8 Gy (*20*). With acute doses of greater than 10 Gy, more concerning and potentially permanent skin damage can occur, including moist desquamation, ulceration, or scarring, as well as late cosmetic changes, such as dermal thinning and telangiectasia (*20*). By comparison, subcutaneous fat cells are replaced at a much slower rate, with approximately 10% turnover annually (*21*). Tissues with particularly slow turnover rates, such as fat and connective tissues, are generally considered to be resistant to radiation. Although data regarding dose–effect relationships are absent from the literature, tolerable subcutaneous doses are likely much higher than thresholds for concerning tissue effects within the dermis and epidermis.

Infiltration Versus Extravasation

Historically, the terms *infiltration* and *extravasation* have been used interchangeably in the nuclear medicine literature. Clinically, extravasation has a specific definition and refers to injectates that are vesicants—chemicals that are irritants capable of causing tissue damage. In context, this has typically meant that they may be capable of causing blistering, tissue sloughing, or necrosis. The results of this study suggest that in PET imaging we do not approach skin doses in sensitive tissues that would cause such symptoms, nor have they been reported in the literature. For these reasons, in this article, the term *infiltration* is specifically and intentionally used.

Implications of Results

The lack of clinically significant infiltration events in the 1,000 patients studied, as discerned by quantitative measurement rather than visually based supposition, suggests that a more meaningful definition of infiltration events, as relates to risk assessment for patients, is necessary. With zero patients having more than 1% of the injected activity found at the injection site, none of the 3 adverse event categories introduced at the beginning of the article (tissue damage, diminished diagnostic image quality, or quantitative accuracy) were identified. That is not to say significant infiltrations do not occur. Instances have clearly been reported in the PET literature for the latter 2 categories (although not for the first), and the field at large must be vigilant. With that said, our data indicate a high level of quality in the administration of radiopharmaceuticals in PET practice.

Of particular interest from the Monte Carlo results was the importance of the ratio of activity in the subcutaneous tissue to the dermis, its impact on dose to the epidermis, and the importance of the β-energy of the radionuclide. Using the data and assumptions from this work, the risk of significant tissue injury from diagnostic PET agents appears negligible, as is consistent with both clinical experience and the literature. More interesting, however, are the implications of this work when extrapolated to therapeutic radionuclides and significantly higher injected activities. Importantly, in a review of reported adverse skin events from extravasated therapy administrations (*1*), most were with ^{90}Y, which has an average β-energy of close to 1 MeV and a mean range of 2.4 mm, which is

much larger than dermal thickness. The small number of literature reports of ^{177}Lu extravasations, with a mean β-range of 0.23 mm (less than dermal thickness), do not yet indicate any significant tissue injury. There is a clear need to extend our current simulation work into therapeutic radionuclides, with therapeutic levels of activity, and to further investigate experimentally the actual quantitative partition of activity between the subcutaneous tissue and the dermis.

CONCLUSION

The observation of zero clinically meaningful infiltration events in our 1,000-patient cohort having more than 1% of injected activity at the injection site drives a conclusion, with 95% confidence, that the rate for PET infiltrations of more than 1% of injected activity lies somewhere between 0% and 0.37%, substantially below previously reported rates relying on visual interpretation. Further, it appears that when taking into account actual skin anatomy and geometry, absorbed dose to the epidermis from infiltration events is lower than previously estimated because of effective β-shielding by the dermal layer beneath.

DISCLOSURE

No potential conflict of interest relevant to this article was reported.

ACKNOWLEDGMENTS

We thank Kimberly Schulz, MD, Ali Jabbari, MD, PhD, FAAD, and Kirk Sidey, MD, for enlightening discussions providing insight into dermal and subcutaneous tissue injections and associated fluid behavior, and we thank Mahmoud Abou Alaiwa, MD, for invaluable help with tumescent injection experiments.

KEY POINTS

QUESTION: What is the relative risk of deterministic skin injury from an infiltrated PET injection, considering both the frequency of injection infiltration and the potential absorbed dose to the skin.

PERTINENT FINDINGS: When characterized by quantitative measurement of activity at the injection site, clinically significant infiltration events for PET radiopharmaceuticals are dramatically less frequent than previously reported in the literature. Absorbed radiation dose to the radiosensitive epidermis is likely substantially lower than previously reported when actual skin anatomy and dose distribution are accounted for.

IMPLICATIONS FOR PATIENT CARE: Even the infiltration of an entire clinical PET patient dose will likely not lead to any deterministic skin injury.

REFERENCES

1. van der Pol J, Voo S, Bucerius J, Mottaghy FM. Consequences of radiopharmaceutical extravasation and therapeutic interventions: a systematic review. *Eur J Nucl Med Mol Imaging.* 2017;44:1234–1243.
2. Osborne D, Lattanze R, Knowland J, et al. The scientific and clinical case for reviewing diagnostic radiopharmaceutical extravasation long-standing assumptions. *Front Med (Lausanne).* 2021;8:684157.
3. Osman MM, Muzaffar R, Altinyay ME, Teymouri C. FDG dose extravasations in PET/CT: frequency and impact on SUV measurements. *Front Oncol.* 2011;1:41.
4. Osborne D, Kiser JW, Knowland J, Townsend D, Fisher DR. Patient-specific extravasation dosimetry using uptake probe measurements. *Health Phys.* 2021;120: 339–343.
5. Shapiro B, Pillay M, Cox PH. Dosimetric consequences of interstitial extravasation following i.v. administration of a radiopharmaceutical. *Eur J Nucl Med.* 1987;12: 522–523.
6. Sandby-Møller J, Poulsen T, Wulf HC. Epidermal thickness at different body sites: relationship to age, gender, pigmentation, blood content, skin type and smoking habits. *Acta Derm Venereol.* 2003;83:410–413.
7. Fredriksson I, Larsson M, Stromberg T. Optical microcirculatory skin model: assessed by Monte Carlo simulations paired with in vivo laser Doppler flowmetry. *J Biomed Opt.* 2008;13:014015.
8. Bray FN, Simmons BJ, Wolfson AH, Nouri K. Acute and chronic cutaneous reactions to ionizing radiation therapy. *Dermatol Ther (Heidelb).* 2016;6:185–206.
9. Jaschke W, Schmuth M, Trianni A, Bartal G. Radiation-induced skin injuries to patients: what the interventional radiologist needs to know. *Cardiovasc Intervent Radiol.* 2017;40:1131–1140.
10. Wong TZ, Benefield T, Masters S, et al. Quality improvement initiatives to assess and improve PET/CT injection infiltration rates at multiple centers. *J Nucl Med Technol.* 2019;47:326–331.
11. Muzaffar R, Frye SA, McMunn A, Ryan K, Lattanze R, Osman MM. Novel method to detect and characterize ^{18}F-FDG infiltration at the injection site: a single-institution experience. *J Nucl Med Technol.* 2017;45:267–271.
12. Koulakis JP, Rouch J, Huynh N, Wu HH, Dunn JCY, Putterman S. Tumescent injections in subcutaneous pig tissue disperse fluids volumetrically and maintain elevated local concentrations of additives for several hours, suggesting a treatment for drug resistant wounds. *Pharm Res.* 2020;37:51.
13. Guyton AC, Scheel K, Murphree D. Interstitial fluid pressure. 3. Its effect on resistance to tissue fluid mobility. *Circ Res.* 1966;19:412–419.
14. Leng Y, Wang H, de Lucio M, Gomez H. Mixed-dimensional multi-scale poroelastic modeling of adipose tissue for subcutaneous injection. *Biomech Model Mechanobiol.* 2022;21:1825–1840.
15. Comely K, Fleck N. Deep penetration and liquid injection into adipose tissue. *J Mech Mater Struct.* 2011;6:127–140.
16. Hamby DM, Mangini CD, Luitjens JM, et al. *VARSKIN+ 1.0: A Computer Code for Skin Contamination and Dosimetry Assessments*, revision 4. U.S. Nuclear Regulatory Commission; 2021
17. Bergonie J, Tribondeau L. Interpretation of some results of radiotherapy and an attempt at determining a logical technique of treatment. *Radiat Res.* 1959;11: 587–588.
18. Fisher LB. Determination of the normal rate and duration of mitosis in human epidermis. *Br J Dermatol.* 1968;80:24–28.
19. Halprin KM. Epidermal "turnover time"—a re-examination. *Br J Dermatol.* 1972; 86:14–19.
20. Hopewell JW. The skin: its structure and response to ionizing radiation. *Int J Radiat Biol.* 1990;57:751–773.
21. Spalding KL, Arner E, Westermark PO, et al. Dynamics of fat cell turnover in humans. *Nature.* 2008;453:783–787.

Voxel-Based Dosimetry Predicts Hepatotoxicity in Hepatocellular Carcinoma Patients Undergoing Radioembolization with ^{90}Y Glass Microspheres

Masao Watanabe[1,2], Hong Grafe[1,2], Jens Theysohn[2,3], Benedikt Schaarschmidt[2,3], Johannes Ludwig[2,3], Leonie Jochheim[2,4], Matthias Jeschke[2,4], Hartmut Schmidt[2,4], Wolfgang P. Fendler[1,2], Alexandros Moraitis[1,2], Ken Herrmann[1,2], Kelsey L. Pomykala[5], and Manuel Weber[1,2]

[1]*Department of Nuclear Medicine, University Clinic Essen, Essen, Germany;* [2]*University of Duisburg–Essen and German Cancer Consortium–University Hospital, Essen, Germany;* [3]*Institute of Diagnostic and Interventional Radiology and Neuroradiology, University Clinic Essen, Essen, Germany;* [4]*Department of Gastroenterology and Hepatology, University Clinic Essen, Essen, Germany; and* [5]*Institute for AI in Medicine, University Medicine Essen, Essen, Germany*

Personalized dosimetry holds promise to improve radioembolization treatment outcomes in hepatocellular carcinoma (HCC) patients. To this end, tolerance absorbed doses for nontumor liver tissue are assessed by calculating the mean absorbed dose to the whole nontumor liver tissue (AD-WNTLT), which may be limited by its neglect of nonuniform dose distribution. Thus, we analyzed whether voxel-based dosimetry could be more accurate in predicting hepatotoxicity in HCC patients undergoing radioembolization. **Methods:** In total, 176 HCC patients were available for this retrospective analysis; of these, 78 underwent partial- and 98 whole-liver treatment. Posttherapeutic changes in bilirubin were graded using the Common Terminology Criteria for Adverse Events. We performed voxel-based and multicompartment dosimetry using pretherapeutic ^{99m}Tc-labeled human serum albumin SPECT and contrast-enhanced CT/MRI and defined the following dosimetry parameters: AD-WNTLT; the nontumor liver tissue volume exposed to at least 20 Gy (V20), at least 30 Gy (V30), and at least 40 Gy (V40); and the threshold absorbed dose to the 20% (AD-20) and 30% (AD-30) of nontumor liver tissue with the lowest absorbed dose. Their impact on hepatotoxicity after 6 mo was analyzed using the area under the receiver-operating-characteristic curve; thresholds were identified using the Youden index. **Results:** The area under the curve for prediction of posttherapeutic grade 3+ increases in bilirubin was acceptable for V20 (0.77), V30 (0.78), and V40 (0.79), whereas it was low for AD-WNTLT (0.67). The predictive value could further be increased in the subanalysis of patients with whole-liver treatment, where a good discriminatory power was found for V20 (0.80), V30 (0.82), V40 (0.84), AD-20 (0.80), and AD-30 (0.82) and an acceptable discriminatory power was found for AD-WNTLT (0.63). The accuracies of V20 ($P = 0.03$), V30 ($P = 0.009$), V40 ($P = 0.004$), AD-20 ($P = 0.04$), and AD-30 ($P = 0.02$) were superior to that of AD-WNTLT but did not differ significantly from each other. The respective thresholds were 78% (V30), 72% (V40), and 43 Gy (AD-30). Statistical significance was not reached for partial-liver treatment. **Conclusion:** Voxel-based dosimetry may more accurately predict hepatotoxicity than multicompartment dosimetry in HCC patients undergoing radioembolization, which could enable dose escalation or deescalation with the intent to optimize treatment response. Our results indicate that a V40 of 72% may be particularly useful in whole-liver treatment. However, further research is warranted to validate these results.

Key Words: SIRT; liver toxicity; voxel-based dosimetry; multicompartment dosimetry; radioembolization

J Nucl Med 2023; 64:1102–1108
DOI: 10.2967/jnumed.122.264996

On the basis of an ever-growing body of evidence, radioembolization guidelines and expert consensuses increasingly recommend the use of multicompartment dosimetry, that is, treatment activity calculations based on a separate pretherapeutic assessment of mean absorbed doses to the tumor and nontumor tissue (*1–4*). Following these recommendations with regard to ^{90}Y glass microspheres, the mean absorbed dose to the whole nontumor liver tissue (AD-WNTLT) should be kept below 75 Gy to minimize the risk of hepatic decompensation, although different thresholds based on baseline bilirubin have been proposed (*4,5*). However, when AD-WNTLT is used, nonuniform dose distribution is not considered. This could potentially be addressed by use of voxel-based dosimetry.

Three-dimensional voxel-based dosimetry evaluates the absorbed dose to each reconstructed voxel, thus taking into account dose heterogeneity and gradients in each region on a small spatial scale (*3,6*), which resembles absorbed dose planning models used in external-beam radiotherapy (*7*). However, the benefits of voxel-based activity calculation for ^{90}Y radioembolization in hepatocellular carcinoma (HCC) have not yet been established (*4*). The limited spatial resolution of ^{99m}Tc-macroaggregated albumin (MAA) SPECT used for pretherapeutic assessment of dose distribution in ^{90}Y radioembolization may not be sufficient to map the voxel-based distribution of tumor lesions because of the presence of image noise and partial-volume effects (*6*). However, the volume of the nontumoral liver is typically larger by an order of magnitude than lesions, potentially allowing for voxel-based dosimetry of the nontumoral liver (*8*). In addition, ^{99m}Tc-MAA SPECT predicts glass ^{90}Y microsphere distribution more reliably in the nontumoral liver than in tumor lesions (*3,8–10*).

So far, there is no consensus on how to parametrize voxel-based dosimetry in radioembolization; however, exploratory considerations are facilitated by literature on external-beam radiation therapy and surgery. In external-beam radiation therapy, the safety threshold of the absorbed dose to the nontumor hepatic tissue ranges from 20 to 40 Gy

Received Oct. 5, 2022; revision accepted Mar. 7, 2023.
For correspondence or reprints, contact Manuel Weber (manuel.weber@uk-essen.de).
Published online Jun. 8, 2023.

(*7,11,12*), whereas in liver surgery, a remnant nontumor liver of 20% and 30% should be aimed for (*13–17*).

This work retrospectively investigated the prognostic impact of various voxel-based dosimetry parameters on short-term (6 mo) hepatotoxicity, compared with multicompartment dosimetry in HCC patients undergoing radioembolization with ^{90}Y glass microspheres.

MATERIALS AND METHODS

Patients

From March 2008 to February 2021, 406 consecutive patients with HCC were screened from the radioembolization registry from our institution, and 176 were excluded because the follow-up period of their laboratory data was less than 6 mo. Of the remaining 230 patients, 3 underwent 2 radioembolization sessions to the identical target volume within 6 mo, impairing the assessment of absorbed dose distribution. Three patients underwent concurrent transarterial chemoembolization. Twenty-three patients underwent subsequent transarterial chemoembolization or radioembolization within 6 mo after the first radioembolization. In 25 patients, dosimetry calculations were not possible because of missing CT or MR images or technical issues. After exclusion of these 54 patients, 176 were finally included in this retrospective study (Fig. 1).

Of these 176 patients, 142 were male and 34 were female; the mean patient age was 67.2 y (range, 20 to 86 y). Seventy-eight patients underwent partial-liver treatment, and 98 underwent whole-liver treatment. Of the latter, 9 received a lobar injection after hemihepatectomy, making it a whole-liver treatment.

In cases of whole-liver treatment with 2 or more injections (e.g., separate injections for left and right lobes), injections were performed in 2 sessions, approximately 4–6 wk apart. The patient characteristics are summarized in Table 1. Of note, 3 patients had very limited extrahepatic metastases (adrenal grand, $n = 1$; lung, $n = 1$, abdominal wall, $n = 1$) (*3*). Seven patients had previously been treated with sorafenib and 1 patient with lenvatinib. In addition, 23 and 30 patients underwent transarterial chemoembolization or radiofrequency ablation and liver resection before radioembolization, respectively. Concerning this retrospective study, all procedures performed were approved in accordance with the ethical standards of the institutional review board of the Medical Faculty of the University Duisburg–Essen (Ethics Committee approval 13-5325BO) and with the principles of the Declaration of Helsinki and its later amendments. All patients gave written informed consent to the analysis of available data.

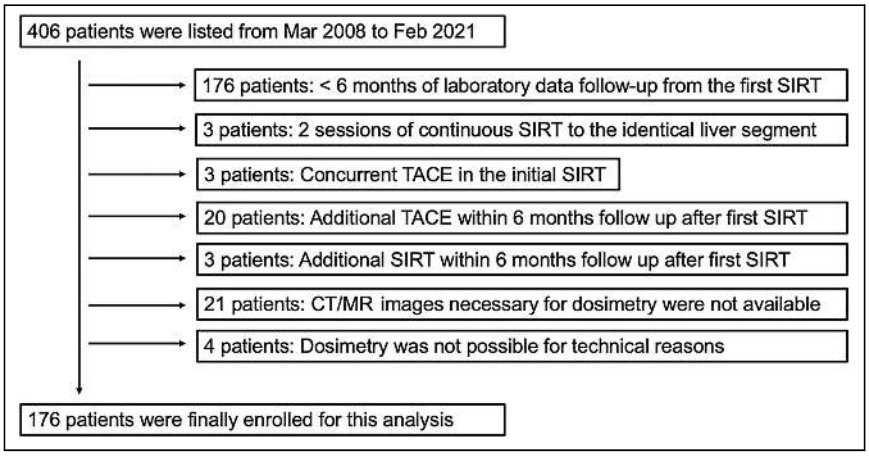

FIGURE 1. CONSORT (consolidated standard of reporting trial) diagram demonstrating patient enrollment. SIRT = selective internal radiation therapy; TACE = transarterial chemoembolization.

Treatment Algorithm

All radioembolization cases were discussed by a multidisciplinary tumor board. Digital-subtraction angiography, ^{99m}Tc-human serum albumin (HSA) planar scintigraphy, and SPECT/CT were performed for treatment planning. A mean of 151.4 MBq (range, 90–193 MBq) of ^{99m}Tc-HSA was administered into the hepatic target vessels, and image acquisition started within 2 h. Images were acquired on a Symbia T2 (Siemens Medical Solutions AG) hybrid SPECT/CT scanner using a 130- to 150-keV energy window, and a total of 64 views were acquired in step-and-shoot mode, with 15 s per view and a 2.8° angular step size. The low-dose CT was performed immediately after emission acquisition. Images were reconstructed into a 128×128 matrix with a cubic voxel size of 4.8 mm^3 using the 3-dimensional ordered-subset expectation maximization algorithm with 8 iterations and 4 subsets and no smoothing filter. All images were corrected for scatter and attenuation.

Calculation of the lung-shunt fraction was based on the planar scintigraphy following guideline recommendations, and visceral shunting was assessed using ^{99m}Tc-HSA SPECT/CT by 2 nuclear medicine physicians as per clinical routine. Treatment activity was calculated using unicompartment dosimetry (mean perfused target volume absorbed dose, 80–150 Gy), aiming for an absorbed dose of 120 Gy (±10%) to the perfused target volume, with further adjustments being based on factors such as liver function, tumor load, ^{99m}Tc-HSA uptake, and the extent of the treated liver fraction. Treatment activity was injected while patient breathed freely in the same catheter position as for the pretherapeutic ^{99m}Tc-HSA scan. The mean duration from dose calibration to the first and second dose injections was 4.5 d (range, 1–12 d).

Dosimetry Calculation

Post hoc multicompartment and voxel-based dosimetry were performed by a board-certified nuclear medicine physician and radiologist in collaboration with a board-certified nuclear medicine physician using Mirada Simplicit90Y (Mirada Medical). The mean durations between the first radioembolization and the ^{99m}Tc-HSA SPECT and between the ^{99m}Tc-HSA SPECT and contrast-enhanced CT/MRI were 40.9 and 19.6 d, respectively.

After manual coregistration of contrast-enhanced CT/MR and ^{99m}Tc-HSA SPECT/CT images, segmentation of whole-liver volume, perfused target volumes, tumor tissue, and nontumor liver tissue was performed both manually and automatically or semiautomatically by use of region-growing and thresholding tools. The whole-liver volume segmentation was performed automatically, whereas tumor lesions were segmented on CT/MR images using region-growing tools and on ^{99m}Tc-HSA SPECT images using visually determined thresholds.

As for dosimetry calculation, we calculated the AD-WNTLT (multicompartment dosimetry) and determined the volume of nontumor liver tissue (voxel-based dosimetry), in which the absorbed doses exceeded 20 Gy (V20), 30 Gy (V30), and 40 Gy (V40). In addition, we determined the absorbed dose threshold level (voxel-based dosimetry) including a volume of 20% (AD-20) and 30% (AD-30) of the total nontumor liver tissue receiving the lowest absorbed doses; that is, 20% of the nontumor liver tissue received less than AD-20 and 30% of the nontumor liver tissue received less than AD-30. The analyses were limited to AD-20, AD-30, V20, V30, and V40 to prevent spurious results and multiple testing problems. The hepatic reserve, that is, the fraction of liver tissue not treated by radioembolization, was measured for all patients undergoing partial-liver treatment, and the percentage of hepatic tumor

TABLE 1
Patient Characteristics (n = 176)

Characteristic	Value	Characteristic	Value
Age (y)	67.2 ± 10.1 (range, 20–86)	ECOG score	
Sex		0	127
Male	142	1+	46
Female	34	NA	3
Origin of cirrhosis		Liver cirrhosis	
Alcohol	24	Positive	115
NASH	18	Negative	61
Hepatitis B	10	Tumor involvement	
Hepatitis C	22	<25%	147
Mixed or unknown	41	≥25%	29
Baseline AST (IU/L)	61.2 ± 47.0	SIRT procedure	
Baseline ALT (IU/L)	51.4 ± 45.8	Partial-liver	78
Baseline bilirubin (mg/dL)	0.8 ± 0.4	Whole-liver	98
Baseline albumin (g/dL)	4.2 ± 0.4	PV thrombosis (//)	
Child–Pugh score		Vp1–3	46
A	109	Vp4	9
B7	6	Negative	121
ALBI score		Tumor invasiveness (positive/negative)	
G1	53	Positive	86
G2	122	Negative	90
G3	1	Treatment-native patients before SIRT	125
BCLC score		Prior therapy*	
A	41	Liver resection	30
B	79	TACE or RFA	23
C	56	Sorafenib or lenvatinib	8

*10/51 patients underwent several prior therapies.
NASH = nonalcoholic steatohepatitis; AST = aspartate transaminase; ALT = alanine transaminase; ALBI = albumin-bilirubin; BCLC = Barcelona Clinic liver cancer; ECOG = Eastern Cooperative Oncology Group; NA = not applicable; SIRT = selective internal radiation therapy; PV = portal vein; tumor invasiveness = tumor with irregular margins invading into surrounding tissues including nontumor liver tissue, portal vein, or hepatic vein; TACE = transarterial chemoembolization; RFA = radiofrequency ablation.
Qualitative data are number and percentage; continuous data are mean ± SD.

burden was obtained by dividing the tumor volume by the whole-liver volume as measured on contrast-enhanced CT/MRI.

Follow-up

The patients who underwent radioembolization were followed up using total bilirubin measurements for at least 6 mo (n = 176). Adverse effects were graded using the Common Terminology Criteria for Adverse Events (CTCAE), version 5. Relevant hepatotoxicity was defined as a binary metric by the occurrence of grade 3+ toxicity in bilirubin levels, on the basis of prior publications identifying it as a particularly suitable marker for hepatotoxicity after radioembolization (*18,19*).

Statistical Analysis

Statistics were analyzed using MedCalc, version 20.113-32 bit (MedCalc Software). To investigate the relationship between the absorbed dose of the nontumor liver and the liver toxicity within the follow-up period of 6 mo, we performed a receiver-operating-characteristic (ROC) curve analysis and identified the cutoffs using the Youden index. ROC curve analyses were compared using Hanley and McNeil's methodology (*20*). Subanalyses were performed for patients undergoing partial-liver and whole-liver treatment; analyses of the latter group involved 9 patients undergoing lobar treatment after contralateral hemihepatectomy. A P value of less than 0.05 was considered statistically significant.

RESULTS

The mean volume and percentage of hepatic tumor burden across all patients were 269.0 mL (range, 0.6–2,534.4 mL) and 12.1% (range, 0.04%–61.1%), respectively. Twenty-nine patients had a high tumor burden (≥25%), and 147 patients had a low tumor burden (<25%). Of the 55 patients with portal tumoral thrombosis, 46 had the first branch or a more distal branch of the portal vein involved, and in 9 patients the main trunk of the portal vein was involved.

In the total cohort (n = 176), CTCAE grade 3+ hyperbilirubinemia was observed in 20 patients. Mean V20, V30, V40, AD-20, AD-30, and AD-WNTLT was 60.5%, 55.6%, 51.1%, 11.1 Gy, 18.2 Gy, and 57.7 Gy, respectively. Comparison of ROC curves (Fig. 2) showed superiority of V20 (area under the ROC curve [AUC], 0.77; P = 0.03), V30 (AUC, 0.78; P = 0.009), and V40

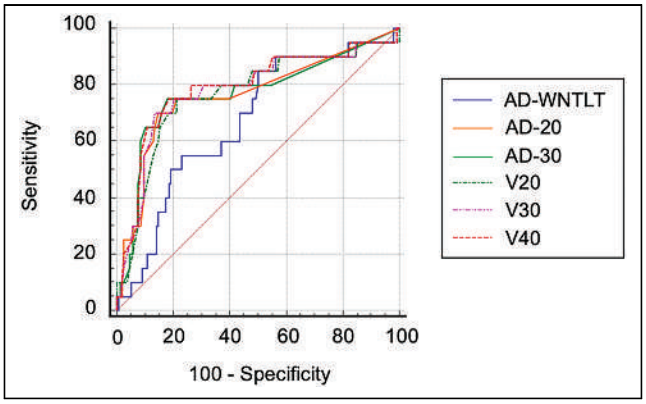

FIGURE 2. ROC analyses of whole patient cohort assessing relationship of absorbed dose parameters and occurrence of liver decompensation within 6 mo.

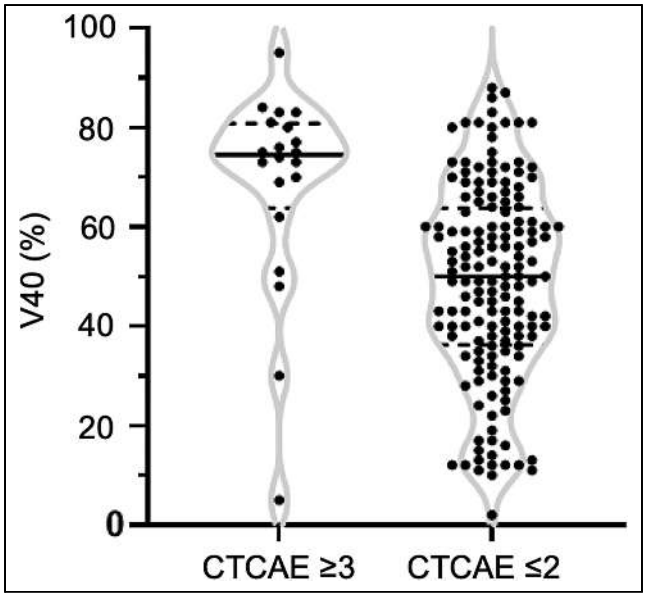

FIGURE 3. Scatterplot of whole patient cohort: comparison of V40 between group of CTCAE for hyperbilirubinemia adverse effects ≥ 3 and group of CTCAE ≤ 2.

(AUC, 0.79; $P = 0.005$) over AD-WNTLT (AUC, 0.67) in predicting 6-mo hepatotoxicity. V40 was significantly more accurate than V20 ($P < 0.05$), whereas no difference was found between V40 and V30 ($P = 0.09$). The cutoffs using the Youden index with the follow-up period of 6 mo, in consideration of the ROC analyses in CTCAE grade 3+ hyperbilirubinemia (Table 2; Figs. 2 and 3), were 56.9 Gy, 80%, 78%, 68%, 27 Gy, and 37 Gy in AD-WNTLT, V20, V30, V40, AD-20, and AD-30, respectively.

In the cohort that underwent partial-liver treatment ($n = 78$), CTCAE grade 3+ hyperbilirubinemia was observed in 4 patients. Mean V20, V30, V40, AD-20, AD-30, AD-WNTLT, and hepatic reserve were 42.7%, 39.7%, 36.9%, 0.1 Gy, 1.4 Gy, 42.1 Gy, and 41.8%, respectively. The AUC of the voxel-based calculations ranged from 0.52 to 0.59 for voxel-based analyses and was 0.58 for AD-WNTLT; however, statistical significance was reached only for AD-30 ($P < 0.001$). The cutoffs using the Youden index with the follow-up period of 6 mo, in consideration of the ROC analyses in CTCAE grade 3+ hyperbilirubinemia (Table 3; Fig. 4; Supplemental Fig. 1; supplemental materials are available at http://jnm.snmjournals.org), were 58.7 Gy, 6%, 6%, 5%, 0 Gy, 0 Gy, and 34% in AD-WNTLT, V20, V30, V40, AD-20, AD-30, and hepatic reserve, respectively.

In the cohort that underwent whole-liver treatment ($n = 98$), CTCAE grade 3+ hyperbilirubinemia was observed in 16 of 98 within 6 mo and in 2 of 49 within 6–12 mo. Mean V20, V30, V40, AD-20, AD-30, and AD-WNTLT were 74.6%, 68.3%, 62.3%, 19.9 Gy, 31.6 Gy, and 70.2 Gy, respectively. The AUC of the voxel-based calculations using histograms (V20, V30, V40, AD-20, and AD-30) (AUC, 0.80–0.84) were superior to that of the AD-WNTLT (AUC, 0.63) (Table 4; Figs. 5 and 6). V20 ($P = 0.03$), V30 ($P = 0.009$), V40 ($P = 0.004$), AD-20 ($P = 0.04$), and AD-30 ($P = 0.02$) were superior to AD-WNTLT in predicting hepatotoxicity, whereas the predictive power between them did not differ significantly. The cutoffs were determined to be 55.6 Gy, 80%, 78%, 72%, 27 Gy, and 43 Gy in AD-WNTLT, V20, V30, V40, AD-20, and AD-30, respectively.

DISCUSSION

Our results indicate superiority for voxel-based dosimetry in the pretherapeutic prediction of hepatotoxicity in HCC patients undergoing radioembolization of the whole liver. All tested voxel-based parameters were more accurate in predicting 6-mo hepatotoxicity than AD-WNTLT, which is considered the state of the art by current guidelines (*3,4*). A V40 of more than 72%, in particular, appears to be an accurate predictor of liver decompensation, showing an accuracy superior to V20, AD-20, AD-30, and AD-WNTLT and a tendency toward higher accuracy than V30.

TABLE 2
ROC Analysis of 6-Month Toxicity of Whole Patient Cohort with 6-Month Follow-up (CTCAE Grade 3+ Hyperbilirubinemia, 20 Positive and 156 Negative)

Parameter	AD-WNTLT	V20	V30	V40	AD-20	AD-30
AUC	0.672	0.768	0.782	0.790	0.765	0.770
P value	0.006	<0.001	<0.001	<0.001	<0.001	<0.001
P value vs AD-WNTLT*		0.025	0.0094	0.0046	0.096	0.055
Cutoff	56.9 Gy	80%	78%	68%	27 Gy	37 Gy

**P* value of ROC comparison between each voxel-based parameter and AD-WNTLT (multicompartment parameter); cutoff was determined by Youden index.

TABLE 3
ROC Subanalysis of 6-Month Toxicity for Patients Who Underwent Partial Liver Treatment (CTCAE Grade 3+ Hyperbilirubinemia, 4 Positive and 74 Negative)

Parameter	AD-WNTLT	HR	V20	V30	V40	AD-20	AD-30
AUC	0.578	0.591	0.534	0.546	0.542	0.520	0.588
P value	0.629	0.452	0.868	0.811	0.818	0.079	<0.001
P value vs AD-WNTLT*		0.90	0.41	0.45	0.30	0.72	0.95
Cutoff	58.7 Gy	33.8%	6%	6%	5%	0 Gy	0 Gy

**P* value of ROC comparison between each voxel-based parameter and AD-WNTLT (multicompartment parameter); cutoff was determined by Youden index.
HR = hepatic reserve, that is, liver volume not treated by radioembolization.

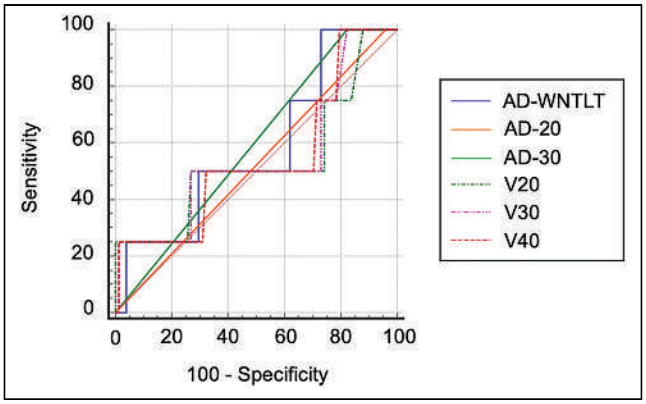

FIGURE 4. ROC analyses of patients undergoing partial-liver radioembolization assessing relationship of absorbed dose parameters and occurrence of liver decompensation within 6 mo.

Of all patients undergoing whole-liver treatment, grade 3+ hepatotoxicity was observed in only 3 of 98 patients with a V40 of no more than 72%, making it a reasonably safe threshold for radioembolization. On the basis of these results, activity escalation within safe margins would have been possible in 65 of 98 patients with a V40 of less than 72% undergoing whole-liver radioembolization. Because prior studies assessing the absorbed dose–response relationship for HCC lesions treated with radioembolization show a wide range of proposed absorbed dose thresholds, it follows that additional increases in tumor-absorbed doses may further increase the likelihood of treatment response (*19,21,22*).

Treatment planning using absorbed dose to the nontumor liver tissue as an additional driving criterion may be of particular interest in the presence of small tumor lesions, where partial-volume effects are expected to lead to a severe underestimation of absorbed doses. Furthermore, the prediction of absorbed doses to nontumor liver tissue by use of ^{99m}Tc-MAA has been shown to be more reliable than the prediction of absorbed doses to tumor lesions, underpinning the robustness of this approach (*9,10*).

To our knowledge, this is the first study to show superiority for voxel-based dosimetry over multicompartment dosimetry in the prediction of liver decompensation of HCC patients undergoing radioembolization with ^{90}Y glass microspheres. However, prior studies have shown some evidence for a potential benefit of voxel-based dosimetry to assess the likelihood of treatment response. Two retrospective studies of patients with liver tumors showed that voxel-based dosimetry of tumor lesions as assessed on posttherapeutic PET was predictive of tumor response after radioembolization with ^{90}Y resin microspheres (*23,24*). Similarly, a slightly higher accuracy than for multicompartment dosimetry was found for response prediction using voxel-based segmentation of the pretherapeutic ^{99m}Tc-MAA SPECT/CT images (*25*).

The analysis of prognostic parameters of hepatotoxicity in HCC patients undergoing partial-liver treatment did not reveal statistically significant results. This may be attributable to low statistical power because of a low event rate in this subcohort. In addition, the prognostic impact of the voxel-based parameters chosen for this study may not be able to accurately reflect radiobiologic effects in a patient cohort, in whom a relevant part of the liver remains untreated.

TABLE 4
ROC Subanalysis of 6-Month Toxicity for Patients Who Underwent Whole Liver Treatment (CTCAE Grade 3+ Hyperbilirubinemia, 16 Positive and 82 Negative)

Parameter	AD-WNTLT	V20	V30	V40	AD-20	AD-30
AUC	0.633	0.796	0.824	0.840	0.803	0.823
P value	0.042	<0.001	<0.001	<0.001	<0.001	<0.001
P value vs AD-WNTLT*		0.032	0.0088	0.0038	0.041	0.015
Cutoff	55.6 Gy	80%	78%	72%	27 Gy	43 Gy

**P* value of ROC comparison between each voxel-based parameter and AD-WNTLT (multicompartment parameter); cutoff was determined by Youden index.

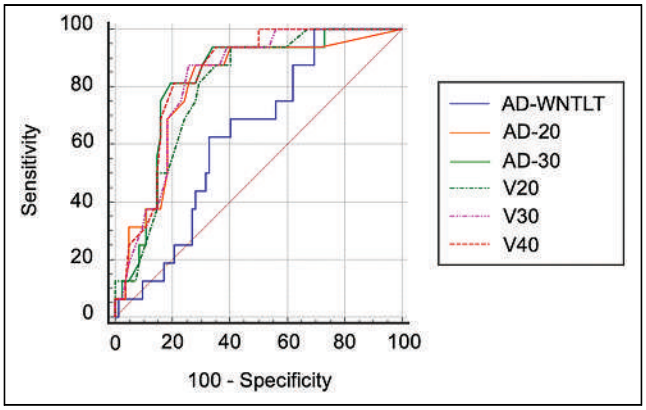

FIGURE 5. ROC analyses of patients undergoing whole-liver radioembolization assessing relationship of absorbed dose parameters and occurrence of liver decompensation within 6 mo.

Limitations of this study include the high rate of patients with insufficient follow-up, as well as its retrospective nature. In addition, absorbed dose distribution was derived from pretherapeutic ^{99m}Tc-HSA SPECT/CT, which has been shown to be a reliable but not perfect predictor of ^{90}Y glass microsphere deposition (*9,10*). Calculated doses will therefore deviate from those achieved during treatment, posing inherent constraints on the reliability of ^{99m}Tc-MAA/HSA-based pretherapeutic prediction of liver decompensation. On the other hand, ^{99m}Tc-MAA/HSA SPECT/CT constitutes the only modality to pretherapeutically assess ^{90}Y microsphere deposition recommended by current guidelines, with no viable alternatives. In addition, for sequential bilobar radioembolization, absorbed doses from both sessions were analyzed cumulatively, with no interim ^{99m}Tc-MAA/HSA SPECT/CT or contrast-enhanced CT, meaning that volumetric changes between treatments were not considered. Though technically a limitation with regard to accurate assessment of dose distribution, this more closely resembles the clinical reality of most physicians and is therefore preferable. The interval from the ^{99m}Tc-MAA/HSA SPECT/CT scan to the first radioembolization (40.9 d) was longer than ideal (15 d) (*3*) and may limit the reliability of the predicted dose distribution.

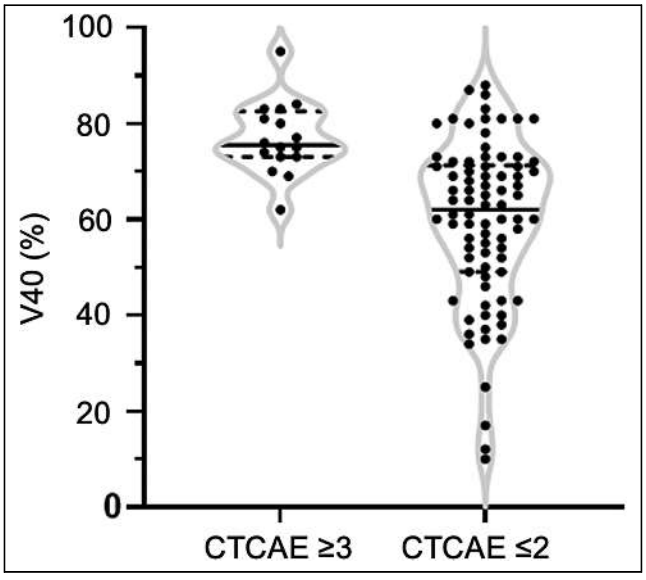

FIGURE 6. Scatterplot of whole-liver treatment patients: comparison of V40 between group of CTCAE for hyperbilirubinemia adverse effects ≥ 3 and group of CTCAE ≤ 2.

CONCLUSION

Our retrospective study showed encouraging results for the prediction of posttherapeutic liver decompensation in HCC patients after whole-liver radioembolization with ^{90}Y glass microspheres using voxel-based absorbed dose metrics. In these patients, exposure of 72% or more of the nontumor liver tissue to more than 40 Gy was associated with an increased risk of liver decompensation. Future research is warranted to confirm these preliminary results and elucidate the interplay of dosimetry results and baseline laboratory and clinical parameters.

DISCLOSURE

Benedikt M. Schaarschmidt received a research grant from PharmaCept for an undergoing investigator-initiated study not related to this paper. Wolfgang P. Fendler is a consultant for Endocyte and BTG and received fees from RadioMedix, Bayer, and Parexel outside the submitted work. Wolfgang P. Fendler reports fees from SOFIE Bioscience (research funding), Janssen (consultant, speakers' bureau), Calyx (consultant), Bayer (consultant, speakers' bureau, research funding), Parexel (image review), and AAA (speakers' bureau) outside the submitted work. Ken Herrmann reports personal fees from Bayer, Sofie Biosciences, SIRTEX, Adacap, Curium, Endocyte, BTG, IPSEN, Siemens Healthineers, GE Healthcare, Amgen, Novartis, ymabs, Aktis Oncology, Theragnostics, and Pharma15; other fees from Sofie Biosciences; nonfinancial support from ABX; and grants from BTG outside the submitted work. Manuel Weber reports personal fees from Boston Scientific, Terumo, Advanced Accelerator Applications, and Eli Lilly outside the submitted work. No other potential conflict of interest relevant to this article was reported.

KEY POINTS

QUESTION: Can voxel-based dosimetry predict hepatotoxicity in HCC patients undergoing radioembolization and thereby improve pretherapeutic activity calculation?

PERTINENT FINDINGS: Voxel-based dosimetry may more accurately predict hepatotoxicity than multicompartment dosimetry, which is currently considered to be the state of the art in procedure guidelines.

IMPLICATIONS FOR PATIENT CARE: Voxel-based dosimetry of selective internal radiation therapy is helpful to assess expected hepatotoxicity and may thereby enable safe escalation or deescalation of treatment activity to optimize tumor control, that is, the efficacy and toxicity trade-off of selective internal radiation therapy.

REFERENCES

1. Garin E, Tselikas L, Guiu B, et al. Personalised versus standard dosimetry approach of selective internal radiation therapy in patients with locally advanced hepatocellular carcinoma (DOSISPHERE-01): a randomised, multicentre, open-label phase 2 trial. *Lancet Gastroenterol Hepatol*. 2021;6:17–29.
2. Levillain H, Bagni O, Deroose CM, et al. International recommendations for personalised selective internal radiation therapy of primary and metastatic liver diseases with yttrium-90 resin microspheres. *Eur J Nucl Med Mol Imaging*. 2021;48:1570–1584.

3. Weber M, Lam M, Chiesa C, et al. EANM procedure guideline for the treatment of liver cancer and liver metastases with intra-arterial radioactive compounds. *Eur J Nucl Med Mol Imaging.* 2022;49:1682–1699.
4. Salem R, Padia SA, Lam M, et al. Clinical and dosimetric considerations for Y90: recommendations from an international multidisciplinary working group. *Eur J Nucl Med Mol Imaging.* 2019;46:1695–1704.
5. Chiesa C, Mira M, Bhoori S, et al. Radioembolization of hepatocarcinoma with ^{90}Y glass microspheres: treatment optimization using the dose-toxicity relationship. *Eur J Nucl Med Mol Imaging.* 2020;47:3018–3032.
6. Chiesa C, Sjogreen-Gleisner K, Walrand S, et al. EANM dosimetry committee series on standard operational procedures: a unified methodology for ^{99m}Tc-MAA pre- and ^{90}Y peri-therapy dosimetry in liver radioembolization with ^{90}Y microspheres. *EJNMMI Phys.* 2021;8:77.
7. Apisarnthanarax S, Barry A, Cao M, et al. External beam radiation therapy for primary liver cancers: an ASTRO clinical practice guideline. *Pract Radiat Oncol.* 2022;12:28–51.
8. Haste P, Tann M, Persohn S, et al. Correlation of technetium-99m macroaggregated albumin and yttrium-90 glass microsphere biodistribution in hepatocellular carcinoma: a retrospective review of pretreatment single photon emission CT and posttreatment positron emission tomography/CT. *J Vasc Interv Radiol.* 2017;28:722–730.e1.
9. Gnesin S, Canetti L, Adib S, et al. Partition model-based ^{99m}Tc-MAA SPECT/CT predictive dosimetry compared with ^{90}Y TOF PET/CT posttreatment dosimetry in radioembolization of hepatocellular carcinoma: a quantitative agreement comparison. *J Nucl Med.* 2016;57:1672–1678.
10. Jadoul A, Bernard C, Lovinfosse P, et al. Comparative dosimetry between ^{99m}Tc-MAA SPECT/CT and ^{90}Y PET/CT in primary and metastatic liver tumors. *Eur J Nucl Med Mol Imaging.* 2020;47:828–837.
11. Burman C, Kutcher GJ, Emami B, Goitein M. Fitting of normal tissue tolerance data to an analytic function. *Int J Radiat Oncol Biol Phys.* 1991;21:123–135.
12. Emami B, Lyman J, Brown A, et al. Tolerance of normal tissue to therapeutic irradiation. *Int J Radiat Oncol Biol Phys.* 1991;21:109–122.
13. TheraSphere® yttrium-90 glass microspheres. Package insert. Biocompatibles UK Ltd.; revision 12.
14. Guglielmi A, Ruzzenente A, Conci S, Valdegamberi A, Iacono C. How much remnant is enough in liver resection? *Dig Surg.* 2012;29:6–17.
15. Kim HJ, Kim CY, Hur YH, et al. Comparison of remnant to total functional liver volume ratio and remnant to standard liver volume ratio as a predictor of postoperative liver function after liver resection. *Korean J Hepatobiliary Pancreat Surg.* 2013;17:143–151.
16. Garin E, Lenoir L, Edeline J, et al. Boosted selective internal radiation therapy with ^{90}Y-loaded glass microspheres (B-SIRT) for hepatocellular carcinoma patients: a new personalized promising concept. *Eur J Nucl Med Mol Imaging.* 2013;40:1057–1068.
17. Garin E, Rolland Y, Pracht M, et al. High impact of macroaggregated albumin-based tumour dose on response and overall survival in hepatocellular carcinoma patients treated with ^{90}Y-loaded glass microsphere radioembolization. *Liver Int.* 2017;37:101–110.
18. Braat MN, van Erpecum KJ, Zonnenberg BA, van den Bosch MA, Lam MG. Radioembolization-induced liver disease: a systematic review. *Eur J Gastroenterol Hepatol.* 2017;29:144–152.
19. Lam M, Garin E, Maccauro M, et al. A global evaluation of advanced dosimetry in transarterial radioembolization of hepatocellular carcinoma with yttrium-90: the TARGET study. *Eur J Nucl Med Mol Imaging.* 2022;49:3340–3352.
20. Hanley JA, McNeil BJ. A method of comparing the areas under receiver operating characteristic curves derived from the same cases. *Radiology.* 1983;148:839–843.
21. Kappadath SC, Mikell J, Balagopal A, Baladandayuthapani V, Kaseb A, Mahvash A. Hepatocellular carcinoma tumor dose response after ^{90}Y-radioembolization with glass microspheres using ^{90}Y-SPECT/CT-based voxel dosimetry. *Int J Radiat Oncol Biol Phys.* 2018;102:451–461.
22. Roosen J, Klaassen NJM, Westlund Gotby LEL, et al. To 1000 Gy and back again: a systematic review on dose-response evaluation in selective internal radiation therapy for primary and secondary liver cancer. *Eur J Nucl Med Mol Imaging.* 2021;48:3776–3790.
23. Kao YH, Steinberg JD, Tay YS, et al. Post-radioembolization yttrium-90 PET/CT—part 2: dose-response and tumor predictive dosimetry for resin microspheres. *EJNMMI Res.* 2013;3:57.
24. Allimant C, Kafrouni M, Delicque J, et al. Tumor targeting and three-dimensional voxel-based dosimetry to predict tumor response, toxicity, and survival after yttrium-90 resin microsphere radioembolization in hepatocellular carcinoma. *J Vasc Interv Radiol.* 2018;29:1662–1670 e1664.
25. Chiesa C, Bardies M, Zaidi H. Voxel-based dosimetry is superior to mean absorbed dose approach for establishing dose-effect relationship in targeted radionuclide therapy. *Med Phys.* 2019;46:5403–5406.

An International Study of Factors Affecting Variability of Dosimetry Calculations, Part 2: Overall Variabilities in Absorbed Dose

Julia Brosch-Lenz[1], Suqi Ke[2], Hao Wang[2], Eric Frey[3,4], Yuni K. Dewaraja[5], John Sunderland*[6], and Carlos Uribe*[1,7,8]

[1]*Department of Integrative Oncology, BC Cancer Research Institute, Vancouver, British Columbia, Canada;* [2]*Division of Quantitative Sciences, Sidney Kimmel Comprehensive Cancer Center, Johns Hopkins University School of Medicine, Baltimore, Maryland;* [3]*Rapid, LLC, Baltimore, Maryland;* [4]*Department of Radiology, Johns Hopkins University, Baltimore, Maryland;* [5]*Department of Radiology, University of Michigan, Ann Arbor, Michigan;* [6]*Department of Radiology, University of Iowa, Iowa City, Iowa;* [7]*Department of Functional Imaging, BC Cancer, Vancouver, British Columbia, Canada; and* [8]*Department of Radiology, University of British Columbia, Vancouver, British Columbia, Canada*

Dosimetry for personalized radiopharmaceutical therapy has gained considerable attention. Many methods, tools, and workflows have been developed to estimate absorbed dose (AD). However, standardization is still required to reduce variability of AD estimates across centers. One effort for standardization is the Society of Nuclear Medicine and Molecular Imaging ^{177}Lu Dosimetry Challenge, which comprised 5 tasks (T1–T5) designed to assess dose estimate variability associated with the imaging protocol (T1 vs. T2 vs. T3), segmentation (T1 vs. T4), time integration (T4 vs. T5), and dose calculation (T5) steps of the dosimetry workflow. The aim of this work was to assess the overall variability in AD calculations for the different tasks. **Methods:** Anonymized datasets consisting of serial planar and quantitative SPECT/CT scans, organ and lesion contours, and time-integrated activity maps of 2 patients treated with ^{177}Lu-DOTATATE were made available globally for participants to perform dosimetry calculations and submit their results in standardized submission spreadsheets. The data were carefully curated for formal mistakes and methodologic errors. General descriptive statistics for ADs were calculated, and statistical analysis was performed to compare the results of different tasks. Variability in ADs was measured using the quartile coefficient of dispersion. **Results:** ADs to organs estimated from planar imaging protocols (T2) were lower by about 60% than those from pure SPECT/CT (T1), and the differences were statistically significant. Importantly, the average differences in dose estimates when at least 1 SPECT/CT acquisition was available (T1, T3, T4, T5) were within ±10%, and the differences with respect to T1 were not statistically significant for most organs and lesions. When serial SPECT/CT images were used, the quartile coefficients of dispersion of ADs for organs and lesions were on average less than 20% and 26%, respectively, for T1; 20% and 18%, respectively, for T4 (segmentations provided); and 10% and 5%, respectively, for T5 (segmentation and time-integrated activity images provided). **Conclusion:** Variability in ADs was reduced as segmentation and time-integration data were provided to participants. Our results suggest that SPECT/CT-based imaging protocols generate more consistent and less variable results than planar imaging methods. Effort at standardizing segmentation and fitting should be made, as this may substantially reduce variability in ADs.

Key Words: radiopharmaceutical therapy; dosimetry; variability; standardization; dosimetry challenge

J Nucl Med 2023; 64:1109–1116
DOI: 10.2967/jnumed.122.265094

Recent clinical trials have demonstrated favorable patient outcomes and led to U.S. Food and Drug Administration approvals of ^{177}Lu-based radiopharmaceuticals for the treatment of neuroendocrine tumors (^{177}Lu-DOTATATE (*1*) in 2018) and metastatic castration-resistant prostate cancer (^{177}Lu-PSMA-617 (*2*) in 2022). These approvals have motivated research for new targets and development of new radiopharmaceuticals by both academia and industry (*3–7*). Despite the initial promising results for radiopharmaceutical therapies, recurrence has also been reported (*8,9*). Patient-specific dosimetry (*10*) may allow personalization of administered activity to deliver maximized absorbed doses (ADs) to lesions while keeping normal-organ ADs below toxic levels. There is evidence that dosimetry-guided therapy increases the survival of patients who undergo liver radioembolization (*11*). However, dosimetry calculations are still not routinely performed for radiopharmaceutical therapies, partly because of the lack of standardized dosimetry tools, methods, and protocols. Dosimetry-based therapy-planning approaches are fundamentally limited by the precision of the AD estimates. However, relatively little is known about variability in ADs and the extent to which the different steps of the dosimetry workflow contribute to it.

Dosimetry calculations involve multiple steps (*12–14*): quantitative imaging of the distribution of the radiopharmaceutical over time, segmentation of lesions and organs of interest, estimation of the total number of disintegrations (time-integrated activity (TIA)) in each target region (e.g., organs and lesions), and conversion of TIA to AD using either organ-level or voxelized dosimetry methods. Alternatively, serial dose-rate images can be calculated first, followed by fitting and integration over time.

To better understand the relative contribution to variability of the various steps of the dosimetry workflow, the Society of Nuclear Medicine and Molecular Imaging (SNMMI) Dosimetry Task Force

Received Oct. 25, 2022; revision accepted Feb. 7, 2023.
For correspondence or reprints, contact Carlos Uribe (curibe@bccrc.ca).
*Contributed equally to this work.
Published online Apr. 6, 2023.

TABLE 1
Patient Characteristics, Administered Activities, and Pre- and Post-therapeutic Imaging Information

Patient	Injected activity (GBq)	Diagnostic images	Post-therapy images	Characteristics
A	7.21	Baseline MRI with contrast medium; ^{68}Ga PET 185 d before baseline CT and 468 d before first SPECT/CT	SPECT/CT and whole-body planar images on day of treatment and days 1, 4, and 5 after treatment	Two liver lesions were selected for the challenge
B	7.31	Baseline CT with contrast medium; ^{68}Ga PET 36 d after baseline CT and 69 d before first SPECT/CT	SPECT/CT and whole-body planar images on day of treatment and days 1, 4, and 8 after treatment	Patient had been splenectomized; 4 lesions were selected for the challenge

launched the ^{177}Lu Dosimetry Challenge in 2021 (*15*). The challenge included 5 tasks (T1–T5). Three tasks investigated variability caused by different imaging protocols: serial SPECT/CT (T1), serial planar images (T2), or a hybrid approach (serial planar and 1 SPECT/CT image) (T3). Two additional tasks provided participants with volumes of interest (VOIs) (T4) and TIA maps (T5) with the aim of removing variability in segmentation and integration by removing sources of variability in the serial SPECT/CT workflow. The challenge did not address the impact of variability in ADs caused by image acquisition, calibration, or reconstruction.

The aim of the analysis presented in this work was to assess the source and magnitude of variability in AD estimates, for both organs and lesions, for the different tasks of the ^{177}Lu dosimetry challenge and to inform standardization efforts.

MATERIALS AND METHODS

Patient Images and Data Collection

Datasets of 2 patients who underwent planar and SPECT/CT imaging at 4 time points after administration of ^{177}Lu-DOTATATE therapy (*16*) were shared via the Deep Blue Data repository (https://deepblue.lib.umich.edu/data/collections/hm50ts030?locale=en) (*17–21*) of the University of Michigan. Sharing of patient images and data was approved by the University of Michigan Institutional Review Board, and both patients gave written informed consent. Table 1 summarizes the data provided. Maximum-intensity-projection images showing the provided VOIs are displayed in Figure 1.

Participants reported results on standardized spreadsheets tailored to each task. No lesion AD results were requested in T2 because of the overlap of lesions with organs on planar images. Separate spreadsheets were submitted for each patient. The data requested included information about methods, software used, intermediate values (e.g., VOI volumes, activities, and TIAs), and final ADs. Details of the methodology used for the challenge were given in our previous publication by Uribe et al. (*15*), including a full list of collected variables. Participants were encouraged to submit multiple calculations for the same patient using different types of software ormethodology (e.g., organ-based vs. voxel-based calculations). Participants were asked to briefly describe their dosimetry workflow in addition to the spreadsheet; unfortunately, however, only 1 participant mentioned partial-volume correction.

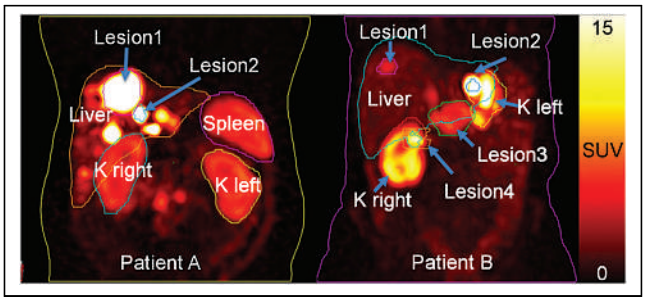

FIGURE 1. Maximum-intensity-projection images at 24 h after injection of ^{177}Lu-DOTATATE for the 2 patients included in the dosimetry challenge. Contours of VOIs provided in T4 and T5 are shown. For patient A, average VOIs as measured from RTstructure files were 1,959 cm^3 for liver, 247 cm^3 for spleen, 467 cm^3 for total kidney, 107 cm^3 for lesion 1, and 3 cm^3 for lesion 2; for patient B, they were 1,693 cm^3 for liver, 229 cm^3 for total kidney, 11 cm^3 for lesion 1, 3 cm^3 for lesion 2, 68 cm^3 for lesion 3, and 22 cm^3 for lesion 4. K = kidney.

Data Collation

Data from all received submissions were extracted using the Python data analysis library (Pandas, version 1.3.5) and Python (version 3.9.5). All data were concatenated into a single data frame with columns corresponding to the specific variables collected. A full glossary of variables and column descriptions can be found in Supplemental Tables 1 and 2 (supplemental materials are available at http://jnm.snmjournals.org), as well as in the GitHub repository of the ^{177}Lu Dosimetry Challenge (https://github.com/carluri/snmmi_dosimetry_challenge).

We curated the data, including identifying typographical, orientation (left/right ambiguity), and unit conversion issues and errors and evaluating data completeness. Participants were contacted for confirmation and clarification as needed. Results that were identified as containing mistakes in the calculations were removed from the analysis. A detailed description of the data curation process can be found in the supplemental material.

Statistical Analysis

Descriptive statistics, such as quartiles, means, and standard deviations (SDs) of ADs, were calculated separately for each task, patient, organ, and lesion. The quartile coefficient of dispersion (QCD) was calculated as the ratio of the difference between the 75th and 25th quartiles and the sum of the 75th and 25th quartiles of the data. The QCD was chosen since it is less sensitive to outliers in the data than is the coefficient of variation. For a normal distribution, the coefficient of variation is 1.4826 times the QCD.

A mixed-effects model was used to compare ADs among T1, T2, and T3 and, separately, among T1, T4, and T5. The model included the task as a fixed effect and the participant as a random effect. The analysis was performed separately for each patient and organ or lesion. Restricted maximum likelihood was applied to estimate the parameters in the models. All tests were 2-sided, and P values of 0.05 or less were considered to indicate statistically significance differences. The analysis was performed with Python (version 3.9.5) and R (version 4.1.0).

TABLE 2
Number of Submissions per Task and per Patient

	Submissions (*n*)				
Patient	T1	T2	T3	T4	T5
A	63	13	16	40	31
B	63	11	14	40	30

16 participants (institutions) submitted all tasks, and 10 submitted T1, T4, and T5.

RESULTS

General Observations

We received 321 submissions from 51 institutions (Asia, 8; Australia, 2; Europe, 18; North America, 22; and South America, 1). Table 2 summarizes the submissions per task and patient. Some participants submitted multiple spreadsheets using different dosimetry methods (e.g. organ-level and voxelized).

Both open-source and commercial dosimetry softwares were used, with details provided in Supplemental Figures 1 and 2. Approximately 27% of submissions used an in-house dose calculation approach.

Absorbed Doses

Figure 2 shows the distribution of mean ADs in organs and lesions from all submissions (after data curation). The numeric values of the descriptive statistics underlying Figure 2 can be found in Supplemental Table 1.

Table 3 shows the percentage difference calculated as the difference between the median of all submissions per task taking the median of all submissions from T1 as a reference, as well as the median of all submissions from T4 and T5 as a reference. Percentage differences were averaged separately for patients and for organs and lesions.

In general, ADs calculated from planar imaging protocols (T2) were lower than pure SPECT or hybrid protocols (Fig. 2). ADs for organs from T2 underestimated those from the pure SPECT protocol of T1 on average by 60%, ranging from −81% to −31% (Table 3). In contrast, the ADs of the hybrid protocol (T3) were similar to those of the pure SPECT/CT protocol (T1) for organs (on average 8% lower, ranging from −17% to 4%, Table 3). On average, the ADs for all organs were within ±10% of one another for T1, T4, and T5 (Table 3), suggesting no substantial bias between SPECT-based tasks. For lesions, a larger spread of values was observed (Fig. 2), but average percentage differences were within ±12%, ranging from −25% to +40% (Table 3). The provision of TIA maps in T5 yielded slightly smaller ranges in percentage difference of the medians of organ and lesion doses of T4 relative to T5 (Table 3).

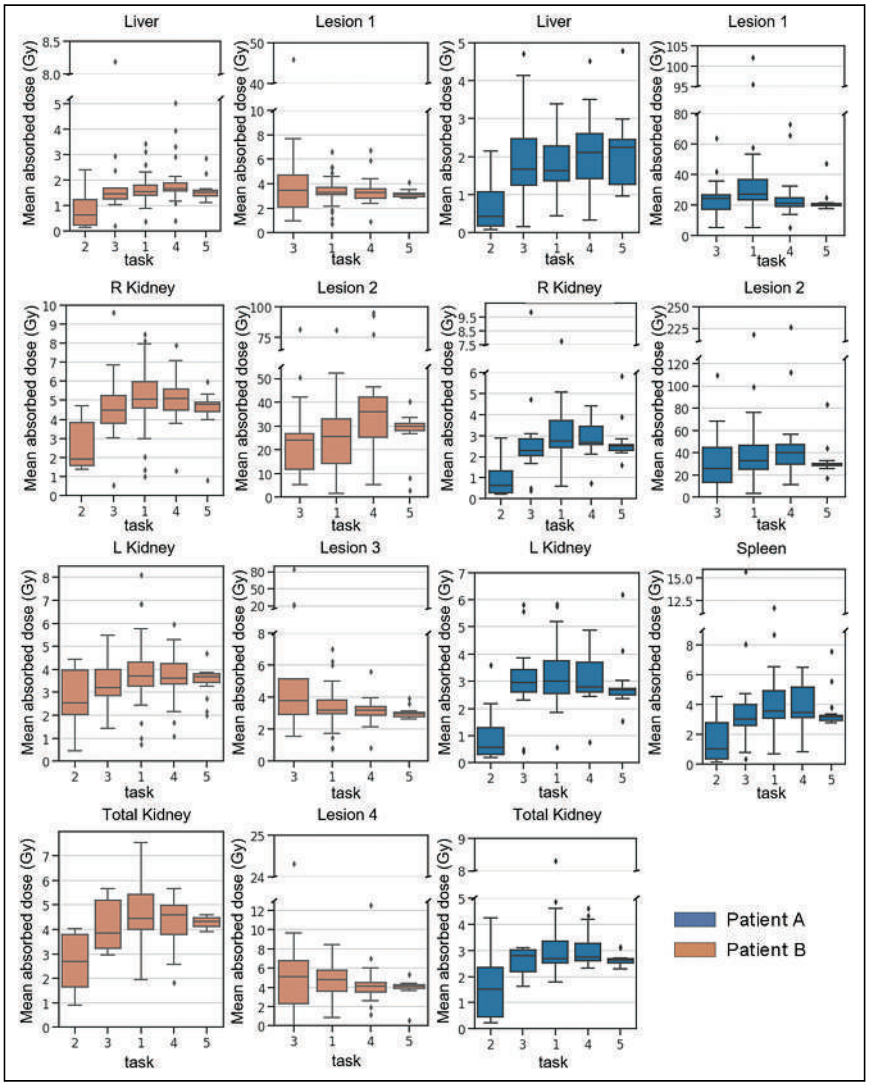

FIGURE 2. Mean organ and lesion AD in Gray per task and per patient. Patient B had been splenectomized. T2 was based on planar images, T3 used hybrid imaging protocol of multiple planar images and 1 SPECT/CT image, T1 used multiple SPECT/CT images, T4 used multiple SPECT/CT images and provided VOIs, and T5 was based on provided TIA image and VOIs.

Quantification of Variability

Figure 3 and Table 4 show the QCDs of ADs for all tasks averaged over organs and lesions. QCDs per organ and patient are provided in Supplemental Table 1. The QCDs for T2 were large, with an average of 69% for patient A and 46% for patient B (Table 4). The hybrid (T3) and pure SPECT (T1) protocols had similar QCDs for organs: on average 20% for patient A and 17% and 14% for patient B. Overall, the variability was reduced as segmentation and TIA activity data were provided (i.e., T1 to T4 to T5) (Figs. 2 and 3; Table 4). For the pure SPECT protocols (T1, T4, and T5), there was an overall reduction by a factor of about 1.5 in lesion QCD when VOIs were given to participants (T1 vs. T4, Table 4); the change for organs was smaller. Larger QCDs were observed for the smaller lesions (lesion 2 of patient A and lesion 2 of

TABLE 3
Percentage Difference Between Medians of All Submissions per Task Relative to T1 and T4 Relative to T5

Patient	Organ	T2 vs. T1	T3 vs. T1	T4 vs. T1	T5 vs. T1	T4 vs. T5
A	Liver	−74%	2%	29%	38%	−6%
	Spleen	−71%	−15%	−2%	−12%	11%
	R kidney	−77%	−17%	−3%	−9%	7%
	L kidney	−81%	−2%	−7%	−11%	4%
	Total kidney	−43%	4%	3%	−2%	5%
	Lesion 1		−10%	−23%	−25%	3%
	Lesion 2		−23%	21%	−10%	34%
B	Liver	−60%	−6%	6%	−3%	9%
	R kidney	−62%	−11%	1%	−5%	6%
	L kidney	−31%	−14%	−3%	−1%	−2%
	Total kidney	−40%	−13%	4%	−2%	6%
	Lesion 1		6%	−1%	−5%	5%
	Lesion 2		−6%	40%	16%	20%
	Lesion 3		19%	0%	−7%	7%
	Lesion 4		6%	−14%	−16%	1%

patient B) in T1, when segmentation and time integration were performed by participants. There was a substantial reduction in QCD for both organs and lesions when both VOIs and TIA maps were given to participants (T5, Table 4), resulting in QCDs of less than 7% for organs (excluding the liver of patient A) and less than 6% for lesions, independent of lesion size.

Statistical Analysis

The results of the statistical comparisons between ADs calculated for the different tasks are given in Table 5. In general, statistically significant differences were observed between T1 (pure SPECT) and T2 (planar imaging) but not between tasks that involved a SPECT scan, although there were a few exceptions.

DISCUSSION

All of the different steps in the dosimetry workflow potentially contribute to variability in AD estimates. First, the choice of imaging protocol (i.e., planar, SPECT, or hybrid imaging) can affect the measurement of the activity estimates that are the basis for dosimetry calculations. Second, the segmentation of organs and lesions can also affect the ADs. For voxel-based dosimetry, segmentation defines the spatial extent of VOIs where the AD is averaged, whereas for organ-based dosimetry it defines the organ mass and activity. The effect of segmentation on the AD is complicated since both the numerator (energy) and the denominator (mass) in the definition of dose (i.e., joules per kilogram) are affected. The estimation of total number of decays performed by curve fitting and time integration is influenced by the choice of fit function and the temporal limits of integration, neither of which is currently standardized. Finally, the choice of dosimetry method, software, and source of S-values or dose kernel can affect the final AD. The SNMMI ^{177}Lu Dosimetry Challenge was designed to assess the variability in ADs caused by imaging protocol (T1, T2, and T3), segmentation (T4), and time-integration and dosimetry method (T5) on the final dosimetry results.

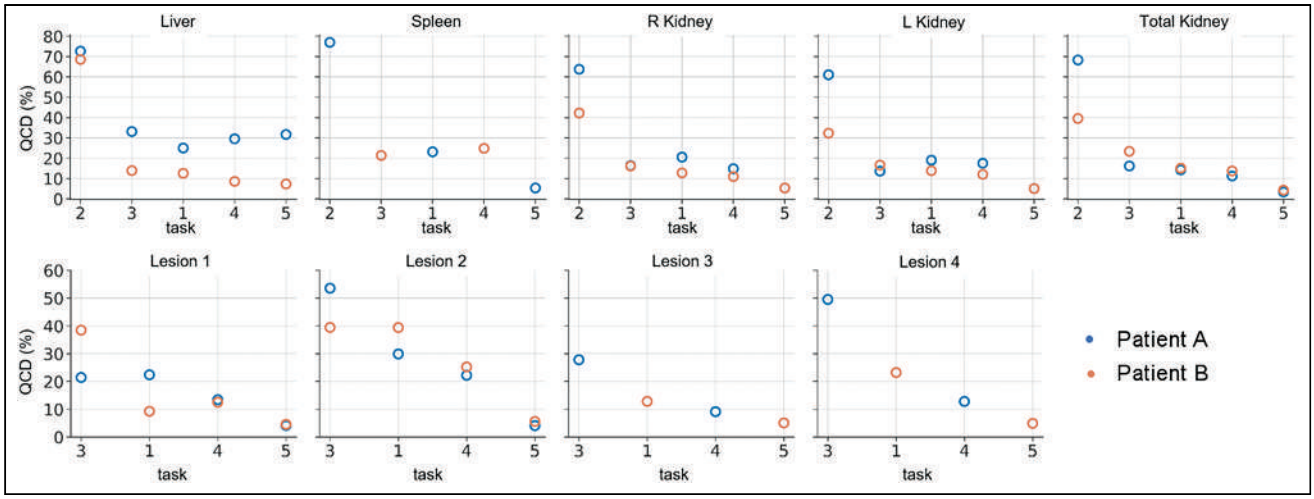

FIGURE 3. QCD per task, organ, and patient.

TABLE 4
QCD per Task, Organ, and Patient

	Patient A					Patient B				
Organ	T2	T3	T1	T4	T5	T2	T3	T1	T4	T5
Liver	73%	33%	25%	30%	32%	69%	14%	13%	9%	7%
Spleen	77%	21%	23%	25%	5%					
R kidney	64%	16%	21%	15%	5%	42%	16%	13%	11%	5%
L kidney	61%	14%	19%	18%	5%	32%	17%	14%	12%	5%
Total kidney	68%	16%	14%	11%	3%	40%	23%	15%	14%	4%
Lesion 1		21%	22%	13%	4%		38%	9%	13%	5%
Lesion 2		54%	30%	22%	4%		39%	39%	25%	6%
Lesion 3							28%	13%	9%	5%
Lesion 4							50%	23%	13%	5%

The planar protocol (T2) resulted in lower ADs by a factor of 2 and higher average QCDs than SPECT-based protocols, and these differences were statistically significant (Table 5). Lesion doses were not requested for T2 (planar protocols) because of the overlap with organs. Of note, T2 had the smallest number of submissions, with only 13 and 11 submissions for patients A and B, respectively.

The differences between ADs from the hybrid (T3) and pure SPECT (T1, T4, and T5) protocols were generally not statistically significant (Table 5). With the hybrid approach, the issues with overlapping structures are substantially reduced by use of the SPECT/CT image but can still affect the shape of the time–activity curve, especially for objects in high-uptake regions such as the lesions (Fig. 1). These results are consistent with previous reported data about the accuracy and precision of SPECT and hybrid protocols as compared with planar protocols (*22–26*).

The differences in ADs for the purely SPECT-based T1, T4, and T5 were generally small (Fig. 2; Table 3) and were not statistically significant for most organs and lesions (Table 5). However, statistically significant differences for the liver were observed, as can be explained by the presence of lesions in the livers of both patients (Fig. 1)—lesions might not have been excluded in the segmentation of healthy liver by all participants. This possibility suggests that standardization of segmentation methodologies should be considered to reduce variability. As demonstrated in Figure 2, the ranges of dose results were reduced when VOIs and TIA maps were provided, that is, comparing T1 with T4 and T5.

The largest average QCDs were found for the planar protocol, that is, T2 (Fig. 3; Table 4). We observed larger QCDs for the smaller lesions (Fig. 3, lesion 2 of patients A and B) than for the larger lesions. This result is expected given the difficulty and subjectivity associated with lesion segmentation and mass definition for those structures. This difficulty can further be related to the partial-volume effect, which is more pronounced for smaller lesions such as lesion 2 of patients A and B. In general, the QCDs, reflecting variation in ADs, were reduced as more information was provided to participants (i.e., T1 to T4 to T5), even for the challenging small lesions. Average organ QCDs changed little when VOIs were provided to participants (T1 to T4, Table 4), whereas lesion QCDs decreased by a factor of approximately 1.5. The

TABLE 5
P Values for Comparisons of ADs Between Various Tasks and T1

	Planar-, hybrid-, and SPECT-based tasks				Purely SPECT-based tasks			
	T1 vs. T2		T1 vs. T3		T1 vs. T4		T1 vs. T5	
Organ	Patient A	Patient B	Patient A	Patient B	Patient A	Patient B	Patient A	Patient B
Liver	<0.01*	0.03*	0.09	0.08	<0.01*	0.01*	<0.01*	0.89
Spleen	<0.01*		0.87		0.63		0.12	
R kidney	<0.01*	0.01*	0.75	0.61	0.65	0.84	0.14	0.07
L kidney	<0.01*	0.13	0.87	0.67	0.86	0.44	0.18	0.22
Total kidney	0.01*	0.15	0.31	0.88	0.59	0.22	0.27	0.73
Lesion 1			0.15	0.02*	0.02*	0.92	<0.01*	0.40
Lesion 2			0.82	0.74	0.08	<0.01*	0.63	0.24
Lesion 3				<0.01*		0.12		0.02*
Lesion 4				0.21		0.14		0.06

*Statistically significant difference.

QCDs of T5 were as low as 10% and 5% on average for all organs and 4% and 5% for all lesions of patients A and B, respectively (Table 4). The vast decrease in QCD between T1 and T5 from 30% to 4% for the small lesion 2 (~3 mL) of patient A and from 39% to 6% for lesion 2 (~3 mL) of patient B, compared with the moderate QCD decrease from 22% to 4% for lesion 1 (~107 mL) of patient A and from 13% to 5% for lesion 3 (~68 mL) of patient B, indicates that both segmentation and integration represent large sources of variability, especially for smaller objects. Segmentation can be further complicated when lesions are within an organ with little difference in contrast. The largest organ QCDs from all submissions for T5 were 32% and 7% for the liver of patients A and B, respectively (Fig. 3; Table 4; Supplemental Table 1). The size of this variation was unexpected given the data provided to the participants in T5. We attribute this variation to the presence of liver lesions and different decisions made by participants about what to include in the liver VOI (i.e., removing all lesions or only the lesions indicated by the challenge, Fig. 1). In general, the segmentation and TIA data provided in T4 and T5 substantially reduced variability as assessed by QCD (Fig. 3) and with respect to Figure 2, strongly suggesting that efforts to standardize segmentation (e.g., whether to include suspected lesions in normal tissues and whether to include the medulla and pelvis in kidney VOIs) may substantially reduce variability. Furthermore, providing TIA maps (i.e., standardization of fitting and integration) strongly reduced the variability in ADs and points to the integration approach as a source of substantial variability and a target for standardization.

The remaining variability in T5 can be attributed to several sources. Since this step included solely the conversion from TIA to AD, it may be related to differences in S values, dose kernels, or Monte Carlo simulations. Generally, these differences have been found to be small (<5%) (*27–29*), as is consistent with our independent findings for this dataset (*30*). Another potential source of variability is application of mass scaling to the S values (*31*) or density weighting to the dose kernels (*27*), both of which options are usually available in dosimetry software. Future analysis will focus on the effect of these factors on T5.

A limitation of this work is that it is based on only 2 patient datasets; this number was selected as a compromise between gaining more information on interpatient variability and the desire to attract a larger number of voluntary participants. The 2 patients chosen, however, illustrate some important characteristics and common challenges in the dosimetry workflow related to imaging protocol (planar vs. SPECT), segmentation, and integration. Specific characteristics of interest included a large tumor burden in the liver, significant differences between right and left kidney volumes, significant differences from standard phantom organ volumes, and lesion size and proximity to other high-uptake structures. In addition, some unintentional sources of variability are inherent in the design and implementation of the SNMMI ^{177}Lu Dosimetry Challenge. For example, VOIs were provided both in the radiotherapy structure set (RTSTRUCT) of the DICOM standard and as voxelized masks to accommodate different capabilities in software available to participants. The process of voxelizing the RTSTRUCT resulted in different volume and activity estimates between the contours and the masks depending on the software used for the analysis. For example, one software package used by the organizers allowed the contours to include subvoxels, but the masks always contained complete voxels. Generally, the contour interpolation into subvoxels should be disabled for dosimetry purposes. This disabling resulted in average differences in volumes of 8% (range, 4%–14%) for organs and of 20% (range, 8%–37%) for lesions. Thus, the use of RTstructure by some participants and masks by others added to the variability in ADs. Similarly, VOIs were provided at each imaging time point, whereas the TIA map for T5 was generated using the first imaging time point as a reference. Applying to the TIA map the VOIs from a time point other than the first will consequently lead to different results. Although reflective of differences that may be observed at different sites in a clinical environment, the magnitude of the contribution of these sources to overall variability is likely specific to the design and implementation of the challenge. We did not expect that the provision of VOIs in RTstructure and mask format at multiple time points would affect the ADs and thus did not act to minimize this source of variability. Nevertheless, this difference when saving VOIs does highlight the potential for variability due to differences in software implementations and settings. Finally, this challenge did not address the impact of image acquisition, reconstruction, and quantification, which are also considered to be major contributors to variability of dose estimates.

The analysis of the SNMMI ^{177}Lu Dosimetry Challenge data on overall dose variability elucidated several areas in which standardization or harmonization may be important to reduce variability across sites and methods. Our initial recommendations to reduce the variability of dose calculations based on the results of our analysis are as follows.

First, pure SPECT or hybrid SPECT/planar imaging protocols should be used for dosimetry instead of planar imaging–only protocols. The results presented here indicate that this recommendation would reduce variability and suggest a reduced bias.

Second, the development of segmentation guidelines for organs and lesions can help standardize the process and reduce the variability observed in this study. For example, guidance can be issued on how to deal with overlapping regions such as lesions in the liver and which regions of the kidney such as the renal pelvis should be included in the segmentation. In the meantime, we believe that publications should explicitly detail how these procedures are being performed to ensure that a correct comparison between results is being made.

Third, standardizing the use of fitting functions and integration methods would achieve some meaningful reduction in dose variability based on the reduction in variability from T4 to T5.

Fourth, more detailed and standardized reporting (*32,33*) of such details as dosimetry method (voxelized vs. organ-based), software used, appropriate use of mass scaling, and user decisions regarding the inclusion of kidney substructures should be developed to enable comparison of results from different centers and in different trials. A standardized nomenclature as emphasized in MIRD pamphlet 21 (*34*) would facilitate this reporting.

CONCLUSION

This analysis of all tasks of the SNMMI ^{177}Lu Dosimetry Challenge highlights the need to move toward SPECT-based imaging protocols for dosimetry of radiopharmaceutical therapies. Standardizing segmentation and fitting methods and decisions is essential to reducing variability in AD. Removing these sources of variation from the dosimetry workflow reduced the variability to below 10% for organs and lesions.

DISCLOSURE

This work was partly supported by the SNMMI Value Initiative. Yuni Dewaraja acknowledges funding from grant R01CA240706

awarded by the National Cancer Institute for patient studies and resources made available by the University of Michigan Deep Blue Data Repository for data sharing. Eric Frey is a cofounder and part-owner of Rapid, LLC; receives royalty income from GE Healthcare; and acknowledges support from grants R44CA213782 and R01CA240779 awarded by the National Cancer Institute. Carlos Uribe acknowledges funding from Natural Science and Engineer Research Council (NSERC) discovery grant RGPIN-2021-02965. No potential conflict of interest relevant to this article was reported.

ACKNOWLEDGMENTS

We thank Bonnie Clarke, the director of research and discovery at the SNMMI, for her excellent support and her continuous help with data collection and communication of the challenge. Special thanks to all the participants: Aaron Scott, Adam Kesner, Albert Bartrés, Alessandro Desy, Alessia Milano, Anne-Laurène Wenger, Antoine Legrand, Arda Könik, Ashok Tiwari, Avery Peterson, Azadeh Akhavan, Benjamin Van, Carlos Montes Fuentes, Chae Moon Hong, Daniel McGowan, Daniele Pistone, David Adam, Diana McCrumb, Domenico Finocchiaro, Edoardo d'Andrea, Eric Brunner, Erin McKay, George Andl, Greta Mok, Heying Duan, Hina J. Shah, Ivan Yeung, Jacob Hesterman, Jeanette Libera-Körner, Joe Grudzinski, Johan Blakkisrud, Joshua Scheuermann, Juan Camilo Ocampo Ramos, Julia Brosch-Lenz, Keon Min Kim, Laetitia Imbert, Lara Bonney, Lawrence Hutton, Lorena Sandoval, Lukas Carter, Naoyuki Ukon, Natalie Cole, Nathaly Barbosa, Nuria Carrasco Vela, O Joo Hyun, Paulo Ferreira, Price Jackson, Rachele Danieli, Raquel Barquero, Richard Laforest, Sean McGurk, Seunggyun Ha, Shalini Subramanian, Sophia Wunder, Stéphanie Lamart, Stephen A. Graves, Su Bin Kim, Tay Young Soon, Teresa Pérez, Tiffany Beaumont, Valentina Ferri, Vikram Adhikarla, William Erwin, William Turner, and Yazdan Salimi

KEY POINTS

QUESTION: What is the overall variability in AD estimates in radiopharmaceutical therapy calculated using different methods at different centers?

PERTINENT FINDINGS: Planar imaging protocols resulted in substantially lower estimates of AD and the largest variability when compared with protocols that used SPECT/CT images. Overall variability using serial SPECT/CT as measured by QCD was less than 26% for organs and lesions. The results suggest that standardization of integration and segmentation may further reduce variability.

IMPLICATIONS FOR PATIENT CARE: Standardization of the dosimetry workflow will reduce variability in AD estimates and ultimately improve reliability—essential for dosimetry-based personalization of radiopharmaceutical therapies.

REFERENCES

1. Strosberg J, El-Haddad G, Wolin E, et al. Phase 3 trial of ^{177}Lu-Dotatate for midgut neuroendocrine tumors. *N Engl J Med.* 2017;376:125–135.
2. Sartor O, de Bono J, Chi KN, et al. Lutetium-177-PSMA-617 for metastatic castration-resistant prostate cancer. *N Engl J Med.* 2021;385:1091–1103.
3. Fendler WP, Pabst KM, Kessler L, et al. Safety and efficacy of ^{90}Y-FAPI-46 radioligand therapy in patients with advanced sarcoma and other cancer entities. *Clin Cancer Res.* 2022;28:4346–4353.
4. Fiedler L, Kellner M, Gosewisch A, et al. Evaluation of ^{177}Lu[Lu]-CHX-A′′-DTPA-6A10 Fab as a radioimmunotherapy agent targeting carbonic anhydrase XII. *Nucl Med Biol.* 2018;60:55–62.
5. Pooja D, Gunukula A, Gupta N, Adams DJ, Kulhari H. Bombesin receptors as potential targets for anticancer drug delivery and imaging. *Int J Biochem Cell Biol.* 2019;114:105567.
6. Wickstroem K, Karlsson J, Ellingsen C, et al. Synergistic effect of a HER2 targeted thorium-227 conjugate in combination with olaparib in a BRCA2 deficient xenograft model. *Pharmaceuticals (Basel).* 2019;12:155.
7. Grob NM, Schibli R, Béhé M, Mindt TL. Improved tumor-targeting with peptidomimetic analogs of minigastrin ^{177}Lu-PP-F11N. *Cancers (Basel).* 2021;13:2629.
8. Ilhan H, Gosewisch A, Böning G, et al. Response to ^{225}Ac-PSMA-I&T after failure of long-term ^{177}Lu-PSMA RLT in mCRPC. *Eur J Nucl Med Mol Imaging.* 2021; 48:1262–1263.
9. Kratochwil C, Bruchertseifer F, Rathke H, et al. Targeted α-therapy of metastatic castration-resistant prostate cancer with ^{225}Ac-PSMA-617: swimmer-plot analysis suggests efficacy regarding duration of tumor control. *J Nucl Med.* 2018;59:795–802.
10. Danieli R, Milano A, Gallo S, et al. Personalized dosimetry in targeted radiation therapy: a look to methods, tools and critical aspects. *J Pers Med.* 2022;12:205.
11. Garin E, Tselikas L, Guiu B, et al. Personalised versus standard dosimetry approach of selective internal radiation therapy in patients with locally advanced hepatocellular carcinoma (DOSISPHERE-01): a randomised, multicentre, open-label phase 2 trial. *Lancet Gastroenterol Hepatol.* 2021;6:17–29.
12. Dewaraja YK, Frey EC, Sgouros G, et al. MIRD pamphlet no. 23: quantitative SPECT for patient-specific 3-dimensional dosimetry in internal radionuclide therapy. *J Nucl Med.* 2012;53:1310–1325.
13. Capala J, Graves SA, Scott A, et al. Dosimetry for radiopharmaceutical therapy: current practices and commercial resources. *J Nucl Med.* 2021;62(suppl 3):3S–11S.
14. Mora-Ramirez E, Santoro L, Cassol E, et al. Comparison of commercial dosimetric software platforms in patients treated with ^{177}Lu-DOTATATE for peptide receptor radionuclide therapy. *Med Phys.* 2020;47:4602–4615.
15. Uribe C, Peterson A, Van B, et al. An international study of factors affecting variability of dosimetry calculations, part 1: design and early results of the SNMMI dosimetry challenge. *J Nucl Med.* 2021;62(suppl 3):36S–47S.
16. Dewaraja YK, Mirando DM, Peterson A, et al. A pipeline for automated voxel dosimetry: application in patients with multi-SPECT/CT imaging following ^{177}Lu peptide receptor radionuclide therapy. *J Nucl Med.* 2022;63:1665–1672.
17. Dewaraja YK, Van BJ. Lu-177 DOTATATE anonymized patient datasets: pre-therapy diagnostic images. Deep Blue Data website. https://doi.org/10.7302/vqmy-g059. Published February 10, 2021. Modified November 18, 2022. Accessed March 15, 2023.
18. Dewaraja YK, Van BJ. Lu-177 DOTATATE anonymized patient datasets: multi-time point Lu-177 planar whole body scans. Deep Blue Data website. https://doi.org/10.7302/y4xd-s758. Published February 10, 2021. Modified November 18, 2022. Accessed March 15, 2023
19. Dewaraja YK, Van BJ. Lu-177 DOTATATE anonymized patient datasets: multi-time point Lu-177 SPECT/CT scans. Deep Blue Data website. https://doi.org/107302/0n8e-rz46. Published February 10, 2021. Modified November 18, 2022. Accessed March 15, 2023.
20. Dewaraja YK, Van BJ. Lu-177 DOTATATE anonymized patient datasets: lesion and organ volumes of interest. Deep Blue Data website. https://doi.org/10.7302/vhrh-qg23. Published May 19, 2021. Modified November 17, 2022. Accessed March 15, 2023.
21. Dewaraja YK, Van BJ. Lu-177 DOTATATE anonymized patient datasets: Lu-177 SPECT time integrated activity maps. Deep Blue Data website. https://doi.org/10.7302/9nct-bk44. Published August 23, 2021. Modified November 18, 2022. Accessed March 15, 2023.
22. He B, Du Y, Song X, Segars WP, Frey EC. A Monte Carlo and physical phantom evaluation of quantitative In-111 SPECT. *Phys Med Biol.* 2005;50: 4169–4185.
23. He B, Frey EC. Comparison of conventional, model-based quantitative planar, and quantitative SPECT image processing methods for organ activity estimation using In-111 agents. *Phys Med Biol.* 2006;51:3967–3981.
24. He B, Wahl RL, Du Y, et al. Comparison of residence time estimation methods for radioimmunotherapy dosimetry and treatment planning: Monte Carlo simulation studies. *IEEE Trans Med Imaging.* 2008;27:521–530.
25. Belli ML, Mezzenga E, Di Iorio V, et al. A whole body dosimetry protocol for peptide-receptor radionuclide therapy (PRRT): 2D planar image and hybrid 2D+3D SPECT/CT image methods. *J Vis Exp.* 2020;158:e60477.
26. Garkavij M, Nickel M, Sjögreen-Gleisner K, et al. ^{177}Lu-[DOTA^0,Tyr^3] octreotate therapy in patients with disseminated neuroendocrine tumors: analysis of dosimetry with impact on future therapeutic strategy. *Cancer.* 2010;116:1084–1092.
27. Dieudonné A, Hobbs RF, Lebtahi R, et al. Study of the impact of tissue density heterogeneities on 3-dimensional abdominal dosimetry: comparison between dose kernel convolution and direct Monte Carlo methods. *J Nucl Med.* 2013;54: 236–243.
28. Brosch-Lenz J, Uribe C, Gosewisch A, et al. Influence of dosimetry method on bone lesion absorbed dose estimates in PSMA therapy: application to mCRPC patients receiving Lu-177-PSMA-I&T. *EJNMMI Phys.* 2021;8:26.

29. Grimes J, Celler A. Comparison of internal dose estimates obtained using organ-level, voxel S value, and Monte Carlo techniques. *Med Phys.* 2014;41:092501.
30. Brosch-Lenz J, Rahmim A, Sunderland J, Frey E, Dewaraja YK, Uribe C. Impact of dosimetry method on healthy organ and tumor absorbed dose estimates for lutetium-177-DOTATATE therapy of neuroendocrine tumors. *Eur J Nucl Med Mol Imaging.* 2022;49(suppl 1):S393–S394.
31. Howell RW, Wessels BW, Loevinger R, et al. The MIRD perspective 1999: medical internal radiation dose committee. *J Nucl Med.* 1999;40:3S–10S.
32. Lassmann M, Chiesa C, Flux G, Bardiès M; EANM Dosimetry Committee. EANM Dosimetry Committee guidance document: good practice of clinical dosimetry reporting. *Eur J Nucl Med Mol Imaging.* 2011;38:192–200.
33. Sgouros G, Bolch WE, Chiti A, et al. ICRU REPORT 96, dosimetry-guided radiopharmaceutical therapy. *J ICRU.* 2021;21:1–212.
34. Bolch WE, Eckerman KF, Sgouros G, Thomas SR. MIRD pamphlet no. 21: a generalized schema for radiopharmaceutical dosimetry—standardization of nomenclature. *J Nucl Med.* 2009;50:477–484.

MIRD Pamphlet No. 28, Part 1: MIRDcalc—A Software Tool for Medical Internal Radiation Dosimetry

Adam L. Kesner[1], Lukas M. Carter[1], Juan C. Ocampo Ramos[1], Daniel Lafontaine[1], Edmond A. Olguin[2], Justin L. Brown[3], Bonnie President[3], Derek W. Jokisch[4,5], Darrell R. Fisher[6], and Wesley E. Bolch[3]

[1]*Department of Medical Physics, Memorial Sloan Kettering Cancer Center, New York, New York;* [2]*Beth Israel Deaconess Medical Center, Department of Radiology, Harvard Medical School, Boston, Massachusetts;* [3]*J. Crayton Pruitt Department of Biomedical Engineering, University of Florida, Gainesville, Florida;* [4]*Department of Physics and Engineering, Francis Marion University, Florence, South Carolina;* [5]*Center for Radiation Protection Knowledge, Oak Ridge National Laboratory, Oak Ridge, Tennessee; and* [6]*University of Washington and Versant Medical Physics and Radiation Safety, Richland, Washington*

Medical internal radiation dosimetry constitutes a fundamental aspect of diagnosis, treatment, optimization, and safety in nuclear medicine. The MIRD committee of the Society of Nuclear Medicine and Medical Imaging developed a new computational tool to support organ-level and suborgan tissue dosimetry (MIRDcalc, version 1). Based on a standard Excel spreadsheet platform, MIRDcalc provides enhanced capabilities to facilitate radiopharmaceutical internal dosimetry. This new computational tool implements the well-established MIRD schema for internal dosimetry. The spreadsheet incorporates a significantly enhanced database comprising details for 333 radionuclides, 12 phantom reference models (International Commission on Radiological Protection), 81 source regions, and 48 target regions, along with the ability to interpolate between models for patient-specific dosimetry. The software also includes sphere models of various composition for tumor dosimetry. MIRDcalc offers several noteworthy features for organ-level dosimetry, including modeling of blood source regions and dynamic source regions defined by user input, integration of tumor tissues, error propagation, quality control checks, batch processing, and report-preparation capabilities. MIRDcalc implements an immediate, easy-to-use single-screen interface. The MIRDcalc software is available for free download (www.mirdsoft.org) and has been approved by the Society of Nuclear Medicine and Molecular Imaging.

Key Words: dosimetry; radiobiology; radionuclide therapy; research methods; dosimetry; MIRD; software

J Nucl Med 2023; 64:1117–1124
DOI: 10.2967/jnumed.122.264225

Methods for radiopharmaceutical dosimetry, that is, estimation of absorbed radiation dose, have evolved gradually since the 1950s. Accurate dose assessment requires an accounting of both the spatial and temporal pharmacokinetics of an administered radiopharmaceutical. This characterization defines the biodistribution of a radiopharmaceutical which is used to estimate absorbed dose to the patient. Measurement-based data may be obtained from clinical quantitative imaging (*1*). The MIRD schema and supporting software represent the standard method for calculating absorbed radiation doses resulting from given biodistributions of administered radiopharmaceuticals (*2*).

Medical internal radionuclide dosimetry comes with unique challenges; clinicians rely on supporting software and user expertise to make dose calculations timely and practical. Existing software tools vary significantly in design and function and are typically based on different models and assumptions. These tools vary in complexity, ranging from simple lookup tables (*3*) to computationally intensive Monte Carlo–based radiation transport models (*4*).

Dosimetry can be performed at different scales, including at the whole-body, organ, suborgan, voxel, and cellular levels. Organ-level dosimetry may stand out in one respect because it provides a balance of relatively personalized dosimetry that can be derived with practical methods based on quantitative PET and SPECT imaging. Calculating absorbed dose to specific organs and tissues allows one to contextualize the dosimetry against known, commonly accepted organ-specific dosimetric thresholds for tissue reactions (*5*).

Organ-level dosimetry software has been used in the field for many years. For example, the OLINDA/EXM software (*6*) based on MIRDOSE (developed in the mid-1980s), demonstrated to the nuclear medicine community the utility of software tools for implementing a standardized dosimetry schema. Other organ-level dosimetry software tools include IDAC-Dose 2.1, which is freely available and is used internally within International Commission on Radiological Protection (ICRP) task group 36 on radiopharmaceuticals (*7*). A companion article is provided which compares dose calculations using the different available software (*8*). Other software tools extend dosimetric analysis beyond the organ level, including voxel Monte Carlo, kernel convolution, cellular-level, and microdosimetric (*9–12*) applications. Across the variety of tools, no solution is demonstrably superior across all use cases (*13*). A contemporary summary of dosimetry software options can be found in chapter 6 of MIRD primer 2022 (*14*).

The dose calculations provided in MIRDcalc software are based on the well-established MIRD schema and other methods needed for calculating absorbed radiation doses (*2*). Thus, MIRDcalc was inspired by MIRDOSE and OLINDA/EXM, with attention to their generalizable suitability and practical application. MIRDcalc uses the organ-level dosimetry paradigm as the starting point from which to innovate, exemplified with new features that include error propagation and dynamic source regions. MIRDcalc itself is not a complete package for absorbed dose calculation workflows. It is a robust tool to support the computational aspect of a dosimetry

Received Apr. 4, 2022; revision accepted Mar. 21, 2023.
For correspondence or reprints, contact Adam L. Kesner (kesnera@mskcc.org).
Published online Jun. 2, 2023.

protocol, given an input of time-integrated activity coefficients (TIACs) of the radiopharmaceutical in organs and tissues and specification of a pertinent anatomic model.

The MIRDcalc software project was undertaken to meet the needs of the community for validated, open-source, flexible, and freely accessible dosimetry tools. MIRDcalc is immediately available to physicists, biomedical researchers, and health-care colleagues worldwide, reducing the time required for, and variability of, dosimetry-related computations. The MIRDcalc project also provides a framework for further development and community cooperation and collaboration.

MIRDCALC SOFTWARE

Organ-Level Dosimetry

The MIRD schema for absorbed dose calculation was originally formulated in the 1960s (*2,15*) as the computational basis for performing dosimetry with models of representative organ geometry, presented in the form of stylized anthropomorphic digital phantoms. The main equations and standardized nomenclature are described in MIRD pamphlet 21 (*16*) and MIRD primer 2022 (*11*).

The MIRD framework allows for the logical separation of tasks in the process of calculating absorbed dose. Computationally intensive processing can be performed a priori to establish reference individual- and radiopharmaceutical-specific dose calculation models, which may later be used with subject-specific biodistributions to provide individualized absorbed dose estimates.

The parameters that characterize the dosimetry model are called S values, which quantitatively relate the mean absorbed dose rate to a target organ (or region) per unit of activity in a given source organ (or region). When a user inputs a time-integrated activity distribution, S values stored within the software, based on an anthropomorphic model, are used to quickly estimate radiation doses using the standard MIRD equations (given in the companion article (*8*)). MIRDcalc provides the models, S values, and interface for performing the absorbed dose calculations.

Absorbed dose estimates calculated in this manner have a limitation because they are usually based on anatomic models of reference individuals (phantoms) of specified sex and age. Models may be extrapolated to represent specific patients. Reference S values account for all dosimetrically relevant anatomy, including regions with complex microstructure (such as bone marrow). MIRDcalc uses a well-established methodology for scaling reference S values for patient-mass–specific absorbed dose calculations (*17*). MIRDcalc also offers a unique feature to support global scaling of all regions between reference phantoms, on the basis of total-body mass.

Development of Radionuclide S Values

The radionuclide S values within the MIRDcalc program were developed according the MIRD schema. The S-value components for the photon, electron/positron, α-particle, and α-recoil components of the radionuclide decay scheme were computed as …

$$S(r_T \leftarrow r_S) = \sum_i E_i \; Y_i \; \Phi(r_T \leftarrow r_S, \; E_i), \qquad \text{Eq. 1}$$

where $\Phi(r_T \leftarrow r_S, \; E_i)$ is the specific absorbed fraction (SAF) for radiation particle i emitted in source region r_S and irradiating target region r_T, whereas E_i and Y_i are, respectively, the energies and yields of radiation emitted during radionuclide decay as taken from the MIRD monograph on radionuclide data and decay schemes (*18*).

The full energy spectrum for both β-particles and positrons was used in lieu of considering only their mean energies. The β-particle component of the S value was computed as

$$S(r_T \leftarrow r_S)_\beta = \int_0^{E_0} P(E) \; E \; \Phi(r_T \leftarrow r_S, \; E) \; dE, \qquad \text{Eq. 2}$$

where E is the energy of emission, ranging from zero to endpoint energy E_0, and $P(E)$ and $\Phi(r_T \leftarrow r_S, E)$ are, respectively, the energy-dependent yield and SAF.

All S values were computed using a Python script with SAF interpolation through particle energies using piecewise cubic Hermite interpolation polynomials. For α-recoils, the SAF values were interpolated at a 2-MeV α-particle, an approach previously adopted by the ICRP (*19*). S values for members of α-emitter decay chains were computed and reported independently for the parent radionuclide and all individual progeny.

For the ICRP reference adult phantoms within MIRDcalc, ICRP publication 133 (*19*) was used as the source of all SAF values in the computation of S values. These 2 phantoms—reference adult male and reference adult female—are fully described in ICRP publication 110 (*20*). For the pediatric reference phantoms, as described in ICRP publication 143 (*21*), SAF values for photons and electrons were taken primarily from the work presented by Schwarz et al. (*22,23*) with subsequent adjustments for source region blood content when $r_T = r_S$. SAF values that were not fully covered in the 2 articles by Schwarz et al., including SAFs for α-particles, SAFs for localized regions in the respiratory and alimentary tracts, and SAFs for intraskeletal sources and targets, were taken from transport studies conducted by ICRP task group 96, which are fully described in a forthcoming ICRP publication (*24*).

Platform

The platform of our software is Microsoft Excel, with additional interface features supported with Visual Basic coding, and is compiled as an executable application for Microsoft Windows operating systems. Advances in Excel over the last decade, including the PowerPivot tools, have made this project possible. The PowerPivot tools allow seamless integration of large reference datasets, such as the reference individual-specific S values, into MIRDcalc. The Excel platform has several advantages over traditional compiled code: the software is familiar, accessible, and easy to install; the platform is highly developed for broad use across industries and supports easy integration of complex computational and visual functions; the tools can be built to fit on an intuitive, user-friendly single-screen interface (Fig. 1); the interface responds instantly to user interaction; the software includes visual graphics that check data integrity, conditional formatting, and selective cell protection; inputs and outputs are inherently formatted for easy access and integration; and the calculations are easy to access for educational purposes and for quality control with transparency. The only part of the code that will not be available to users is the Visual Basic patches, but this portion of the code provides support only for executable protection and input and output functionality.

User Manual

MIRDcalc comes with a comprehensive user manual in searchable portable document file format, available within the software and online (https://mirdsoft.org/mirdcalc). The manual covers all relevant elements of software use, including the topics presented in this article. The manual also provides background theory to

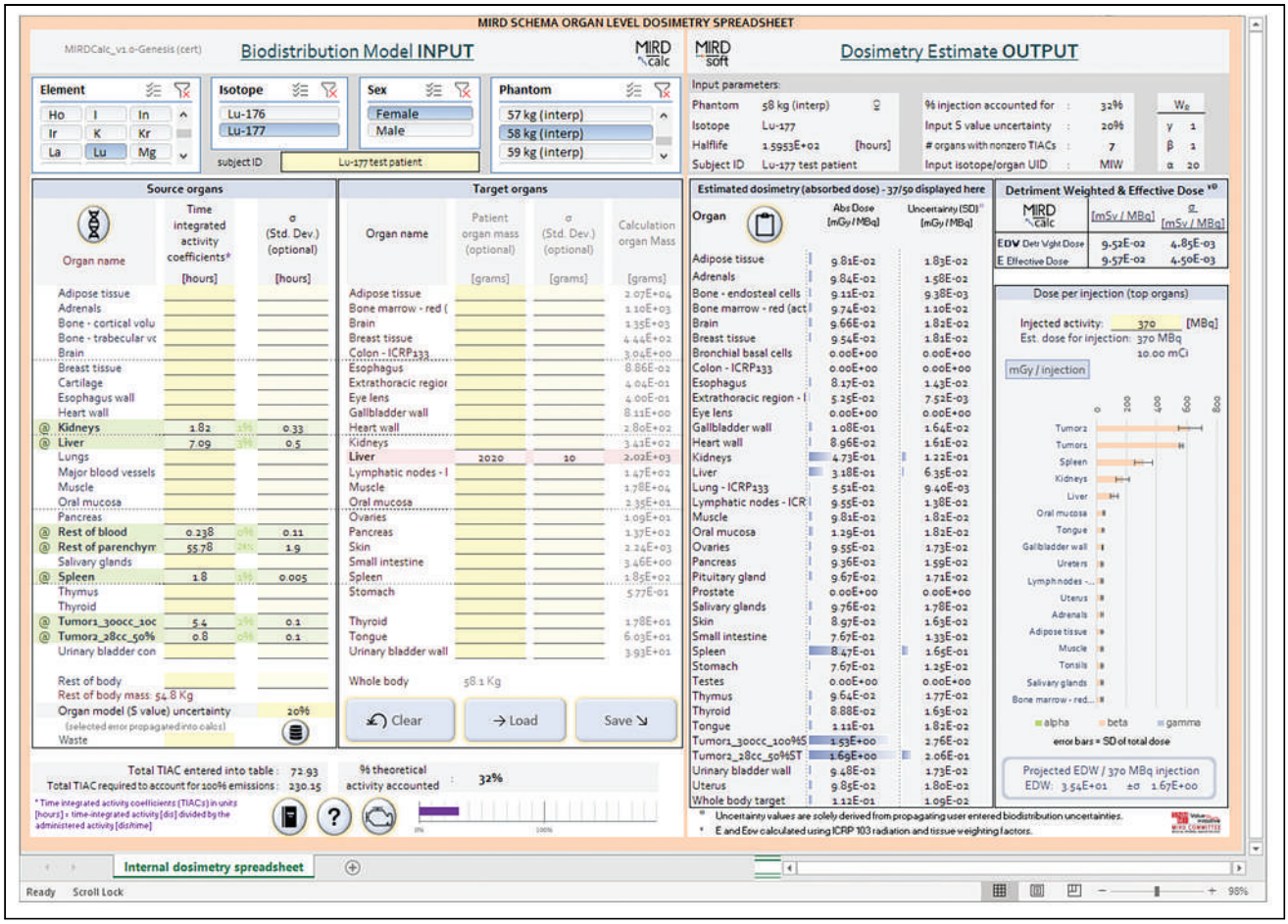

FIGURE 1. Screenshot of MIRDcalc software.

help users understand basic concepts of radiopharmaceutical internal dosimetry.

Classic Use

Analogous to other software, MIRDcalc allows users to select a radionuclide and reference patient model and enter the TIACs that characterize the radiopharmaceutical biodistribution in a subject. Given this input information, an organ-level dosimetry report is generated on-screen and may be copied to the clipboard or exported. An example classic absorbed dose calculation is provided in Supplement A (supplemental materials are available at http://jnm.snmjournals.org) (*25–30*).

Software Validation

MIRDcalc version 1.0 was beta tested and validated by benchmarking against published references (*8*). The results of MIRDcalc were compared with reference values in ICRP publication 128 (*3*) using biokinetic data for 71 radiopharmaceuticals. Absorbed dose coefficients estimated with MIRDcalc were systematically compared against dose coefficients derived using other software; the absorbed dose coefficients are the dose quantity per organ or tissue that, when multiplied by administered activity, provide the organ or tissue dose estimates. The dosimetry computed with MIRDcalc agreed closely with results from another dosimetry software implementing the ICRP publication 133 reference adult SAFs, IDAC-Dose 2 (*19*), and showed partial agreement with dose coefficients derived using stylized or hybrid phantoms with reference masses derived from ICRP publication 89 (*31*) in OLINDA/EXM version 2.0 (*32*).

A comparison of different organ-level dosimetry software calculations, derived using a standard ^{18}F-FDG biodistribution published in ICRP publication 128, calculated for an adult male anthropomorphic model, is presented in Fig 2. The figure illustrates general concordance between organ-absorbed doses and the effective dose calculations across different software platforms. It also demonstrates a certain degree of variability in dose calculations in reported relevant organs, largely within 20%. Systematic differences are also seen in the bladder wall dose, and an analysis of this issue is presented in the Design Considerations section below.

Innovative Features

Single-Screen Interface. MIRDcalc provides full absorbed dose calculation tools on a single-screen interface, facilitating usability, inspection, and interpretation of results (Fig. 1).

Free Distribution. MIRDcalc is freely downloadable from the MIRDsoft.org website, together with other dosimetry-related tools developed within the MIRDsoft initiative.

Quality Control Graphics: Real-Time Dose Calculations. MIRDcalc provides useful quality control and safety check metrics

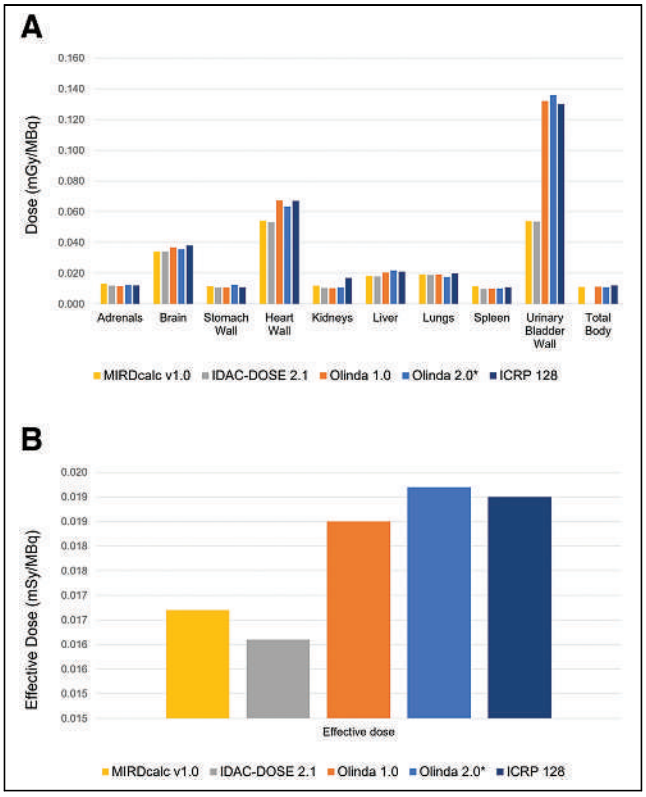

FIGURE 2. Comparison of different organ-level dosimetry software calculations for typical ^{18}F-FDG case, calculated for adult male anthropomorphic model. (A) Absorbed dose calculations for various organs. (B) Effective dose presented by different software.

and graphics to protect against user error. These include checks on activity accounted for and ability to account for activity excreted and eliminated. MIRDcalc also displays a unique isotope/input organ identification code.

Fully Accessible Calculations (Open Source). Dose calculations are performed within an accessible spreadsheet that permits a user to review all math operations. Users may edit and change values in designated input cells, whereas the other portions of the interface are locked to prevent code corruption.

Comprehensive Case Documentation. Subject dose calculations may be saved in a comma-separated-value file format to document output results, as well as input parameters and phantom S values.

Uncertainty Propagation. MIRDcalc propagates estimated uncertainty values of radiopharmaceutical biodistribution parameters and organ masses to calculate an associated uncertainty for calculated absorbed doses. Users may optionally enter custom uncertainties for TIACs or organ masses. Users may also select a global S-value uncertainty (coefficient of variation), which is propagated to all calculations that are derived from the S values; this feature may ideally be used to insert a global uncertainty that provides a general accounting of the expected mismatch between anthropomorphic reference models and any given patient geometry. The uncertainties entered are propagated through all TIAC-to-dose calculations using the Joint Committee for Guides in Metrology *Guide to the Expression of Uncertainty in Measurement* (*33*) generalized schema for propagating uncertainties. To propagate the error of parameters when these are added or subtracted ($f(A,B) = \mathrm{aA} \pm \mathrm{bB}$) or multiplied or divided ($f(A,B) = AB$ or $f(A,B) = A/B$) in the dosimetry calculations, Equations 3 and 4 are used (assuming only 2 variables are combined in the operation), respectively.

$$\sigma_f = \sqrt{a^2\sigma_A^2 + b^2\sigma_B^2 + 2ab\sigma_{AB}}, \quad \text{Eq. 3}$$

$$\sigma_f = f(A,B) \times \left(\sqrt{\left(\frac{\sigma_A}{A}\right)^2 + \left(\frac{\sigma_B}{B}\right)^2 + 2\frac{\sigma_{AB}}{2AB}}\right), \quad \text{Eq. 4}$$

where A and B are real variables, with SDs σ_A and σ_B, respectively; σ_{AB} is covariance. Both Equations 3 and 4 include a covariance term at the end. In the context of dosimetry, this term is complex and derived from many physical and biologic variables. To provide a generally applicable and implementable tool, MIRDcalc assumes that the covariance of all variables in the dosimetry calculations is zero, with justification from *Guide to the Expression of Uncertainty in Measurement* clause F.1.2.1.c (*33*). Thus, the propagation of error equations implemented in all but one situation in MIRDcalc are shown in Equations 5 and 6.

$$\sigma_f = \sqrt{a^2\sigma_A^2 + b^2\sigma_B^2}, \quad \text{Eq. 5}$$

$$\sigma_f = f(A,B) \times \left(\sqrt{\left(\frac{\sigma_A}{A}\right)^2 + \left(\frac{\sigma_B}{B}\right)^2}\right). \quad \text{Eq. 6}$$

Zero covariance, however, is not assumed in uncertainty calculation for effective dose, which includes male and female dose averaging. In this instance, the covariance between male and female doses is set to be 1, as the two are highly correlated. For users interested in performing more complex error propagation calculations, MIRDcalc outputs all data required for in-house calculations in the standard MIRDcalc output files.

Incorporating uncertainty propagation into dosimetry calculations remains a relatively new concept for the field of internal dosimetry (*34*). The community has yet to reach consensus and develop standards for how to properly use this information. MIRDcalc includes this feature to promote the development of a standard for error integration in the field. However, all uncertainty estimates presented by MIRDcalc are based on the above-mentioned covariance assumptions and are entirely dependent on uncertainty values provided by the user. Reported uncertainty values of the outputs are therefore only as accurate as the user's data and assumptions.

Mass Accounting with New Source and Target Regions. MIRDcalc accounts for the complete subject using published values for reference man and woman (*19,20*) and pediatric phantoms (*21*). Two additional source regions were added: heart contents and major blood vessels. A detailed accounting of tissue masses can be found in Supplement B to this article.

Users are also given access to new suborgan combination target regions, which aggregate dose to subregions defined in ICRP publication 133: colon, extrathoracic region, lung, lymphatic nodes, and whole-body target. A description of these regions can be found in the original reference from the ICRP (*19*) and the MIRDcalc user manual.

Dynamic Source Regions. MIRDcalc introduces 3 dynamic source regions: rest of body, rest of blood, and rest of parenchyma. This option allows users to assign TIAC values across entire body tissues.

TIACs entered into the "rest-of" regions are distributed among unaccounted-for organs and tissues, weighted by mass. Unaccounted-for source regions are defined as the nonoverlapping source regions for which the user has not explicitly assigned a coefficient. The rest-of regions are dynamic; as the user assigns TIACs to static source organs, the total mass of the rest-of regions adjusts accordingly.

This strategy is modeled after the additive approach described by the ICRP for handling other tissues as presented in ICRP publication 133, Equation 2.10 (*19*). MIRDcalc distributes the dynamic TIAC into nonassigned organs rather than updating SAFs.

The explicit makeup of the subregions that comprise the MIRDcalc-defined rest-of regions are presented in the MIRDcalc user manual.

Blood Source Model. Modeling blood separate from soft tissues and bone can be difficult but important since the biokinetics of blood are different from the biokinetics of tissue-bound activity. Although other dosimetry approaches assume parenchyma and blood within each organ as a single region, MIRDcalc offers the option to treat the different biokinetics separately. Coefficients entered for the source regions may be associated with either the combined blood and parenchyma in each source region (accommodating imaging-derived input) or parenchyma only to accommodate pharmacokinetic models that address tissue parenchyma and total-body blood separately. MIRDcalc keeps track of the separate blood and parenchyma masses accounted for in the regions of user-entered TIACs and removes them from the rest-of-body, rest-of-blood, and rest-of-parenchyma input terms as appropriate. These rest-of terms can then be used to distribute radionuclides into unaccounted-for tissues.

Coefficients associated with the blood may be assigned to organ regions (defining blood and parenchyma), blood regions (heart content and major blood vessels), rest-of-body source region (distributes to all unaccounted-for blood and soft and hard tissues), and separate rest-of-blood and rest-of-parenchyma source regions (which separately distribute TIACs to the blood and parenchyma, respectively).

The blood source region models provided in MIRDcalc are depicted in Figure 3. The choice of regions to use depends on the user's activity measurement methods and assumptions. For example, if a user defines the remainder (or unaccounted-for activity) from imaging, a background measurement derived from a background region or volume of interest measured from images may be used for the rest of body TIAC, accounting for both remainder blood and remainder parenchyma. Alternatively, if blood activity measurements are available from specimens or blood pool imaging, the input values may be entered for separate blood and parenchyma inputs.

Integrated Spheric Tumor Dosimetry. MIRDcalc supports simplistic tumor dosimetry by calculating the self-dose that a sphere receives from uniformly incorporated activity. MIRDcalc allows selection of sphere volume, volume uncertainty, tissue composition (bone/soft-tissue mixture), radionuclide, TIAC, and TIAC uncertainty. These dose calculations are based on S values provided by Olguin et al. (*35*). MIRDcalc implementation utilizes S-value interpolation or extrapolation of published data points for user-specified volumes. Interpolation and extrapolation are accomplished via log–log interpolation between the 2 nearest sampling points. Propagation of uncertainty in tumor dosimetry is estimated from the inherent uncertainty of the tissue volume and coefficient values, as described in Equation 67 of Gear et al. (*34*).

MIRDcalc tumor dosimetry is performed independently from organ dosimetry. Only tumor self-dose is provided; cross-organ contributions from all other source regions are not included in the tumor dose calculation.

Command Line and Batch Processing. MIRDcalc supports 2 methods of running absorbed dose calculations: via the user interface or via spool processing. The batch-processing feature allows MIRDcalc dose calculations to run without an interface or user interaction and supports batch processing of population data.

Organ Mass Interpolation. It is recognized that organ masses from specific subjects may not match those from the standard phantoms, causing an error in organ dose estimation. A first-order approximation for correcting these differences was presented in MIRD pamphlet 11 and is implemented in MIRDcalc (*36*). Specifically, it was recommended that the impact of differences in nonreference organ sizes can be accounted for through scaling the self-dose by the ratio of the organ masses to a constant power. The value of the power was set to $-2/3$ for photon self-dose scaling and -1 for electron and α-self-dose scaling. Estimations of cross-dose contributions are unchanged when using user-modified organ masses.

The option to add associated uncertainty to the user-modified mass is also available. This will impact only mass scaling calculations and therefore are relevant only for organs that have had their mass changed.

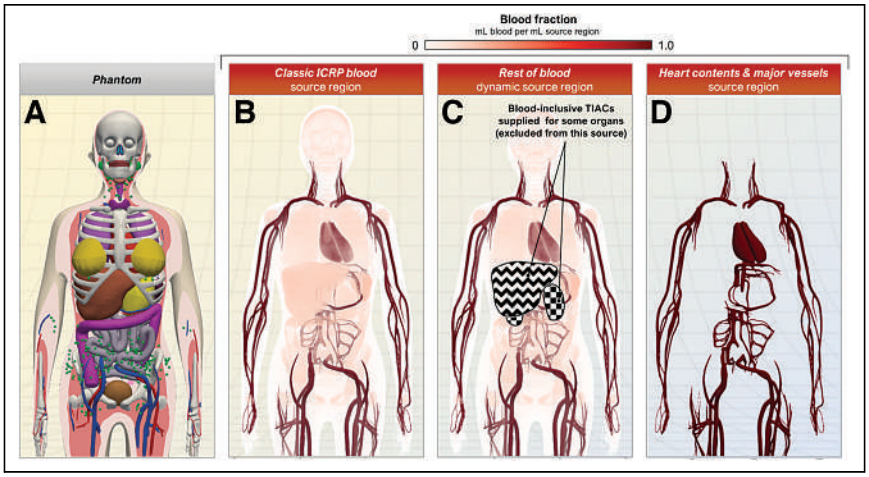

FIGURE 3. MIRDcalc blood source options support different strategies for defining source region TIACs. (A) Example phantom (ICRP 15-y-old female) shown for anatomic reference. (B) Classic ICRP blood source region accounts for entire volume of blood in phantom and spatially overlaps with volumes of blood-perfused source regions. (C) Rest-of-blood source region accounts for total remaining blood after input of blood-inclusive TIACs into various organs. (D) Heart contents and major vessel source regions do not overlap with parenchyma of any source regions.

Whole-Phantom Mass Interpolation. The user may select among multiple phantom models for dose calculations; these include the ICRP phantom series (newborn, 1-y-old, 5-y-old, 10-y-old, 15-y-old, and adult male and female) (*20,21*). In addition, the user may select a phantom model based on weight. A representation of the MIRDcalc phantom library is shown in Figure 4. Selection of a weight-based phantom will load a linearly interpolated mass phantom model from the 2 closest-by-mass phantoms in the ICRP reference series. Reference region masses are scaled linearly, and S values are interpolated with log–log scaling, relative to the user-selected phantom mass (identified by the phantom name) and the 2 closest ICRP reference individuals.

ICRP Publication 128 Case Library. The ICRP published reference biokinetic data in the form of TIACs for radiopharmaceuticals (ICRP publication 128) (*3*).

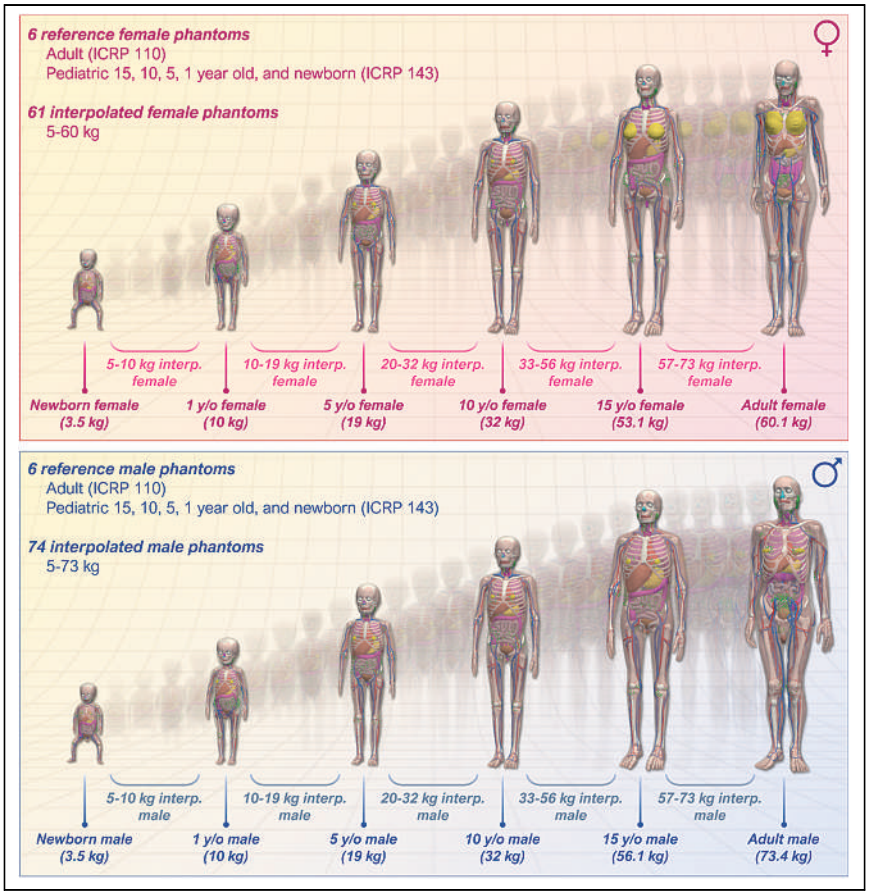

FIGURE 4. Visualization of MIRDcalc phantom library, including 12 ICRP reference phantoms (publications 110 and 143), and graphical representation of MIRDcalc interpolation feature.

These reference coefficients were incorporated into MIRDcalc case library, formatted for direct import. Processing of these files is performed using the batch-processing capability and is the basis of the comparisons reported in the companion validation article (*8*).

Effective Dose, Detriment-Weighted Dose, and Risk Index. In addition to absorbed doses, MIRDcalc also calculates the detriment-weighted dose and effective dose (*19,37*). Effective dose is a risk-related weighted construct based on organ doses. It is calculated using radiation-weighting factors and tissue-weighting factors described in ICRP publication 103 (*38*). Effective dose is specific to the ICRP reference individuals and is averaged over both male and female phantoms.

The detriment-weighted dose is also a risk-related weighted sum of organ-absorbed doses calculated using radiation-weighting factors and tissue-weighting factors described in ICRP publication 103 (*38*). Detriment-weighted dose is calculated similarly to effective dose but is specific to the phantom model used for dose calculations (single sex, potentially modified organ masses) (*37*).

MIRDcalc calculates a risk index, a ratio of the estimated added risk of cancer from specific radiation exposure relative to the estimated natural risk of cancer according to a concept known as lifetime attributable risk of cancer (National Cancer Institute's Radiation Risk Assessment Tool (*39*)). The baseline natural incidence of cancer in a population with an absence of radiation exposure was derived from the Surveillance, Epidemiology, and End Results database (*40*) as defined in the Radiation Risk Assessment Tool. The risk index was recently introduced in the literature (*41,42*). The intent behind the concept of risk index was to provide an alternative to effective dose for risk assessment. However, the validity and applicability of this quantity is limited by its dependence on the linear no-threshold model, a radiation dose risk model whose applicability at low radiation doses continues to be questioned (*43,44*). It also ignores the potential benefit that a diagnostic or therapeutic radiopharmaceutical may have.

DESIGN CONSIDERATIONS

The specialty of internal dosimetry is evolving, and the number of software tools has increased. Software packages provide different results and should therefore be compared and scrutinized. For the organ-level dosimetry tools, most discrepancies come from the differences in phantom models; MIRDcalc uses the ICRP publication 133 reference adult series and SAFs based on the ICRP publication 143 pediatric phantoms (Fig. 3) (*21*) and MIRD decay schemes (*18*), whereas OLINDA/EXM version 2.0 uses RADAR phantoms (*45,46*).

In comparing the similar dosimetry software packages, we can take note some differences. First, calculated absorbed doses to the urinary bladder were factors of 2–3 times higher in ICRP publication 128 than in MIRDcalc because of advances in the stylized dosimetry model used to compute absorbed fractions of energy deposited in the bladder wall from emissions in the urinary bladder contents (*47,48*). Next, MIRDcalc spheric tumor β-dosimetry was modeled using the entire β-energy spectrum, rather than the mean β-emission energy. Finally, the skeletal target (endosteum) was redefined in ICRP publication 110, enlarged to a thickness of 50 μm from 10 μm (*49*). This change produced significant differences, relative to other organs, for calculated SAFs and S values for charged particles emitted within skeletal tissues (*19,50*).

The MIRDcalc software and the MIRDsoft.org webspace provide platforms for continued expansion and evolution of community dosimetry software tools. Future improvements will include new utilities for curve fitting, pregnant phantom/fetus dosimetry, and suborgan dosimetry. We can also expect to see an analogous CT dosimetry software, MIRDct, to be released shortly. These additions will complement the already-released MIRDcell software, which performs cellular and multicellular dosimetry and bioeffect modeling (*11*)

SUMMARY AND CONCLUSIONS

MIRDcalc represents a new software solution for medical internal radiation dosimetry. The software was developed by the MIRD committee of the Society of Nuclear Medicine and Molecular Imaging to benefit an international user community. MIRDcalc implements the basic MIRD schema, equations, and nuclear databases with molecular imaging data for applications to patient-specific dosimetry and radionuclide therapy planning.

As clinical nuclear medicine evolves with the ability to acquire more detailed quantitative molecular imaging data on radiopharmaceutical uptake, distribution, and biokinetics, the need has intensified for more powerful and more accurate computational tools for calculating radiation dose to organs, suborgan regions, tissues, and tumors. Integration of advanced quantitative imaging data with more flexible and detailed anatomic models, such as those recently developed by the ICRP, necessitated development of software that could make best use of these models. New radionuclide applications also suggested the need for an expanded and updated nuclear emissions database. Although greater complexity may provide additional key features and capabilities, the need remained to provide the user community with a software platform that was readily available, simple to execute, and affordable.

The design of a next-generation computing package necessarily focused first on addressing the technical gaps, weaknesses in, deficiencies with, and elements missing from all other available software platforms. In response to calls for improvements in personalization, standardization, and contextualization of dosimetry calculations, MIRDcalc increases user ability to incorporate custom organ sizes obtained from medical imaging, to interpolate between standard models, and to customize biokinetic modeling to more accurately calculate a full suite of organ and tissue doses. Accordingly, the MIRDcalc developers collaborated closely with the leadership of ICRP Task Group 96, a group which has been responsible for producing anatomically realistic reference voxel phantoms, dosimetric models, and specific absorbed fractions for use in internal dosimetry. Going forward, MIRDcalc will be revised and updated as scientific progress in nuclear medicine physics dose modeling continues.

DISCLOSURE

The MIRDcalc software aids a user in performing dose calculations for a variety of diagnostic and therapeutic isotopes. MIRDcalc is intended for educational and research use only. MIRDcalc has not been approved by the U.S. Food and Drug Administration and is not intended for clinical use or use as a medical device. MIRDcalc and any results generated from its use are not substitutes for medical diagnosis, advice, or treatment of specific medical conditions. A physician should always be consulted for any health problem or medical condition. This research was funded in part through the NIH/NCI Cancer Center support grant P30 CA008748 and NIH U01 EB028234. Lukas Carter acknowledges support from the Ruth L. Kirschstein NRSA postdoctoral fellowship (NIH F32 EB025050). No other potential conflict of interest relevant to this article was reported.

ACKNOWLEDGMENTS

This work was done in collaboration with the Society of Nuclear Medicine and Molecular Imaging MIRD Committee: Vikram Adhikarla, Rachael M. Barbee, Wesley E. Bolch, Yuni K. Dewaraja, William D. Erwin, Darrell R. Fisher, Roger W. Howell, Adam L. Kesner, Richard Laforest, Joseph G. Rajendran, George Sgouros, and Pat B. Zanzonico (chair). We thank Dr. Pat Zanzonico from Memorial Sloan Kettering Cancer Center for providing guidance and support to the MIRDcalc development effort. We thank Dr. Keith Eckerman from Oak Ridge National Laboratory for help in validating the MIRDcalc S values. We thank Dr. Jazmin Schwartz from Memorial Sloan Kettering Cancer Center for providing statistics support.

REFERENCES

1. Siegel JA, Thomas SR, Stubbs JB, et al. MIRD pamphlet no. 16: techniques for quantitative radiopharmaceutical biodistribution data acquisition and analysis for use in human radiation dose estimates. *J Nucl Med.* 1999;40(suppl): 37S–61S.
2. Loevinger R, Budinger TF, Watson EE. *MIRD Primer for Absorbed Dose Calculations.* Society of Nuclear Medicine and Molecular Imaging; 1991.
3. Mattsson S, Johansson L, Svegborn LS, et al. ICRP publication 128: radiation dose to patients from radiopharmaceuticals: a compendium of current information related to frequently used substances. *Ann ICRP.* 2015;44:1–321.
4. Villoing D, Marcatili S, Garcia MP, Bardiès M. Internal dosimetry with the Monte Carlo code GATE: validation using the ICRP/ICRU female reference computational model. *Phys Med Biol.* 2017;62:1885–1904.
5. ICRP publication 41: nonstochastic effects of ionizing radiation. *Ann ICRP.* 1984; 14:1–33.
6. Stabin MG, Sparks RB, Crowe E. OLINDA/EXM: the second-generation personal computer software for internal dose assessment in nuclear medicine. *J Nucl Med.* 2005;46:1023–1027.
7. Andersson M, Johansson L, Eckerman K, Mattsson S. IDAC-Dose 2.1, an internal dosimetry program for diagnostic nuclear medicine based on the ICRP adult reference voxel phantoms. *EJNMMI Res.* 2017;7:88.
8. Carter LM, Ramos JCO, Olguin EA, et al. MIRD pamphlet no. 28, part 2: comparative evaluation of MIRDcalc dosimetry software across a compendium of diagnostic radiopharmaceuticals. *J Nucl Med.* In press.
9. Vergara Gil A, Amato E, Auditore L, et al. OpenDose3D: a free, collaborative 3D Slicer module for patient-specific dosimetry. *Eur J Nucl Med Mol Imaging.* 2020; 47(suppl 1):S314–S315.
10. Capala J, Graves SA, Scott A, et al. Dosimetry for radiopharmaceutical therapy: current practices and commercial resources. *J Nucl Med.* 2021;62(suppl 3): 3S–11S.
11. Katugampola S, Wang J, Rosen A, Howell RW. MIRD pamphlet no. 27: MIRDcell V3, a revised software tool for multicellular dosimetry and bioeffect modeling. *J Nucl Med.* 2022;63:1441–1449.
12. Vaziri B, Wu H, Dhawan AP, Du P, Howell RW. MIRD pamphlet no. 25: MIRDcell V2.0 software tool for dosimetric analysis of biologic response of multicellular populations. *J Nucl Med.* 2014;55:1557–1564.
13. Chiesa C, Bardiès M, Zaidi H. Voxel-based dosimetry is superior to mean absorbed dose approach for establishing dose-effect relationship in targeted radionuclide therapy. *Med Phys.* 2019;46:5403–5406.
14. Bartlett RM, Bolch WE, Brill AB, et al. *MIRD Primer 2022: A Complete Guide to Radiopharmaceutical Dosimetry.* Society of Nuclear Medicine and Molecular Imaging; 2022.
15. Loevinger R. A schema for absorbed-dose calculations for biologically-distributed radionuclides. *J Nucl Med.* 1968;9(suppl 1):9–14.
16. Bolch WE, Eckerman KF, Sgouros G, Thomas SR. MIRD pamphlet no. 21: a generalized schema for radiopharmaceutical dosimetry—standardization of nomenclature. *J Nucl Med.* 2009;50:477–484.
17. Petoussi-Henss N, Bolch WE, Zankl M, Sgouros G, Wessels B. Patient-specific scaling of reference S-values for cross-organ radionuclide S-values: what is appropriate? *Radiat Prot Dosimetry.* 2007;127:192–196.
18. Eckerman KF, Endo A. *MIRD: Radionuclide Data and Decay Schemes.* 2nd ed. Society of Nuclear Medicine and Molecular Imaging; 2008.
19. Bolch WE, Jokisch D, Zankl M, et al. ICRP publication 133: the ICRP computational framework for internal dose assessment for reference adults: specific absorbed fractions. *Ann ICRP.* 2016;45:5–73.
20. Menzel HG, Clement C, DeLuca P. ICRP Publication 110: adult reference computational phantoms. *Ann ICRP.* 2009;39:1–164.
21. Bolch WE, Eckerman K, Endo A, et al. ICRP publication 143: paediatric reference computational phantoms. *Ann ICRP.* 2020;49:5–297.
22. Schwarz BC, Godwin WJ, Wayson MB, et al. Specific absorbed fractions for a revised series of the UF/NCI pediatric reference phantoms: internal photon sources. *Phys Med Biol.* 2021;66:035006.
23. Schwarz BC, Godwin WJ, Wayson MB, et al. Specific absorbed fractions for a revised series of the UF/NCI pediatric reference phantoms: internal electron sources. *Phys Med Biol.* 2021;66:035005.
24. Jokisch DW, Bolch WE, Schwarz BC, et al. Specific absorbed fractions for reference paediatric individuals. *Ann ICRP.* In press.
25. Silberstein EB, Alavi A, Balon HR, et al. The SNMMI practice guideline for therapy of thyroid disease with ^{131}I 3.0. *J Nucl Med.* 2012;53:1633–1651.
26. Hobbs RF, Wahl RL, Lodge MA, et al. ^{124}I PET-based 3D-RD dosimetry for a pediatric thyroid cancer patient: real-time treatment planning and methodologic comparison. *J Nucl Med.* 2009;50:1844–1847.

27. Thierens HM, Monsieurs MA, Bacher K. Patient dosimetry in radionuclide therapy: the whys and the wherefores. *Nucl Med Commun.* 2005;26:593–599.
28. Benua R, Leeper R. A method and rationale for treating metastatic thyroid carcinoma with the largest safe dose of ^{131}I. *Front Thyroidol.* 1986;2:1317–1321.
29. Hänscheid H, Lassmann M, Luster M, et al. Iodine biokinetics and dosimetry in radioiodine therapy of thyroid cancer: procedures and results of a prospective international controlled study of ablation after rhTSH or hormone withdrawal. *J Nucl Med.* 2006;47:648–654.
30. Sgouros G, Song H, Ladenson PW, Wahl RL. Lung toxicity in radioiodine therapy of thyroid carcinoma: development of a dose-rate method and dosimetric implications of the 80-mCi rule. *J Nucl Med.* 2006;47:1977–1984.
31. ICRP publication 89: basic anatomical and physiological data for use in radiological protection: reference values. *Ann ICRP.* 2002;32:5–265.
32. Stabin M, Farmer A. OLINDA/EXM 2.0: the new generation dosimetry modeling code [abstract]. *J Nucl Med.* 2012;53(suppl 1):585.
33. Working Group 1 of the Joint Committee for Guides in Metrology. *Evaluation of Measurement Data: Supplement 2 to the "Guide to the Expression of Uncertainty in Measurement"—Extension to Any Number of Output Quantities.* Bureau International des Poids et Mesures; 2011.
34. Gear JI, Cox MG, Gustafsson J, et al. EANM practical guidance on uncertainty analysis for molecular radiotherapy absorbed dose calculations. *Eur J Nucl Med Mol Imaging.* 2018;45:2456–2474.
35. Olguin E, President B, Ghaly M, Frey E, Sgouros G, Bolch WE. Specific absorbed fractions and radionuclide S-values for tumors of varying size and composition. *Phys Med Biol.* 2020;65:235015.
36. Snyder WS, Ford MR, Warner GG, Watson SB. *MIRD Pamphlet No. 11: "S," Absorbed Dose per Unit Cumulated Activity for Selected Radionuclides and Organs.* Society of Nuclear Medicine and Molecular Imaging; 1975.
37. Kofler C, Domal S, Satoh D, Dewji S, Eckerman K, Bolch WE. Organ and detriment-weighted dose rate coefficients for exposure to radionuclide-contaminated soil considering body morphometries that differ from reference conditions: adults and children. *Radiat Environ Biophys.* 2019;58:477–492.
38. ICRP publication 103: the 2007 recommendations of the International Commission on Radiological Protection. *Ann ICRP.* 2007;37:1–332.
39. Berrington de Gonzalez A, Iulian Apostoaei A, Veiga LH, et al. RadRAT: a radiation risk assessment tool for lifetime cancer risk projection. *J Radiol Prot.* 2012; 32:205–222.
40. SEER Cancer Statistics Review (CSR), 1975–2018. National Cancer Institute website. https://seer.cancer.gov/csr/1975_2018/. Published April 15, 2021. Accessed April 25, 2023.
41. O'Reilly SE, Plyku D, Sgouros G, et al. A risk index for pediatric patients undergoing diagnostic imaging with ^{99m}Tc-dimercaptosuccinic acid that accounts for body habitus. *Phys Med Biol.* 2016;61:2319–2332.
42. Brown JL, Sexton-Stallone B, Li Y, et al. Body morphometry appropriate computational phantoms for dose and risk optimization in pediatric renal imaging with Tc-99m DMSA and Tc-99m MAG3. *Phys Med Biol.* 2020;65:235026.
43. Siegel JA, Brooks AL, Fisher DR, et al. A critical assessment of the linear no-threshold hypothesis: its validity and applicability for use in risk assessment and radiation protection. *Clin Nucl Med.* 2019;44:521–525.
44. Shore RE, Dauer LT, Beck HL, et al. *NCRP Commentary No. 27: Implications of Epidemiologic Studies for the Linear-Nonthreshold Model and Radiation Protection.* National Council on Radiation Protection and Measurement; 2018.
45. Segars WP, Lalush DS, Frey EC, Manocha D, King MA, Tsui BM. Improved dynamic cardiac phantom based on 4D NURBS and tagged MRI. *IEEE Trans Nucl Sci.* 2009;56:2728–2738.
46. Segars PW, Tsui BM. MCAT to XCAT: the evolution of 4-D computerized phantoms for imaging research—computer models that take account of body movements promise to provide evaluation and improvement of medical imaging devices and technology. *Proc IEEE Inst Electr Electron Eng.* 2009;97:1954–1968.
47. Carter LM, Choi C, Krebs S, et al. Patient size-dependent dosimetry methodology applied to ^{18}F-FDG using new ICRP mesh phantoms. *J Nucl Med.* 2021;62:1805–1814.
48. Stabin MG, Siegel JA. Physical models and dose factors for use in internal dose assessment. *Health Phys.* 2003;85:294–310.
49. ICRP publication 110: adult reference computational phantoms. *Ann ICRP.* 2010;39:1–164.
50. Bolch WE, Shah AP, Watchman CJ, et al. Skeletal absorbed fractions for electrons in the adult male: considerations of a revised 50-μm definition of the bone endosteum. *Radiat Prot Dosimetry.* 2007;127:169–173.

The Role of Pretherapy Quantitative Imaging and Dosimetry in Radioiodine Therapy for Advanced Thyroid Cancer

Jan Taprogge[1,2], Carla Abreu[1,2], Siraj Yusuf[3], Gemma Ainsworth[4], Rachel H. Phillip[4], Jonathan I. Gear[1,2], Rebecca Gregory[1,2], Francesca Leek[1,2], Iain Murray[1,2], Amy B. Coulson[4], Sarah R. Brown[4], Yong Du[3], Kate Newbold[5], Jonathan Wadsley[6], and Glenn D. Flux[1,2]

[1]Joint Department of Physics, Royal Marsden NHSFT, Sutton, United Kingdom; [2]Institute of Cancer Research, London, United Kingdom; [3]Department of Nuclear Medicine and PET/CT, Royal Marsden NHSFT, Sutton, United Kingdom; [4]Clinical Trials Research Unit, Leeds Institute of Clinical Trials Research, University of Leeds, Leeds, United Kingdom; [5]Thyroid Unit, Royal Marsden NHSFT, Sutton, United Kingdom; and [6]Department of Oncology, Weston Park Hospital, Sheffield, United Kingdom

Radioactive iodine is well established as a successful treatment for differentiated thyroid cancer (DTC), although around 15% of patients have local recurrence or develop distant metastases and may become refractory to radioactive iodine (RAI). A personalized approach to treatment, based on the absorbed radiation doses delivered and using treatments to enhance RAI uptake, has not yet been developed. **Methods:** We performed a multicenter clinical trial to investigate the role of selumetinib, which modulates the expression of the sodium iodide symporter, and hence iodine uptake, in the treatment of RAI-refractory DTC. The iodine uptake before and after selumetinib was quantified to assess the effect of selumetinib. The range of absorbed doses delivered to metastatic disease was calculated from pre- and posttherapy imaging, and the predictive accuracy of a theranostic approach to enable personalized treatment planning was investigated. **Results:** Significant inter- and intrapatient variability was observed with respect to the uptake of RAI and the effect of selumetinib. The absorbed doses delivered to metastatic lesions ranged from less than 1 Gy to 1,170 Gy. A strong positive correlation was found between the absorbed doses predicted from pretherapy imaging and those measured after therapy ($r = 0.93$, $P < 0.001$). **Conclusion:** The variation in outcomes from RAI therapy of DTC may be explained, among other factors, by the range of absorbed doses delivered. The ability to assess the effect of treatments that modulate RAI uptake, and to estimate the absorbed doses at therapy, introduces the potential for patient stratification using a theranostic approach. Patient-specific absorbed dose planning might be the key to more successful treatment of advanced DTC.

Key Words: dosimetry; radioiodine; theragnostics; advanced thyroid cancer

J Nucl Med 2023; 64:1125–1130
DOI: 10.2967/jnumed.122.264913

Differentiated thyroid cancer (DTC) has been treated with radioactive iodine (RAI) for over 80 y (*1*). More than 580,000 new DTC cases were estimated worldwide for 2020 (*2*). Although 84% of patients survive for 10 y or more (*3*), over 15% of patients have local recurrence or develop distant metastases, and 5%–10% eventually become RAI-refractory (*4,5*). This status carries a poor prognosis with a median overall survival of 3–5 y. Treatment with lithium carbonate, retinoic acid, or histone deacetylase inhibitors has been attempted to resensitize disease to RAI treatment, but no significant clinical benefit has been demonstrated (*3,4*).

Initial results have shown that mitogen-activated protein kinase/extracellular-signal–regulated kinase pathway inhibitors such as the mitogen-activated protein kinase inhibitor selumetinib (ARRY-1428860) might be used to increase sodium iodide symporter expression and restore or enhance uptake of RAI (*6–8*). Further benefit may be gained from a theranostic approach (*9*), which offers the possibility of personalized treatments by combining therapeutics and diagnostics. In the case of RAI for DTC, the widely available imaging isotope ^{123}I-NaI may be used to guide treatment with ^{131}I-NaI and to predict the absorbed doses delivered to lesions and to healthy organs (*10,11*).

Here, we report the imaging and dosimetry results from a phase 2 trial (SEL-I-METRY, EudraCT no. 2015-002269-47) to resensitize RAI-refractory DTC to further RAI therapy (*12,13*). The aims of this aspect of the trial were to establish the quantitative increase in RAI uptake due to selumetinib and the range of absorbed doses delivered to metastatic disease from fixed levels of administered activity. In addition, we aimed to determine the accuracy with which the absorbed doses delivered at therapy may be predicted from pretherapy diagnostic studies and to establish the percentage of lesions responding to treatment.

MATERIALS AND METHODS

Study Design

Patient inclusion and exclusion criteria are provided in Supplemental Table 1 (supplemental materials are available at http://jnm.snmjournals.org). Iodine-refractory disease was defined as one or more lesions with no measurable iodine uptake or an iodine-avid lesion that progressed within 12 mo of RAI. An exploratory endpoint of the SEL-I-METRY trial was to assess the feasibility of quantitative imaging and SPECT/CT-based lesion dosimetry to personalize treatment for patients with advanced DTC.

Participants received 75 mg of selumetinib orally twice daily for 4 wk (Fig. 1). Pre- and postselumetinib quantitative ^{123}I-NaI SPECT/CT and whole-body scans were used to predict the increase in ^{131}I-NaI uptake for subsequent treatment after the initial 4 wk of selumetinib. Patients with an increase in ^{123}I-NaI uptake of more than 30% after selumetinib

Received Sep. 14, 2022; revision accepted Feb. 7, 2023.
For correspondence or reprints, contact Jan Taprogge (jan.taprogge@icr.ac.uk).
Published online Apr. 28, 2023.

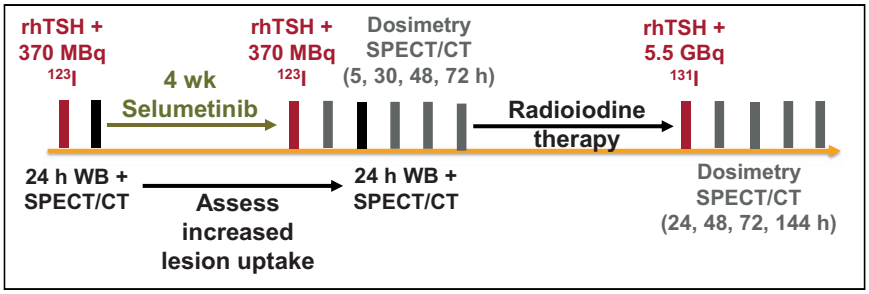

FIGURE 1. SEL-I-METRY imaging schedule consisting of 24-h whole-body and SPECT ^{123}I-NaI scans before selumetinib, 24-h whole-body and SPECT ^{123}I-NaI scans after selumetinib, up to 4 additional dosimetry SPECT/CT ^{123}I-NaI scans after selumetinib, and up to 4 dosimetry SPECT/CT scans after treatment with 5.5 GBq of ^{131}I-NaI. rhTSH = recombinant human thyroid-stimulating hormone; WB = whole body.

in at least one lesion went on to receive RAI therapy with a fixed activity of 5.5 GBq of ^{131}I-NaI (*13*). Patients continued receiving selumetinib until the ^{131}I-NaI therapy (maximum, 18 d) during the ^{123}I-NaI scan review.

For patients eligible for therapy, ^{123}I-NaI dosimetry was performed after the 4 wk of selumetinib administration (referred to here as pretherapy dosimetry) and lesional dosimetry was performed after ^{131}I-NaI therapy (referred to here as posttherapy dosimetry). Pretherapy dosimetry consisted of up to 5 SPECT/CT scans (at 5, 24, 30, 48, and 72 h) after administration of 370 MBq of ^{123}I-NaI. After ^{131}I-NaI therapy, SPECT/CT was performed at 24, 48, 72, and 144 h (Fig. 1). Recombinant human thyroid-stimulating hormone stimulation was administered before ^{123}I-NaI and ^{131}I-NaI. The imaging and reconstruction protocols are provided in Supplemental Tables 2 and 3.

The study was approved by East Midlands, the Leicester South Research Ethics Committee (15/EM/0455), the institutional review boards of participating centers, and the Medicines and Health Care Products Regulatory Agency. All patients provided written informed consent before trial registration.

Quantitative Imaging to Assess Effect of Selumetinib

γ-cameras at participating centers were configured for quantitative imaging including the determination of calibration factors for ^{123}I-NaI and ^{131}I-NaI and dead-time correction factors for ^{131}I-NaI (*14*). Anatomic lesion volumes were outlined by a trained radiologist on each of the CT components of up to 5 postselumetinib ^{123}I-NaI SPECT/CT scans. Lesions were excluded from the analysis if the largest diameter was smaller than 10 mm. Oversized volumes of interest, encompassing all activity visible within the lesions, were delineated to determine activity retention in all ^{123}I-NaI and ^{131}I-NaI SPECT/CT images. This approach was used to minimize problems arising from breathing motion and partial-volume effects and, therefore, allows for dosimetry estimates of small lesions.

The effect of selumetinib was assessed by calculating the absolute and relative differences in ^{131}I-NaI lesion uptake during therapy, as predicted from the pre- and postselumetinib ^{123}I-NaI images. These were converted to predictions of ^{131}I-NaI uptake during therapy, taking into account the differences in physical half-lives and administered activities.

Predictive Accuracy of Pretherapy Dosimetry and Treatment Planning

Pretherapy dosimetry was performed to predict lesional absorbed doses during ^{131}I-NaI therapy, taking into account the differences in physical half-life and injected activities, to investigate the potential of personalized treatment planning in this cohort. Dosimetry was performed according to the MIRD formalism (*15*) using mass-adjusted S values and taking into account only self-dose (*16*). Uncertainties regarding absorbed doses were estimated according to the guidance of the European Association of Nuclear Medicine (*17*).

The predictive accuracy of the pretherapy dosimetry was assessed by calculating the absolute and relative differences between the absorbed doses predicted before therapy and those measured after therapy.

Lesion Response Assessment

Response after RAI treatment was assessed using RECIST (*18*). The analysis was performed on a lesion-by-lesion basis between the baseline CT scan and the latest follow-up CT scan (maximum, 12 mo) after RAI treatment. Complete response (CR) was defined as lesion disappearance. Partial response (PR) was a decrease in lesion size by at least 30% (longest axis, in mm). Progressive disease was an increase in lesion size by at least 20% (longest axis, in mm). Stable disease was a case with no CR, PR, or progressive disease. Overall response was observation of either CR or PR, whereas clinical benefit was achievement of CR, PR, or stable disease.

Statistical Analysis

The Kruskal–Wallis test was used to assess whether relative changes in quantitative lesional uptake before and after selumetinib treatment significantly differed between patients. The relationship between relative changes in quantitative uptake before and after selumetinib treatment and baseline uptake was assessed using the Spearman rank correlation coefficient. The relationship between absorbed doses from pretherapy and posttherapy dosimetry was assessed using Pearson product-moment correlation coefficients. To account for the possibility of multiple, nonindependent lesions within a single patient, all correlation coefficients were calculated on group-mean–centered data.

The relationships between postselumetinib uptake and absorbed doses, and among the baseline data, biomarker, and selumetinib treatment parameters, were explored. A multilevel modeling approach was used to account for the nested data structure, incorporating random effects with respect to each patient. Lesional variables (baseline CT lesion size) were explored as fixed effects within the model. Patient-level variables (cancer subtype, sum of CT lesion size, thyroglobulin, and total selumetinib dose) were explored as random effects in the model. All models were adjusted for preselumetinib lesion uptake or pretherapy predicted absorbed doses, respectively, as a fixed effect. A forward selection approach with χ^2 testing was used to decide which variables to include in the model. χ^2 tests were used to test the difference between the nested models and determine whether inclusion of a variable improved the model fit.

The association between treatment success and quantitative absorbed doses from pre- and postselumetinib ^{123}I-NaI and ^{131}I-NaI imaging was investigated using univariate logistic regression modeling. Additionally, receiver-operating-curve analysis of the data was explored to establish a threshold absorbed dose for overall response rate and clinical benefit rate, using cutoffs at the median, one-third and two-thirds quantiles.

All statistical tests were exploratory because the trial was not formally powered to detect statistically significant effects on the dosimetry endpoints. Testing was performed at the 2-sided 5% significance level and did not account for multiple testing. Statistical analysis was performed using R, version 4.0.2 or later versions, and the Kruskal–Wallis test was performed using GraphPad Prism, version 9.3.1 (GraphPad Software), for Microsoft Windows.

RESULTS

Thirty RAI-refractory DTC patients were recruited to SEL-I-METRY, of whom 28 received selumetinib treatment. After 4 wk

TABLE 1
Patient Characteristics

Characteristic	Value
Age (y)	48 (45–78)
Female	3 (33%)
Histology subtype	
Papillary	2 (22%)
Follicular	7 (78%)
Cumulated activity of RAI before study registration (GBq)	7.6 (3.7–14.6)
Baseline thyroglobulin (μg/L)	742 (36–7,530)

Qualitative data are number and percentage; continuous data are median and range.

of selumetinib, 9 patients (Table 1) demonstrated an increase in ^{123}I-NaI uptake of 30% or more (Fig. 2) and were administered RAI treatment after a median of 12.5 d (range, 2–15 d). During this time, the patients continued to take selumetinib. Within these 9 patients, 39 lesions were identified. Median lesion volume was 2.6 cm^3 (minimum, 0.3 cm^3; 25th percentile, 0.7 cm^3; 75th percentile, 9.6 cm^3; maximum, 43.1 cm^3). Eighteen lesions were in the lungs, 14 in bone, and 7 in soft tissues (4 in lymph nodes and 3 in the area of the thyroid bed or the neck).

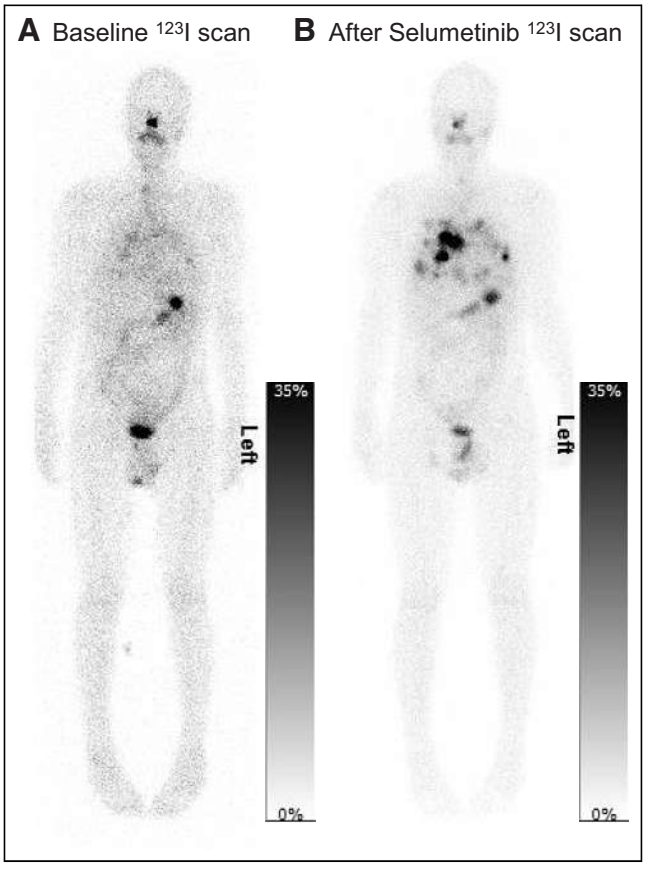

FIGURE 2. Example of whole-body planar scans at 24 h after ^{123}I-NaI administration at baseline, before selumetinib was administered (A), and after 4 wk of treatment with selumetinib (B).

Quantitative Imaging to Assess Effect of Selumetinib

Quantitative SPECT before and after treatment with selumetinib was used to assess the effect on RAI uptake. Two lesions were excluded from this analysis because they were not included in the range of the preselumetinib scan. The median predicted ^{131}I-NaI uptake per lesion volume (MBq/cm^3) at 24 h in 37 lesions before and after selumetinib was 0.2 MBq/cm^3 (range, 0.001–11.5 MBq/cm^3) and 2.1 MBq (range, 0.01–175.4 MBq/cm^3), respectively. The median absolute change (predicted uptake after selumetinib minus predicted uptake before selumetinib) and the median relative change (predicted uptake after selumetinib divided by uptake before selumetinib) were 1.9 MBq/cm^3 (range, −0.4 to 174.9 MBq/cm^3) and 16.7 (range, 0.7–819.1), respectively. Figure 3 shows the relative change in predicted ^{131}I-NaI uptake. The absolute and relative changes in uptake are presented in Figures 4 and 5, respectively, with respect to the baseline uptake.

A large inter- and intrapatient variability was observed for the relative change in uptake on a lesional basis. A Kruskal–Wallis test showed that the relative increase in uptake significantly differed between patients ($H_{(8)} = 22.48$, $P = 0.004$). There was a weak, positive correlation between the group-mean–centered data of the relative uptake change and the baseline uptake before selumetinib (Supplemental Fig. 1), $r_{(37)} = 0.011$; however, the relationship was not significant ($P = 0.946$).

A multilevel modeling approach was used to assess the relationships between postselumetinib uptake, adjusted for preselumetinib lesion uptake, and baseline data, biomarkers, and selumetinib treatment parameters. No variables of interest improved the multilevel model fit over the null model according to the χ^2 difference tests, with many models demonstrating singular fit, likely caused by the small sample size's being unable to support the complexity of the modeling approach. The intraclass correlation coefficient was calculated as 0.093 for patients, indicating large variability.

Predictive Accuracy of Pretherapy Dosimetry

To assess the feasibility of applying theranostic and dosimetry-based treatment planning in this patient cohort, pre- and posttherapy dosimetry was performed to assess the absorbed doses delivered to the lesions and to investigate whether pretherapy imaging can be used for treatment planning. All 39 lesions were evaluated for dosimetry. The median predicted absorbed doses from pretherapy and posttherapy dosimetry were 17.2 Gy (range, 0.1–1,292.1 Gy) and 10.4 Gy (range, 0.3–1,169.9 Gy), respectively. The median relative

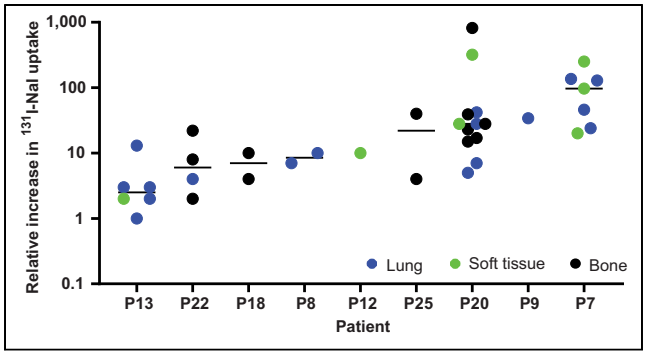

FIGURE 3. Relative change in predicted ^{131}I-NaI uptake after treatment with selumetinib with respect to uptake before selumetinib administration. Relative increase in uptake is shown for 9 patients who progressed to RAI therapy. P = patient.

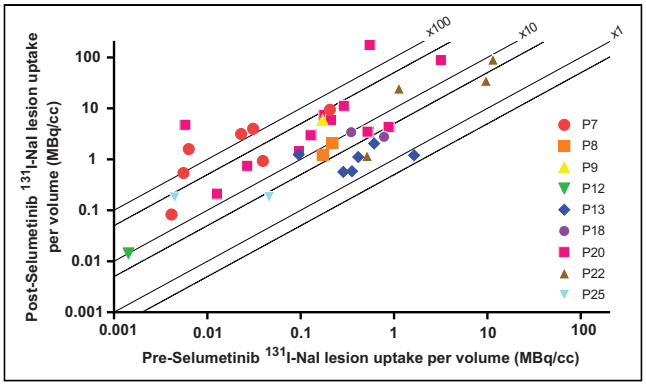

FIGURE 4. Uptake of ^{131}I-NaI before and after treatment with selumetinib. Solid lines represent relative increase in uptake by factors of 1, 10, and 100, respectively, to illustrate relative effect of selumetinib in individual patients and lesions. P = patient.

percentage difference between pretherapy and posttherapy dosimetry was −33% (range, −98% to 764%).

Comparison of predicted absorbed doses before RAI therapy and measured absorbed doses after RAI therapy are shown in Figure 6, illustrating the wide range of absorbed doses delivered. Pearson product-moment correlation analysis of the group-mean–centered data (Supplemental Fig. 2) resulted in a strong positive correlation between the predicted absorbed doses from pretherapy dosimetry and posttherapy dosimetry, r (37) = 0.93, $P < 0.001$. Figure 7 shows a Bland–Altman plot of the difference between predicted and measured absorbed doses. The estimated bias was 37.0 Gy (SD, 71.9 Gy), illustrating that predicted absorbed doses were higher than delivered absorbed doses. Supplemental Figures 3 and 4 show Bland–Altman plots of the 24-h uptake and the retention half-lives, respectively, comparing the predicted values using pretherapy dosimetry and the values measured after therapy.

A multilevel modeling approach was used to assess the relationships between posttherapy absorbed doses, adjusted for pretherapy predicted absorbed doses, and baseline data, biomarkers, and selumetinib treatment parameters. No variables of interest improved the multilevel model fit over the null model according to the χ^2 difference tests, again with many models demonstrating singular fit. The intraclass correlation coefficient was calculated as 0.062 for patients.

Lesion Response Analysis

Follow-up CT scans were collected for 7 patients (last follow-up: at 3 mo in 1 patient, 6 mo in 1 patient, 9 mo in 1 patient, and 12 mo in 4 patients), with a total of 24 lesions included in the analysis. Response was assessed using RECIST (*18*) but on an individual-lesion basis by comparing the baseline CT scan with the latest follow-up scan for each patient. Overall response was defined as either CR (disappearance of the lesion) or PR (≥30% decrease in lesion size as defined by the longest axis, in mm). Clinical benefit was taken to be CR, PR, or stable disease (<30% decrease or increase in lesion size). Overall response and clinical benefit were observed in 13% (3/24) and 83% (20/24) of lesions, respectively.

Univariate logistic regression modeling was used to assess the association between quantitative absorbed doses from pre- and post-selumetinib therapy imaging and treatment success. The logistic

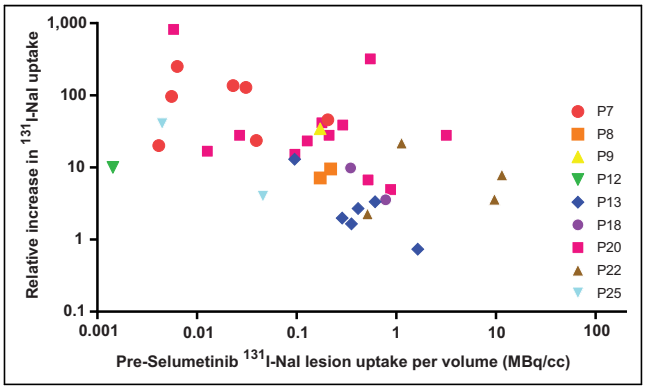

FIGURE 5. Relative increase in ^{131}I-NaI uptake after treatment, with selumetinib plotted against baseline uptake of ^{131}I-NaI before treatment. P = patient.

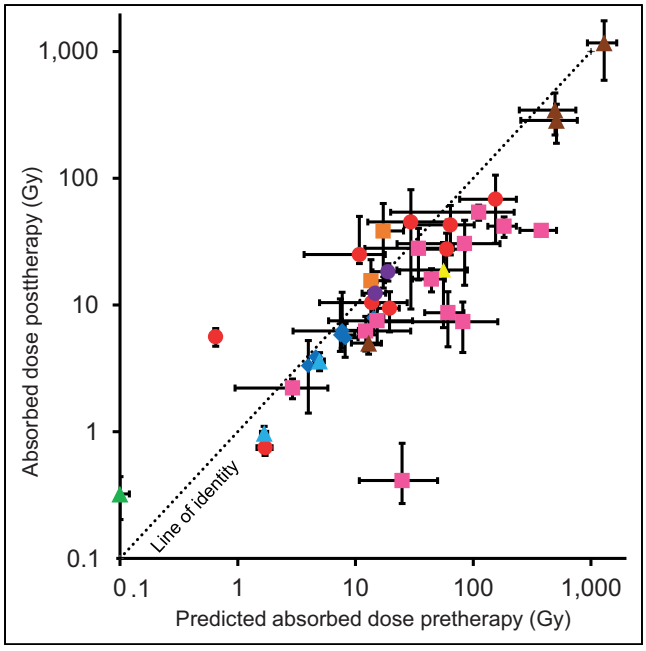

FIGURE 6. Comparison of absorbed doses for each lesion as predicted from pretherapy dosimetry and measured from posttherapy dosimetry.

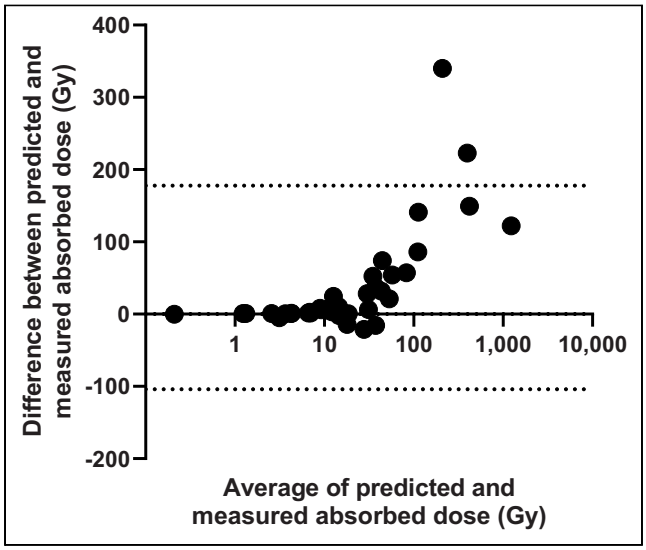

FIGURE 7. Bland–Altman plot for comparison of absorbed doses predicted and measured for each lesion, showing difference of predicted absorbed doses minus actual delivered absorbed doses.

models demonstrated poor fit due to small sample size, were highly influenced by outliers in the data, and are therefore not presented. Receiver-operating-curve analysis was also limited by the small sample size, and a threshold absorbed dose could not established.

DISCUSSION

Quantitative ^{123}I-NaI imaging has shown great potential to assess whether further ^{131}I-NaI treatment is warranted after attempted resensitization of RAI-refractory DTC with selumetinib. Significant inter- and intrapatient variability in the relative change in RAI uptake after selumetinib treatment was found in the present cohort. This variability suggests that, to fulfil the justification principle, patient-specific uptake changes should be assessed before RAI therapy proceeds. Furthermore, the RAI concentration within lesions before and after selumetinib treatment markedly differed between and within patients. No patient- or lesion-specific biomarkers were found to be predictive of uptake. Results of studies by Ho et al. suggest that a biomarker-directed strategy may be required, as redifferentiation using selumetinib in $BRAF^{V600E}$-mutant patients appeared to be less successful (*7,19*).

The relative change in uptake did not correlate with baseline uptake, suggesting that selumetinib might also be effective in nonrefractory patients, who still have a degree of iodine uptake in lesions before starting treatment. Ho et al. (*19*) used selumetinib plus RAI therapy in a phase 3 randomized clinical trial on the adjuvant treatment of high-risk, resected DTC patients but could not show a statistically significant difference in complete remission when compared with RAI therapy alone. Further investigations are warranted on the use of selumetinib or other related drugs to improve the outcome in cohorts of advanced-DTC patients at risk of becoming RAI-refractory.

The wide range of RAI uptake observed is also reflected by the wide range of absorbed dose delivered to lesions from a fixed 5.5-GBq administration to patients with advanced DTC. This administration is considered standard practice in the United Kingdom and in line with national guidelines and was therefore used in the current study (*20*). The wide range agrees with results presented previously (*21,22*) and might explain the variations in outcome observed among patients. Personalized treatment planning based on the absorbed doses delivered could, therefore, potentially be warranted in this cohort.

The results suggest that personalized treatment planning using pretherapy ^{123}I-NaI is feasible. Although the absolute accuracy decreases for absorbed doses higher than 50 Gy, pretherapy dosimetry correlated fairly well with posttreatment dosimetry. The average difference of −33% may be due to differences in imaging schedules, the possibility of a stunning effect of ^{123}I-NaI or self-stunning of ^{131}I-NaI (*23,24,25*), a delayed action of the selumetinib during the time before therapy, alterations of biokinetics due to prior administration of recombinant human thyroid-stimulating hormone (*26*), saturation of receptors, or the continued use of selumetinib before RAI therapy. The last of these possibilities has not yet been studied. To our knowledge, this is the first time that ^{123}I-NaI pretherapy dosimetry has been shown to be indicative of the absorbed doses delivered from treatment in metastatic DTC patients. This result might have wide implications for molecular radiotherapy, by allowing for personalized treatment planning in combination with dosimetric methods to assess absorbed doses to organs at risk, such as whole-body and bone marrow dosimetry (*27*).

The large uncertainties in absorbed doses, brought about by the use of oversized volumes of interest, reflect the volume estimate uncertainties for small lesions and the significantly shorter half-life of ^{123}I-NaI (*28*). Uncertainties are potentially smaller with ^{124}I-NaI pretherapy dosimetry, which was not available for this study. The longer physical half-life of ^{124}I-NaI than of ^{123}I-NaI would allow for more accurate determination of the retention half-lives. ^{123}I-NaI pretherapy dosimetry potentially overestimates the retention half-life (Supplemental Fig. 3) and, therefore, the absorbed dose delivered.

The present analysis has some limitations. The trial was not designed to have sufficient power to detect statistically significant effects on the dosimetry endpoints, and statistical testing did not account for multiple testing. The relatively small number of patients undergoing both pre- and posttherapy dosimetry is a limiting factor, and the statistical analysis should be considered exploratory. When feasible, future studies should be sufficiently powered to detect statistically significant effects and to identify key parameters affecting both the response to treatments before RAI therapy and the absorbed doses delivered. Additionally, since these types of data have a nested structure of lesions within patients, careful consideration should be given to the design of trials aiming to capture these data. Such a design will aid in avoiding or mitigating potential issues that may arise when using a multilevel modeling approach, such as the issues with model singularity encountered here. Follow-up analysis was limited by the short follow-up time, leading to inconclusive results with respect to the absorbed dose relationship due to a poor model fit. Response measurements of bone lesions using RECIST are considered difficult but can be performed for osteolytic lesions, the predominant type in thyroid cancer. Nevertheless, the lack of an absorbed dose relationship potentially reflects that 14 of the 39 lesions were found in bone. Similarly, an absorbed dose threshold could not be identified. Most absorbed doses delivered were estimated to be lower than the proposed absorbed dose thresholds for soft-tissue (*29*) and bone metastases (*30*), as is in line with the low overall response rate of 13%.

Absorbed dose–response relationships for advanced DTC (*30*) should be confirmed in multicenter clinical trials. Together with the results presented here, these future results would facilitate personalized treatment planning of RAI administrations.

CONCLUSION

Quantitative SPECT/CT has shown large inter- and intrapatient variability in the effect of selumetinib on increasing the lesional RAI uptake in advanced RAI-refractory DTC. In addition, a large range of RAI uptake concentrations was observed in lesions at baseline. The absorbed doses delivered at therapy in this cohort can be estimated from a pretherapy dosimetry study. These findings suggest that future studies of redifferentiation therapy should use the combination of pretherapy quantitative imaging (to assess the effect of treatments to enhance RAI uptake) and dosimetry (to plan the activity of RAI administered to patients) to ensure that those patients achieving increased iodine uptake obtain maximum benefit from subsequent therapy. Our findings also likely have implications for the personalized treatment planning of patients with iodine-sensitive DTC.

DISCLOSURE

Financial support was received from Cancer Research U.K. (CRUK) (CRUK reference CRUK/14/041), AstraZeneca U.K. Limited, the NIHR Biomedical Research Centre at RMH/ICR, and the National Institute for Health Research (NIHR). Sanofi Genzyme provided recombinant human thyroid-stimulating hormone. Sarah Brown, Glenn Flux, Jonathan Wadsley, Jan Taprogge, Iain Murray, Jonathan Gear, and Carla Abreu report funding or

provision of study materials from CRUK, AstraZeneca, and Sanofi Genzyme during the conduct of the study. Jan Taprogge, Carla Abreu, Jonathan Gear, Iain Murray, and Glenn Flux report funding from the National Health Service to the NIHR Biomedical Research Centre at the Royal Marsden and the ICR and grants from Euratom research and training program 2014–2018 and the NIHR and NIHR Royal Marsden Clinical Research Facility. Jonathan Gear reports personal fees and honoraria from the European Association of Nuclear Medicine. Jonathan Wadsley reports personal fees and honoraria from Lilly, Eisai, Novartis, AAA, Bayer, Ipsen, and Roche. Amy Coulson reports grants and nonfinancial support from BMS/Celgene, Merck Sharpe & Dohme, Amgen, and Takeda. Sanofi Genzyme provided recombinant human thyroid-stimulating hormone. The research was developed with support from NCRI CTRad. NHS funding was provided to the NIHR Biomedical Research Centre at the Royal Marsden and the ICR. The RTTQA group is funded by the NIHR. We acknowledge infrastructure support from NIHR Royal Marsden Clinical Research Facility funding. This report is independent research funded by the NIHR. The views expressed in this publication are those of the authors and not necessarily those of the NHS, the NIHR, or the Department of Health and Social Care. No other potential conflict of interest relevant to this article was reported.

ACKNOWLEDGMENTS

We are deeply indebted to the participants and their families and carers. We are grateful to the SEL-I-METRY teams at the participating hospitals and the Trial Steering Committee and Data Monitoring and Ethics Committee members, without whom this trial would not have been possible.

KEY POINTS

QUESTION: Can quantitative imaging and SPECT/CT-based lesional dosimetry be used to personalize RAI treatment for advanced thyroid cancer, which currently has a poor prognosis?

PERTINENT FINDINGS: Pretherapy imaging was found to be a powerful tool to assist with the stratification of patients before further RAI therapy, and a strong positive correlation was found between pre- and posttherapy absorbed doses, indicating the suitability of pretherapy dosimetry for treatment planning.

IMPLICATIONS FOR PATIENT CARE: Pretherapy quantitative imaging and dosimetry in RAI therapy for advanced thyroid cancer has the potential to inform treatment planning for individual patients and to alter patient management.

REFERENCES

1. Hertz S, Roberts A. Radioactive iodine in the study of thyroid physiology: VII. The use of radioactive iodine therapy in hyperthyroidism. *J Am Med Assoc.* 1946; 131:81–86.
2. Pizzato M, Li M, Vignat J, et al. The epidemiological landscape of thyroid cancer worldwide: GLOBOCAN estimates for incidence and mortality rates in 2020. *Lancet Diabetes Endocrinol.* 2022;10:264–272.
3. Schlumberger M, Brose M, Elisei R, et al. Definition and management of radioactive iodine-refractory differentiated thyroid cancer. *Lancet Diabetes Endocrinol.* 2014;2:356–358.
4. Jin Y, Van Nostrand D, Cheng L, Liu M, Chen L. Radioiodine refractory differentiated thyroid cancer. *Crit Rev Oncol Hematol.* 2018;125:111–120.
5. Durante C, Haddy N, Baudin E, et al. Long-term outcome of 444 patients with distant metastases from papillary and follicular thyroid carcinoma: benefits and limits of radioiodine therapy. *J Clin Endocrinol Metab.* 2006;91:2892–2899.
6. Chakravarty D, Santos E, Ryder M, et al. Small-molecule MAPK inhibitors restore radioiodine incorporation in mouse thyroid cancers with conditional BRAF activation. *J Clin Invest.* 2011;121:4700–4711.
7. Ho AL, Grewal RK, Leboeuf R, et al. Selumetinib-enhanced radioiodine uptake in advanced thyroid cancer. *N Engl J Med.* 2013;368:623–632.
8. Rothenberg SM, McFadden DG, Palmer EL, Daniels GH, Wirth LJ. Redifferentiation of iodine-refractory BRAF V600E-mutant metastatic papillary thyroid cancer with dabrafenib. *Clin Cancer Res.* 2015;21:1028–1035.
9. Arnold C. Theranostics could be big business in precision oncology. *Nat Med.* 2022;28:606–608.
10. Van Nostrand D, Aiken M, Atkins F, et al. The utility of radioiodine scans prior to iodine-131 ablation in patients with well-differentiated thyroid cancer. *Thyroid.* 2009;19:849–855.
11. Brans B, Bodei L, Giammarile F, et al. Clinical radionuclide therapy dosimetry: the quest for the "Holy Gray." *Eur J Nucl Med Mol Imaging.* 2007;34:772–786.
12. Wadsley J, Gregory R, Flux G, et al. SELIMETRY: a multicentre I-131 dosimetry trial—a clinical perspective. *Br J Radiol.* 2017;90:20160637.
13. Brown SR, Hall A, Buckley HL, et al. Investigating the potential clinical benefit of selumetinib in resensitising advanced iodine refractory differentiated thyroid cancer to radioiodine therapy (SEL-I-METRY): protocol for a multicentre UK single arm phase II trial. *BMC Cancer.* 2019;19:582.
14. Gregory RA, Murray I, Gear J, et al. Standardised quantitative radioiodine SPECT/CT imaging for multicentre dosimetry trials in molecular radiotherapy. *Phys Med Biol.* 2019;64:245013.
15. Bolch WE, Eckerman KF, Sgouros G, Thomas SR. MIRD pamphlet no. 21: a generalized schema for radiopharmaceutical dosimetry—standardization of nomenclature. *J Nucl Med.* 2009;50:477–484.
16. Stabin MG, Siegel JA. Physical models and dose factors for use in internal dose assessment. *Health Phys.* 2003;85:294–310.
17. Gear JI, Cox MG, Gustafsson J, et al. EANM practical guidance on uncertainty analysis for molecular radiotherapy absorbed dose calculations. *Eur J Nucl Med Mol Imaging.* 2018;45:2456–2474.
18. Eisenhauer EA, Therasse P, Bogaerts J, et al. New response evaluation criteria in solid tumours: revised RECIST guideline (version 1.1). *Eur J Cancer.* 2009;45:228–247.
19. Ho AL, Dedecjus M, Wirth LJ, et al. Selumetinib plus adjuvant radioactive iodine in patients with high-risk differentiated thyroid cancer: a phase III, randomized, placebo-controlled trial (ASTRA). *J Clin Oncol.* 2022;40:1870–1878.
20. Wadsley J, Armstrong N, Bassett-Smith V, et al. Patient preparation and radiation protection guidance for adult patients undergoing radioiodine treatment for thyroid cancer in the UK. *Clin Oncol (R Coll Radiol).* 2023;35:42–56.
21. de Keizer B, Brans B, Hoekstra A, et al. Tumour dosimetry and response in patients with metastatic differentiated thyroid cancer using recombinant human thyrotropin before radioiodine therapy. *Eur J Nucl Med Mol Imaging.* 2003;30:367–373.
22. Sun F, Gerrard GE, Roberts JK, et al. Ten year experience of radioiodine dosimetry: is it useful in the management of metastatic differentiated thyroid cancer? *Clin Oncol (R Coll Radiol).* 2017;29:310–315.
23. Lassmann M, Luster M, Hänscheid H, Reiners C. Impact of ^{131}I diagnostic activities on the biokinetics of thyroid remnants. *J Nucl Med.* 2004;45:619–625.
24. McDougall IR, Iagaru A. Thyroid stunning: fact or fiction? *Semin Nucl Med.* 2011; 41:105–112.
25. Canzi C, Zito F, Voltini F, Reschini E, Gerundini P. Verification of the agreement of two dosimetric methods with radioiodine therapy in hyperthyroid patients. *Med Phys.* 2006;33:2860–2867.
26. Hänscheid H, Lassmann M, Luster M, et al. Iodine biokinetics and dosimetry in radioiodine therapy of thyroid cancer: procedures and results of a prospective international controlled study of ablation after rhTSH or hormone withdrawal. *J Nucl Med.* 2006;47:648–654.
27. Lassmann M, Hänscheid H, Chiesa C, et al. EANM Dosimetry Committee series on standard operational procedures for pre-therapeutic dosimetry I: blood and bone marrow dosimetry in differentiated thyroid cancer therapy. *Eur J Nucl Med Mol Imaging.* 2008;35:1405–1412.
28. Flux GD, Guy MJ, Beddows R, Pryor M, Flower MA. Estimation and implications of random errors in whole-body dosimetry for targeted radionuclide therapy. *Phys Med Biol.* 2002;47:3211–3223.
29. Maxon HR, Thomas SR, Hertzberg VS, et al. Relation between effective radiation dose and outcome of radioiodine therapy for thyroid cancer. *N Engl J Med.* 1983; 309:937–941.
30. Jentzen W, Verschure F, van Zon A, et al. ^{124}I-PET assessment of response of bone metastases to initial radioiodine treatment of differentiated thyroid cancer. *J Nucl Med.* 2016;57:1499–1504.

Optimized SPECT Imaging of ^{224}Ra α-Particle Therapy by ^{212}Pb Photon Emissions

Lars Tore Gyland Mikalsen[1,2], Monika Kvassheim[1,3], and Caroline Stokke[1,4]

[1]*Division of Radiology and Nuclear Medicine, Oslo University Hospital, Oslo, Norway;* [2]*Department of Life Sciences and Health, Oslo Metropolitan University, Oslo, Norway;* [3]*Faculty of Medicine, University of Oslo, Oslo, Norway; and* [4]*Department of Physics, University of Oslo, Oslo, Norway*

In preparation for an α-particle therapy trial using 1–7 MBq of ^{224}Ra, the feasibility of tomographic SPECT/CT imaging was of interest. The nuclide decays in 6 steps to stable ^{208}Pb, with ^{212}Pb as the principle photon-emitting nuclide. ^{212}Bi and ^{208}Tl emit high-energy photons up to 2,615 keV. A phantom study was conducted to determine the optimal acquisition and reconstruction protocol. **Methods:** The spheres of a body phantom were filled with a ^{224}Ra-$RaCl_2$ solution, and the background compartment was filled with water. Images were acquired on a SPECT/CT system. In addition, 30-min scans were acquired for 80- and 240-keV emissions, using triple-energy windows, with both medium-energy and high-energy collimators. Images were acquired at 90–95 and 29–30 kBq/mL, plus an explorative 3-min acquisition at 20 kBq/mL (using only the optimal protocol). Reconstructions were performed with attenuation correction only, attenuation plus scatter correction, 3 levels of postfiltering, and 24 levels of iterative updates. Acquisitions and reconstructions were compared using the maximum value and signal-to-scatter peak ratio for each sphere. Monte Carlo simulations were performed to examine the contributions of key emissions. **Results:** Secondary photons of the 2,615-keV ^{208}Tl emission produced in the collimators make up most of the acquired energy spectrum, as revealed by Monte Carlo simulations, with only a small fraction (3%–6%) of photons in each window providing useful information for imaging. Still, decent image quality is possible at 30 kBq/mL, and nuclide concentrations are imageable down to approximately 2–5 kBq/mL. The overall best results were obtained with the 240-keV window, medium-energy collimator, attenuation and scatter correction, 30 iterations and 2 subsets, and a 12-mm gaussian postprocessing filter. However, all combinations of the applied collimators and energy windows were capable of producing adequate results, even though some failed to reconstruct the 2 smallest spheres. **Conclusion:** SPECT/CT imaging of ^{224}Ra in equilibrium with daughters is possible, with sufficient image quality to provide clinical utility for the current trial of intraperitoneally administrated activity. A systematic scheme for optimization was designed to select acquisition and reconstruction settings.

Key Words: optimization; SPECT; Ra224; Pb212; α-particle therapy

J Nucl Med 2023; 64:1131–1137
DOI: 10.2967/jnumed.122.264455

Targeted α-particle therapy has seen increasing interest during the last decade (*1*). α-particles are densely ionizing with short-range and high-energy (HE) transfer. Imaging of the patient-specific uptake is commonly considered difficult, because only small amounts of activity are used. Still, a few studies have investigated imaging of different nuclides and found that relevant clinical information can be obtained. Planar imaging has been performed, and although ^{223}Ra-$RaCl_2$ (Xofigo; Bayer) is the most extensively studied (*2,3*),

TABLE 1
^{224}Ra Decay Chain Photon Emissions (Cutoff, 40 keV and 0.5%)

Nuclide	Energy	*P* (%)	Ray type
^{208}Tl, α	73.0	0.8	x
^{212}Pb	75.1	10.6	x
^{208}Tl, α	75.3	1.4	x
^{212}Pb	**77.4**	**17.7**	x
^{212}Pb	87.1	2.0	x
^{212}Pb	87.7	3.8	x
^{212}Pb	90.2	0.9	x
^{212}Pb	115	0.6	γ
^{212}Pb	**239**	**43.3**	γ
^{224}Ra	241	4.1	γ
^{208}Tl, α	277	2.3	γ
^{212}Pb	300	3.3	γ
^{208}Tl, α	511	8.1	γ
^{208}Tl, α	583	30.3	γ
^{212}Bi, β	727	4.2	γ
^{208}Tl, α	763	0.7	γ
^{212}Bi, β	785	0.7	γ
^{208}Tl, α	861	4.5	γ
^{212}Bi, β	1621	1.0	γ
^{208}Tl, α	2615	35.6	γ

P = probability of emission per ^{224}Ra decay obtained from International Commission on Radiological Protection publication 107 (*8*); β = β-decay branch of ^{212}Bi, 64%; α = α-decay branch of ^{212}Bi, 36%.

Value of highest-frequency photon emission, in bold, within each window was used for AC.

Received Oct. 7, 2022; revision accepted Mar. 10, 2023.

For correspondence or reprints, contact Lars Tore Gyland Mikalsen (ltmikals@ous-hf.no).

Published online Jun. 2, 2023.

TABLE 2
SPECT Acquisition Windows

Candidate imaging window	Lower scatter window	Emission window	Upper scatter window	AC	$\bar{e}$	$\sum P$ (%)
X-ray window, 80 keV	48-64	64-96	96-112	77.4	79.2	43
ME γ-window, 240 keV	204-216	216-264	264-276	239	239	48

$\bar{e}$ = theoretic average energy of primary emissions within window; $\sum P$ = Total probability of emission within the energy window per ^{224}Ra decay.

other α-particle therapeutics have also been investigated by imaging (*4*). SPECT imaging has rarely been performed, although images of decent quality have been obtained on a few occasions, for example, in a trial using a ^{213}Bi-labeled substance for therapy of gliomas (*5*) and for ^{225}Ac-PSMA (*6*). ^{149}Tb is in a special position among α-emitters, because it also emits positrons and allows PET imaging (*7*).

^{224}Ra adsorbed to calcium carbonate microparticles is being investigated for intraperitoneal therapeutic use in 2 phase 1 trials. The nuclide has a half-life of 3.63 d and emits 4 α-particles as it decays to stable ^{208}Pb (*8*). The shorter half-life of ^{224}Ra than of ^{223}Ra is considered an advantage for this treatment (*9*). X-ray and medium-energy (ME) γ-emissions, predominantly from ^{212}Pb, can facilitate imaging (Table 1). In the trials, activity will be escalated from 1 to 7 MBq, a range quite typical for α-emitter therapy. The relatively small intraperitoneal distribution volume contributes to expectations of increased concentrations at these activity levels, relative to systemic therapies, and a corresponding minimal background outside the intraperitoneal cavity. In addition to low amounts of activity providing little signal, imaging is complicated by the high background of scattered photons. Hence, a highly optimized imaging protocol is necessary. Although an earlier study that performed planar imaging of 3 patients with intraperitoneal ^{212}Pb-TCMC-trastuzumab (*10*) gave an idea of the possibility for imaging, we have been unable to find previous imaging studies for ^{224}Ra.

The primary objective of the present work was to determine whether SPECT/CT imaging is meaningful under the conditions for the current clinical trial and to identify the optimal imaging protocol. To this end, we aimed to develop a general optimizing routine to maximize the contrast of phantom spheres relative to scatter-induced noise and compared each evaluated acquisition protocol using individually optimized reconstruction settings.

MATERIALS AND METHODS

Image Acquisition and Energy Spectra Measurements

A NEMA IEC PET Body Phantom Set (Capintec) was applied without the lung cylinder insert, using a ^{224}Ra-$RaCl_2$ solution in the spheres and nonradioactive water in the background chamber. ^{224}Ra was produced with a generator based on the parental nuclide ^{228}Th (*9*). The phantom contained 6 spheres with diameters of 10, 13, 17, 22, 28, and 37 mm and volumes of 0.52, 1.15, 2.57, 5.57, 11.49, and 26.52 mL, for a total of 47.82 mL. The spheres were filled with ^{224}Ra-$RaCl_2$ solution containing ethylenediaminetetraacetic acid and saline water. Imaging was performed at ^{224}Ra concentrations of 90–95 kBq/mL (4.4–4.6 MBq total) and 29–30 kBq/mL (1.4 MBq total) in the spheres, denoted as 90 and 30 kBq/mL, respectively. Acquisitions were made on a Symbia Intevo Bold system (Siemens) with a 1-cm (3/8 inch) crystal size using ME and HE collimators, a 20% energy window centered at 240 keV, and a 40% window centered at 80 keV, with dual scatter windows of 5% and 20%, respectively (Table 2). A single bed position was acquired using a 256 × 256 matrix, noncircular orbit, acquisition during steps, and 60 views of 30 s each. CT was acquired at 130 kVp with 2.49 mGy CTDIvol and reconstructed with a soft filter (B08). Quality-assurance procedures were followed according to manufacturer recommendations.

In addition, a single acquisition was performed with ME collimators, 3 s/view, and the 240-keV triple-energy window. The phantom spheres contained 20 kBq/mL at the time of imaging. Because of the short acquisition time, the dataset is considered equivalent to 2 kBq/mL using the standard protocol of 30 min. Energy spectra were acquired with and without the water-filled phantom hull and with and without collimators mounted.

Monte Carlo Simulations of Energy Spectra

To gain better insight into the composition of energy spectra, and the nature of the observed high scatter, Monte Carlo simulations were performed using the Geant4 Application for Tomographic Emission (version 9.0; OpenGATE Collaboration) (*11,12*). The SPECT detectors were modeled with collimators, crystals, back compartments, and shielding. The back compartments were described in detail, with lightguides, electronics, and photomultiplier tubes, to accurately model the backscatter of HE photons (*13,14*). The source was simulated using a UserSpectrum, including all photon emissions from the decay chain with emission probabilities larger than 0.1% per ^{224}Ra decay. Energy blurring was modeled using a linear law with 13% resolution at 80 keV and a slope of −0.091/MeV after calibration with the experimental spectra. The electromagnetic option 4 physics list was used. The obtained spectra were validated against experimental results with ME collimators, HE collimators,

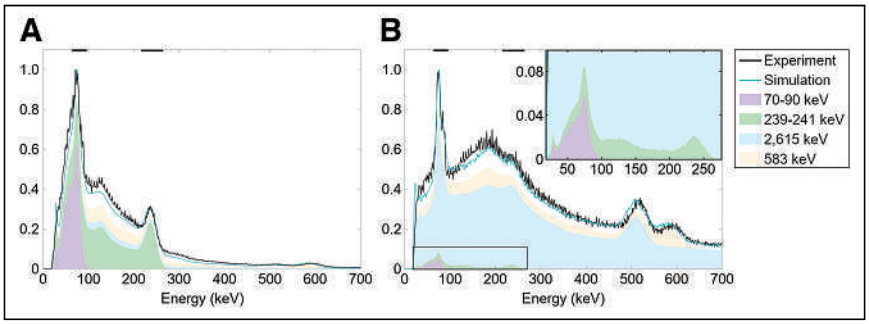

FIGURE 1. Captured (experiment) and Monte Carlo–simulated (cyan line) normalized energy spectra without (A) and with (B) ME collimator. Energy windows are marked with black lines on top axis. Stacked areas show contribution of imageable x-ray (70–90 keV) and γ-ray (239–241 keV) emissions, as well as scattered photons produced by 2,615-keV and 583-keV emissions. Presence of collimators greatly increased scatter; only low percentage of captured counts are from primary emissions. Supplemental Figure 1 shows for further panels.

TABLE 3
Number of Ordered-Subset Expectation Maximization Updates in Individually Optimized Reconstructions

Parameter	Gaussian filter (mm)	No. of OSEM updates for maximized SSR								ME240 (20 kBq/mL), 3-min scan
		HE80 (95 kBq/mL)	HE240 (94 kBq/mL)	ME80 (90 kBq/mL)	ME240 (90 kBq/mL)	HE80 (30 kBq/mL)	HE240 (29 kBq/mL)	ME80 (29 kBq/mL)	ME240 (29 kBq/mL)	
AC	9	75	90	120	180	42	48	180	90	12
	12	900	120	240	720	42	90	900	300	12
	16	900	600	900	600	120	120	900	300	16
SC+AC	9	90	42	42	75	34	75	120	360	12
	12	120	30	42	90	20	90	120	60	12
	16	180	34	120	120	24	180	120	42	12

OSEM = ordered-subsets expectation maximization; HE80 = HE collimator with x-ray window; HE240 = HE collimator with γ-ray window; ME80 = ME collimator with x-ray window; ME240 = ME collimator with γ-ray window.

Table shows optimal number of ordered-subset expectation maximization updates, according to SSR, for each acquisition, as well as ^{224}Ra concentration in phantom at time of imaging. Scan time was 30 min where not otherwise stated.

and no collimators. After validation, the simulations were repeated including only selected emissions from the ^{224}Ra decay chain; the γ-emission of 2,615 keV, γ-emission of 583 keV, x-ray emissions of 70–90 keV, and γ-emissions of 239 and 241 keV were simulated separately.

Reconstructions

Images were reconstructed in Syngo MI Applications, version VB20B (Siemens Healthcare and Toshiba Medical Systems Corp.), using Flash3d. Images were reconstructed with and without scatter correction (SC) at 24 levels of iterative updates (iteration × subsets), ranging from 5 to 900 total updates (Supplemental Table 1 [supplemental materials are available at http://jnm.snmjournals.org]); iterations were preferentially increased over subsets. CT-based attenuation correction (AC) was used. Triple-energy windows were used for SC (Table 2).

Next, 9-, 12-, and 16-mm gaussian filters were used for postfiltering (AC and SC+AC), and SC input data were prefiltered using 9-, 16-, and 20-mm gaussian kernels, respectively, for increasing postprocessing filter strength. The reconstructed matrix was 256 × 256 × 164, with isotropic 2.40-mm voxels. In total, 1,296 reconstructions were performed, 144 per acquisition. Images are shown on a linear gray scale from zero to the maximum intensity value.

Image Analysis

Analysis was performed semiautomatically using MATLAB, version 2017 (MathWorks, Inc.). Sphere positions were found on CT images. For each reconstruction, spheric volumes of interest (VOIs) approximating the physical sphere volumes were placed optimally on the SPECT images within 20 mm of the CT position by maximizing the total intensity enclosed. When there was no local maximum, the CT-derived position was used. For each spheric VOI in each reconstruction, the maximum and mean were extracted and normalized by activity and scan duration. A 2.8-L large background VOI was constructed containing the water-filled phantom hull with 40.2-mm margins to spheres and a 26.8-mm margin to the phantom hull. Scatter-induced noise in the background compartment was assessed by peak measurements (largest mean of a fixed-size spheric VOI across all locations in the background VOI) using peak VOI sizes matching each spheric VOI. Signal-to-scatter peak ratio (SSR) was defined as the mean sphere value divided by the volume-matched background peak value.

Iterative Reconstruction Optimization

The optimal number of iterative updates was defined as the reconstruction that maximized the combined normalized SSR. The SSRs of each sphere, as a function of iterative updates, were smoothed using a 3-element floating average, normalized against the maximum value, and added together, omitting spheres without local maxima.

Acquisition and Reconstruction Comparisons

The normalized maximum values for the largest sphere, and the combined normalized SSR results for each combination of collimator, energy window, and SC, were compared at the individually obtained optimal number of iterations.

RESULTS

Energy Spectra and Contributions from Different Emissions

Energy spectra (Fig. 1) acquired without collimators showed prominent peaks in the x-ray region (70–90 keV) and around 239 keV and minor peaks near 115, 511, and 583 keV. With collimators, a high background of photons was observed throughout the spectrum, obscuring the 239-keV peak. The Monte Carlo–simulated spectra matched the experimental spectra with reasonable visual agreement (Fig. 1; Supplemental Fig. 1). The results show that the collimator-induced background can be almost entirely explained by secondary photons—from pair production, Compton scatter,

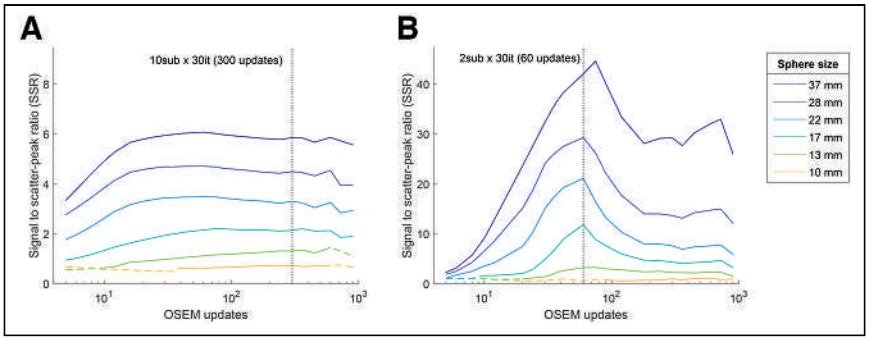

FIGURE 2. SSR as function of ordered-subset expectation maximization updates (logarithmic scale) for each phantom sphere for selected dataset (ME collimator, 240-keV window, and 12-mm gaussian filter), without (A) and with (B) SC. Dashed segments signify reconstructions where spheres did not show local intensity maximum. Setting that maximized total normalized SSR of all spheres was considered optimal (dashed vertical line). Supplemental Figures 4–7 show further panels.

and x-ray production in lead—resulting from the 2,615-keV ^{208}Tl emission. This accounts for most of the counts in the energy windows as well.

In the acquired image raw data, the total counts were 4.6–10 megacounts (Supplemental Table 2). They were 16% higher in the 240-keV window than in the 80-keV window for both collimators. The ME collimator had 79% more counts than the HE collimator. The triple-energy window estimates of scatter ratios underestimated scatter according to Monte Carlo results. The estimates showed 66% in the 80-keV window for both collimators and 91% and 89% in the 240-keV window for ME and HE collimators, respectively. However, the Monte Carlo simulations estimated that only 4% and 6% of counts in the 80-keV window with ME and HE collimators, respectively, and 3% of counts in the 240-keV window with either collimator originated from the desired radionuclide emissions. The remaining detections (94%–97%) in each window were secondary photons of higher-energy emissions.

Optimal Iteration Levels

The optimal iterative levels for each combination of collimator, energy window, AC or SC+AC correction, and filters are listed in Table 3. Examples of SSR as a function of iterative updates, used to determine the optimal iterative levels, are shown in Figure 2. Overall, more iterations were tolerated when reconstructing without SC, with a stronger postprocessing filter, or with higher ^{224}Ra concentrations. Optimal iterative updates with respect to SSR were 42–900 for AC-only reconstructions and 20–360 for SC+AC. Transaxial slices for a selected protocol at the optimal iterative level are shown in Figure 3. SSR curves for all acquisitions and further image examples are shown in Supplemental Figs. 2–10.

Reconstructed Sphere Counts

The maximum values of the spheres reflect a combination of sensitivity and resolution recovery and mostly increased with the number of iterative updates. The larger spheres often reached a plateau, whereas the smaller spheres continued to increase (example in Fig. 4; full results in the supplemental materials). At the SSR-optimized iterative level, we found that the maximum count rate of the largest sphere varied from 3.6 to 10.2 counts/h for 1 kBq/mL depending on window, collimator, and SC (Fig. 5). It was mostly somewhat higher at 90 than 30 kBq/mL; however, near-identical results were obtained with the ME collimator with SC, and consistent results were obtained in the 2 kBq/mL equivalent scan (Fig. 4).

Acquisition and Reconstruction Comparisons

Based on the combined normalized SSR (Fig. 6, and detailed further in the following paragraphs), the optimal acquisition and reconstruction setting for the current investigations was suggested to be ME collimator and 240-keV energy window with SC, AC, and 12-mm gaussian filter. This combination is used for the examples given in Figures 2B, 3, 4, and 7B. Additional figures are available in the supplemental materials, detailing results for all investigated acquisition protocols and reconstruction settings.

SC. SC resulted in a higher overall SSR for all collimator and energy window combinations (Fig. 6). However, for some iteration levels, the HE collimator acquisitions failed to reconstruct local maxima for the smallest spheres with SC enabled.

Collimator. With AC-only reconstruction, the HE collimator scored higher SSRs than the ME collimator for the 4 largest spheres, and they were equal for the 13-mm sphere. However, the ME collimator outperformed HE for the smallest sphere (Fig. 6). Using SC, the ME collimator had overall better performance in nearly all cases. The ME collimator resulted in higher maximum counts than the HE collimator, when comparing the largest sphere at the optimal iterative update level, for all combinations.

Energy Windows. The 2 energy windows gave comparable SSRs, except for scatter-corrected 240-keV images with the ME collimator, which had approximately twice the SSR of the 80-keV window. The 80-keV window provided 29%–80% higher counts than 240 keV, when comparing the largest sphere at the optimal iterative level, as determined by maximized SSR (Fig. 6).

Postprocessing filters. Increased postfiltering decreased the maximum counts of both spheres and scatter. In most cases, SSRs decreased as well (Fig. 7), and the best results were obtained with 9-mm postfilters, the smallest examined. The ME-collimated 240-keV window with SC was a notable exception, where the 12-mm filter provided much higher SSR than the 9-mm filter, which gave the poorest result.

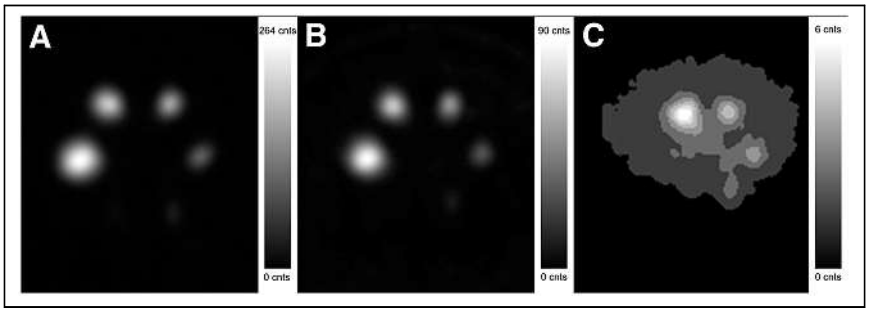

FIGURE 3. Example of image quality. (A–C) Transaxial slices at each exposure level: 90 kBq/mL (A), 30 kBq/mL (B), and 2 kBq/mL equivalent scan (C), captured using ME collimator and 240-keV window and reconstructed using SC and 12-mm gaussian filter at individually optimal number of iterations. (C) Spheres' positions are rotated 60° clockwise.

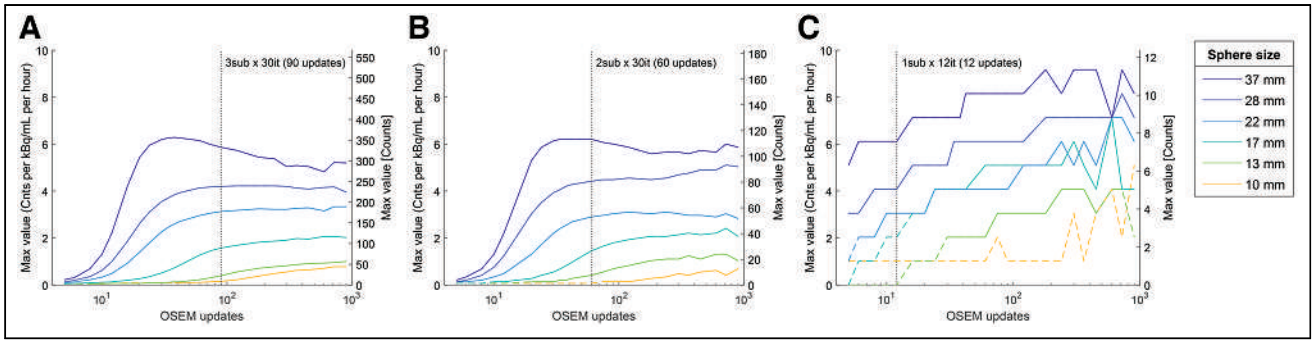

FIGURE 4. Maximum value in each sphere at each exposure level: 90 kBq/mL (A), 30 kBq/mL (B), and 2 kBq/mL (C) equivalent for selected dataset using ME collimator, 240-keV window, AC, SC, and 12-mm gaussian filter. Exposure-normalized count rates are shown on left axis, and absolute number of counts are shown on right axis. Dashed segments signify reconstructions where spheres did not show local intensity maximum. Supplemental Figures 11–14 show further panels. OSEM = ordered-subsets expectation maximization.

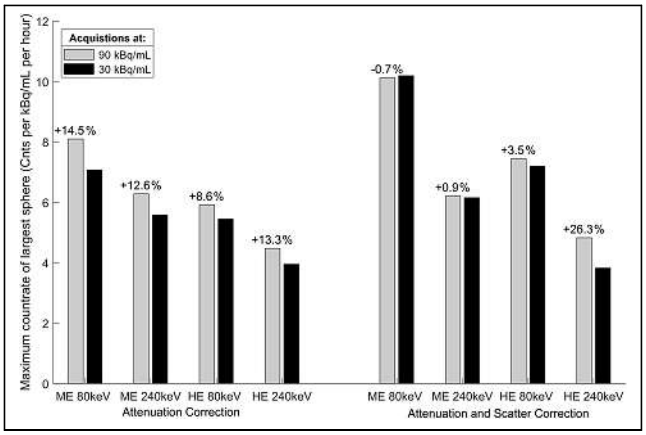

FIGURE 5. Comparison of maximum voxel count rate in largest sphere at 90 kBq/mL (gray) and 30 kBq/mL (black). Difference in normalized count rates at 90 kBq/mL relative to 30 kBq/mL is shown on top of bars. Acquisitions were reconstructed using optimal settings at 30 kBq/mL for both concentrations.

DISCUSSION

We have here established a scheme to optimize independently each combination of collimator, energy window, postprocessing filter, and use of SC for different concentrations of ^{224}Ra in equilibrium with daughters, before comparison. Here, the ME collimator with the 240-keV energy window and SC outperformed all other protocols, with SSRs 2–3 times higher than any other combination. Overall, the phantom study shows that tomographic imaging of ^{224}Ra in equilibrium with daughters is possible even with low activity. The main contributors to image information are ^{212}Pb and daughters; therefore, the findings may be relevant for imaging of ^{212}Pb as well.

All 4 combinations of collimators and energy windows were capable of reproducing activity distribution with acceptable accuracy. The maximum number of visible spheres is comparable, but the optimal ordered-subset expectation maximization settings vary, as do the resulting visual texture, contrast, and counts. The most significant factor in the protocol was the use of SC, which was preferable in terms of SSR for all acquisitions, but the ME collimator with the 240-keV window benefited the most (Fig. 6). Overall, we recommend this combination, but the smallest sphere was slightly more visible than with other protocols yet was never clearly defined above the noise floor (SSR < 1). When only HE collimators are available and only the major hot spots are of interest, we suggest using SC. When both weak and strong uptake is important, non–scatter-corrected images may also be produced to visualize the smallest nuclide deposits. Our results suggest that 80- and 240-keV images provide similar SSRs for the HE collimator. Because 80-keV imaging gave higher maximum values, it might be preferable for medium-sized and small patients, but 240 keV is expected to deteriorate less in larger patients. In addition, the scatter triple-energy-window correction appears more accurate for 240 keV, as shown by the Monte Carlo simulations.

In our relevant clinical setting, we expect no or extremely low amounts of activity adjacent to the peritoneal cavity where ^{224}Ra therapeutics would be delivered, and no activity was added in the background compartment of the phantom. It can be argued that this is an idealized setup. Still, a high number of counts was reconstructed in the background because of scatter. This led to the definition of SSR to determine image quality instead of more common measures such as signal-to-noise ratio, which often measures noise in a homogeneous background region. SSR is directly interpretable as the contrast ratio between lesions and

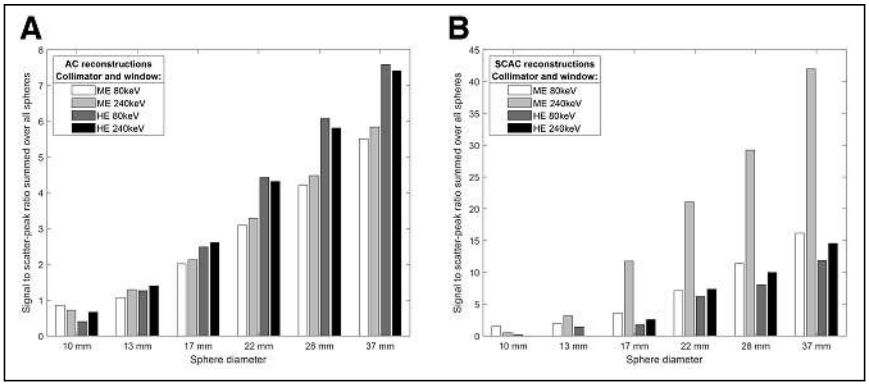

FIGURE 6. Comparison of maximized aggregated SSR values for each collimator and energy window combination, reconstructed without (A) and with (B) SC. Scatter-corrected images have higher SSRs and are plotted on wider scale. SCAC = Scatter and attenuation corrected.

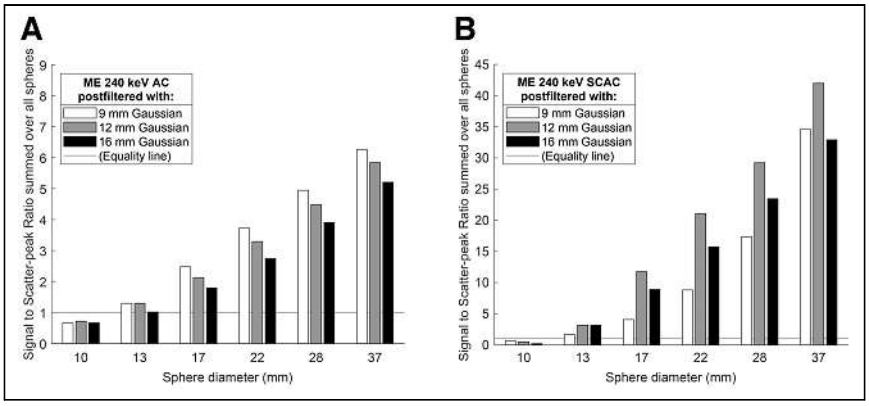

FIGURE 7. Effect of gaussian postprocessing filter widths on resulting SSRs, for example, setting with ME collimator and 240-keV window, each at individually optimal number of ordered-subset expectation maximization updates. Reconstruction without (A) and with (B) SC. Supplemental Figure 8 shows further panels. SCAC = Scatter and attenuation corrected.

scatter-induced noise peaks. During optimization, we weighted the SSR of each sphere size equally, which might not be favorable in all clinical circumstances. For specialized uses, conclusions may be drawn from the plotted results (Supplemental Figs. 4–8 and 11–15).

In most cases, SSR was optimized at high iterations, in particular without SC, where several datasets maximized the SSR at 900 updates, the software upper limit (Table 3; Supplemental Figs. 2 and 3). We found that the 9-mm filter (the smallest used) provided the best SSR in nearly all instances, despite high iterations. Our results do not provide a clear recommendation for postprocessing filters but indicate that, depending on the clinical purpose, heavy filtering should be used cautiously. For lower activity, the SSR was typically maximized at lower ordered-subset expectation maximization updates. In particular, the scan equivalent to 2 kBq/mL maximized SSR at only 12 iterations. However, the largest sphere typically achieved convergence after 20–30 iterations, and fewer iterations than this should likely be avoided (Fig. 4; Supplemental Figs. 11–14). Visually, the scan equivalent to 2 kBq/mL also holds up well in this range; encouragingly, the visibility of spheres 3 and 4 increased compared with that of 12 iterations (Supplemental Figs. 9 and 10).

The smallest imageable activity appears to be limited by the resulting desired intensity range of images as the maximum value decreases toward zero. The observed sensitivity values for maximum measurements indicate that to obtain 10 counts in the maximum voxel with a 30-min scan duration, larger lesions need a concentration of about 3–5 kBq/mL and smaller lesions need total activity of about 4 kBq with the suggested protocol. Imaging at the equivalent of 2 kBq/mL confirms that this is achievable, at least for larger spheres. In a therapeutic setting, a steady-state concentration of 4 kBq/mL corresponds to cumulative absorbed doses of up to 8.2 and 0.31 Gy for ^{224}Ra and ^{212}Pb, respectively, assuming no relocalization (*8*). Thus, the imageable range encompasses most of the therapeutic range for tumors, although with respect to normal tissues, a negative scan might not be enough to rule out toxicity. The Monte Carlo simulations show that most scattered photons originate in the collimators, not the phantom. This means that activity in the patient easily may contribute to degraded image quality and reduce the visibility of low-concentration deposits, possibly even at large distances. Consequently, the total amount of activity in the patient may be a limiting factor for low-activity detection.

Although phantom studies are a convenient way of determining an imaging protocol before a trial, phantom imaging is highly simplified compared with in vivo patient imaging. We believe that the overall trade-offs of different collimators, energy windows, and SC application will remain similar for this system, but parameters such as iterations and postfilters should be revisited for each clinical context, given the large variation in use for these nuclides. In the context of the 2 phase 1 trials for intraperitoneal administration of ^{224}Ra adsorbed in calcium carbonate microparticles, most activity is assumed to be retained within a single bed position without physiologic washout, hence the high starting concentrations in the study design. For the same reason, the study was performed without background in the phantom. Depending on the time of imaging and the location of the VOI—whether a lesion or organs at risk—this needs to be considered, because a blood-pool background or parenchymal uptake will complicate partial-volume effects and reduce visibility, adding the challenge of contrast to that of imaging at low concentrations. The results are most easily interpretable for high-contrast lesions and organs at risk. We have not directly evaluated the possibility of quantitative imaging for dosimetry purposes, but our results indicate that this may be possible (Fig. 5). One should always be aware of the clinical limitations of imaging a selection of nuclides (or a single nuclide) of a decay chain, because this introduces possible relocalization between therapeutic dose deposition and imaging. Although separation of ^{227}Th from ^{223}Ra has been attempted by spectral decomposition of different windows (*15*), the relative amount of photons emitted from pre-^{212}Pb nuclides in the decay chain of ^{224}Ra is probably not sufficient for similar investigations in either window (Tables 1 and 2). Therefore, potential relocalization between ^{224}Ra and ^{212}Pb will need investigation with supplementary methods (such as blood sampling) in the clinical trials.

CONCLUSION

The results indicate that low counts are fairly unproblematic for the reconstruction algorithm. The detection limit appears to be in the region of 1–10 kBq/mL with 30-min acquisitions for ^{224}Ra and, by extension, ^{212}Pb. The HE photons from ^{208}Tl produce high amounts of scatter in the collimators, explaining the observed importance of SC. The best results were obtained with the ME collimator.

DISCLOSURE

No potential conflict of interest relevant to this article was reported.

KEY POINTS

QUESTION: Is clinical SPECT imaging of ^{224}Ra- and ^{212}Pb-based α-particle therapy possible?

PERTINENT FINDINGS: The results show meaningful image quality at clinically relevant concentrations. We provide recommendations for an optimized imaging protocol.

IMPLICATIONS FOR PATIENT CARE: The use of SPECT/CT to verify tumor or normal tissue uptake of α-emitters greatly simplifies imaging endpoints in clinical studies.

REFERENCES

1. Sgouros G, Bodei L, McDevitt MR, Nedrow JR. Radiopharmaceutical therapy in cancer: clinical advances and challenges. *Nat Rev Drug Discov.* 2020;19: 589–608.
2. Pacilio M, Ventroni G, De Vincentis G, et al. Dosimetry of bone metastases in targeted radionuclide therapy with alpha-emitting (^{223})Ra-dichloride. *Eur J Nucl Med Mol Imaging.* 2016;43:21–33.
3. Hindorf C, Chittenden S, Aksnes AK, Parker C, Flux GD. Quantitative imaging of ^{223}Ra-chloride (Alpharadin) for targeted alpha-emitting radionuclide therapy of bone metastases. *Nucl Med Commun.* 2012;33:726–732.
4. Sgouros G, Frey E, Du Y, Hobbs R, Bolch W. Imaging and dosimetry for alpha-particle emitter radiopharmaceutical therapy: improving radiopharmaceutical therapy by looking into the black box. *Eur J Nucl Med Mol Imaging.* 2021;49:18–29.
5. Cordier D, Forrer F, Bruchertseifer F, et al. Targeted alpha-radionuclide therapy of functionally critically located gliomas with ^{213}Bi-DOTA-[Thi^{8},Met$(O_2)^{11}$]-substance P: a pilot trial. *Eur J Nucl Med Mol Imaging.* 2010;37:1335–1344.
6. Gosewisch A, Schleske M, Gildehaus FJ, et al. Image-based dosimetry for (^{225})Ac-PSMA-I&T therapy using quantitative SPECT. *Eur J Nucl Med Mol Imaging.* 2021;48:1260–1261.
7. Müller C, Vermeulen C, Köster U, et al. Alpha-PET with terbium-149: evidence and perspectives for radiotheragnostics. *EJNMMI Radiopharm Chem.* 2017;1:5.
8. Eckerman K, Endo A. ICRP publication 107. Nuclear decay data for dosimetric calculations. *Ann ICRP.* 2008;38:7–96.
9. Westrøm S, Malenge M, Jorstad IS, et al. Ra-224 labeling of calcium carbonate microparticles for internal alpha-therapy: preparation, stability, and biodistribution in mice. *J Labelled Comp Radiopharm.* 2018;61:472–486.
10. Meredith RF, Torgue J, Azure MT, et al. Pharmacokinetics and imaging of ^{212}Pb-TCMC-trastuzumab after intraperitoneal administration in ovarian cancer patients. *Cancer Biother Radiopharm.* 2014;29:12–17.
11. Sarrut D, Bardies M, Boussion N, et al. A review of the use and potential of the GATE Monte Carlo simulation code for radiation therapy and dosimetry applications. *Med Phys.* 2014;41:064301.
12. Jan S, Santin G, Strul D, et al. GATE: a simulation toolkit for PET and SPECT. *Phys Med Biol.* 2004;49:4543–4561.
13. Rault E, Staelens S, Van Holen R, De Beenhouwer J, Vandenberghe S. Accurate Monte Carlo modelling of the back compartments of SPECT cameras. *Phys Med Biol.* 2011;56:87–104.
14. Robinson AP, Tipping J, Cullen DM, Hamilton D. The influence of triple energy window scatter correction on activity quantification for ^{177}Lu molecular radiotherapy. *Phys Med Biol.* 2016;61:5107–5127.
15. Murray I, Rojas B, Gear J, Callister R, Cleton A, Flux GD. Quantitative dual-isotope planar imaging of thorium-227 and radium-223 using defined energy windows. *Cancer Biother Radiopharm.* 2020;35:530–539.

^{161}Tb-DOTATOC Production Using a Fully Automated Disposable Cassette System: A First Step Toward the Introduction of ^{161}Tb into the Clinic

Chiara Favaretto[1,2], Pascal V. Grundler[1], Zeynep Talip[1], Stefan Landolt[1], Lebogang Sepini[3], Ulli Köster[4], Cristina Müller[1], Roger Schibli[1,2], Susanne Geistlich[1], and Nicholas P. van der Meulen [1,5]

[1]*Center for Radiopharmaceutical Sciences, ETH–Paul Scherrer Institute, Villigen-PSI, Switzerland;* [2]*Department of Chemistry and Applied Biosciences, ETH, Zurich, Switzerland;* [3]*Radiochemistry, South African Nuclear Energy Corp., Brits, South Africa;* [4]*Institut Laue-Langevin, Grenoble, France; and* [5]*Laboratory of Radiochemistry, Paul Scherrer Institute, Villigen-PSI, Switzerland*

^{161}Tb is an interesting radionuclide for application in the treatment of neuroendocrine neoplasms' small metastases and single cancer cells because of its conversion and Auger-electron emission. Tb has coordination chemistry similar to that of Lu; therefore, like ^{177}Lu, it can stably radiolabel DOTATOC, one of the leading peptides used for the treatment of neuroendocrine neoplasms. However, ^{161}Tb is a recently developed radionuclide that has not yet been specified for clinical use. Therefore, the aim of the current work was to characterize and specify ^{161}Tb and to develop a protocol for the synthesis and quality control of ^{161}Tb-DOTATOC with a fully automated process conforming to good-manufacturing-practice guidelines, in view of its clinical use. **Methods:** ^{161}Tb, produced by neutron irradiation of ^{160}Gd in high-flux reactors followed by radiochemical separation from its target material, was characterized regarding its radionuclidic purity, chemical purity, endotoxin level, and radiochemical purity (RCP) in analogy to what is described in the European Pharmacopoeia for no-carrier-added ^{177}Lu. In addition, ^{161}Tb was introduced into a fully automated cassette-module synthesis to produce ^{161}Tb-DOTATOC, as used for ^{177}Lu-DOTATOC. The quality and stability of the produced radiopharmaceutical in terms of identity, RCP, and ethanol and endotoxin content were assessed by means of high-performance liquid chromatography, gas chromatography, and an endotoxin test, respectively. **Results:** ^{161}Tb produced under the described conditions showed, as the no-carrier-added ^{177}Lu, a pH of 1–2, radionuclidic purity and RCP of more than 99.9%, and an endotoxin level below the permitted range (175 IU/mL), indicating its appropriate quality for clinical use. In addition, an efficient and robust procedure for the automated production and quality control of ^{161}Tb-DOTATOC with clinically applicable specifications and activity levels, that is, 1.0–7.4 GBq in 20 mL, was developed. The radiopharmaceutical's quality control was also developed using chromatographic methods, which confirmed the product's stability (RCP $\geq$ 95%) over 24 h. **Conclusion:** The current study demonstrated that ^{161}Tb has appropriate features for clinical use. The developed synthesis protocol guarantees high yields and safe preparation of injectable ^{161}Tb-DOTATOC. The investigated approach could be translated to other DOTA-derivatized peptides; thus, ^{161}Tb could be successfully applied in clinical practice for radionuclide therapy.

Key Words: ^{161}Tb; specifications; DOTATOC; GMP compliant; automated

J Nucl Med 2023; 64:1138–1144
DOI: 10.2967/jnumed.122.265268

In recent years, peptide receptor radionuclide therapy (PRRT) has emerged as an option in metastatic or nonresectable neuroendocrine neoplasms (NENs) expressing high levels of somatostatin receptor (*1,2*). DOTATOC and DOTATATE are most commonly used for PRRT in NENs (*3*). In particular, in the neuroendocrine tumors therapy phase 3 randomized trial (*4*), ^{177}Lu-DOTATATE treatment was confirmed as effective in tumor control with only minor side effects. It was approved by the European Medicines Agency in 2017 and the U.S. Food and Drug Administration in 2018 (Lutathera; Advanced Accelerator Applications) for the treatment of well-differentiated gastroenteropancreatic NENs (*5,6*). Despite its efficacy, studies have since shown partial remission of no more than 50%, with complete response of no more than 18% (*4,7,8*). The radionuclide ^{161}Tb (Mean β^- energy, 154 keV [100%]; half-life, 6.96 d) (*9,10*) is proposed as a potential alternative to ^{177}Lu (Mean β^- energy, 134 keV [100%]; half-life, 6.65 d) (*11*) because of their similar physical decay characteristics with regard to β^--particle emission, suitability for PRRT, and concomitant emission of photons, which can be used for SPECT imaging purposes (Table 1) (*12,13*). In addition, Tb has similar coordination chemistry to Lu (*14*); therefore, it can be stably coordinated with a DOTA chelator and respective tumor-targeting peptides, for example, DOTATOC or DOTATATE. ^{161}Tb is regarded as superior to ^{177}Lu because it coemits a substantial number of conversion and Auger electrons ($\sim$12 e^-, $\sim$37 keV per decay for ^{161}Tb, $\sim$1 e^- and $\sim$1.0 keV per decay for ^{177}Lu, respectively) (*9,11,13*), which would be more effective in the treatment of the smallest metastases, as well as single cancer cells (*13,15–19*). ^{161}Tb production for radiopharmaceutical application was developed and is regularly performed at the Paul Scherrer Institute. It is produced by neutron irradiation of enriched ^{160}Gd targets. The separated ^{161}Tb product yields $^{161}TbCl_3$ in a quality suitable for highly specific radiolabeling, which is useful for preclinical applications (*13,18–20*). At a clinical level, phantom studies were performed that demonstrated the feasibility of imaging ^{161}Tb in high resolution when using low-energy, high-resolution collimators (*21*); a first-in-humans study was also

Received Nov. 29, 2022; revision accepted Mar. 1, 2023.
For correspondence or reprints, contact Nicholas P. van der Meulen (nick.vandermeulen@psi.ch).
Published online May 18, 2023.

TABLE 1
^{161}Tb Specifications Until Shelf-Life Expiration Date (9 Days After End of Separation)

Characteristic	Test	$^{161}TbCl_3$ specification
Appearance	Visual inspection	Clear and colorless solution
Identity	γ-spectrometry (keV)	74.6 ± 1, 87.9 ± 1, 103.1 ± 1, 106.1 ± 1, 292.4 ± 1, and 550.3 ± 1
pH	pH paper	1–2
Chemical purity	ICP-MS (μg/GBq)	Cu: <1.0
		Fe: <0.5
		Pb: <0.5
		Zn: <1.0
Sterility		Not required
Bacterial endotoxins	LAL test	<175 IU/mL (injectable dose)
Radionuclidic purity	γ-spectrometry	^{160}Tb ≤ 0.1%
RCP	TLC	≥99.0% as $^{161}TbCl_3$

ICP-MS = inductively coupled plasma–mass spectrometry; LAL = *Limulus* amebocyte lysate; TLC = thin-layer chromatography.

conducted (*22*). The next step in the development of this radionuclide toward medical application is its introduction into drug manufacture under good manufacturing practice (GMP) to be able to demonstrate the higher efficacy of ^{161}Tb-based radiopharmaceuticals than of ^{177}Lu-labeled counterparts in clinical trials. An approach to demonstrate the sufficient quality of the $^{161}TbCl_3$ solution for clinical purposes was to compare it with the specifications of commercially available no-carrier-added $^{177}LuCl_3$, because the latter is approved for the preparation of several radiopharmaceuticals for clinical studies (*4,23*). One purpose of this study was to characterize ^{161}Tb for clinical use. After this assessment, a protocol for the production of ^{161}Tb-DOTATOC was developed, conforming to GMP principles, on an automated synthesis module.

MATERIALS AND METHODS

^{161}Tb Production and Quality Control (QC)

^{161}Tb was produced by neutron irradiation of enriched $^{160}Gd_2O_3$ targets (98.2% enrichment; Isoflex; Supplemental Table 1 [supplemental materials are available at http://jnm.snmjournals.org]), via the $^{160}Gd(n,\gamma)^{161}Gd \rightarrow {}^{161}Tb$ nuclear reaction at the South African Fundamental Atomic Research Installation (South African Nuclear Energy Corp.; $\sim 2 \cdot 10^{14}$ n·cm^{-1}·s^{-1} neutron flux) or the Institut Laue-Langevin's High Flux Reactor ($\sim 1 \cdot 10^{15}$ n·cm^{-1}·s^{-1} neutron flux). The quartz ampoule, containing the irradiated target material, was processed at the Paul Scherrer Institute for radiochemical separation of the produced ^{161}Tb from the target material, as described previously (*20*). An approach to demonstrate the high quality of the $^{161}TbCl_3$ product was to compare it with the specifications of commercially available no-carrier-added ^{177}Lu, approved for the preparation of radiopharmaceuticals for clinical studies, described in the European Pharmacopoeia (Ph. Eur.) monograph (*24*).

Identity, pH, and Radionuclidic Purity. The identification and radionuclidic purity of ^{161}Tb were examined by γ-spectrometry using a high-purity germanium detector (Canberra), in combination with the InterWinner software package (version 7.1; Itech Instruments; supplemental materials and Supplemental Fig. 1). The choice of γ-rays used for a reliable radionuclide identification accounted for possible interferences from other radionuclides that could create artifacts (supplemental materials). The pH of the $^{161}TbCl_3$ solution was assessed by means of pH paper.

Chemical Purity. The chemical purity of the $^{161}TbCl_3$ solution was assessed via inductively coupled plasma–mass spectrometry (Element HR; Thermo Fisher Scientific; supplemental materials). Four batches of ^{161}Tb were analyzed after the radiochemical purification for contents of Cu, Fe, Pb, Zn, Gd, and Tb, as described in the Ph. Eur. monograph for ^{177}Lu (*24*). The purity was also investigated in all 7 ^{161}Tb productions performed during this study by means of apparent molar activity (AMA) determination through hand-operated labeling of the product to DOTATOC (supplemental materials), as described elsewhere (*13,20*).

Endotoxin Level. Because ^{161}Tb is considered a radiopharmaceutical precursor, the bacterial endotoxin level needs to be tested. Pyrogens were tested according to Ph. Eur. standards using a chromogenic *Limulus* amebocyte lysate test (supplemental materials) (*25*). In the evaluation of the endotoxin level, international units per milliliter were used, considering that the unit used in the Ph. Eur. monograph is international units per volume, indicating the maximum volume to be used for the preparation of a single patient dose, which corresponds to 1 mL of ^{161}Tb (maximum volume at the end of separation).

Radiochemical Purity (RCP). The RCP of 3 ^{161}Tb batches was assessed by thin-layer chromatography, as described in the Ph. Eur. monograph for ^{177}Lu (supplemental materials) (*24*). Quantification of the thin-layer chromatography signals with the indicated software enabled the determination of the area of the peak of ^{161}Tb in ionic form (R_f = 0.4–0.7), over the total activity.

Automated Synthesis of ^{161}Tb-DOTATOC

Ten syntheses of ^{161}Tb-DOTATOC were performed using a Modular-Lab PharmTracer fully automated cassette synthesis system (Eckert & Ziegler; Fig. 1A), installed in a hot cell so that high activities of the radionuclide could be manipulated with no radiation dose exposure to the operator. For each synthesis, the sterile synthesis cassettes were prepared with the necessary reagents and attached to the Modular-Lab's synthesis module (supplemental materials). A synthesis protocol was adequately adapted and optimized, and the production of ^{161}Tb-DOTATOC was run by the Modular-Lab PharmTracer software (Modular-Lab SoftPLC; Eckert & Ziegler), which provided a graphical display of each step and the progress of the synthesis together with audit trail as required by GMP (Fig. 1B) (*26,27*). To ensure sterility, the final product was finally passed through a 0.22-μm filter (Medical Millex-GV Syringe Filter, Hydrophilic Polyvinylidene Fluoride,

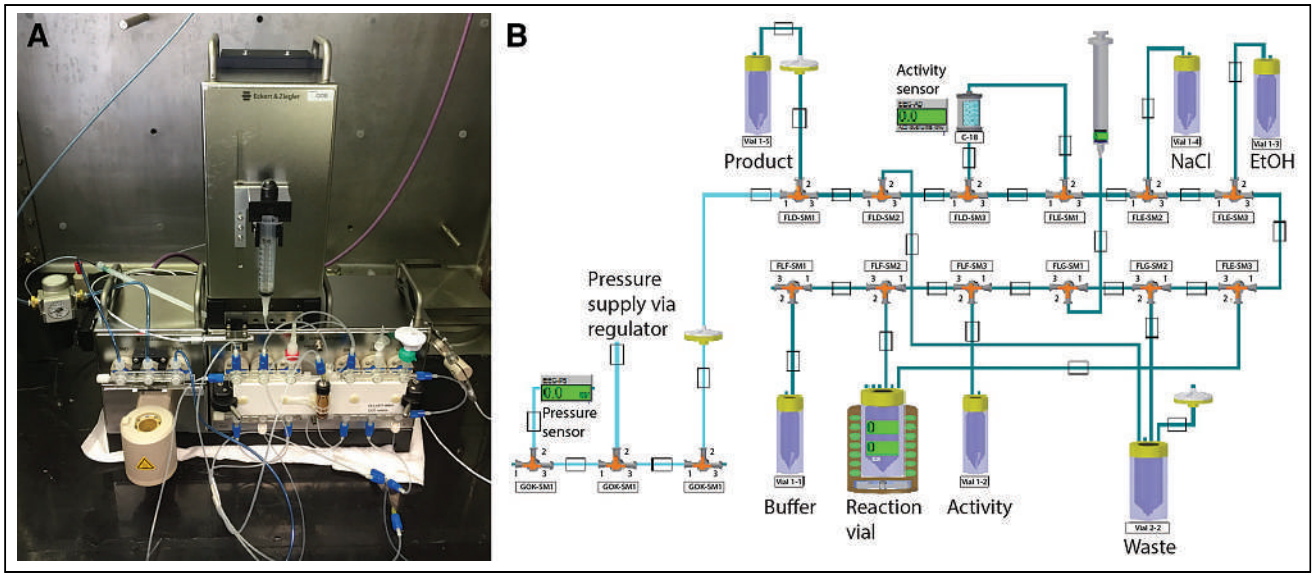

FIGURE 1. (A) Eckert & Ziegler Modular-Lab PharmTracer fully automated cassette synthesis system. (B) Graphical display of cassette components and synthesis process.

γ-sterilized; Merck Millipore). At the end of the synthesis, the final product activity and the residual radioactivity remaining in the principal components (activity vial, reaction vial, C18 cartridge, and waste) were measured (Isomed Dose Calibrator 2010) (*28*). Aliquots were withdrawn from the total volume for QC purposes.

^{161}Tb-DOTATOC QC

High-Performance Liquid Chromatography (HPLC). QC was performed to determine the RCP of ^{161}Tb-DOTATOC, as well as the identification of the compound and possible impurities, by means of HPLC (Dionex P680 LGP Pump). First, the retention times of the product peaks in the radiochromatogram and UV chromatogram were assessed (Supplemental Figs. 2 and 3). Eventually, during the QC of ^{161}Tb-DOTATOC, 20 μL of the synthesis product were analyzed by means of HPLC to estimate the RCP of ^{161}Tb-DOTATOC from the HPLC radiodetector chromatogram and to identify the compound and possible impurities in the UV chromatogram.

Further evaluations of the method were performed to investigate the suitability and robustness of the QC. In particular, the linearity, limit of detection, and limit of quantification for both the radiodetector and the UV detector were assessed (Supplemental Fig. 4), together with the setup of a system suitability test (Supplemental Fig. 5).

Gas Chromatography. The ethanol content in the synthesis product was assessed by means of gas chromatography. The quantification of ethanol was based on the acetonitrile internal standard (supplemental materials). The linearity of the gas chromatography method was assessed by linear regression analysis for 6 ethanol concentrations between 1% and 15% (Supplemental Fig. 6).

Sterility and Endotoxin Level. Although the synthesis was not performed under GMP-compliant clean conditions, the pyrogenicity of the product and the integrity of the sterilization filter were evaluated to assess the suitability of the methods and to prove the acceptable quality of ^{161}Tb-DOTATOC. Pyrogens were tested according to

TABLE 2
^{161}Tb Activity at EOS ^{161}Tb Activity and Measured Before and at End of Synthesis for Each ^{161}Tb-DOTATOC Production

Activity EOS (GBq)	Labeling yield at 100 MBq/nmol AMA (%)	Synthesis	Initial activity (GBq)	Bulk product activity (GBq)	Production yield (%)
13.4	99.9	1	1.29	1.12	86.8
		2	1.16	1.08	93.1
15.3	99.9	3	1.19	1.13	95.0
15.2	100	4	8.80	8.77	99.7
5.78	68.0	5	1.33	1.25	94.0
		6	2.87	2.79	97.2
11.7	99.9	7	9.26	8.92	96.3
11.8	99.7	8	9.17	9.08	99.0
14.3	100	9	9.39	9.26	98.6
		10	1.56	1.50	96.2

EOS = end of separation.

TABLE 3
Composition of ^{161}Tb-DOTATOC (bulk product)

Characteristic	Data
Range of ^{161}Tb activity (shelf-life expiration date)	1–7.4 GBq
Volume	24 mL
DOTATOC and metal complexes	1 μg/37 MBq (maximum, 200 μg)
Calcium-DTPA	19.5 mg (0.1 mL, 195 mg/mL)
Ascorbic acid	250 mg (2.5 mL, 100 mg/mL)
Ethanol	1.25 mL (2.5 mL, ethanol 50%)
Saline	19 mL

DTPA = diethylenetriaminepentaacetic acid.
All syntheses produced ^{161}Tb-DOTATOC within ±10% of stated parameters.

Ph. Eur. standards with a chromogenic *Limulus* amebocyte lysate test, as described earlier for the endotoxin test on the $^{161}TbCl_3$ solution (*25*).

To ensure the integrity of the sterilization filter used at the end of the synthesis, a bubble point test was developed. The threshold value of the pressure depends on the matrix of the sterilized solution; therefore, it was assessed for the product in question (supplemental materials) (*29*). The bubble point test was then performed on the filter used during the synthesis of the batch tested for bacterial endotoxins.

Stability. The stability of the synthesis product, ^{161}Tb-DOTATOC, was tested in both normal and stress conditions. To establish the stability of the radiolabeled peptide, all synthesized batches of ^{161}Tb-DOTATOC were stored at room temperature and the RCP was assessed 3 and 24 h after synthesis. In addition, 1 batch of DOTATOC radiolabeled with high activity (8.77 GBq) was stored at room temperature for 96 h and the RCP was assessed by means of HPLC every 24 h with the method described earlier. After 96 h at room temperature, the product was incubated at 40 °C for an additional 72 h and HPLC analyses were conducted every 24 h.

RESULTS

^{161}Tb Production and QC

Multiple productions of ^{161}Tb were analyzed, compared with the Ph. Eur. monograph for ^{177}Lu, and found to comply with all requirements (Table 1).

Radionuclidic Purity. The content of the long-lived impurity ^{160}Tb (half-life, 72.3 d) (*30*) was less than 0.005% of the total ^{161}Tb activity at end of bombardment (EOB), as reported previously by our group (*20*). Three weeks after EOB, the level of ^{160}Tb was still no more than 0.03% (Supplemental Fig. 1; Supplemental Table 2). Therefore, the specification for radionuclidic purity, which must apply until the end of shelf life, was prudently proposed for ^{160}Tb at a level of 0.1%. With this level of impurity, the additional radiation dose to the patient was estimated to be about 0.4% (supplemental materials) (*31*).

Chemical Purity. The content of Cu, Fe, Pb, and Zn measured in the ^{161}Tb samples was far below the limit for metal impurities reported for ^{177}Lu (Supplemental Table 3). The Gd content was less than 0.4 ppm. Moreover, 6 of the 7 ^{161}Tb productions were tested for AMA and successfully labeled DOTATOC at 100 MBq/nmol. Even so, the ^{161}Tb production that allowed labeling of only the lower AMA was sufficiently pure to be used for ^{161}Tb-DOTATOC synthesis (Table 2). Thanks to Tb quantification, the specific activity was also calculated and resulted in values greater than 3.5 GBq/μg.

Endotoxin Level. The endotoxin content of the 3 batches tested was less than 1.20, 1.00, and 1.65 IU/mL, respectively, considerably lower than the requirement of less than 175 IU/mL.

RCP. In all productions tested, the peak of ^{161}Tb in ionic form (R_f = 0.4–0.7) over the total activity (^{161}Tb-diethylenetriaminepentaacetic acid, R_f = 0.9) was above 99.0%, thereby allowing the RCP of ^{161}Tb to be established as greater than 99.0%.

Automated Synthesis of ^{161}Tb-DOTATOC

Ten preparations of ^{161}Tb-DOTATOC were performed and form part of this work. For all syntheses, the ^{161}Tb-labeled radioactivity at the shelf-life expiration date was in the range from 1 to 7.4 GBq ± 10%, which was the target to obtain a product comparable to a patient dose for ^{177}Lu-DOTATOC (*32*). In particular, 5 syntheses produced ^{161}Tb-DOTATOC with the minimum activity, 4 syntheses produced ^{161}Tb-DOTATOC with the maximum activity, and 1 synthesis produced ^{161}Tb-DOTATOC with intermediate activity (Table 2). The AMA was maintained at a constant of approximately 50 MBq/nmol, varying the peptide amount from 27 μg to a maximum of 200 μg (*32*). The duration of the process was approximately 45 min, and the total volume of the bulk product at the end of the synthesis was 24 mL, of which 4 mL were intended for QC and 20 mL were intended as final product. The final formulation was established in analogy to that of ^{177}Lu-DOTATOC (Table 3).

Residual radioactivity was detected in the activity vial, the reaction vial, the C18 cartridge, and the waste (Supplemental Table 4). Unlike the bulk product and initial activity measurements, which were performed with appropriate calibration for each container (*28*), the residual activity measurements were not comparable to

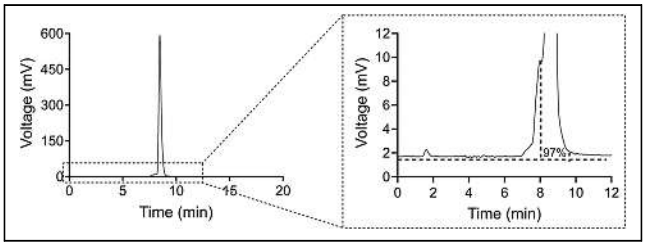

FIGURE 2. Representative HPLC radiochromatogram of high-activity batch of ^{161}Tb-DOTATOC with RCP of 97.0% (1.6-min retention time would indicate ^{161}Tb-diethylenetriaminepentaacetic acid, whereas 8.5 min indicates ^{161}Tb-DOTATOC).

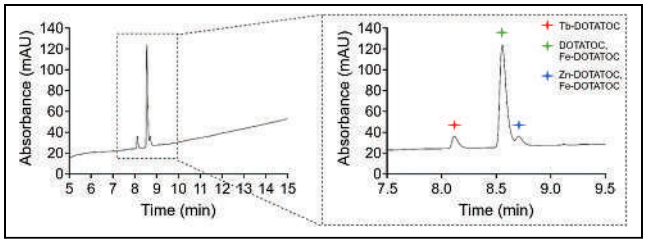

FIGURE 3. Representative HPLC UV chromatogram obtained during QC of synthesis product. Product peaks (DOTATOC, Tb-DOTATOC, Fe-DOTATOC, and Zn-DOTATOC) were identified, and no other peaks (impurities) were observed. milli Absorbance Unit.

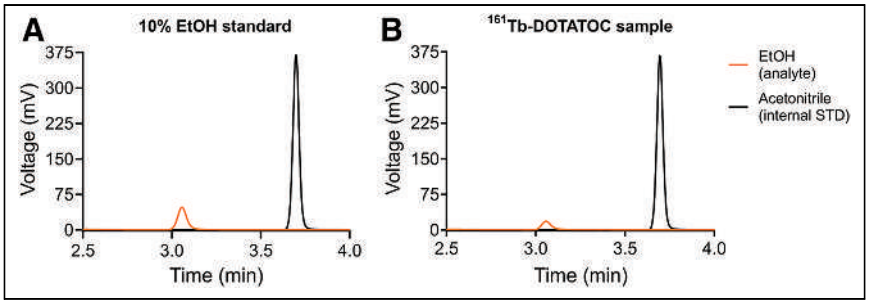

FIGURE 4. Representative gas chromatograms of 10% ethanol standard solution (A) and of sample of synthesis product (B). In both solutions, acetonitrile was added as internal standard (STD).

one another, or to the initial activity, because of the distinct geometries of the samples. Nevertheless, the measurements indicated losses mainly in the waste or because of bound activity on the C18 cartridge. However, a total yield of more than 85% of ^{161}Tb-DOTATOC, in reference to the initial ^{161}Tb activity, was determined (Table 2).

^{161}Tb-DOTATOC QC

The synthesis product complied with the established specifications (Table 4).

HPLC. The results of the HPLC analysis of the synthesis products demonstrated that the RCP of ^{161}Tb-DOTATOC was, on average, approximately 98% at the end of synthesis ($n = 10$; 98.2% ± 0.82; Supplemental Table 5), which meets the 95% specification level normally applied to these types of products (Fig. 2) (*33,34*).

The UV chromatograms showed low levels or complete nonappearance of impurities. The peaks of the unlabeled peptide (DOTATOC), together with those of Tb-DOTATOC, Fe-DOTATOC, and Zn-DOTATOC, established during the development of the HPLC method, were identified during the QC of the synthesis product and considered product peaks (Fig. 3).

Gas Chromatography. The ethanol content in the synthesis product was demonstrated to be less than 10%, which is the acceptable limit for radiopharmaceutical preparation for intravenous injection (*35*). In particular, the area of the ethanol peak in the analyzed sample of the synthesis product was normalized to the internal standard peak area and then compared with the normalized area of the ethanol peak in the 10% ethanol standard solution. In Figure 4, the ethanol peaks of the standard solution and the synthesis product are visually compared, with the lower ethanol content in the synthesis product displayed.

Sterility and Endotoxin Level. The synthesis resulted in a clear, colorless, particle-free product with a low level of bacterial endotoxins in the batch tested (<6.15 international units/mL). This endotoxin content was compliant with the specification for radiopharmaceutical products defined by the Ph. Eur. monograph (≤175 international units/20 mL) (*25,33*).

Although the sterility of the final product requires further validation, the integrity of the sterilization filter used at the end of the synthesis was successfully proven with a bubble point test. In particular, the bubble point was less than 2.75 bar, as specified for the product matrix (Supplemental Table 6).

Stability. ^{161}Tb-DOTATOC presented RCP of more than 95% up to 24 h for all batches tested ($n = 9$; 97.6% ± 1.0 at 24 h; Supplemental Table 5). In addition, the RCP results of the batch selected for the stability test under stress conditions indicated that ^{161}Tb-DOTATOC was highly stable at room temperature for up to 4 d (Fig. 5A). When the product was incubated at 40 °C, it demonstrated RCP of less than 95% over a period of 48 h, with increased released ^{161}Tb and radiolysis (Fig. 5B).

DISCUSSION

The aim of this work was to characterize ^{161}Tb for clinical use, creating a list of parameters that can be the basis for future official specifications and monographic standards. The study compared ^{177}Lu specifications with ^{161}Tb features, showing that the latter comply with all requirements reported in the Ph. Eur. monograph for ^{177}Lu (*24*). With regard to radionuclidic purity, long-lived ^{160}Tb (half-life, 72.3 d) (*30*) was found as an impurity; it is coproduced by the ^{159}Tb(n,γ)^{160}Tb nuclear reaction, and the multistep reactions on the residual ^{159}Tb, ^{158}Gd, and ^{157}Gd present as impurities in the target material. However, the content did not exceed 0.005% of the total ^{161}Tb activity at EOB. Three weeks after EOB, the ingrowth of ^{160}Tb was still no more than 0.03%. These results were observed in several productions after the irradiation of various amounts of target material with different neutron fluxes. According to previous studies by our group (*20*), the quality of ^{161}Tb in terms of radiolabeling yield and AMA was comparable to that of commercially available ^{177}Lu for 9 d after end of separation. This would prudently set the specifications to a shelf life of 9 d after end of separation and a radionuclidic purity of at least 99.9%. Because the latter would be true until 21 d after EOB, to comply with these specifications, the separation cannot be performed later than 12 d after EOB. However, these assumptions may no longer appear to be true if the target material has a different enrichment level from that used in this study; hence, more research is foreseen to examine this subject in greater detail. In addition, our earlier reports on the radiolabeling yield were supported by the results from this study with regard to ^{161}Tb chemical purity and RCP. RCP tests showed that more than 99% of ^{161}Tb was present in the chloride form, which is the expected chemical form after radiochemical separation,

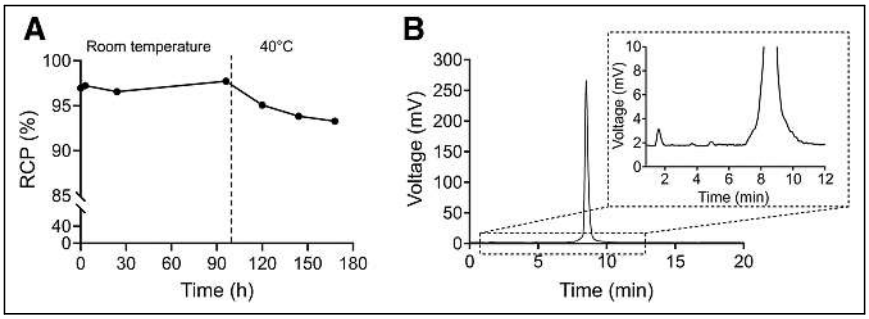

FIGURE 5. (A) ^{161}Tb-DOTATOC (8.77-GBq batch) stability for 4 d at room temperature and additional 3 d at 40 °C. (B) HPLC radiochromatogram of ^{161}Tb-DOTATOC after 48 h at 40 °C (RCP of 93.8%).

TABLE 4
^{161}Tb-DOTATOC Specifications Until Shelf-Life Expiration Date

Characteristic	Test	Specification
Appearance	Visual inspection	Clear, colorless solution, without visible particles
pH	pH paper	4–8
Activity concentration	Dose calibrator	50–370 MBq/mL
RCP	HPLC	≥95%
^{161}Tb-DOTATOC identity	HPLC	Peaks at defined RT in radio- and UV chromatograms
Impurities and degradation products	HPLC	Each impurity ≤ 100 μg/patient dose
Ethanol content	GC	<10%
Bacterial endotoxin level	LAL test	<175 IU/20 mL
Filter integrity (matrix-based)	bubble point test	Bubble point > 2.75 bar
Shelf life		24 h

RT = retention time; GC = gas chromatography.

ensuring its direct use for radiolabeling. In terms of chemical impurities, the tested metals complied with the same requirement as stated for ^{177}Lu. Moreover, only trace amounts of Gd were measured, implying the success of the radiochemical separation from the target material to provide ^{161}Tb with a quality suitable for clinics. The specific activity resulted in more than 3.5 GBq/μg, which is comparable to what was achieved for commercially available no-carrier-added ^{177}Lu (*36*). Because $^{161}TbCl_3$ solution is not intended for direct administration to humans or for use in kit-type products at this stage of development, sterility does not need to be guaranteed (*24*). However, the product needs to be nonpyrogenic; therefore, pyrogens were tested according to Ph. Eur. standards with a chromogenic *Limulus* amebocyte lysate test (*25*), resulting in values below the recommended level.

Taking the preceding observations into consideration, one can see that ^{161}Tb-labeled radiopharmaceuticals can easily be produced and made GMP-compliant for routine clinical use. The production, including synthesis and QC, of ^{161}Tb-DOTATOC, the ^{161}Tb equivalent of the somatostatin analogs currently used with ^{177}Lu in clinical practice (*37,38*), was demonstrated. An Eckert & Ziegler cassette synthesis module, with a modified sequence, was applied to radiolabel DOTATOC with levels of ^{161}Tb radioactivity suitable for a patient dose comparable to that used for ^{177}Lu-DOTATOC, that is, 7.4 GBq in 20 mL (*32*). Ten productions were performed, yielding approximately 50 MBq/nmol AMA with up to 9.3 GBq of ^{161}Tb-DOTATOC produced, which was enough to guarantee the required activity dose for a shelf life of 24 h. Precise activity measurement of ^{161}Tb, which emits γ-radiation mainly with energies below 100 keV, becomes inaccurate with radionuclide dose calibrators used without appropriate calibration factors. An intensive investigation for the calibration of the dose calibrators with the geometries used in the manufacturing process was conducted in collaboration with the certified Institut de Radiophysique and is reported elsewhere (*28*). The 24 h-shelf life was established to reduce the activity use during the development work, but according to the stability studies, it could easily be extended for up to 4 d. The design of the synthesis system was based on disposable and sterilized flow paths that, together with the final filtration through a 0.22-mm filter, are expected to deliver a pharmaceutically adequate product (*33,34*). In addition, during the synthesis, ^{161}Tb-DOTATOC was passed through a C18 cartridge to guarantee the removal of unreacted ^{161}Tb. However, the final formulation contained diethylenetriaminepentaacetic acid to ensure the coordination of possible traces of released ^{161}Tb, which is then quickly eliminated via renal excretion, preventing bone uptake of activity after the administration (*39*). The final product was then tested for RCP and ethanol and endotoxin content, which were determined to be in the acceptable ranges for pharmaceutical preparations. A tendency toward a lower RCP was observed in batches with high activity levels, which may be attributed to the greater activity concentration that caused the peptide to undergo more radiolysis. However, the RCP values for all products were far higher than the criterion for RCP of more than 95%. As a result of these assessments, further purification of the peptide was not required.

CONCLUSION

In the present work, it was demonstrated that ^{161}Tb shows quality standards comparable to those of ^{177}Lu, implying its suitability for potential clinical use. In addition, an efficient and robust procedure for the automated production and QC of ^{161}Tb-DOTATOC was developed using an automated cassette synthesis module and appropriate analytic techniques. The process described was evaluated in accordance with existing guidelines and quality standards. This will form the foundation of monographic standards for this nuclide and further attempts to introduce the use of Tb radioisotopes in clinical applications.

DISCLOSURE

This work was financially supported by the Swiss National Science Foundation (200021_188495) and the NET Research Foundation Petersen Award. No other potential conflict of interest relevant to this article was reported.

ACKNOWLEDGMENTS

We acknowledge Prof. Dr. Jan Rijn Zeevaart for the supervision and arrangement of the neutron irradiations at the South Africa Fundamental Atomic Research Installation facility, as well as Colin C. Hillhouse for technical support in the radiochemical separations. We thank David E. Schmid and Valeria Farsaci for the quality assurance/QC support and Rolf Hesselmann for regulatory counsel. We also

thank Matthias Martin, Dr. Peter Sprung, and Adelheid Fankhauser for the inductively coupled plasma–mass spectrometry analysis and evaluations, as well as Dr. Francesca Borgna for her contribution in the previous work that led to this project. We are grateful to Prof. Dr. Peter Bernhard for his support in the dosimetry calculations.

KEY POINTS

QUESTION: Why is it important to develop a robust production of ^{161}Tb and derived radiopharmaceuticals for the treatment of NENs?

PERTINENT FINDINGS: The newly developed radionuclide ^{161}Tb was characterized for clinical use, and fully automated synthesis of ^{161}Tb-DOTATOC was achieved, showing positive results regarding the safety and quality of the product.

IMPLICATIONS FOR PATIENT CARE: These findings would form the foundation of the introduction of ^{161}Tb for clinical applications in the treatment of NENs, which could improve the outcome of the therapy because of its conversion and Auger electron emission targeting small metastases and single cancer cells.

REFERENCES

1. Modlin IM, Oberg K, Chung DC, et al. Gastroenteropancreatic neuroendocrine tumours. *Lancet Oncol.* 2008;9:61–72.
2. Camus B, Cottereau AS, Palmieri LJ, et al. Indications of peptide receptor radionuclide therapy (PRRT) in gastroenteropancreatic and pulmonary neuroendocrine tumors: an updated review. *J Clin Med.* 2021;10:1267.
3. Kam BLR, Teunissen JJM, Krenning EP, et al. Lutetium-labelled peptides for therapy of neuroendocrine tumours. *Eur J Nucl Med Mol Imaging.* 2012;39(suppl 1): S103–S112.
4. Strosberg J, El-Haddad G, Wolin E, et al. Phase 3 trial of ^{177}Lu-DOTATATE for midgut neuroendocrine tumors. *N Engl J Med.* 2017;376:125–135.
5. Committee for Medicinal Products for Human Use. *Assessment Report: Lutathera.* European Medicines Agency; 2017:1–132. EMA/506460/2017.
6. Food and Drug Administration (FDA), Department of Health and Human Services. NDA Approval 208700 (reference ID 4212675). FDA website. https://www.accessdata.fda.gov/drugsatfda_docs/nda/2018/208700Orig1s000Approv.pdf. Published January 26, 2018. Accessed May 3, 2023.
7. van Essen M, Krenning EP, Bakker WH, De Herder WW, Van Aken MO, Kwekkeboom DJ. Peptide receptor radionuclide therapy with ^{177}Lu-octreotate in patients with foregut carcinoid tumours of bronchial, gastric and thymic origin. *Eur J Nucl Med Mol Imaging.* 2007;34:1219–1227.
8. Sansovini M, Severi S, Ambrosetti A, et al. Treatment with the radiolabelled somatostatin analog ^{177}Lu-DOTATATE for advanced pancreatic neuroendocrine tumors. *Neuroendocrinology.* 2013;97:347–354.
9. Reich CW. Nuclear data sheets for A=161. *Nucl Data Sheets (NY NY).* 2011;112: 2497–2713.
10. Durán MT, Juget F, Nedjadi Y, et al. Determination of ^{161}Tb half-life by three measurement methods. *Appl Radiat Isot.* 2020;159:109085.
11. Kondev FG. Nuclear data sheets for A=177. *Nucl Data Sheets (NY NY).* 2019;159: 1–412.
12. Lehenberger S, Barkhausen C, Cohrs S, et al. The low-energy β^- and electron emitter ^{161}Tb as an alternative to ^{177}Lu for targeted radionuclide therapy. *Nucl Med Biol.* 2011;38:917–924.
13. Müller C, Reber J, Haller S, et al. Direct in vitro and in vivo comparison of ^{161}Tb and ^{177}Lu using a tumour-targeting folate conjugate. *Eur J Nucl Med Mol Imaging.* 2014;41:476–485.
14. Amoroso AJ, Fallis IA, Pope SJA. Chelating agents for radiolanthanides: applications to imaging and therapy. *Coord Chem Rev.* 2017;340:198–219.
15. Hindié E, Zanotti-Fregonara P, Quinto MA, Morgat C, Champion C. Dose deposits from ^{90}Y, ^{177}Lu, ^{111}In, and ^{161}Tb in micrometastases of various sizes: implications for radiopharmaceutical therapy. *J Nucl Med.* 2016;57:759–764.
16. Bernhardt P, Benjegård SA, Kölby L, et al. Dosimetric comparison of radionuclides for therapy of somatostatin receptor-expressing tumors. *Int J Radiat Oncol Biol Phys.* 2001;51:514–524.
17. Bernhardt P, Svensson J, Hemmingsson J, et al. Dosimetric analysis of the short-ranged particle emitter ^{161}Tb for radionuclide therapy of metastatic prostate cancer. *Cancers (Basel).* 2021;13:2011.
18. Müller C, Umbricht CA, Gracheva N, et al. Terbium-161 for PSMA-targeted radionuclide therapy of prostate cancer. *Eur J Nucl Med Mol Imaging.* 2019;46: 1919–1930.
19. Borgna F, Haller S, Monné Rodriguez JM, et al. Combination of terbium-161 with somatostatin receptor antagonists: a potential paradigm shift for the treatment of neuroendocrine neoplasms. *Eur J Nucl Med Mol Imaging.* 2022;49: 1113–1126.
20. Gracheva N, Müller C, Talip Z, et al. Production and characterization of no-carrier-added ^{161}Tb as an alternative to the clinically-applied ^{177}Lu for radionuclide therapy. *EJNMMI Radiopharm Chem.* 2019;4:12.
21. Marin I, Rydèn T, Van Essen M, et al. Establishment of a clinical SPECT/CT protocol for imaging of ^{161}Tb. *EJNMMI Phys.* 2020;7:45.
22. Baum RP, Singh A, Kulkarni HR, et al. First-in-human application of terbium-161: a feasibility study using ^{161}Tb-DOTATOC. *J Nucl Med.* 2021;62:1391–1397.
23. Sartor O, de Bono J, Chi KN, et al. Lutetium-177-PSMA-617 for metastatic castration-resistant prostate cancer. *N Engl J Med.* 2021;385:1091–1103.
24. European Directorate for the Quality of Medicines and Health Care. Lutetium (^{177}Lu) solution for radiolabelling. In: *European Pharmacopoeia.* EDQM; 2020: 1218–1219.
25. European Directorate for the Quality of Medicines and Health Care. Bacterial endotoxins. In: *European Pharmacopoeia.* EDQM; 2020:209–213.
26. European Commission. Good manufacturing practice medicinal products for human and veterinary use. Annex 11: computerised systems. *EudraLex.* 2011;4: 2005–2007.
27. Food and Drug Administration (FDA), Department of Health and Human Services. *Guidance for Industry: Part 11, Electronic Records; Electronic Signatures*. FDA; 2003:1–9.
28. Juget F, Talip Z, Nedjadi Y, et al. Precise activity measurements of medical radionuclides using an ionization chamber: a case study with terbium-161. *EJNMMI Phys.* 2022;9:19.
29. Hayashi K, Douhara K, Kashino G. Evaluation of the bubble point test of a 0.22-μm membrane filter used for the sterilizing filtration of PET radiopharmaceuticals. *Ann Nucl Med.* 2014;28:586–592.
30. Nica N. Nuclear data sheets for A=160. *Nucl Data Sheets (NY NY).* 2021;176: 1–428.
31. Chauvin M, Borys D, Botta F, et al. OpenDose: open-access resource for nuclear medicine dosimetry. *J Nucl Med.* 2020;61:1514–1519.
32. Bodei L, Mueller-Brand J, Baum RP, et al. The joint IAEA, EANM, and SNMMI practical guidance on peptide receptor radionuclide therapy (PRRNT) in neuroendocrine tumours. *Eur J Nucl Med Mol Imaging.* 2013;40:800–816.
33. European Directorate for the Quality of Medicines and Health Care. General monograph: radiopharmaceutical preparations. In: *European Pharmacopoeia.* EDQM; 2020:884–887.
34. European Commission. Good Manufacturing Practice Medicinal Products for Human and Veterinary Use Annex 3 Manufacture of Radiopharmaceuticals. EudraLex; 2008:1–8.
35. Serdons K, Verbuggen A, Bormans G. The presence of ethanol in radiopharmaceutical injections. *J Nucl Med.* 2008;49:2071.
36. Committee for Medicinal Products for Human Use. *Assessment Report: Endolucin-Beta.* European Medicines Agency. 2016:1–58. EMA/404078/2016.
37. Baum RP, Kluge AW, Kulkarni HR, et al. [^{177}Lu-DOTA]^0-D-Phe^1-Tyr^3-octreotide (^{177}Lu-DOTATOC) for peptide receptor radiotherapy in patients with advanced neuroendocrine tumours: a phase-II study. *Theranostics.* 2016;6:501–510.
38. Uccelli L, Boschi A, Cittanti C, et al. ^{90}Y/^{177}Lu-DOTATOC: from preclinical studies to application in humans. *Pharmaceutics.* 2021;13:1463.
39. Breeman WAP, van der Wansem K, Bernard BF, et al. The addition of DTPA to [^{177}Lu-DOTA^0, Tyr^3]octreotate prior to administration reduces rat skeleton uptake of radioactivity. *Eur J Nucl Med Mol Imaging.* 2003;30:312–315.

Fully Automated, Fast Motion Correction of Dynamic Whole-Body and Total-Body PET/CT Imaging Studies

Lalith Kumar Shiyam Sundar[1], Martin Lyngby Lassen[2], Sebastian Gutschmayer[1], Daria Ferrara[1], Anna Calabrò[3], Josef Yu[1], Kilian Kluge[4], Yiran Wang[3], Lorenzo Nardo[3], Philip Hasbak[2], Andreas Kjaer[2], Yasser G. Abdelhafez[3], Guobao Wang[3], Simon R. Cherry[3,5], Benjamin A. Spencer[3], Ramsey D. Badawi[3,5], Thomas Beyer[1], and Otto Muzik[6]

[1]*Quantitative Imaging and Medical Physics Team, Center for Medical Physics and Biomedical Engineering, Medical University of Vienna, Vienna, Austria;* [2]*Department of Clinical Physiology, Nuclear Medicine, and PET and Cluster for Molecular Imaging Section 4011, Rigshospitalet, University of Copenhagen, Copenhagen, Denmark;* [3]*Department of Radiology, University of California–Davis, Davis, California;* [4]*Department of Biomedical Imaging and Image-Guided Therapy, Division of Nuclear Medicine, Medical University of Vienna, Vienna, Austria;* [5]*Department of Biomedical Engineering, University of California–Davis, Davis, California; and* [6]*Department of Pediatrics, Children's Hospital of Michigan, Wayne State University School of Medicine, Detroit, Michigan*

We introduce the Fast Algorithm for Motion Correction (FALCON) software, which allows correction of both rigid and nonlinear motion artifacts in dynamic whole-body (WB) images, irrespective of the PET/CT system or the tracer. **Methods:** Motion was corrected using affine alignment followed by a diffeomorphic approach to account for nonrigid deformations. In both steps, images were registered using multiscale image alignment. Moreover, the frames suited to successful motion correction were automatically estimated by calculating the initial normalized cross-correlation metric between the reference frame and the other moving frames. To evaluate motion correction performance, WB dynamic image sequences from 3 different PET/CT systems (Biograph mCT, Biograph Vision 600, and uEXPLORER) using 6 different tracers (^{18}F-FDG, ^{18}F-fluciclovine, ^{68}Ga-PSMA, ^{68}Ga-DOTATATE, ^{11}C-Pittsburgh compound B, and ^{82}Rb) were considered. Motion correction accuracy was assessed using 4 different measures: change in volume mismatch between individual WB image volumes to assess gross body motion, change in displacement of a large organ (liver dome) within the torso due to respiration, change in intensity in small tumor nodules due to motion blur, and constancy of activity concentration levels. **Results:** Motion correction decreased gross body motion artifacts and reduced volume mismatch across dynamic frames by about 50%. Moreover, large-organ motion correction was assessed on the basis of correction of liver dome motion, which was removed entirely in about 70% of all cases. Motion correction also improved tumor intensity, resulting in an average increase in tumor SUVs by 15%. Large deformations seen in gated cardiac ^{82}Rb images were managed without leading to anomalous distortions or substantial intensity changes in the resulting images. Finally, the constancy of activity concentration levels was reasonably preserved (<2% change) in large organs before and after motion correction. **Conclusion:** FALCON allows fast and accurate correction of rigid and nonrigid WB motion artifacts while being insensitive to scanner hardware or tracer distribution, making it applicable to a wide range of PET imaging scenarios.

Key Words: whole-body PET; total-body PET; motion correction; diffeomorphic registration; automation; quantification

J Nucl Med 2023; 64:1145–1153
DOI: 10.2967/jnumed.122.265362

Received Dec. 22, 2022; revision accepted Mar. 9, 2023.
For correspondence or reprints, contact Otto Muzik (otto@pet.wayne.edu).
Published online Jun. 8, 2023.

PET is a widely used medical imaging technique that enables noninvasive visualization of molecular processes in the body. New PET/CT systems with an extended axial field of view now allow for total-body (TB) PET imaging using a single bed position (*1*), offering improved volume sensitivity and the ability to acquire TB pharmacokinetic data with short frame durations (*2*). However, these advances require improved methods for motion correction to enable improved whole-body (WB) image analysis, such as parametric imaging. Currently, there is no motion correction software that works effectively for both WB (acquisition of multiple bed positions) or TB (one large axial FOV bed position) dynamic PET imaging or that is universal across all tracers and organs.

Rigid motion is typically encountered in brain studies, and many methods have been proposed to correct subject head motion effectively (*3–5*). Likewise, numerous nonrigid motion compensation approaches (*6–9*) have been proposed to selectively compensate for respiratory and cardiac motion in PET imaging studies. However, the literature is rather sparse (*10,11*) regarding TB/WB motion correction approaches that can universally and automatically compensate for both rigid and nonrigid motion.

WB/TB dynamic PET motion correction aims to achieve voxelwise correspondence in a series of image frames. Motion artifacts arise from involuntary movements, such as breathing and cardiac motion or voluntary changes in body position due to patient fatigue or pain. Motion correction for WB/TB PET imaging is a complex problem because of 2 main challenges: the time-dependent changes in tracer distribution and the variable rigidity profiles of different organs, some being rigid (e.g., brain) and others being deformable (e.g., heart). Therefore, it is challenging for a single alignment algorithm to account for both profiles robustly. Likewise, different tracers produce unique tracer distribution images because of varying kinetics. Therefore, a motion compensation paradigm that works on one tracer might not necessarily work on another.

To add complexity, different acquisition protocols can present different challenges for realignment. For example, in research, dynamic studies are often initiated contemporaneously with tracer injection, showing significant variation in tracer distribution. Consequently, motion correction is seldom performed during the first 10 min after injection. To date, there are no promising techniques to perform robust motion correction in the early frames (<10 min after injection). In clinical scenarios, studies with a small number of

image frames are acquired during the equilibrium phase (when tracer changes are negligible) to enable accurate correction of motion artifacts. Because clinical or research studies likely fall between these 2 extreme protocols, developing multiple alignment strategies tailored to one or the other acquisition protocol is impractical.

In response to these challenges, we focused on creating a generic, fully automated motion correction tool that gracefully adapts to these challenges. We present the Fast Algorithm for Motion Correction (FALCON) tool, a new WB/TB motion correction tool based on multiscale Greedy diffeomorphic registration paradigms (*12*). Diffeomorphism refers to a type of mathematic transformation that is smooth and invertible. This type of registration has been extensively used in computational neuroanatomy (*13–16*) because it can handle large, nonlinear deformations while preserving image topology. Since diffeomorphisms have shown great success in aligning highly deformable organs (*17*), we hypothesized that a diffeomorphic algorithm would be well suited to aligning different WB image frames of a subject across time. In addition to developing an accurate motion compensation scheme, we also focused on addressing the problem of rapidly changing uptake patterns during the initial part of the study (<10 min after injection), which renders accurate motion correction of early frames an ill-conditioned problem.

MATERIALS AND METHODS

Ethics Declaration

All data were acquired in accordance with the Declaration of Helsinki. Written informed consent was obtained from all subjects before the examinations. Approval numbers for the various datasets are presented in Table 1.

Identification of Frames Eligible for Motion Correction

In dynamic PET series, not all frames can be accurately aligned with the reference frame (typically the last frame). Early frames (those occurring within the first 10 min) differ notably from the reference frame. It would be advantageous to objectively select the frames for which alignment with the reference frame can be reliably performed. Therefore, a precomputational step was devised to enable automated identification of frames on which motion correction can robustly be performed (termed candidate frames), irrespective of the acquisition protocol (Fig. 1).

A voxelwise normalized cross-correlation (NCC) image was calculated between the 3-dimensional (3D) reference frame F and the moving frames $I_{i,j}$ (varying from time point i to j) by…

$$\mathrm{NCC}_{i,j}=\frac{\sum_{x,y,z}\left(I_{i,j}(x,y,z)-\mu_{i,j}\right)\left(F(x,y,z)-\mu_F\right)}{\sqrt{\sum_{x,y,z}\left(I_{i,j}(x,y,z)-\mu_{i,j}\right)^2}\sqrt{\sum_{x,y,z}\left(F(x,y,z)-\mu_F\right)^2}}, \quad \text{(Eq. 1)}$$

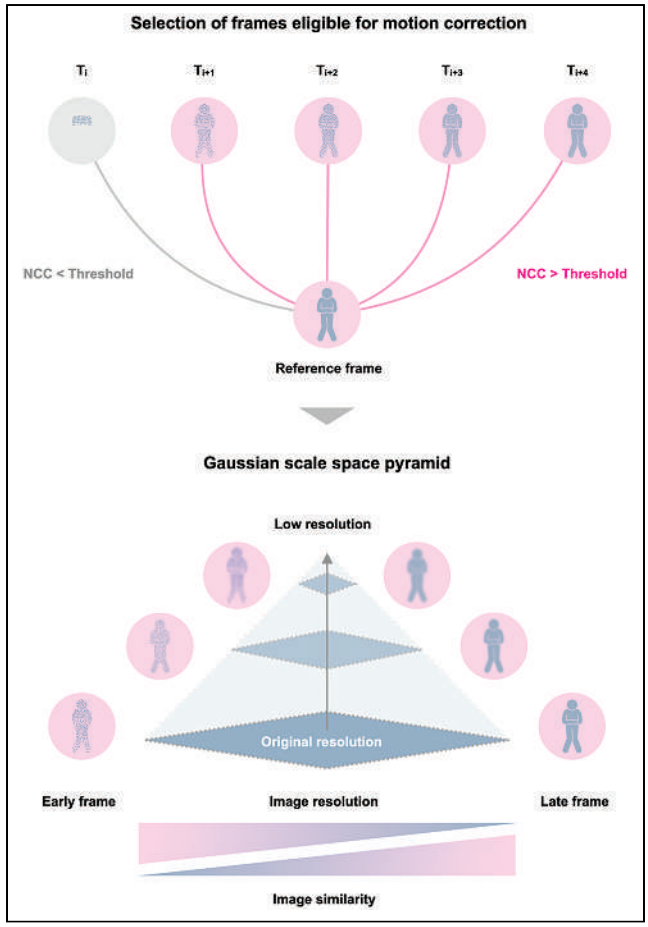

FIGURE 1. FALCON algorithm begins by selecting frames eligible for motion correction using customized threshold for NCC. These frames are then embedded in gaussian scale space pyramid and registered using multiscale registration. As resolution decreases, image similarity increases.

where $\mu_{i,j}$ and μ_F are the mean intensities of $I_{i,j}$ and F. After calculation of the voxelwise NCC image for each image pair, the corresponding mean NCC $\mu_{\mathrm{NCC}_{i,j}}$ was calculated for the so-derived NCC images:

$$\mu_{\mathrm{NCC}_{i,j}}=\frac{\sum_{x,y,z}\mathrm{NCC}_{i,j}(x,y,z)}{N}, \quad \text{(Eq. 2)}$$

where N is the total number of voxels in the image. Finally, frames on which motion correction can effectively be performed

TABLE 1
Dataset Approvals

Dataset	Acquisition system	Institutional review board	Reference number
^{18}F-FDG (n = 8)	Biograph Vision 600	Medical University of Vienna	EK1907/2020
^{68}Ga-PSMA (n = 8)	Biograph Vision 600	Medical University of Vienna	EK1907/2020
^{11}C-PIB (n = 6)	Biograph Vision 600	Medical University of Vienna	EK1907/2020
^{18}F-FDG (n = 10)	uEXPLORER	University of California, Davis	IRB # 1374902
^{68}Ga-DOTATATE (n = 8)	uEXPLORER	University of California, Davis	IRB # 1470016
^{18}F-fluciclovine (n = 8)	uEXPLORER	University of California, Davis	IRB # 1470016
^{82}Rb (n = 11)	Biograph mCT	Rigshospitalet Copenhagen	H-15009293

were identified using the following criteria:

$$I_{i,j} \mid \mu_{\mathrm{NCC}_{i,j}} > 0.6 \cdot \max_{i,j}(\mu_{\mathrm{NCC}_{i,j}}), \quad \text{(Eq. 3)}$$

where $I_{i,j}$ represents the set of images with a corresponding mean NCC ($\mu_{\mathrm{NCC}_{i,j}}$) greater than 60% of the maximum mean NCC across all frames.

A threshold of 60% was chosen as the minimum acceptable level of similarity for an image to be considered a candidate frame in a dynamic series. The rationale behind this threshold is that an image with a mean NCC of more than half of the observed maximum mean NCC in a dynamic series is likely to have sufficient similarity to the reference image, making it a good candidate for motion correction.

Motion Correction Methodology and Scale Space

Motion correction was performed on only the candidate frames using 2 sequential steps. First, an affine alignment was used to correct for global motion, such as movement of the head and extremities. Second, a Greedy diffeomorphic approach was used to account for precise nonrigid motion such as lung deformation, intestine movement, and bladder distention. The diffeomorphic approach is "greedy," as the optimization is performed by making a locally optimal choice to find a global optimum subsequently (*18*). The paradigm uses a nonlinear optimization approach to align 2 images by iteratively deforming one image to the other by maximizing their similarity metric. In both steps, images are registered in gaussian scale space following a multiscale alignment approach (Fig. 1). Specifically, the algorithm conducts affine and diffeomorphic alignment between images starting at a coarse scale that is then used to initialize registration at the next finer scale, a process repeated until it reaches the finest possible scale. The multiscale methodology has several advantages that facilitate fast and robust alignment of images: first, the computational load is reduced significantly since most iterations are performed at the coarse levels of the pyramid. Second, the algorithm is less likely to get trapped in a local optimum because the initial search is performed on a coarse grid (*19*). In addition, using an approach with gaussian scale space improves the similarity between early and late frames in an image sequence by suppressing high-frequency information, such as noise in the early frames and structural information in the late frames (Fig. 1).

Unlike most registration algorithms, which apply a normalized-mutual-information metric, we chose the NCC as the similarity metric. Our choice was guided by the understanding that the normalized-mutual-information metric is poorly suited to deformable registration because of the many degrees of freedom, which lead to nonrealistic spatial deformations (*12,16*). In contrast, the NCC metric uses small-volume patches and is therefore much more constrained, thus resulting in more realistic alignments (*12*).

Mathematically, we can represent the images being registered as I_1 and I_2 and the deformation field as ϕ. The NCC between the images is then given by…

$$\mathrm{NCC}(I_1, I_2, \phi) = \frac{\sum_{x \in \Omega}(I_1(x) - \mu_{I_1})(I_2(\phi(x)) - \mu_{I_2})}{\sqrt{\sum_{x \in \Omega}(I_1(x) - \mu_{I_1})^2}\sqrt{\sum_{x \in \Omega}(I_2(x) - \mu_{I_2})^2}}, \quad \text{(Eq. 4)}$$

where μ_{I_1} and μ_{I_2} are the means of the images I_1 and I_2, and omega is the domain over which the NCC is calculated. The Greedy diffeomorphic algorithm aims to find a deformation field ϕ that maximizes the NCC.

Software Implementation

The software is built around the Greedy Registration Toolkit (*12*) and Kitware's Insight Segmentation and Registration Toolkit (*20,21*). A comprehensive exposition on the image registration procedure and the corresponding hyperparameter specifications can be found in the supplemental materials (available at http://jnm.snmjournals.org). Images are aligned at 3 different resolution levels of a scale space pyramid: coarse (one-eighth resolution), medium (one-fourth resolution), and fine (original resolution) (*19*). Moreover, the user can select the number of maximum iterations for aligning the images at each resolution level, with 100, 50, and 25 (coarse, medium, and fine, respectively) iterations set as the default, which proved to be a solid choice on testing during development to compromise speed and robustness. The software runs the alignment in parallel by default, and the speed of the motion correction increases with the number of available central-processing-unit cores.

The code for FALCON is freely available under an open-source license. Interested users can access the code by visiting the FALCON GitHub page (https://github.com/QIMP-Team/FALCON). The code is regularly updated and maintained by the FALCON development team. Instructions for downloading and installing the software can be found on the GitHub page. Sample videos of before and after motion correction can be found on YouTube (http://bit.ly/3FXxDO0).

Performance Assessment

We applied the developed software to studies of patients with various cancer types who underwent dynamic imaging procedures using different tracers on 2 different PET/CT systems (Siemens Biograph Vision 600 and United Imaging uExplorer). Specifically, 3 separate studies were acquired using the Biograph Vision 600 (axial field of view, 26 cm). In the first study, 8 lung cancer patients (47–77 y old, 50–88 kg, 4 women and 4 men) underwent WB PET using ^{18}F-FDG as a tracer (injected dose, 309 ± 52 MBq). Likewise, 8 additional prostate cancer patients (51–77 y, 63–164 kg) underwent WB PET using ^{68}Ga-PSMA as a tracer (injected dose, 161 ± 22 MBq). The acquisition protocol for both studies was identical. After intravenous injection of the activity, a 6-min dynamic scan with the bed fixed at the chest region was followed by a 60-min dynamic WB PET scan consisting of 14 continuous-bed-motion passes. From the 66-min PET acquisition, only the continuous 6- to 66-min WB PET scan was considered for motion correction since it covered the entire body. The PET list-mode data were rebinned into a dynamic frame sequence (6 × 180 s and 8 × 330 s). In the third study, 6 patients with cardiac amyloidosis (48–82 y old, 58–91 kg, 2 women and 4 men) were scanned using ^{11}C-Pittsburgh compound B (PIB) (703 ± 51 MBq), and a 25-min list-mode acquisition with continuous-bed-motion passes was initiated from 10 min after injection. The list-mode data were subsequently rebinned into a 5 × 300 s dynamic sequence. Images of all studies were reconstructed into 220 × 220 matrices (voxel size, 3.3 × 3.3 × 2.0 mm) using 3D point-spread function plus time-of-flight ordered-subsets expectation maximization with all corrections applied.

In addition, 3 studies with different tracers were acquired using the uEXPLORER (axial field of view, 194 cm). In the first study, 10 patients with genitourinary cancer (56–82 y old, 64–101 kg, 9 men and 1 woman) underwent a 60-min PET list-mode acquisition after injection of ^{18}F-FDG (351 ± 17 MBq); the acquisition was subsequently rebinned into a dynamic frame sequence (6 × 10 s, 2 × 30 s, 6 × 60 s, 5 × 120 s, 4 × 180 s, and 6 × 300 s). In the second study, 8 patients with recurrent prostate cancer (66–90 y old, 71–109 kg) were scanned using ^{18}F-fluciciclovine (310 ± 4 MBq), with the resulting list-mode data being rebinned into a 25-min dynamic frame sequence (12 × 5 s, 3 × 10 s, 3 × 30 s, 6 × 60 s, and 8 × 120 s). In the third study, 8 patients with neuroendocrine tumors (49–92 y old, 47–102 kg, 3 men and 5 women) underwent a 20-min list-mode acquisition using ^{68}Ga-DOTATATE (181 ± 18 MBq) starting at 60 min after injection, with the data rebinned into a dynamic frame sequence (20 × 60 s). All images acquired using the uEXPLORER were reconstructed into 150 × 150 matrices (voxel size, 4 × 4 × 4 mm) using 3D time-of-flight

ordered-subsets expectation maximization with all corrections (except for point-spread-function modeling).

As a result, the performance of the motion correction algorithm was evaluated for 5 tracers (^{18}F-FDG, ^{68}Ga-PSMA, ^{11}C-PIB, ^{18}F-fluciclovine, and ^{68}Ga-DOTATATE) using 3 different measures. First, correction of overall gross body motion across the dynamic sequence was assessed on the basis of the volume mismatch between the individual WB image volumes. Specifically, a 3D body surface was determined semiautomatically using thresholding across the dynamic sequence, thereby defining a body volume for each frame. The so-derived body volumes were then subtracted in 3D space from the reference body volume (last) frame, yielding a mismatch volume (mm^3). Mismatch volumes were determined for both the motion-corrected and the uncorrected dynamic sequences. The percentage decrease in mismatch volume was then used to measure motion correction performance concerning gross body motion artifacts. In addition, the segmented body volumes were averaged across the frames for both the motion-corrected and the uncorrected dynamic sequences for all tracers. The resulting penumbra images, or the probabilistic binary masks, ranged from 0 to 1, where 0 indicates complete mismatch and 1 indicates complete overlay. This approach was especially useful in evaluating the motion correction performance for the head and extremities. The proposed approach is analogous to the calculation of a Dice coefficient. However, it is much more sensitive in highlighting mismatches.

Second, to evaluate the accuracy of the developed method to correct for involuntary motion within the torso due to respiration, the superior surface of the liver (termed the liver dome) was defined manually by a nuclear medicine expert in 3 coronal slices that were 2 cm apart in all motion-corrected and uncorrected images. The absolute difference between the so-defined liver dome of the reference frame (last) and all other dynamic frames was calculated and compared for both motion-corrected and uncorrected images for all tracers. Finally, the absolute average distance (mm) was reported.

Third, to evaluate the impact of the motion correction algorithm on lesion intensity in clinical oncologic scans, we manually defined a small (<10 cm^3) tumor tissue nodule on the average image of the dynamic series of each patient and calculated the associated SUV_{mean}. Only small tumors (<10 cm^3) were selected because they were more prone to motion artifacts. The tumors were segmented by a nuclear medicine physician using a semiautomated segmentation tool (PETTumorSegmentation plugin, 3D Slicer, version 5.2.1) proposed by Beichel et al. (*22*). The SUV_{mean} was then compared between the motion-corrected and uncorrected average images. The hypothesis was that an increase in SUV should be seen after motion correction because smearing of activity due to motion artifacts is removed.

Robustness and Stability

In addition to the 3 performance measures, we used a fourth measure to characterize the robustness of our algorithm. An ideal diffeomorphic registration algorithm must perfectly align the 2 disparate images and not introduce notable intensity changes during the alignment process. Extreme deformations are observed in the different phases of the contracting heart. We used gated cardiac images to test the robustness and stability of FALCON in preserving image topology and avoiding the introduction of artifacts or intensity changes while handling large deformations. To test the performance of the motion correction, we applied our motion correction algorithm to gated myocardial data obtained using ^{82}Rb PET performed on a Siemens Biograph mCT scanner. This study comprised 11 healthy volunteers who underwent rest myocardial perfusion scans using ^{82}Rb. Each dataset was reconstructed into 8 electrocardiogram phases using an optimized reconstruction window (*23*). All 8 electrocardiogram phases (including the end-systolic phase) were coregistered to the end-diastolic phase. An ideal image-registration algorithm will fully align the end-systolic volume with the end-diastolic volume, yielding stroke volumes and left ventricular ejection fractions of 0 mL and 0, respectively. Although clinically irrelevant, the alignment of all electrocardiogram phases with end-diastole will probe the ability of FALCON to handle large deformations quantitatively. The volumetric analyses were performed in QPET (Cedars-Sinai).

Besides volumetric analyses, left ventricular wall motion is reported for the septum (basal, midventricular, and apical parts) before and after motion correction. In theory, the ideal registration of all phases to the end-diastolic phase would reduce motion to 0 mm for each segment. In contrast, any motion greater than 0 mm reflects residual motion in the image after motion correction. We also report the true motion observed in the heart before motion correction, thus providing insight into how much the motion is constricted when TB motion correction is used. We also investigated the change in intensity introduced by motion correction by generating gated mean images before and after motion correction and compared their line profiles with the reference diastolic phase.

In addition, we quantified the intensity change introduced by the diffeomorphic registration process in noncardiac tracer studies by manually segmenting the brain, kidneys, liver, and spleen in all dynamic frames before and after motion correction. Mean activities (Bq/mL) from all 4 regions were derived for frames before and after motion correction, and the absolute percentage difference was reported.

Statistical Analysis

To test whether applying the motion correction algorithm significantly decreased gross body motion across frames, mismatch volumes derived from the motion-corrected and uncorrected dynamic images were compared using a 2-sample *t* test. Moreover, a 2-sample *t* test was used to determine whether the absolute average distance between the liver dome defined in the reference frame and all other frames differs before and after motion correction. To determine whether SUVs in small tumor nodules increase significantly after motion correction, a paired *t* test was applied between the SUVs before and after motion correction. A *P* value of 0.05 was assumed to indicate statistical significance.

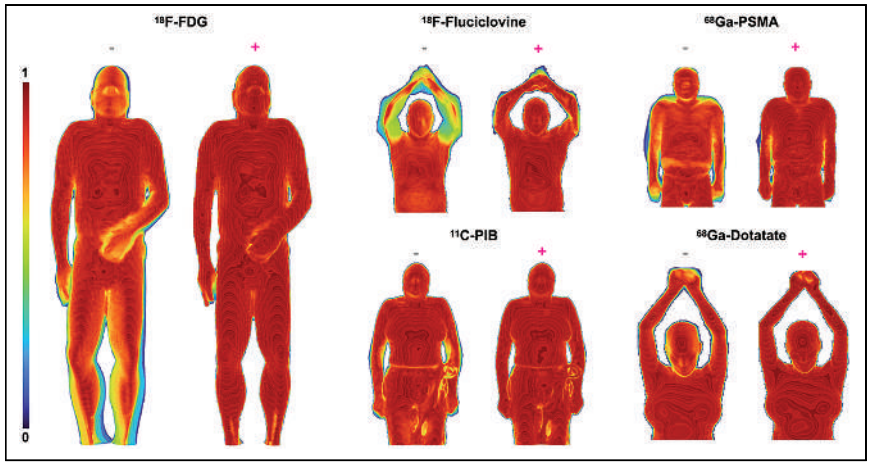

FIGURE 2. Penumbra images generated before (−) and after (+) motion correction for various tracers. Penumbra around extremities is significantly reduced after motion correction.

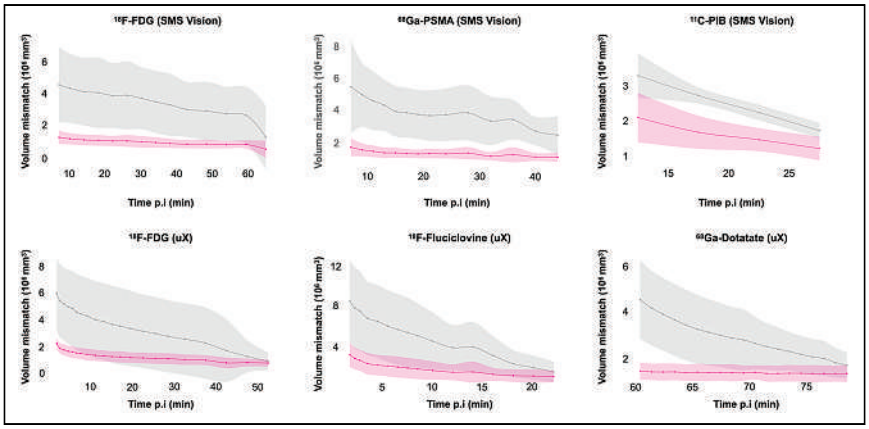

FIGURE 3. Group comparison of average volume mismatch (mm^3) before (gray line) and after (pink line) motion correction across dynamic frames for various tracers and systems. Shaded areas represent 1 SD. After motion correction, both average volume mismatch and associated variance are significantly reduced. p.i = after injection; SMS = Siemens; uX = uEXPLORER.

RESULTS

Selection of Frames for Motion Correction

The candidate frames for motion correction varied depending on the tracer and subject. Therefore, we report the median and interquartile range for each tracer. For dynamic studies using the ^{18}F-FDG and ^{18}F-fluciclovine tracers on the uEXPLORER system, the candidate frames started after 2.5 min (0.7) and 1.8 min (1) after injection, respectively. For ^{68}Ga-DOTATATE scans obtained during the equilibrium phase (60–80 min after injection), the candidate frames started after 2.5 ± 0.7 min and 1.8 ± 1.0 min after injection, respectively. Likewise, for WB imaging studies of ^{18}F-FDG and ^{68}Ga-PSMA involving continuous-bed-motion passes (6–66 min after injection), the candidate frames started 6 min after injection. Finally, for ^{11}C-PIB (10–35 min after injection), the candidate frames began 10 min after injection. Only the candidate frames were subsequently used for motion correction and evaluation purposes.

Correction of Gross Anatomic Motion

Figure 2 shows examples of the penumbra images across the dynamic WB sequence when accounting for gross motion compared with voxel overlap obtained using the uncorrected image volumes. The figure demonstrates improvement in voxel overlap after motion correction, and this improvement can be most clearly appreciated in the decreased shades of the penumbra around the extremities (arms and legs) and the head. Quantitative assessment of gross motion correction showed a substantial reduction in both volume mismatch and the associated variance across the dynamic sequence and various tracers (Fig. 3). On average, volume mismatch decreased by about 50% for ^{18}F-FDG, ^{18}F-fluciclovine, and ^{68}Ga-PSMA image volumes, whereas for ^{11}C-PIB and ^{68}Ga-DOTATATE, it decreased by about 40%. The extended metrics are shown in Table 2.

TABLE 2
Gross Motion Analysis Evaluation for Different Tracer Studies Using Volume Mismatch Metrics

PET/CT system	Tracer	Volume mismatch (%)	*P*
uEXPLORER	^{18}F-FDG	46 ± 14	<0.01
uEXPLORER	^{18}F-fluciclovine	52 ± 9	<0.01
uEXPLORER	^{68}Ga-DOTATATE	43 ± 11	<0.01
Biograph Vision 600	^{18}F-FDG	63 ± 8	<0.01
Biograph Vision 600	^{68}Ga-PSMA	56 ± 10	<0.01
Biograph Vision 600	^{11}C-PIB	36 ± 13	<0.05

Correction of Involuntary Organ Motion

Figure 4 demonstrates virtually perfect alignment of the liver dome across the dynamic sequence in 70% of frames after motion correction. After motion correction, the absolute average distance across the dynamic frames was significantly lower than that determined for the uncorrected images ($P < 0.05$), as seen in Table 3.

Correction of Tumor Tissue Motion

Mean tumor SUVs showed a trend toward an increase in average tracer concentration (15%, $P < 0.01$) between non–motion-corrected images (4.0 ± 2.2) and motion-corrected images (4.6 ± 2.2) (Fig. 5). However, we also observed slight decreases in average tracer concentration in some tumors (presumably tumors without motion) because of the effect of reslicing small volumes.

Assessment of Motion Correction Robustness

Figure 6 shows a representative comparison between the diastolic myocardium and the motion-corrected systolic myocardium from the gated ^{82}Rb images. Our results indicate a substantial decrease (76% ± 3%) in stroke volume after motion correction (from 58 ± 17 mL to 14 ± 4 mL, $P < 0.01$), without leading to anomalous or aberrant distortions in the resulting images. After motion correction, the residual left ventricular wall motion in the basal, mid, and apical anteroseptal regions was reduced by 86%, 81%, and 73%, respectively. In addition, from the intensity profiles of the reference (end-diastolic phase) mean motion-corrected and mean non–motion-corrected images shown in Figure 6, we observe a better overlay of the peaks of the line profile for the mean motion-corrected and reference images than for the mean non–motion-corrected image. The customized analysis clearly indicates preservation of quantitative values.

Likewise, for all noncardiac studies with different tracers, the average absolute percentage difference in intensity in major organs (brain, kidneys, spleen, and liver) was less than 2%, as shown in Supplemental Figures 1–3.

DISCUSSION

We introduce an accurate, fully automated, diffeomorphic motion compensation scheme using both affine alignments and nonrigid deformations of dynamic WB PET images. The algorithm is stable and computationally robust in the presence of substantial organ deformations between image frames, yields subvoxel accuracy in compensating for involuntary body motion over a large range of

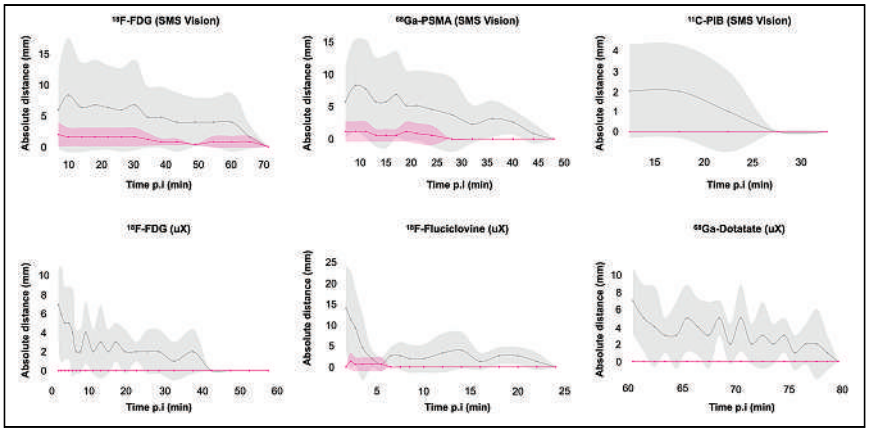

FIGURE 4. Group comparison of absolute difference between reference liver dome (last frame) and remaining dynamic frames for all tracers before (gray line) and after (pink line) motion correction across dynamic frames. Shaded areas represent 1 SD. After motion correction, absolute difference is minimized to zero in most cases. p.i = after injection; SMS = Siemens; uX = uEXPLORER.

PET tracer distribution patterns, and is independent of the acquisition system.

Scale Space Theory for Dynamically Changing Uptake Pattern

Although the time course of distribution is specific for each tracer, the last frame of a dynamic sequence is most commonly selected as the reference frame for alignment of all previous frames. However, accurate alignment of the reference frame with early frames (<10 min after injection) is challenging because of the vastly different uptake patterns and poor count statistics typical of early frames. Therefore, motion correction is typically not performed during the first 10 min (*11*). In our previous work (*4,10*), we used conditional generative adversarial networks to generate PET navigators by converting early frames to frames resembling late frames. The idea was to artificially increase the information in the early frames to resemble the late frames. However, the proposed approach required dedicated hardware (graphics processing unit) and pixelwise spatial correspondence between image pairs, which demanded extensive network training for different tracers—untenable in clinical routine.

Here, we chose a simplified approach that is computationally fast, largely tracer-independent, and does not require any special hardware. First, we identify whether the information in a particular frame is sufficient for alignment based on an objective criterion of uptake pattern similarity. Second, we embed the images in gaussian scale space and conduct the alignment in multiple resolutions. Doing so increases image similarity between early and late frames by suppressing high-frequency information in both frames (*24*). Using this approach, we found that motion could be corrected for frames later than about 2 min after injection for tracers such as ^{18}F-FDG and ^{18}F-fluciclovine.

Motion Correction Assessment

Validation of nonlinear motion correction schemes for organs within the torso is difficult. In radiology, projects such as the Nonrigid Image Registration Project have been established to provide guidelines for validating nonlinear motion correction algorithms for MR and CT images (*25*). Predominantly, these investigators suggest segmenting a specific volume of interest (e.g., liver) in the images to be aligned and quantifying the segmentation overlap before and after alignment. However, this segmentation is not practical in PET imaging, as organ contours in dynamic frames change because of the changing activity distribution and noise over time. Therefore, consensus on a gold standard is needed in the evaluation of nonlinear motion correction algorithms for WB/TB PET motion correction.

In the absence of such a consensus, validation of our method was based on a set of complementing measures that collectively provide a comprehensive assessment of our algorithm's performance. These measures test for the ability to correct for gross body motion, to correct for involuntary movement of a large organ due to respiration within the torso (liver dome), to correct for smearing effects due to motion when small nodules are averaged over multiple frames, and to maintain activity concentration levels even under conditions of substantial deformation.

Clinical Performance

Evaluation of the clinical viability of the method was based on alignment of dynamic image sequences with vastly different uptake

TABLE 3
Organ Motion Evaluation Due to Respiration Before and After Motion Correction for Different Tracer Studies Using Absolute Average Distance Between Liver Dome in Reference Frame and Liver Dome in All Other Frames

		Absolute average distance (mm)		
PET/CT system	Tracer	Before motion correction	After motion correction	*P*
uEXPLORER	^{18}F-FDG	2.7 ± 1.9 (0.0–6.9)	0 (0)	<0.01
uEXPLORER	^{18}F-fluciclovine	4.2 ± 3.9 (0.7–14)	0.3 ± 0.4 (0.0–1.3)	<0.01
uEXPLORER	^{68}Ga-DOTATATE	3.3 ± 1.6 (1.0–7.0)	0 (0)	<0.01
Biograph Vision 600	^{18}F-FDG	5.3 ± 1.7 (1.6–8.4)	1.2 ± 0.5 (0.4–2.0)	<0.01
Biograph Vision 600	^{68}Ga-PSMA	4.8 ± 2.1 (0.9–8.3)	0.6 ± 0.5 (0.0–1.1)	<0.01
Biograph Vision 600	^{11}C-PIB	1.3 ± 1.0 (0.0–2.0)	0 (0)	<0.1

Data in parentheses are range.

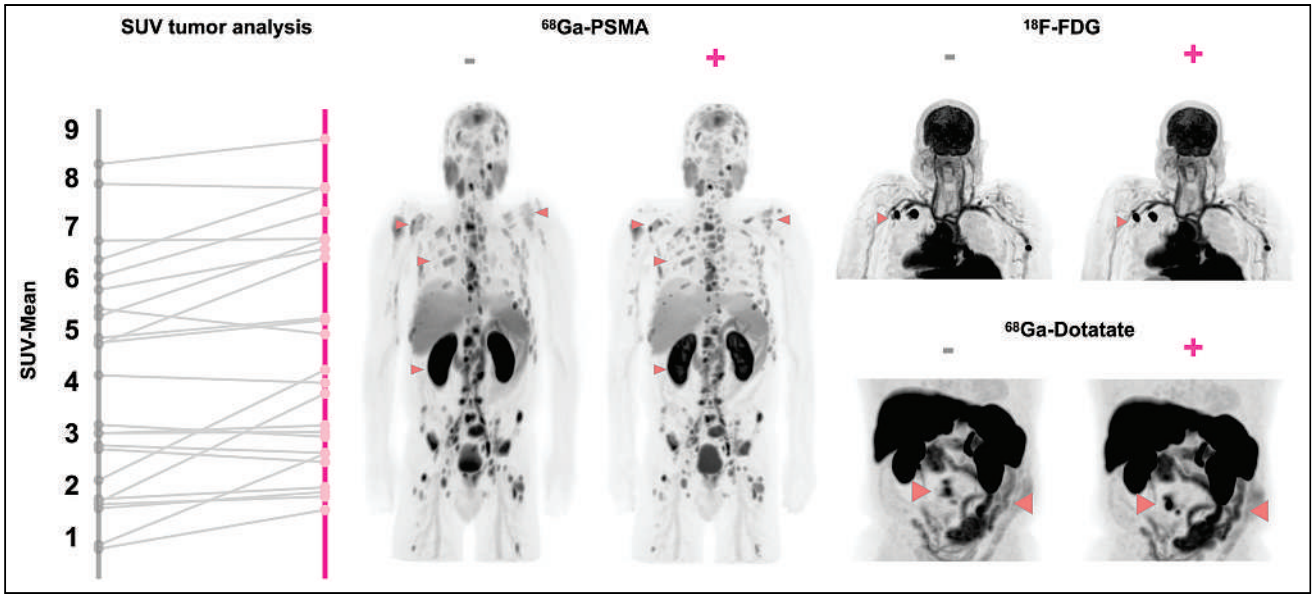

FIGURE 5. Comparison of tumor SUVs from mean images of dynamic series of different tracers before (gray, −) and after (pink, +) motion correction. PET images demonstrate improvement in image quality after correction.

patterns. FALCON proved to serve as a strong baseline motion correction approach that works across different PET/CT systems, tracers, and fields of view. Figures 2 and 3 show the decrease in volume mismatch across the whole body after motion correction. Specifically, one can clearly appreciate the improved diagnostic quality of ^{68}Ga-PSMA images after motion correction (Fig. 5) and a significant decrease in organ movement caused by respiration. This result also suggests the potential of this methodology for correcting motion artifacts in respiration-gated data.

Moreover, one of the major concerns of nonlinear motion correction algorithms is preservation of quantitative aspects of PET data. We investigated these aspects via the intensity profiles of end-diastolic (reference) images, mean motion-corrected images, and mean non–motion-corrected images (Fig. 6) and via multiorgan analysis (Supplemental Figs. 1–3). Our results showed preservation of quantitative values even after large deformations, demonstrated by the improved overlay of line profile peaks in the mean motion-corrected and reference images compared with the mean

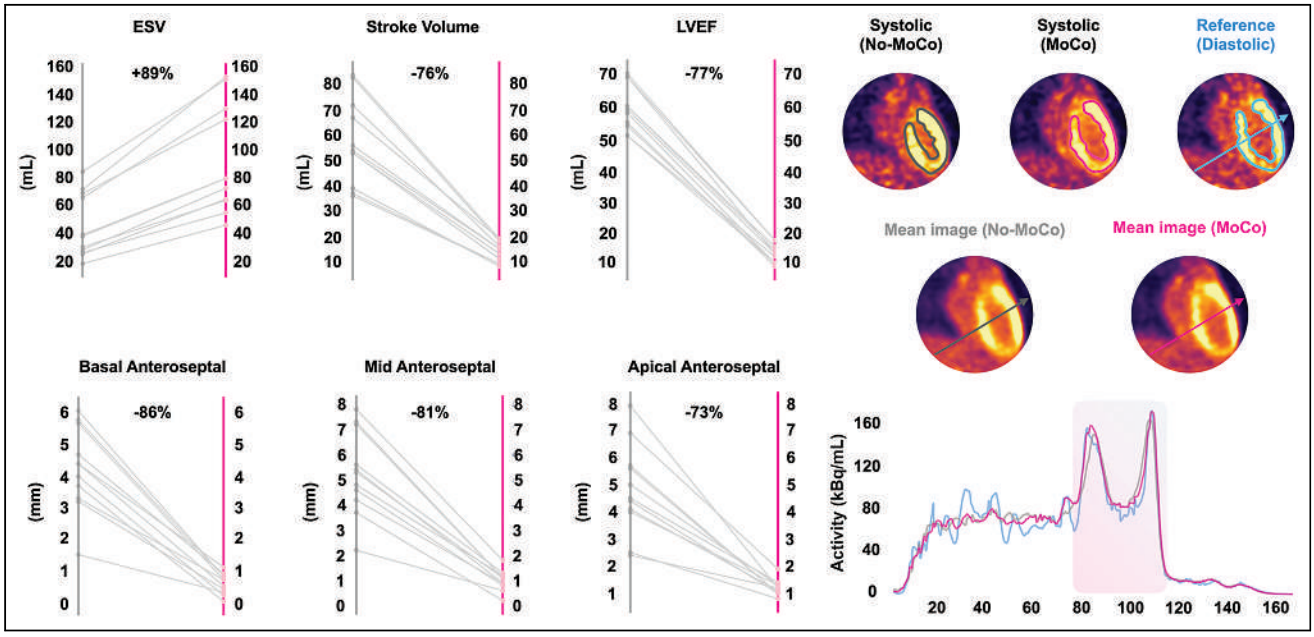

FIGURE 6. Alignment of different gates to end-diastolic phase significantly reduced stroke volume and left ventricular ejection fraction and increased end-systolic volume. Residual motion in basal, mid, and apical regions also was significantly reduced after motion correction. In addition, mean images generated with and without motion correction are shown, with their respective line profiles (motion correction in pink and no motion correction in gray) in comparison to reference diastolic phase (blue). ESV = end-systolic volume; LVEF = left ventricular ejection fraction; MoCo = motion correction.

non–motion-corrected image. In addition, Figure 5 illustrates improved correction of activity smearing, which is clearly visible in the non–motion-corrected images. The average time required for aligning each frame is about 2 min for a TB dataset (typical matrix size, $150 \times 150 \times 486$), with processing time increasing linearly with matrix size. Moreover, using parallel processing on a standard reconstruction server with 32 central-processing-unit cores, FALCON takes about 10 min to correct motion in a dynamic TB dataset consisting of 29 frames.

Limitations

There are several limitations associated with the current implementation. First, we used a static attenuation map that is not motion-corrected; therefore, quantitative errors due to attenuation mismatches are unavoidable (*26,27*). Further, intraframe motion is not addressed in this work. Nonetheless, our results from real-world dynamic studies indicated that even if intraframe motion is not considered, correction of interframe motion can contribute significantly to the quality of summed and parametric images (Supplemental Fig. 4). Finally, FALCON does not allow correction for motion at the beginning of a dynamic sequence (<2 min after injection), when the tracer distribution pattern differs substantially from the reference image. Using FALCON to correct for frames during the first pass will provide poor results. Our validation studies suggest that the tracer distribution patterns in image frames acquired during the initial 120 s are significantly different from the pattern in the reference image (even at the lowest-resolution scale), precluding successful application of our method in these very early frames. Although these frames are generally less important from a clinical point of view, they carry information about the blood input function, which is often of interest to obtain an image-derived input function for kinetic modeling (*28*) and quantification (*29*). Consequently, motion correction of these early frames will require a separate alignment strategy.

Finally, because of filling of the bladder, FALCON tends to warp the semifilled bladder of the moving frames to the filled bladder of the reference frame. Therefore, care should be taken in interpreting the bladder area after motion correction. Likewise, we have observed that FALCON performs poorly in correcting large-angle joint flexions and extensions, such as large finger motions.

CONCLUSION

The developed motion correction tool, FALCON, allows correction of rigid and nonlinear motion that might be present in WB dynamic imaging studies. Our software tool can potentially improve the accuracy of PET scans, ultimately leading to better diagnosis and treatment.

DISCLOSURE

This work was partly supported by NIH research grant R01CA29422 and by ERA-PERMED 2021-324 PETictCAC. No other potential conflict of interest relevant to this article was reported.

KEY POINTS

QUESTION: Is there a clinically viable method of correcting motion in WB dynamic PET imaging data?

PERTINENT FINDINGS: FALCON, a fast, fully automated WB motion correction tool that is independent of vendor, tracer distribution, and axial field of view, is proposed. FALCON is based on Greedy diffeomorphic registration paradigms and shows promise in improving voxel overlap, reducing gross volume mismatch, and increasing tumor contrast. FALCON is computationally stable and robust, permitting correction of even large deformations associated with the beating heart without leading to topologic or intensity aberrations.

IMPLICATIONS FOR PATIENT CARE: FALCON allows accurate and consistent correction of motion artifacts in WB PET scans regardless of the external markers, tracer, or scanner geometry. Consequently, FALCON might contribute to improved performance in the clinical setting.

REFERENCES

1. Badawi RD, Shi H, Hu P, et al. First human imaging studies with the EXPLORER total-body PET scanner. *J Nucl Med.* 2019;60:299–303.
2. Zhang X, Cherry SR, Xie Z, Shi H, Badawi RD, Qi J. Subsecond total-body imaging using ultrasensitive positron emission tomography. *Proc Natl Acad Sci USA.* 2020;117:2265–2267.
3. Lu Y, Naganawa M, Toyonaga T, et al. Data-driven motion detection and event-by-event correction for brain PET: comparison with Vicra. *J Nucl Med.* 2020;61:1397–1403.
4. Shiyam Sundar LK, Iommi D, Muzik O, et al. Conditional generative adversarial networks aided motion correction of dynamic ^{18}F-FDG PET brain studies. *J Nucl Med.* 2021;62:871–879.
5. Spangler-Bickell MG, Khalighi MM, Hoo C, et al. Rigid motion correction for brain PET/MR imaging using optical tracking. *IEEE Trans Radiat Plasma Med Sci.* 2019;3:498–503.
6. Rubeaux M, Doris MK, Alessio A, Slomka PJ. Enhancing cardiac PET by motion correction techniques. *Curr Cardiol Rep.* 2017;19:14.
7. Lassen ML, Tzolos E, Pan T, et al. Anatomical validation of automatic respiratory motion correction for coronary ^{18}F-sodium fluoride positron emission tomography by expert measurements from four-dimensional computed tomography. *Med Phys.* 2022;49:7085–7094.
8. Nehmeh SA. Respiratory motion correction strategies in thoracic PET-CT imaging. *PET Clin.* 2013;8:29–36.
9. Kesner AL, Schleyer PJ, Büther F, Walter MA, Schäfers KP, Koo PJ. On transcending the impasse of respiratory motion correction applications in routine clinical imaging: a consideration of a fully automated data driven motion control framework. *EJNMMI Phys.* 2014;1:8.
10. Sundar LS, Iommi D, Spencer B, et al. Data-driven motion compensation using cGAN for total-body [^{18}F]FDG-PET imaging [abstract]. *J Nucl Med.* 2021;62(suppl 1):35.
11. Sun T, Wu Y, Wei W, et al. Motion correction and its impact on quantification in dynamic total-body ^{18}F-fluorodeoxyglucose PET. *EJNMMI Phys.* 2022;9:62.
12. Venet L, Pati S, Feldman MD, Nasrallah MP, Yushkevich P, Bakas S. Accurate and robust alignment of differently stained histologic images based on Greedy diffeomorphic registration. *Appl Sci (Basel).* 2021;11:1892.
13. Miller MI, Joshi SC, Christensen GE. Large deformation fluid diffeomorphisms for landmark and image matching. In: *Brain Warping.* Elsevier; 1999:115–131.
14. Vercauteren T, Pennec X, Perchant A, Ayache N. Symmetric log-domain diffeomorphic registration: a demons-based approach. *Med Image Comput Comput Assist Interv.* 2008;11:754–761.

15. Ashburner J. A fast diffeomorphic image registration algorithm. *Neuroimage.* 2007;38:95–113.
16. Avants BB, Epstein CL, Grossman M, Gee JC. Symmetric diffeomorphic image registration with cross-correlation: evaluating automated labeling of elderly and neurodegenerative brain. *Med Image Anal.* 2008;12:26–41.
17. Santos J, Chaudhari AJ, Joshi AA, et al. Non-rigid registration of serial dedicated breast CT, longitudinal dedicated breast CT and PET/CT images using the diffeomorphic demons method. *Phys Med.* 2014;30:713–717.
18. Cormen TH, Leiserson CE, Rivest RL, Stein C. *Introduction to Algorithms.* 4th ed. MIT Press; 2001.
19. Thevenaz P, Ruttimann UE, Unser M. Iterative multi-scale registration without landmarks. In: *Proceedings, International Conference on Image Processing.* Vol 3. IEEE; 1995:228–231.
20. McCormick M, Liu X, Jomier J, Marion C, Ibanez L. ITK: enabling reproducible research and open science. *Front Neuroinform.* 2014;8:13.
21. Yoo TS, Ackerman MJ, Lorensen WE, et al. Engineering and algorithm design for an image processing Api: a technical report on ITK—the Insight Toolkit. *Stud Health Technol Inform.* 2002;85:586–592.
22. Beichel RR, Van Tol M, Ulrich EJ, et al. Semiautomated segmentation of head and neck cancers in ^{18}F-FDG PET scans: a just-enough-interaction approach. *Med Phys.* 2016;43:2948–2964.
23. Lassen ML, Wissenberg M, Byrne C, Kjaer A, Hasbak P. Optimization of the left ventricle ejection fraction estimate obtained during cardiac adenosine stress ^{82}rubidium-PET scanning: impact of different reconstruction protocols. *J Nucl Cardiol.* 2022;29:3369–3378.
24. Gutschmayer S, Muzik O, Chalampalakis Z, et al. A scale space theory based motion correction approach for dynamic PET brain imaging studies. *Front Phys.* 2022;10:1034783.
25. Christensen GE, Geng X, Kuhl JG, et al. Introduction to the non-rigid image registration evaluation project (NIREP). In: *Biomedical Image Registration: Lecture Notes in Computer Science.* Springer; 2006:128–135.
26. Le Meunier L, Maass-Moreno R, Carrasquillo JA, Dieckmann W, Bacharach SL. PET/CT imaging: effect of respiratory motion on apparent myocardial uptake. *J Nucl Cardiol.* 2006;13:821–830.
27. Emond EC, Bousse A, Machado M, et al. Effect of attenuation mismatches in time of flight PET reconstruction. *Phys Med Biol.* 2020;65:085009.
28. Shiyam Sundar LK, Muzik O, Rischka L, et al. Promise of fully integrated PET/MRI: noninvasive clinical quantification of cerebral glucose metabolism. *J Nucl Med.* 2020;61:276–284.
29. Wang G, Nardo L, Parikh M, et al. Total-body PET multiparametric imaging of cancer using a voxelwise strategy of compartmental modeling. *J Nucl Med.* 2022; 63:1274–1281.

High-Temporal-Resolution Lung Kinetic Modeling Using Total-Body Dynamic PET with Time-Delay and Dispersion Corrections

Yiran Wang[1,2], Benjamin A. Spencer[1,2], Jeffrey Schmall[3], Elizabeth Li[2], Ramsey D. Badawi[1,2], Terry Jones[1], Simon R. Cherry[1,2], and Guobao Wang[1]

[1]Department of Radiology, University of California Davis Medical Center, Sacramento, California; [2]Department of Biomedical Engineering, University of California at Davis, Davis, California; and [3]United Imaging Healthcare of America, Inc., Houston, Texas

Tracer kinetic modeling in dynamic PET has the potential to improve the diagnosis, prognosis, and research of lung diseases. The advent of total-body PET systems with much greater detection sensitivity enables high-temporal-resolution (HTR) dynamic PET imaging of the lungs. However, existing models may become insufficient for modeling the HTR data. In this paper, we investigate the necessity of additional corrections to the input function for HTR lung kinetic modeling. **Methods:** Dynamic scans with HTR frames of as short as 1 s were performed on 13 healthy subjects with a bolus injection of about 370 MBq of ^{18}F-FDG using the uEXPLORER total-body PET/CT system. Three kinetic models with and without time-delay and dispersion corrections were compared for the quality of lung time–activity curve fitting using the Akaike information criterion. The impact on quantification of ^{18}F-FDG delivery rate K_1, net influx rate K_i and fractional blood volume v_b was assessed. Parameter identifiability analysis was also performed to evaluate the reliability of kinetic quantification with respect to noise. Correlation of kinetic parameters with age was investigated. **Results:** HTR dynamic imaging clearly revealed the rapid change in tracer concentration in the lungs and blood supply (i.e., the right ventricle). The uncorrected input function led to poor time–activity curve fitting and biased quantification in HTR kinetic modeling. The fitting was improved by time-delay and dispersion corrections. The proposed model resulted in an approximately 85% decrease in K_1, an approximately 75% increase in K_i, and a more reasonable v_b (~0.14) than the uncorrected model (~0.04). The identifiability analysis showed that the proposed models had good quantification stability for K_1, K_i, and v_b. The v_b estimated by the proposed model with simultaneous time-delay and dispersion corrections correlated inversely with age, as would be expected. **Conclusion:** Corrections to the input function are important for accurate lung kinetic analysis of HTR dynamic PET data. The modeling of both delay and dispersion can improve model fitting and significantly impact quantification of K_1, K_i, and v_b.

Key Words: total-body PET; kinetic modeling; dynamic PET; lung; high temporal resolution

J Nucl Med 2023; 64:1154–1161
DOI: 10.2967/jnumed.122.264810

PET with ^{18}F-FDG or other radiotracers is a promising method for studying a variety of lung diseases, including lung cancer (*1*), acute lung injury (*2,3*), asthma (*4*), lung fibrosis (*5*), and recently coronavirus disease 2019 (*6*). The SUV is a traditional semiquantitative measure for evaluating lung ^{18}F-FDG uptake (*7,8*), whereas kinetic analysis through compartment modeling (*9*) has shown the potential to provide more quantitative tracer kinetics, for example, the ^{18}F-FDG delivery rate K_1 (*10*), net influx rate K_i (*11–15*), and fractional blood volume v_b (*13,16*), to better characterize lung diseases in previous human and animal studies. However, conventional PET scanners have a relatively poor sensitivity and limited temporal resolution (e.g., 10–40 s/frame) for dynamic imaging, which in turn affects the performance of lung kinetic quantification.

The advent of the uEXPLORER (United Imaging) total-body PET and other scanners with a long axial field of view (*17–19*) has brought new opportunities to improve lung kinetic modeling by offering a large axial field of view to cover the entire lungs with improved detection efficiency, allowing high-temporal-resolution (HTR) imaging, such as with 1 s or even a subsecond per frame (*20,21*). The HTR ability is especially useful for capturing the rapidly changing early phase of tracer uptake in lung tissues. Meanwhile, image-derived input functions (IDIFs) can also be extracted with HTR from major blood pools (e.g., ventricles and large blood vessels) for kinetic modeling (*21,22*). In this work, we investigate the use of HTR data for lung kinetic quantification with total-body PET, expecting improvement especially for those parameters that are sensitive to the early kinetics, such as ^{18}F-FDG K_1 and v_b.

One challenge with using HTR data is the potential need for additional corrections for the IDIF. Recent work on total-body PET kinetic modeling has considered time-delay correction to account for the difference between the tracer arrival time in a tissue and the arrival in the blood pool, where the IDIF is extracted (*21–23*). However, dispersion (*24,25*) may also occur when the tracer travels from the location at which the IDIF is determined to the capillaries of the lungs. The correction for either time delay or dispersion has only rarely been investigated in previous studies of lung kinetic modeling and is usually omitted (*2,26–28*), partly because of the limited temporal resolution (e.g., 10 s/frame) of conventional dynamic PET. Here, we hypothesize that a simultaneous correction for both the time-delay and dispersion effects is essential for accurate kinetic modeling in HTR dynamic PET imaging of the lungs.

MATERIALS AND METHODS

HTR Dynamic Data Acquisition on uEXPLORER

Thirteen healthy human subjects (age [mean±SD], 49 ± 15 y; weight 82 ± 18 kg; 6 men, 7 women) gave written informed consent

Received Aug. 22, 2022; revision accepted Feb. 22, 2023.
For correspondence or reprints, contact Yiran Wang (yrdwang@ucdavis.edu).
Published online Apr. 28, 2023.

and were scanned on a uEXPLORER total-body PET/CT system (*29,30*). The study was approved by the Institutional Review Board at the University of California, Davis. After an ultralow-dose CT scan (140 kVp, 5 mAs), each participant underwent a dynamic ^{18}F-FDG PET scan with intravenous bolus administration of a dose of approximately 370 MBq. Total-body PET imaging was performed for 60 min starting immediately before the injection. The resulting list-mode data were reconstructed into dynamic images using the vendor-supplied time-of-flight ordered-subset expectation maximization algorithm with 4 iterations and 20 subsets and a voxel size of $4 \times 4 \times 4$ mm^3. The dynamic framing protocol contains 120 frames over 60 min: 60×1 s, 30×2 s, 6×10 s, 6×30 s, 12×120 s, and 6×300 s, with HTR frames (1–2 s/frame) over the first 2 min. For each subject, a region of interest (ROI) was placed in the right ventricle to extract an IDIF $C_{RV}(t)$ to represent the pulmonary blood supply, the dominant blood input to the lungs (*31,32*). Five ROIs were placed in the left and right lungs (1 in each of the 5 lung lobes) to extract lung time–activity curves from the dynamic images with diminished effects of motion and spillover. The 5 lung-ROI time–activity curves were averaged to generate a global lung time–activity curve $\check{C}_T(t)$ for each of the 13 subjects. An additional ROI was also placed in the left ventricle to extract the time–activity curve $C_{LV}(t)$ for the purpose of comparison. In addition to the HTR time–activity curves, time–activity curves of low temporal resolution were generated using 10 s/frame for the first 3 min for all the ROIs.

Compartmental Modeling

^{18}F-FDG kinetics in the extravascular lung is described by a 2-tissue irreversible (2Ti) compartmental model (*33*) and is illustrated in Figure 1A. Suppose that $C_p(t)$ is the blood input function and that $C_f(t)$ and $C_m(t)$ are the concentration of free and phosphorylated ^{18}F-FDG in the extravascular lung tissue. We would then have the following differential equations to describe the system states:

$$\frac{d}{dt}\begin{bmatrix} C_f(t) \\ C_m(t) \end{bmatrix} = \begin{bmatrix} -k_2-k_3 & 0 \\ k_3 & 0 \end{bmatrix}\begin{bmatrix} C_f(t) \\ C_m(t) \end{bmatrix} + \begin{bmatrix} K_1 \\ 0 \end{bmatrix} C_p(t), \quad \text{Eq. 1}$$

where K_1 (mL/min/cm^3) and k_2 (/min) indicate the blood-to-tissue and tissue-to-blood ^{18}F-FDG delivery rate constants, respectively. k_3 (/min) is the ^{18}F-FDG phosphorylation rate constant. This irreversible model assumes that the dephosphorylation process is negligible (i.e., the dephosphorylation rate constant $k_4 = 0$) (*13*).

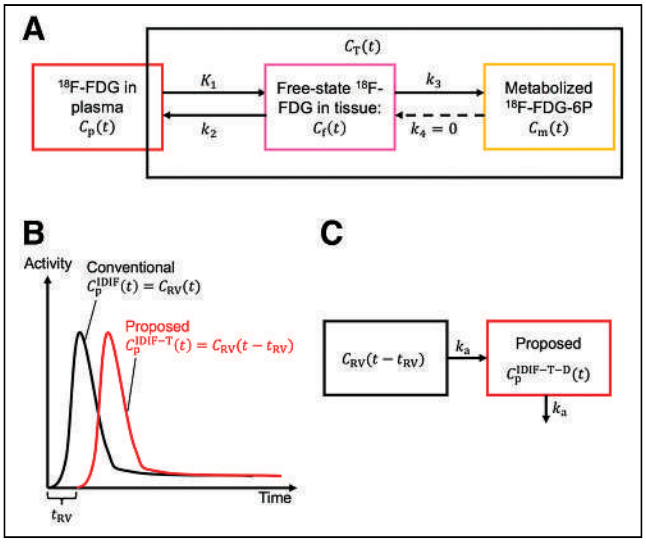

FIGURE 1. (A) Compartmental model of lung kinetics. (B) Proposed IDIF-T model with correction of time delay in input function. (C) Proposed IDIF-T-D model with both time-delay and dispersion corrections included.

The ^{18}F-FDG concentration in lung parenchyma, $C_t(t)$, is the summation of the free and the phosphorylated ^{18}F-FDG,

$$C_t(t) = C_f(t) + C_m(t) = H(t;\boldsymbol{\kappa}) \otimes C_p(t), \quad \text{Eq. 2}$$

where $\boldsymbol{\kappa} = [K_1,\ k_2,\ k_3]^T$, $\otimes$ denotes the convolution operation, and $H(t;\boldsymbol{\kappa})$ is the impulse response function of the 2Ti model:

$$H(t;\boldsymbol{\kappa}) = \frac{K_1}{k_2+k_3}\left(k_3 + k_2 e^{-(k_2+k_3)t}\right). \quad \text{Eq. 3}$$

The measured lung time–activity curve obtained by PET is modeled by $C_T(t)$, a mixture of the blood compartment and the tissue compartment,

$$C_T(t) = (1-v_b)H(t;\boldsymbol{\kappa}) \otimes C_p(t) + v_b C_{wb}(t). \quad \text{Eq. 4}$$

$C_{wb}(t)$ is the whole blood activity and is usually approximated by $C_p(t)$ for ^{18}F-FDG.

Following previous studies (*2,34,35*), the right ventricle IDIF can be used for the blood input,

$$C_p^{IDIF}(t) = C_{RV}(t), \quad \text{Eq. 5}$$

because the pulmonary circulation accounts for most of the total blood input to the lung (*32*).

The measured lung time–activity curve $\check{C}_T(t)$ was fitted with the model time–activity curve $C_T(t)$ using a nonlinear least-squares formulation:

$$\hat{\boldsymbol{\theta}} = \arg\min_{\boldsymbol{\theta}} WRSS(\boldsymbol{\theta}),\ WRSS(\boldsymbol{\theta}) = \sum_{m=1}^{M} w_m[\check{C}_T(t_m) - C_T(t_m)]^2 \quad \text{Eq. 6}$$

where $WRSS(\boldsymbol{\theta})$ denotes the weighted residual sum of squares of the curve fitting. $\boldsymbol{\theta}$ is the unknown parameter set, $\boldsymbol{\theta} = [v_b, K_1,\ k_2,\ k_3]^T$. t_m is the time of the m-th frame in a total of M frames, and w_m is the weight for frame m considering the time length and nuclear decay (*36*):

$$w_m = \Delta t_m \exp(-\lambda t_m). \quad \text{Eq. 7}$$

Here Δt_m is the length of the m-th frame, $\lambda = \frac{\ln(2)}{T_{1/2}}$ is the decay constant, and the half-life $T_{1/2} = 109.8$ min for ^{18}F-FDG. This time-varying weight was based on our initial studies of model fitting.

Modeling of Time-Delay Effect

Corrections for time delay were seldom considered in previous studies of lung kinetic modeling (*2,26–28*) because the delay was usually only several seconds and tended to be blurred out by conventional dynamic imaging of limited temporal resolution (e.g., 10 s/frame). However, the time-delay effect will no longer be concealed with the HTR measurement (e.g., 1 s/frame) and is likely to affect parameter quantification if not accounted for.

To model the time-delay effect of the IDIF extracted from the right ventricle, we include a time-delay parameter t_{RV} (s) in the input function (Fig. 1B):

$$C_p^{IDIF-T}(t) = C_{RV}(t - t_{RV}). \quad \text{Eq. 8}$$

The proposed input function model with time-delay correction is noted as IDIF-T. The time-delay parameter t_{RV} is included in $\boldsymbol{\theta}$ and will be jointly estimated with other kinetic parameters during time–activity curve fitting.

Simultaneous Correction for Dispersion

Dispersion may occur when the tracer travels from the right ventricle to the lung capillaries. Here, we model the actual lung blood input as the convolution of the measured IDIF with a parameterized dispersion function following Iida's monoexponential form (*24,37*),

$$C_{\mathrm{p}}^{\mathrm{IDIF-T-D}}(t) = C_{\mathrm{p}}^{\mathrm{IDIF-T}}(t) \otimes k_{\mathrm{a}}\exp(-k_{\mathrm{a}}t) = C_{\mathrm{RV}}(t-t_{\mathrm{RV}}) \otimes k_{\mathrm{a}}\exp(-k_{\mathrm{a}}t). \quad \text{Eq. 9}$$

This input function model is denoted as IDIF-T-D (Fig. 1C), in which both the dispersion parameter k_{a} (/min) and time delay t_{RV} (s) are included in $\boldsymbol{\theta}$ for joint parameter estimation.

Note that here the simultaneous dispersion correction is different from those explored for brain PET (*25*). Previous work focused on a backward dispersion-correction problem (*24,25*). The measured input function, such as by arterial blood sampling from the radial artery, is a dispersed version of the actual input function. Therefore, the dispersion needs to be removed from the measured input function. In comparison, our work here is a forward dispersion-correction problem. The actual lung input function is a dispersed version of the measured IDIF, to which the dispersion needs to be added.

Evaluation of Time–Activity Curve Fit Quality

The Akaike information criterion (AIC) was used to compare the statistical fit quality of different models (*38,39*),

$$\mathrm{AIC} = M\ln\left(\frac{WRSS}{M}\right) + 2N + \frac{2N^2+2N}{M-N-1}, \quad \text{Eq. 10}$$

where N is the number of unknown parameters to be optimized in $\boldsymbol{\theta}$ and M is the number of dynamic frames. AIC reflects the trade-off between the goodness of fit and the simplicity of the model and thus accounts for the difference in the number of parameters that need to be estimated. A lower AIC value indicates better fitting quality.

Evaluation of the Impact on Kinetic Quantification

We evaluated the impact of the corrections on the quantification of 3 kinetic parameters of interest: ^{18}F-FDG delivery rate K_1, net influx rate K_{i}, and fractional blood volume v_{b}. K_{i} was calculated from the microparameters:

$$K_{\mathrm{i}} = \frac{K_1 k_3}{k_2 + k_3}. \quad \text{Eq. 11}$$

The change in each kinetic parameter by a given model was reported relative to the parameter estimate by the standard IDIF model, and the reason for the quantification changes was studied by analyzing the time–activity curve fittings of different models.

Identifiability Analysis of Kinetic Parameter Estimates

As the proposed models have more parameters to estimate than the standard 2Ti model with the uncorrected IDIF, their kinetic parameter identifiability may be a concern. That is because a more complex model is more likely to be sensitive to random noise and may have reduced parameter stability. To evaluate the parameter identifiability, a noisy lung tissue time–activity curve $\tilde{C}_{\mathrm{T}}(t_m)$ was simulated using a time-varying gaussian model (*40–42*):

$$\tilde{C}_{\mathrm{T}}(t_m) \sim N(\overline{C}_{\mathrm{T},m},\ S_{\mathrm{c}}\delta_m). \quad \text{Eq. 12}$$

where $\overline{C}_{\mathrm{T},m}$ is the m-th frame of the noise-free time–activity curve generated by the curve fitting of the tested model. S_{c} is the scaling factor controlling the noise level and δ_m is the unscaled standard deviation given by:

$$\delta_m = \sqrt{\frac{\overline{C}_{\mathrm{T},m}\exp(\lambda t_m)}{\Delta t_m}} \quad \text{Eq. 13}$$

S_{c} was estimated using the residual error between the measured $\check{C}_{\mathrm{T}}(t)$ and the modeled $C_{\mathrm{T}}(t)$ using the model that demonstrated the best fitting by assuming that the fitting error of that model comes mostly from random noise. We simulated 500 noisy lung tissue time–activity curve realizations for each $\tilde{C}_{\mathrm{T}}(t)$ and analyzed the bias and noise SD of each parameter estimate. The analysis was conducted for the 3 models (i.e., the IDIF, IDIF-T, and IDIF-T-D) using the HTR data. By summing the corresponding HTR frames together, the IDIF model using a more conventional low temporal resolution (10 s/frame in the first 3 min) was also included for comparison.

Correlation of Lung ^{18}F-FDG Kinetics with Age

Aging effects are evident in healthy lungs. Previous human studies have observed an inverse relationship between age and pulmonary blood volume (*43,44*). Therefore, we hypothesize that the v_{b} in the lungs tends to decrease with aging. Although we do not have longitudinal data on individuals in this study, we aim to explore any association between the ^{18}F-FDG kinetic parameters and age using the available healthy subject cohort. We performed the Pearson regression analysis

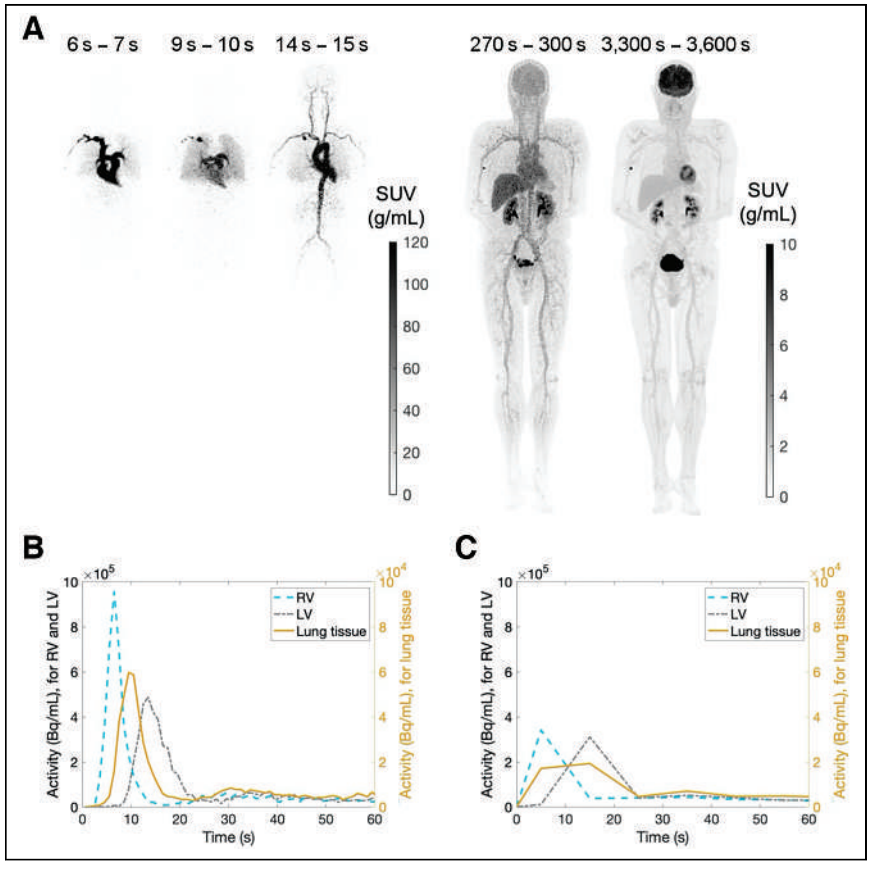

FIGURE 2. (A) HTR (1 s/frame) total-body ^{18}F-FDG dynamic images of example subject acquired using uEXPLORER system. (B) Regional time–activity curves extracted from HTR dynamic images. *y*-axis on left is for time–activity curves of right ventricle and left ventricle, whereas *y*-axis on right is for time–activity curve of lung tissue, which has lower range by factor of 10. (C) Conventional low-temporal-resolution (10 s/frame) regional time–activity curves. LV = left ventricle; RV = right ventricle.

between age and kinetic parameters. Body mass index was also included in the regression to consider potential confounding factors.

Demonstration of Total-Lung Parametric Imaging

In addition to the ROI-based kinetic analysis, we implemented the proposed kinetic modeling approach voxel by voxel. Parametric images of different kinetic parameters (e.g., K_1, K_i, and v_b) were then generated for the entire lung. Kernel smoothing was applied to both the dynamic images and the parametric images for noise reduction (*23*).

RESULTS

Example of HTR Dynamic Images and Time–Activity Curves

Figure 2 shows the acquired HTR total-body dynamic data for a representative subject. The ^{18}F-FDG dynamics in the very early phases after injection were captured by the HTR, as illustrated by the total-body maximum-intensity projections of the SUV image in the coronal direction (Fig. 2A) and the HTR time–activity curves (Fig. 2B). To begin, the tracer was injected into a vein in the right arm before traveling to the right ventricle through the vena cava (Fig. 2A, 6–7 s of the scan time). The tracer next traveled through the pulmonary circulation by flowing into the lungs via the pulmonary artery (Fig. 2A, 9–10 s) and flowing out of the lungs to the left ventricle through the pulmonary veins (Fig. 2A, 14–15 s).

As a comparison, time–activity curves with the conventional temporal resolution are shown in Figure 2C. With a 10-s temporal resolution, the time–activity curves have lost much of the information about the early-phase ^{18}F-FDG kinetics. Both the shape and the amplitude of the time–activity curves were distorted and inaccurate because of the poor temporal resolution.

Model Fitting of Lung Time–Activity Curve

The proposed approaches for modeling the input function can clearly impact the time–activity curve fitting, as shown by the fitting results for an example subject in Figure 3A along with the residual fitting errors in Figure 3B. These figures focus on the early dynamic phase, given that the late phase is similar among different models. Without the time-delay correction, the conventional IDIF model failed to fit the early-phase data even though the time delay is approximately 3 s (Supplemental Fig. 1A; supplemental materials are available at http://jnm.snmjournals.org). The dispersion correction in the IDIF-T-D model further improved the fitting of the first peak because it accounts for the deformation of the input function caused by the tracer dispersion effect (Supplemental Fig. 1B). The improved fitting by the proposed models (IDIF-T and IDIF-T-D) is further demonstrated by the decreased AIC (Fig. 3C; Table 1). The IDIF-T-D model achieved the best average AIC across all subjects.

Kinetic Parameter Estimation

The means and SDs of lung kinetic parameters are reported in Table 2. Figure 4 shows the resulting impact on the quantification of K_1, K_i, and v_b.

When the IDIF model without time-delay or dispersion correction is used, the K_1 value of 0.350 ± 0.092 mL/min/cm^3 seems unreasonable because of the poor fitting. This further supports that the direct application of the IDIF without corrections is not appropriate for the HTR data. The model IDIF-T was also likely to overestimate K_1 given the poor early-phase fitting. The IDIF-T-D estimate of K_1 is 0.056 ± 0.033 mL/min/cm^3, with an approximately 85% decrease compared with the conventional IDIF model. The IDIF-T-D model estimated v_b to be 0.144 ± 0.030, much higher than the estimate obtained with the IDIF (0.042 ± 0.022) and IDIF-T (0.107 ± 0.024) models. A previous study showed a

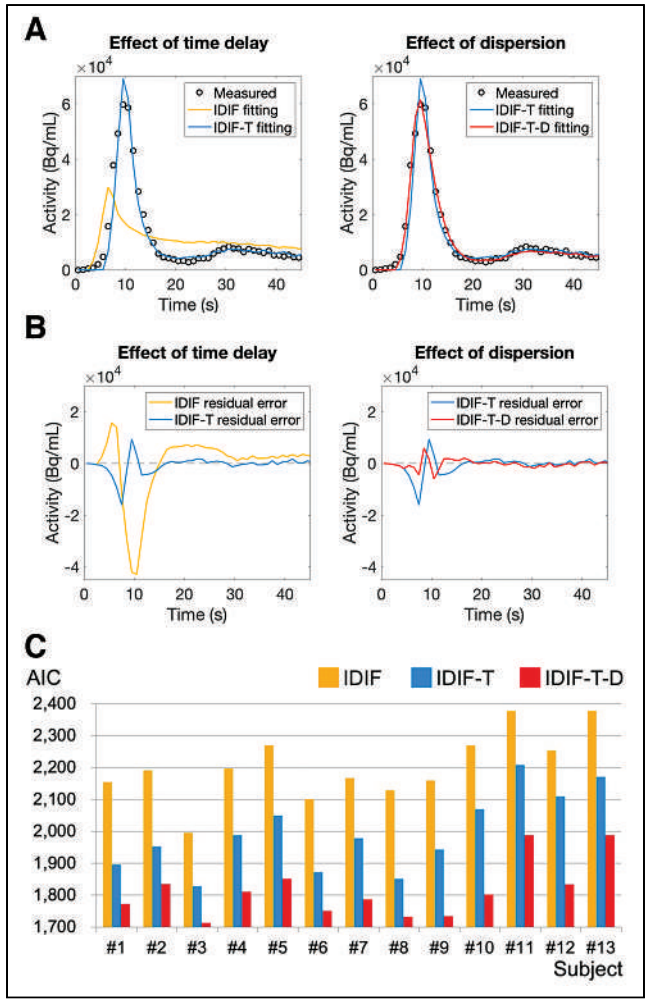

FIGURE 3. (A) Effects of modeling time delay and dispersion on fitting of measured lung time–activity curve. (B) Effects on residual error of time–activity curve fitting. (C) AIC of different models in 13 subjects.

blood fraction of 0.16 in the normal human lungs (*13*). Thus, the v_b estimates by IDIF and IDIF-T are likely biased, whereas the estimates by IDIF-T-D are more consistent with the expected v_b values. For K_i quantification, the proposed IDIF-T-D had an average increase of approximately 75% compared with the conventional IDIF model.

To understand the observed changes in parameter estimation, we analyzed the predicted activity of individual compartments (Supplemental Fig. 2). The vascular component $v_bC_p(t)$ was much increased in the IDIF-T-D model as compared with the IDIF due to the increased v_b estimate. Therefore, the total extravascular component $C_t(t)$ was decreased (Eqs. 2 and 4; Supplemental Fig. 2C), and K_1 became smaller accordingly (Eq. 3). In addition,

TABLE 1
AIC Values of Different Kinetic Models Averaged from 13 Subjects

Model	AIC
IDIF	2,203.2 ± 106.6
IDIF-T	1,993.6 ± 121.3
IDIF-T-D	1,815.2 ± 87.9

TABLE 2
Lung ^{18}F-FDG Kinetic Quantification of K_1, v_b, K_i, t_{RV}, and k_a Using Different Models

Parameter	IDIF	IDIF-T	IDIF-T-D
K_1(mL/min/cm^3)	0.350 ± 0.092	0.190 ± 0.066	0.056 ± 0.033
v_b	0.042 ± 0.022	0.107 ± 0.024	0.144 ± 0.030
K_i(mL/min/cm^3)	0.00034 ± 0.00032	0.00072 ± 0.00039	0.00060 ± 0.00033
t_{RV}(s)	—	3.2 ± 0.5	2.1 ± 0.4
k_a(/min)	—	—	25.8 ± 7.1

K_i was higher in IDIF-T-D than in IDIF because of the increased $C_m(t)$ (Supplemental Fig. 2D), which was associated with decreased K_1 and k_2 but increased k_3.

Identifiability of Kinetic Parameters

Table 3 shows the absolute value of relative bias and the SD of kinetic parameter estimates by different models. To clarify, this analysis is to study the robustness of models against random noise, whereas the systematic bias introduced by model oversimplification (e.g., neglecting the time-delay effect) is not involved. The HTR IDIF model had a lower bias and SD for K_1 and v_b, along with worse K_i estimation, than the low-temporal-resolution IDIF. Among the HTR cases, both the IDIF-T-D and the IDIF models have a small bias (<2%) for K_1 quantification, whereas the SD level of the IDIF-T-D (13.6%) was higher than that of the HTR IDIF (2.4%). The proposed IDIF-T-D model achieved a low bias (<1%) and a low SD (<3%) for quantifying v_b. For K_i, the IDIF-T-D had bias (0.4%) and SD (6.2%) levels comparable to those of the HTR IDIF. The time-delay and dispersion parameters t_{RV} and k_a had good identifiability.

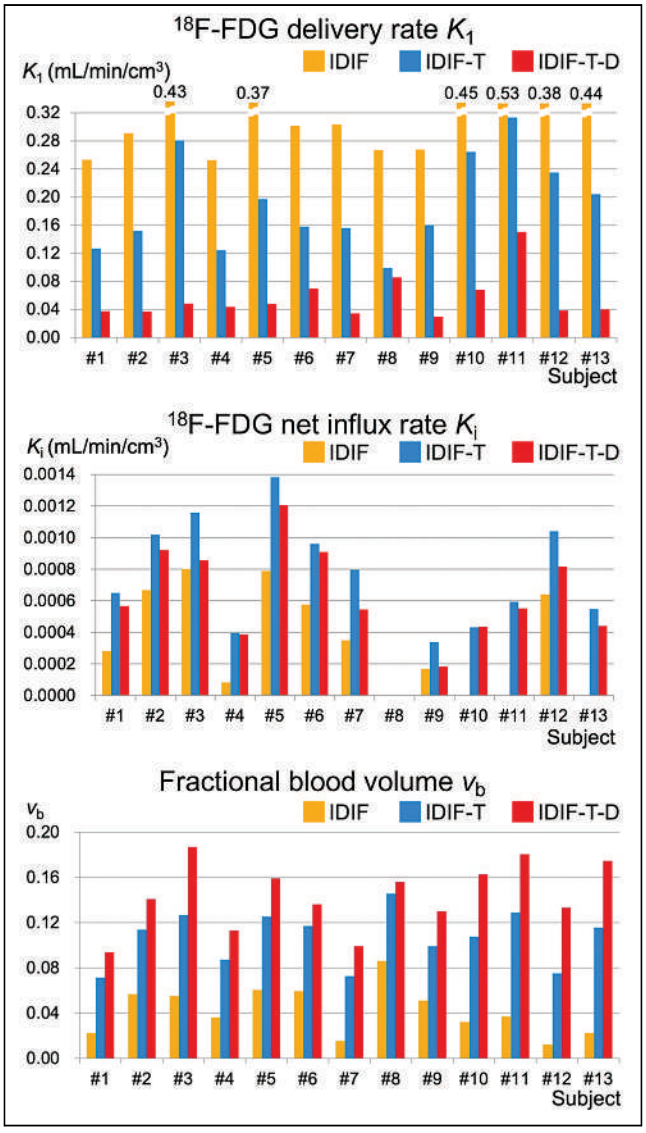

FIGURE 4. Kinetic parameter estimates by different lung kinetic models (IDIF, IDIF-T, and IDIF-T-D).

Correlation with Age

Figure 5 shows the correlation plots between age and v_b estimated by different approaches. For comparison, the result by a traditional low-temporal-resolution protocol (10 s/frame) is also included. Neither the v_b estimates by the low-temporal-resolution approach nor the v_b estimates by the HTR approaches without time-delay or dispersion correction showed a statistically significant correlation with age (all $P > 0.1$). In comparison, the v_b by the proposed IDIF-T-D model correlated with age with statistical significance ($r^2 = 0.45$, $P = 0.01$). The observed age–v_b relationship is consistent with the results reported in previous studies (*43,44*) that show aging to be associated with decreased pulmonary blood volume. Neither age nor body mass index correlated with other kinetic parameters.

Demonstration of Total-Lung Parametric Images

Figure 6A shows the total-lung SUV and multiparametric images using the proposed IDIF-T-D model for a single subject. These images are overlaid on the corresponding CT image. The different parametric images demonstrate complementary spatial information. Figure 6B further shows the parametric images of v_b for a young subject (aged 26 y) and an old subject (aged 78 y). The lung v_b was much lower in this old subject than in the young subject. We also noticed that in the parametric images generated by the IDIF-T-D model, the posterior part of the lungs had a higher v_b than the anterior part, and the posterior lung base had a higher v_b than the apex (Supplemental Fig. 3), which are also within expectation (*45*).

DISCUSSION

In this work, we studied the time-delay and dispersion corrections to the IDIF for lung kinetic modeling with HTR. Traditionally, limited by the temporal resolution of dynamic PET imaging, these corrections were not considered in most existing studies of pulmonary ^{18}F-FDG kinetics (*2,26,46*), especially when the focus

TABLE 3
Relative Bias (Absolute Value) and SD of Kinetic Parameters in Identifiability Study

	IDIF, LTR		IDIF, HTR		IDIF-T, HTR		IDIF-T-D, HTR	
Parameter	Bias (%)	SD (%)	Bias (%)	SD (%)	Bias (%)	SD (%)	Bias (%)	SD (%)
K_1	4.0	9.3	1.3	2.4	6.2	6.4	1.4	13.6
v_b	0.8	6.3	0.5	4.8	1.6	2.7	0.1	2.3
K_i	0.9	4.9	2.4	8.6	4.9	5.4	0.4	6.2
t_{RV}	—	—	—	—	4.5	0.1	0.4	2.8
k_a	—	—	—	—	—	—	1.2	7.2

LTR = low temporal resolution.

was on ^{18}F-FDG K_i (*2,13*), a macroparameter of which the estimation is dominated more by the late-phase dynamic data and is expected to be less sensitive to these corrections. However, a model without these corrections resulted in a poor fitting performance for the HTR data acquired with total-body PET in this work (Figs. 3A and 3C).

The proposed approaches to correcting time delay and dispersion for the IDIF led to much-improved lung time–activity curve fitting (Figs. 3A and 3B) with much lower AIC values (Table 1). Along with the improved fitting, the proposed modeling approaches had a significant impact on kinetic parameter quantification, especially for K_1 and v_b (Table 2). This impact can be explained by the improved estimation of the vascular component in the fitted lung time–activity curves (Supplemental Fig. 2). We also noted that the time delay t_{RV} tended to correlate with the inverse of the dispersion parameter k_a ($r = 0.44$, $P = 0.14$) in the proposed model, as is consistent with the expectation that a longer time delay (larger t_{RV}) is likely to be accompanied by a larger dispersion (smaller k_a). Although the proposed model is more complex, the identifiability analysis results suggested the robustness of the proposed model to random noise (Table 3).

Although there is no ground truth, the v_b estimates by the proposed model are in general more consistent with the literature-reported pulmonary blood volume values and have led to an improved inverse correlation with age (Fig. 5). This correlation aligns with previous findings of decreased pulmonary capillary blood volume with aging (*43,44*). The same correlation would be otherwise missed if the conventional IDIF models with or without time-delay correction were used. Together with the improved time–activity curve fit quality (Fig. 3), our results here indicate the importance of simultaneous time-delay and dispersion corrections as compared with no correction or time-delay correction only (Fig. 5).

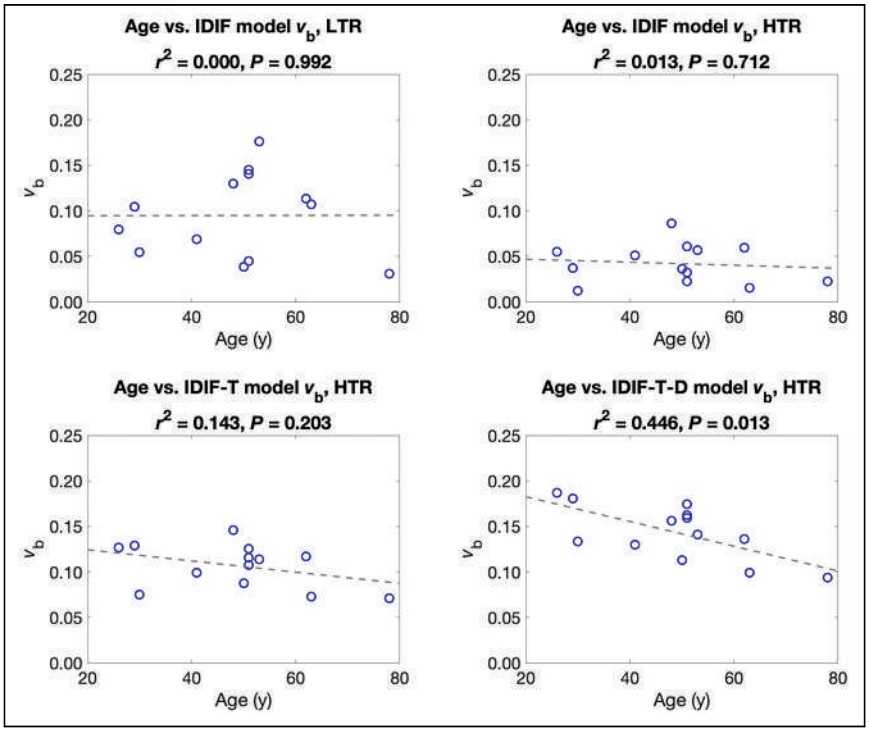

FIGURE 5. Correlation between subject age and v_b using standard IDIF model with 10 s/frame low temporal resolution (top left), IDIF model with 1 s/frame HTR (top right), IDIF-T model with HTR (bottom left), and proposed model IDIF-T-D with HTR (bottom right). LTR = low temporal resolution.

It is worth noting that simultaneous correction for time delay and dispersion was explored previously in dynamic brain PET studies (*25*). However, the method cannot be directly applied in our work on lung kinetic modeling because the prior study tackled a backward dispersion-correction problem that removes dispersion from the measured input function (e.g., from the radial artery), whereas this paper focuses on a forward dispersion-correction problem that adds dispersion to the measured IDIF for modeling the actual blood input. The latter approach is developed in response to the availability of IDIF in total-body HTR dynamic PET imaging.

In addition to the use of the right ventricle for deriving the IDIF, the region of the pulmonary arteries may be used directly for their closer location to the lung tissues. Similar results were obtained using the pulmonary arteries as the input function compared with using the right ventricle, including the input function after corrections (Supplemental Fig. 4A), lung time–activity curve fitting (Supplemental Fig. 4B), and kinetic parameter quantification (Supplemental Table 1),

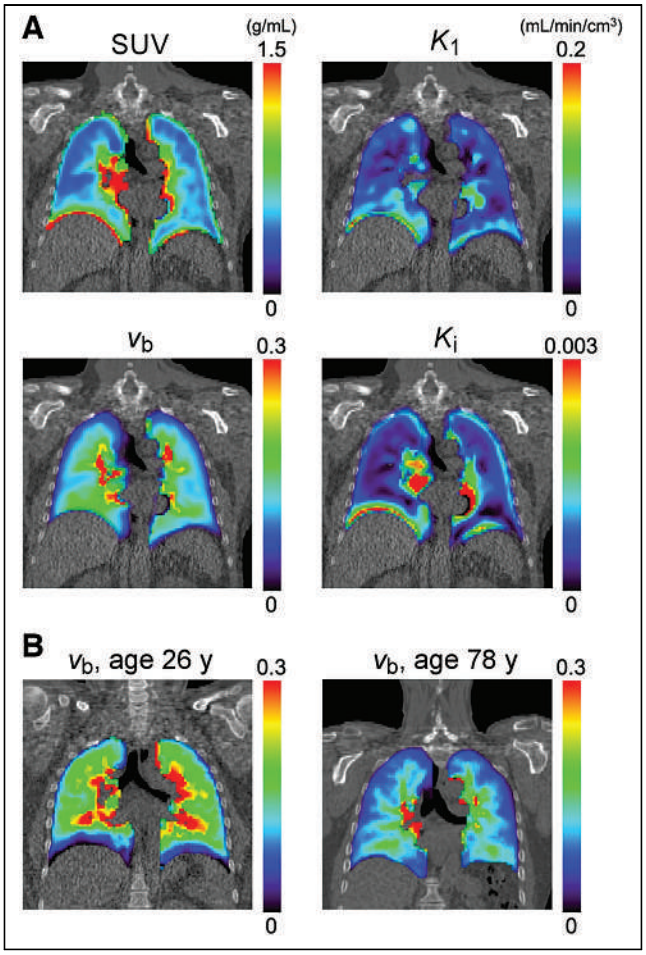

FIGURE 6. (A) ^{18}F-FDG PET images of segmented lung for example subject (subject 4): SUV image of 55–60 min, and multiparametric images of ^{18}F-FDG delivery rate K_1, fractional blood volume v_b, and net influx rate K_i generated with IDIF-T-D model. These images are superimposed on corresponding CT images. (B) v_b images of young subject (subject 3) and old subject (subject 1).

confirming the benefits of time-delay and dispersion corrections. The IDIFs from the left and right pulmonary arteries can also be used for kinetic modeling of individual lungs (Supplemental Table 1). However, use of the pulmonary arteries for IDIF needs to be done more carefully because the smaller size may make ROI placement more challenging to reduce the partial-volume effect.

This work has several limitations. First, the sample size is relatively small as the 13 healthy subjects vary in age and body weight. Second, subject motion can affect the kinetic quantification results (*47*). We tried to minimize the motion effect by carefully placing the ventricular ROIs to reduce the partial-volume effect of the myocardium. We also drew 5 ROIs in the lung lobes and extracted the global lung time–activity curve to decrease the respiratory motion effect and avoid a partial-volume effect from the liver. Third, the air fraction in the lungs may affect the absolute quantification of K_1 and K_i (*27,48*), but the correction is not included here. It does not, however, influence the comparison of kinetic models because this tissue-fraction effect introduces only a scaling factor on K_1 and K_i and can be corrected after kinetic modeling.

Our future work will include a larger subject cohort and apply the method to study lung diseases, such as coronavirus disease 2019. The kinetic quantification approach can be also used to assess the lungs in other systemic diseases, for example, cancer and nonalcoholic fatty liver disease. Motion correction and air fraction correction will be implemented to optimize the HTR kinetic modeling and parameter estimation further. Another direction is to model the dual blood-input function to account for the fraction of tracer delivery from the bronchial circulation (*49*). This dual-input effect may be small in healthy lung tissues but can be significant in lung tumors (*50*), which will be explored in a future study.

CONCLUSION

We studied lung kinetic modeling for HTR dynamic PET imaging on the uEXPLORER total-body PET/CT system. Direct application of the standard IDIF model resulted in poor time–activity curve fitting. We developed an approach to jointly correcting the effects of time delay and dispersion in the IDIF. The proposed model greatly improved time–activity curve fitting and had a large impact on lung kinetic quantification. It also improved the correlation of v_b with age. Total-body HTR dynamic PET has the potential to be a sensitive tool for studying healthy lungs and lung diseases.

DISCLOSURE

This research is supported in part by National Institutes of Health grants R01 CA206187 and R01 DK124803. The University of California at Davis has a research agreement and revenue-sharing agreement with United Imaging Healthcare. No other potential conflict of interest relevant to this article was reported.

ACKNOWLEDGMENTS

We gratefully acknowledge the technologists and staff of the University of California, Davis, EXPLORER Molecular Imaging Center for acquiring and processing the data.

KEY POINTS

QUESTION: Is simultaneous correction of time delay and dispersion essential for high-temporal resolution kinetic modeling of the lungs in total-body dynamic PET imaging?

PERTINENT FINDINGS: The proposed time-delay and dispersion corrections can largely improve model fitting and have a significant impact on lung kinetic quantification, leading to an improved correlation between age and fractional blood volume v_b.

IMPLICATIONS FOR PATIENT CARE: Total-body dynamic PET with HTR kinetic modeling may offer a sensitive tool to evaluate the lungs in health and disease.

REFERENCES

1. Dimitrakopoulou-Strauss A, Hoffmann M, Bergner R, et al. Prediction of short-term survival in patients with advanced nonsmall cell lung cancer following chemotherapy based on 2-deoxy-2-[F-18]fluoro-D-glucose-positron emission tomography: a feasibility study. *Mol Imaging Biol.* 2007;9:308–317.
2. de Prost N, Tucci MR, Melo MFV. Assessment of lung inflammation with ^{18}F-FDG PET during acute lung injury. *AJR.* 2010;195:292–300.
3. Rodrigues RS, Miller PR, Bozza FA, et al. FDG-PET in patients at risk for acute respiratory distress syndrome: a preliminary report. *Intensive Care Med.* 2008;34:2273–2278.
4. Castro M, Fain SB, Hoffman EA, Gierada DS, Erzurum SC, Wenzel S. Lung imaging in asthmatic patients: the picture is clearer. *J Allergy Clin Immunol.* 2011;128:467–478.

5. Chen DL, Schiebler ML, Goo JM, van Beek EJR. PET imaging approaches for inflammatory lung diseases: current concepts and future directions. *Eur J Radiol.* 2017;86:371–376.
6. Fields BKK, Demirjian NL, Dadgar H, Gholamrezanezhad A. Imaging of COVID-19: CT, MRI, and PET. *Semin Nucl Med.* 2021;51:312–320.
7. van den Hoff J, Oehme L, Schramm G, et al. The PET-derived tumor-to-blood standard uptake ratio (SUR) is superior to tumor SUV as a surrogate parameter of the metabolic rate of FDG. *EJNMMI Res.* 2013;3:77.
8. Hellwig D, Graeter TP, Ukena D, et al. ^{18}F-FDG PET for mediastinal staging of lung cancer: which SUV threshold makes sense? *J Nucl Med.* 2007;48:1761–1766.
9. Carson RE. Tracer kinetic modeling in PET. In: *Positron Emission Tomography.* Springer; 2005:127–159.
10. Mullani NA, Herbst RS, O'Neil RG, Gould KL, Barron BJ, Abbruzzese JL. Tumor blood flow measured by PET dynamic imaging of first-pass ^{18}F-FDG uptake: a comparison with ^{15}O-labeled water-measured blood flow. *J Nucl Med.* 2008;49: 517–523.
11. Laffon E, Calcagni ML, Galli G, et al. Comparison of three-parameter kinetic model analysis to standard Patlak's analysis in ^{18}F-FDG PET imaging of lung cancer patients. *EJNMMI Res.* 2018;8:24.
12. de Prost N, Feng Y, Wellman T, et al. ^{18}F-FDG kinetics parameters depend on the mechanism of injury in early experimental acute respiratory distress syndrome. *J Nucl Med.* 2014;55:1871–1877.
13. Chen DL, Cheriyan J, Chilvers ER, et al. Quantification of lung PET images: challenges and opportunities. *J Nucl Med.* 2017;58:201–207.
14. Chen DL, Schuster DP. Positron emission tomography with [^{18}F]fluorodeoxyglucose to evaluate neutrophil kinetics during acute lung injury. *Am J Physiol Lung Cell Mol Physiol.* 2004;286:L834–L840.
15. Wellman TJ, de Prost N, Tucci M, et al. Lung metabolic activation as an early biomarker of acute respiratory distress syndrome and local gene expression heterogeneity. *Anesthesiology.* 2016;125:992–1004.
16. Dimitrakopoulou-Strauss A, Georgoulias V, Eisenhut M, et al. Quantitative assessment of SSTR2 expression in patients with non-small cell lung cancer using ^{68}Ga-DOTA-TOC PET and comparison with ^{18}F-FDG PET. *Eur J Nucl Med Mol Imaging.* 2006; 33:823–830.
17. Cherry SR, Badawi RD, Karp JS, Moses WW, Price P, Jones T. Total-body imaging: transforming the role of positron emission tomography. *Sci Transl Med.* 2017;9:eaaf6169.
18. Surti S, Pantel AR, Karp JS. Total body PET: Why, how, what for? *IEEE Trans Radiat Plasma Med Sci.* 2020;4:283–292.
19. Nadig V, Herrmann K, Mottaghy FM, Schulz V. Hybrid total-body pet scanners: current status and future perspectives. *Eur J Nucl Med Mol Imaging.* 2022;49:445–459.
20. Zhang X, Cherry SR, Xie Z, Shi H, Badawi RD, Qi J. Subsecond total-body imaging using ultrasensitive positron emission tomography. *Proc Natl Acad Sci USA.* 2020;117:2265–2267.
21. Feng T, Zhao Y, Shi H, et al. Total-body quantitative parametric imaging of early kinetics of ^{18}F-FDG. *J Nucl Med.* 2021;62:738–744.
22. Li EJ, Spencer BA, Schmall JP, et al. Efficient delay correction for total-body PET kinetic modeling using pulse timing methods. *J Nucl Med.* 2022;63:1266–1273.
23. Wang G, Nardo L, Parikh M, et al. Total-body PET multiparametric imaging of cancer using a voxel-wise strategy of compartmental modeling. *J Nucl Med.* 2022; 63:1274–1281.
24. Iida H, Kanno I, Miura S, Murakami M, Takahashi K, Uemura K. Error analysis of a quantitative cerebral blood flow measurement using $H_2{}^{15}O$ autoradiography and positron emission tomography, with respect to the dispersion of the input function. *J Cereb Blood Flow Metab.* 1986;6:536–545.
25. Meyer E. Simultaneous correction for tracer arrival delay and dispersion in CBF measurements by the $H_2{}^{15}O$ autoradiographic method and dynamic PET. *J Nucl Med.* 1989;30:1069–1078.
26. Chen DL, Mintun MA, Schuster DP. Comparison of methods to quantitate ^{18}F-FDG uptake with PET during experimental acute lung injury. *J Nucl Med.* 2004; 45:1583–1590.
27. Holman BF, Cuplov V, Millner L, et al. Improved correction for the tissue fraction effect in lung PET/CT imaging. *Phys Med Biol.* 2015;60:7387–7402.
28. Schroeder T, Vidal Melo MF, Musch G, Harris RS, Venegas JG, Winkler T. Modeling pulmonary kinetics of 2-deoxy-2-[^{18}F]fluoro-D-glucose during acute lung injury. *Acad Radiol.* 2008;15:763–775.
29. Spencer BA, Berg E, Schmall JP, et al. Performance evaluation of the uEXPLORER total-body PET/CT scanner based on NEMA NU 2-2018 with additional tests to characterize PET scanners with a long axial field of view. *J Nucl Med.* 2021;62:861–870.
30. Leung EK, Berg E, Omidvari N, et al. Quantitative accuracy in total-body imaging using the uEXPLORER PET/CT scanner. *Phys Med Biol.* 2021;66:205008.
31. West JB. Evolution of the pulmonary circulation and the right heart. In: *Pulmonary Circulation.* CRC Press; 2016:22–30.
32. Walker CM, Rosado-de-Christenson ML, Martínez-Jiménez S, Kunin JR, Wible BC. Bronchial arteries: anatomy, function, hypertrophy, and anomalies. *Radiographics.* 2015;35:32–49.
33. Cherry SR, Sorenson JA, Phelps ME. Tracer kinetic modeling. In: *Physics in Nuclear Medicine.* 4th ed. Elsevier Health Sciences; 2012:379–405.
34. de Prost N, Costa EL, Wellman T, et al. Effects of surfactant depletion on regional pulmonary metabolic activity during mechanical ventilation. *J Appl Physiol.* 2011; 111:1249–1258.
35. Schroeder T, Vidal Melo MF, Musch G, Harris RS, Venegas JG, Winkler T. Image-derived input function for assessment of ^{18}F-FDG uptake by the inflamed lung. *J Nucl Med.* 2007;48:1889–1896.
36. Thiele F, Buchert R. Evaluation of non-uniform weighting in non-linear regression for pharmacokinetic neuroreceptor modelling. *Nucl Med Commun.* 2008;29:179–188.
37. Wang G, Corwin MT, Olson KA, Badawi RD, Sarkar S. Dynamic PET of human liver inflammation: impact of kinetic modeling with optimization-derived dual-blood input function. *Phys Med Biol.* 2018;63:155004.
38. Akaike H. A new look at the statistical model identification. *IEEE Trans Automat Contr.* 1974;19:716–723.
39. Glatting G, Kletting P, Reske SN, Hohl K, Ring C. Choosing the optimal fit function: comparison of the Akaike information criterion and the F-test. *Med Phys.* 2007;34:4285–4292.
40. Carson RE, Yan Y, Daube-Witherspoon ME, Freedman N, Bacharach SL, Herscovitch P. An approximation formula for the variance of PET region-of-interest values. *IEEE Trans Med Imaging.* 1993;12:240–250.
41. Wu Y, Carson RE. Noise reduction in the simplified reference tissue model for neuroreceptor functional imaging. *J Cereb Blood Flow Metab.* 2002;22:1440–1452.
42. Zuo Y, Sarkar S, Corwin MT, Olson K, Badawi RD, Wang G. Structural and practical identifiability of dual-input kinetic modeling in dynamic PET of liver inflammation. *Phys Med Biol.* 2019;64:175023.
43. Georges R, Saumon G, Loiseau A. The relationship of age to pulmonary membrane conductance and capillary blood volume. *Am Rev Respir Dis.* 1978;117:1069–1078.
44. Chang S-C, Chang H-I, Liu S-Y, Shiao G-M, Perng R-P. Effects of body position and age on membrane diffusing capacity and pulmonary capillary blood volume. *Chest.* 1992;102:139–142.
45. Galvin I, Drummond GB, Nirmalan M. Distribution of blood flow and ventilation in the lung: gravity is not the only factor. *Br J Anaesth.* 2007;98:420–428.
46. Grecchi E, Veronese M, Moresco RM, et al. Quantification of dynamic [^{18}F]FDG PET studies in acute lung injury. *Mol Imaging Biol.* 2016;18:143–152.
47. Hunter CRRN, Klein R, Beanlands RS, deKemp RA. Patient motion effects on the quantification of regional myocardial blood flow with dynamic PET imaging. *Med Phys.* 2016;43:1829–1840.
48. Coello C, Fisk M, Mohan D, et al. Quantitative analysis of dynamic ^{18}F-FDG PET/CT for measurement of lung inflammation. *EJNMMI Res.* 2017;7:47.
49. Deffebach ME, Charan NB, Lakshminarayan S, Butler J. The bronchial circulation. *Am Rev Respir Dis.* 1987;135:463–481.
50. Yuan X, Zhang J, Ao G, Quan C, Tian Y, Li H. Lung cancer perfusion: can we measure pulmonary and bronchial circulation simultaneously? *Eur Radiol.* 2012; 22:1665–1671.

Incidental Detection of a Tenosynovial Giant Cell Tumor of the Thigh on [^{68}Ga]Ga-FAPI PET/CT: Presentation of an Unusual Case

Timur Sellmann[1,2], Felicitas Staak[3], Clemens Maurer[4], Gernot Rott[5], Oliver Witzke[6], Wolfgang Fendler[7,8], Hans-Ulrich Schildhaus[9], Lars Erik Podleska[10], Ken Herrmann[7,8], and Christoph Rischpler[7,8,11]

[1]Department of Anesthesiology and Intensive Care Medicine, Bethesda Krankenhaus Duisburg, Duisburg, Germany; [2]Department of Anesthesiology 1, Witten/Herdecke University, Witten, Germany; [3]Witten/Herdecke University, Witten, Germany; [4]Department of Pneumology and Allergology, Bethesda Krankenhaus Duisburg, Duisburg, Germany; [5]Department of Radiology, Bethesda Krankenhaus Duisburg, Duisburg, Germany; [6]Department of Infectious Diseases, West German Centre of Infectious Diseases, University Hospital Essen, University of Duisburg–Essen, Essen, Germany; [7]West German Cancer Center, University Hospital Essen, Essen, Germany; [8]Department of Nuclear Medicine, University Hospital Essen, Essen, Germany; [9]Department of Pathology, University Hospital Essen, Essen, Germany; [10]Department of Tumor Orthopedics and Sarcoma Surgery, University Hospital Essen, Essen, Germany; and [11]Department of Nuclear Medicine, Bethesda Krankenhaus Duisburg, Duisburg, Germany

A 55-y-old man underwent [^{68}Ga]Ga-fibroblast activation protein inhibitor (FAPI) PET/CT because of persistent pulmonary symptoms after recovery from coronavirus disease 2019 (*1*). No increased pulmonary tracer uptake was found; however, as shown in Figures 1A and 1C, focally increased [^{68}Ga]Ga-FAPI uptake was observed in a mass within the dorsal musculature of the left thigh. Tracer uptake colocalized with a sharply circumscribed, inhomogeneously contrast-enhancing mass on MRI without relevant diffusion restriction (Fig. 1B).

Consequently, CT-guided percutaneous biopsy was undertaken, and an aggressive angiomyxoma was suspected, a rare tumor affecting predominantly female patients and typically occurring in the perineum or pelvis (*2*). Although generally benign, this tumor grows infiltratively and is prone to recurrence.

Because of the proximity to the sciatic nerve, the tumor was completely resected in July 2021. The tumor showed a fine capsule encased by multiple layers. Subsequent to the operation, pathologic reassessment showed a definite diagnosis of a tenosynovial giant cell tumor (Fig. 1D), which is extremely rare in this location. Tenosynovial giant cell tumor is an unusual primary soft-tissue tumor that is completely distinct from and should not be confused with any giant cell–rich tumor of bone or soft tissue. Tenosynovial giant cell tumor belongs to the group of benign fibrohistiocytic tumors (*3*).

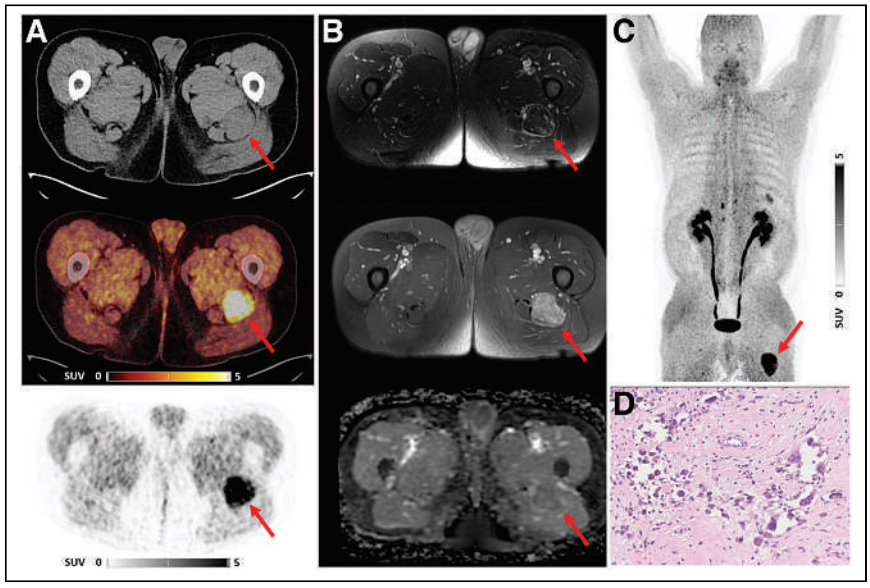

FIGURE 1. Images of tenosynovial giant cell tumor (arrows). (A, B, and C) Axial [^{68}Ga]Ga-FAPI PET/CT (A) and maximum-intensity PET projection (C) showing increased pulmonary tracer uptake. (B) Axial MRI showing colocalization of uptake with enhancing mass. (D) Hematoxylin- and eosin-stained histologic section showing tenosynovial giant cell tumor.

This report demonstrates the high sensitivity of [^{68}Ga]Ga-FAPI PET/CT to detect previously unknown tumors, making it a promising test in cases of suspected tumor disease or in cancers of unknown primary (*4*).

DISCLOSURE

Wolfgang Fendler reports fees from SOFIE Bioscience (research funding), Janssen (consultant, speakers' bureau), Calyx (consultant), Bayer (consultant, speakers' bureau, research funding), Parexel

Received Dec. 19, 2022; revision accepted Dec. 22, 2022.
For correspondence or reprints, contact Timur Sellmann (t.sellmann@bethesda.de).
Published online Jan. 26, 2023.

DOI: 10.2967/jnumed.118.207761

(image review), and AAA (speakers bureau) outside the submitted work. Ken Herrmann reports personal fees from Bayer, Sofie Biosciences, SIRTEX, Adacap, Curium, Endocyte, BTG, IPSEN, Siemens Healthineers, GE Healthcare, Amgen, Novartis, ymabs, Bain Capital, and MPM Capital; nonfinancial support from ABX; grants from BTG; and other fees from Sofie Biosciences outside the submitted work. Christoph Rischpler reports speaker honoraria from Adacap, Alnylam, BTG, Curium, GE Healthcare, Pfizer, Siemens Healthineers; a consultancy for Adacap and Pfizer; and a research grant from Pfizer, all outside the submitted work. No other potential conflict of interest relevant to this article was reported.

REFERENCES

1. Bergmann C, Distler JHW, Treutlein C, et al. ^{68}Ga-FAPI-04 PET-CT for molecular assessment of fibroblast activation and risk evaluation in systemic sclerosis-associated interstitial lung disease: a single-centre, pilot study. *Lancet Rheumatol.* 2021;3:e185–e194.
2. Zou R, Xu H, Shi Y, Wang J, Wang S, Zhu L. Retrospective analysis of clinicopathological features and prognosis for aggressive angiomyxoma of 27 cases in a tertiary center: a 14-year survey and related literature review. *Arch Gynecol Obstet.* 2020;302:219–229.
3. Jo VY, Fletcher CDM. WHO classification of soft tissue tumours: an update based on the 2013 (4th) ed. *Pathology.* 2014;46:95–104.
4. Kratochwil C, Flechsig P, Lindner T, et al. ^{68}Ga-FAPI PET/CT: tracer uptake in 28 different kinds of cancer. *J Nucl Med.* 2019;60:801–805.

Clinical Potential of HER2 PET as a Predictive Biomarker to Guide the Use of Trastuzumab Deruxtecan in Breast Cancer Patients

TO THE EDITOR: We have read with great interest the results of the DESTINY-Breast04 trial, "Trastuzumab Deruxtecan in Previously Treated HER2-Low Advanced Breast Cancer," from Modi et al. and published in *The New England Journal of Medicine* (*1*). These impressive findings have also earned a standing ovation after the plenary session presentation at the American Society of Clinical Oncology annual meeting in June 2022 and led to the Food and Drug Administration approval of a novel anti–human epidermal growth factor receptor-2 (HER2) therapy, trastuzumab deruxtecan (T-DXd), for the treatment of patients with HER2-low metastatic breast cancer (mBC) in August 2022. We strongly believe that the nuclear medicine community should be familiar with the results of this pivotal clinical trial, which is opening new, exciting prospects for HER2-targeted PET imaging.

HER2 is a membrane protein encoded by the ERBB2 oncogene. ERBB2 is amplified in 10%–15% of invasive breast carcinomas and classified as HER2-positive for clinical practice. These tumors are identified by immunohistochemistry both as being scored 3+ or 2+ and as having a gene amplification as assessed by fluorescence in situ hybridization. Until now, only HER2-positive breast cancers could be targeted by anti-HER2 therapies. The rest of the tumors have no detectable HER2 or low levels, with the patients known as, respectively, "HER2-zero" and "HER2-low" patients.

Within DESTINY-Breast04, T-DXd provided clinically meaningful benefits compared with standard chemotherapy in patients with HER2-low mBC. T-DXd successfully prolonged both progression-free survival and overall survival among patients with HER2-low mBC (*1*). Patients in the T-DXd group had a median progression-free survival of 10 mo, compared with a median progression-free survival of 5 mo in the chemotherapy group, and, thus, a 50% reduction in the risk of disease progression or death (hazard ratio, 0.50; 95% CI, 0.40–0.63; $P < 0.0001$).

The findings are necessarily changing the way advanced breast cancers are classified. We are rethinking the way of assessing the HER2 status. However, the current standard immunohistochemistry assays were not standardized to distinguish HER2-low from HER2-zero patients (*2*) but to identify HER2-positive patients. Pathologists are currently modifying their methods of interpreting the staining to identify HER2-low patients accurately. The question remains open, and whether the development of new strategies based on immunofluorescence or mass spectrometry currently under investigation would improve patients' HER2 status assessment is under investigation (*3*). In a metastatic context, the HER2 status heterogeneity between metastatic sites remains challenging to assess and is known to impact response to therapies (*4*) and spatiotemporal intratumoral HER2 heterogeneity.

HER2 PET thus appears a promising alternative tool for monitoring whole-body HER2 expression quantitatively and noninvasively. Although most published studies focused mainly on HER2-positive patients (*5,6*), a critical paper by Ulaner et al. published in *The Journal of Nuclear Medicine* in October 2016 demonstrated that imaging with a HER2-targeted PET tracer can detect HER2-positive metastases in patients with HER2-negative primary breast cancer (*7*). Such interesting findings highlight that HER2 PET can identify additional candidates for HER2-targeted therapy, such as T-DXd.

However, in these studies, the authors used the cancer treatment drug trastuzumab, a monoclonal antibody that specifically binds to the HER2 protein, as the imaging agent (*5–7*). Although uptake of ^{64}Cu-DOTA-trastuzumab in mBC is strongly associated with patient HER2 status (*5*), such HER2-targeted PET imaging does not assess strictly HER2 status but measures the uptake of trastuzumab, which provides pharmacokinetic information. Furthermore, as stated by Mortimer et al., ^{64}Cu-DOTA-trastuzumab PET/CT could help determine which patients will respond to HER2-targeted therapy (*6*).

The development of specific radiotracers, including radiolabeled Affibody molecules (Affibody AB) (*8,9*) or single-domain antibodies (*10*), directly targeting the HER2 protein and enabling accurate assessment of the HER2 status is an area of intensive investigation within the nuclear medicine community. For example, by labeling the Affibody molecule with a radioactive tracer, such as ^{68}Ga or ^{18}F (*9*), it is possible to visualize the distribution and uptake of the tracer in cancer cells that express HER2. In addition, such novel radiolabeled Affibody molecules or single-domain antibodies could allow imaging within hours of tracer administration and reduce radiation dose to patients.

Finally, none of these studies specifically looked at HER2-low patient populations, and such studies now need to be deepened and sustained, given the results of the DESTINY-Breast04 trial.

First, whereas patients with HER2-zero mBC are not eligible for T-DXd, HER2 PET could allow visualization of lesions with low HER2 expression in these patients, making them potentially eligible for T-DXd. Second, HER2 PET could eventually become a predictive marker of T-DXd efficacy among patients who are currently eligible for this treatment and identify those who do not benefit from T-DXd: in DESTINY-Breast04, up to 30% of patients experienced disease progression within the first 6 mo of T-DXd therapy, although their tumor was classified as HER2-low by immunohistochemistry (*1*). Such a biomarker could prove its clinical utility in the context of new treatments becoming available targeting other membrane antigens, such as tumor-associated calcium signal transducer 2.

In conclusion, the DESTINY-Breast04 findings have revolutionized the therapeutic strategy for HER2-low mBC patients and also raised several questions about determining HER2 status. HER2 PET imaging is a serious candidate modality that may provide most of these answers and could become the novel cornerstone of therapeutic decisions. The next step is to pursue clinical studies that would ensure a deeper understanding of how HER2 PET could be used as a clinical decision-support tool in patients with HER2-low mBC treated with novel HER2-targeted therapies, as well as T-DXd.

DISCLOSURE

Francois-Clement Bidard received research grants from GE Healthcare and Astra-Zeneca and advisory board honoraria from

GE Healthcare, Astra-Zeneca, and Daichii-Sankyo. No other potential conflict of interest relevant to this article was reported.

REFERENCES

1. Modi S, Jacot W, Yamashita T, et al. Trastuzumab deruxtecan in previously treated HER2-low advanced breast cancer. *N Engl J Med.* 2022;387:9–20.
2. Fernandez AI, Liu M, Bellizzi A, et al. Examination of low ERBB2 protein expression in breast cancer tissue. *JAMA Oncol.* 2022;8:1–4.
3. Moutafi M, Robbins CJ, Yaghoobi V, et al. Quantitative measurement of HER2 expression to subclassify ERBB2 unamplified breast cancer. *Lab Invest.* 2022;102:1101–1108.
4. Tarantino P, Curigliano G, Tolaney SM. Navigating the HER2-low paradigm in breast oncology: new standards, future horizons. *Cancer Discov.* 2022;12:2026–2030.
5. Mortimer JE, Bading JR, Park JM, et al. Tumor uptake of ^{64}Cu-DOTA-trastuzumab in patients with metastatic breast cancer. *J Nucl Med.* 2018;59:38–43.
6. Mortimer JE, Bading JR, Frankel PH, et al. Use of ^{64}Cu-DOTA-trastuzumab PET to predict response and outcome of patients receiving trastuzumab emtansine for metastatic breast cancer: a pilot study. *J Nucl Med.* 2022;63:1145–1148.
7. Ulaner GA, Hyman DM, Ross DS, et al. Detection of HER2-positive metastases in patients with HER2-negative primary breast cancer using ^{89}Zr-trastuzumab PET/CT. *J Nucl Med.* 2016;57:1523–1528.
8. Sörensen J, Sandberg D, Sandström M, et al. First-in-human molecular imaging of HER2 expression in breast cancer metastases using the ^{111}In-ABY-025 affibody molecule. *J Nucl Med.* 2014;55:730–735.
9. Kenny LM, Gilbert FJ, Gopalakrishnan G, et al. The HERPET study: imaging HER2 expression in breast cancer with the novel PET tracer [^{18}F]GE-226, a first-in-patient study [abstract]. *J Clin Oncol.* 2022;40(suppl):3069.
10. Keyaerts M, Xavier C, Heemskerk J, et al. Phase I study of ^{68}Ga-HER2-nanobody for PET/CT assessment of HER2 expression in breast carcinoma. *J Nucl Med.* 2016;57:27–33.

Romain-David Seban*
Laurence Champion
Audrey Bellesoeur
Anne Vincent-Salomon
Francois-Clement Bidard
**Institut Curie*
Saint-Cloud, France
E-mail: romaindavid.seban@curie.fr

Published online May 25, 2023.
DOI: 10.2967/jnumed.123.265434

BE PREPARED. GET CERTIFIED.

2023 SNMMI Nuclear Medicine Review Course – Live Virtual Meeting

This comprehensive review course is designed to help individuals prepare for their ABNM board certification, as well as providing a refresher for more experience clinicians. The program will be offered in a live virtual environment over two days, covering the following topics:

Day 1 Program – September 9, 2023

- Neurology
- Thyroid/Parathyroid/Head & Neck
- Pediatrics
- PET/CT
- Pulmonary/Thoracic
- Cardiovascular
- Infection/Inflammation
- Musculoskeletal

Day 2 Program – September 10, 2023

- Renal
- Gastrointestinal
- Male/Female-Benign/Malignant
- Therapies
- Treatment Response-Criteria/Imaging
- NRC Regulations/Radiation Safety
- Artifacts/Corrections
- Physics/Instrumentation

Register Today:
www.snmmi.org/nmrc

SNMMI | SOCIETY OF NUCLEAR MEDICINE & MOLECULAR IMAGING

2023 ACNM/SNMMI **HOT TOPICS** Webinar Series

SNMMI and ACNM are excited to announce the lineup for the 2023 Hot Topics Webinar Series. **These informative webinars will take place at 12:00 pm ET on the second Tuesday of each month and are complimentary for ACNM and SNMMI members.**

- **Theranostics for Prostate Cancer**
  On Demand | *Speaker: Stephan Probst, MD*
- **Theranostics for Pheochromocytoma/ Paraganglioma**
  On Demand | *Speaker: Erik Mittra, MD, PhD*
- **FDG PET/CT for Infection Imaging**
  On Demand | *Speaker: Gad Abikhzer, MDCM, FRCPC*
- **From Beta to Alpha in Theranostics**
  On Demand | *Speaker: Chandrasekhar Bal, MD*
- **Myocardial Flow Reserve**
  On Demand | *Speaker: Ron Schwartz, MD*
- **PET/MR**
  June 25 | *Speaker: Andrei Iagaru, MD*
  in-person during the SNMMI 2023 Annual Meeting
- **Theranostics for Neurodegenerative Disease-Final Frontier for Health Span**
  July 11 | *Speaker: Phillip Kuo, MD, PhD*
- **Cardiac Infection and Inflammation Imaging**
  August 8 | *Speaker: Vasken Dilsizian, MD*
- **Whole Body PET**
  September 12 | *Speaker: Ramsey Badawi, PhD*
- **FAPI PET: Make it or break it?**
  October 10 | *Speaker: Ken Herrmann, MD*
- **Landscape of Molecular Imaging and Fluid Biomarkers in Neurodegeneration**
  November 14 | *Speaker: Alexander Drzezga, MD*
- **PSMA PET**
  December 12 | *Speaker: Jeremie Calais, MD*

SNMMI SOCIETY OF NUCLEAR MEDICINE & MOLECULAR IMAGING

ACNM American College of Nuclear Medicine

Register today!

www.acnmonline.org/webinars

SPECTRUM
DYNAMICS MEDICAL

VERITON-CT®

DIGITAL SPECT/CT

Optimization of Every Step

Spectrum Dynamics has integrated its ground-breaking BroadView Technology design into the VERITON-CT system, providing a digital platform enabling routine 3D imaging in Nuclear Medicine. The result is optimization of every step, from image acquisition to interpretation.

VERITON-CT digital SPECT/CT combines the best-in-class CZT detectors, novel system design, high resolution CT, and advanced software technology to elevate the performance of 360° digital SPECT/CT.

BroadView Technology
Proprietary swiveling detector design provides increased sensitivity for faster scans

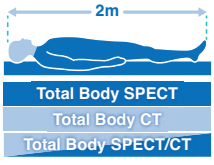

Total Body 3D Imaging
200cm continuous coverage vertex to feet
SPECT | CT | SPECT/CT

80cm NM and CT bore
Wide Bore SPECT/CT
80cm NM and CT bore

Choice of 16/64 slice
Choice of high-resolution CT for diagnostic applications and low dose total body CTAC

TruView Console
One platform, one location for clinical care decision-making:

1. Acquisition
2. Advanced quantitative reconstruction
3. Both 3D and 4D data analysis and review

VERITON-CT Feature Application: 3D Dynamic Imaging

TruFlow for VERITON-CT offers real-time 3D in-vivo fast dynamic imaging to capture the radiopharmaceutical distribution, uptake, or clearance over time in 3D SPECT/CT parametric imaging.

TruFlow

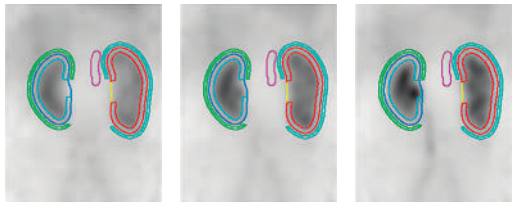

spectrum-dynamics.com

7/23

The Journal of Nuclear Medicine

July 2023 ■ Vol. 64 ■ Pages 997–1165